PROCEEDINGS BOOK

IMPRS
19-21 May **2025**

IMPRS 2025

2nd International
Mineral Processing
Reasearchers
Symposium

IRAN - KARAJ

Preface

It is with great pleasure that we present the proceedings of the 2nd International Mineral Processing Researchers Symposium (IMPRS 2025), held from May 19 to 21, 2025, and hosted by the Iran Mineral Processing Research Center (IMPRC). This biennial symposium is dedicated to fostering collaboration among scientists, engineers, and professionals from around the world who are engaged in advancing the science and practice of mineral processing.

The IMPRS serves as a unique platform for the exchange of knowledge, experiences, and innovative ideas in response to the challenges facing the mineral industry. With a focus on both fundamental research and industrial application, the symposium emphasizes the importance of integrating scientific insight with practical solutions.

In this event, we received 61 paper submissions, of which 48 were accepted following a thorough review process. These include 24 oral presentations and 24 poster presentations, alongside a series of keynote speeches and expert panels. The contributions reflect a wide range of current research interests and technological developments across various areas of mineral processing.

We are also pleased to announce that the symposium has been officially licensed by the Islamic World Science Citation Center (ISC 0450-17097), under the authority of the Institute for Scientific Information and Technology Monitoring of the Islamic World, adding further credibility and recognition to the event.

In recognition of the quality of the submitted work, a selection of outstanding papers has been approved for publication in reputable scientific journals. Specifically, 12 papers will be published in the International Journal of Mining and Geo-Engineering (University of Tehran), 9 papers in the Journal of Mining and Environment (Shahrood University of Technology, ISI indexed), and 9 papers in the Journal of Environment and Sustainable Mining (University of Sistan and Baluchestan).

We extend our sincere appreciation to all participants, including invited speakers, authors, reviewers, and attendees, whose efforts and enthusiasm have been instrumental in the success of IMPRS 2025. Special thanks are also due to the organizing and scientific committees, as well as our sponsors and institutional supporters.

With the growing interest and engagement in this symposium, we look forward to continuing IMPRS as a biennial event and invite all interested professionals and researchers to take part in future editions. We hope these proceedings will serve as a valuable reference and contribute meaningfully to the continued progress of mineral processing worldwide.

Dr. Bahram Rezai   Dr. Ziaeddin Pourkarimi

Scientific Secretary of Symposium (IMPRS 2025)   Executive Committee Chair of Symposium (IMPRS 2025)

Executive Policy Council Members

- Dr. Mohammad Aghajanlou: Chairman of the IMIDRO Executive Board
- Ms. Somayeh Kholousi: Deputy for Planning and Empowerment, IMIDRO
- Dr. Omid Emami: Deputy for Mining and Mineral Industries Development Projects, IMIDRO
- Dr. Farhad Farshad: Director of Research and Technology of IMIDRO
- Dr. Majid Vafaifard: Executive Board Member of IMPRC.
- Dr Ziaeddin Pourkarimi: Managing Director, Iran Mineral Processing Research Center (IMPRC)

Scientific Policy Council Members

- Prof. Bahram Rezai: Symposium Secretary
- Prof. Seyed Ziaeddin Shafaie Tonekabeni: Secretary of the Hydrometallurgy Section
- Prof. Mohammad Noaparast: Secretary of the Comminution and Physical Separation Section
- Dr. Ali Akbar Abdollahzadeh: Secretary of the Simulation, Modeling, Control, and Design of Mineral Processing Plants Section
- Dr. Mohammad Karamouzian: Secretary of coal processing Section
- Dr. Seyed Mohammad Razavian: Secretary of the Recycling and Tailings Management in Mining and Mineral Industries Section
- Dr. Ziaeddin Pourkarimi: Secretary of the Flotation and Surface Chemistry Section
- Dr. Mehdi Rahimi: Secretary of the Water and Energy Resources Management in mineral processing Plants Section

Scientific Committee Members

- Prof. Bahram Rezai, Amirkabir University of Technology
- Prof. Mohammad Noaparast, University of Tehran
- Prof. Seyed Zaieddin Shafaie Tonekaboni, University of Tehran
- Prof. Parviz Pourghahremani, Sahand University of Technology
- Prof. Ali Ahmadi, Isfahan University of Technology
- Dr. Abbas Sam, Shahid Bahonar University of Kerman
- Dr. Ali Akbar Abdollahzadeh, Amirkabir University of Technology
- Dr. Mohammad Mokmeli, University of Tehran
- Dr. Hadi Abdollahi, University of Tehran
- Dr. Mohammadreza Khalesi, Tarbiat Modares University
- Dr. Sima Mohammadnezhad, Tarbiat Modares University
- Dr. Reza Dehghan, University of Yazd
- Dr. Mohammad Masinayi, University of Birjand
- Dr. Mohammad Karamouzian, Shahrood University of Technology
- Dr. Seyed Mohammad Razavian, University of Kashan

- Dr. Rahman Ahmadi, Imam Khomeini International University (Qazvin)
- Dr. Kianoush Barani Beyranvand, Lorestan University
- Dr. Faraz Soltani, Arak University of Technology
- Dr. Ziaeddin Pourkarimi, Iran Mineral Processing Research Center (IMPRC)
- Dr. Mehdi Rahimi, Iran Mineral Processing Research Center (IMPRC)
- Dr. Behrouz Karimi Shahraki, Iran Mineral Processing Research Center (IMPRC)
- Prof. Mehmet Sabri Çelik, Istanbul Technical University, Turkey
- Prof. Mohsen Yahyaei, University of Queensland, Australia
- Prof. Laurindo Leal Filho, University of Sao Paulo, Brazil
- Prof. Pablo Brito Parada, Imperial College London, UK
- Prof. Bern Klein, University of British Columbia, Canada
- Dr. Ahmad Hassanzadeh, Norwegian University of Science and Technology (NTNU), Norway
- Dr. Hasan Sedighi Project manager for critical and strategic elements, IMIDRO

Executive Committee Members

Dr. Ziaeddin Pourkarimi, Managing Director of IMPRC and Executive Committee Chair of Symposium (IMPRS 2025)

Scientific Support Group:

- Dr. Mehdi Rahimi
- Dr. Behrooz Karimi
- Mr. Gholamreza Parvareh
- Mr. Seyed Javad Mousavi
- Mr. Alireza Parvizi
- Ms. Dorna Pirouzan
- Mr. Ramin Banihashemi
- Mr. Mohsen Mirzaie

Technical Support Group:

- Mr. Mohammad Homayouni
- Mr. Reza Sakian
- Mr. Hamidreza Pourjanabi
- Mr. Reza Vahedi
- Mr. Mehran Rabani

Language Editor:

Dr. Payman Bayat

Coordination and Communication Group:

- Ms. Mahrang Keshvardoust
- Ms. Najmeh Khajeh'i
- Mr. Iman Shafiee

Website Design and IT Support Group:

- Ms. Sepideh Ahmadi
- Mr. Seyed Javad Mousavi
- Mr. Alireza Parvizi
- Mr. Mohammad Homayouni

Logistics and General Support Group:

- Mr. Ali Asghar Khodashenas
- Mr. Abdolreza Ebrahimi
- Mr. Omid Karimi
- Mr. Abbas Zare
- Mr. Mohammad Reza Radfar
- Mr. Mehdi Nazari

Security Group:

- Mr. Abdollah Almasi
- Mr. Amir Mobaraki
- Mr. Ahmad Ramazani

Other Colleagues:

Dr. Abolfazl Farahani, Mr. Hossein Hashemi, Mr. Amir Firoozi, Mr. Morteza Dehghani, Mr. Hossein Habibi, Mr. Amir Masoud Karamiyar, Mr. Hassan Vafaei, Mr. Hooman Hassani, Mr. Mohammad Ali Moradzadeh, Mr. Ali Pour Asghar, Ms. Masoumeh Madanipour, Ms. Farank Razzaghi, Ms. Samira Moradkhani, Ms. Mojdeh Papen, Mr. Amir Afsari Kohneshahri

Scientific Topics

- Comminution
- Physical separation
- Flotation and surface chemistry
- Hydrometallurgy
- Geometallurgy
- Biological processing methods
- Fine and ultrafine particles processing
- Coal processing
- Critical Minerals Processing
- Gold and precious metals processing
- Industrial minerals processing
- Recycling and tailings management
- Water and energy resources management in mineral processing
- Modern methods of mineral processing
- Dry and low-water processing methods
- Application of AI in mineral processing
- Process mineralogy and modern methods of mineral characterization

Contents

Feasibility Study on Apatite Recovery from Iron Ore Beneficiation Tailings Using Flotation Process

Mohadeseh Rajabi[1], Parviz Pourghahramani[1*]

[1] Mining Engineering Department, Tabriz University of Technology, Tabriz, Iran

*Corresponding author: pourghahramani@sut.ac.ir (Parviz Pourghahramani)

Abstract:

With phosphorus demand for fertilizers and pharmaceuticals increasing and high-grade deposits diminishing, this study surveys the feasibility of recovering apatite from iron ore beneficiation tailings of the Sangan Company in Yazd Province, Iran, as a secondary resource. Optimization of the direct flotation process was examined through a full factorial experimental design considering collector dosage, pH, starch dosage, and sodium silicate dosage, with data processed by Umetrics MODDE software and a multiple linear regression (MLR) model. The direct flotation process was designed to separate apatite; however, due to the surface similarities between apatite and carbonate minerals such as calcite and dolomite, efficient separation could not be achieved, making an additional reverse flotation step necessary to remove carbonate minerals. To this end, the direct flotation concentrate underwent acid scrubbing to remove adsorbed collectors and was prepared with a mixture of phosphoric and sulfuric acids to depress apatite, followed by reverse flotation with sodium oleate as collector at pH 4.5. Reverse flotation yielded a final concentrate exceeding 30% P_2O_5 content and 70% recovery. These findings show that these tailings can be processed as an apatite source, offering an economic resource while reducing tailings and reusing them for environmental preservation.

Keywords: apatite recovery, secondary resource, direct flotation, reverse flotation, iron ore tailings

1. Introduction

Phosphorus is a critical element for the production of fertilizers, detergents, and pharmaceuticals and occurs naturally in the form of phosphates, mainly as apatite ($Ca_5(PO_4)_3(F, Cl, OH)$), which is a major component of the global biogeochemical phosphorus cycle (Lishmund et al., 1982; Filippelli, 2002, 2008; Cordell et al., 2009; Vaneeckhaute et al., 2016). Apatite is a mineral found extensively as an accessory in multiple geological deposits. In specific instances, such as phosphorites and apatite-magnetite deposits, it emerges as a principal mineral, gaining economic importance (Harlov, 2015).

Effective beneficiation of phosphate ore can be realized through a multitude of methodologies, contingent upon the liberation size of phosphate and gangue minerals, as well as other phosphate ore characteristics, such as the type of associated gangue minerals. A variety of techniques, including screening, scrubbing, heavy media separation, roasting, calcination, leaching, and flotation, may be employed (Gharabaghi et al., 2010). The most common method to beneficiate phosphate ore is flotation, generating more than 60% of the world's marketable phosphate by separating minerals according to their surface properties (Abouzeid, 2008). The occurrence of carbonate gangue minerals such as calcite and dolomite, which also have similar surface characteristics to phosphate minerals, makes their separation through flotation difficult. Anionic fatty acid collectors, employed in direct flotation, adsorb on both surfaces, lowering selectivity and efficiency (Kawatra & Carlson, 2013). To overcome this challenge, reverse flotation has been employed to remove carbonate gangue by floating carbonates while depressing apatite. This is often achieved using fatty acids as collectors for

carbonates and inorganic acids (such as H_3PO_4 or H_2SO_4) as apatite depressants (Amirech et al., 2018; Huang & Zhang, 2024). Also, novel collectors and depressants have improved apatite flotation efficiency and selectivity. For instance, 2-chloro-9-octadecanoic acid (2-Cl-9-ODA) effectively separates apatite from dolomite and calcite. When combined with sodium pyrophosphate as a depressant, it achieves high recovery while reducing gangue flotation (W. Zhang et al., 2025). Carbon dioxide supplanted air during the preliminary flotation phase to selectively extricate carbonates. This was succeeded by a subsequent phase to float apatite, culminating in a concentrate with an excess of 21% P_2O_5. Nevertheless, residual contaminants such as magnetite and carbonates underscored the necessity for further process optimization. (Carvalho et al., 2022). A novel collector synthesized from waste frying oils was found to exhibit selective adsorption on carbonate minerals like calcite and dolomite. This reagent showed excellent performance in separating carbonate gangue minerals from apatite, achieving over 80% recovery of calcite and dolomite, while the recovery of apatite in the carbonate concentrate remained below 10%, indicating high selectivity (El-bahi et al., 2024).

Due to an increasing demand for phosphorus fertilizers and depletion of high-grade deposits, research and extraction efforts have focused on secondary resources. The circular economy approach is another alternative in this context to manage mineral wastes and recover valuable elements (Alsafasfeh & Alagha, 2017). Magnetic tailings from iron oxide-apatite deposits have been a potential sustainable phosphorus-supplying tool, and previous experiments have confirmed that apatite is recoverable from these sources with high grade and recovery obtained via flotation (Valderrama et al., 2024). Studies on the recovery of apatite from iron ore beneficiation tailings in Iran are neglected, particularly with respect to tailings generated by the Sangan Company. Moreover, previous investigations have not yielded satisfactory or industrially viable results.

In this study, the tailings produced during the iron ore beneficiation process at the Sangan Company in Yazd Province, Iran were investigated to evaluate the feasibility of apatite recovery from secondary resources. The average P_2O_5 grade of this tailings deposit is around 4%. First, in order to determine the optimal operation conditions to achieve a proper grade and recovery, the effect of variables, which affect direct apatite flotation (collector dosage, pH, depressant dosage) was investigated. Then, a reverse flotation stage was tested to separate carbonate minerals from apatite, in order to produce an acceptable industrial grade of concentrate (P_2O_5 grade above 30%).

2. Material and methods

2.1. Sample Collection and Preparation

Random sampling was conducted on the iron ore beneficiation tailings from the Sangan Company to obtain representative samples. A total of 250 kilograms of dry, mostly agglomerated tailings were collected for laboratory studies. Fig. 1 presents the cumulative particle size distribution of a representative tailings sample, with a D_{80} of 460 μm. Approximately 39% of the particles are smaller than 37 μm, accounting for 44.85% of the total P_2O_5 content. This fine fraction may increase entrainment during flotation and reduce the selectivity of separation.
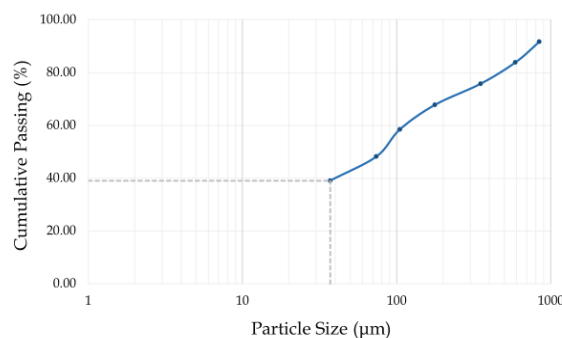
Fig. 1. Cumulative particle size distribution of the representative tailings sample.

2.2. Mineralogical Studies

Mineralogical investigations on different fractions from sieve size analysis were performed with the preparation of thin sections to analyze both mineral composition and distribution. Thin sections were observed under ordinary and polarized light using a polarizing microscope to identify minerals based on optical properties. The observation of plastic xenomorphic texture in the samples indicates the simultaneous formation of minerals under intense metamorphic conditions and high pressure and temperature. Thin section mineralogy revealed that most constituent minerals of the sample were alkali feldspar, amphibole, calcite, dolomite, and quartz. Most alkali feldspar minerals have undergone intense alteration processes and have been transformed into secondary minerals such as clay minerals, epidote, and chlorite.The investigation results suggest that part of the calcite present in the sample was formed due to the alteration of primary minerals, while another part has a primary origin. Plagioclase occurred as widely distributed, liberated fine-grained crystals. As shown in Fig. 2, apatite grains in the coarse fractions showed internal fractures and most of them were associated with iron oxides. Degree of liberation analyses revealed that over 85% of apatite liberates in particle sizes below 75 µm.
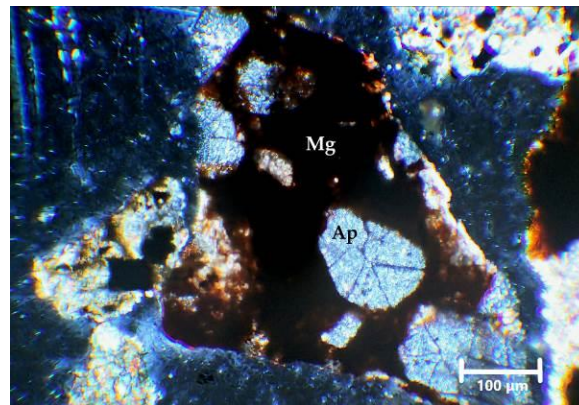
Fig. 2. Apatite grains associated with magnetite under cross-polarized light (-350 +177 µm).

2.3. Reagents

Procoll flo-ys20, sodium oleate, and Linaz-20 were used as collectors in this study. The collectors had frothing properties; thus, no additional frothing agent was required. pH was adjusted with sodium hydroxide and sulfuric acid. Sodium silicate and starch were used as depressants, where sodium silicate depressed silicate and aluminosilicate minerals while dispersing the pulp, and starch depressed iron oxides and carbonate minerals. Sulfuric and phosphoric acids were used to depress apatite.

2.4. Direct Flotation Tests

2.4.1. Experimental Design

A full factorial experimental design was employed to conduct flotation experiments for investigating effects of several variables on the process. Four important parameters were evaluated at two levels for each factor: collector dosage (500 and 1500 g/t), pH (9.5 and 11.5), sodium silicate dosage (0 and 500 g/t), and starch dosage (0 and 400 g/t). The levels of the parameters were determined based on preliminary experiments. In total, 16 experiments were conducted along with 3 additional replicate tests at the central points of the parameters to ensure statistical reliability.

2.4.2. Conditions

Flotation tests were carried out in a Denver flotation machine with a 5-liter cell, and the flotation feed particle size was kept below 75 microns so that most of the apatite was liberated. At the start of each test, the pulp pH was adjusted according to the experimental design. If required, depressants were introduced first, followed by a combination of Procoll flo-ys20 and Linaz-20 collectors, with 70% added during the rougher stage and 30% in the scavenger stage. The solids content (25%), impeller speed (1000 rpm), aeration rate, and pulp conditioning time were held constant throughout all experiments, and the flotation time for each sample was set at 20 minutes. After completing the flotation process, the concentrate was collected, filtered, dried, weighed, and analyzed to assess its grade.

2.5. Reverse Flotation Test

2.5.1. Acid Scrubbing

Based on the similarity in the surface properties among calcite, dolomite, and apatite, their separation through direct flotation is difficult (Kawatra & Carlson, 2013). Accordingly, a reverse flotation stage was necessary. First, the direct flotation concentrate underwent acid scrubbing to eliminate adsorbed collectors. The concentrate, with a solids content of 50%, was agitated at pH 4.5 (adjusted with sulfuric acid) for 15 minutes to desorb the collectors. Subsequently, the pulp was washed and filtered to remove the acid and collectors, thereby improving the performance of the reverse flotation.

2.5.2. Conditions

Reverse flotation of carbonate minerals was also carried out in a Denver flotation machine with a 5-liter cell, similar to the direct flotation tests. To depress apatite, the solid recovered from the acid scrubbing was conditioned with a mixture of sulfuric and phosphoric acids at pH 4.5 and a solids content of 50% for 10 minutes. Following conditioning, the carbonate minerals were floated with 500 g/t sodium oleate as collector at a solids content of 25%, and other conditions, such as flotation time, aeration rate, and impeller speed, were consistent with those of direct flotation. Subsequently, the concentrate was collected, weighed, and analyzed for grade determination.

2.6. Analysis and Evaluation of Results

The concentrates, from direct flotation and reverse flotation, were analyzed using a UV Specord 200 spectrophotometer by colorimetry. Apatite initially was dissolved in a nitric acid and water solution (1:5), and then phosphorus-specific chemical reagents were added, resulting in the formation of phosphate ions in the complex phase and colored solutions. The P_2O_5 grade of the samples was then determined by comparing the color intensity of the test samples with those of standard solutions. Data from the direct flotation experiments were evaluated using Umetrics MODDE software and the multiple linear regression (MLR) method. Model quality was evaluated using key statistical metrics (R^2 close to 1, $Q^2 > 0.5$, reproducibility > 0.5, model validity > 0.25, and R^2–$Q^2 < 0.3$) where compliance with these criteria confirms a robust fit to laboratory data, together with a reliable prediction of new outcomes.

3. Results and Discussion

3.1. Direct Flotation Tests

3.1.1. Model Fitting

Table 1 presents the experimental design along with the results of 19 direct flotation tests. The values of the MLR model evaluation metrics are provided in Table 2. The $R^2 = 0.80$ and $Q^2 = 0.57$ obtained for the grade response are representative of suitable values, with model validity (0.80) and reproducibility (0.80) values that exceed the model validity and reproducibility thresholds (0.25 and 0.5 respectively) and the R^2–Q^2 difference (0.23) within the acceptable range. For recovery response, fitted values were strong ($R^2 = 0.93$; $Q^2 = 0.82$) and highly predictive, with model validity (0.58), reproducibility (0.97), and R^2–Q^2 difference (0.11), all within acceptable limits. All of these indicators confirm the model adequately describes the experimental data and can be employed in optimizing the direct flotation process. Relative relationships between the operational parameters and grade and recovery responses were analyzed through regression coefficients of the multiple linear regression (MLR) model at a confidence level of 95%. The outputs of this analysis are shown as plots of regression coefficients for grade and recovery in Fig. 3.

Table 1. Experimental design and results of direct flotation tests (Continued on the next page).

Exp No	Factors				Responses	
	Collector (g/t)	pH	Sodium silicate (g/t)	Starch (g/t)	Grade (%)	Recovery (%)
1	500	9.5	0	0	7.32	47.46
2	1500	9.5	0	0	8.63	83.47
3	500	11.5	0	0	4.78	38.79
4	1500	11.5	0	0	6.46	87.89
5	500	9.5	500	0	4.99	12.53
6	1500	9.5	500	0	9.68	76.96
7	500	11.5	500	0	3.78	34.14
8	1500	11.5	500	0	5.15	66.97
9	500	9.5	0	400	3.75	9.09
10	1500	9.5	0	400	9.18	71.4
11	500	11.5	0	400	4.35	34.22
12	1500	11.5	0	400	6.49	81.25
13	500	9.5	500	400	5.01	14.58
14	1500	9.5	500	400	9.68	78.97
15	500	11.5	500	400	4.1	30.8
16	1500	11.5	500	400	6.2	80.52
17	1000	10.5	250	200	8.7	68

Table 1. Experimental design and results of direct flotation tests (Continued).

Exp No	Factors				Responses	
18	1000	10.5	250	200	7.8	70
19	1000	10.5	250	200	6.9	74

Table 2. Summary of the MLR fit values for model.

	R2	Q2	Model Validity	Reproducibility
Grade	0.80	0.57	0.80	0.80
Recovery	0.93	0.82	0.58	0.97
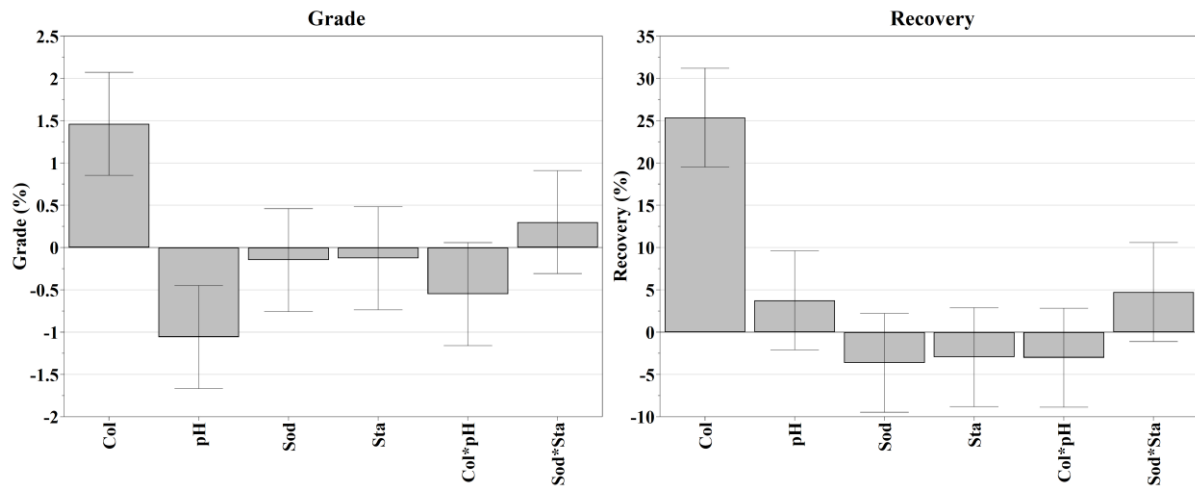
Fig. 3. Regression coefficient plots for grade (left) and recovery (right) at 95% confidence level.

Based on the final refined model, the collector dosage is the most significant main effects affecting concentrate grade and recovery at 95% confidence level. The factor pH appears to be the second most important statistically significant factor influencing the concentrate assay. In addition, the interaction between two depressants affect statistically the responses in a different manner. A more detailed explanation is given in the following sections.

3.1.2. Collector Dosage Effect

As depicted in Fig. 3, collector dosage had a significant (P-value < 0.05) and positive effect on both grade and recovery, making it the key parameter with the greatest influence on apatite flotation. The influence of collector dosage on flotation performance was evaluated by examining its effect on both grade and recovery, as illustrated in Fig. 4, using a main effects plot. The plot on the left-hand side illustrates a positive relationship between the grade of the final concentrate and the dosage of collector. By increasing collector from 500 g/t to 1500 g/t, concentrate assay increases from 5 to almost 8% in P_2O_5. The recovery curve on the right plot reveals that by increasing collector to 1500 g/t, the recovery of apatite increases up to 81%. The confidence intervals (dotted lines) for both grade and recovery curves suggest a statistically reliable trend. In summary, an increase in grade and recovery can both be achieved through a higher collector dosage. However, the recovery rates are more significantly improved.

One of the major reasons why higher collector dosages are imperative is because the feed comprises a considerable fraction of fine particles (<37μm). The reagent demand is reasonably high for these fine particles due to their greater surface area. The other reason which would demand more quantity of collector to improve flotation efficiency is the greater sensitivity of fatty acid collectors to dissolved ions (e.g., Mg^{2+}) present in the pulp. Due to the quality of the process water, along with mineral dissolution and the abrasion of grinding media, certain metal ions such as Ca^{2+}, Mg^{2+}, Al^{3+}, and Fe^{3+} are inevitably present in the flotation pulp under actual operating conditions (Ruan et al., 2018). Fatty acid collectors have the tendency to easily form complexes with these ions, and thus there is greater collector consumption required for effective flotation (dos Santos et al., 2010). Also a higher collector dosage results in higher hydrophobicity of apatite particles, resulting in better recovery and grade (Santana et al., 2010; Testa, 2016). The collector concentration also has a significant effect on the flotation kinetics of apatite in alkaline environments. For example, a study found an improvement in flotation rate and recovery when collector concentration was increased (Testa, 2016).
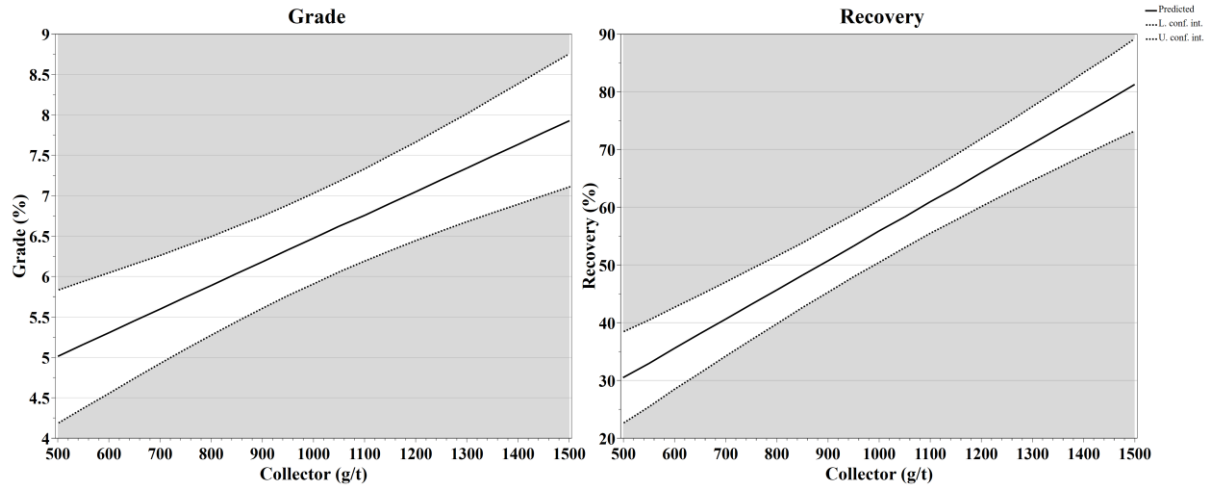
Fig. 4. Main effects plot of collector dosage on grade (right) and recovery (left) of apatite in direct flotation.

3.1.3. pH Effect

Based on Fig. 5, the effect of pH on apatite flotation demonstrates an inverse relationship between grade and recovery. As pH increases from 9.5 to 11.5, the P_2O_5 grade of the concentrate drops from approximately 7.5% to below 5.5%, while recovery slightly increases from around 52% to nearly 60%. However, according to the regression coefficients shown in Fig. 3, the effect of pH on recovery is not statistically significant at the 95% confidence level. Nonetheless, the declining trend in grade appears more consistent and meaningful.

This pattern can be partially attributed to the influence of solution chemistry and pH on flotation behavior. In fact, although the flotation of quartz cannot be achieved using fatty acid collectors, it may be activated using multivalent cations like Mg^{2+}, Fe^{3+}, and Al^{3+} to enhance its floatability within a pH range of 9 to 10. In addition, the addition of Ca^{2+} ions have also been proven to increase the flotation of the quartz within the pH range of 9.5 to 11.5 (Ruan et al., 2018). In addition, this effect may be explained by the impact of alkaline conditions on the behavior of fatty acid collectors. Specifically, high pH values cause the collectors to exhibit an increased frothing ability and reduced average bubble size, which enhances gas retention in the flotation cell. Under such conditions, excessive froth stability can entrap gangue particles within the froth phase (Atrafi et al., 2012). Together, these factors impair the selectivity of separation, thereby reducing concentrate purity despite the presence of a marginal increase in recovery levels. Thus, accurate pH adjustment is needed to obtain a trade-off between grade and recovery.

3.1.4. Interaction Effects

According to Fig. 3, the only significant interaction affecting the process is the effect of the starch and sodium silicate interaction on recovery. Fig. 6 shows the interaction plot. At low starch dosages, with an increased amount of sodium silicate, recovery decreased sharply from approximately 67% to 50%. In contrast, at high starch dosages, recovery increased slightly from about 51.7% to 54%. This implies
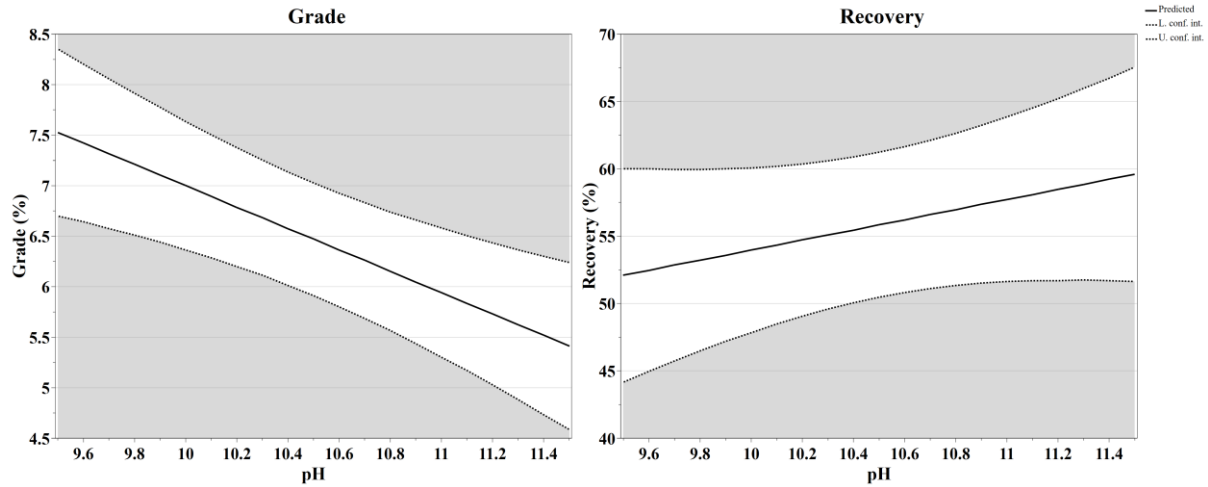
Fig. 5. Main effects plot of pH on grade (right) and recovery (left) of apatite in direct flotation.

that at low starch concentrations, sodium silicate causes excessive depression that significantly reduces recovery, but at higher starch dosages, this effect is partially mitigated. These results highlight the importance of the interaction between these two depressants on the flotation performance.
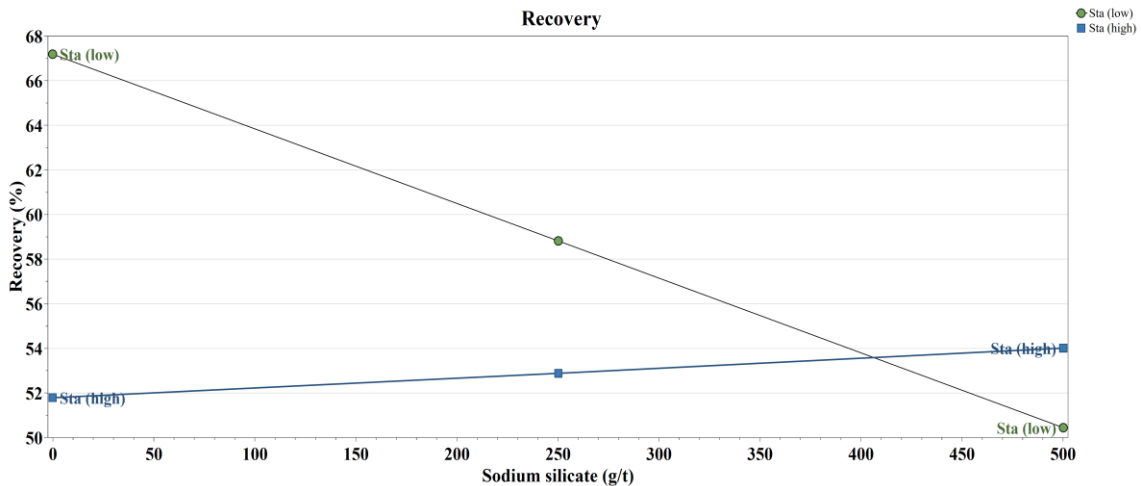
Fig. 6. Interaction plot of sodium silicate and starch on recovery.

3.1.5. Process Optimization

Optimization of the direct flotation process was performed using response surface plots for grade and recovery (Fig. 7). The plots that are shown depict the effect of collector dosage and pH levels when keeping starch dosage constant at zero because its effect on flotation efficiency is statistically insignificant and slightly detrimental. Sodium silicate was maintained at an optimized level of 100 g/t to support pulp dispersion. The maximum grade (9-10%) was achieved at a pH range of 9.5-10.1 and high collector dosage (1220-1500 g/t), while raising pH to 11.5 and reducing collector dosage to 500 g/t decreased the grade to its lowest value (~5%), as shown by the response surface plots. This decline in grade at higher pH levels can be attributed to the reduced selectivity of fatty acid collectors. The negative effect of increased pH on grade and positive effect of collector dosage on grade and recovery are validated from these results. Also, the significant grade drop evident at lower collector doses indicates the increased reagent consumption for this sample, suggesting that a high enough collector dosage is necessary to maintain good flotation performance. In contrast, a maximum recovery (80-

90%) was achieved over a wide pH range (9.5 to 11.5) and high collector dosage (1300-1500 g/t), but decreased to 45-50% with decreasing pH to 10.5 and collector dosage of 560 g/t.

Using a sweet spot plot, which ascertains the operational conditions under which multiple response criteria are concurrently fulfilled, the direct flotation conditions were optimized. The plot is for simultaneous high grade and recovery (≥9% and ≥80%, respectively) with sodium silicate (100 g/t) and starch (0 g/t) set constant. The upper limits for grade and recovery are as per the experimental design outcome that showed the maximum ranges of responses. The results (Fig. 8) revealed that the desirable region (green) is located at pH 9.5-9.7 and collector dosage 1373-1500 g/t. At higher pH and lower collector dosage, only one criterion (blue) or neither (white) is met. This plot shows the appropriate pH range between 9.5 and 9.7 and collector dosage of 1373 to 1500 g/t to achieve optimal grade and recovery for direct flotation, with sodium silicate dosage of 100 g/t and no starch addition. Using the optimizer tool in MODDE software, the precise optimal conditions were determined to be a pH of 9.5, a collector dosage of 1500 g/t, and a sodium silicate dosage of 100 g/t. In these conditions, a concentrate of approximately 9.8% grade and 82% recovery can be obtained. Similar results in tests conducted under these optimal conditions also validate the authenticity of such data.
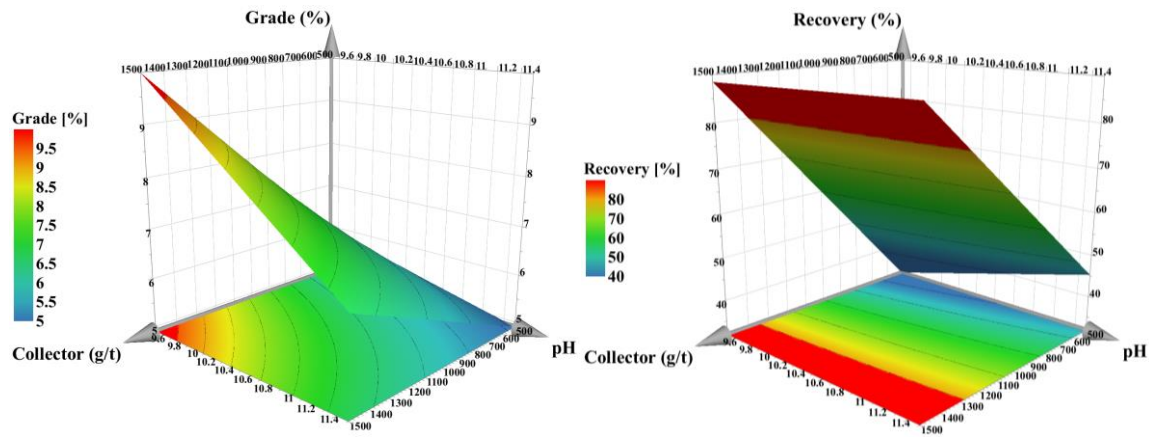
Fig. 7. Response surface plots of grade (left) and recovery (right).
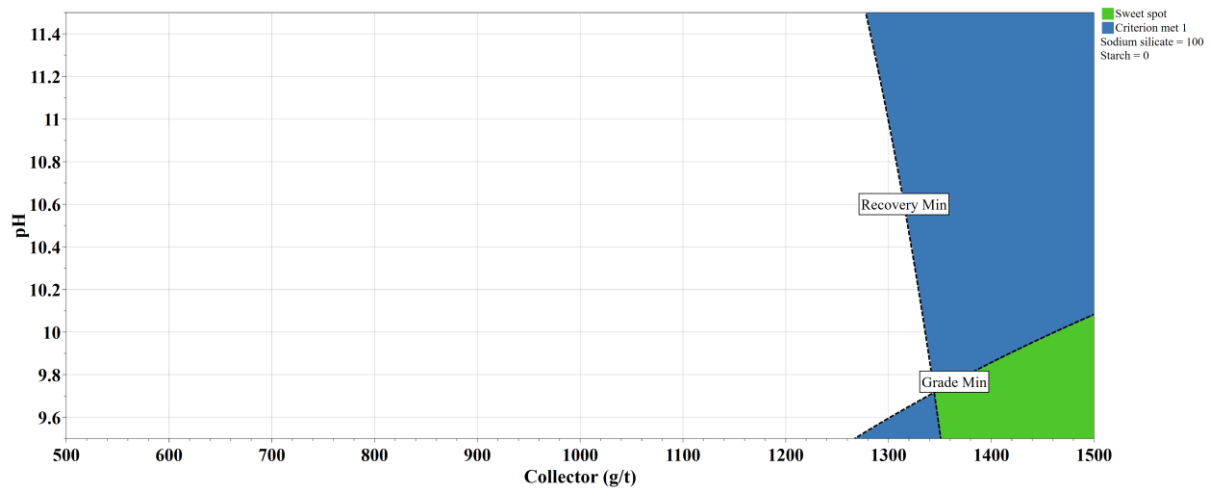
Fig. 8. Sweet spot plot for optimal grade and recovery conditions.

3.2. Reverse Flotation Test

As described in Section 2.5, the reverse flotation test was performed to separate carbonate minerals from the direct flotation concentrate, though due to surface similarities between carbonate minerals

like calcite and dolomite and apatite, their separation via direct flotation was not feasible, necessitating a reverse flotation step to float carbonate minerals. The findings demonstrated the successful removal of carbonate minerals by reverse flotation, resulting in a final product with above 30% P_2O_5 content and above 70% recovery. The final process flowsheet is presented in Fig. 9. The acid scrubbing step (Section 2.5.1) enhanced the selectivity of carbonate flotation by desorbing collectors from the concentrate. It has been established that phosphoric acid and sulfuric acid are effective depressants for reverse flotation of phosphate ores under acidic conditions (Huang & Zhang, 2024). Previous studies have confirmed that using a mixture of sulfuric and phosphoric acids is more effective for apatite depression than using either acid alone. This is why a mixed acid system was used in the present work. The mixed acid system does decrease the contact angle of apatite to the lowest state, which is effective depression (Lai et al., 2023). The mechanism for the depression of apatite by phosphoric acid and sulfuric acid at pH 4.5 employs further chemical adsorption of H_3PO_4 onto apatite surfaces, leading to the formation of hydrophilic species including $CaHPO_4$, $Ca(H_2PO_4)_2$, $CaH_2PO_4^+$, which restricts collector adsorption on apatite surfaces. Among these, $CaHPO_4$ is considered the primary species responsible for effective apatite depression (Liu, Ruan, et al., 2017; Huang & Zhang, 2024). In addition, sulfuric acid contributed further to the overall effect by forming a poorly soluble $CaSO_4$ layer on apatite surfaces preventing collector access to the calcium sites (Liu, Luo, et al., 2017; H. Zhang et al., 2025). These results indicated that reverse flotation is a suitable complementary method to direct flotation, improving the quality of the apatite concentrate for industrial use. These grade and recovery can be further optimized by adjusting collector consumption in this stage or by fine-tuning pH during the acid scrubbing or preparation with sulfuric and phosphoric acids for apatite depression. These findings show that these tailings can be processed as an apatite source, offering an economic resource while reducing tailings and reusing them for environmental preservation.
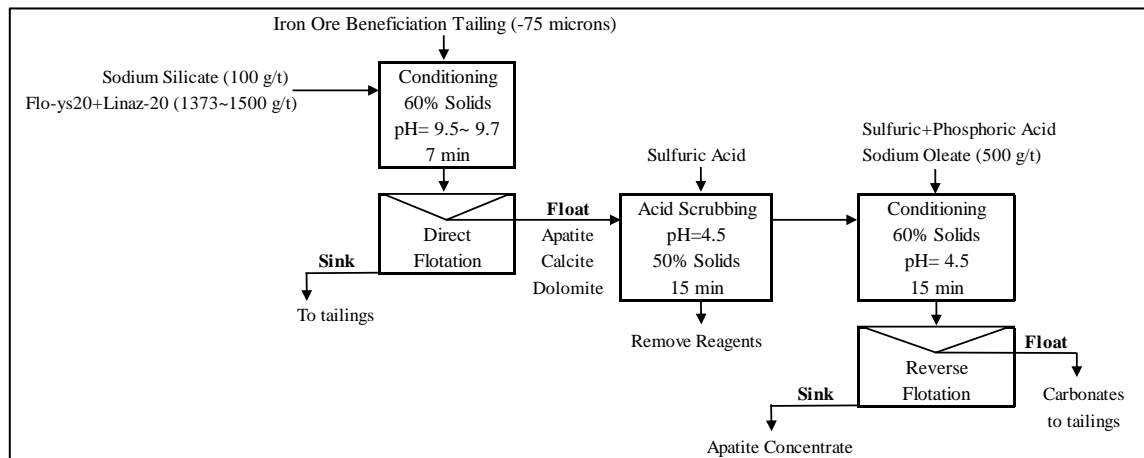
Fig. 9. Final flowsheet for the recovery of apatite from iron ore beneficiation tailings.

4.   Conclusions

The feasibility of apatite recovery from secondary resources was studied using the tailings from iron ore beneficiation at the Sangan company in Yazd Province, Iran. Mineralogical investigations demonstrated that the dominant gangue minerals in the tailings, in turn, are alkali feldspar, quartz, calcite and dolomite. A full factorial experimental design was employed to optimize the direct flotation process, and the results were processed using Umetrics MODDE software and the MLR model. High grade and recovery (≥9% and ≥80%, respectively) in the direct flotation were achieved under optimized conditions at a pH range of 9.5-9.7 and collector dosage of 1373-1500 g/t, with sodium silicate dosage of 100 g/t and no starch addition. Microscopic examinations revealed that more than 85% of the apatite in the sample is fully liberated in the size fraction below 75 μm, indicating that selectivity, rather than liberation, is the primary challenge in this flotation process. The

subsequent reverse flotation test successfully removed the carbonate minerals and improved the concentrate quality, resulting in a final grade above 30% P_2O_5 and a final recovery above 70% for the entire process. In reverse flotation, both phosphoric and sulfuric acids were used to depress apatite, leading to an increase in selectivity. These results demonstrate that the integration of direct and reverse flotation is indeed a potential route for producing high-quality apatite concentrates, with strong potential for industrial scale-up and further process enhancement.

Acknowledgments

References

Abouzeid, A.-Z. M. (2008). Physical and thermal treatment of phosphate ores — An overview. *International Journal of Mineral Processing*, *85*(4), 59-84. doi: https://doi.org/10.1016/j.minpro.2007.09.001

Alsafasfeh, A., & Alagha, L. (2017). Recovery of phosphate minerals from plant tailings using direct froth flotation. *Minerals*, *7*(8), 145. doi: 10.3390/min7080145

Amirech, A., Bouhenguel, M., & Kouachi, S. (2018). Two-stage reverse flotation process for removal of carbonates and silicates from phosphate ore using anionic and cationic collectors. *Arabian Journal of Geosciences*, *11*(19), 593. doi: 10.1007/s12517-018-3951-2

Atrafi, A., Gomez, C. O., Finch, J. A., & Pawlik, M. (2012). Frothing behavior of aqueous solutions of oleic acid. *Minerals Engineering*, *36*, 138-144. doi: https://doi.org/10.1016/j.mineng.2012.03.020

Carvalho, I. d. S. B., Brandao, P. R. G., Henriques, A. B., & Ferreira, E. E. (2022). Characterization of a complex carbonate-silicate apatite ore and its concentration by a two-stage anionic flotation method. *REM-International Engineering Journal*, *75*, 353-359. doi: 10.1590/0370-44672021750080

Cordell, D., Drangert, J.-O., & White, S. (2009). The story of phosphorus: global food security and food for thought. *Global environmental change*, *19*(2), 292-305. doi: 10.1016/j.gloenvcha.2008.10.009

dos Santos, M. A., Santana, R. C., Capponi, F., Ataíde, C. H., & Barrozo, M. A. (2010). Effect of ionic species on the performance of apatite flotation. *Separation and Purification Technology*, *76*(1), 15-20. doi: https://doi.org/10.1016/j.seppur.2010.09.014

El-bahi, A., Taha, Y., Ait-Khouia, Y., Elghali, A., & Benzaazoua, M. (2024). Enhancing sustainability in phosphate ore processing: Performance of frying oil as alternative flotation collector for carbonate removal. *International Journal of Mining Science and Technology*, *34*(4), 557-571. doi: https://doi.org/10.1016/j.ijmst.2024.04.003

Filippelli, G. M. (2002). The global phosphorus cycle. *Reviews in mineralogy and geochemistry*, *48*(1), 391-425. doi: doi: 10.2138/rmg.2002.48.10

Filippelli, G. M. (2008). The global phosphorus cycle: past, present, and future. *Elements*, *4*(2), 89-95. doi: 10.2113/GSELEMENTS.4.2.89

Gharabaghi, M., Irannajad, M., & Noaparast, M. (2010). A review of the beneficiation of calcareous phosphate ores using organic acid leaching. *Hydrometallurgy*, *103*(1-4), 96-107. doi: https://doi.org/10.1016/j.hydromet.2010.03.002

Harlov, D. E. (2015). Apatite: A fingerprint for metasomatic processes. *Elements*, *11*(3), 171-176. doi: 10.2113/gselements.11.3.171

Huang, X., & Zhang, Q. (2024). Depression mechanism of acid for flotation separation of fluorapatite and dolomite using ToF-SIMS and XPS. *Journal of Molecular Liquids*, *394*, 123584. doi: https://doi.org/10.1016/j.molliq.2023.123584

Kawatra, S. K., & Carlson, J. (2013). *Beneficiation of phosphate ore*. Society for Mining, Metallurgy, and Exploration.

Lai, X., Cheng, W., Pan, X., & Huang, W. (2023). Flotation Behavior and Interface Characteristics of Apatite with Co-Depression by Sulfuric Acid and Phosphoric Acid. *Minerals*, *13*(10), 1275. doi: https://doi.org/10.3390/min13101275

Lishmund, S., Holmes, G., & Oakes, G. M. (1982). *A review of industrial minerals and rocks in New South Wales*. New South Wales Dept. of Mineral Resources.

Liu, X., Luo, H., Cheng, R., Li, C., & Zhang, J. (2017). Effect of citric acid and flotation performance of combined depressant on collophanite ore. *Minerals Engineering*, *109*, 162-168. doi: doi: 10.1016/j.mineng.2017.03.010

Liu, X., Ruan, Y., Li, C., & Cheng, R. (2017). Effect and mechanism of phosphoric acid in the apatite/dolomite flotation system. *International Journal of Mineral Processing*, *167*, 95-102. doi: https://doi.org/10.1016/j.minpro.2017.08.006

Ruan, Y., Zhang, Z., Luo, H., Xiao, C., Zhou, F., & Chi, R. (2018). Effects of metal ions on the flotation of apatite, dolomite and quartz. *Minerals*, *8*(4), 141. doi: 10.3390/min8040141

Santana, R. C. d., Santos, M. A., Ataíde, C. H., & Barrozo, M. A. S. (2010). Evaluation of the Influence of Process Variables on Flotation of Phosphate. *Materials Science Forum*, *660-661*, 555 - 560. doi: 10.4028/www.scientific.net/MSF.660-661.555

Testa, F. G. (2016). *Influência da dissipação de energia na cinética da flotação aniônica direta de apatita em meio básico* (Universidade de São Paulo).

Valderrama, L., Gómez, O., Pavez, O., & Santander, M. (2024). Recovery of Apatite from Magnetic Concentration Tailings by Flotation. *Minerals*, *14*(5), 441. doi: 10.3390/min14050441

Vaneeckhaute, C., Janda, J., Vanrolleghem, P. A., Tack, F. M., & Meers, E. (2016). Phosphorus use efficiency of bio-based fertilizers: Bioavailability and fractionation. *Pedosphere*, *26*(3), 310-325. doi: 10.1016/S1002-0160(15)60045-5

Zhang, H., Zhou, F., Liu, M., Jin, Y., Xiao, L., & Yu, H. (2025). Employing sulfur–phosphorus mixed acid as a depressant: A novel investigation in flotation of collophanite. *Energy Sources, Part A: Recovery, Utilization, and Environmental Effects*, *47*(1), 3015-3028. doi: 10.1080/15567036.2020.1849458

Zhang, W., Tu, R., Ren, Q., Liu, S., Guo, Z., Liu, P., & Tian, M. (2025). The selective flotation separation of apatite from dolomite and calcite utilizing a combination of 2-chloro-9-octadecenoic acid collector and sodium pyrophosphate depressant. *Separation and Purification Technology*, *353*, 128446. doi: https://doi.org/10.1016/j.seppur.2024.128446

Upgrading of low-grade iron ore: optimization of recovery and reduction of feed volume

Mahdieh Seyfi[1], Parviz Pourghahramani[1]*

[1]Mining Engineering Department, Tabriz University of Technology, Tabriz, Iran

* Corresponding author: pourghahramani@sut.ac.ir (Parviz Pourghahramani)

Abstract:

The present study investigated the potential for iron recovery from magnetite-bearing iron ore tailings at the Sangan Company's old dumps, aiming to reduce environmental challenges through wet magnetic separation as a pre-beneficiation stage. This method selectively removed coarse gangue while maximizing magnetite recovery. A full factorial experimental design evaluated the effects of magnetic field intensity (1200, 2700, 3400 Gauss), drum speed (1, 1.4 m/s), and pulp solids content (25%, 35%). Concentrate analysis was performed using titration and Satmagan methods. Partial Least Squares (PLS) modeling revealed that higher magnetic field intensities significantly improved magnetite recovery, enabling a feed mass reduction of 18–22% with negligible magnetite loss (~2–3%). Magnetite recovery from tailings represents a novel approach, achieving up to 97.21% recovery under optimal conditions. Davis Tube tests confirmed that lost magnetite, with iron grades below 13.63%, is unsuitable for the final concentrate, enhancing overall concentrate quality by its removal. This pre-upgrading process improves concentrate quality, reduces operating costs, and supports sustainable tailings management.

1. Introduction

Steel is the foundation of industrial development. It is widely used in various fields, such as construction, the automotive industry, industrial equipment, transportation, and energy (Comtois & Slack, 2016). Iron ores are crucial for providing raw materials to the steel industry. Notable iron minerals encompass hematite (Fe_2O_3), magnetite (Fe_3O_4), goethite ($FeO(OH)$), and siderite ($FeCO3$). Iron ores, such as hematite and magnetite, have been effectively processed for a long time. However, significant iron reserves remain unexploited due to technical and economic challenges, accumulating as tailings in mines (Carmignano et al., 2021; Lu, 2015). With increasing global demand and limited primary resources, recovering iron from mine tailings has become critical for preserve resources and minimizing environmental degradation (Arol & Aydogan, 2004; Jyolsna et al., 2016).

Iron ore beneficiation occurs in processing plants to produce materials suited for iron smelters. These methods include flotation (Ghasemi et al., 2019), combined gravity and magnetic techniques (Zare et al., 2023), magnetic roasting (Li et al., 2010), and magnetic separation (Herrera-Pérez et al., 2024; Luttrell et al., 2004). Importantly, particularly in the recovery of valuable materials from iron ore tailings, many of these technologies are also widely used (Roy & Das, 2008). Conventional processing methods are often cost-prohibitive or inefficient for low-grade tailings due to their complex mineralogy and high gangue content. Magnetic separation, an effective mineral processing technique, relies on differences in the magnetic properties of iron minerals (Chen & Xiong, 2015). This method is highly efficient for extracting magnetite from iron ore tailings (Sahin, 2020). Recent studies on magnetite processing highlight diverse approaches to enhancing the efficiency of magnetic separation. One study utilized a hydrocyclone prior to high-intensity wet magnetic separation, achieving a recovery of 89.2% (Jyolsna et al., 2016). Similarly, another investigation combining hydrocyclone and magnetic separation produced a concentrate with a grade of 63% and a recovery of 70.7% (Jena et al., 2015). Additionally, a different study employing low-intensity magnetic separation yielded a concentrate with a grade of 47.5% and a recovery of 68.56% (Behnamfard & Khaphaje, 2019). Another research suggested increasing the size of ultra-fine magnetite particles as a method to reduce losses during magnetic separation (Arol & Aydogan, 2004). Among magnetic separation techniques, the wet method is considered an efficient and cost-effective option for tailings containing magnetite due to its superior particle attraction, energy efficiency, and suitability for the mineralogical properties of the tailings. These findings underscore the importance of optimizing processing conditions and selecting appropriate methods to achieve higher efficiency in magnetic separation processes.

As a pioneer in the iron ore mining and processing industry in Iran, Sangan Company has deposited a large amount of low-grade material and mischievous ore in storage sites over the years. Despite their low initial grade, these deposits offer significant potential for recovery and reuse in production due to their high magnetite content. pre-processing these tailings, particularly using magnetic separation, can be considered an economic and environmental solution. However, optimizing this process faces challenges, including the oxidation of magnetite to hematite, high operating costs, and varied mineralogical properties.

The main objective of this study is to selectively remove a significant portion of the coarse-grained gangue in the pre-processing stage. For this purpose, the magnetic separation method was used, which is considered to be an efficient, and cost-effective method in mineral processing. This study also seeks to substantially reduce the feed rate of material entering downstream processing stages by optimizing pre-processing. To this end, experiments were designed using a full factorial experimental design, investigating key parameters of magnetic separation, including magnetic field intensity, separator speed, and pulp solids content. The results were analyzed using the Partial Least Squares (PLS) method to optimize the efficiency of magnetic separation.

2. Material and Methods

2.1. Material

The initial representative sample, weighing 900 kg, was prepared after grinding to a maximum particle size of 6 mm. Particle size analysis (see Fig. 1) indicated that 80% of the particles were smaller than 2700 μm. This particle sizes are well suited for wet magnetic separation of magnetite, particularly with medium-to-high magnetic field intensities.
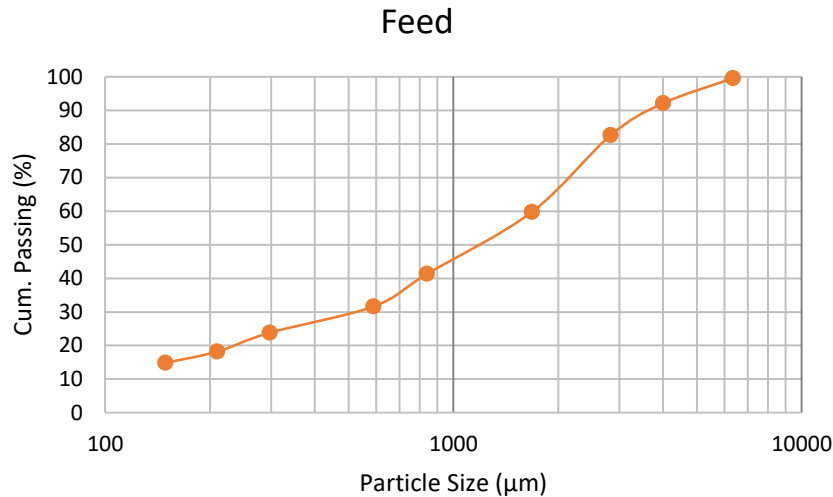
Fig. 1. Feed size analysis for initial representative sample.

In this study, experiments were conducted using a drum magnetic separator in the mineral processing laboratory of Sahand University of Technology, Tabriz. This apparatus, capable of adjusting the drum speed via electric current control, allowed experiments across a range of drum speed. The separator was equipped with an adjustable mechanical feeder and agitator to control the feed rate and mixing speed. This allowed for uniform feeding, ensured a constant flow rate, and ensured optimal pulp homogeneity.

2.2. Experimental Design

The efficiency of the magnetic separation process depends on key operating parameters. Accurate identification of these factors and the extent to which each influences the process is of particular importance. The experimental design of this study involved the use of a full factorial design, which was implemented after conducting preliminary experiments and identifying salient factors. The experimental design was used to conduct a comprehensive investigation of the effects of three variables: magnetic field intensity, separator speed, and pulp solids content. These variables were found to have a significant effect on two primary indicators: grade and recovery of iron and iron oxides. The range of these parameters was determined based on preliminary studies and is presented in Table 1.

Table 1. Range of variation of operating parameters

Parameters	Intensity (G)	Speed (m/s)	Solid (%)
Levels	1200	1	25
	2700	1.4	35

15

3400	-	-

2.3. Results Analysis Method

Mineralogical studies of the sample were performed through the preparation of thin and polished sections. The sections were analyzed using a polarizing microscope equipped with a digital image processing system. Chemical analysis of the concentrates obtained from the experiments was carried out using two methods: titration and Satmagan magnetic analyzer.

Experiments data were analyzed using the Partial Least Squares (PLS) regression in MODDE software. PLS was chosen for its ability to simultaneously examine the relationships between independent and dependent variables while handling multiple response variables. Unlike multivariate linear regression (MLR), which ignores the covariance between responses, PLS enables robust analysis of variable relationships by taking into account their covariance and variance. Given the presence of several related and non-independent responses in this study, the PLS method was selected as a more robustness approach than MLR. This approach made it possible to extract more accurate information from the data structure and identify complex relationships between process parameters (Eriksson et al., 2000).

2.4. Mineralogical Studies

Mineralogical analyses of the sample using optical microscope revealed that the main transparent minerals predominantly consist of, in turn, alkali feldspars and quartz and plagioclase. Amphiboles and micas were also identified in thin sections, with investigations indicating that amphiboles and biotite transformed into epidote and chlorite assemblages in early alteration stages and into actinolite and serpentine in more advanced stages. Furthermore, the saussuritization process in plagioclases and alkali feldspars was observed, resulting in the formation of secondary iron-bearing minerals, such as epidote and zoisite. Magnetite, the primary iron ore, constitutes over 40% of the sample's composition. Microscopic examinations showed that magnetite by 5-10 micron in size presents within the silicate gangue. Silicate gangue with 5-10 micron in size is observed within the magnetite particles. In some cases, martitization—the alteration of magnetite to hematite—was noted, particularly at crystal edges and along fracture surfaces.
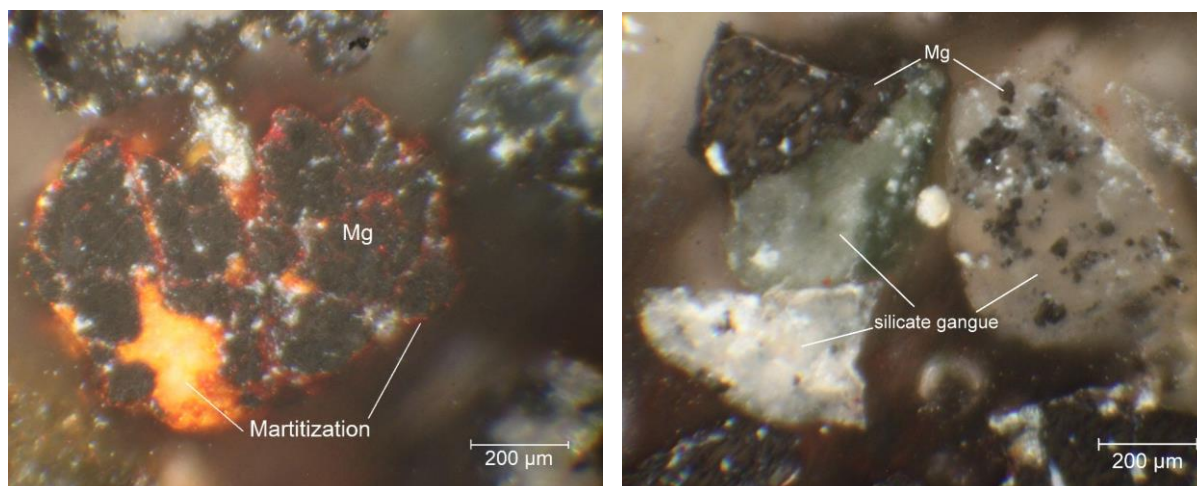
Fig. 2. Magnetite and martitization phenomenon in fractures and edges (left), magnetite within silicate gangue (right), (-60 microns).

2.5. Initial Experiments

In this section, the effects of magnetic field intensity and speed of the separator, on the separation performance is investigated. Initially, initial experiments were designed with a constant pulp solids content of 35%, magnetic field intensity at three levels of 1200, 2700, and 3400 Gauss, and separator linear speed at two levels of 1 and 1.4 m/s. It is noteworthy that the inlet pulp flow rate and the washing water flow rate were kept constant at 3 liters per minute (L/min) and 2 L/min, respectively, throughout all experiments.

2.6. Supplemental Experiments

Preliminary tests have demonstrated that a high-intensity magnetic field is essential to prevent further magnetite loss and enhance process efficiency. These tests were conducted with the magnetic field intensity adjusted to 2700 and 3400 Gauss, the separator linear speed set at 1 and 1.4 m/s, and the pulp solids content configured at 25% and 35%. Notably, other parameters, such as inlet pulp and washing water flow rates,kept constant throughout the experiments.

2.7. Assessing the Quality of Lost Magnetite

According to the results of the initial beneficiation stage, the optimal FeO Satmagan recovery, representing magnetite recovery, reached 97.39%, indicating approximately 2.61% magnetite loss. To evaluate the quality of the lost magnetite, a series of experiments was conducted using a Davis tube. Tailings from the initial beneficiation were crushed to a final grind size below 63 µm, and reference samples were prepared. Magnetic separation tests were performed at field intensities of 1000, 2000, 3500, and 5000 Gauss.

3.   Results and Discussion

3.1. Initial Experiment Results

The experimental conditions, the results obtained, and the metallurgical calculations are presented in Table 2. Based on the data presented in Table 2, the total iron grade in the sample under study varied between 48.11 to 50.21 percent depending on the operating conditions and the weight recovery of the concentrate ranged from 77.90 to 81.98 percent. Also, the total iron recovery ranged from 93.62 to 96.08 percent and the recovery of FeO based on the Satmagan analysis ranged from 97.05 to 98.83 percent. Since the Satmagan analysis fairly reflects the amount of magnetite present in the concentrate, it can be concluded that the recovery of magnetite in the pre-upgrading process was very satisfactory and more than 97 percent of magnetite could be recovered. A comparative analysis of iron oxide content obtained through titration and Satmagan methods revealed that titration consistently yielded higher values. This is attributed to the presence of divalent iron in non-magnetite iron-bearing minerals, such as silicates or secondary oxides, which are not detected by the Satmagan method.

The analysis of the results highlights the critical influence of operational parameters on separation performance. Specifically, increasing the magnetic field intensity of the separator was found to enhance both magnetite and total iron recovery, likely due to the stronger attraction of fine magnetite particles to the magnetic field. Conversely, an increase in the linear speed of the magnetic separator led to a relative decrease in concentrate grade, possibly because higher speeds reduce the residence time of particles on rotating drum , allowing some non-magnetic gangue minerals to be entrained in the concentrate. These findings are consistent with the mineralogical characteristics of the sample.

From an industrial perspective, the high magnetite recovery (>97%) achieved in this study underscores the efficiency of high-intensity wet magnetic separation for processing magnetite-rich ores. This approach not only minimizes losses but also aligns with energy-efficient and cost-effective beneficiation strategies, as discussed previously. However, the slight reduction in concentrate grade at

higher separator speeds suggests a trade-off between recovery and quality, which warrants careful optimization in large-scale operations. These findings contribute to the optimization of magnetic separation processes and provide a foundation for further research into enhancing concentrate quality and minimizing losses in magnetite ore processing

Table 2. Initial test conditions and results.

Test ID	Parameters			Concentrate			Recovery			Head (Cal)		
	Intensity (G)	Speed (m/s)	C/F (%)	Fe (%)	FeO (%)	FeOsat (%)	RFe (%)	RFeO (%)	RFeOsat (%)	Fe (%)	FeO (%)	FeOsat (%)
R1	3400	1.4	81.52	48.11	13.19	12.40	95.79	93.72	98.83	40.95	11.47	10.23
R2	3400	1	81.98	48.27	13.80	13.33	96.08	94.50	98.77	41.18	11.97	11.06
R5	2700	1.4	79.58	48.11	13.80	12.71	94.73	93.73	97.73	40.42	11.72	10.35
R12	2700	1	79.71	49.51	14.40	14.01	94.65	93.09	98.62	41.70	12.33	11.32
R16	1200	1.4	77.90	50.21	14.85	12.96	93.62	92.90	97.05	41.78	12.45	10.40
R17	1200	1	80.66	49.20	14.05	13.48	95.20	93.98	98.53	41.69	12.06	11.04

3.2. Supplemental Experiment Results

The experimental conditions, results, and metallurgical calculations for the magnetic separation process are summarized in Table 3. The data presented in Table 3 illustrate the significant influence of operating parameters—namely magnetic field intensity, separator linear speed, and pulp solids content—on the performance and quality of magnetic separation during the pre-beneficiation stage. The total iron grade of the concentrate ranged from 50.82% to 52.55%, reflecting the combined effects of these parameters. The weight recovery of the concentrate varied between 76.70% and 80.11%, indicating a direct correlation with operating conditions. Specifically, lower pulp solids content and optimized field intensities contributed to higher weight recoveries by improving the selectivity of magnetic separation. Total iron recovery ranged from 92.27% to 94.97%, with higher recoveries observed at elevated magnetic field intensities, consistent with the enhanced attraction of magnetite particles under stronger fields. The recovery of iron oxide (FeO), as determined by Satmagan analysis, ranged from 96.68% to 98.47%, underscoring the exceptional efficiency of the pre-beneficiation process for magnetite recovery. Additionally, the FeO content in the concentrate, measured by Satmagan, varied between 12.40% and 14.47%, influenced primarily by magnetic field intensity and pulp solids content. These results align with earlier mineralogical findings, where magnetite was identified as micron-sized grains dispersed within a silicate gangue matrix, necessitating high-intensity separation to achieve optimal recovery.

From an industrial perspective, the high FeO recovery (up to 98.47%) achieved in this study demonstrates the efficacy of high-intensity wet magnetic separation for processing magnetite-rich ores. This approach not only maximizes resource utilization but also aligns with energy-efficient and cost-effective beneficiation strategies, as noted in earlier sections. However, the observed trade-off between concentrate grade and drum speed underscores the need for careful process optimization to balance recovery and quality in large-scale operations. For instance, operating at moderate speeds (e.g., 1 m/s) with high field intensities could strike an optimal balance, as evidenced by the upper range of iron grades and recoveries reported.

Table 3. Conditions of supplementary tests and their results.

Test	Parameters	Concentrate	Recovery	Head(Cal)

ID	Intensity (G)	Speed (m/s)	Solid (%)	C/F (%)	Fe (%)	FeO (%)	FeOsat (%)	RFe (%)	RFeO (%)	RFeOsat (%)	Fe (%)	FeO (%)	FeOsat (%)
N1	3400	1.4	25	76.70	52.55	15.20	13.33	92.27	91.58	98.47	43.68	12.73	10.38
N2	3400	1.4	35	79.08	51.20	14.80	13.83	93.83	92.62	97.72	42.61	12.48	11.05
N3	3400	1	25	77.38	50.82	14.25	12.71	93.62	92.42	97.58	42.00	11.93	10.08
N4	3400	1	35	80.11	52.55	15.00	14.47	94.97	93.79	97.21	44.33	12.81	11.92
N6	2700	1.4	25	77.83	52.10	14.90	13.86	94.29	92.73	97.69	43.01	12.51	11.04
N7	2700	1.4	35	78.67	51.16	14.60	13.73	93.99	92.92	96.68	42.82	12.36	11.17
N8	2700	1	25	79.12	51.80	14.85	12.40	94.69	93.21	97.51	43.28	12.60	10.06
N9	2700	1	35	79.28	52.03	15.00	13.79	94.70	93.33	97.92	43.56	12.74	11.17

In conclusion, the findings from supplementary experiments demonstrate that increasing magnetic field intensity, combined with precise control of separator speed and pulp solids content, significantly enhances iron recovery and minimizes magnetite loss. Specifically, optimal conditions of 3400 Gauss, 1 m/s separator speed, and 35% pulp solids content achieved a magnetite recovery of 97.21%, as determined by Satmagan analysis. A final flowsheet illustrating this optimized process is presented in Figure 3. These results confirm the high efficiency of wet magnetic separation in the pre-beneficiation process for magnetite recovery. The iron grades and recoveries obtained, supported by the optimal performance under these conditions, are highly satisfactory and efficient in ore processing.
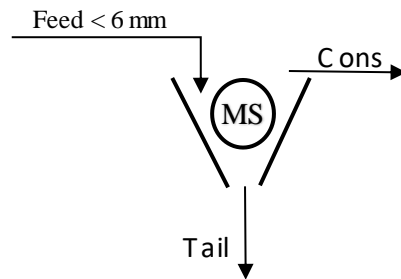
Fig. 3. Final flowsheet. Feed finer than 6 mm is separated by a wet magnetic separator.

3.2.1. PLS modeling

Following the implementation of the PLS model, the model fit criteria were utilized to assess the model's performance. In this diagram, it is imperative to examine R2 and the discrepancy between R2 and Q2. The R2 parameter, designated as the "goodness factor," quantifies the extent to which the raw data aligns with the regression model. Its value ranges from zero to one. A higher R2 value indicates the better fit between the raw data and the regression model. However, it is imperative to note that the R2 parameter is subject to limitations. Specifically, if there are many terms in the model, it may artificially produce a large value. Another appropriate index that shows the usefulness of the regression model is the Q2 index, known as the model's goodness of prediction. This parameter estimates the predictive power of the model. For a very good model, the R2 and Q2 parameters should have high values and their difference should not exceed 0.3. The next index in the summary fit plot is the repeatability and reproducibility index, whose high values indicate a lower repeatability error compared to the overall design variability, a value less than 0.5 for this index indicates a large net error and poor control of the experimental steps (Eriksson et al., 2000).

The model fit diagram is shown in Figure 2. By examining the values of the aforementioned indices on the multiple responses in the model, it is observed that the fitted model is appropriate and acceptable.
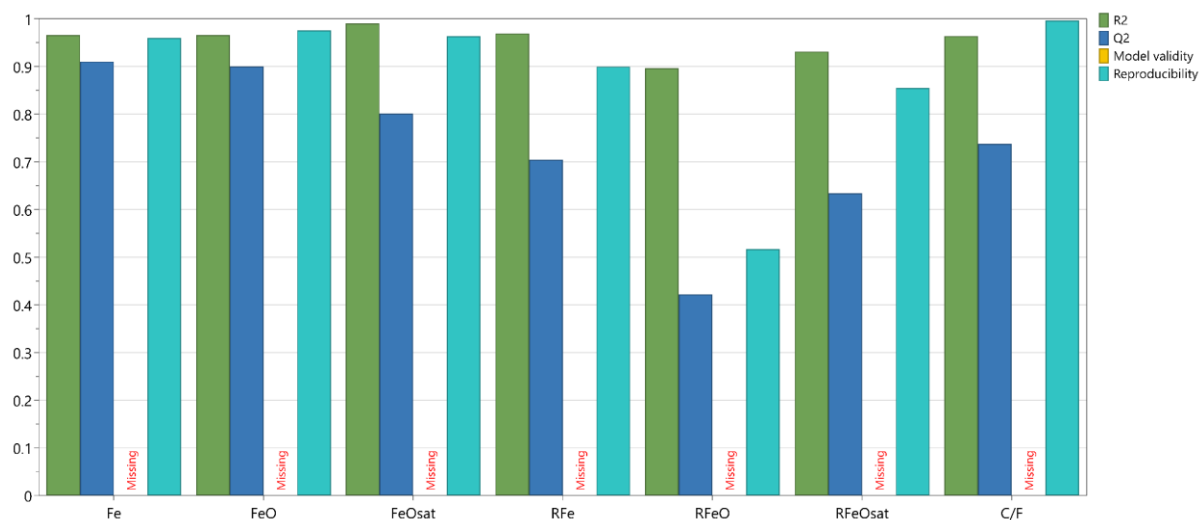
Fig. 4. Summary of the fit for the PLS model.

3.2.2. Variable importance

The Variable Importance Plot (VIP) of the final model to examine the parameters that affect all the responses is shown in Figure 3. As can be seen from the VIP diagram, the quadratic expressions of solid percentage, magnetic intensity, and separator speed have the greatest impact on the responses, with a VIP value of 1.257. After the quadratic terms, the solid percentage parameter has the largest impact, followed by the speed by solid percentage interaction (spe*sol), the speed parameter, the magnetic intensity by speed interaction (int*spe), and the magnetic intensity by solid percentage interaction (int*sol). Finally, the magnetic intensity with a VIP value of 0.63 has little effect on the responses. The insignificant effect of magnetic intensity may be due to the ferromagnetic property of magnetite and the proximity of the factor surface to each other, this property causes the recovery of magnetite even at low magnetic intensities.
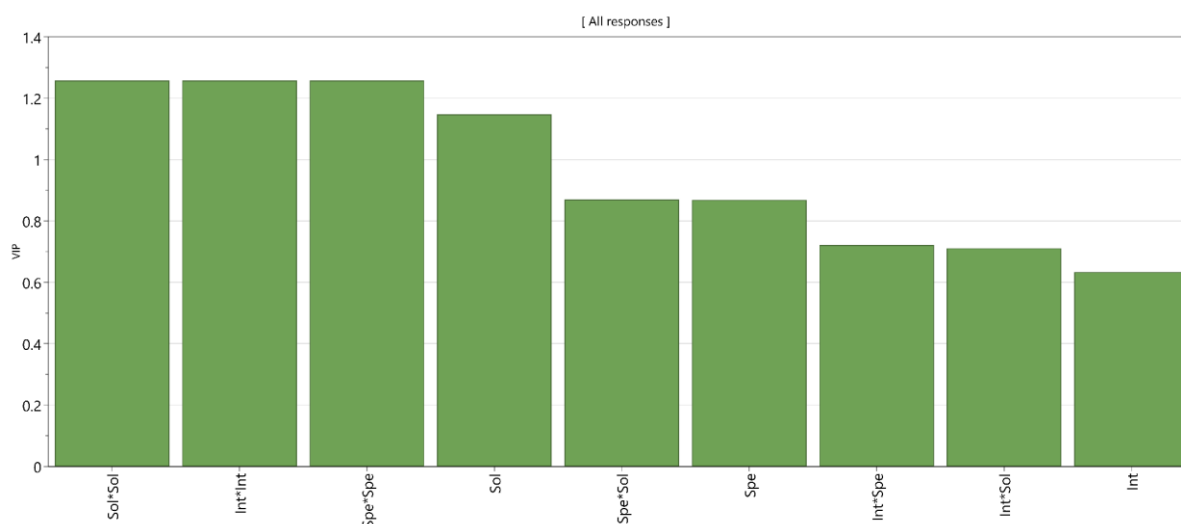
Fig. 5. Variable importance plot of the final model.

3.2.3. Interaction Effects

The interaction between magnetic intensity and separator linear speed is one of the interaction effects in the process shown in Figure 4 for the responses of grade and recovery of iron oxide from iron ore. However, there are some other interaction effects that have a lesser effect on the responses and are not shown here. From Figure 4, it can be seen that in the response of the iron oxide grade from the iron ore at low speed, the grade increases slightly with increasing magnetic intensity, but after an intensity of 3050 Gauss, the grade increases with a steep slope. This is in the case that at high speed, with increasing intensity, the grade initially decreases, but after an intensity of 3050 Gauss, the grade increases slightly. It appears that with increasing speed of the magnetic separator, due to the ferromagnetic nature of magnetite, the iron grade recovered from the iron ore at both separator speeds has an almost increasing trend, with the rate of increase being greater at lower speeds.

The interaction between magnetic intensity and separator speed on the response related to the recovery of iron oxide obtained from the iron ore shows that at low speeds, with increasing magnetic intensity, the recovery initially increases, but after a magnetic intensity of 3050 Gauss, the recovery decreases. At high speeds, with increasing magnetic intensity up to 3050 Gauss, the recovery increases with a steep slope, but after a magnetic intensity of 3050 Gauss, the recovery increases gently.
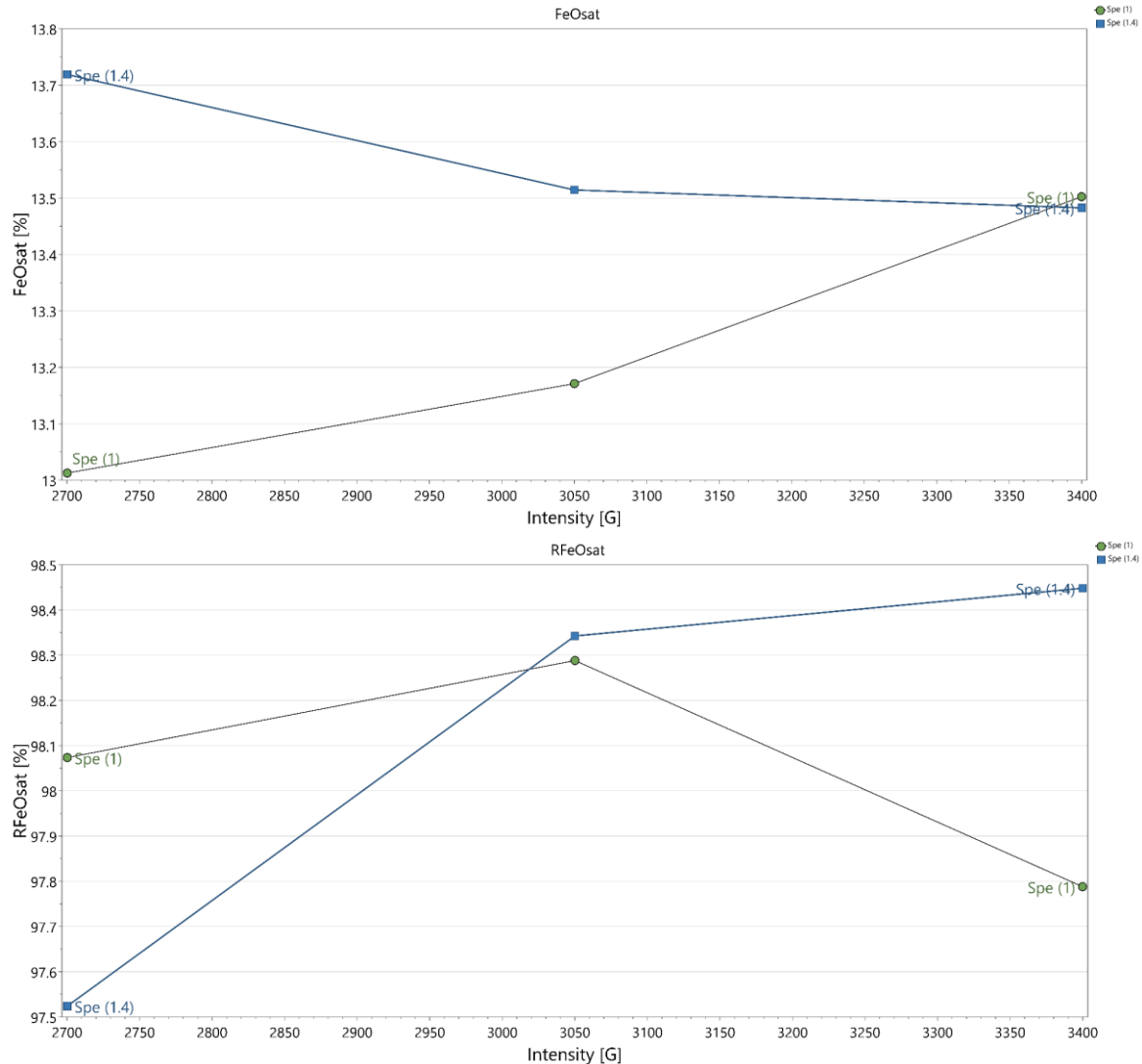
Fig. 6. Interaction of parameters on the responses of grade and recovery of iron oxide from satmagan.

3.2.4. Contour Plots

After studying the effects of the parameters on the process, equipotential surfaces were created to better understand the model. The purpose of constructing equipotential surfaces is to find the appropriate range of parameters for the experiments. Figure 5 shows the changes in the responses of the grade and recovery of iron oxide from the slag in terms of magnetic intensity and separator speed, and the intermediate limit of the solid percentage parameter is considered. The results obtained show that high grades can be obtained by setting the separator speed to the maximum and the magnetic intensity to the lowest limit. In addition, the speed and magnetic intensity simultaneously shift the recovery of iron oxide from the slag so that the highest recovery is obtained at the maximum speed and magnetic intensity. According to the explanations, it is clear that the effect of both speed and intensity parameters on the above responses is large.
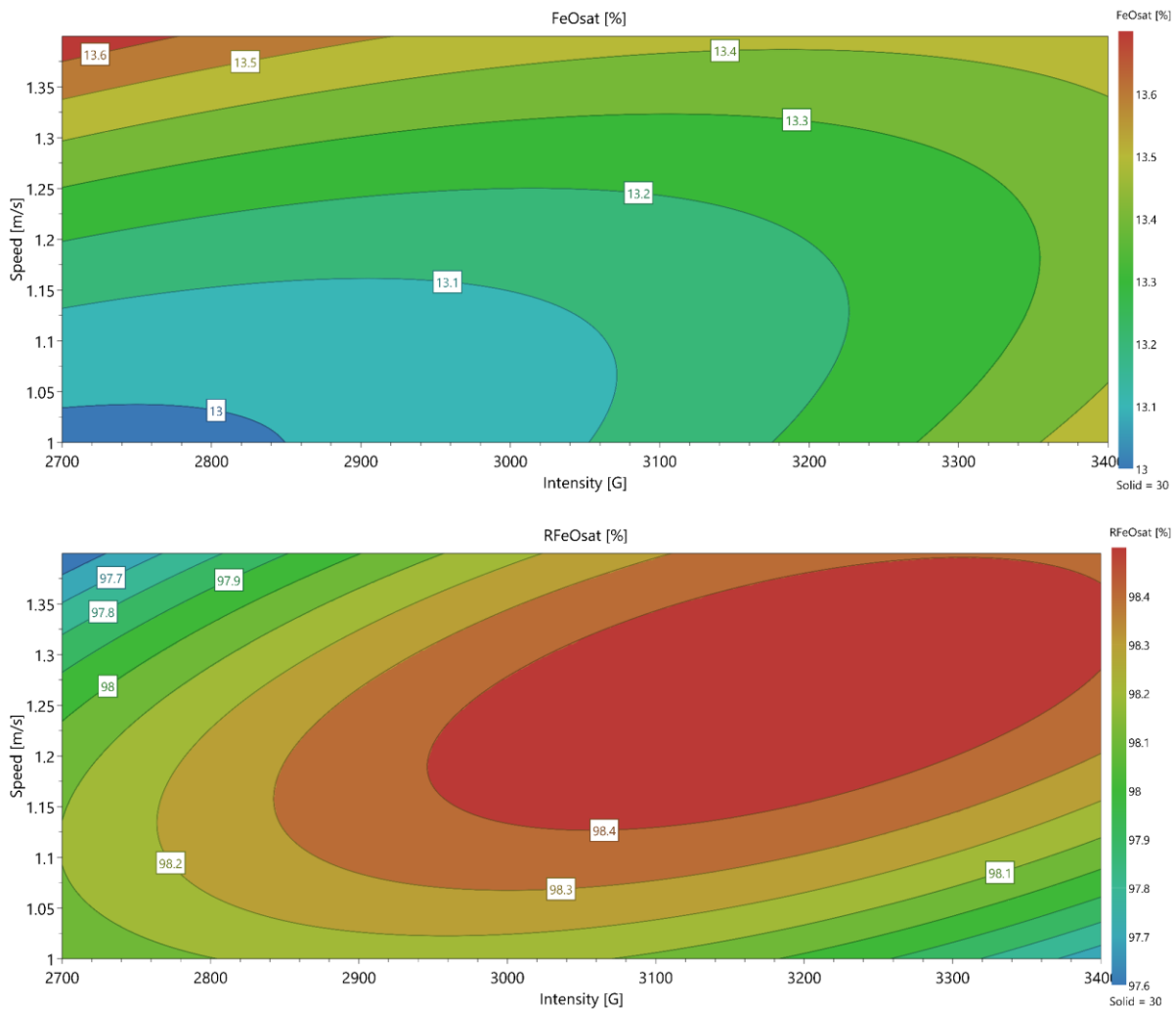
Fig. 7. Contour plots related to the grade response and recovery of iron oxide from the satmagan.

3.3. Lost Magnetite Quality Assessment Results

The results of the quality assessment of lost magnetite, derived from Davis Tube tests, are presented in Table 4. These experiments were conducted to evaluate the characteristics of magnetite lost during the pre-beneficiation stage. According to the data in Table 4, the weight recovery of magnetic materials from the tailings was consistently low, ranging from 0.30% to 0.84% across magnetic field intensities of 1000, 2000, 3500, and 5000 Gauss, corroborating the high efficiency of the pre-upgrading process

22

reported previously. As magnetic field intensity increased, the iron and FeO content in the concentrates, as determined by titration analysis, decreased progressively. Specifically, the iron content ranged from 63.13% at 1000 Gauss to 57.22% at 5000 Gauss, while FeO content varied from 21.30% to 17.0% over the same range.

These results indicate that the magnetite recovered from the tailings via the Davis Tube has low quality. This low quality is likely attributable to the presence of fine-grained, disseminated magnetite inclusions entrapped within the silicate gangue matrix, as observed in earlier mineralogical analyses. The small particle size (<63 µm, as prepared for these tests) and the association with non-magnetic gangue minerals further explain the poor quality of the recovered magnetite. Consequently, it can be inferred that the magnetite lost during the pre-beneficiation stage is not suitable for inclusion in the final concentrate, as its incorporation would likely reduce the overall concentrate grade.

Table 4. The conditions of the davis test and the results together with the metallurgical calculations.

Test ID	Parameters	Concentrate			Recovery		Head(Cal)	
	Intensity (G)	C/F (%)	Fe (%)	FeO (%)	RFe (%)	RFeO (%)	Fe (%)	FeO (%)
H1	1000	0.30	63.13	21.30	2.10	1.80	8.86	3.50
H2	2000	0.49	61.26	21.50	3.40	3.02	8.86	3.50
H3	3500	0.67	59.40	19.80	4.50	3.80	8.86	3.50
H4	5000	0.84	57.22	17.30	5.41	4.14	8.86	3.50

The low quality of the lost magnetite supports the strategic advantage of allowing minor magnetite losses in the pre-beneficiation stage to enhance the quality of the final concentrate.The Davis Tube results suggested that the small fraction of magnetite lost (approximately 2–3%, as noted earlier) consists primarily of low-grade material, which, if recovered, could compromise the high-grade concentrate achieved. Thus, the trade-off of sacrificing a minor portion of low-quality magnetite is justified to maintain the superior quality of the final product.

4. Conclusion

In conclusion, the results underscore the efficacy of high-intensity wet magnetic separation for valorizing magnetite-bearing tailings at the Sangan Company. The optimal conditions (3400 Gauss, 1 m/s, 35% solids) achieved a magnetite recovery of 97.21% and an FeO content of 14.47%, demonstrating the process's ability to produce high-quality concentrates while reducing tailings mass by 18–22%. The low quality of lost magnetite, as confirmed by Davis Tube tests, justifies the strategic acceptance of minor losses to enhance final concentrate quality. PLS modeling further elucidated the critical influence of quadratic parameter interactions, providing a robust framework for process optimization. These findings contribute to sustainable tailings management by enabling efficient magnetite recovery and reducing waste volume. From an industrial perspective, the process aligns with cost-effective and resource-efficient beneficiation strategies, offering significant potential for large-scale implementation. Conducting pilot-scale trials with industrial wet magnetic separators under optimal conditions (3400 Gauss, 1 m/s, 35% solids) to assess scalability, throughput, and economic viability is proposed.

Acknowledgments

References

Arol, A., & Aydogan, A. (2004). Recovery enhancement of magnetite fines in magnetic separation. Colloids and Surfaces A: Physicochemical and Engineering Aspects, 232(2-3), 151-154.

Behnamfard, A., & Khaphaje, E. (2019). Characterization of Sangan low-grade iron ore and its processing by dry low-intensity magnetic separation. International Journal of Mining and Geo-Engineering, 53(2), 111-116.

Carmignano, O. R., Vieira, S. S., Teixeira, A. P. C., Lameiras, F. S., Brandão, P. R. G., & Lago, R. M. (2021). Iron ore tailings: characterization and applications. Journal of the Brazilian Chemical Society, 32, 1895-1911.

Chen, L., & Xiong, D. (2015). Magnetic techniques for mineral processing. In Progress in Filtration and Separation (pp. 287-324). Elsevier.

Comtois, C., & Slack, B. (2016). Dynamic determinants in global iron ore supply chain (Vol. 6). CIRRELT Montréal, Canada.

Eriksson, L., Johansson, E., Kettaneh-Wold, N., Wikström, C., & Wold, S. (2000). Design of experiments. Principles and Applications, Learn ways AB, Stockholm.

Ghasemi, S., Behnamfard, A., & Arjmand, R. (2019). Reprocessing of Sangan iron ore tailings by flotation. Journal of Mining and Environment, 10(3), 729-745.

Herrera-Pérez, J. G., Legorreta-García, F., Reyes-Pérez, M., Reyes-Cruz, V. E., Chávez-Urbiola, E. A., & Trujillo-Villanueva, L. E. (2024). Analysis of the Effect of Magnetic Separation Processing Parameters for the Treatment of Mining Waste. Polish Journal of Environmental Studies, 33(2).

Jena, S., Sahoo, H., Rath, S., Rao, D., Das, S., & Das, B. (2015). Characterization and processing of iron ore slimes for recovery of iron values. Mineral processing and extractive metallurgy review, 36(3), 174-182.

Jyolsna, J., Rath, R. K., & Kumar, A. (2016). Recovery of Iron Values from Waste Iron Ore Slime. Journal of Materials & Metallurgical Engineering, 6, 1-7.

Li, C., Sun, H., Bai, J., & Li, L. (2010). Innovative methodology for comprehensive utilization of iron ore tailings: Part 1. The recovery of iron from iron ore tailings using magnetic separation after magnetizing roasting. Journal of Hazardous Materials, 174(1-3), 71-77.

Lu, L. (2015). Iron ore: mineralogy, processing and environmental sustainability. Elsevier.

Luttrell, G., Kohmuench, J., & Mankosa, M. (2004). Optimization of magnetic separator circuit configurations. Mining, Metallurgy & Exploration, 21, 153-157.

Roy, S., & Das, A. (2008). Characterization and processing of low-grade iron ore slime from the Jilling area of India. Mineral Processing & Extractive Metallurgy Review, 29(3), 213-231.

Sahin, R. (2020). Beneficiation of low/off grade iron ore: a review. Int. J. Res.-GRANTHAALAYAH, 8(8), 328-335.

Zare, A., Noaparast, M., & Dehghan, S. (2023). Recovery of Iron Ore From The Tailings of Tang Zagh Iron Beneficiation Plant: A Comparative Study of Gravity and Magnetic Separation Methods. Journal of Geomine, 1(3), 137-143.

The Beneficiation Study of Manganese Carbonate Ore By Calcination And Magnetic Separation

Seyed Ramin Banihashemi[1]*, Gholamreza Parvareh[1], Morteza Dehghani[1], Hasan Vafaei Jirsaraei[1]

[1]IMPRC (Iran Mineral Processing Research Center)

*Corresponding author: r.banihashemi@imprc.ir (Seyed Ramin Banihashemi)

Abstract:

Manganese carbonate mines in Iran are one of the significant potentials of this applied element in Iran. This research investigates the enrichment of manganese from rhodochrosite mineral found in a mine in eastern Iran. Chemical analysis and mineralogical studies showed that the manganese content of the sample was 9.1% (MnO_2 14.4%) and rhodochrosite was present as the main manganese mineral along with manganite with a relatively low degree of freedom. Calcination experiments were performed in feed size of -3 mm at 700-900°C for 2 hours with the aim of converting carbonate minerals into oxidant minerals. The optimized calcined product has undergone a magnetic separation process in different size fractions to enrich the manganese present in it. Magnetic separation at a magnetic field strength of 12000 Gauss at a grain size of less than 0.5 mm from the calcination product resulted in the production of MnO_2 concentrate with a grade of 34.9% and a recovery of 76.3%. Also, the MnO_2 content of the resulting tail has been reduced to 2.5%.

Keywords: Manganese, Carbonate ore, Calcination, Magnetic separation

1. Introduction

Manganese (Mn) is the 12th most abundant element in the earth's crust, with ~1,000 ppm (~0.1%) concentration and the fourth most-used metal after iron, aluminum, and copper (Dunne et al. 2019).

Manganese can take on a variety of valence states, primarily from 2+ to 7+. Because of this speciation, many manganese minerals can form. Water-stable manganese oxide minerals include pyrolusite (MnO2, 4+ valence), bixbyite (Mn2O3, 3+ valence), hausmannite (Mn3O4, two 3+ and one 2+ valence), and pyrochroite (Mn(OH)2, 2+ valence). Other important manganese minerals include rhodochrosite (MnCO3, 2+ valence), braunite (Mn7SiO12, six 3+ and one 2+ valence), cryptomelane ((K,Ba) Mn8O16 · xH2O or K2Mn8O16, seven 4+ and one 3+ valence), and manganite (MnOOH, 3+ valence). Rhodochrosite is the primary manganese mineral in about 33% of manganese deposits (Hudson Institute of Mineralogy, 2015).

Manganese has several uses. The largest use is in the steel industry, which typically consumes about 90% of the manganese produced each year. Other important uses include batteries and electronics, aluminum and copper alloys, fertilizers and micronutrients, water treatment, and as a colorant in materials, including glass, textiles, and plastic (Matos and Corathers, 2005).

Manganese ore deposits may be of four different types: hydrothermal manganese deposits, sedimentary manganese deposits, residual manganese deposits, and metamorphic manganese deposits (Sivrikaya, 2017). The increasing demand for the metal encouraged the mining industry to exploit all manganese-bearing resources recently. Even, the seabed may become a viable source of minerals in the future since manganese nodules have been known since the beginning of the nineteenth century (Mukherjee et al., 2004; Wills and Napier-Munn, 2006).

Over 80% of the known world, manganese resources are found in South Africa and Ukraine. Other important manganese deposits are in China, Australia, Brazil, Gabon, India, and Mexico (Baba et al. 2014). There are a lot of manganese deposits and numerous mineral occurrences in Iran. The major tectonic/structural zones of Iran that host manganese deposits are: (1) Urumieh-Dokhtar magmatic assemblage (UDMA), (2) the Central Iran (CI), (3) the Sabzevar zone (SZ), (4) the Alborz magmatic belt (AMB), and (5) the Cretaceous ophiolites (Maghfouri et al. 2019).

In this paper, the beneficiation of manganese carbonate using calcination and magnetic separation was comprehensively investigated.

2. Material and methods

Calcination of rhodochrosite to manganese oxide as the main type of pyrometallurgical pretreatments is used in the combined pyro-physical separation treatments of manganese carbonate ores. In the calcination of rhodochrosite, the ore is heated to drive off the CO2 gas, typically at temperatures of 800°C or greater (You et al. 2015). At these temperatures in an air atmosphere, the MnO formed oxidizes to MnO2, which is then cooled and subject to subsequent process.

At present, the process of manganese carbonate resources mainly includes ore washing, gravity separation, magnetic separation, flotation, leaching, and combined process. The magnetic separation process by high intensity magnetic separator (HIMS) requires more advanced equipment, so the investment cost is high, but it has the advantages of simple operation, environmental friendliness, and low subsequent operating costs. The concentration of manganese carbonate obtained by magnetic separation is higher than that of heavy concentrate, which is an important means of separating modern industrial manganese ore resources (Wu, 2015; Zou, 2021).

2.1. Material

A manganese carbonate ore containing 9.1% Mn from a deposit in Razavi Khorasan province, Iran, was used for all the experiments. The mineralogical properties of the ore sample were characterized based on optical mineralogy methods using the polished and thin sections by ZEISS polarizing microscope images and XRD analysis. XRD analysis showed that the ore contains calcite, dolomite, quartz, rhodochrosite, and manganite are present in the ore. For major elemental analysis, inductively coupled plasma (ICP), and X-ray fluorescence (XRF) were used (Tables 1 and 2).

Table 1. ICP analysis result

Ca (%)	Mn (%)	Fe (%)	Mg (%)	Al (%)	K (%)	S (%)	Na (%)
10.7	9.1	5.7	1.6	1.2	0.6	0.2	0.1
Zn (ppm)	Pb (ppm)	Sr (ppm)	Ba (ppm)	Cu (ppm)	As (ppm)	Cr (ppm)	Ni (ppm)
620.2	349.7	272.0	155.1	153.6	27.8	22.2	15.6

Table 2. XRF analysis result

SiO_2 (%)	Al_2O_3 (%)	CaO (%)	MgO (%)	MnO (%)	SO_3 (%)	Fe_2O_3 (%)	K_2O (%)	L.O.I (%)
12.3	2.9	27.5	3.5	12.0	0.6	10.1	0.8	31.7

According to Table 3, the liberation degree of Mn mineral was studied in different-size fractions. Mineral liberation degree is the ratio of the number of unlocked particles of mineral to the sum of the number of locked and unlocked particles of mineral. The calculation formula is as follows:

$$df = \frac{n_1}{n_1 + n_2} \times 100 \qquad (1)$$

where *df* is the mineral liberation degree, n_1 is the unlocked content of the mineral, and n_2 is the content of locked particles.

The degree of liberation of Mn mineral has a value of 80% for size fraction (-150+106) μm, slightly increasing to the value of 90% for particles below 38 μm. As shown in Figure 1, gangue minerals are closely related to Mn minerals in coarse sections. With the decrease in the size of the grains, most of the minerals correlation has occurred in binary status, which includes types of correlation between Mn mineral and waste minerals such as manganite-hematite, and manganite-quartz.

Table 3. Degree of liberation of Mn mineral

size fractions (micron)	Mn mineral degree of liberation (%)
+1180	17
-1180, +600	36
-600, +420	48
-420, +300	68
-300, +212	74
-212, +150	77
-150, +106	81
-106, +75	83
-75, +38	87
-38	90
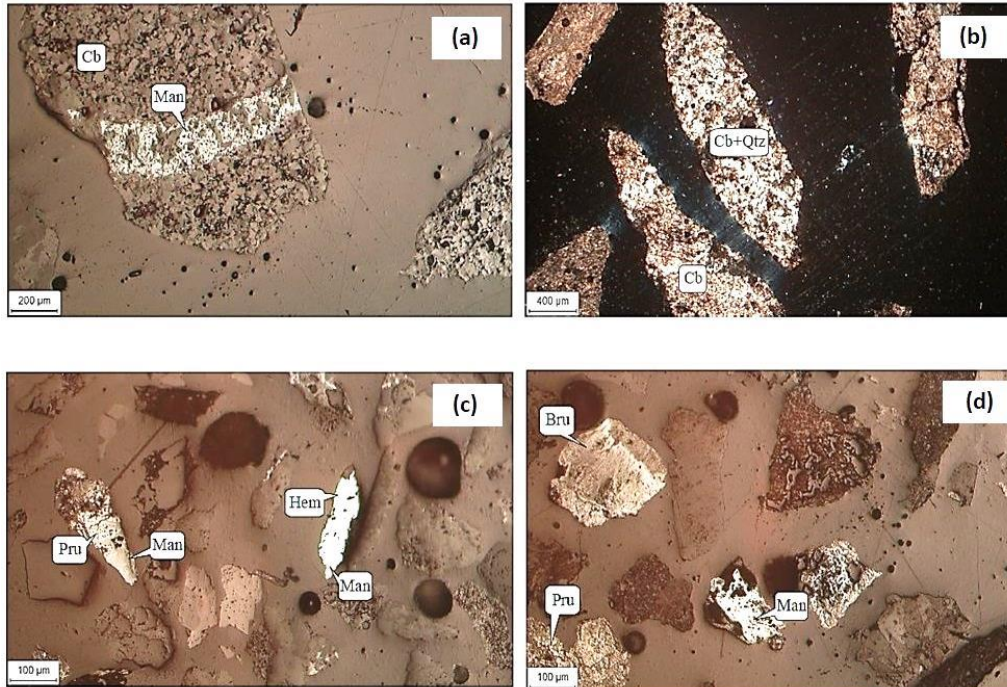
Fig. 1. Mn mineral liberation in different size fractions. (a) manganite-carbonate mineral correlation in (-1180,+600 mic.) fraction (by plane polarized light), (b) carbonate mineral -quartz correlation in +1180 mic.) fraction (by cross polarized light), (c) manganite-hematite and manganite-pyrolusite correlations in (-150, +106 mic.) fraction (by plane polarized light), (d) manganite, pyrolusite and braunite in (-212, +150 mic.) fraction (by plane polarized light).

2.2. Method

Calcination is a thermal treatment process applied to ores and other solid materials in order to bring about thermal decomposition, phase transition, or the removal of a volatile fraction. When it comes to the calcination of manganese carbonate minerals like rhodochrosite ($MnCO_3$), the process typically involves heating the mineral in the absence or limited supply of air (oxygen) to decompose the carbonate into manganese oxide (MnO) and carbon dioxide (CO_2).

Here's a general reaction that describes the calcination of rhodochrosite:

$$MnCO_3 \rightarrow MnO + CO_2 \uparrow \qquad\qquad (2)$$

This reaction usually occurs at temperatures between 450°C and 900°C, depending on the specific conditions and the desired end product. The carbon dioxide is released as a gas, leaving behind manganese(II) oxide. It's important to control the calcination conditions carefully, as excessive temperatures or improper atmosphere control can lead to the formation of unwanted phases or the loss of material through sublimation or volatilization.

After calcination, the resulting manganese oxide can be further processed to produce manganese concentrate using magnetic separation due to turning a diamagnetic mineral (manganese carbonate) into a magnetic mineral (manganese oxide).

2.2.1. Calcination studies

Experimental studies were carried out by using a muffle furnace, which has 30 cm height and 20 cm inner diameter. The temperature could be adjusted to the desired level and kept constant by automatic control. A series of calcination experiments were carried out at the size of -3 mm with various temperatures at 700°C, 800°C, and 900°C (a temperature higher than 900°C is not suitable for the calcination process of manganese carbonate because, according to the experiments conducted, it causes the sample to sinter), and 2 hours as the retention time. After the calcination process, the products were cooled in the furnace atmosphere, and weighted and representative samples were taken for chemical and XRD analyses.

Figure 2 shows the results of manganese oxide analysis in calcined products as well as their weight loss at different temperatures. The results show that as the calcination temperature increases, the weight loss of the calcined product increases, and subsequently the manganese content also increases. At 900°C, 30.8% of the sample weight was lost and the manganese content improved from 9.1% to 11.9%.

The XRD analysis result of calcination experiments is given in Figure 3. As shown in Figure 3, the peaks of carbonate minerals are clearly visible in the products obtained from calcination at 700 and 800 °C, but the product of calcination at 900 °C is completely oxidized compounds.
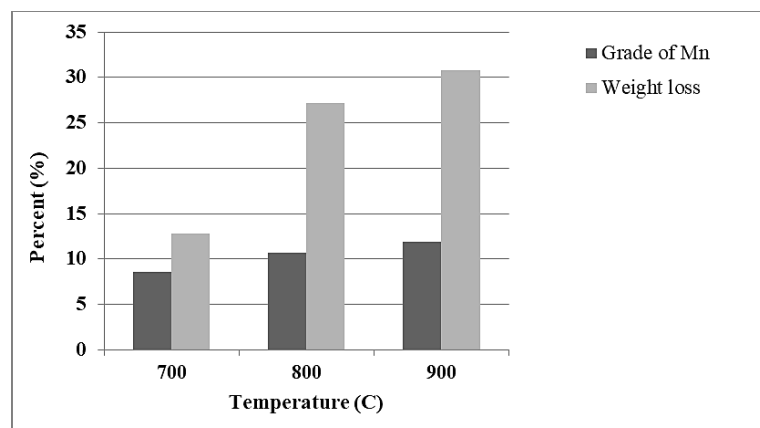
Fig. 2. Calcination result in different temperatures
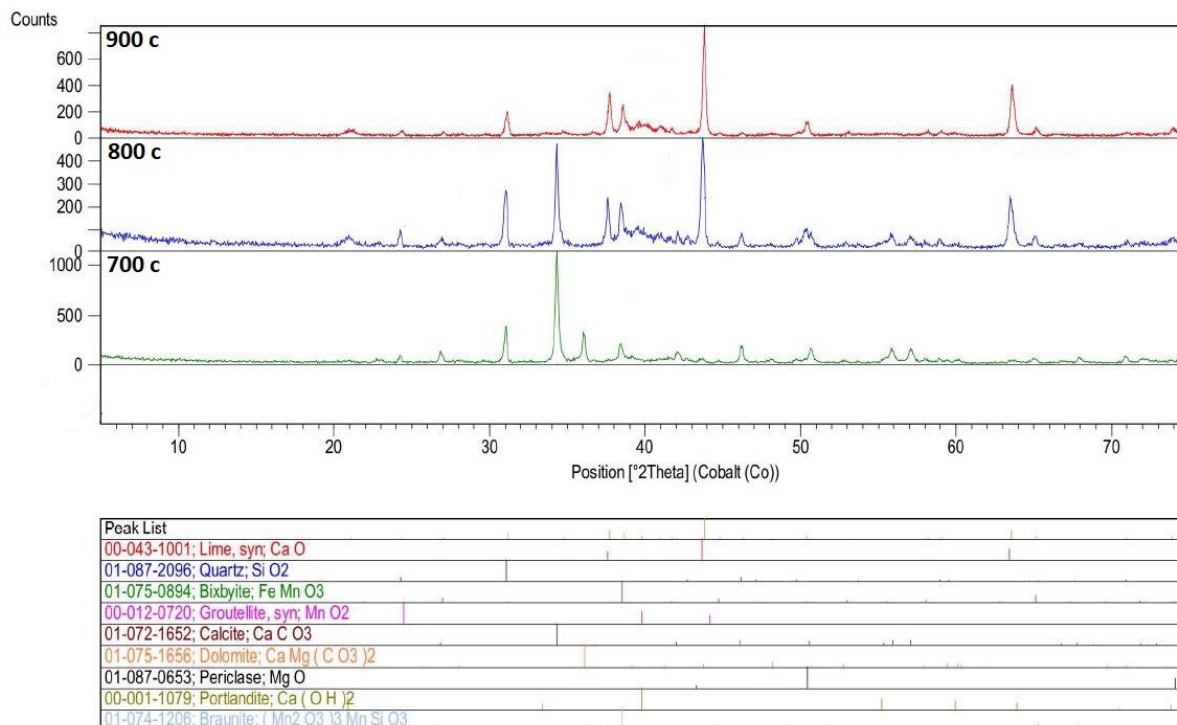
Fig. 3. The XRD analysis in different temperatures

Based on the calcination results, it can be claimed that due to the predominant presence of oxidized compounds (such as bixbyite, and groutelite), as well as the weight loss and significant increase in grade in the calcined product, 900°C is the appropriate calcination temperature.

2.2.2. Optimization of magnetic separation

The calcined product at 800°C undergoes a magnetic separation process in the next purification step. High intensity magnetic separation has been performed on both uncrushed (-3 mm) and crushed (to less than 0.5 mm) calcination products. In high-intensity magnetic separation for particles with a grain size of -3 mm, a belt separator with a dry separation mechanism is used. However, a matrix magnetic separator with a wet separation mechanism is used for particles with a grain size of 0-0.5 mm. Figure 4 shows magnetic separator devices and their operation. Magnetic separation has been done on desliming particles with a grain size of 0.075-0.5 mm and the resulting fine particles (<0.075 mm) separately.

The results of magnetic separation experiments aimed at investigating different grain sizes at a magnetic field intensity of 12,000 Gauss are given in Table 4.

Although the use of a dry belt separator for the calcined product with a grain size of -3 mm and a magnetic field intensity of 12,000 Gauss had a high grade recovery and was able to absorb about 95% of manganese, the manganese grade experienced a relatively small increase from 10.7% to 14%. The very high magnetic absorption indicates a proper calcination process and acceptable conversion of carbonate minerals to oxidized minerals.

Particles smaller than -75 microns do not have good magnetic field absorption and therefore the size of 75-500 microns has the highest manganese recovery in the concentrate. Also, the size of 0-500 microns leads to a manganese grade of 22% with a recovery of 76.3%, and the manganese grade in the

tailings is reduced to about 4%. Therefore, it can be claimed that the calcination process and subsequent magnetic separation at the size of -500 microns leads to achieving the optimal amount of grade and manganese recovery.

Table 4. Results of magnetic separation experiments at various grain sizes (magnetic field intensity of 12,000 Gauss)

Particle size (mm)	Feed		Concentrate			Tail		
	Weight percent (%)	Mn grade (%)	Weight percent (%)	Mn grade (%)	Mn recovery (%)	Weight percent (%)	Mn grade (%)	Mn recovery (%)
-3	100	10.7	72.0	14.1	94.9	28.0	2.0	5.1
-500	100	10.7	37.1	22.0	76.3	62.9	4.0	23.7
75-500	100	10.2	51.8	18.0	91.4	48.2	1.8	8.5
-75	100	10.9	27.4	22.5	56.6	72.6	6.5	43.3
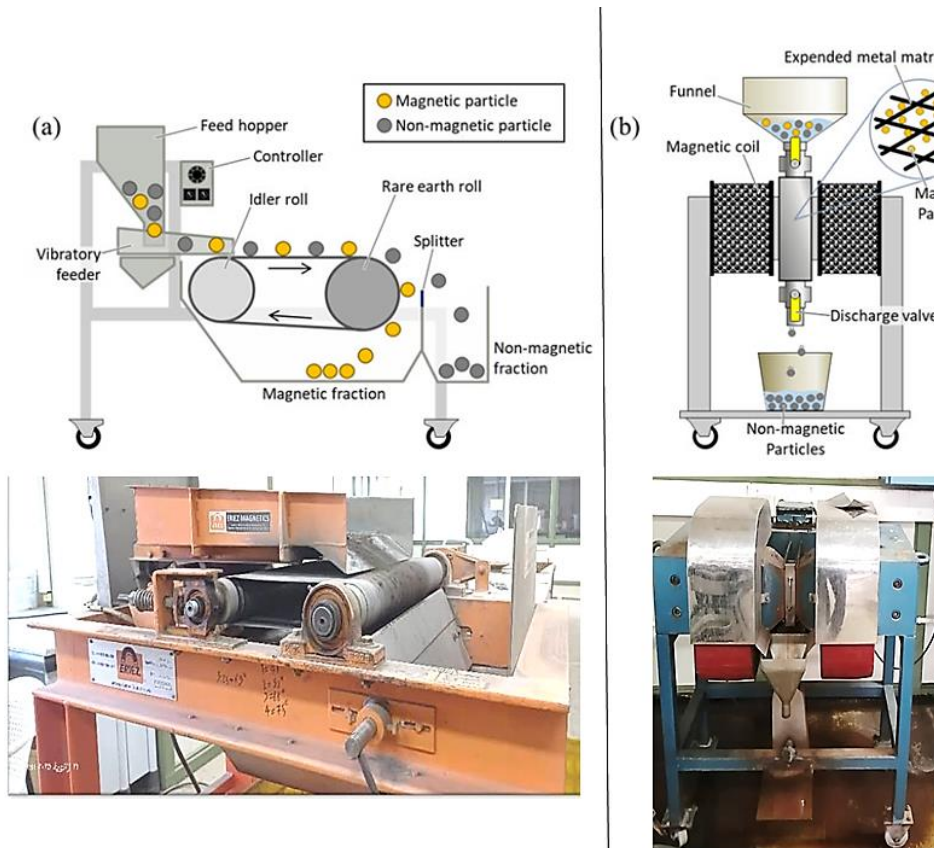
Fig. 4. Schematic diagrams and devices of (a) dry high-intensity magnetic belt separator and (b) wet high-intensity magnetic matrix separator

According to the results obtained from determining the appropriate grain size for magnetic separation, by grinding calcined products at temperatures of 700, 800, and 900°C up to grain size of less than 0.5 mm, magnetic field strengths of 8,000 Gauss and 12,000 Gauss have been used for manganese enrichment. The purpose of these experiments is to investigate the enrichment ability of

calcined manganese at different magnetic field intensities. The result of magnetic separation experiments aimed at investigating different magnetic field intensities is shown in Table 5.

Table 5. results of magnetic separation experiments at various magnetic field intensities (grain size of -3 mm)

Temperature of calcination (^{o}C)	magnetic field intensity (G)	Feed		Concentrate			Tail		
		Weight percent (%)	Mn grade (%)	Weight percent (%)	Mn grade (%)	Mn recovery (%)	Weight percent (%)	Mn grade (%)	Mn recovery (%)
700	8000	100	8.6	23.2	20.1	54.2	76.8	5.1	45.8
	12000	100	8.6	32.0	19.4	72.2	68.0	3.5	27.8
800	8000	100	10.7	32.6	23.0	70.4	67.4	4.7	29.6
	12000	100	10.7	37.1	22.0	76.3	62.9	4.0	23.7
900	8000	100	11.9	54.0	18.2	82.6	46.0	4.5	17.4
	12000	100	11.9	70.0	15.2	89.4	30.0	4.2	10.6

In accordance with Table 5, the calcined product at higher temperatures resulted in better recovery at magnetic field strengths of 8000 and 12000 Gauss, but the maximum manganese grade was only achieved in the calcined product at 800°C. Magnetic separation of the calcined product at 800°C with field strengths of 8,000 and 12,000 Gauss has resulted in the production of manganese concentrate with grades of 23% and 22%, as well as recoveries of 70.4% and 76.3%, respectively. By applying a coefficient of 1.58 to the values of manganese content in the concentrate, it is possible to estimate manganese dioxide (MnO_2) contents of more than 34% for the concentrates of both magnetic field intensities of the calcined product at 800°C.

3. Conclusions

The study investigated the beneficiation of manganese carbonate ore from a deposit in eastern Iran using calcination and magnetic separation. Although the optimum calcination temperature was 900°C, which increased the manganese content from 9.1% to 11.9% by converting carbonate minerals to oxides, better magnetic separation occurred in the product calcined at 800°C. Magnetic separation at 12,000 Gauss on calcined products with a grain size of less than 0.5 mm yielded a manganese concentrate with a grade of 34.9% MnO_2 and a recovery of 76.3%. The results demonstrated that the combined process of calcination and magnetic separation is effective for enriching manganese from low-grade carbonate ores, with the potential for industrial application. The study concluded that controlling calcination temperature and optimizing magnetic separation parameters are crucial for achieving high-grade manganese concentrates.

Acknowledgments

References

Baba, A. , Ibrahim, L. , Adekola, F. , Bale, R. , Ghosh, M. , Sheik, A. , Pradhan, S. , Ayanda, O. and Folorunsho, I. (2014). Hydrometallurgical Processing of Manganese Ores: A Review. *Journal of Minerals and Materials Characterization and Engineering*, 2, 230-247. doi: 10.4236/jmmce.2014.23028.

Dunne, R., Komar Kawatra, S.,bYoung, C. (2019). *SME mineral processing and extractive metalurgy handbook*. (vol. 1): society for mining, metallurgy and exploration.

Hudson Institute of Mineralogy (2015). *Mindat.org database [various minerals]*. www.mindat.org/. Accessed March 2025.

Maghfouri, S., Rastad, E., Movahednia, M., David-R. L. , Hosseinzadeh, M. R., Lin Ye, Mousivand, F. (2019). Metallogeny and temporal–spatial distribution of manganese mineralizations in Iran: Implications for future exploration. *Ore Geology Reviews*, 115. doi: https://doi.org/10.1016/j.oregeorev.2019.103026.

Matos, G.R., Corathers, L.A. (2005). *Manganese end-use statistics*. Reston, V A: U.S. Geological Survey.

Mukherjee, A., Raichur, A.M., Natarajan, K.A., and Modak, J.M. (2004). Recent developments in processing ocean manganese nodules- A critical review. *Mineral Processing and Extractive Metallurgy Review*, 25,2, 91-127. doi: 10.1080/08827500490433188.

Sivrikaya, Osman & Arol, A. (2017). *Investigation of Beneficiation of a Manganese Ore by Jig*. XVII Balkan Mineral Processing Congress.

Wills Barry A., Tim Napier-Munn (2006). *Wills' Mineral Processing Technology*, An Introduction to the Practical Aspects of Ore Treatment and Mineral, Recovery, 7th edition, Elsevier Science & Technology Books.

Wu, Yan, Shi, B., Ge, W., Yan, C., Yang, X. (2014). Magnetic Separation and Magnetic Properties of Low-Grade Manganese Carbonate Ore. *The journal of the Minerals, Metals and Materials Society*. 67. 361-368. doi: 10.1007/s11837-014-1212-8.

You, Zhixiong, Li, Guanghui, Zhang, Yuanbo, Peng, Zhiwei. (2015). Extraction of manganese from iron rich MnO_2 ores via selective sulfation roasting with SO_2 followed by water leaching. *Hydrometallurgy*. 156. doi:10.1016/j.hydromet.2015.05.017.

Zou, Song & Wang, Shuai & Zhong, Hong & Qin, Wenqing. (2020). Hydrophobic agglomeration of rhodochrosite fines in aqueous suspensions with sodium oleate. *Powder Technology*, 377. doi: 10.1016/j.powtec.2020.08.019.

Optimization of effective parameters in the leaching of sodium and potassium salts from electric arc furnace dust

Hossein Habibi[1]*, Ziaeddin Pourkarimi[1], Seyed Hossein Hashemi[1], Dorna Pirouzan[1], Gholamreza Parvareh[1] ,Mahdi Rahimi[1]

[1] Iran Mineral Processing Research Center (IMPRC)

*Corresponding author: PSDKHabibi@gmail.com (Hossein Habibi)

Abstract:

This study optimized water-based leaching parameters for recovering Na and K salts from Electric Arc Furnace (EAF) dust, while enhancing iron content in the residue. Characterization revealed the dust contained 14% Na_2O, 10.7% K_2O, and 45.3% Fe_2O_3, with particles <15 µm. Response Surface Methodology (RSM) identified temperature (60-70°C) as the most critical factor, achieving 83% Na and 68% K recovery at 25% solid content over 60 minutes. The process enriched the iron grade in the residue by 25% (from 32% to 40% Fe), as validated through large-scale experiments. The method offers dual environmental and economic benefits by minimizing waste and recovering valuable salts.

Keywords: Electric Arc Furnace (EAF) Dust , Sodium and Potassium, Water-Based Leaching, Environmental Sustainability , Waste Minimization

1. Introduction

During the melting and steelmaking process in an electric arc furnace (EAF), a significant amount of dust is generated when charging iron-bearing materials and steel scrap into the furnace. On average, 10 to 20 kg of dust is produced per ton of steel. The large volume of dust creates major challenges. First, transportation and storage require extensive space and high costs. Additionally, the current method of storing the produced dust is not a sustainable solution, as it continuously demands more space and poses environmental risks.

Since the introduction of dust collection systems, the steel industry has been dealing with similar materials such as dust or sludge. Environmental concerns, rising transportation costs, and collection expenses have become critical challenges in this industry. Therefore, from the early days, the reuse of dust and sludge in steel production was considered. However, significant progress was only made when the economic benefits of dust recycling became evident. The first successful attempts involved reusing dust in processes such as sintering, blast furnaces, converters, and EAFs .

The primary sources of elements entering EAF dust are raw materials such as scrap and additives. According to previous studies, EAF dust can be categorized based on its chemical composition:

a) Dust from plants that use galvanized scrap, which contains high levels of zinc and lead. These elements contribute to environmental pollution, making their extraction economically valuable. Various products can be obtained, such as crude zinc oxide for further metallurgical refining, iron-rich materials for furnace charging, or useful slag and sponge iron for steelmaking.

b) Dust from alloy and stainless steel production plants. This type of dust contains significant amounts of nickel and chromium. Several recycling methods for EAF dust have been developed, including raw pelletization , PTC , briquetting, Calx briquetting , and direct injection into the furnace [16]. These methods involve mixing dust with other byproducts such as mill scale and slag, with or without binders and reductants (e.g., coke or ferrosilicon), forming pellets or briquettes, and reintroducing them into the

furnace. Such methods are particularly suitable for alloy steel plants, where the dust contains valuable materials like nickel and chromium, which can be effectively recovered in the furnace .

c) Dust from plants that use charge materials with low zinc and lead content but significant amounts of sodium, potassium, and iron. A common method for recycling EAF dust is returning it to the furnace to recover Fe and C. However, this approach reintroduces other elements like potassium, sodium, zinc, and lead into the furnace, which can negatively affect its operation. Recovering sodium and potassium salts is economically beneficial.

EAF dust recycling methods often have limitations, such as requiring high capacity for economic feasibility and significant capital investment. Currently, the combination of hydrometallurgical and pyrometallurgical methods for recovering zinc, lead, potassium, sodium, copper, nickel, and other valuable elements on a smaller scale has gained importance. Research on EAF dust recovery in the steel industry has been ongoing for years, with numerous process proposals involving hydrometallurgical, pyrometallurgical, or hybrid approaches. Some solutions suggest integrating EAF dust with other materials at ambient or high temperatures. However, only pyrometallurgical processes (high-temperature metal recovery, HTMR) have achieved significant commercial success, primarily based on modifications of the Waelz process.

Since most steel plants generate dust with high zinc and lead content, most research has focused on processing EAF dust based on its iron and zinc content. In many cases, zinc recovery is the primary driver, as its recovery rate directly affects process economics. Over the past 22 years, many EAF dust recovery projects in the United States have failed, leading to the abandonment of older technical approaches such as the Waelz process. Economic challenges, lack of technical refinement, and insufficient prior studies have contributed to these failures. Consequently, EAF dust processing remains complex, with several influencing factors, including:

Particle size and bulk density: Most particles are smaller than 10 microns, and the bulk density of EAF dust ranges from 1.1 to 2.5 g/cm³ [17,21]. Due to the fine particle size, agglomeration (pelletization or briquetting) is often required before pyrometallurgical recovery to prevent pneumatic dispersion .

Zinc content: The presence of zinc is the main reason for EAF dust recovery. Its concentration significantly impacts process economics.

Zinc mineralogy: Zinc in EAF dust typically appears as franklinite (Fe_2ZnO) and zincite (ZnO). This distinction is crucial in hydrometallurgical processing, as zincite dissolves easily in leaching solutions, whereas franklinite is a stable oxide that requires harsh hydrodynamic conditions for dissolution.

Halide compounds: Most halides exist as potassium and sodium chlorides. Depending on the composition and process, halides can have varying degrees of negative effects.

Other metals: EAF dust contains lead, cadmium, chromium, nickel, and copper in varying amounts. In hydrometallurgical processes, these metals often need to be separated before zinc recovery due to technical constraints.

Copper contamination: Copper can contaminate the recovered iron from EAF dust, particularly in pyrometallurgical processes where iron recovery occurs alongside zinc extraction.

At Mobarakeh Steel Company, large amounts of Electric Arc Furnace (EAF) dust are produced, requiring collection and recovery to avoid environmental pollution. About 80% of the charge materials are sponge iron, leading to a higher iron content in the dust compared to plants using only scrap. The dust also contains significant levels of zinc, sodium, and potassium, which pose environmental risks. The proposed recovery process involves extracting iron concentrate, recovering sodium and potassium salts, and safely disposing of the remaining waste, reducing iron loss and mitigating environmental concerns..

2. Material and methods

The dust sample was prepared by Mobarakeh Steel Company (Isfahan) from the stockpile of collected dust from the electric arc furnaces in the plant and provided to the researchers. The particle size distribution of the sample was determined using a laser particle size analyzer.

For precise determination of the total iron content in the sample, wet chemistry methods and titration were employed. To identify the chemical composition of the sample, two representative samples were analyzed using Inductively Coupled Plasma (ICP) and X-ray Fluorescence (XRF) spectroscopy.

For mineralogical studies, X-ray diffraction (XRD) and scanning electron microscopy (SEM) were used.

leaching experiments were conducted using a water-based system to investigate the influence of critical variables—temperature, solid content, and leaching time—on the recovery of sodium and potassium. The primary objective was to optimize the dissolution of sodium and potassium salts while maximizing the iron content in the residual filter cake. The experimental design was based on Response Surface Methodology (RSM), using the DX7 software to explore the interaction between these variables and determine their optimal levels for efficient leaching. Each test was carried out with 300 grams of the sample, using ordinary water in a glass vessel placed on a hot plate, accompanied by mechanical stirring to ensure uniform mixing. The factors chosen—temperature, solid content, and time—were selected based on their known influence on the solubility and leaching kinetics of the target elements.

The pregnant leach solution (PLS) was analyzed by ICP while the leach residues were characterized using both titration and ICP techniques.

3. Results and Discussion

3.1. Particle Size Distribution of the Sample

The particle size distribution of the sample, and the distribution chart is presented in Figure 1. Based on the analysis, the d_{80} of the sample is 4 microns, and 100% of the material is finer than 15 microns.
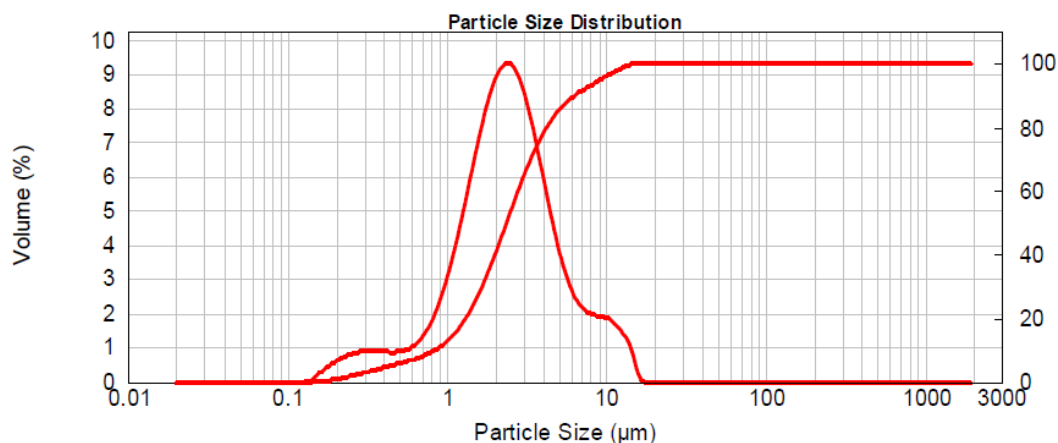
Figure 1 .Particle size distribution of the sample.

3.2. Chemical Characterization of the Sample

The total iron content in the sample was found to be approximately 32%. The results of other analyses are presented in Table 1 and Table. 2.

Table 1. XRF analysis results of the feed sample

SiO$_2$ (%)	Al$_2$O$_3$ (%)	CaO (%)	MgO (%)	Fe$_2$O$_3$ (%)	MnO (%)	SO$_3$ (%)	P$_2$O$_5$ (%)	Na$_2$O (%)	K$_2$O (%)	ZnO (%)	Cl (%)	Rb$_2$O (%)	SUM (%)	L.O.I (%)
3.62	0.35	5.10	2.54	45.29	0.52	0.56	0.39	14.12	10.74	2.14	0.21	0.12	85.7	14.07

Based on the XRF analysis, the sample contains approximately 14% Na$_2$O, 7.1% K$_2$O, and 32% iron as key valuable components. The sample also contains 2% zinc oxide, 5% calcium oxide, and 2.5% magnesium oxide.

Table. 2. ICP analysis results of the feed sample

Al (%)	As (ppm)	Ca (%)	Cr (ppm)	Cu (ppm)	Fe (%)	K (%)	La (ppm)	Mg (%)
0.41	18.5	4.1	63	72	15	5.01	15	2.21
Mn (ppm)	Na (%)	Ni (ppm)	P (%)	Pb (ppm)	Sr (ppm)	Ti (%)	V (ppm)	Zn (ppm)
1557	8.88	14.5	0.24	616	16.00	0.04	554.00	6917.50

The ICP results indicate that the sample contains 5% potassium and 8.88% sodium, with the zinc content being below 0.7%.

3.3. Mineralogical Characterization of the Sample

3.3.1. X-ray Diffraction (XRD) Studies

X-ray diffraction (XRD) analysis revealed that the sample primarily consists of iron oxide phases such as magnetite and wüstite, along with phosphosiderite (iron phosphate), sodium carbonate, and diopside. The XRD pattern for the sample is shown in Figure 2.
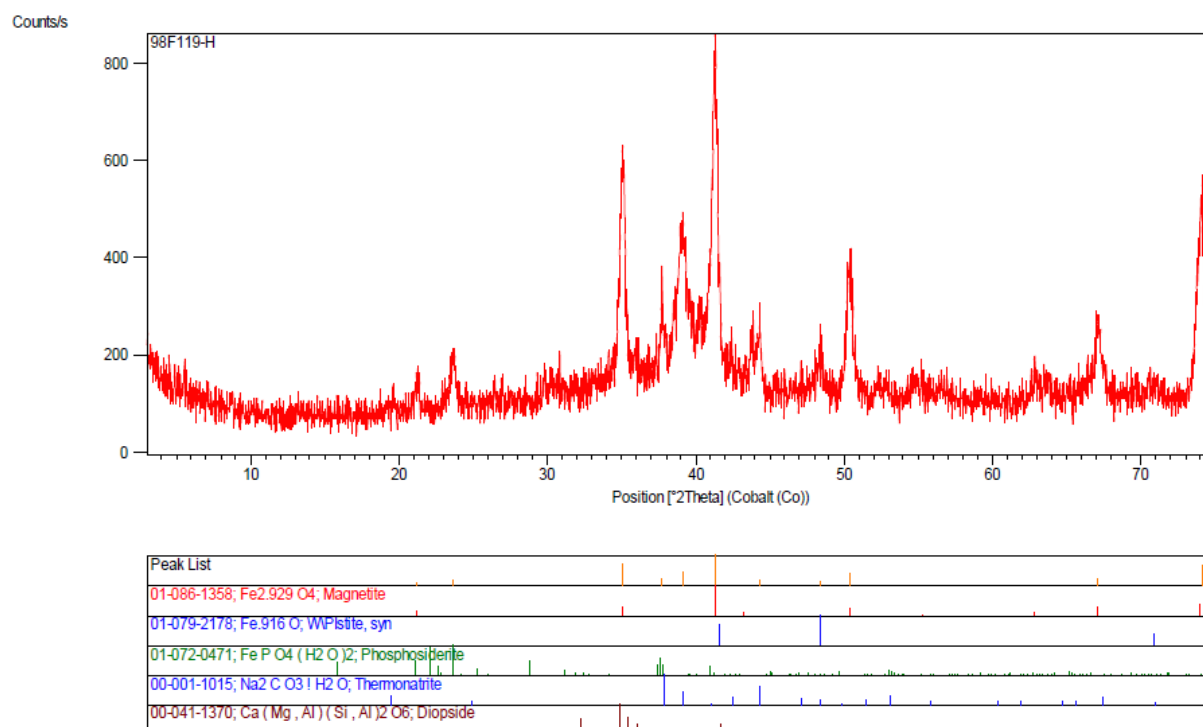
Figure 2 .X-ray diffraction pattern of the dust sample.

3.3.2. Scanning Electron Microscopy (SEM) Studies

Electron microscopy studies were conducted on a polished thin section of the sample. Significant amounts of iron oxides (mainly magnetite, with traces of hematite and goethite) were observed as fine and coarse particles dispersed throughout the sample. In some regions, calcium and potassium were also identified in association with iron oxides. Some iron carbonate, specifically siderite, was identified within the sample. Other minerals and phases identified include a significant amount of pyroxene, some calcite, and minor amounts of silicate minerals such as diaspore and biotite. The Energy Dispersive X-ray Spectroscopy (EDS) analysis results obtained from the SEM are provided in the appendix. Most of the oxides are spherical in shape, and dendritic iron solidification particles, fine and coarse oxide particles, siderite, calcite, biotite, pyroxene, as well as calcium- and potassium-containing iron oxides were observed throughout the sample. In Figure 3, one of the EDS analyses obtained by the SEM is shown.
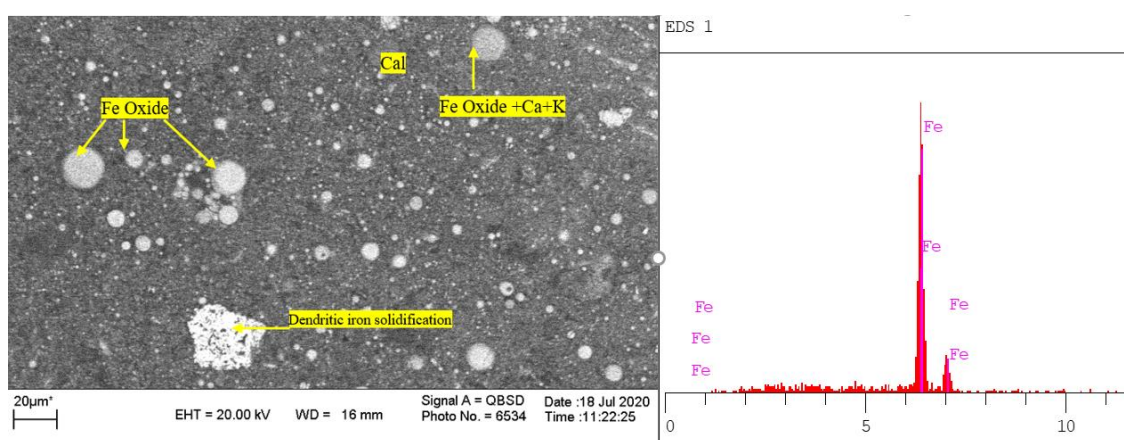
Figure 3 .One of the EDS analyses obtained by the SEM

3.4. Leaching

The experimental parameters and their respective ranges are summarized in Table 3.

Table 3. Experimental Variables for Salt Leaching

Variable Name	Unit	Lower Limit	Upper Limit
A: Temperature	°C	25	60
B: Solid content	%	15	25
C: Time	min	30	60

After conducting the leaching experiments, the samples were filtered, with the filter cake undergoing one or two washing steps before being sent for chemical analysis. It is important to note that the fine particle size of the sample posed challenges during filtration, which was a slow process due to the high specific surface area of the particles. The results from these experiments, focusing on the recovery of sodium and potassium as well as the iron concentration in the filter cake relative to its initial content, are presented in Table 4.

Table 4. Results of the water-based salt leaching experiments with agitation

	Experimental conditions			Products		Solid grade			Solution grade		Results and recovery		
run	Temp (°C))	SR (%)	Time (min)	V (cc)	W (gr)	Fe (%)	Na (%)	K (%)	Na (ppm)	K ppm	Na (%)	K (%)	*Ratio Fe
1	25	25	60	1010	244.3	37	3.38	6.75	13886	17005	68.7	26.7	1.17
2	40	20	45	1200	233.2	39	2.92	5.55	14988	18840	74.2	42.5	1.22
3	70	20	45	1240	207	42	1.8	3.1	16758	21075	88.8	74.6	1.31
4	40	10	45	1630	235.5	39	2.82	5.13	12264	15280	74.8	46.3	1.23
5	40	20	45	1240	238.8	39	3.03	5.8	15444	19490	72.6	38.4	1.21
6	40	20	45	1190	237.7	39	2.88	5.24	16074	20480	74.1	44.6	1.22
7	25	15	30	1800	224.2	40	2.9	5.56	11430	14025	75.4	44.6	1.25
8	40	30	45	700	209.4	39	2.94	6.12	24150	30160	76.7	43.0	1.23
9	40	20	45	1230	234	40	2.6	4.62	16302	20285	77.0	52.0	1.25
10	13	20	45	1330	238.8	38	3.24	6.5	14130	17025	70.7	31.0	1.19
11	60	25	60	960	216.2	41	2.03	3.25	22254	27600	83.4	68.8	1.28
12	40	20	70	1240	229.2	39	2.64	4.66	16566	20790	77.1	52.5	1.23
13	25	25	30	1050	213.2	39	2.72	5.42	18198	22005	78.0	48.6	1.22
14	60	15	30	1720	208.7	42	2.1	3.57	12804	15860	83.4	66.9	1.30
15	60	15	60	1650	209.7	42	1.86	3.1	13434	16780	85.2	71.1	1.30
16	40	20	20	1230	222.2	40	2.58	4.68	16434	20180	78.3	53.8	1.25
17	40	20	45	1210	218.7	40	2.36	4.72	17034	20444	80.4	54.1	1.24
18	40	20	45	1160	221.2	40	2.58	4.81	17466	21295	78.4	52.7	1.25
19	60	25	30	890	219.2	42	2.63	4.24	22602	28510	78.2	58.7	1.31
20	25	15	60	1850	238.2	38	2.8	5.45	11154	13485	74.736	42.3	1.19

*The iron grade increase ratio is equal to the ratio of the iron grade in the product to the iron grade in the feed

3.5. Investigation of Potassium Dissolution

3.5.1. ANOVA Analysis

Based on p-values less than 0.05, the factors influencing potassium dissolution were determined. According to Table 5 , only the temperature variable individually affects potassium dissolution. Additionally, there is a minor interaction between temperature and dissolution time. Solid percentage and time alone did not have a significant impact on dissolution within the selected range, but the combined effect of temperature and time is worth investigating.

Table 5 .ANOVA for Potassium Dissolution

Source	Sum of Squares	df	Mean Squares	F value	p-value (Prob > F)
Model	2022.91	2	1011.46	34.25	< 0.0001
A-temp	1870.04	1	1870.04	63.33	< 0.0001
AC	152.87	1	152.87	5.18	0.0361
Residual	501.97	17	29.53	-	-

Source	Sum of Squares	df	Mean Squares	F value	p-value (Prob > F)
Lack of Fit	332.13	12	27.68	0.81	0.6451
Pure Error	169.84	5	33.97	-	-
Cor Total	2524.88	19	-	-	-
Statistics					
Std. Dev.	5.43		R-Squared	0.8012	
Mean	46.81		Adj R-Squared	0.7778	
C.V. %	11.61		Pred R-Squared	0.7256	
PRESS	692.81		Adeq Precision	18.702	

Model: The proposed model is significant (p-value < 0.0001) and explains 80.12% of the data variability (R-Squared = 0.8012).

Temperature (A): Temperature has a highly significant effect on potassium dissolution (p-value < 0.0001).

Interaction of Temperature and Time (AC): The interaction between temperature and time also has a significant effect (p-value = 0.0361).

Lack of Fit: The model fits the data well (p-value = 0.6451).

Effect of Temperature and Time on Potassium Dissolution

Effect of Temperature: Increasing temperature significantly enhances potassium recovery and dissolution (Figure 5).

Effect of Time: At low temperatures (ambient temperature), increasing time reduces dissolution, whereas at high temperatures, increasing time improves recovery (Figure 6).

3.5.2. Mathematical Model

Based on the obtained model, the relationship for potassium recovery as a function of temperature and time is defined as follows:

Potassium Recovery (K)=50.66+12.92×A+4.82×A×C   (Equation 1)

Where:

A: Coded temperature (based on software coding) -C: Coded time (based on software coding)
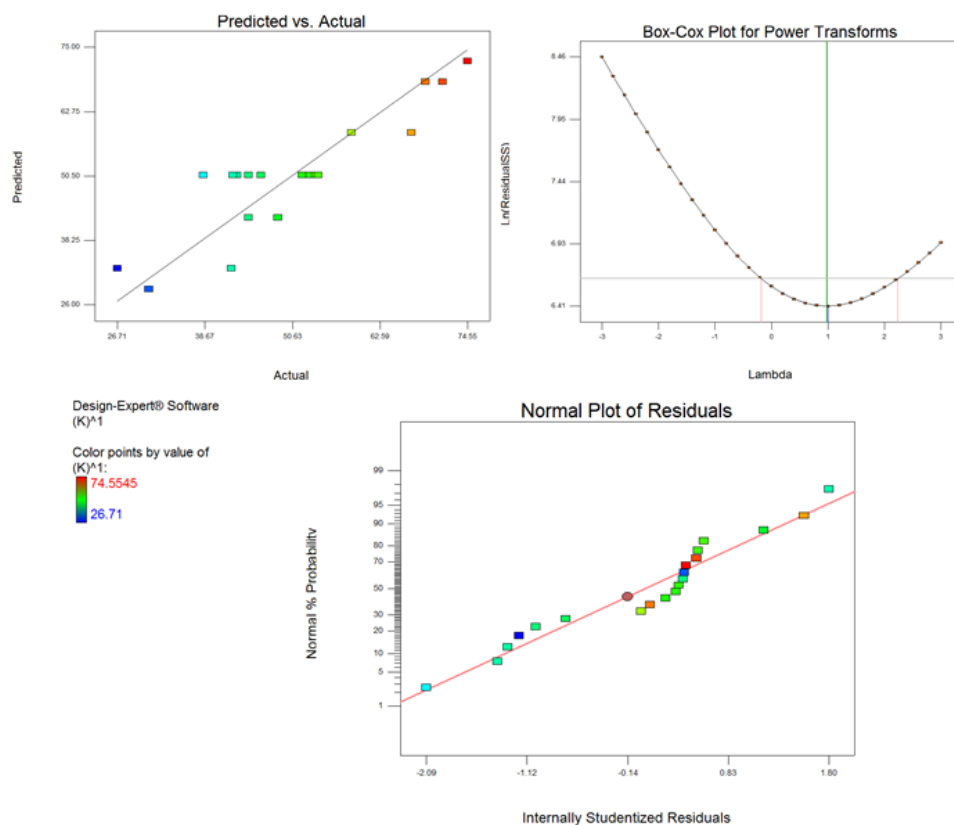
Figure 4 .BOX-COX plots, normal residuals, and actual vs. predicted values for the experimental design of potassium recovery
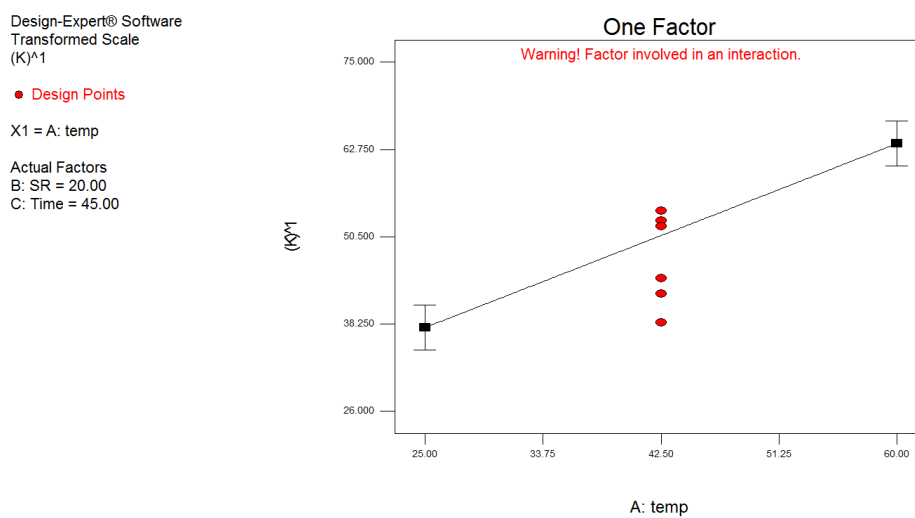
Figure 5 .Graph of potassium dissolution recovery as a function of temperature.
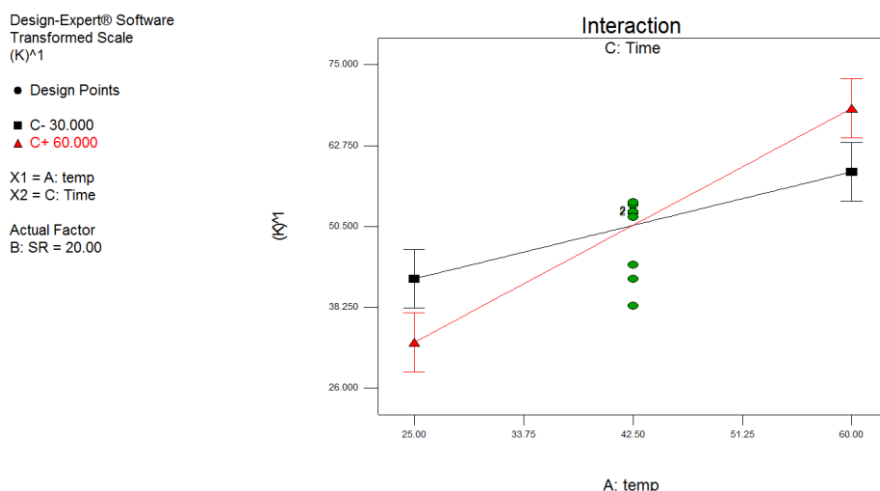
Figure 6 .Interaction plot of time and temperature for potassium dissolution recovery.

3.6. Investigation of Sodium Dissolution

3.6.1. ANOVA Analysis

Based on p-values less than 0.05, the factors influencing sodium dissolution were determined. According to Table 3–4, only the temperature variable individually affects sodium dissolution. Additionally, there is a minor interaction between temperature and dissolution time. Solid percentage and time alone did not have a significant impact on dissolution within the selected range, but the combined effect of temperature and time is worth investigating.

Table 6 .ANOVA for Sodium Dissolution

Source	Sum of Squares	df	Mean Squares	F value	p-value (Prob > F)
Model	1.840E-005	2	9.201E-006	22.54	< 0.0001
A-temp	1.623E-005	1	1.623E-005	39.77	< 0.0001
AC	2.169E-006	1	2.169E-006	5.32	0.0340
Residual	6.938E-006	17	4.081E-007	-	-
Lack of Fit	4.231E-006	12	3.526E-007	0.65	0.7489
Pure Error	2.707E-006	5	5.413E-007	-	-
Cor Total	2.534E-005	19	-	-	-
Statistics					
Std. Dev.	6.39E-04		R-Squared	0.7262	
Mean	0.021		Adj R-Squared	0.694	
C.V. %	3.06		Pred R-Squared	0.6106	
PRESS	9.87E-06		Adeq Precision	14.821	

Model: The proposed model is significant (p-value < 0.0001) and explains 72.62% of the data variability (R-Squared = 0.7262).

Temperature (A): Temperature has a highly significant effect on sodium dissolution (p-value < 0.0001).

41

Interaction of Temperature and Time (AC): The interaction between temperature and time also has a significant effect (p-value = 0.0340).

Lack of Fit: The model fits the data well (p-value = 0.7489).

Effect of Temperature: Increasing temperature significantly enhances sodium recovery and dissolution (Figure 3–5).

Effect of Time: At low temperatures (ambient temperature), increasing time reduces dissolution, whereas at high temperatures, increasing time improves recovery (Figure 3–6).

3.6.2. Mathematical Model

Based on the obtained model, the relationship for sodium recovery as a function of temperature and time is defined as follows:

Sodium Recovery (Na)−0.89=0.021−1.090×10−3×A−5.207×10−4×A×C   *(Equation 2)*

Where:

A: Coded temperature (based on software coding)

C: Coded time (based on software coding)
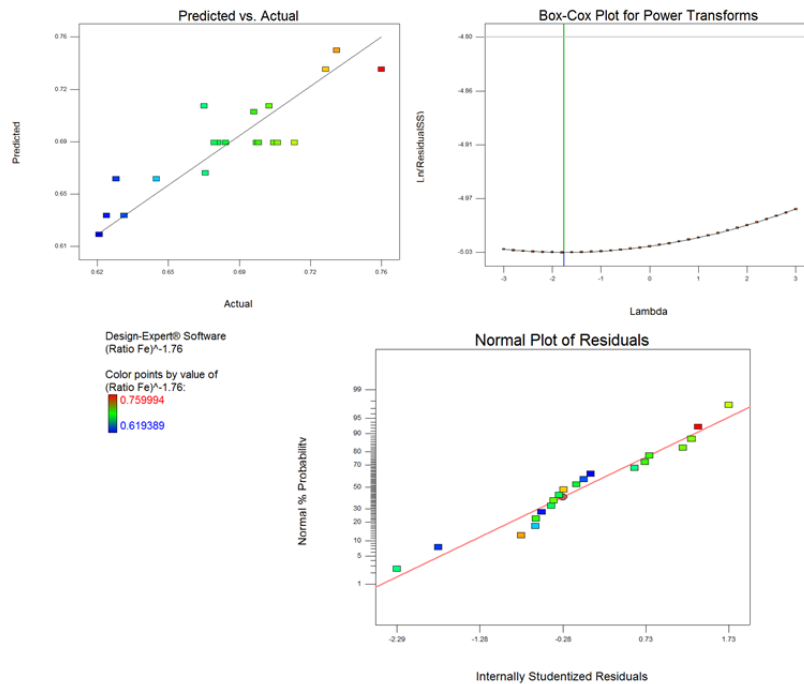
Figure 7. BOX-COX plots, normal residuals, and actual vs. predicted values for the experimental design of sodium recovery.
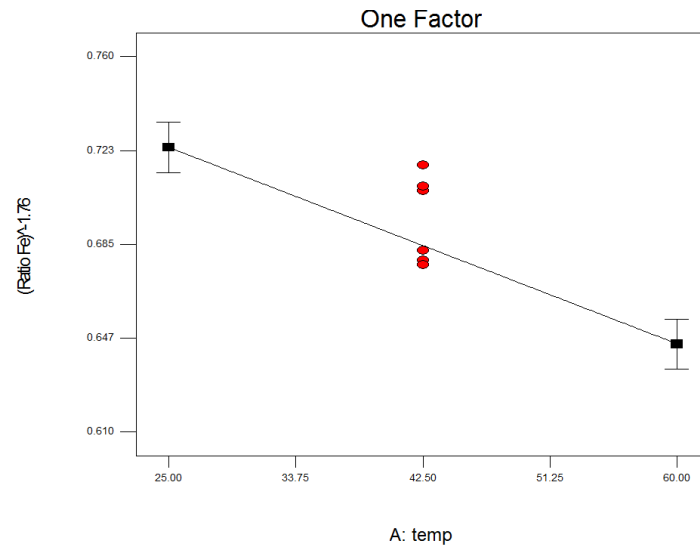
Figure 8. Graph of sodium dissolution recovery as a function of temperature.
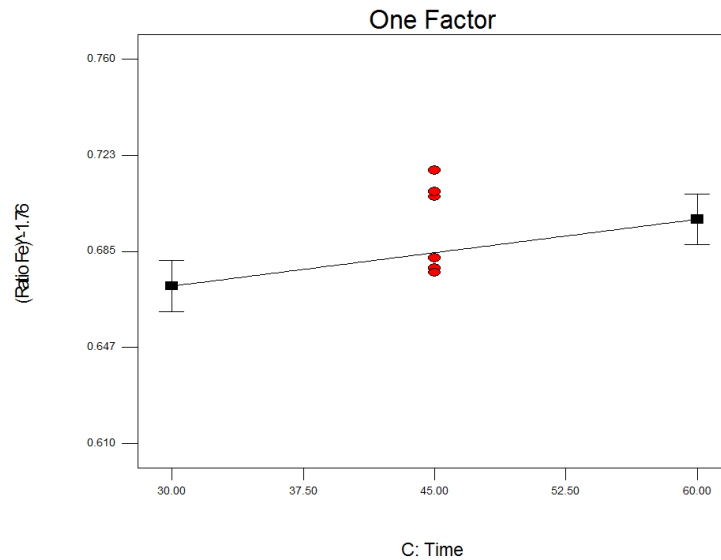
Figure 9. Interaction plot of time and temperature for sodium dissolution recovery.

3.7. Optimization

Based on the obtained results, optimization was performed using software to maximize the recovery of potassium and sodium, as well as to achieve the highest iron ratio in the product relative to the feed, with a desirability of 85%. The optimal conditions were determined to be:

Time: 60 minutes , Temperature: 60–70°C , Solid content: 25%

Under these conditions, the following results were achieved:

Potassium recovery: 68% , Sodium recovery: 83% , Iron grade increase ratio: 1.25

To validate the proposed model, a verification experiment was conducted under conditions similar to Experiment No. 11 in Table 3–2. The results were consistent, with potassium recovery at approximately 68.8%, sodium recovery at 83%, and an iron grade increase ratio of 1.28.

3.8. Large-Scale Leaching Experiment

A large-scale leaching experiment was conducted using 20 kg of the sample under the optimized laboratory conditions. The sample was washed with 60 liters of water at a temperature above 60°C for 1 hour. The chemical analysis of the solid residue is presented in Table 7, and the analysis of the resulting solution is provided in Table 8.

Table 7. ICP Analysis of the Washed Solid Residue

Al (%)	Bi (ppm)	Ca (%)	Ce (ppm)	Cr (ppm)	Cu (ppm)	K (%)	La (ppm)	Mg (%)	Mn (ppm)
0.53	256	5.28	162	70	398	1.75	37	2.67	3300
Na (%)	Ni (ppm)	P (%)	Pb (ppm)	S (%)	Fe (%)	Sr (ppm)	Ti (%)	V (ppm)	Zn (ppm)
1.94	37	0.36	739	0.35	41	49	0.87	622	14233

Table 8. ICP Analysis of the Leach Solution

Al (ppm)	As (ppm)	Ba (ppm)	Ca (ppm)	Cr (ppm)	Fe (ppm)	K (ppm)
27.53	11	0.01	3.09	29.02	0.85	19100
Mg (ppm)	Mo (ppm)	Na (ppm)	P (ppm)	Sb (ppm)	Si (ppm)	V (ppm)
0.73	0.98	21500	87.26	0.18	70.64	120.8

Large-scale experiments demonstrated the feasibility of scaling up the process, with significant recovery of sodium and potassium and enrichment of iron in the solid residue.

4. Conclusions

This study investigated the recovery of sodium and potassium salts from Electric Arc Furnace (EAF) dust generated during steelmaking processes at Mobarakeh Steel Company. The research focused on optimizing the leaching process to maximize the dissolution of sodium and potassium while increasing the iron grade in the residue solid. Analysis of the EAF dust revealed that the sample contained significant amounts of sodium (14% Na_2O), potassium (10.7% K_2O), and iron (45.3% Fe_2O_3), with a particle size distribution showing 100% of particles finer than 15 microns (d80 = 4 microns). Water-based leaching experiments, optimized using Response Surface Methodology (RSM), demonstrated that temperature is the most influential factor in sodium and potassium recovery. Higher temperatures (60–70°C) with a solid content of 25% over 60 minutes achieved recovery rates of 83% for sodium and 68% for potassium. The process increased the iron grade in the residue by a factor of 1.25, making it suitable for further processing. The optimized conditions (60 minutes, 60–70°C, 25% solid content) were validated through large-scale experiments, confirming the model's reliability. The results demonstrated the feasibility of scaling up the process for industrial applications. The proposed method reduces environmental risks by minimizing waste and offers economic benefits through the recovery of valuable salts and enhanced iron grade.

Acknowledgments

References

Aune, J.: "Electric Arc Furnace Dust Symposium", 1991, Pittsburgh, USA.

Buzin, P.J.W.K., Heck, N.C., Vilela, A.C.F.: "EAFD – A Thermodynamic Analysis and Classification of Dust Types", Proceedings of the 45th ggSteelmaking Seminar – International, 2014.

Chaubad, P.C., Okeefe, T.J.: "Ironmaking and Steelmaking", 2 (1982) No.6, P.258-260.

Chung-Lee Li, Shing, M.: "ISIJ International", 33 (1993) No.2, P.248-290.

Cruells, M., Rocu, A., Nunez, C.: "Hydrometallurgy", 31 (1992) No. 3, P.213-231.

Hagni, A.M., Hagani, R.D., Demars, C.: "Journal of Metals", 43 (1991) No. 4, P.28-30.

Hopkins, D.W., Johnson, W., Davies, R.: "Ironmaking and Steelmaking", 2 (1975) No.1, P.25-29.

International Iron and Steel Institute (IISI): "The Management of Steel Industry By-Product and Waste", 1987.

Kawala: "Proceedings of International Symposium on Extractive Metallurgy of Zinc", 14-19 1985, Tokyo, Japan, P.759-805.

Kotrota, N.I.: "Electric Arc Furnace Dust Symposium", 1989, Pittsburgh, USA.

Lightfoot, R.: "Electric Arc Furnace Dust Symposium", 1991, Pittsburgh, USA.

Medonnell, C.F., Triger, D.R., Argent, B.: "Ironmaking and Steelmaking", 16 (1989) No. 6, P.435-445.

Nyirenda, R.L.: "The Processing of Steelmaking Flue Dust: A Review", Minerals Engineering, 1991;4(7–11):1003–25.

Pedro Jorge Walburga Keglevich de Buzina, Nestor Cezar Heck, Antônio Cezar Faria Vilela: "EAF Dust: An Overview on the Influences of Physical, Chemical and Mineral Features in Its Recycling and Waste Incorporation Routes", Journal of Materials Research and Technology, 2017;6(2):194–202.

Pickles, C.A.: "Thermodynamic Analysis of the Selective Chlorination of Electric Arc Furnace Dust", Journal of Hazardous Materials, 2008;166(2–3):1030–42.

Pirect, N.I. Muler, D.: "Criteria for the Selection of Recycling Process for Low Zinc Containing Residuals from the Iron/Steel Industry", in Residues and Effluents-Processing for Environmental Considerations Conference. 5 Mar 1992, The Minerals, Metals & Materials Society. San Diego, California, P.613-646.

Pustrip, J.F.: "Electric Arc Furnace Dust Symposium", 1991, Pittsburgh, USA.

Shahverdi, H.R., Mohammad, M.: "Investigation of Steelmaking Dust in Electric Arc Furnace", Ministry of Mines and Metals, Alloy Steel Company of Iran, Steel Symposium 75, 3-5 Mehr 1375, Materials Engineering Faculty, Isfahan University of Technology.

Southwick, L.M.: "Still No Simple Solution to Processing EAF Dust", Steel Times International, 2010, p.43–45. Available from: www.steeltimesint.com/contentimages/features/EAF dustMar10.pdf [cited 15.07.13].

Svoboda, J.M.: "AFS Transaction", vol 99 (1991), p.405-409.

West, N.G.: "Iron and Steel International", (1976), June, P.173-185.

Implementation of Coupled DEM-FEM to Investigate the Mechanical Behavior of Roller Screen Rolls in Classification of Green İron Ore Pellets

Mehrshad Asghari[1]*, Mohammad Noaparast[1], Mohammad Jahani Chegeni[2]

[1] School of Mining Engineering, University College of Engineering, University of Tehran, P.O. Box 14395-515, Tehran, Iran.

[2] Faculty of Mining, Petroleum & Geophysics Engineering, Shahrood University of Technology, Shahrood, Iran.

*Corresponding author: m.asghari@ut.ac.ir (Mehrshad Asghari)

Abstract:

Because roller screens are connected to the pelletizing discs on one side and the green iron ore induration furnaces on the other side in pelletizing plants, they play a crucial role in the plant's productivity and steel production process. Consequently, an optimal performance and structural design are essential in this context. A significant issue with roller screens during the classification of green pellets is the deformation of the rolls caused by the force exerted by the pellets during operation. This deformation disrupts the uniformity of the gap between the rolls, thereby reducing the efficiency of the screen, and the overall performance of the circuit, as well. Despite the importance of this issue, no studies have been conducted to investigate the force exerted by the pellets during classification on the screen or the subsequent mechanical behavior of the rolls. Therefore, this study employs the discrete element method–finite element method (DEM-FEM) coupling simulation technique to examine, for the first time, the mechanical behavior of rolls and to optimize their structural design. The results indicated that decreasing the roll diameter from 80 mm to 30 mm led to 1088 times increase in the average total deformation of the rolls. Furthermore, increasing the thickness of the polyurethane liner from 3 mm to 14 mm caused the average total deformation to rise by 54 times.

Keywords: Roller screen, DEM, FEM, Coupling, Total deformation

1. Introduction

The roller screen utilized for the classification of green iron ore pellets has become increasingly prevalent owing to its numerous advantages, which play a crucial role in enhancing the efficiency and productivity of the pelletizing circuits. Its benefits include high efficiency and capacity in classifying green pellets, low noise generation, minimal space requirements, ability to handle highly sticky materials with elevated moisture content, and reduced damage to green pellets. These features have made this equipment essential for preparing a suitable feed for induration kilns. The roller screen serves as a vital link between the pelletizing and balling equipment, such as pelletizing discs or drums and induration furnaces, which effectively connect these machines and create a closed circuit. Thus, ensuring the optimal design, construction, and operational efficiency of the roller screen is critical, as it significantly contributes to increasing the productivity of the pelletizing plant (Carvalho et al., 2023). Green pellets produced from pelletizing disks or drums are transferred to a roller screen for size classification and typically range from 6 to 22 mm in diameter. As illustrated in Fig. 1, the roller screen utilized in both laboratory and industrial settings consists of several rolls with a specific diameter, inclined at a particular angle, and rotating at a designated speed. This design facilitated the movement of pellets along the roller screen. During this process, the gaps between the rolls allow for the separation of green pellets based on their dimensions. According to Fig. 1, there is an area referred to as the initial three-quarters of the screen length that features a gap opening of 9.5 mm. This

configuration enables fine-grained pellets measuring 6–9.5 mm to pass through. In the remaining quarter of the screen, the gap opening increases to 15.5 mm, allowing for the separation of on-size pellets ranging from 9.5 to 16 mm which are subsequently directed to the induration furnace as the feed (Asghari et al., 2024c). The appropriate gap opening size assigned to each segment of the roller screen area depends on the pelletizing plant strategy and downstream flow requirements (Andrade Steve; Athayde, Maycon, 2022).
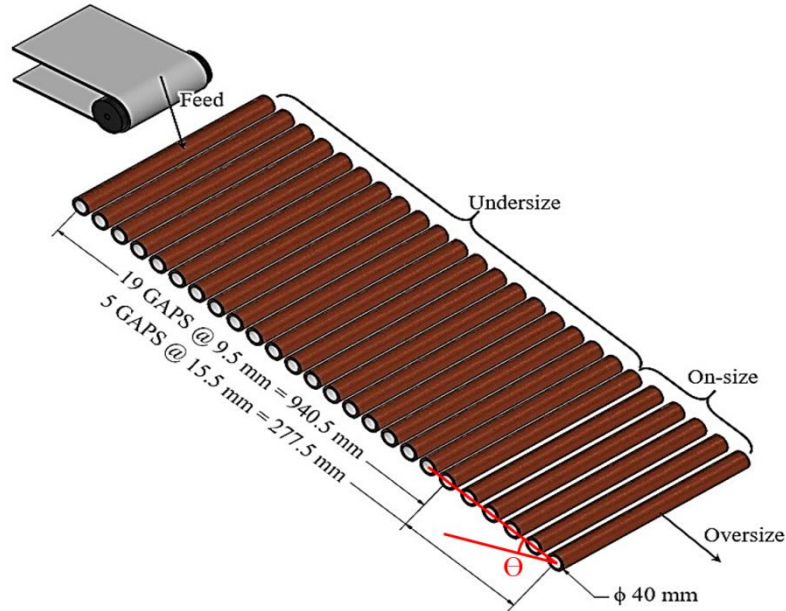
Fig. 1. Different constituent parts of the roller screen.

As shown in Fig. 2(a), during the sizing process of green pellets, the continuous collisions of the pellets with the surface of the rolls generate an impact, resulting in a sustained force exerted by the pellets onto the rolls. Based on Fig. 2(b), F_T represents the total force exerted by the pellets on the rolls. Therefore, the rolls remain consistently under load throughout the roller screen operation.
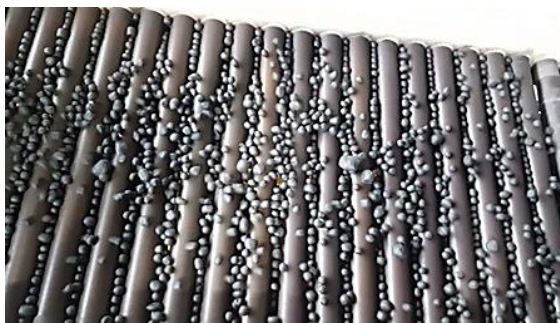
a): classification of green iron ore pellets by roller screen   b): applied total force of F_T to the surface of the roll
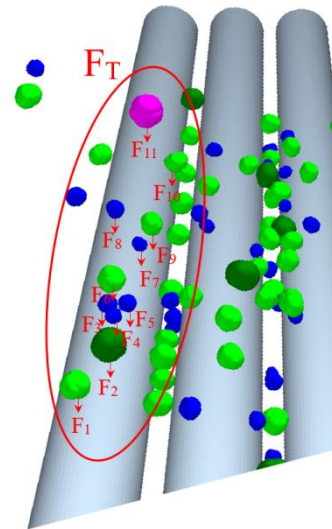
Fig. 2. Applied forces to the surface of the roll due to the collision of each pellet and consequently the total force of F_T.

In this context, the application of F_T to the rolls, along with the reaction forces exerted by the supports that connect and stabilize the rolls on the body of the roller screen, essentially functioning as bearings, can be analyzed. As illustrated in Fig. 3(a), these factors establish the boundary conditions for the rolls

of the roller screen during the green pellet classification process. As shown in Fig. 3(b), the applied force of F_T on the surface of the roll consistently induces a bending stress along its length. As illustrated in Fig. 3(a), the bending stress results in elastic deflection. Ultimately, when the stress exceeds the yield strength, permanent plastic deformation occurs, particularly in the central region of the roll (Beer et al., 2020).

a): applied forces to the roll. F_T and reaction forces are applied to the roll by collision of pellet and supports (bearings), respectively.

b): applied bending stress to the roll along its length.
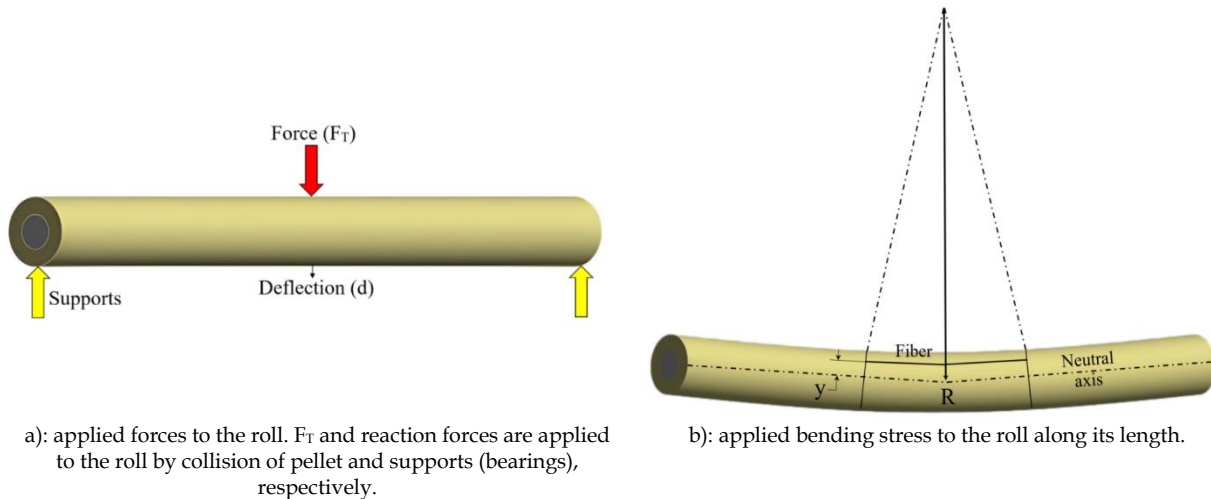
Fig. 3. Applied forces and resultant bending stress to the roll while classification of pellet.

According to Fig. 3(b), the elastic or plastic deformation of the roll, essentially roll bending, results in a loss of straightness. Under the influence of bending, the uniformity of the gap opening deviates significantly from the ideal state. As a result, transferring on-size pellets to the fine-grained area and fine grain pellets to the product area leads to both a quantitative and qualitative decrease in the efficiency of the roller screen (Andrade Steve; Athayde, Maycon, 2022). Maintaining appropriate gaps between rolls is essential for effectively separating fine-grained materials from product materials and improving the performance of the roller screen. A review of the literature indicates that there is limited research on the comprehensive performance of roller screens during the pelletizing process. Consequently, the impact of key parameters on the proficiency of the roller screen remains unclear. Therefore, there is a lack of established knowledge regarding the screening process that utilizes roller screens. Furthermore, the suboptimal performance of the roller screen contributes to losses in pelletizing plants. Thus, it would be essential to conduct theoretical and practical research to evaluate and optimize its design, construction, and performance. This research is crucial for enhancing the efficiency and productivity of the entire plant, and is both justified and necessary (de Carvalho et al., 2021). Understanding the rolling screening process, particularly the interactions between the pellets and the roll surface, necessitates particle-scale studies. However, conducting experimental research in full-scale industrial plants poses significant challenges. However, online analysis is often hindered by spatial constraints. Even when space is available, investment costs associated with such installations are frequently deemed unjustifiable. While experimental tests yield valuable and reliable information, the inherent heterogeneity, discreteness, and anisotropy of particulate solids complicate the dynamic behavior of bulk materials owing to the interactions between particles and between particles and geometry. Moreover, the complexity and high costs associated with manufacturing laboratory equipment, along with the time and difficulty involved in conducting experimental studies, render it impractical to perform comprehensive investigations and parametric studies of particle systems (Aikins et al., 2023).

Simulations have become a widely utilized tool in the design and optimization of industrial processes. Owing to the highly discrete nature of granular materials, it is anticipated that particulate media will require a discrete simulation method. Mechanical modeling and numerical simulation using the discrete element method (DEM) can be employed, in order to investigate the classification behavior of green pellets on a roller screen. when properly calibrated and validated, this approach can effectively predict the dynamic and bulk behavior of pellets on rolls by considering both pellet-pellet and pellet-

roll interactions. DEM is a widely utilized research and development tool that predicts the macroscopic behavior of particles through a microscopic approach (Yang et al., 2024). By employing DEM, it is possible to simulate the interactions between pellets, including pellet-pellet and pellet-roll interactions. This results in the calculation of the force (F_T) exerted when a pellet collides with the roll surface (Brandt et al., 2024). After simulating the DEM and calculating the forces resulting from the pellet's impact on the roll surface, it is essential to evaluate the mechanical behavior of the roll, including the total deformation and equivalent stress. Finite Element Method (FEM) is the most effective method for simulating and calculating these behaviors. FEM is considered a robust and mature approach for addressing complex engineering problems involving materials with varying properties, intricate geometries, diverse loading conditions, and multiple boundary constraints (Xu et al., 2024). Considering the advantages of FEM for investigating the reactions and behavior of roller screen rolls under the impact loads generated by green pellets, it is essential to transfer the forces calculated through DEM simulations to the FEM platform. The process of connecting and transferring data obtained from the discontinuous DEM simulation to the continuous FEM simulation is referred to as the coupled DEM-FEM method. This approach facilitates an accurate simulation of the interaction between the forces exerted by the impact of the pellets and the resulting deformation of the rolls caused by this impact (Cheng et al., 2023). The coupled DEM-FEM numerical simulation method effectively integrates the strengths of the DEM in characterizing granular particle behavior with the FEM which excels in addressing bending problems in rolls (Shen et al., 2019). In this research work, the performance of roller screen rolls was modeled using FEM based on the principles of continuum mechanics, whereas the pellets were represented as distinct and independent particles through DEM to account for discontinuities.

Unlike vibrating screens, which have been extensively studied to simulate their operational and mechanical behaviors using DEM, FEM, and DEM-FEM coupling methods, comprehensive research on the functional simulation of roller screens using the DEM-FEM coupling method and FEM remains limited. Current simulation studies of roller screens are primarily restricted to the use of DEM alone. Cherepakha et al. employed DEM simulations to examine the effects of the diameter, length, and rotational speed of the rolls, as well as the inclination angle of the roller screen's surface and the number of rolls (length of the roller screen) on the efficiency and performance of the roller screen (Cherepakha et al., 2019). Javaheri et al. simulated and investigated various regimes of roll rotation speed and inclination angle of the roller screen's surface on the performance criteria of the roller screen using DEM simulations (Javaheri et al., 2022). Jafari et al. also employed DEM to examine the effects of various performance parameters, including the inclination angle, diameter, and rotation speed of the rolls on the efficiency of the roller screen (Jafari et al., 2022). Silva et al. utilized DEM to examine the effects of rotation speed and diameter of the rolls, fine grain area gap, inclination angle of the roller screen surface, and feeding rate on the efficiency of single- and double-deck roller screens (e Silva et al., 2017). In another study, Silva et al. employed a DEM to investigate the effects of the moisture content and granulation distribution of the input feed on the performance of a single-deck roller screen. They also analyzed the impact of gap opening in a fine grain area (e Silva et al., 2018). Carvalho et al. conducted a DEM simulation study on a double-deck roller screen to investigate its performance concerning various factors, including load capacity, the number of constituent rolls, the length of the first deck, the inclination angle, and the gap opening between the rolls of the second deck (Carvalho et al., 2023).

In summary, previous studies on DEM simulation of roller screens have primarily focused on evaluating the performance of these screens in relation to structural and process parameters. However, the physical and dynamic behavior of particles, particularly the forces generated during collisions with the geometry of the roller screen, especially the rolls, has not been simulated or analyzed. Therefore, a comprehensive study addressing the interaction between continuous geometry and discrete particles for the design and optimization of roller screens, both structurally and functionally, is lacking. Several studies have been conducted on various types of vibrating screens (linear, circular, or flip-flow) using the DEM method. These studies not only simulated particle movement but also investigated the dynamics and interactions between the particles and the screen plates and meshes. Consequently, the inertia and forces exerted on the screen plates by the particles

were simulated effectively (Moncada & Rodríguez, 2018). Thus, the positive outcomes of these studies highlight the potential benefits and effectiveness of employing DEM in roller screens. It is important to note that all of the aforementioned DEM studies of roller screen utilized a spherical pellet shape and the Hertz-Mindlin elastic contact model. Previous research (Asghari et al., 2024b), along with results from experimental tests conducted on a laboratory roller screen and the calibration of contact parameters, indicates that employing the actual shape of the pellet and a hysteretic spring contact model, owing to its elastoplastic properties, produces DEM simulation results that are more consistent with realistic experimental outcomes. So, these results are considered more reliable and repeatable. In this study, a roller screen is investigated for the first time using DEM and FEM techniques to develop a coupled DEM-FEM model. Following the establishment of this coupling as a novel design tool for the roller screen, the mechanical behavior of the rolls, including the total deformation and equivalent stress experienced, are assessed in response to the impact load of the pellets during the classification process. The coupled DEM-FEM method used in this study represents an innovative approach that enables parametric design analysis of roller screen. To address issues such as bending which can reduce the efficiency of the screening process during the classification of green pellets, a thorough parametric design analysis is conducted. Consequently, optimal construction conditions are proposed, along with design recommendations concerning the roll diameter and thickness of the polyurethane (PU) liner for the rolls. These recommendations aim to minimize the adverse effects of the deformation and bending of the rolls, thereby addressing the significant technical and financial challenges encountered by pelletizing plants.

2. Material and methods

2.1. Laboratory roller screen tests

At the outset, experimental tests of the roller screen were conducted using the laboratory roller screen illustrated in Fig. 4, with the structural and functional characteristics detailed in Table 1 and Fig. 5. These experimental studies on the roller screening process of green pellets provide the foundation for the coupled DEM-FEM simulations discussed in this study. They are comprehensively detailed in reference (Asghari et al., 2024c).

Fig. 4. Performing laboratory roller screen tests for classifying green iron ore pellets.

Table 1. Specifications and operating parameters of the laboratory roller screen.

Specification		Value
Construction parameters	Roll diameter (mm)	40
	Roll length (mm)	480
	Material type of roll liner	Polyurethane (PU)
	Material type of roll shaft	Structural steel
	Roll number	25
Operational parameters	Feeding rate (t/h)	1-1.5
	Feeding conveyor belt speed (m/s)	0.35
	Roll rotation speed (rpm)	10-500
	Inclination angle (degrees)	Adjustable to 20
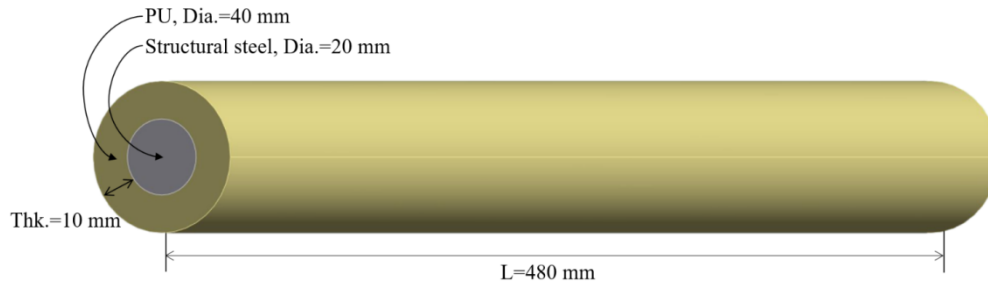
Fig. 5. Specification of the roll of laboratory roller screen.

2.2. Pellet shape modeling

Modeling the actual shape of magnetite green pellets which contain 8% moisture and 1% bentonite, was conducted based on the analysis of images obtained from experimental tests. The results of these tests are shown in Fig. 6. EDEM software version 2021.2 (Edinburgh DEM Solutions) was utilized to perform both pellet shape modeling tests and DEM roller screen tests (*Altair EDEM Software, EDEM 2021.2 Documentation*, 2022; Asghari et al., 2024a). Additionally, Digimizer software was utilized to analyze the pellet images (Asghari et al., 2024a). Details of pellet shape modeling, along with experimental tests measuring contact parameters and their calibration, are presented in reference (Asghari et al., 2024a).

a): real shape of pellet   b): simulated shape of pellet.
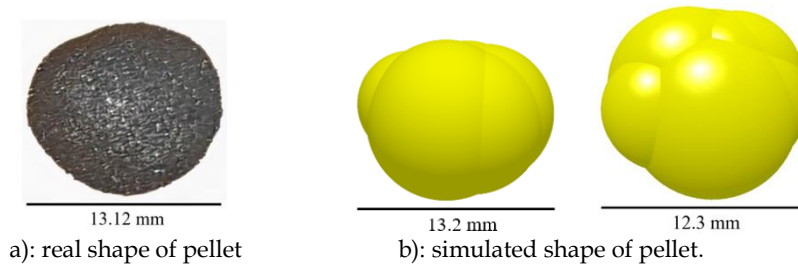
Fig. 6. Modeling the shape of magnetite pellet with 8% moisture and 1% bentonite in EDEM (Asghari et al., 2024a).

2.3. Determination of contact parameters

In this study, for the first time, experimental tests regarding the green pellet were conducted to determine the contact parameters of the magnetic pellet, including drop, inclined plane, sliding, angle of repose (AOR), and tumbling drum tests. Additionally, physical tests, such as specific gravity and dimensional distribution, as well as mechanical tests, including Young's modulus and yield strength tests, were performed. Calibration tests for pellet-pellet and pellet-roll interactions were conducted using DEM simulations as a novelty, the results are presented in Table 2 (Asghari et al., 2024a).

Table 2. Properties and interaction parameters utilized in EDEM simulation of the roller screen test for magnetite pellets with actual shape (Asghari et al., 2024a).

Parameters	Unit	Values
Pellet properties		
Pellet type	-	Magnetite
Pellet moisture content	%	8
Pellet bentonite dosage	%	1
Pellet density (ρ)	kg/m^3	4893
Geometry density (ρ)	kg/m^3	1215
Poisson's ratio (v)-(Pellet; Geometry)	-	0.25; 0.41
Shear modulus (G)-(Pellet; Geometry)	Pa	2.015e+06; 1.02e+08
Pellet yield strength	Pa	0.0554e+06
Pellet shape model	-	Overlapping spheres

51

Pellet size distribution		mm	6–22
Test method		-	Bulk pellet
Pellet mass		kg	26, 30, 40, 50 and 70
Feed rate		kg/s	0.417
Time step		s	2.93e-05
Time step		%	20
Simulation time		s	85
Contact parameters			
Physics for interaction	Pellet-pellet	-	Hertz-Mindlin with JKR
	Pellet-geometry	-	Hysteretic spring
Surface energy for the interaction of pellets 6–9.5 mm to pellets 9.5–22 mm		J/m²	1.9
Damping factor		-	-0.0077
Stiffness factor		-	0.125
[1]COR$_{P-P}$; COR$_{P-G}$		-	0.104; 0.09
[2]μ_{sP-P}; μ_{sP-G}		-	0.23; 0.6
[3]μ_{rP-P}; μ_{rP-G}		-	0.31; 0.2

[1]COR$_{P-P}$ and COR$_{P-G}$=coefficient of restitution for pellet-pellet and pellet-roll interactions, respectively
[2]μ_{sP-P} and μ_{sP-G} = static friction coefficient for pellet-pellet and pellet-roll interactions, respectively
[3]μ_{rP-P} and μ_{rP-G} = rolling friction coefficient for pellet-pellet and pellet-roll interactions, respectively

The dimensional distribution of the pellet feed used for the simulation is illustrated in Fig. 7 (Asghari et al., 2024a).

Undersize pellet (6–9.5 mm) **On-size pellet** (9.5–12.5 mm) **On-size pellet** (12.5–16 mm) **Oversize pellet** (16–19 mm) **Oversize pellet** (19–22 mm)
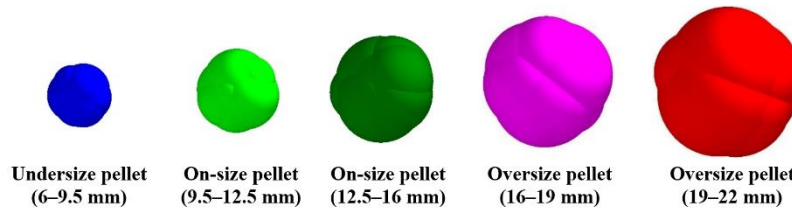
Fig. 7. Different particle sizes of pellet for DEM simulation of roller screen (Asghari et al., 2024a).

A DEM simulation test of the roller screen was conducted based on the contact parameters listed in Table 2. The specifications of the roller screen used to conduct the DEM tests are shown in Fig. 8. The DEM simulation test is illustrated in Fig. 9. In this test, the operational parameters were as follows: feed rate=1.5 t/h, deck angle=13°, roll speed=225 rpm, roll diameter=40 mm, roll length=480 mm, undersize gap=9.5 mm, on-size gap=15.5 mm, and particle shape=real shape.
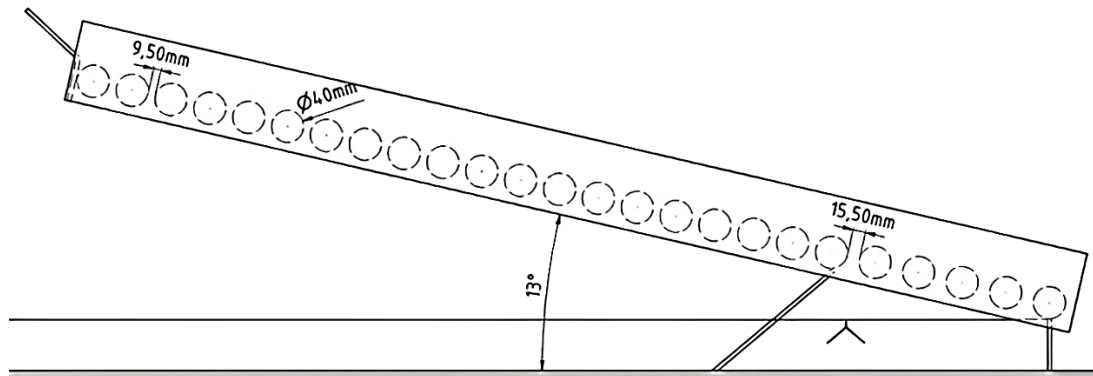
Fig. 8. Specification of applied roller screen for DEM simulation tests.

a)   b)
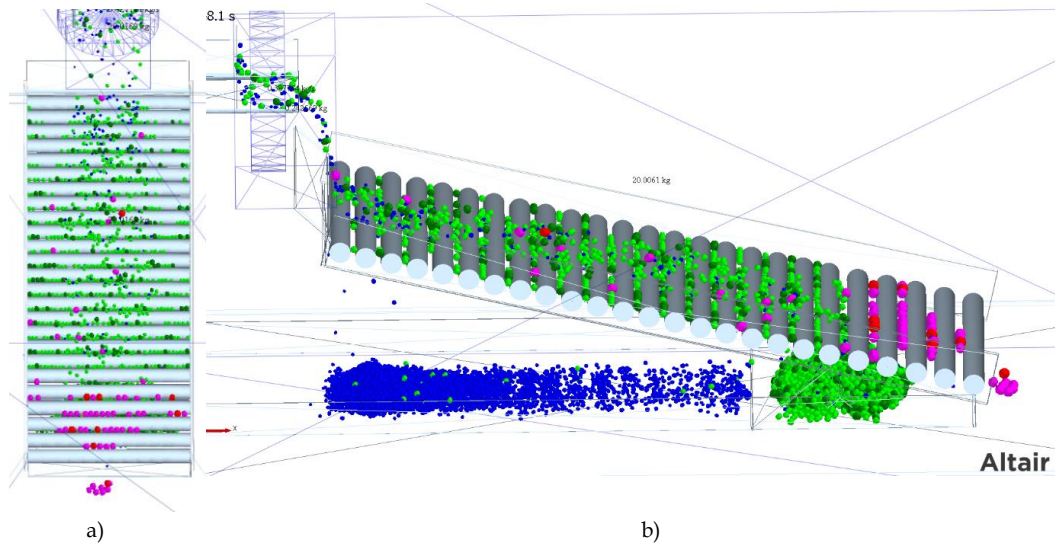
Fig. 9. EDEM simulation of roller screen to classify green pellets.

2.4. Modeling roll geometry

To conduct FEM simulation tests on the roller screen, analysis of the mechanical behavior of the rolls, including the total deformation and equivalent stress are aimed in response to the forces exerted by the pellets during dimensional separation. According to Fig. 10(a), the geometry of the roller screen, particularly its rolls, was modeled using Autodesk Inventor software and Design Modeler in ANSYS version 2022 R2, in accordance with the specifications provided for the laboratory roller screen (Table 1). The boundary conditions for the roll shown in Fig. 5, utilized in the FEM simulations, are illustrated in Fig. 10(b).
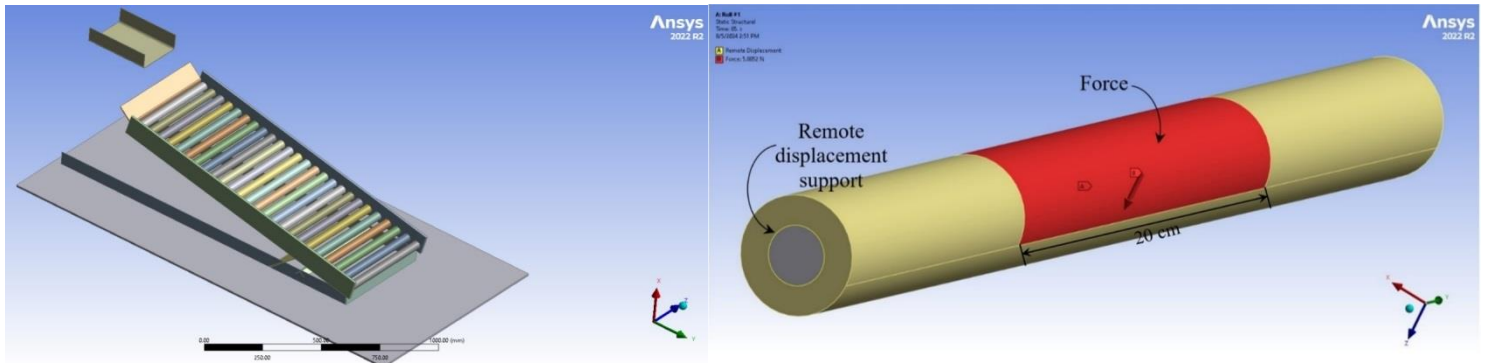
a): a three-dimensional geometry of the roller screen prepared by Autodesk Inventor software and imported to the ANSYS software.

b): applied boundary conditions for FEM simulation of roll

Fig. 10. Modeling geometry of roller screen rolls and applied boundary conditions for FEM simulations

2.5. Investigation of affecting parameters on the mechanical behavior of roll

After conducting a simulation of the DEM-FEM coupling method for the roller screen, investigation of the mechanical behavior of the first roll of the roller screen which is the most critical component during the roller screening process, aimed to establish a comprehensive study methodology. In this section, additional simulation tests for performing parametric study of roller screen roll were examined for the first time which includes some of the most significant parameters that influence the structural design of the roll.

2.5.1. Diameter of roll

Because the diameter of the roll is a critical geometric parameter that influences its mechanical behavior, various FEM simulations of the first roll were conducted to examine the effect of the roll diameter. The conditions for the FEM simulation were as follows: roll diameters of 30 mm, 40 mm, 50 mm, 60 mm, 70 mm, and 80 mm, a PU thickness of 10 mm, and PU shear modulus of 102 MPa.

2.5.2. Thickness of PU

Because PU is used as a liner for roller screen rolls owing to its high wear resistance, various FEM simulation tests of the first roll were conducted under different PU thickness conditions. The parameters for the FEM simulation were as follows: roll diameter=40 mm, PU thickness=3 mm, 6 mm, 8 mm, 10 mm, 12 mm, and 14 mm, and PU shear modulus of 102 MPa.

2.5.3. Shear modulus of PU

In addition to the thickness and geometric characteristics of PU, its mechanical properties, such as the shear modulus, are crucial for analyzing the mechanical behavior of rolls during the roller screening process. As PU is a polymer and a chemical substance, altering its molecular structure, particularly its molecular weight, changes its mechanical properties. To optimize the mechanical behavior of the roll in response to impact forces, it is essential to consider the effects of these changes on the characteristics of PU. Accordingly, various FEM simulation tests were conducted under different PU shear modulus conditions. In tests, the parameters for FEM simulations were as follows: roll diameter=40 mm, PU thickness=10 mm, PU shear modulus=5 MPa, 10 MPa, 20 MPa, 50 MPa, 102 MPa, 150 MPa, and 200 MPa.

3. Results and discussion

3.1. Applied force resulting from the impact load of pellets

The total force (F_T) applied to each roll during the pellet classification process, along with the average total force exerted on the rolls, is shown in Fig. 11. The highest force is exerted on the first roll where the pellets collide during their transfer from the chute to the roller screen. This force measures 6.67 N, which is 3.05 times greater than the average force applied to the rolls of the roller screen.
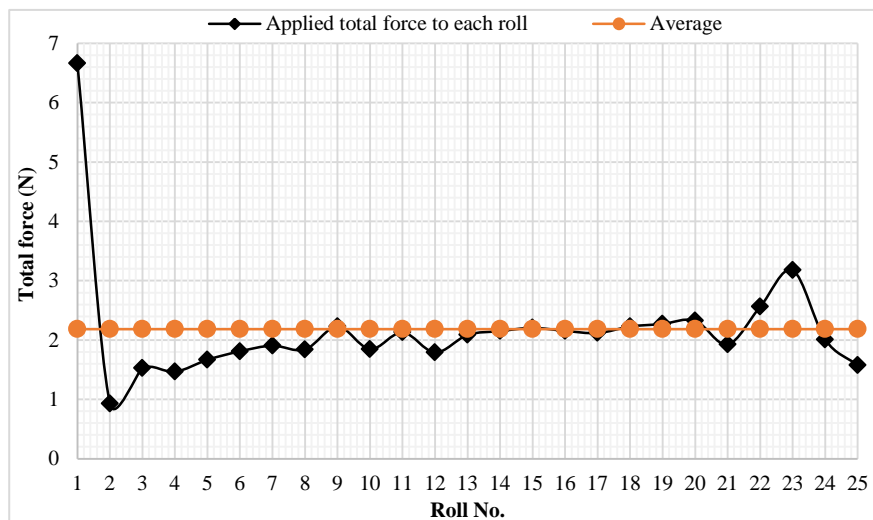
Fig. 11. Analysis results of applied total force by collision of green pellets on the rolls.

3.2. Analysis results of mechanical behaviors of roll

The results of the analysis of the mechanical behaviors of the first roller screen roll, along with their distribution, are presented in Fig. 12.

a): total deformation (mm) along roll length and across its cross-section

b): equivalent stress (MPa) along roll length and across its cross-section

c): equivalent stress in surface path (MPa)

d): equivalent stress in axial path (MPa)
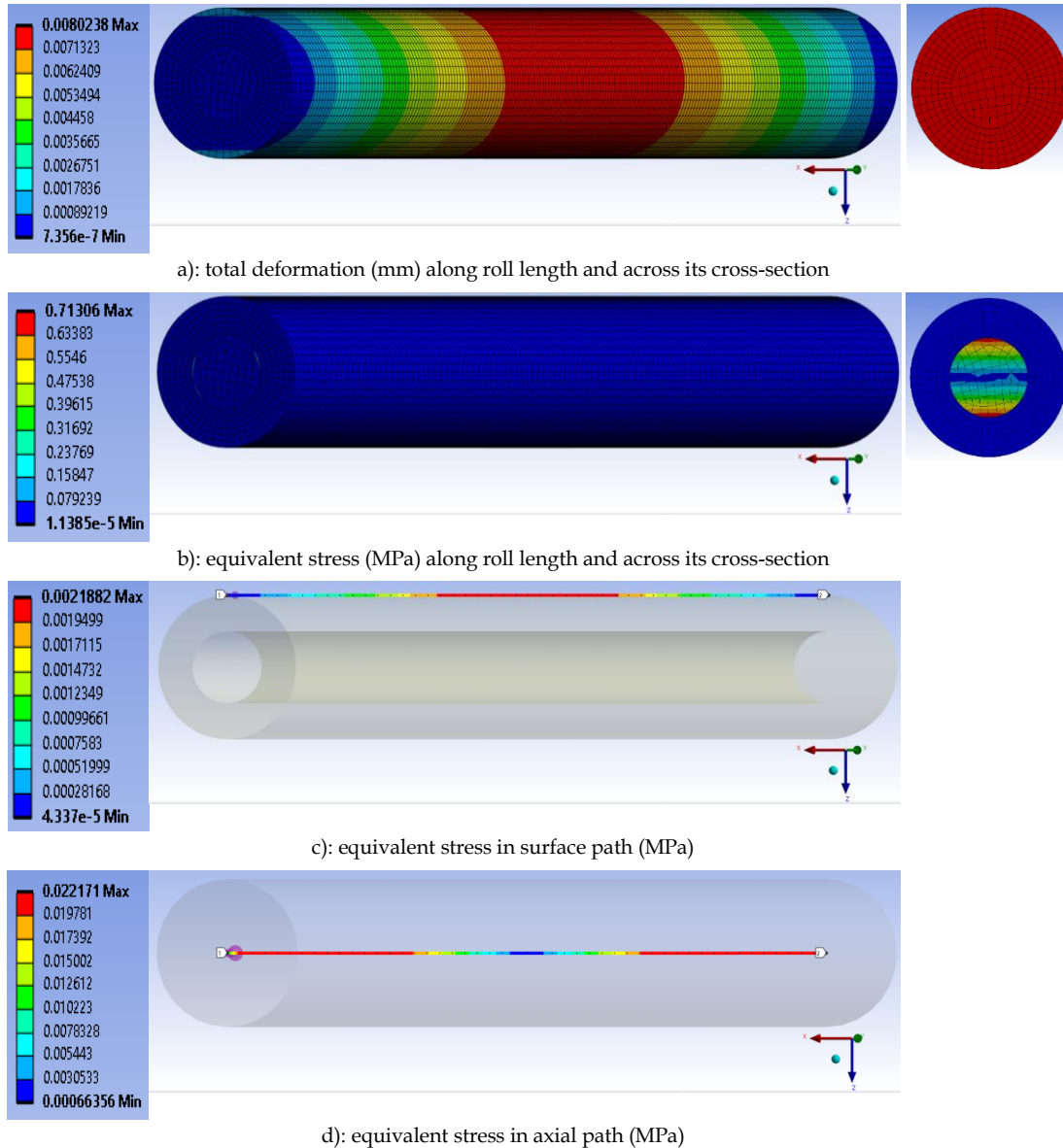
Fig. 12. Distribution contours of mechanical behaviors of roll 1 along its length and across its cross-section, accompanied by a legend to illustrate the corresponding values.

Based on Figs. 12(a), it is evident that total deformation reaches its maximum value in the central region of the roll, encompassing its entire cross-section, including the surface area near the point of force application and the roll axis. A concentration of deformation was primarily observed in these areas. Conversely, the minimum value of the total deformation occurs at the edges of the roll, specifically at the base where the support and bearing are connected. According to Fig. 12(b), the equivalent stress applied to the surface and axis of the roll which demonstrates a uniform distribution, was minimal. However, at the connection points between the structural steel shaft and PU liner in the upper and lower sections of the roll shaft axis, there is a concentration of stress. As the stress

concentration approaches to the axis of the roll, its magnitude diminishes, ultimately reaching a minimum value. According to Fig. 12(c), the stress applied to the surface path of the roll was maximized in the central region. As one moves toward the edges of the roll, values decrease, ultimately reaching their minimum at the edges. Furthermore, Fig. 12(d) indicates that the stress along the roll axis path is at its minimum in the central region, with values rising toward the edges and ultimately reaching a maximum value.

3.3. Analysis of the effects of structural variables on the mechanical behavior of rolls

3.3.1. Diameter of roll

As illustrated in Fig. 13, for a roll with a diameter of 30 mm, the average values of total deformation and equivalent stress applied were 1088 and 51 times greater than those for a roll with a diameter of 80 mm, respectively. This indicates that the diameter of the roll has an inverse relationship with the average values of its mechanical behavior in response to the forces generated by the pellet impact. In this scenario, with the force exerted on the roller screen roll held constant, the general relationship of the stress suggests that as the diameter of the roll increases, the surface area also increases, leading to a decrease in the stress experienced by the roll. Under a consistent load, increase in roll diameter enhances the resistance to deformation within the roll, which consequently results in reduced strain values. Therefore, the deformation resulting from the collision and impact of the pellet on the roll surface is also reduced. To mitigate the deformation and stress and to minimize the negative effects on the alignment and spacing between the rolls, it is recommended that the diameter of the primary roll, designated as the impact roll, be larger than that of the other rolls.

a): effect of roll diameter variation on the total deformation b): effect of roll diameter variation on the equivalent stress
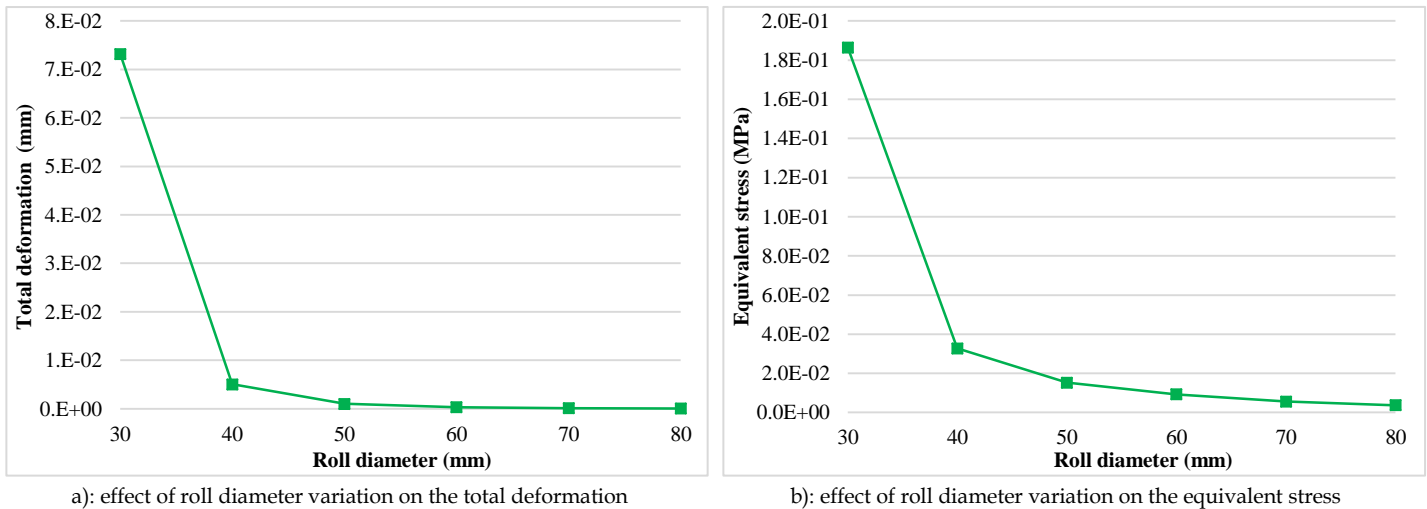
Fig. 13. Variation of the mechanical behaviors of roll 1 with different diameters.

3.3.2. Thickness of PU

In this section, the impact of variations in the thickness of the PU liner on the mechanical behavior of the first roll of the screen was examined. As illustrated in Fig. 14, the roll with a PU liner thickness of 14 mm exhibited average values of total deformation and equivalent stress that were 54 and 8 times greater, respectively, than those of the roll with a PU liner thickness of 3 mm. This indicates a direct relationship between the thickness of the PU liner and the average mechanical performance of the roll in response to the forces generated by the pellet impacts. The underlying reason for this phenomenon is the lower shear modulus of the PU compared to that of the structural steel shaft; the shear modulus of the roll shaft is 754 times greater than that of the PU liner. This disparity is resulted in increased deformation and stress on the roll. To mitigate deformation and stress and ultimately reduce bending effects on the rolls, thereby preserving their straightness and maintaining the gap between them, it is

recommended to minimize the thickness of the PU liner on the first roll as much as possible while still considering its anti-wear function. This should be balanced with the maximum thickness of the structural steel shaft.
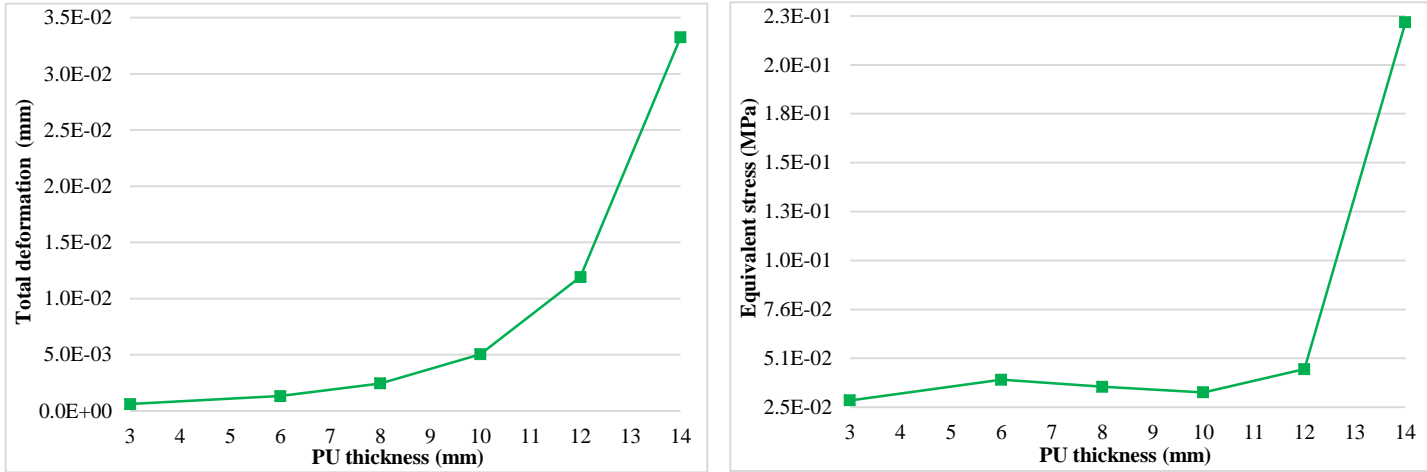
a): effect of PU thickness variation on the total deformation   b): effect of PU thickness variation on the equivalent stress

Fig. 14. Variation of the mechanical behaviors of roll 1 with different PU thickness.

3.3.3. Shear modulus of PU

This section examines the impact of variations in the shear modulus of the PU liner on the mechanical behavior of the first roll of the roller screen. As shown in Fig. 15, for the roll with a PU liner modulus of 5 MPa, the average values of total deformation and equivalent stress are 1.07 and 1.02 times greater, respectively, compared to those for the roll with a PU liner modulus of 200 MPa. This finding indicates an inverse relationship between the modulus of the PU liner and the average values of its mechanical behavior. To minimize deformation and stress, as well as the bending caused by the collision of pellets with the roll, which adversely affects the efficiency of the roller screen, it is recommended that the modulus of the PU liner for the first roll be maximized.
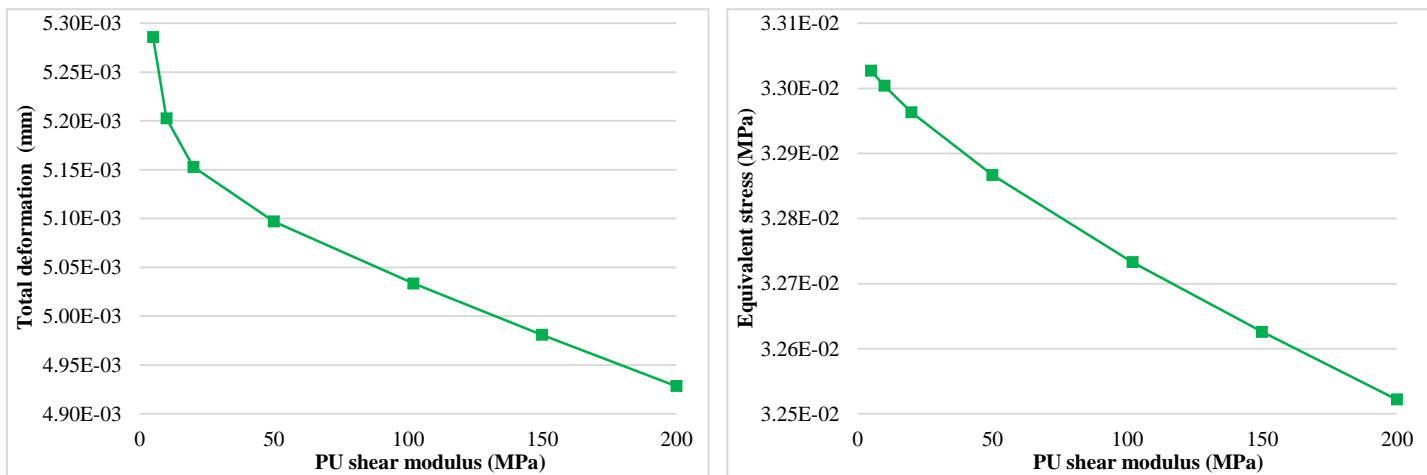
a): effect of PU shear modulus variation on the total deformation   b): effect of PU shear modulus variation on the equivalent stress

Fig. 15. Variation of the mechanical behavior of roll 1 with different PU shear modulus.

The results of the examination of the mechanical behavior of the roller screen's initial roll related to structural design factors were analyzed using statistical methods and the Pearson correlation coefficient with a 95% confidence interval using SPSS software. These findings are presented in Fig. 16.
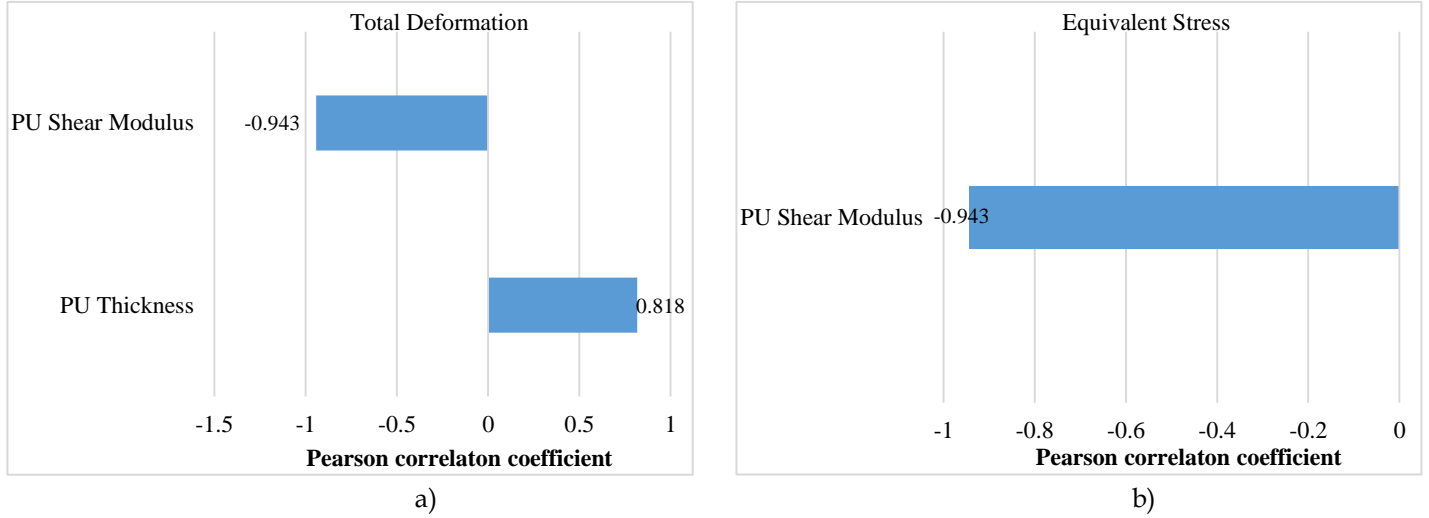
Fig. 16. Analysis results of Pearson correlation coefficient of mechanical behavior of initial roll related to structural design factors.

Based on Fig. 16(a), it is evident that the total deformation of the first roll exhibits an inverse relationship with the PU shear modulus and a direct relationship with the PU thickness whereas Fig. 16(b) indicates that the equivalent stress is inversely related to the shear modulus of PU. Therefore, the following relationships can be derived to describe the mechanical behavior of the roll in relation to its structural parameters:

$$Total\ deformation \ \propto \frac{T_{PU}}{G_{PU}} \tag{1}$$

$$Equivalent\ stress \ \propto \frac{1}{G_{PU}} \tag{2}$$

where:
T_{PU} = thickness of PU (mm)
G_{PU} = shear modulus of PU (MPa)

By identifying the stress concentration points during the operation of the screen used for classifying the green pellets, it is possible to extend the lifespan of the rolls, which are the most critical components of the screen. This can be achieved by modifying the geometric characteristics, such as the roll diameter and mechanical properties, including the shear modulus and thickness of the PU liner. Consequently, utilizing the obtained results allows for the design of an optimal structure, thereby enhancing the performance of the screen. This improvement ultimately increases both the quantitative and qualitative efficiencies of the screen, as well as those of the induration furnace and pelletizing circuit. The frequency and duration of screen downtime were significantly reduced, which, in turn, enhanced plant productivity. A larger volume of material can be processed using a roller screen. The results obtained can be applied to the study of other processing equipment such as ball mill lifters.

3.4. Validation of obtained results

Considering the low values of the forces exerted by the pellets during the laboratory tests, as well as the industrial studies conducted, it is evident that the stresses applied to the rolls occur over extended periods of screen operation. This prolonged exposure leads to deformation of the rolls and, consequently, a decrease in their efficiency. To validate the findings of the laboratory tests and coupled DEM-FEM simulations regarding the effects of roll diameter, particularly for the first roll, which serves as an impact roll and endures the highest levels of force, deformation, and stress, as well as the mechanical strength and thickness of its liner in industrial screens, the diameter of the roll should be increased. Additionally, a polyurethane liner with a higher shear modulus and reduced

thickness should be used. After a specified period, the results should be examined and compared with the state prior to the changes, which will be the focus of future research.

4. Conclusions

According to studies and simulation tests conducted in the fields of DEM and FEM, and more importantly, the coupled method employed in this study, the following results were obtained:

- The actual shape of the green pellet, determined through image analysis and employing the elastic-plastic hysteretic spring contact model, was utilized in the DEM studies of the green pellet classification process.
- It was evident that the DEM simulation facilitated the calculation of the average force exerted on the roller screen rolls owing to the impact load from the pellets during the screening operation. Furthermore, this method allows for the identification of both the maximum values and specific locations where these forces are concentrated.
- According to the DEM studies on the rolls of the roller screen, the average force resulting from the impact of the green pellet on the first roll is 3.05 times greater than the average force applied to all rolls, respectively.
- The highest levels of total deformation occurred in the central section of the roll. This deformation results in a loss of straightness, which subsequently affects the uniformity of the gap opening between the rolls and ultimately diminishes the efficiency of the roller screen.
- As the diameter of the roll decreased from 80 mm to 30 mm, the average values of the total deformation and equivalent stress applied to the roll increased by 1088 and 51 times, respectively. Therefore, the diameter of the roll, particularly the first roll, can be increased to mitigate the negative effects of deformation on the roll and resulting gap.
- By increasing the thickness of the PU liner of the rolls from 3 mm to 14 mm, while maintaining a constant roll diameter, the values of the total deformation and equivalent stress applied to the roll increased by 54 and 8 times, respectively. In this context, it is advisable to reduce the thickness of the PU liner while maintaining its anti-wear properties, considering the relationship between the liner thickness and the deformation and stress experienced by the roll.
- By decreasing the shear modulus of the PU liner of the rolls from 200 MPa to 5 MPa, the values of the total deformation and equivalent stress applied to the roll increased by 1.07 and 1.02 times, respectively. Therefore, maximizing the shear modulus of the PU liner is advisable to minimize the deformation of the roller screen rolls.
- Finally, it was concluded that the coupled DEM-FEM numerical simulation method is a suitable and effective approach for improving the design, structure, and efficiency of roller screens.

References

Aikins, K. A., Ucgul, M., Barr, J. B., Awuah, E., Antille, D. L., Jensen, T. A., & Desbiolles, J. M. A. (2023). Review of Discrete Element Method Simulations of Soil Tillage and Furrow Opening. *Agriculture (Switzerland)*, *13*(3). https://doi.org/10.3390/agriculture13030541

Altair EDEM software, EDEM 2021.2 Documentation. (2022).

Andrade Steve; Athayde, Maycon, A. G. B. (2022). Impact of key parameters on the iron ore pellets roller screening performance. *Metallurgical Research & Technology*, *119*(3), 311. https://doi.org/10.1051/metal/2022045

Asghari, M., Noaparast, M., & Jahani, M. (2024a). Implementation of DEM to calibrate contact parameters, as a novel simulation of the elastoplastic behavior of green iron pellet classified by roller screen. *Advanced Powder Technology*, *35*(5), 104457. https://doi.org/https://doi.org/10.1016/j.apt.2024.104457

Asghari, M., Noaparast, M., & Jahani, M. (2024b). Improving the roller screen efficiency to classify green iron pellets using DEM simulation , novel roll design and implementing banana configuration. *Advanced Powder Technology*, *35*(11), 104675. https://doi.org/10.1016/j.apt.2024.104675

Asghari, M., Noaparast, M., & Jahani, M. (2024c). Investigation of cigarette effect and elastic-plastic behavior of green iron pellets on the roller screen efficiency. *Advanced Powder Technology*, *35*(2), 104321. https://doi.org/https://doi.org/10.1016/j.apt.2023.104321

Beer, F. P., Johnston, E. R., DeWolf, J. T., & Mazurek, D. F. (2020). *Mechanics of materials (Eighth)*. New York, NY: McGraw-Hill Education.

Brandt, V., Grabowski, J., Jurtz, N., Kraume, M., & Kruggel-Emden, H. (2024). DEM and DEM-CFD modeling of systems with geometric constrictions using a new particle location based multi-level coarse graining approach. *Powder Technology*, *436*(October 2023), 119447. https://doi.org/10.1016/j.powtec.2024.119447

Carvalho, R. M., Thomazini, A. D., Cunha, E. R., e Silva, B. B., & Tavares, L. M. (2023). Simulation of Classification and Stratification in Double-Deck Roller Screening of Green Iron Ore Pellets using DEM. *Transactions of the Indian Institute of Metals*. https://doi.org/10.1007/s12666-023-02958-6

Cheng, H., Thornton, A. R., Luding, S., Hazel, A. L., & Weinhart, T. (2023). Concurrent multi-scale modeling of granular materials: Role of coarse-graining in FEM-DEM coupling. *Computer Methods in Applied Mechanics and Engineering*, *403*, 115651. https://doi.org/10.1016/j.cma.2022.115651

Cherepakha, D., Johnson, J., & Kulchitsky, A. (2019). Examining roller screen performance to categorize iron ore green pellets to optimize pellet induration. *Proceedings Of The 8th International Conference On Discrete Element Methods(DEM8)*, *Figure 1*, 1–7.

de Carvalho, R. M., Jafari, A., Baradaran, G. H., Saidi, A., Javaheri, M., & Jafari, A. (2021). Effects of Rollers Speed Regime on the Roller Screen Efficiency. *Mineral Processing and Extractive Metallurgy Review*, *00*(00), 1–8. https://doi.org/10.1080/08827508.2021.1916926

e Silva, B. B., Carvalho, R. M., Cunha, E. R., Cavalcanti, P. P., & Tavares, L. M. (2017). Modeling of classification of iron ore green pellets on roller screens using the discrete element method. *5º Simpósio Brasileiro de Aglomeração de Minérios*, *47*, 211–221.

e Silva, B. B., Cunha, E. R., Carvalho, R. M., & Tavares, L. M. (2018). Modeling and simulation of green iron ore pellet classification in a s ingle deck roller screen using the discrete element method. *Powder Technology*, *332*, 359–370. https://doi.org/10.1016/j.powtec.2018.04.005

Jafari, A., Javaheri, M., & Baradaran, G. (2022). *Computer simulation to optimize roller screen settings providing higher efficiency in green pellets classification*. *161*.

Javaheri, M., Jafari, A., Baradaran, G. H., & Saidi, A. (2022). Effects of rollers speed regime on the roller screen efficiency. *Mineral Processing and Extractive Metallurgy Review*, *43*(5), 648–655.

Moncada, M., & Rodríguez, C. G. (2018). Dynamic Modeling of a Vibrating Screen Considering the Ore Inertia and Force of the Ore over the Screen Calculated with Discrete Element Method. *Shock and Vibration*, *2018*. https://doi.org/10.1155/2018/1714738

Shen, J., Wheeler, C., Ilic, D., & Chen, J. (2019). Application of open source FEM and DEM simulations for dynamic belt deflection modelling. *Powder Technology*, *357*, 171–185. https://doi.org/10.1016/j.powtec.2019.08.068

Xu, N., Wang, X., Lin, D., & Zuo, W. (2024). Numerical Simulation and Optimization of Screening Process for Vibrating Flip-Flow Screen Based on Discrete Element Method–Finite Element Method–Multi-Body Dynamics Coupling Method. *Minerals*, *14*(3). https://doi.org/10.3390/min14030278

Yang, Z. J., Lian, X., Savari, C., & Barigou, M. (2024). Evaluating the effectiveness of CFD-DEM and SPH-DEM for complex pipe flow simulations with and without particles. *Chemical Engineering Science*, *288*(October 2023), 119788. https://doi.org/10.1016/j.ces.2024.119788

The impact of nano-micro bubbles on the zinc oxide ore flotation performance

Mohammad Omidifar[1]*, Sied Ziaedin Shafaei Tonkaboni[2]

[1]Master's Student in Mineral Processing Engineering, Faculty of Mining Engineering, University of Tehran, Tehran, Iran.

[2]Professor, Faculty of Mining Engineering, University of Tehran, Tehran, Iran.

*Corresponding author: Mohammadomidifar95@gmail.com (Mohammad Omidifar), zshafaie@ut.ac.ir (Sied Ziaedin Shafaei Tonkaboni)

Abstract:

The major challenge in zinc oxide ores flotation is primarily the excessive production of fines during comminution, which leads to increased reagent consumption and the loss of zinc minerals. One of the most effective methods to enhancing recovery is the using nano-micro bubbles in the flotation. In this study, the effect of using nano-micro bubbles in the flotation of an zinc oxide ore sample with a Zn content of 15.67% provided from Zanjan province, Iran, was studied with the aim of eliminating the desliming stage. By generating nano-micro bubbles using a vortex pump under specific conditions, nano-micro bubbles with an average size of 300 nm were produced and utilized in the experiment. A software based statistical design of experiments, DOE, using a demo version of DX11 software was applied to design and statistically analysis of the results. The parameters were labeled as: using nano-micro bubbles water (A), sodium sulfide concentration as a sulfidant (B), Armac C concentration as a collector (C) and particle size (D). The zinc concentrate recovery was evaluated as response in the design. Analysis of the results showed that the influence of parameters and their interactions on response followed the order: B>D>C>BD>BC>CD>A>BCD. The maximum recovery was achieved in the presence of nano-micro bubbles, sodium sulfide concentration 4000 g/t, Armac C concentration 1000 g/t, and the d_{80} of the feed particles 92 μm. Under these conditions, a concentrate with Zn grade of 25.89% and 88.81% recovery was obtained and in the absence of both nano-micro bubbles an PAX as a promoter, the concentrate grade and recovery were 27.31% and 81.74%, respectively. The results showed that using PAX (200 g/t) led to a lower recovery increase (~1%) compared to using nano-micro bubbles (~7%).

Keywords: *Nano-micro bubbles, Zinc oxide flotation, DOE*

1. Introduction

Various methods exist to overcome the limitations of flotation caused by the presence of fine particles in the flotation feed. These methods are primarily based on increasing particle size through selective aggregation (including selective agglomeration and flocculation), reducing bubble size (using nano-micro bubbles), or employing specialized flotation cells. The low flotation rate of fine particles is mainly due to the low probability of collision between these particles and air bubbles. previous studies showed that reducing the size of air bubbles can enhance the flotation of fine particles. However, using only small bubbles in the absence of larger bubbles can increase flotation time due to the lower rising velocity and carrying capacity of small bubbles, necessitating the use of taller flotation cells. Therefore, the improvement in flotation is largely attributed to the synergy between normal-sized bubbles and fine bubbles (Farrokhpay et al., 2021). In addition, the use of small bubbles increases the entrainment of particles, which occurs due to the higher recovery of water. Consequently, it can be concluded that the grade of the product decreases as a result of the entrainment of gangue particles

into the concentrate (Trahar and Warren, 1976). Nanobubbles are extremely small gas cavities in an aqueous solution, with sizes smaller than 1 μm, and they have a lifespan ranging from several days to weeks. Since the work of adhesion between a solid particle and water is always less than the work of adhesion of water, nano-micro bubbles selectively accumulate on the surface of hydrophobic particles. Additionally, the work of adhesion decreases with increasing hydrophobicity of the solid particle surface (Maoming et al., 2010). Nano-micro bubbles create a capillary bridge between the surfaces of hydrophobic solid particles, causing these particles to adhere to each other (Hampton and Nguyen, 2010). It has also been established that the flotation rate is strongly influenced by bubble diameter, such that when the bubble diameter decreases from 665 μm to 75 μm, the flotation rate increases by up to 100 times. Thus, it is clear that reducing bubble diameter can lead to enhanced flotation of fine particles (Tao, 2005). Nazari et al. concluded that the presence of nano-micro bubbles increased the lithium-ion batteries-graphite (LIBG) flotation recovery and its kinetic rate by 15% and 33%, respectively (Nazari at al., 2022). In addition, one of the influential parameters on the quality of the concentrate and the achievable recovery in the flotation process is froth stability. Due to the presence of an electrical repulsion between the surfaces of nanobubbles, which prevents their coalescence and growth, the presence of nanobubbles significantly impacts froth stability (Sobhy and Tao, 2019). In a study on copper sulfide flotation, the presence of nano-micro bubbles was found to reduce collector and frother consumption by 50% and 66.6%, respectively (Nikouei Mahanni et al., 2024). Numerous factors influence the size of nano-micro bubbles produced, including the method of nano-micro bubble generation, the type of frother, frother concentration, gas solubility, solution temperature, gas type, solution pH, and the hydrophobicity of particles (Pourkarimi et al., 2017; Holl, 1970; Meegoda et al., 2018). If the generated nanobubbles possess high surface charge density or zeta potential, they will remain stable (Meegoda et al., 2018).

One of the major challenges in zinc oxide ores processing is the generation of fines during comminution, which are often separated by hydrocyclones, leading to the loss of valuable material. One of the methods employed in the flotation of fines is the use of nano-micro bubbles alongside conventional bubbles, which is an effective approach for increasing particle recovery. These bubbles enhance the hydrophobicity of particles (in fact, nano-micro bubbles are referred to as promoter) to increase the probability of particle-bubble attachment, thereby improving the efficiency of particle collisions. It has also been demonstrated that nano-micro bubbles can expand the size range of particles in flotation. Consequently, this study aims to compare the performance of flotation in the presence and absence of nano-micro bubbles, without desliming stage, to evaluate the impact of these bubbles on the zinc oxide ore flotation.

2. Sample characterization

The sample studied in this research was provided from the Iran Lead and Zinc Plant located in the industrial town of Zanjan Province, Iran. Qualitative and quantitative analysis methods was carried out for characterization of sample. X-ray diffraction (XRD) was used for minerals identification, and X-ray fluorescence (XRF) was used to determine the content of various elements or chemical compounds. Additionally, thin and polished section were used for microscopic mineralogical studies and determination of degree of liberation of valuable minerals in the sample.

2.1. Mineralogy

According to the XRD analysis results presented in Table 1, the minerals present in the sample, in order of abundance, include: calcite, smithsonite, quartz, hemimorphite, dolomite, clinochlore, and phlogopite. Therefore, the studied sample is of zinc oxide ore type, where smithsonite and hemimorphite are the valuable and economically significant zinc minerals, while the other minerals are considered gangue.

Table 1. Minerals identified in the studied sample using XRD analysis.

Phase	Formula	Semi-quantitative percentage
Calcite	$CaCO_3$	36.2
Smithsonite	$ZnCO_3$	20.7
Quartz	SiO_2	15.9
Hemimorphite	$Zn_4Si_2O_7(OH)_2.H_2O$	9.1
Dolomite	$CaMg(CO_3)_2$	9.1
Clinochlore	$(Mg,Al,Fe)_6(Si,Al)_4O_{10}(OH)_8$	4.5
Phlogopite	$KMg_3AlSi_3O_{10}(OH)_2$	4.5
Amorphous	-	-

2.2. Chemical composition

XRF analysis (Table 2), showed that the sample zinc grade was 15.67%. with 0.42 % lead which was negligible.

Table 2. Sample quantitative XRF analysis.

Element/Compound	SiO_2	BaO	CaO	Fe_2O_3	K_2O	MgO	MnO	SO_3	TiO_2	Pb	Zn	LOI
Percentage	19.40	0.24	15.65	3.86	0.57	1.36	0.14	0.41	0.20	0.42	15.67	24.67

2.3. Microscopic mineralogical studies

Microscopic studies were conducted on size-by-size polished sections with fraction range of 1400 μm to 75 μm. According to the results presented in Table 3, a degree of liberation exceeding 80% for both smithsonite and hemimorphite occurs at sizes below 106 μm, as illustrated in Figure 1.

Table 3. Microscopic Degree of liberation study (calculation is based on the ratio of liberated particles to the sum of liberated and locked particles).

Fraction (μm)	1400	600	212	150	106	75
Degree of liberation of smithsonite (%)	65-70	70-75	75-80	85-90	90-95	95
Degree of liberation of hemimorphite (%)	50-60	60-65	70-75	75-80	85-90	95
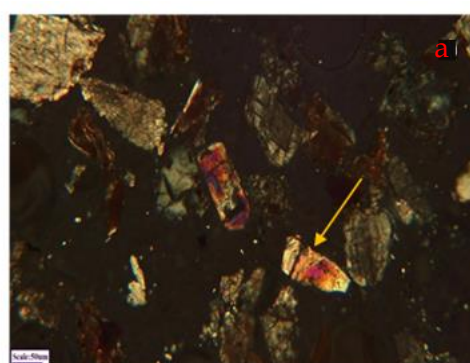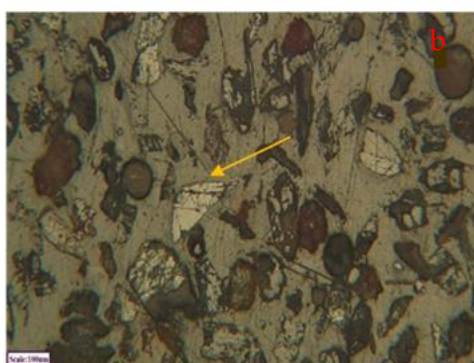
Fig. 1. Microscopic images of the 106 μm fraction. liberated particles of a) hemimorphite b) lsmithsonite

3. Materials and methods

The samples were initially crushed to below 3.36 mm in a closed circuit using primary and secondary jaw crushers with a control screen. Finally, the material remaining on the screen was fed into a roll crusher in a closed circuit with a control screen to obtain the final product with a size below 3.36 mm. The resulting product was homogenized using a riffle splitter, and ultimately, it was divided into 1-kilogram representative samples for further analysis and experiments.

To determine the optimal grinding time for the wet rod mill to achieve the desired degree of liberation (above 80%), the grinding of the mill feed with a weight of 1000 gr, 50% solids, and a grinding load of 3539 gr was conducted at times of 4, 5:30, 7, 8:30, and 10 minutes, with the results presented in Table 4. Based on the degree of liberation results, grinding times of 7 and 8:30 minutes were selected. The desliming test (using a 25-micrometer sieve and wet method) of the ground product at 7 and 8:30 minutes showed that 23.65% and 40.3% of the zinc metal, respectively, reported to the slimes.

Table 4. Grinding time and d80 of the ground product.

Grinding time (min)	4	5:30	7	8:30	10
d_{80} (μm)	150	110	92	75	69
Weight of -25 μm (gr)	196	224	285	331	412

The chemicals used in the flotation experiments are listed in Table 5 (Ejtemaei et al., 2011). In all experiments, the following parameters were kept constant: pulp pH of 11, sodium silicate (500 g/t), sodium hexametaphosphate (250 g/t), pine oil (120 g/t), pulp solid percentage (14.8%), rotor speed (1000 rpm), feed weight, and cell volume. scraping was conducted for 10 minutes in all tests, with intervals of 15 seconds. It is worth mentioning that the flotation experiments in this study were conducted without prior desliming of the feed.

Table 5. The chemicals used in flotation experiments.

Surfactant	Concentration (%)	Role	Conditioning time (min)
Sodium silicate	97	Depressant/Dispersant	5
Sodium hexametaphosphate	96	Depressant	5
Sodium sulfide	75	Sulfidant	10
Sodium hydroxide	-	pH regulator	Simultaneously with sodium sulfide
Acetate of coco amine (Armac C)	99	Collector	10
Pine oil	99	Frother	2

In this study, a two-phase vortex pump was used to generate nano-micro bubbles, and its various parameters are presented in Table 6. Dynamic light scattering (DLS) method were utilized to characterize nano-micro bubbles. According to Figure 2, the nano-micro bubbles produced by this pump have size distribution ranges between 100 and 500 nm, with the mean diameter of 300 nm and zeta potential of approximately -10 mV, which were utilized in the flotation experiments.

Table 6. Conditions of generating nano-micro bubbles.

Frother concentration in the pump tank (g/t)	Frother addition time (min)	Circulation time of the solution in the pump (min)	Input air flow rate of the pump (L/min)	Input pressure difference of the pump (mmHg)	Output pressure difference of the pump (bar)	Average size of nano-bubbles (nm)
10	0	10	2	180	2.6	300
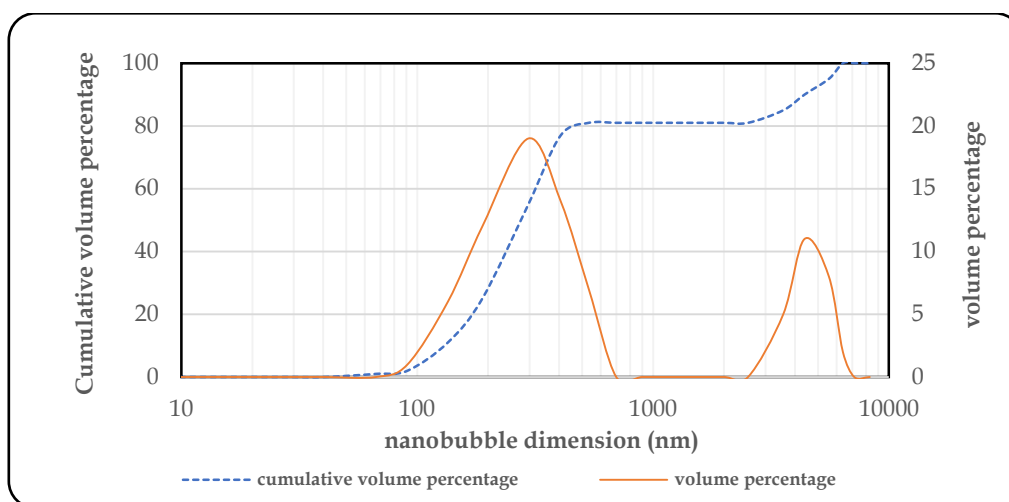
Fig. 2. Size distribution diagram of the nano-micro bubbles generated under the mentioned conditions determined by DLS.

4. Results and Discussion

In this research, to investigate the effect of the presence and absence of nano-micro bubbles on the flotation process, parameters such as feed particle size, sodium sulfide concentration, and Armac C concentration were evaluated. The experiments were conducted using DX11 design expert software and a two-level full factorial design method. The matrix of various conditions of the experiments related to this design, as well as the results, are presented in Table 7.

Table 7. The proposed experiments by the DX11 software using a two-level full factorial design method.

Test No.	Particle size (μm)	Armac C concentration (g/t)	Sodium sulfide concentration (g/t)	using nano-micro bubbles water (%)	Concentrate grade (%)	Concentrate recovery (%)
1	92	1000	4000	100	25.89	88.81
2	92	1000	4000	0	27.31	81.74
3	92	1000	3000	0	17.08	30.52
4	75	800	4000	0	24.13	58.52
5	92	1000	3000	100	15.18	33.42
6	83	900	3500	50	19.20	50.24
7	92	800	4000	100	24.41	69.86
8	75	1000	3000	0	14.87	25.62
9	75	800	4000	100	22.99	62.35
10	75	1000	4000	100	23.97	68.07
11	83	900	3500	50	18.61	52.20
12	83	900	3500	50	19.83	48.10
13	83	900	3500	50	18.56	55.20
14	92	800	3000	100	13.73	27.16
15	92	800	4000	0	25.88	66.06
16	75	1000	4000	0	25.20	65.13
17	75	800	3000	100	12.42	23.38
18	92	800	3000	0	14.39	25.71
19	75	800	3000	0	13.61	22.15
20	75	1000	3000	100	13.48	27.96

ANOVA analysis was used to evaluate the results of the experiments, to determine the factors and interactions effects on the grade, recovery and the validity of the model proposed by the software. The results are presented in Table 8. The findings indicate that the proposed model is valid, and the parameters influencing the model include the using nano-micro bubbles water (A), sodium sulfide concentration (B), Armac C concentration (C), particle size (D), as well as the interactions BC, BD, CD,

and BCD. In addition, the statistical analysis of the model evaluation shows that the model has sufficient accuracy.

Table 8. ANOVA analysis.

Source	Sum of squares	df	Mean square	F value	P value Prob>F	
Model	8230.55	8	1028.82	171.14	<0.0001	Significant
A- using nano-micro bubble water	40.83	1	40.83	79.6	<0.0244	
B- Sodium sulfide concentration	7422.68	1	7422.68	1234.76	<0.0001	
C- Armac C concentration	272.91	1	272.91	45.40	<0.0001	
D- Particle size	307.13	1	307.13	51.09	<0.0001	
BC	48.44	1	48.44	8.06	0.0161	
BD	75.26	1	75.26	12.52	0.0046	
CD	40.07	1	40.07	6.67	0.0255	
BCD	23.23	1	23.23	3.86	0.0751	
Residual	66.13	11	6.01			
Lack of fit	38.82	8	4.85	0.5330	0.7880	Not significant
Pure error	27.31	3	9.10			
Cor Total	8296.68	19				

Standard deviation=2.45, R^2=0.9920, Adjusted R^2=0.9862, Predicated R^2=0.9832, Adequate precision=39.9487

Based on the results presented in Figure 3, it is evident that the presence of nano-micro bubbles (A) has led to an enhancement in zinc recovery. This improvement can be attributed to the unique characteristics of nano-micro bubbles. Their significantly small size provides a considerable specific surface area, resulting in a substantial increase in the number of bubbles per unit volume of the flotation cell. Consequently, this notably improves the probability of effective collision between fine and ultrafine zinc oxide particles and the bubbles. Furthermore, at the nano scale, the larger contact area and stronger capillary forces can establish a more robust attachment between particles coated with a nano bubble film and larger bubbles. This more stable attachment reduces the probability of coarse particle detachment from the bubbles under the influence of shear forces within the flotation cell, ultimately improving the recovery. Additionally, the slower ascent velocity of nano-micro bubbles compared to conventional bubbles may increase the residence time of the bubbles, providing more opportunity for hydrophobic particles to adhere to the bubble surfaces. Finally, the bursting of nano-micro bubbles in the vicinity of particle surfaces can lead to the generation of localized micro turbulences, which facilitates a more effective transfer of particles to the froth phase. As the results demonstrate, increasing the share of nano-micro bubble water from 0 to 100% while keeping other parameters constant (at their midpoint) led to an increase in zinc recovery from 47.51% to 50.71%. Among the investigated parameters, the concentration of sodium sulfide (B) had the most significant impact on zinc recovery in the concentrate. When its concentration increased from 3000 g/t to 4000 g/t (with other parameters held constant), the zinc recovery increased from 27.57% to 70.65%. This improvement can be attributed to the reaction of sulfide ions (S^{2-}) present in the solution with the

surface of oxide minerals, leading to the formation of a metal sulfide layer (such as ZnS) on their surface. This surface sulfidation, by creating more active sites, facilitates collector adsorption and consequently results in the formation of a stronger hydrophobic layer on the particles, increasing their tendency to attach to air bubbles. The high concentration of sodium sulfide is likely attributed to two factors: its role as a pH regulator (hydrolysis of sodium sulfide yields hydroxide ions, resulting in an elevation of the solution's pH), and the potential increase in sodium sulfide consumption due to presence of slimes. Additionally, increasing the concentration of Armac C collector (C) from 800 g/t to 1000 g/t (with other parameters held constant) resulted in an 8.26% increase in recovery, with zinc recovery rising from 44.98% to 53.24%. This improvement is likely due to increased surface hydrophobicity caused by the higher collector concentration and the increased contact angle at higher concentrations, which enhances particle-bubble attachment. Furthermore, increasing the feed particle size (D) leads to better flotation performance because fewer fines are generated during grinding. For instance, when the feed particle size was increased from -75 μm to -92 μm, the zinc recovery increased from 44.73% to 53.49%.

As indicated, the interactions of parameters BC, BD, CD, and BCD had a significant effect on the response, and their Contour and three-dimensional plots are presented in Figure 4. The interactions of all parameters on the response were positive, resulting in an increase in recovery.
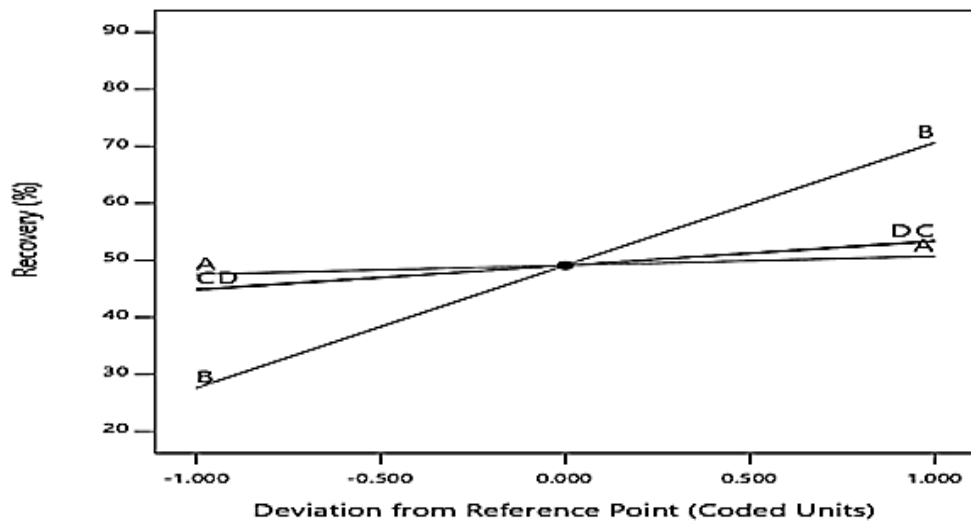
Fig. 3. Perturbation plot

a)

68
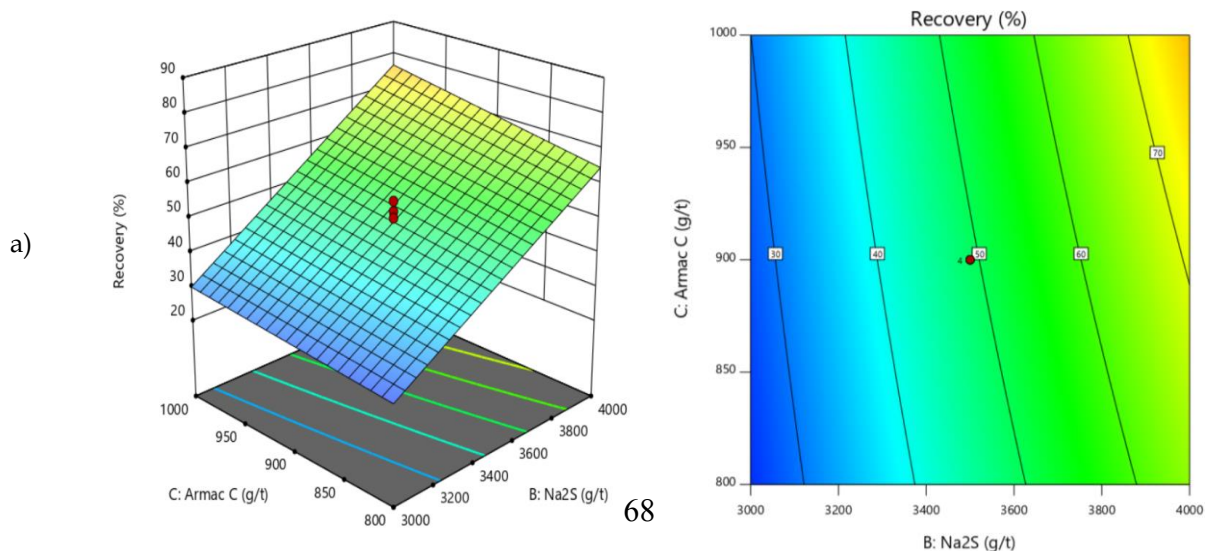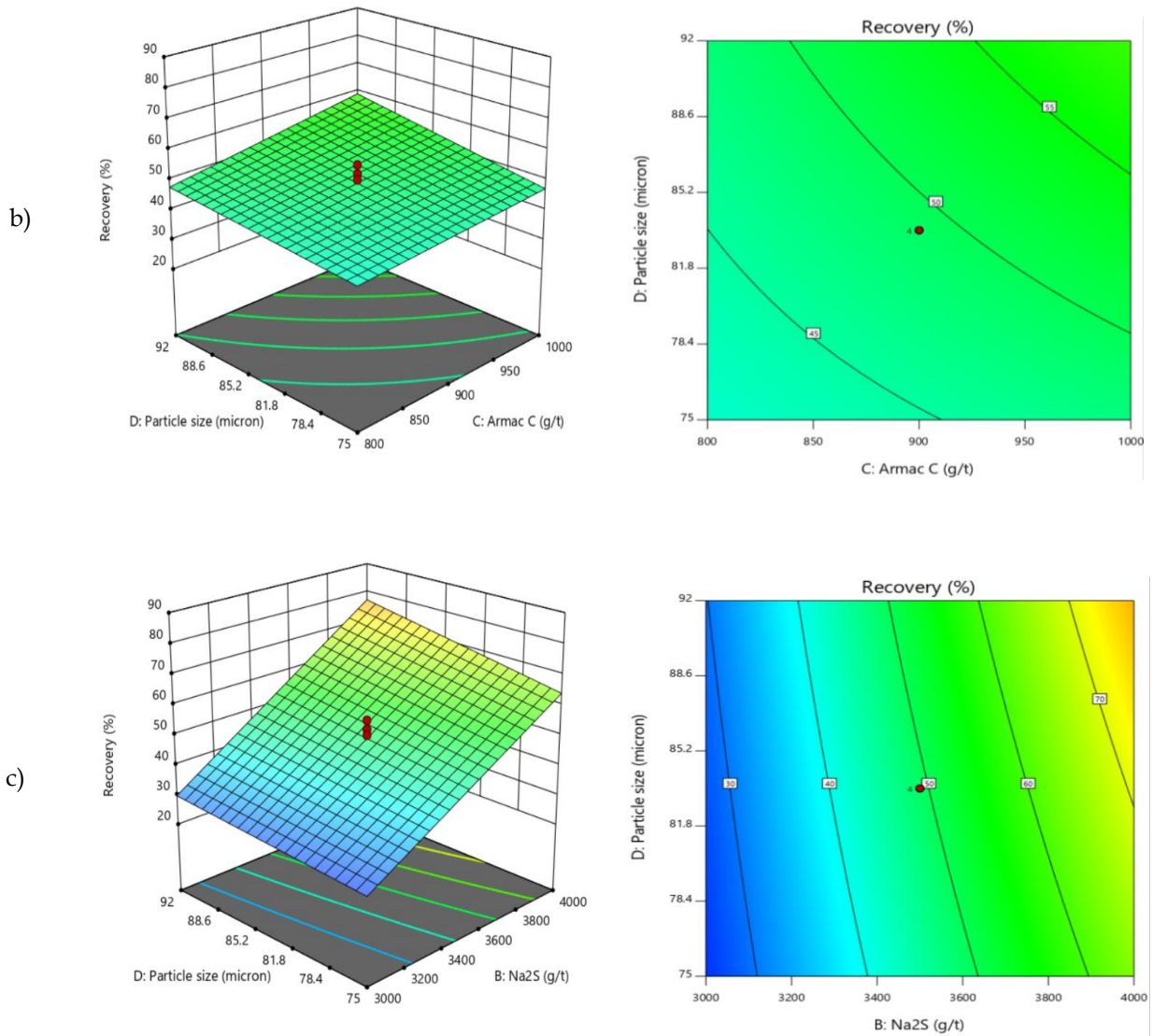
Fig 4. Contour and three-dimensional plots showing the interaction effects of: a) BC, b) BD, c) CD, on recovery.

Based on the response surface equation the optimization of effective parameters to achieve the maximum zinc recovery in the concentrate is shown in Figure 5. According to these results, the maximum zinc recovery was achieved when the using nano-micro bubbles water was 100%, the sodium sulfide concentration was 4000 g/t, the Armac C concentration was 1000 g/t, and the d_{80} of the feed particles was 92 μm. Under these conditions, a concentrate with a grade of 25.74% and a recovery of 87.45% was obtained. Compared to the absence of nano-micro bubbles, this represents an approximate 7% increase in zinc recovery.
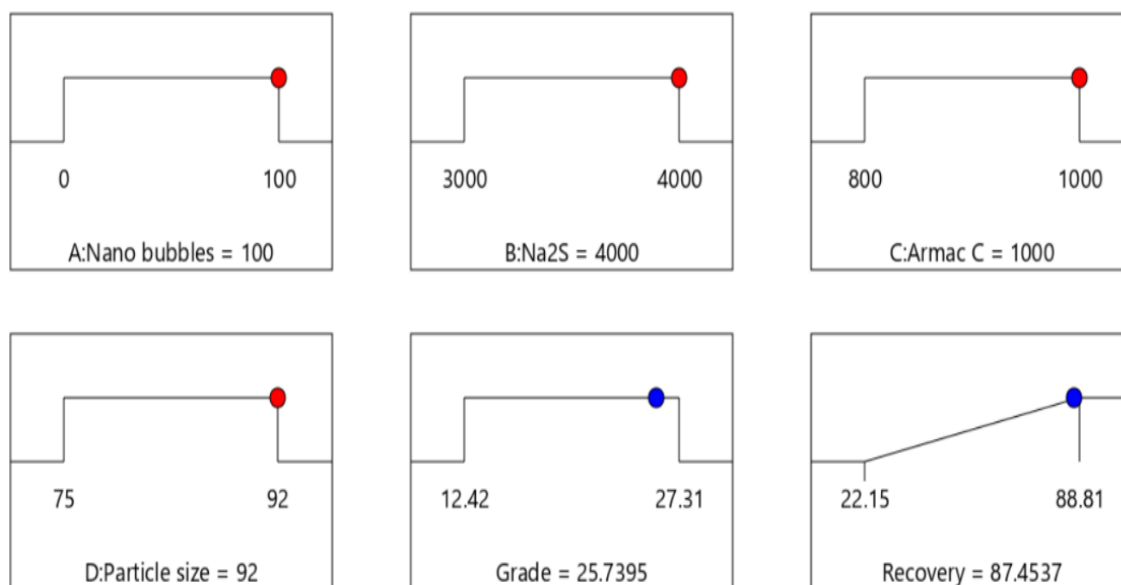
Fig 5. Optimization results to achieve maximum zinc recovery.

Given the role of nano-micro bubbles as a promoter, a comparison was made between the impact of using nano-micro bubbles and potassium amyl xanthate (PAX) as a promoter under optimized condition. The results are presented in Table 9. The application of PAX at 100 g/t and 200 g/t concentrations resulted in marginal recovery increase of 0.35% and 0.84%, respectively, which was significantly lower than the 7.07% improvment observed when nano-micro bubbles were used. The superior performance of nano-micro bubbles as a promoter in enhancing zinc recovery is likely attributed to their ability to establish a more efficient and uniform hydrophobic coating on the particle surface. İn contrast, the effectivness of PAX in inducing hydrophobicity relies on its chemical or physical adsorption at the active sites of the mineral surface.

Table 9. comparison of the effect of PAX with nano-micro bubbles under optimized condition.

Test No.	using nano-micro bubbles water (%)	PAX (g/t)	Concentrate grade (%)	Concentrate recovery (%)
1	0	0	27.31	81.74
2	0	100	26.02	82.09
3	0	200	25.92	82.58
4	0	300	24.21	77.20
5	100	0	25.89	88.81

5. Conclusion

In contrast to previous studies, this reseach aimed to investigate the effect of the presence and absence of nano-micro bubbles in the flotation process of zinc oxide minerals without feed desliming, provided from the Iranian Lead and Zinc Plant located in Zanjan Province, which contains valuable minerals such as smithsonite and hemimorphite. Four parameters were examined: the using nano-micro bubble water, sodium sulfide concentration, Armac C concentration, and feed particle size. By examining the using nano-micro bubble water from 0% to 100% while keeping other factors at their

midpoint values, it was found that zinc recovery increased from 47.51% to 50.71%. This 3.2% increase may be attributed to the higher probability of fine particle collisions and the enhanced probability of coarse particles attaching to conventional bubbles. When evaluating sodium sulfide concentrations of 3000, 3500, and 4000 g/t, it was determined that this parameter had the most significant impact on flotation among the studied parameters. Increasing the sodium sulfide concentration from 3000 g/t to 4000 g/t resulted in a 43.08% increase in zinc recovery, rising from 27.57% to 70.65%. This improvement could be attributed to enhanced sulfidation of the zinc oxide mineral surfaces, which improves collector adsorption on the particle surfaces. To investigate the effect of Armac C concentration on flotation, concentrations of 800, 900, and 1000 g/t were examined. The results showed that increasing the Armac C concentration from 800 to 1000 g/t (while keeping other parameters at their midpoint values) increased zinc recovery from 44.98% to 53.24%. This improvement was likely due to an increase in the particle-bubble contact angle. Additionally, it was found that reducing the particle size, d_{80}, from 92 μm to 75 μm led to a decrease in zinc recovery from 53.49% to 44.73%. This was because the rod mill grinding product contained more slimes, which may increase chemical consumption and reduce recovery. Finally, by optimizing the studied parameters, it was concluded that maximum zinc recovery was achieved when the using nano-micro bubble water was 100%, the sodium sulfide concentration was 4000 g/t, the Armac C concentration was 1000 g/t, and the d_{80} of the feed particles was 92 μm. Under these conditions, a concentrate with a grade of 25.89% and a recovery of 88.81% was obtained, representing an approximately 7% increase in zinc recovery compared to the absence of nano-micro bubbles. Furthermore the results indicated that the application of potassium amyl xanthate as a promoter, compared to the presence of nono-micro bubbles, resulted in a lower recovery increase, approximately 1% at a PAX concentration of 200 g/t. In conditions where neither nano-micro bubbles nor PAX were used, the concentrate grade and recovery were 27.31% and 81.74% respectively.

References

Ejtemaei, S., Filippov, L., & Farnasiero, D. (2011). Influence of important factors on flotation of zinc oxide mineral using cationic, anionic and mixed (cationic/anionic) collectors, *Minerals Engineering,* Vol. 24 (13), 1402-1408. doi: 10.1016/j.mineng.2011.05.018

Farrokhpay, M., Irannajad, M., & Gharabaghi, M. (2021). Flotation of fine particles: A review, *Mineral Processing and Extractive Metallurgy Review,* Vol. 42 (7), 473-483. doi: 10.1080/08827508.2020.1793140

Nikouei Mahanni, N., Karamoozian, M., Jahani Chegeni, M., & Mahmoodi Meymand, M. (2024). Effect of stable nano-microbubbles on sulfide copper flotation and reduction of chemicals dosage. *Journal of Mining and Enviroment, Vol. 15* (1). 261-283. doi: 10.22044/jme.2023.13205.2413

Hampton, M. A., Nguyen, A. V. (2010). Nanobubbles and the nanobubble bridging capillary force. *Advances in colloid and interface science, vol. 154* (1-2), 30-55. doi: 10.1016/j.cis.2010.01.006

Holl, J. W. (1970). Nuclei and Cavitation. *The American Society of Mechanical Engineerings,* 681–688. Doi: 10.1115/1.3425105

Maoming, Fan, et al. (2010). Nanobubble generation and its applications in froth flotation (part II): fundamental study and theoretical analysis. *Mining Science and Technology (China), vol. 20* (2), 159-177. doi: 10.1016/S1674-5264(09)60179-4

Meegoda, J. N., Aluthgun Hewage, S., & Batagoda, J. H. (2018). Stability of nanobubbles. *Environmental Engineering Science, vol. 35* (11). 1216-1227. doi: 10.1089/ees.2018.0203

Nazari, S., Zhou, S., Hassanzadeh, A., Li, J., Bu, X., & Kowalczuk, P. B. (2022). Influence of operating parameters on nanobubbles -assisted flotation of graphite. *Journal of Materials Research and Technology , vol.* 20, 3891-3904. doi: 10.1016/j.jmrt.2022.08.137

Pourkarimi, Z., Rezai, B., & Noaparast, N. (2017). Effective parameters on generation of nanobubbles by cavitation method for froth flotation applications *Physicochemical Problems of Mineral Processing, vol. 53*(2), 920-942. doi: 10.5277/ppmp170220

Sobhy, A., Tao, D. (2019). Effects of nanobubbles on froth stability in flotation column. *International Journal of Coal Preparation and Utilization, vol. 39* (4), 183-198. doi: 10.1080/19392699.2018.1459582

Tao, D. (2005). Role of bubble size in flotation of coarse and fine particles—a review. *Separation science and technology, vol. 39* (4), 741-760. doi: 10.1081/SS-120028444

Trahar, w., Warren, L. (1976). The flotability of very fine particles—A review. *International Journal of Mineral Processing, vol. 3(2),* 103-131. doi: 10.1016/0301-7516(76)90029-6

Assessment of Zinc Precipitation from Sulfate Solutions Using Magnesium-Rich Ores

Saeid Karimi[1], Bahram Behnajady[2,*], Javad Moghaddam[3]

[1] Assistant professor, Department of Metallurgy and Materials Engineering, Hamedan University of Technology, Hamedan, Iran

[2] Assistant professor, Research Centre of Advanced Materials, Faculty of Materials Engineering, Sahand University of Technology, Sahand New Town, Iran

[3] Professor, Materials and Metallurgical Engineering Department, University of Zanjan, Zanjan, Iran

*Corresponding author: b_behnajady@sut.ac.ir (Bahram Behnajady)

Abstract:

This study systematically investigates the mechanisms and optimization of zinc precipitation from sulfate solutions using magnesium-containing ores. The dominant reaction pathway leads to the formation of zinc hydroxysulfate ($Zn_5(OH)_6(SO_4)_2$) at moderate pH (4–6.5), as confirmed by a consistent final pH of 6.5 in all experiments. Temperature critically influences reaction kinetics, with 80 °C identified as optimal for maximizing zinc recovery (73.4 %) and ensuring effective magnesium participation in precipitation reactions. Process efficiency is governed by ore dosage, where 100 g/L of magnesium-rich ore yields peak zinc recovery, beyond which marginal improvements occur. Time-dependent studies reveal that 150 min represents the practical equilibrium for zinc precipitation at 80 °C, achieving 73.4% recovery with diminishing returns thereafter. Key findings demonstrate that controlled parameters—pH 6.5, 80°C, 150-min reaction time, and optimized ore dosage—collectively enhance zinc recovery while minimizing reagent consumption and energy costs. Under the optimized conditions (T = 80°C, ore dosage = 100 g/l, time = 150 min), the magnesium content demonstrated a significant reduction from 7.0 g to 5.1 g, corresponding to an absolute decrease of 1.9 g (27.1% decrement), which clearly indicates effective magnesium participation in the precipitation process, where the combination of elevated temperature and controlled ore dosage synergistically enhanced magnesium removal efficiency while minimizing residual content, ultimately contributing to improved process performance.

Keywords: *Zinc precipitation, Basic zinc sulfate, Magnesium-rich ore, Magnesium removal.*

1. Introduction

With the increasing global demand for zinc and the depletion of high-grade zinc reserves, low-grade zinc ores have gained significant attention from producers (Ashtari et al., 2025; Karimi et al., 2017). Zinc oxide deposits may contain minerals such as smithsonite, hemimorphite, or willemite, while low-grade ores often include gangue minerals like calcite, dolomite, quartz, and iron oxides (Khanmohammadi Hazaveh et al., 2020). Among the soluble impurities in zinc sulfate solutions, magnesium is particularly problematic as it is not removed during the purification stages of the zinc production process, including iron precipitation or hot/cold purification processes. Due to magnesium's higher standard potential compared to zinc, it cannot be deposited on aluminum cathodes during electrowinning (MacKinnon & Brannen, 1991), leading to its accumulation in the solution over time. Increased magnesium concentration raises energy consumption and reduces current efficiency in the electrowinning process. The permissible magnesium concentration in zinc

solutions is typically limited to 10-15 g/L, making its removal crucial in zinc production (Mosayebi et al., 2021).

Current pretreatment methods for zinc concentrate include dilute sulfuric acid leaching, magnesium fluoride precipitation (Booster et al., 2000; Georgalli et al., 2008), lime neutralization (Matthew et al., 1980; Sharma, 1990), solvent extraction (Abutalebi et al., 2019; Cheng et al., 2010), and freezing crystallization (Jin et al., 2023). During dilute sulfuric acid leaching of zinc concentrate, magnesium oxide (MgO) and magnesium carbonate ($MgCO_3$) dissolve along with zinc oxide (ZnO) and zinc carbonate ($ZnCO_3$), resulting in zinc losses. In fluoride precipitation, fluoride ions act as ligands, reacting with magnesium to form low-solubility magnesium fluoride (MgF_2), which is removed as a precipitate (Jin et al., 2023). However, increased fluoride concentration can cause zinc sheets to stick to aluminum cathodes, reducing their effectiveness. The lime neutralization method exploits the difference in hydrolysis pH between zinc and magnesium, adjusting the pH to 10-11 using calcium hydroxide ($Ca(OH)_2$). This process consumes significant amounts of lime and produces gypsum as a byproduct, requiring further treatment (Heimala, 1981). Solvent extraction is effective for separating specific metals from polymetallic solutions, but residual organic phases in the aqueous phase and high chemical costs limit its application (Haghighi et al., 2015). The high energy consumption of freezing crystallization has prevented its industrial adoption. Currently, lime neutralization at pH 10-11 remains the primary industrial method for magnesium removal.

This study investigates the feasibility of precipitating zinc from sulfate solutions using magnesium-rich soil, aiming to separate magnesium from zinc through a displacement precipitation reaction where magnesium enters the solution while zinc is incorporated into the final precipitates. The research focuses on optimizing key parameters such as temperature, reaction time, and the quantity of magnesium-rich soil to achieve efficient separation.

2. Material and methods

2.1. Material

The main experimental material was a magnesium-rich zinc concentrate containing approximately 11.7% zinc and 7.1% magnesium. The zinc sulfate solution used had concentrations of 21.4 g/L zinc and 9.2 g/L magnesium. Both the concentrate and the solution were provided by Zanjan Zinc Khales Sazan Industries Company (ZZKICo) in Zanjan, Iran.

2.2. Experimental Procedure

In this study, the precipitation of zinc from a one-liter zinc sulfate solution was investigated using magnesium-rich ore as a precipitant. The key parameters evaluated included temperature (ranging from 65 to 85 °C), reaction time (ranging from 30 to 180 min), and ore dosage (between 50 and 150 g/L). The process begins by heating the zinc sulfate solution to the target temperature, followed by the controlled addition of a predetermined amount of ore. The solution was continuously stirred at 1000 rpm using a mechanical stirrer to ensure uniform mixing and enhance the precipitation process.

All experiments were conducted in a 2-liter beaker, with temperature precisely controlled to maintain accuracy within ±1 °C. Once the reaction was complete, the entire mixture was subjected to solid-liquid separation using vacuum filtration, ensuring effective removal of the precipitated solids. The collected precipitates were then dried in an oven at 110 °C for 24 h to remove residual moisture, preserving their composition for further analysis.

Subsequently, the dried precipitates were analyzed using atomic absorption spectroscopy (Varian 240AA) to determine their zinc content. The efficiency of zinc removal was quantified by comparing the zinc concentration in the initial solution with that of the final precipitates. The percentage of zinc precipitation was calculated using a defined equation, providing a measure of the process's effectiveness in precipitating zinc from the solution.

$$R_{Zn\ Prec.} = \frac{Zn_{prec.} \times m_{prec.} - Zn_{ore} \times m_{ore}}{Zn_{ore} \times m_{ore}} \times 100 \tag{1}$$

In this equation, $Zn_{prec.}$ represents the zinc grade in the final precipitates (in %), $m_{prec.}$ denotes the weight of the final precipitates (in g), Zn_{ore} refers to the zinc grade in the initial material (in %), and m_{ore} indicates the weight of the initial material (in g).

3. Results and Discussion

3.1. Proposed precipitation reactions

To determine the mechanism of zinc precipitation during the process of adding magnesium-containing ore, the possible reactions can be considered as follows. The formation of zinc hydroxysulfate ($Zn_5(OH)_6(SO_4)_2$) via reaction (2), where carbonate hydrolysis releases OH^- ions to precipitate zinc while evolving CO_2 gas and leaving soluble $MgSO_4$ in solution. The direct precipitation of zinc hydroxide ($Zn(OH)_2$) under higher pH conditions, as shown in reaction (3). The dominant product (hydroxysulfate vs. hydroxide) depends on pH, with hydroxysulfate favored at moderate pH (4–6) and hydroxide at higher pH (>7). With all experiments reaching an identical final pH of 6.5, the data confirmed zinc hydroxysulfate as the prevailing reaction phase. In addition, temperature plays a critical role, with accelerating kinetics and promoting hydroxysulfate formation based on the measured pH in the final solution.

$$5ZnSO_{4(aq)} + 3MgCO_{3(s)} + 3H_2O_{(aq)} \rightarrow Zn_5(OH)_6(SO_4)_{2(s)} + 3MgSO_{4(aq)} + 3CO_{2(g)} \tag{2}$$

$$ZnSO_{4(aq)} + MgCO_{3(s)} + H_2O_{(aq)} \rightarrow Zn(OH)_{2(s)} + MgSO_{4(aq)} + CO_{2(g)} \tag{3}$$
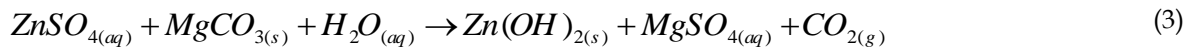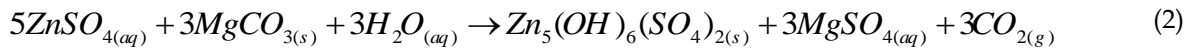
If calcium is present in the ore, the zinc precipitation reaction can also proceed as follows. In industrial zinc recovery processes, the precipitation reaction using calcium carbonate ($CaCO_3$) proceeds primarily through the formation of zinc hydroxysulfate under moderately acidic to neutral conditions (pH ~4-6.5), as described by the reaction (4). This pathway is industrially preferred due to the stability and filterability of the hydroxysulfate precipitate, though it generates $CaSO_4$ (gypsum) as a byproduct, which requires management to prevent equipment scaling. The process is typically conducted at elevated temperatures (70-80 °C) to enhance reaction kinetics, with the CO_2 off-gas necessitating proper handling. The consistent final pH of 6.5 in these experiments confirms the dominance of hydroxysulfate formation, as this pH range optimally suppresses competing zinc hydroxide ($Zn(OH)_2$) precipitation while maximizing zinc recovery efficiency, in agreement with established hydrometallurgical practices (Dutrizac, 2002). The carbonate-to-zinc stoichiometry (3:5 ratio) is carefully controlled to ensure complete zinc precipitation while minimizing excess reagent consumption.

$$5ZnSO_{4(aq)} + 3CaCO_{3(s)} + 3H_2O_{(aq)} \rightarrow Zn_5(OH)_6(SO_4)_{2(s)} + 3CaSO_{4(s)} + 3CO_{2(g)} \tag{4}$$

$$ZnSO_{4(aq)} + CaCO_{3(s)} + H_2O_{(aq)} \rightarrow Zn(OH)_{2(s)} + CaSO_{4(s)} + CO_{2(g)} \tag{5}$$
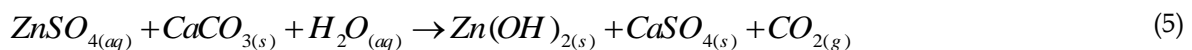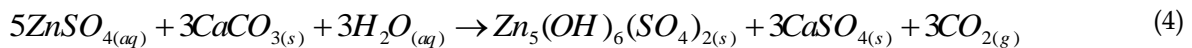
Fig. 1 illustrates the relationship between zinc precipitation recovery (%) and the amount of magnesium-rich ore (g) used in the process at 75 °C for 150 min, highlighting the impact of ore dosage on zinc removal efficiency. As the ore dosage increases from 50 to 150 g/L, a significant improvement in zinc precipitation recovery is observed, emphasizing the role of ore quantity in facilitating the reaction. At 50 g/L of ore dosage, the recovery rate is relatively low at 28.6 %, indicating that the available reactive components are insufficient for effective zinc precipitation. As the ore addition is

increased to 100 g/L, the recovery rate improves notably to 55.8 %, demonstrating a more favorable condition for precipitation, likely due to better interaction between zinc ions and the active sites of the ore. The highest recovery of 62.6 % is recorded at 150 g/L of ore dosage, suggesting that this dosage provides an optimal balance of reactants, maximizing zinc removal while ensuring efficient resource utilization. However, beyond this point, further increasing the ore dosage may not result in a significant improvement in recovery efficiency and could lead to excessive material consumption, making the process less economical.
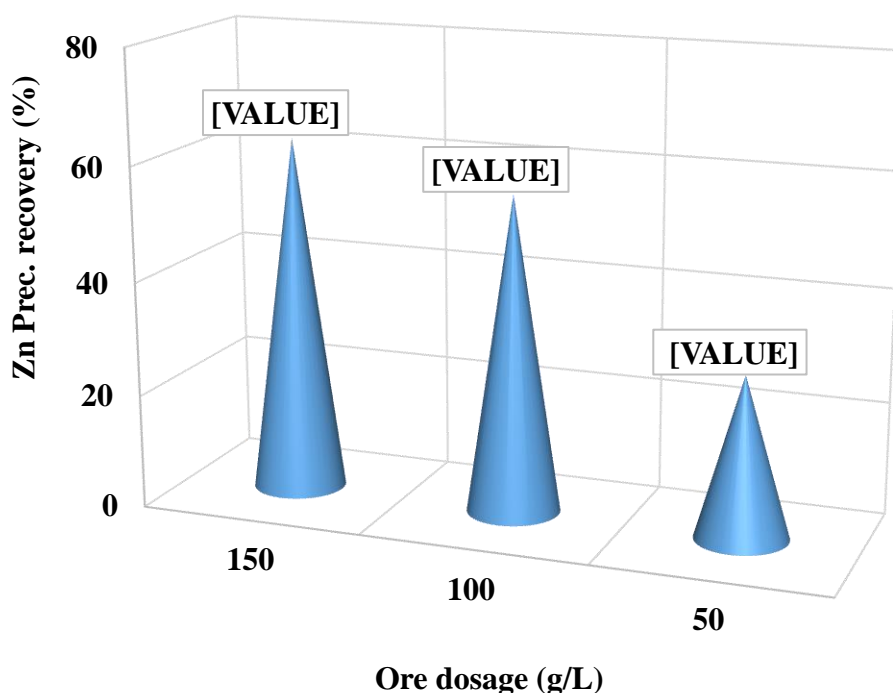
Fig. 1. Effect of magnesium-rich ore addition on zinc precipitation recovery at conditions of 75 °C for 150 min.

Table 1 presents the magnesium content measured before and after the zinc precipitation reaction conducted at 75°C for 150 min using various amounts of magnesium-bearing ores. The experimental results demonstrate that the amount of added ore has a direct impact on magnesium behavior in the precipitation process. In the 150 g/L treatment, the slight increase in magnesium after precipitation (from 10.5 to 12 g) indicates that the excessive ore quantity prevented effective magnesium participation in zinc precipitation reactions. Conversely, when the ore amount was reduced to 100 and 50 g/L, significant decreases in magnesium were observed (from 7 to 5.7 g and from 3.5 to 2.4 g, respectively), demonstrating more active magnesium involvement in precipitation reactions at lower ore quantities. This pattern suggests that for optimal magnesium removal from waste, controlled and reduced amounts of ore should be used to create favorable conditions for magnesium reactivity, while ensuring sufficient time for reaction completion. These findings can be applied to the design of industrial processes for managing magnesium-containing waste.

Table 1. Magnesium content before and after the zinc precipitation process using various magnesium-bearing ores

Ore dosage (g/L)	Before (g)	After (g)
150	10.5	12.0
100	7	5.7

50	3.5	2.4

Fig. 2 illustrates the effect of temperature on zinc precipitation recovery (%) within the range of 65 to 85 °C, under the conditions of 150 min reaction time and 100 g/L of magnesium-rich ore. As the temperature increases, zinc precipitation recovery improves significantly, highlighting the positive influence of temperature on the reaction kinetics and precipitation efficiency. At 65 °C, the recovery is relatively low at 18.2%, suggesting insufficient thermal energy to drive the reaction effectively. Increasing the temperature to 70 °C slightly enhances recovery to 23.7%, but a more substantial improvement is observed at 75 °C, where recovery reaches 55.8 %. The highest recovery rates are achieved at 80 °C (73.4 %) and 85 °C (75.6 %), with only a minor difference of 2.2 % between them. This suggests that 80 °C is the optimum temperature, as further increasing it to 85 °C does not provide a significant improvement in zinc removal while leading to higher energy consumption. Thus, 80°C offers the best balance between efficiency and energy use for maximizing zinc precipitation recovery.
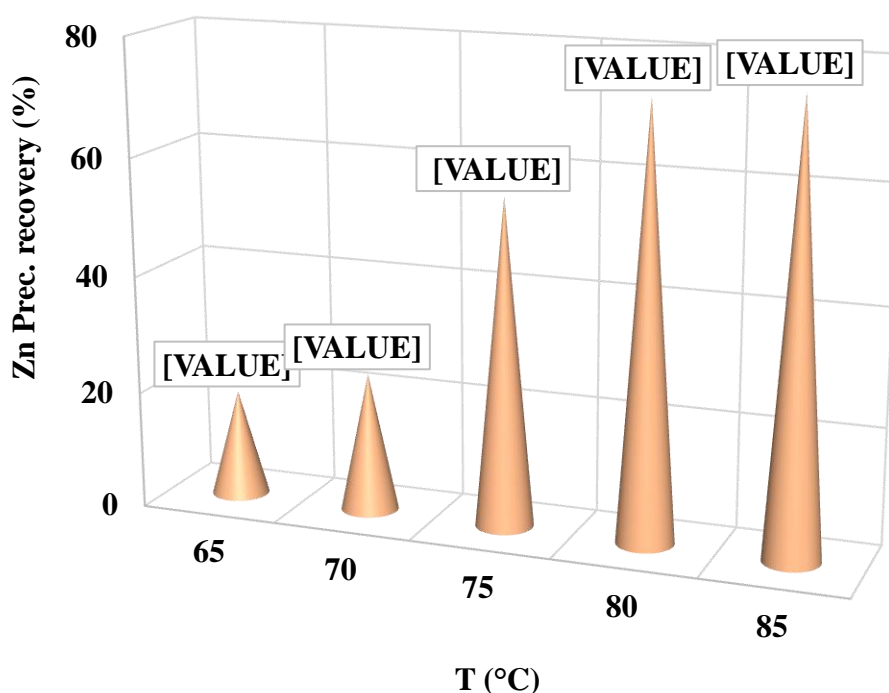
Fig. 2. Effect of temperature on zinc precipitation recovery at conditions of 100 g/L magnesium-rich ore for 150 min.

Table 2 shows the magnesium content measured before and after the zinc precipitation reaction conducted with 100 g/L magnesium-bearing ore for 150 min at various temperatures. The results of investigating the temperature effect on the zinc precipitation process demonstrate that temperature variations significantly influence magnesium behavior in the system. At lower temperatures (65 and 70 °C), the slight increase in magnesium to 7.4 and 7.5 g, respectively, indicates that magnesium does not effectively participate in precipitation reactions. When the temperature reaches 75 °C, a noticeable decrease in magnesium to 5.7 g reveals the beginning of magnesium's effective participation in precipitation mechanisms. At 80 and 85 °C, the stabilization of magnesium content at 5.1 g demonstrates maximum effective participation of magnesium in the reactions, where magnesium either fully incorporates into the precipitate structure or forms stable compounds. These observations emphasize that maintaining 80 °C is essential for achieving optimal and effective magnesium participation in the precipitation process, as this temperature simultaneously maximizes removal

efficiency and prevents incomplete magnesium involvement. The current findings are fully consistent with known mechanisms in mineral compound precipitation studies.

Table 2. Magnesium content before and after the zinc precipitation process using various temperatures

Temperature (°C)	Before (g)	After (g)
65	7	7.4
70	7	7.5
75	7	5.7
80	7	5.1
85	7	5.1

Fig. 3 shows zinc precipitation recovery (%) over time (30 to 180 min) at a constant temperature of 80 °C with an ore mass of 100 g/L. Initially, the recovery increases rapidly, reaching approximately 27.9 % at 30 min, indicating a fast precipitation rate due to favorable kinetic conditions at the elevated temperature. As time progresses, the recovery continues to rise but at a slower pace, reaching 45.4 % at 60 min, 53.7 % at 90 min, and 68.9 % at 120 min, suggesting a gradual approach towards equilibrium. By 150 and 180 min, the recovery plateaus at around 73.4 % and 74.6 %, respectively, indicating that most of the recoverable zinc has been precipitated, and further time yields diminishing returns. The 150 min mark emerges as the optimum precipitation time for zinc recovery, achieving 73.4% efficiency—a near-maximum yield with minimal further gains beyond this point. At 80°C, the reaction kinetics are initially rapid, but by 150 min, the system approaches practical equilibrium, where additional time (e.g., 180 min, 74.6%) only marginally improves recovery (just 1.2% higher) at the cost of extended processing. This plateau suggests that most accessible zinc has already been precipitated, and further retention is economically unjustified due to diminishing returns. Thus, 150 min strikes the best balance between recovery efficiency and operational practicality, optimizing both energy use and throughput in industrial applications.
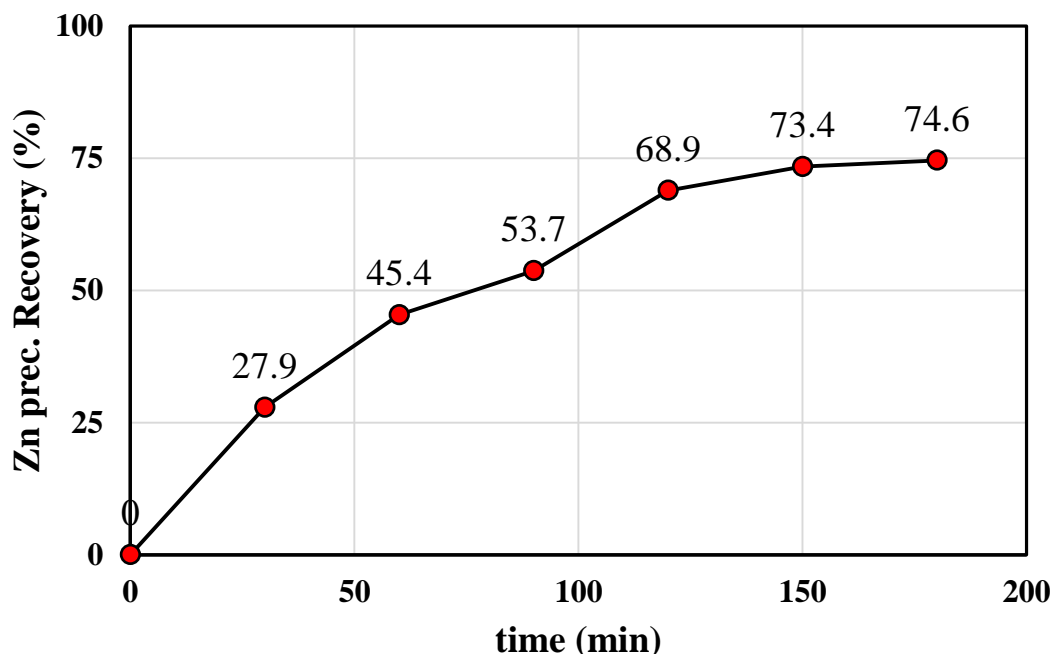
Fig. 3. Effect of time on zinc precipitation recovery at a condition of 100 g/L magnesium-rich ore at 80 °C.

Zinc precipitation from sulfate solutions employs various agents under optimized conditions, with patented methods enhancing selectivity and efficiency. Lime ($Ca(OH)_2$) or hydrated lime is another widely used agent, particularly for precipitating zinc as zinc oxide (ZnO) and simultaneously forming gypsum ($CaSO_4$) as a byproduct. This process operates optimally at pH 6.5–7.5 and temperatures between 70–95°C. The resulting ZnO particles are typically fine (<30 μm), while gypsum crystals are larger, enabling efficient separation by filtration or sedimentation (Habashi, 1997). Lime is cost-effective and suitable for large-scale operations, though careful pH control is necessary to prevent excessive zinc coprecipitation (Voigtm, 2012). This method minimizes magnesium coprecipitation and allows gypsum recycling. Basic zinc sulfate formation is achieved at lower pH (5.5–6.5) and temperatures ≤95 °C using calcium-based agents, producing distinct gypsum and zinc sulfate particles separable via granulometric sizing (Choi, 2014). Limestone ($CaCO_3$) can also be used to precipitate zinc, forming zinc carbonate ($ZnCO_3$) at pH 4.5–6.5 and elevated temperatures (~90°C). However, limestone reacts more slowly than lime, so excess reagent is often required, and unreacted material is typically recycled. This method is less common industrially due to kinetic limitations, but may be chosen where carbonate byproducts are desired or where lime is not readily available (Gupta & T. K. Mukherjee, 1990). In summary, the selection of a precipitation agent for zinc sulfate solutions depends on the specific impurities present, desired selectivity, operational costs, and downstream processing requirements. Each method offers distinct advantages and trade-offs, and process optimization is essential to maximize zinc recovery and solution purity. If a low-cost agent can be effectively utilized for zinc precipitation while improving economic efficiency, its continued use and potential replacement of conventional methods could become viable.

4. Conclusions

In conclusion, this study systematically investigated the mechanisms and optimization of zinc precipitation from sulfate solutions using magnesium-containing ores, demonstrating that the dominant reaction pathway leads to the formation of zinc hydroxysulfate ($Zn_5(OH)_6(SO_4)_2$) under

moderate pH conditions, as evidenced by the consistent final pH of 6.5 across all experiments. The research identified 80 °C as the optimal temperature for maximizing zinc recovery and ensuring effective magnesium participation, while an ore dosage of 100 g/L provided peak zinc recovery with minimal marginal gains beyond this point. Time-dependent analysis revealed that 150 min represents the practical equilibrium for zinc precipitation at 80 °C, achieving 73.4 % recovery before diminishing returns set in. Notably, under these optimized conditions (80 °C, 100 g/L ore dosage, 150 min), magnesium content decreased significantly from 7.0 to 5.1 g (a 27.1 % reduction), highlighting the synergistic effect of temperature and ore dosage in enhancing magnesium removal efficiency and minimizing residual content. These findings collectively establish that controlled parameters—pH 6.5, 80 °C reaction temperature, 150 min, and 100 g/L ore dosage—work in concert to optimize zinc recovery while reducing reagent consumption and energy costs, providing valuable insights for industrial-scale hydrometallurgical applications.

References

Abutalebi, M. R., Saneie, M., & Moghaddam, J. (2019). Investigation on the Zn separation behavior from solution contain Mg from a leaching solution of zinc filter cake by Solvent Extraction. *Metallurgical Engineering*, *22*(2), 96–103. https://doi.org/10.22076/me.2019.103493.1231

Ashtari, P., Surani-Yancheshmeh, H., Karimi, S., & Saghafi Yazdi, M. (2025). Developing a facile process for cobalt recycling from zinc plant residues using various environmentally friendly reductants towards a green and sustainable application in water splitting. *Journal of Industrial and Engineering Chemistry*. https://doi.org/10.1016/j.jiec.2025.01.055

Booster, J. L., Van Sandwijk, A., & Reuter, M. A. (2000). Magnesium removal in the electrolytic zinc industry. *Minerals Engineering*, *13*(5), 517–526. https://doi.org/10.1016/S0892-6875(00)00032-7

Cheng, C. Y., Zhang, W., & Pranolo, Y. (2010). Separation of Cobalt and Zinc from Manganese, Magnesium, and Calcium using a Synergistic Solvent Extraction System Consisting of Versatic 10 and LIX 63. *Solvent Extraction and Ion Exchange*, *28*(5), 608–624. https://doi.org/10.1080/07366299.2010.499299

Choi, Y. (2014). *Production of zinc sulphate concentrates from a dilute zinc sulphate solution*. Google Patents.

Dutrizac, J. E. (2002). Calcium sulphate solubilities in simulated zinc processing solutions. *Hydrometallurgy*, *65*(2–3), 109–135. https://doi.org/10.1016/S0304-386X(02)00082-8

Georgalli, G. A., Eksteen, J. J., Pelser, M., Lorenzen, L., Onyango, M. S., & Aldrich, C. (2008). Fluoride based control of Ca and Mg concentrations in high ionic strength base metal sulphate solutions in hydrometallurgical circuits. *Minerals Engineering*, *21*(3), 200–212. https://doi.org/10.1016/j.mineng.2007.09.010

Gupta, C. K., & T. K. Mukherjee. (1990). Hydrometallurgy in extraction processes Vol. 1. *CRC Press*, *1*.

Habashi, F. (1997). Handbook of extractive metallurgy. *Handbook of Extractive Metallurgy, Vol.2*, *1*.

Haghighi, H. K., Moradkhani, D., & Salarirad, M. M. (2015). Separation of zinc from manganese, magnesium, calcium and cadmium using batch countercurrent extraction simulation followed by scrubbing and stripping. *Hydrometallurgy*, *154*, 9–16. https://doi.org/10.1016/j.hydromet.2015.03.007

Heimala, S. O. (1981). *Process for electrolytic recovery of zinc from zinc sulfate solutions*. Google Patents.

Jin, X., Zhen, Y., Li, X., Du, M., Luo, X., Wei, C., Deng, Z., & Li, M. (2023). Removal of Magnesium in Zinc Hydrometallurgical System via Freezing Crystallization: From Laboratory Experiments to Industrial Application. *Sustainability*, *15*(23), 16275. https://doi.org/10.3390/su152316275

Karimi, S., Rashchi, F., & Moghaddam, J. (2017). Parameters optimization and kinetics of direct atmospheric leaching of Angouran sphalerite. *International Journal of Mineral Processing*, *162*, 58–68. https://doi.org/10.1016/j.minpro.2017.03.004

Khanmohammadi Hazaveh, P., Karimi, S., Rashchi, F., & Sheibani, S. (2020). Purification of the leaching solution of recycling zinc from the hazardous electric arc furnace dust through an as-bearing jarosite. *Ecotoxicology and Environmental Safety*, *202*, 110893. https://doi.org/10.1016/j.ecoenv.2020.110893

MacKinnon, D. J., & Brannen, J. M. (1991). Effect of manganese, magnesium, sodium and potassium sulphates on zinc electrowinning from synthetic acid sulphate electrolytes. *Hydrometallurgy*, *27*(1), 99–111. https://doi.org/10.1016/0304-386X(91)90081-V

Matthew, I. G., Newman, O. M. G., & Palmer, D. J. (1980). Water balance and magnesium control in electrolytic zinc plants using the E.Z. selective zinc precipitation process. *Metallurgical Transactions B*, *11*(1), 73–82. https://doi.org/10.1007/BF02657174

Mosayebi, H., Abdollahi, M., & Khalesi, M. reza. (2021). Magnesium removal from pregnant solution of acid leaching of zinc oxidised ore. *Journal of Separation Science and Engineering*, *13*(1), 124–131. https://doi.org/10.22103/jsse.2021.3001

Sharma, K. D. (1990). An approach to reduce magnesium from zinc electrolyte with recovery of zinc from disposed residue of an effluent treatment plant. *Hydrometallurgy*, *24*(3), 407–415. https://doi.org/10.1016/0304-386X(90)90102-8

Voigtm, P. B. (2012). *Precipitation of zinc from solution*.

Spongy Zinc Powder Production from Cold Filter Cake to Use in Cold Purification Stage

Bahram Behnajady[1],*, Saeid Karimi[2], Javad Moghaddam[3]

[1] Assistant professor, Research Centre of Advanced Materials, Faculty of Materials Engineering, Sahand University of Technology, Sahand New Town, Iran

[2] Assistant professor, Department of Metallurgy and Materials Engineering, Hamedan University of Technology, Hamedan, Iran

[3] Professor, Materials and Metallurgical Engineering Department, University of Zanjan, Zanjan, Iran

*Corresponding author: b_behnajady@sut.ac.ir (Bahram Behnajady)

Abstract:

The hydrometallurgical extraction of zinc often involves a crucial cold purification stage to remove impurities such as cadmium, cobalt, and nickel from the zinc sulfate electrolyte. The efficiency of this purification hinges on the availability of high-quality zinc dust as a cementation agent. A cost-effective approach to procuring this vital reactant involves processing cold filter cake (CFC), a byproduct of the leaching and purification processes. This study focuses on the production of zinc powder from CFC and its application in the cold purification stage of impure zinc sulfate solutions. The research begins with the alkaline leaching of CFC using a 7 molar NaOH solution at a temperature of 75 °C for 2 hours. During the leaching process, 84 % of zinc was dissolved while keeping cadmium and nickel mostly in the residue. The filtrate from the leaching process was then used as an electrolyte in an electrowinning process to produce spongy zinc powder with around 82 % current efficiency. Subsequently, the cold purification of the industrial zinc sulfate solution is performed using spongy zinc powder. The solution is heated to 50 °C and agitated at 300 rpm. A pre-determined quantity of spongy zinc powder is introduced to facilitate the cementation of impurities, specifically cadmium and nickel, which are present at concentrations of 60 ppm and 250 ppm, respectively. The purification process is optimized by adjusting the zinc powder dosage to 5 grams, resulting in cadmium and nickel concentrations reduced to 1.4 and 1.5 ppm, respectively, thus meeting the stringent requirements for electrowinning.

Keywords: Cold filter cake, Zinc alkaline leaching, Basic electrowinning, Spongy zinc powder, Cold purification.

1. Introduction

Zinc production and recovery from secondary sources is increasingly vital due to the finite nature of primary zinc resources and the growing demand for sustainable practices. Secondary zinc, primarily sourced from scrap materials like galvanized steel and metallurgical waste, can be effectively recovered through various innovative methods. Zinc is predominantly extracted from sulfide ores through the hydrometallurgical process, accounting for approximately 80% of global production. This method, favored for its efficiency and reduced environmental impact compared to pyrometallurgy, involves a multi-stage process beginning with ore concentration via froth flotation to yield a zinc concentrate. The concentrate then undergoes roasting at high temperatures, converting zinc sulfide to zinc oxide and releasing sulfur dioxide. Critically, the captured sulfur dioxide is converted into sulfuric acid, a key reagent in subsequent leaching stages. Leaching, conducted in dilute sulfuric acid,

dissolves the zinc oxide, generating a zinc sulfate solution. This process is typically conducted in two stages: a neutral leach targeting zinc oxide and a hot acid leach to break down zinc ferrites. The resulting zinc sulfate solution invariably contains impurities, necessitating rigorous purification. Iron is removed through oxidation and precipitation as jarosite, goethite, or hematite. Subsequently, zinc dust cementation is employed to displace copper, cadmium, cobalt, and nickel in two cold and hot purification stages. The purified zinc sulfate solution is then subjected to electrowinning, where zinc ions are reduced at the cathode, yielding high-purity zinc (Abbott et al., 2009; Freeman et al., 1977; Gharabaghi et al., 2012; Raghavan et al., 2000).

However, the hydrometallurgical process is not without its environmental challenges. Significant waste streams are generated, including roasting residue, iron precipitation residues (most notably jarosite), purification residues such as hot and cold filter cakes, and electrolyte bleed. Jarosite, containing hazardous traces of heavy metals, requires careful management through secure landfills or stabilization/solidification techniques. Purification residues, rich in zinc and other valuable metals, are often reprocessed for metal recovery (Behnajady et al., 2012; Behnajady & Moghaddam, 2014, 2015, 2017b; Gharabaghi et al., 2012; Karimi et al., 2017, 2021; Raghavan et al., 2000).

Zinc recovery from cold filter cake (CFC) is a significant area of research, particularly due to the environmental implications of managing hazardous waste. The CFC, a byproduct of the zinc plant, contains valuable metals such as cadmium, nickel, and zinc, which can be recovered through various leaching and extraction processes. The leaching process typically involves using aqueous solutions, such as sulfuric acid, to dissolve metals from the filter cake. This method is effective for extracting zinc and other metals like cadmium and nickel. Filter cakes from zinc processing contain toxic heavy metals, which pose environmental risks if not properly managed. Leaching processes must be designed to minimize environmental impact and ensure safe disposal or reuse of the treated residues. Research focuses on optimizing leaching conditions to selectively extract zinc while minimizing the extraction of other metals. This selective approach helps in improving the purity of the zinc product and reducing waste. Studies have explored the use of additives to stabilize filter cakes and reduce the leachability of heavy metals. However, the focus on zinc leaching specifically may require different strategies to enhance zinc extraction efficiency and selectivity (Asadollahfardi et al., 2022; Behnajady et al., 2024; Jafari-Basirabad et al., 2024; Moradkhani et al., 2012; Nusen et al., 2015).

Behnajady and Moghadam (2017a) focused on selective zinc leaching from hazardous As-bearing zinc plant purification filter cakes using pH-dependent tests and optimal conditions, achieving nearly 95% Zn extraction while minimizing impurities, specifically under conditions of 333 K, 120 min, pH 5, and 150 g/L. Balesini et al. (2011) leached zinc from the cold purification filter cake using sulfuric acid to extract zinc, and then utilized D2EHPA for solvent extraction. This study achieved 98.8 % zinc recovery under optimized conditions of 40 vol. % extractant, pH 2.5-3, and a 4:1 phase ratio. Sombhatla et al. (2019) used ammoniacal carbonate leaching. This method has been validated for cold purification cake, which contains 10-20% zinc. The leaching process is influenced by parameters such as temperature, agitation, and solvent concentration, with successful implementation in commercial settings. Ashtari and Pourghahramani (2015) applied sodium hydroxide to alkali leach zinc from a hot purification filter cake. Research indicates that NaOH concentrations of 3 to 9 M can significantly impact zinc extraction from hot filter cake, achieving up to 83.4% recovery under optimal conditions.

In this study, zinc powder recovery from zinc plant cold purification stage filter cake (often called Cold Filter Cake, CFC) was achieved through selective alkaline leaching followed by electrowinning. The produced zinc powder was used in the cold purification of zinc sulphate solution to cementite cadmium and nickel. Zinc powder dosage and purification time were adjusted to reduce cadmium and nickel concentration in the zinc sulphate solution to less than 2 mg.L^{-1}.

2. Materials and methods

2.1. Material

Sodium hydroxide (NaOH) was purchased from Mojallali Co. The main experimental material was CFC, containing approximately 19.5 % zinc, 21.5 % cadmium, and 4.5 % nickel. The zinc sulfate solution's pH was 3.5 and had 70 g/L zinc. The zinc sulfate solution, cadmium and nickel impurities were 60 and 250 mg.L^{-1}, respectively. Both the CFC and the zinc sulphate solution were provided by Zanjan Zinc Khales Sazan Industries Company (ZZKICo) in Zanjan, Iran.

2.2. Experimental Procedure

The flowchart is shown in Figure 1 with details of the experiment. The alkaline leaching of zinc was done in a 5 L Erlenmeyer flask with the following conditions: NaOH concentration 7 M, pulp density 100 g/L, reaction temperature 75 °C, and reaction duration 2 h. The process begins by adding 400 g CFC to a 4 L 7 M NaOH solution and heating the pulp to 75 °C. The solution was continuously stirred at 500 rpm using a mechanical stirrer to ensure uniform mixing and enhance the leaching process. Finally, the leaching slurry was filtered immediately, and the filtrate was analyzed by atomic abortion spectroscopy, Varian 240AA.
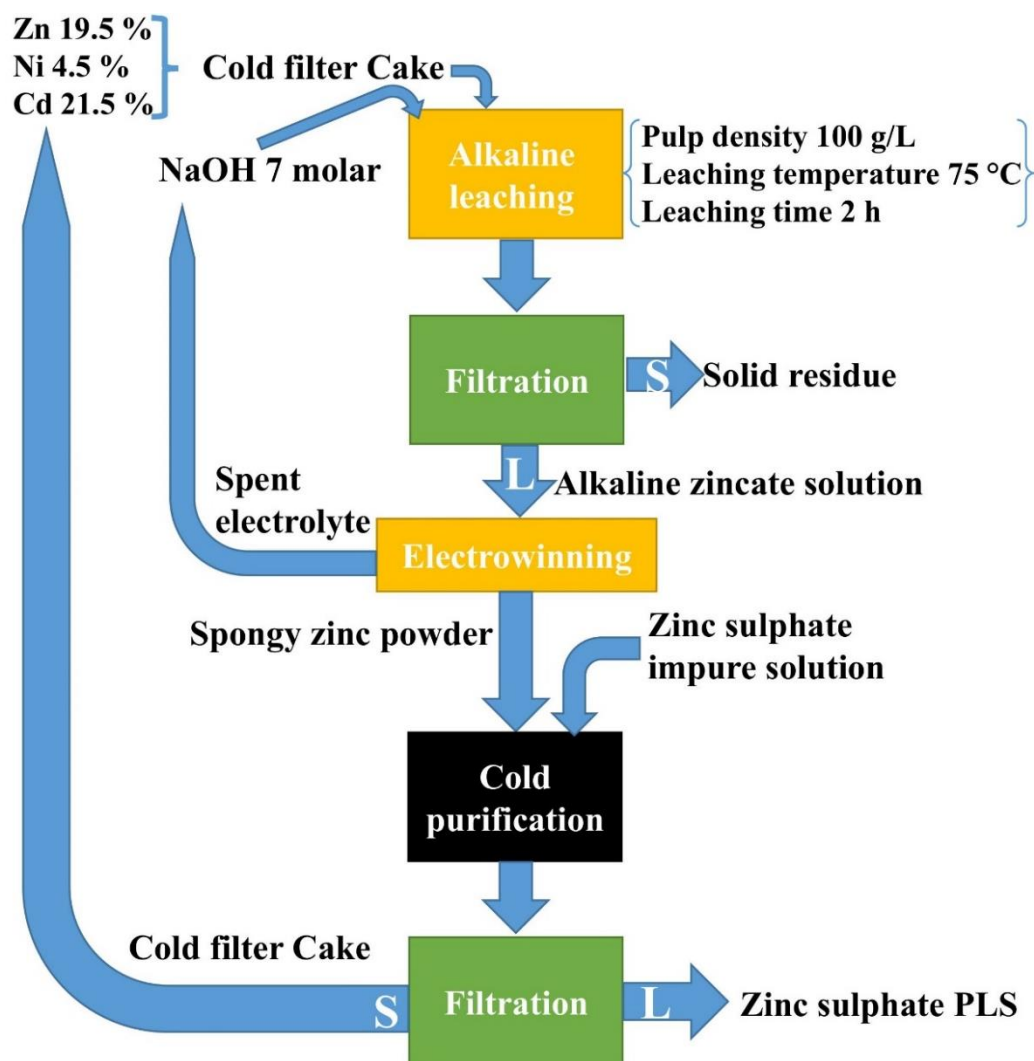
Fig. 1. Flowchart of experiments.

84

3.5 L of alkaline leaching filtrate was used as an electrolyte in electrowinning to produce zinc powder. The electrolysis of the alkaline solution, conducted using two stainless steel sheets of dimensions 12×9 cm² units serving as electrodes, resulted in an average applied voltage of 3.3 V and an average current of 5 A at ambient temperature (electrolyte not heated) for 10 h.

The cold purification of industrial zinc sulfate solutions is a critical step in the refinement of zinc. Experiments were conducted utilizing spongy zinc powder in a 2-liter beaker to achieve this purification. The procedure involved introducing 1 liter of impure zinc sulfate solution into the beaker, which was then placed on a heater and agitated at 300 rpm. The solution temperature was elevated to 50 °C, and the pH, measured at approximately 3.5, was deemed appropriate for initiating the purification process. Following this, a pre-determined quantity of spongy zinc powder was added, facilitating the cementation of impurities by the metallic zinc under continuous stirring. Once the designated purification time had elapsed, the solution was filtered. The concentration of nickel and cadmium after cold purification was measured in the resulting purified solution via atomic absorption spectroscopy.

3. Results and Discussion

3.1. Alkaline leaching of CFC

Alkaline leaching offers a selective approach to extracting zinc from complex mixtures such as CFC. Under alkaline conditions, a significant portion (84%) of zinc is dissolved according to reaction (1) as sodium zincate ($Na_2(Zn(OH)_4)$), while cadmium and nickel remain largely in the solid residue. This selectivity stems from the formation of an anionic zinc complex (ZnO_2^{2-}) in the caustic solution. This complex formation effectively solubilizes zinc, allowing for its separation from cadmium and nickel. These latter metals, unlike zinc, exhibit limited solubility in alkaline media, preventing their co-dissolution and thereby simplifying the subsequent process. Consequently, alkaline leaching represents a promising technique for isolating zinc while minimizing contamination from undesirable metallic impurities.

$$ZnO + 2NaOH + H_2O = Na_2Zn(OH)_4 \tag{1}$$

3.2. Electrowinning to produce zinc powder

The electrowinning of zinc from an alkaline zincate solution, derived from leaching processes, offers a compelling alternative to traditional zinc production methods. This approach leverages direct powder production, bypassing the energy-intensive steps of melting and atomization. In this study, the obtained zincate solution containing 16.5 g/L zinc was utilized as an electrolyte at a current density of 463 A/m². After a 10-hour electrowinning process, the zinc concentration decreased to below 3 g/L.

While Faraday's Laws predicted a zinc deposition of 61 g on the stainless steel cathode, only 50 g of zinc powder was recovered, resulting in a current efficiency of approximately 82%. This reduced efficiency is attributed to the depletion of zincate concentration during the process. The resulting deposit exhibited a spongy, powdery morphology, readily amenable to purification through washing. The product boasts a high purity (>99%) as evidenced by impurity analysis in Table 1. Despite the less-than-ideal current efficiency, the direct powder production method holds promise for a more sustainable and efficient zinc extraction pathway.

Table 1. Zinc powder's impurities chemical analysis

Elements	Cd	Ni	Co	Mn	Fe	Cu
Content (mg.kg⁻¹)	725	53	7	49	112	12

3.3. Cold purification using spongy zinc powder

The efficiency of spongy zinc powder obtained from electrowinning in the cold purification stage of metal extraction processes is significantly affected by its inherent composition and the cementation conditions employed. The initial analysis of the spongy zinc powder, as referenced in Table 1, reveals cadmium as the main impurity. This necessitates careful consideration of process parameters to optimize the removal of cadmium and other impurities like nickel. Due to the carbonation or oxidation of zinc metal when exposed to air, these powders are first washed in a dilute sulfuric acid solution for one minute and then immediately placed in water to be used in the cold purification stage.

Cementation experiments, summarized in Table 2, demonstrate the reduction of nickel and cadmium impurities through metallic zinc precipitation. Initial trials using 4 g of spongy zinc powder over an hour reaction period demonstrably reduced the concentrations of nickel and cadmium to 5.7 and 1.6 mg.L^{-1}, respectively. While this initial success validated the basic principle of cementation, the resulting nickel concentration of 5.7 mg.L-1 remained unacceptably high for direct electrowinning. This finding indicated a need for further optimization of the experimental parameters to achieve the required levels of purity.

Extending the purification time to two hours, in an attempt to further reduce the nickel concentration, yielded unexpected and problematic results. While the nickel concentration did decrease, a paradoxical increase in the cadmium concentration was observed, suggesting the re-dissolution of previously cemented cadmium. This phenomenon underscores the importance of understanding the dynamic equilibrium governing the cementation process. Factors such as the limited availability of zinc surface area for continued deposition and alterations in the solution chemistry over time can contribute to the re-dissolution of previously precipitated metals.

The ultimate successful optimization of the cold purification process was achieved by increasing the dosage of spongy zinc powder to 5 g. This single modification led to a significant reduction in both cadmium and nickel concentrations, reaching levels of 1.4 and 1.5 mg.L-1 respectively. These concentrations are deemed acceptable for direct use in the electrowinning process. The success of this adjustment highlights the crucial role of sufficient zinc powder availability in driving the cementation reaction to completion. A greater quantity of zinc provides more surface area for the effective scavenging of both cadmium and nickel impurities, minimizing the potential for re-dissolution and ensuring efficient purification.

Table 2. Conditions and results of cold purification using spongy zinc powder obtained from alkaline electrowinning

Experiment	Conditions		Impurity concentration	
	Zinc powder amount (g)	Time (h)	Ni	Cd
1	4	1	5.7	1.6
2	4	2	4	2.5
3	5	1	1.5	1.4

4. Conclusions

Alkaline leaching is an effective method for selectively extracting zinc from complex mixtures like CFC (cadmium, nickel, and zinc) containing materials. The process dissolves a large portion (84%) of zinc as sodium zincate under alkaline conditions, while cadmium and nickel largely remain in the

solid residue. This treatment simplifies the separation process, minimizing contamination from undesired metallic impurities. This method offers a promising technique for isolating zinc efficiently while reducing the presence of other unwanted metals. The study focuses on electrowinning zinc from a zincate solution as an environmentally friendly alternative to conventional zinc production methods. Current efficiency was around 82%, lower due to zincate concentration depletion. But the produced zinc deposit has a spongy, powdery structure that allows easy purification, and zinc powder has high purity (>99%). Despite the efficiency challenges, the direct powder production method shows promise for sustainable and efficient zinc extraction. The efficiency of spongy zinc powder in cold purification during metal extraction depends on its composition and the cementation conditions used. The powder, containing cadmium as the main impurity, requires careful optimization to remove cadmium and other impurities like nickel efficiently.

Utilizing zinc powder derived from cold filter cake offers several advantages. Firstly, it minimizes waste disposal and contributes to a more sustainable process. Secondly, it reduces the reliance on purchased zinc dust, leading to significant cost savings. Finally, by controlling the production process, the purity and reactivity of the zinc dust can be tailored to optimize the cold purification stage, ensuring efficient removal of detrimental impurities and ultimately contributing to the production of high-grade zinc metal. Therefore, the recovery of zinc from CFC for use in cold purification represents a valuable and economically viable practice in modern zinc hydrometallurgy.

References

Abbott, A. P., Collins, J., Dalrymple, I., Harris, R. C., Mistry, R., Qiu, F., Scheirer, J. & Wise, W. R. (2009). Processing of electric arc furnace dust using deep eutectic solvents. *Australian Journal of Chemistry*, *62*(4), 341–347. https://doi.org/10.1071/CH08476

Asadollahfardi, G., Yazdani, M., Sarmadi, M. S. & Khodadadi Darban, A. (2022). Evaluation of Enhanced Electrokinetic Remediation of Arsenic from Cold Filter Cake: Zinc-Leaching Sediment. *Journal of Environmental Engineering*, *148*(12), 4022079.

Ashtari, P. & Pourghahramani, P. (2015). Zinc extraction from zinc plants residue using selective alkaline leaching and electrowinning. *Journal of The Institution of Engineers (India): Series D*, *96*, 179–187.

Balesini, A. A., Razavizadeh, H. & Zakeri, A. (2011). *Solvent extraction of zinc from acidic solution obtained from cold purification filter cake of angouran mine concentrate using D2EHPA*.

Behnajady, B. & Moghaddam, J. (2014). Optimization of Lead and Silver Extraction from Zinc Plant Residues in the Presence of Calcium Hypochlorite Using Statistical Design of Experiments. *Metallurgical and Materials Transactions B: Process Metallurgy and Materials Processing Science*, *45*(6), 2018–2026. https://doi.org/10.1007/s11663-014-0130-z

Behnajady, B. & Moghaddam, J. (2015). Statistical evaluation and optimization of zinc electrolyte hot purification process by Taguchi method. *Journal of Central South University*, *22*(6), 2066–2072. https://doi.org/10.1007/s11771-015-2730-4

Behnajady, B. & Moghaddam, J. (2017a). Selective leaching of zinc from hazardous As-bearing zinc plant purification filter cake. *Chemical Engineering Research and Design*, *117*, 564–574.

Behnajady, B. & Moghaddam, J. (2017b). Separation of arsenic from hazardous As-bearing acidic leached zinc plant purification filter cake selectively by caustic baking and water leaching. *Hydrometallurgy*, *173*, 232–240. https://doi.org/10.1016/j.hydromet.2017.08.016

Behnajady, B., Moghaddam, J., Behnajady, M. A. & Rashchi, F. (2012). Determination of the optimum conditions for the leaching of lead from zinc plant residues in NaCl-H2SO4-Ca(OH)2 media by the taguchi method. *Industrial and Engineering Chemistry Research*, *51*(10), 3887–3894. https://doi.org/10.1021/ie202571x

Behnajady, B., Najafi, M. & Karimi, S. (2024). Green leaching of cold filter cakes using choline

chloride–maleic acid deep eutectic solvent and molecular dynamics simulation. *Physical Chemistry Chemical Physics*, *26*(37), 24407–24422.

Freeman, G. M., Dulson, J. E. & Morris, M. F. (1977). *Zinc hydrometallurgical process*. US Patents 4049514.

Gharabaghi, M., Irannajad, M. & Azadmehr, A. R. (2012). Leaching behavior of cadmium from hazardous waste. *Separation and Purification Technology*, *86*, 9–18. https://doi.org/10.1016/j.seppur.2011.10.014

Jafari-Basirabad, M., Behnajady, B. & Ojaghi-Ilkhchi, M. (2024). Selective Leaching of Cadmium from Cold Filter Cake Using Green Deep Eutectic Solvent Choline Chloride-Oxalic Acid. *JOM*, 1–10.

Karimi, S., Rashchi, F. & Ghahreman, A. (2021). The evaluation of sphalerite surface formed during oxidative leaching in acidic ferric sulfate media. *Journal of Sustainable Metallurgy*, *7*(3), 1304–1313.

Karimi, S., Rashchi, F. & Moghaddam, J. (2017). Parameters optimization and kinetics of direct atmospheric leaching of Angouran sphalerite. *International Journal of Mineral Processing*, *162*, 58–68.

Moradkhani, D., Rasouli, M., Behnian, D., Arjmandfar, H. & Ashtari, P. (2012). Selective zinc alkaline leaching optimization and cadmium sponge recovery by electrowinning from cold filter cake (CFC) residue. *Hydrometallurgy*, *115*, 84–92.

Nusen, S., Yottawee, N., Cheng, C. Y. & Chairuangsri, T. (2015). Characterisation of Zinc Plant, Cold-Purification Filter Cake and Leaching of Indium by Aqueous Sulphuric Acid Solution. *CHIANG MAI JOURNAL OF SCIENCE*, *42*(3), 718–729.

Raghavan, R., Mohanan, P. K. & Swarnkar, S. R. (2000). Hydrometallurgical processing of lead-bearing materials for the recovery of lead and silver as lead concentrate and lead metal. *Hydrometallurgy*, *58*(2), 103–116. https://doi.org/10.1016/S0304-386X(00)00108-0

Sombhatla, S. S., Kumar, A. & Rokkam, K. K. (2019). Validation and Implementation of Cold Purification Cake Leaching in Ammoniacal Carbonate Solutions at Hindustan Zinc Hydro Refineries. *Transactions of the Indian Institute of Metals*, *72*(3), 613–621.

Feasibility Study for Gold Processing in Graphite Schists in the Band-e-Cherk district, Anarak Metallogenic Zone, Isfahan Province

Hamed Ebrahimi Fard[1]*, Majid Ghasemi Siani[2], Behrouz Karimi Shahraki[3], Amirhossein Heidari Bafruie[4]

[1] Ph.D. student, Department of Geochemistry, Faculty of Earth Sciences, Kharazmi University, Tehran, Iran

[2] Associate Professor, Department of Geochemistry, Faculty of Earth Sciences, Kharazmi University, Tehran, Iran

[3] Ph.D, Iranian Mineral Processing Research Center, Karaj, Iran

[4] Engineer of deputy of mining affairs, Isfahan Mobarakeh Steel Company, Isfahan, Iran

*Corresponding author: hamedebrahimi772@gmail.com (Hamed Ebrahimi Fard)

Abstract:

The Band-e-Cherk district is located in the Kuh-e-Dom metamorphic zone, in the central part of central Iran and the Yazd block. The Band-e-Cherk district includes metamorphic units of the Kuh-e-Dom complex consisting of schists (muscovite schists, epidote-hornblende-calcite schists, muscovite-chlorite schists, biotite-graphite-calcite schists), marbles and crystalline limestones of Paleozoic age with an east-west trend. This study evaluated the distribution of metamorphic units of the Kuh-e-Dom Complex in the study area, the potential for gold mineralization in the area, and the feasibility of gold processing from graphitic schist units and adjacent rock units in the Band-e-Cherk district. Based on the results of the SEM analysis of the samples, gold anomalies (92.71 to 100.00 wt.%) were identified in the form of native gold and electrum (gold + silver) disseminated throughout the rock and along fractures. Based on the results of the fire assay, the amount of gold in the gold-bearing veins is significant with grades of 11.05, 19.78 and 27.66 ppm gold, while the amount of gold in the schist units is 154 and 120 ppm gold, which is considered unacceptable. According to the results of the processing tests, the gold is of a refractory gold ore type and requires a pre-processing step to dissolve the gold. This may be due to the presence of sulfur and arsenic as confirmed by the analytical results.

Keywords: Gold mineralization, graphitic schist, fire assay, gold processing tests, Band-e-Cherk, Kuh-e-Dom metamorphic zone.

1. Introduction

Most metamorphic sedimentary terranes, especially greenschist facies belts, host orogenic gold deposits that formed during and after the peak of regional metamorphism (e.g., Goldfarb et al., 2005a; Large et al., 2011; Majumdar et al., 2020). Orogenic gold deposits associated with carbonaceous and organic graphitic materials are commonly reported from the Paleozoic, Mesozoic and Tertiary periods (Williams, 2007). In some gold deposits, carbonaceous host rocks are closely associated with gold mineralization and are considered indicator rock units (Craw, 2002). Gold and graphite are spatially closely associated in many orogenic gold deposits, and a genetic relationship between them is commonly inferred (Mishra and Pal, 2008). This relationship is particularly strong in orogenic gold deposits formed in metamorphic turbidite terranes where the host rocks are typically graphitic (MacKenzie et al. 2010). Graphite in these host rocks is generally metamorphosed from organic matter deposited by sediments derived from and associated with the host rocks (Zoheir et al. 2008), and there is extensive evidence for these processes in many gold-bearing metamorphic sedimentary terranes (Kribeck et al. 2008).

The role of carbonaceous materials in gold mineralization remains controversial, including the accumulation of invisible gold and other metals during the depositional-diagenetic process (Large et al., 2011), the production of carbon dioxide and methane when carbonaceous materials react with hydrothermal fluids (Zoheir et al, 2008), the facilitation of shear zone formation in orogenic belts (Cao and Neubauer, 2019), or the reduction of gold disulfide complexes as ore-bearing fluids flow through carbonaceous rocks (Hu et al., 2017). However, when graphite is introduced as a hydrothermal mineral associated with gold, the structures controlling the hydrothermal fluids are the primary exploration target, regardless of the host rock. These results highlight the role of carbonaceous materials present in gold mineralization, but lack explicit constraints on the deposition of solid carbon (e.g., graphite) in the orogenic gold system. This is partly due to the difficulty in distinguishing graphite of different origins and the lack of a clear link between graphite deposition and gold deposition.

Gold recovery from graphitic schist host rocks is challenging due to the complex composition of these rocks. Gold in graphite schist can occur as 1) native gold between schist or graphite layers, 2) gold associated with sulfides (e.g., pyrite, arsenopyrite), or 3) invisible gold trapped within the crystal structure of the minerals (Adams, 2016). Challenges in processing gold from graphite slate include 1) the nature of the carbon (graphite): The carbon in graphite can interfere with flotation and cyanidation processes because carbon tends to adsorb gold and cyanide. In addition, if carbon is present in the ore, any cyanidation test should be performed in the presence of active carbon (CIL); 2) the fineness of the gold: If the gold is in very fine particles or within the structure of minerals, conventional processing methods such as crushing and milling may not sufficiently release it; 3) the presence of interfering impurities: Elements such as arsenic, antimony and sulfides can complicate chemical processes. Possible methods for processing gold from graphite slate include: 1) Preprocessing: a) Crushing and grinding: to native gold particles from the rock matrix, b) Gravity separation (vibrating table): if the gold is coarse grained, c) Flotation: to separate gold-bearing sulfides from the graphite (but graphite carbon may cause problems). 2) Chemical processing: cyanidation (a common method for gold extraction, but can have low efficiency in the presence of graphite, as carbon absorbs gold and cyanide), chlorination, bioleaching (using bacteria), advanced technologies, pressure oxidation processing, thermal processes (Adams, 2016). It is possible to extract gold from graphite schist, but this requires detailed laboratory testing (such as XRD, SEM, Fire Assay analysis). The optimal method depends on the gold grade, particle size and chemical composition of the ore. The cost of processing can be high, so it should be economically investigated. If you have a sample of the ore, it is recommended to perform preliminary processing (metallurgical) tests in specialized laboratories. In Iran, most of the high-grade orogenic gold deposits (average 8 to 18 ppm) with graphitic schist units are formed in the Sanandaj-Sirjan metamorphic zone (Ghorbani, 2007). This zone, along with the association of gold-bearing zones with graphitic schist, poses a challenge to the gold extraction and recovery process. This makes it necessary to perform processing operations on them as an important process in the industry. In terms of national divisions, the Band-e-Cherk district is located in Isfahan province and from the perspective of sediment-structural zones (Aghanabati, 2013), in the Anarak metallogenic zone in the central part of Iran and in the Yazd block. This area, approximately 30 square kilometers in size, is located in central Iran and northeastern Isfahan Province and is confined to the operational quadrangle of 52'36°45.22" to 52'40°41.45" east longitude and 33'57°23.26" to 33'59°29.95" north latitude. Considering the distribution of regional metamorphic units of the Kuh-e-Dom complex in the study area and the possibility of graphite and gold mineralization in them, the need to sample these units and evaluate the possibility of gold processing and enrichment in the Band-e-Cherk district was investigated in this study. During this research, gold was extracted from graphitic schist units and other host rock units using various processing methods while conducting mineralogical studies of gold-bearing zones.

2. A brief overview of the geology of the study area

The Anarak Metallogenic Zone, with its metallogenic, magmatic, metamorphic and distribution of Upper Proterozoic rocks, is considered one of the most interesting geological regions of Iran. This region is one of the richest mineral regions of Iran in terms of mineralization diversity and has a specific metallogenic boundary. This region is one of the oldest mining regions and modern mining in Iran has also largely started from this region (Ghorbani, 2007). In the Anarak area, from north of Naein to around Saghand-Posht-e-Badam, a dark-colored schist complex is exposed, accompanied by graphitic phyllites, quartzite, crystallized limestone, chlorite-epidote schist, micaschist, and epigneiss. Davoudzadeh et al. (1969) believe that this complex is Precambrian in age and have called it (Anarak metamorphisms). According to the work of geologists from Technoexport Company, in the Anarak area this complex includes 5 complexes: Chahgorbeh, Morghab, Patyar, Mohammadabad and Doshakh. But in the Khour region, the five complexes of Chahgorbeh, Patyar, Kaboudan, Doshakh, and Posh-e-Badam are the creators of the Anarak's metamorphoses.

The Kuh-e-Dom mining district consists of Lower Eocene tuff, ignimbrite, rhyolite tuff, tuffite, dacite, rhyolite, basaltic andesite, diorite, granodiorite, marl and limestone units (Fig. 1). The Kuh-e-Dom metamorphic complex is also of Lower Paleozoic age and includes various types of schists and crystalline limestones. Most of the rocks in this metamorphic complex are greenschists and phyllites associated with crystallized limestones and rarely metamorphosed sandstones. The primary composition or parent rocks of the Paleozoic metamorphic rocks in the Kuh-e-Dom district are destructive sedimentary rocks, argillite, crystalline silica limestone, and volcanic rocks that have been altered to greenschist facies under the influence of regional metamorphism in the area. In this complex, metaplite, metabasalt, marble, chlorite schists and metamorphosed sandstones are visible. Based on field evidence, evidence of folding and foliation is visible in the schists of the area, and late quartz veins are abundant in these rock units. As for the lithology of the Band-e-Cherk district, it includes metamorphic units of the Kuh-e-Dom complex consisting of schists (muscovite schist, epidote-hornblende-calc schist, muscovite-chlorite schist, biotite-graphite-calc schist), marbles and crystalline limestones of Paleozoic age, the main part of which is seen in the Band-e-Cherk district with an east-west trend (Fig. 2). After this unit, the Lower Cretaceous limestones are the oldest units, which are mainly found in the northern and central parts of the Band-e-Cherk district and are overlain by the metamorphic rocks of the Kuh-e-Dom complex. Andesitic, andesitic-basaltic volcanic intrusive rocks and Eocene tuffs also cover the northern part of the Band-e-Cherk district in large quantities. Small, strongly altered intrusive bodies with diorite composition are also located on the metamorphic rocks of the Kuh-e-Dom complex with a fault boundary. Conglomerate deposits are the most common Paleocene rocks in the Band-e-Cherk district, resulting from the erosional cycles of the Laramide event. They are mainly conglomerate and sandstone deposits that overlie older rocks such as the schists of the Kuh-e-Dom metamorphic complex, both discontinuously and sometimes congruently.
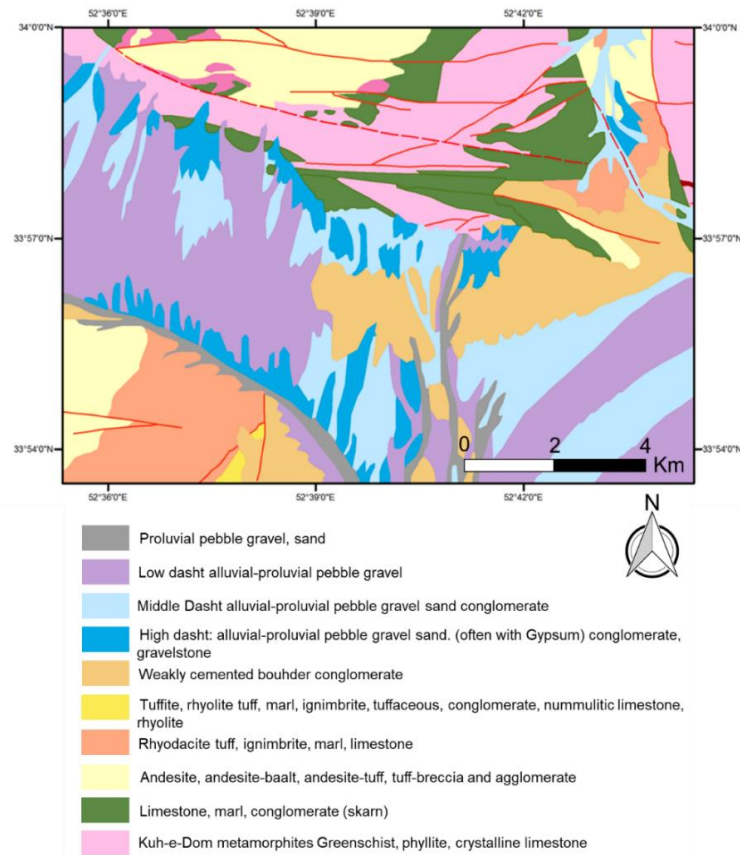
Fig. 1. Simplified geological map of the Kuh-e-Dom district (modified from Technoexport, 1981).

Legend:
- Proluvial pebble gravel, sand
- Low dasht alluvial-proluvial pebble gravel
- Middle Dasht alluvial-proluvial pebble gravel sand conglomerate
- High dasht: alluvial-proluvial pebble gravel sand. (often with Gypsum) conglomerate, gravelstone
- Weakly cemented bouhder conglomerate
- Tuffite, rhyolite tuff, marl, ignimbrite, tuffaceous, conglomerate, nummulitic limestone, rhyolite
- Rhyodacite tuff, ignimbrite, marl, limestone
- Andesite, andesite-baalt, andesite-tuff, tuff-breccia and agglomerate
- Limestone, marl, conglomerate (skarn)
- Kuh-e-Dom metamorphites Greenschist, phyllite, crystalline limestone

Proluvial pebble gravel, clayey sand

Middle Dasht: Alluvial-proluvial gravel, clayey sand, conglomerate

Low Dasht: Alluvial-proluvial gravel

High Dasht: Alluvial-proluvial pebble gravel and sand, conglomerate, gravelly sandstone

Marl

Altered andesite

Andesite, andesite-basalt, tuff

Rhyolite

Trachyte, trachy-andesite

Conglomerate

Gray limestone

Yellow limestone with marl

Koh-e-Dom metamorphose: biotite-graphite calc schist, quartzite

Koh-e-Dom metamorphose: biotite-graphite calc schist

Koh-e-Dom metamorphose: crystalized limestone

Koh-e-Dom metamorphose: epidote-hornblende calc schist

Koh-e-Dom metamorphose: muscovite schist covered by marl

Koh-e-Dom metamorphose: muscovite schist

Altered diorite

Diorite

Feldspar

Fault

Inferred fault

Fig. 2. Simplified geological map of the Band-e-Cherk district.

3. Material and methods

To conduct this research, 300 mineral samples were collected from various units of the Band-e-Cherk Dam during a one-day field visit and survey. A total of 90 microscopic sections (thin-polished and polished) of metamorphic, igneous and sedimentary units were prepared at the Microscopic Section Preparation laboratory of Kharazmi University of Tehran. After preparation, the samples were examined at the Optical Mineralogy Laboratory of Kharazmi University of Tehran and Iranian Mineral Processing Research Center (IMPRC) using a ZEISS Axioplan 2 microscope. In addition, to

further investigate the sample and the possibility of the presence of precious elements and other rare and rare earth elements in the study area, 20 polished and thin-polished section samples were analyzed by SEM with EDAX transmission spectrum at the central laboratory of Kharazmi University of Tehran. SEM studies were performed using a FEI ZEISS 650 FEG-ESEM model in the aforementioned unit. SEM-EDS analyses and SEM-SE images were obtained using beam currents of 5 to 15 nA and electron acceleration potentials of 5 to 20 kV for mineral identification and textural studies. After microscopic examination, 26 samples of graphite schists were chemically analyzed at Iranian Mineral Processing Research Center and Zarazma to measure the abundance of major elements by XRF method and for minor elements and rare earth elements by ICP-MS method. For this purpose, the samples were first crushed with a steel crusher to a size of approximately 5 mesh (4 mm) and then pulverized in an agate mill for 2 minutes to a size of approximately 200 mesh (74 microns). After preparation, 20 grams of the sample powder was sent to the aforementioned laboratories and analyzed for major, trace and rare earth element content using ICP-OES and ICP-MS methods.

4. Results and Discussion

4.1. Mineralogy and Petrography

Microscopic studies of the siliciclastic unit indicate that it is an altered metamorphic rock with high silica and alkaline elements, in which quartz crystals have been formed by hydrothermal processes. These crystals lack wave extinction, indicating formation by hydrothermal processes. This rock belongs to the group of quartz-feldspar (meta psammite) protoliths, which are recrystallized primary cherts and sandstones. The matrix quartz crystals have wave extinction. The texture of the sample is somewhat similar to the corresponding micrographic texture of igneous rock, except that the matrix crystals are quartz and the phenoblast crystals are chlorite (Fig. 3B). Phenoblast crystals show no specific orientation, indicating that the rock has not been affected by regional metamorphism (Fig. 3A). Abundant and intertwined veins of iron hydroxides cut through quartz crystals deposited in earlier stages (Fig. 3C and D). Hematite is observed along the fracture space and also scattered throughout the rock (Fig. 3E and F). Additional SEM studies are recommended to identify gold-bearing phases in the sample. Microscopic sections of strongly silicified schists and SEM studies have identified gold mineralization as disseminated throughout the rock texture, mainly along fractures and weak surfaces, with the presence of Au anomalies in the form of native gold and electrum (gold + silver) (Fig. 4). Gold values (92.71 to 100.00 wt.% on a 2 to 50 micron) were obtained by SEM (Fig. 4). Silver values (6.45 to 8.09 wt.% on a 2 to 20 micron) were also determined.
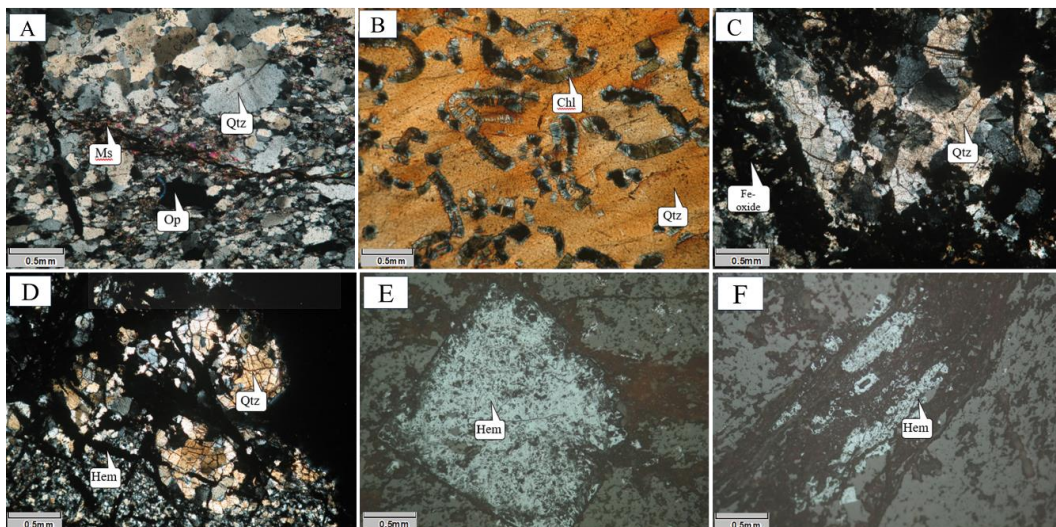
Fig. 3. Microscopic images of the silica alteration unit of the Band-e-Cherk district (transmitted light images were taken in XPL mode and reflected light images were taken in PPL mode). A) Orientation

and subgraining and jagged edges of schistosity surfaces in quartz and muscovite crystals, B) A quartz-feldspar igneous rock with an initial micrographic texture that has been recrystallized by contact metamorphic processes, C and D) Formation of quartz crystals due to silicic alteration in the sample, E) Hematite is disseminated and euhedral along fractures and in the matrix of the rock, F) Hematite is concentrated along fractures and in the matrix of the rock.
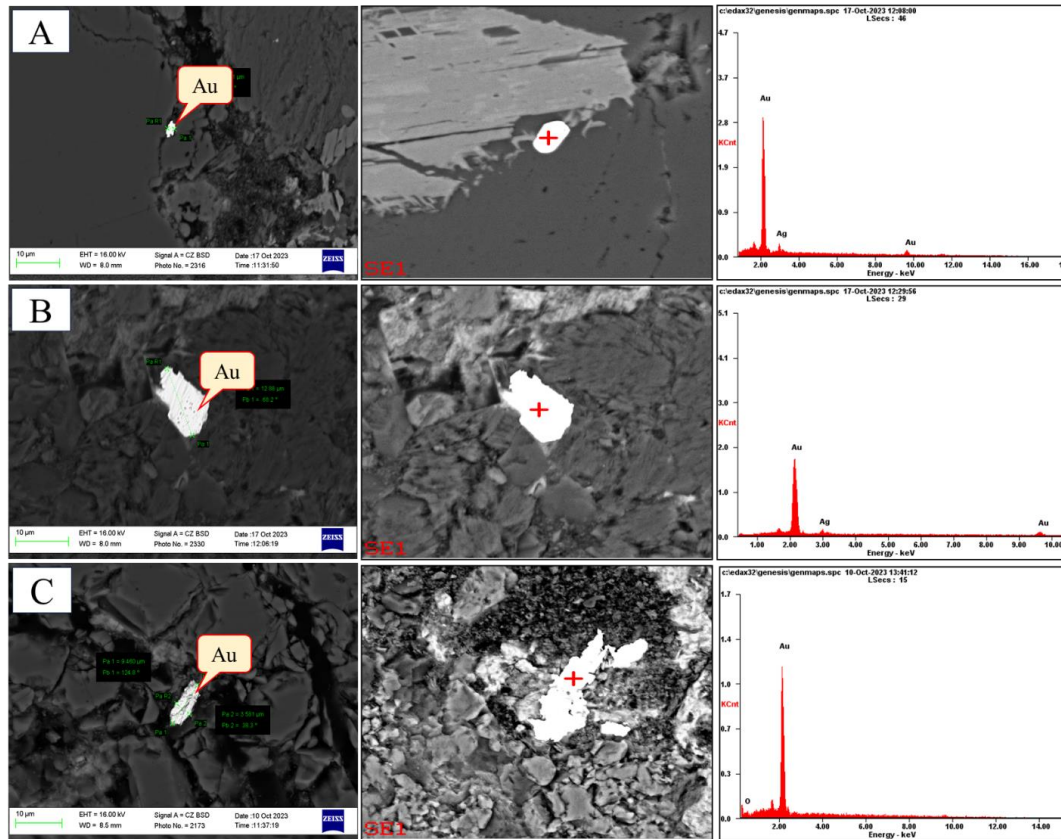
Fig. 4. Gold and partially silver mineralization along fractures and also disseminated throughout the rock.

4.2. Gold Vein Geochemistry

Three samples from the gold-bearing veins and two samples from the surrounding schists were taken for gold analysis, the results of which are presented in Table 1. The results show that the amount of gold in the samples is very significant with values of 11.05, 19.78 and 27.66 ppm. The amount of gold in the schists was 154 and 120 ppm of gold, which is not significant.

Table 1. Gold analysis results of gold-bearing samples analyzed by fire assay at the Iranian Mineral Processing Research Center.

Au (ppb)	Sample No
19784	BC-TR9-Au
154	BC-03-16
116	BC-20
11054	BC-TR3-22
27662	BC-TR3-20

4.3. Gold processing tests

Three types of rock samples were provided by the client to Everest Novin Mining and Processing Engineering Company for gold recovery testing. Initial analyses and gold assays were performed on the gold-bearing rock samples. Samples for analysis had to be crushed to a fine size. Sample crushing was performed in two stages: primary crushing using jaw crushers and a 1-inch control screen, and secondary crushing using roller and cone crushers and a 3.36 mm control screen. The output of the primary crusher, after homogenization, division and sampling for archiving, went to the secondary crusher. Roller and cone crushers were used in the secondary crushing process, the schematic diagram of which is shown below.

4.4. Sample Identification

Homogeneous and representative samples were prepared from the crushed samples of each type and these samples were analyzed. The results of various analyses on these samples are presented in Tables 2 and 3. According to these tables, it can be said that no obvious accompanying element is observed for the samples, but the sulfur and arsenic levels in the samples are high, which can cause problems in the Cyanidation process.

Table 2. Initial feeding results.

Row	Sample code	Gold content (ppm)
1	bc-tr3-20	10.10
2	bc-tr3-21	6.92
3	bc-tr3-22	17.45
4	Average of samples	11.49

Table 3. ICP and XRF results of the samples.

Elements	1086-bc-tr3-20	1086-bc-tr3-21	1086-bc-tr3-22	Elements	1086-bc-tr3-20	1086-bc-tr3-21	1086-bc-tr3-22
SiO_2 (%)	39.99	35.94	60.95	Be	<2	<2	<2
Al_2O_3	8.43	9.54	6.8	Bi	<10	<10	<10
Fe_2O_3	6.97	8.59	7.03	Ce	26	31	28
TiO_2	1.58	1.77	1.24	Co	26	34	22
Na_2O	1.41	1.63	2.51	Cd	<2	<2	<2
K_2O	1.01	1.02	0.6	Cr	122	157	104
CaO	15.91	17.07	9.47	Cu	38	27	10
MgO	2.03	1.93	0.75	La	20	22	21
MnO	0.16	0.22	0.14	Li	109	169	55
P_2O_5	0.47	0.53	0.58	Mo	1.2	1.21	2.06
SO_3	4.08	3.17	0.56	Ni	73	87	30
SrO	0.06	0.06	0.05	Pb	11	12	10
ZrO_2	0.02	0.02	0.01	Sb	26	218	9
V_2O_5	0.02	0.03	0.2	Sc	10	12	7
BaO	0.21	0.17	<0.01	Sr	449	505	420
LOI	17.65	18.3	9.27	V	99	114	60
Ag (ppm)	<2	<2	<2	Y	13	18	11
As	4326	3921	18479	Zn	26	43	19
Ba	1454	1767	114	Zr	41	77	44

5.4. Primary Gold Extraction Assays

Six cyanidation tests were performed on homogenized and powdered samples less than 75 microns in size from a total of three other samples. The test conditions were 40% solids, pH 11.5, different sodium cyanide concentrations and different time periods. The test results are shown in Table 4. Tests 1 to 3 were conducted at a cyanide concentration of 2 kg/ton solid and durations of 24, 48, and 72 hours, and tests 4 to 6 were conducted at a cyanide concentration of 5 kg/ton solid and durations of 24, 48, and 72 hours. The results indicate that the gold is a refractory gold ore type and requires a pre-

processing step to dissolve the gold. The presence of sulfur and arsenic, which were also observed in the analyses, indicates this. It is suggested that diagnostic leaching, flotation and oxidation methods be investigated to obtain better and more accurate results given the high grade of the sample. The results show that, despite the high gold grade of the ore (11 g/t), even with a high sodium cyanide dosage (7 kg/t), only 39% of the gold was extracted.

Table 4. Cyanidation results.

Row	Feed weight (gr)	Feed grade (ppm)	Solution volume (ml)	Solution concentration (ppm)	Cyanide concentration (ppm)	Gold recovery in solution (%)
1	1000	11.49	1500	0.66	3.5	8.62
2	1000	11.49	1500	1.08	4.0	14.10
3	1000	11.49	1500	1.45	4.5	18.93
4	1000	11.49	1500	2.11	5.0	27.55
5	1000	11.49	1500	2.30	6.0	30.03
6	1000	11.49	1500	3.00	7.0	39.16

5. Conclusion

In terms of national divisions, the Band-e-Cherk district is located in the province of Isfahan and in terms of sediment-structural zones, in the Anarak metallogenic zone located in the central part of Iran and in the Yazd block. The Band-e-Cherk district includes metamorphic units of the Kuh-e-Dom Complex consisting of schists (muscovite schists, epidote-hornblende-calcite schists, muscovite-chlorite schists, biotite-graphite-calcite schists), marbles and crystalline limestones of Paleozoic age, the main part of which is seen in the Band-e-Cherk district with an east-west trend. Gold mineralization has been identified as native gold and electrum (gold + silver) mineralization has been identified as disseminated and mainly along fractures and weak surfaces of the silicic alteration unit. The gold content in the gold-bearing veins that make up the graphitic schist units has been highly upgraded, while the gold content in the schist units is not significant. The results of the processing tests showed that the gold is a refractory gold ore and requires a pre-processing step to dissolve the gold. The presence of sulfur and arsenic in the assay results also confirms this point.

Acknowledgments

References

Adams, M. D. (2016). Gold ore processing: project development and operations (Vol. 15). Elsevier.

Aghanabati, S. A. (2013). Geology of Iran. *Geological Survey of Iran*, 587p.

Cao, S. & Neubauer, F. (2019). Graphitic material in fault zones: Implications for fault strength and carbon cycle. *Earth-Science Reviews*, 194, 109-124. DOI: https://doi.org/10.1016/j.earscirev.2019.05.008

Craw, D. (2002). Geochemistry of late metamorphic hydrothermal alteration and graphitisation of host rock, Macraes gold mine, Otago Schist, New Zealand. *Chemical Geology*, 191(4), 257-275. DOI: https://doi.org/10.1016/S0009-2541(02)00139-0

Davoudzadeh, M. (1969). Geologie und Petrographie des Gebietes nördlich von Nain, Zentral-Iran (Doctoral dissertation, ETH Zurich).

Ghorbani, M. (2007). Economic Geology of Mineral Deposits and Natural Resources of Iran, 1st edition, Arian Zamin Publishers, 492p.

Goldfarb, R. J., Baker, T., Dubé, B., Groves, D. I., Hart, C. J. & Gosselin, P. (2005). Distribution, character, and genesis of gold deposits in metamorphic terran. DOI: https://doi.org/10.5382/AV100.14

Hu, S. Y., Evans, K., Craw, D., Rempel, K. & Grice, K. (2017). Resolving the role of carbonaceous material in gold precipitation in metasediment-hosted orogenic gold deposits. *Geology*, 45(2), 167-170. DOI: https://doi.org/10.1130/G38462.1

Kříbek, B., Sýkorová, I., Machovič, V. & Laufek, F. (2008). Graphitization of organic matter and fluid-deposited graphite in Palaeoproterozoic (Birimian) black shales of the Kaya-Goren greenstone belt (Burkina Faso, West Africa). *Journal of Metamorphic Geology*, 26(9), 937-958. DOI: https://doi.org/10.1111/j.1525-1314.2008.00796.x

Large, R. R., Bull, S. W. & Maslennikov, V. V. (2011). A carbonaceous sedimentary source-rock model for Carlin-type and orogenic gold deposits. *Economic Geology*, 106(3), 331-358. DOI: https://doi.org/10.2113/econgeo.106.3.331

MacKenzie, D., Craw, D., Cooley, M. & Fleming, A. (2010). Lithogeochemical localisation of disseminated gold in the White River area, Yukon, Canada. *Mineralium Deposita*, 45, 683-705. DOI: https://doi.org/10.1007/s00126-010-0301-z

Majumdar, S., Singh, S. & Sahoo, P. R. (2020). Characterization of organic matter and its implications for pyrite hosted refractory gold mineralization along the South Purulia Shear Zone, eastern India. *Ore Geology Reviews*, 124, 103584. DOI: https://doi.org/10.1016/j.oregeorev.2020.103584

Mishra, B. & Pal, N. (2008). Metamorphism, fluid flux, and fluid evolution relative to gold mineralization in the Hutti-Maski Greenstone Belt, Eastern Dharwar Craton, India. *Economic Geology*, 103(4), 801-827. DOI: https://doi.org/10.2113/gsecongeo.103.4.801

Technoexport (1981). Detail geology prospecting in the Anarak Area Central Iran. Geological Survey of Iran, Report No. 9.

Zoheir, B. A., El-Shazly, A. K., Helba, H., Khalil, K. I. & Bodnar, R. J. (2008). Origin and evolution of the Um Egat and Dungash orogenic gold deposits, Egyptian Eastern Desert: evidence from fluid inclusions in quartz. *Economic Geology*, 103(2), 405-424. DOI: https://doi.org/10.2113/gsecongeo.103.2.405

Processing of a Low-Grade Gold Refractory Sulfide Ore by Flotation-Biooxidation-Cyanidation Route

Sepide Sedighi[1], Ali Ahmadi[2, *]

[1]M.Sc. in Mineral Processing, Department of Mining Engineering, Isfahan University of Technology.

[2]Professor of Mineral Processing, Department of Mining Engineering, Isfahan University of Technology.

*Corresponding author: _a.ahmadi@iut.ac.ir_ (Ali Ahmadi)

Abstract:

By depleting high-grade and easy-to-treat gold ores and the increase in gold price, the extraction of gold from low-grade and refractory ores such as sulfide ores has been given attention. Biooxidation is one of the efficient, relatively low-cost and environmentally friendly processes to enhance gold extraction by releasing fine gold encapsulated in sulfide phases. So in this research, the efficiency of concentrate biooxidation-flotation system in increasing gold recovery from sulfide-refractory low-grade ores was investigated. biooxidation experiments with mesophilic and moderate thermophilic microorganisms were conducted on the flotation concentrate. Finally, cyanidation experiments were conducted on the flotation concentrate, and biooxidized flotation concentrate. Gold recovery from non-biooxidized flotation concentrate was 63.59%, while it was increased to 80.21% after biooxidation with mesophilic microorganisms and to 79.84% after biooxidation with moderate thermophilic microorganisms.

Keywords: _Biooxidation, Concentrate, Microorganism_

1. Introduction

Currently, biotechnology has attracted much attention for gold recovery from sulfidic refractory gold ores (Natal'ya, Muravyov, & Kondrat'eva, 2010). In refractory gold ores, the gold particles are very fine and may be locked within particle boundaries or the structure of sulfide minerals such as pyrite and arsenopyrite (Wang et al., 2020). Direct cyanidation method is not effective for extracting gold from refractory sulfide ores; Therefore, a pretreatment process such as roasting, pressure oxidation or biooxidation should be considered to liberate encapsulated gold from the sulfide minerals. Compared to other processes, biooxidation of sulfide refractory gold ores has several advantages, including low investment cost and environmental friendliness (Wu, 2018)(N. V. Fomchenko, Kondrat'eva, & Muravyov, 2016). In this process, metal sulfides are oxidized by iron- and sulfur-oxidizing microorganisms, forming soluble metal sulfates and sulfuric acid. Pyrite and arsenopyrite are well-known minerals that are easily biooxidized (Olson, 1994). During this process, microorganisms are catalytically used for oxidizing pyrite and arsenopyrite to release and expose gold for more processing (N. V. Fomchenko et al., 2016). In general, biooxidation for processing of refractory gold concentrate involves a typical flowsheet that involves crushing, milling, producing concentrate from the flotation process, followed by cyanidation and recovery of gold from biooxidized residues (Miller & Brown, 2016).

The operation temperature of a biooxidation process is very important because each microbial culture has its own optimal temperature for growth and oxidation (Muravyov, 2019). The bioleaching process of sulfide minerals involves two chemical and biological stages (N. Fomchenko, Muravyov, & Microbiology, 2017). Nouhi et al. (Nouhi & Ahmadi, 2025) used acid drainage for the biooxidation of a high-grade refractory sulfide gold ore, and gold recovery increased from 73% (without biooxidation) to

99% (in the biooxidized residue). Beiranvand et al. (Beiranvand, Ahmadi, & Hosseini, 2023) investigated the effect of mechanical activation on the oxidation and extraction of gold from a high-grade flotation concentrate using mesophilic and moderate thermophilic microorganisms. Gold recovery from the non-mechanically activated and non-biooxidized concentrate was 83.9%, while after biooxidation this value reached 98.8%. Also, gold recovery from the activated but non-oxidized concentrate was 77.3%, which reached 97.6% after biooxidation.

By decreasing easy-to-treat gold ores, developing technologies and increasing in gold price, the recoverable grade of gold ores has been decreased gradually. The development and optimization of biooxidation technology for increasing the recovery of gold from lean grade refractory sulfide wastes have not been previously well investigated. Flotation followed by biooxidation and cyanidation processes, as one of the potential routes to treat such low-grade and refractory ores and tailings. So, in this research the ability of this strategy was evaluated to extract gold from the low-grade stock piles of Mouteh gold mine.

2. Material and methods

2.1. Material

Samples were taken from low-grade refractory sulfide gold ore stackpiles of Mouteh gold mine (Isfahan province, Iran). At first, the sample was homogenized. Crushing was performed in two stages to achieve the desired particle size. To achieve a particle size of -75 μm, the samples were ground using a rod mill with ratio of 1:8 (1 kg samples: 8 kg rod) after crushing. The representative samples were used to analyze chemical and mineralogical parameters by XRD, XRF and Fire Assay methods.

2.2. Flotation

Flotation tests were conducted using a Denver flotation machine with a cell volume of 2200 ml to provide required concentrate for biooxidation experiments. In flotation tests, 150 g/t potassium amyl xanthate (PAX) was used as a main collector, 30 g/t dithiophosphate as a secondary collector, and 30 g/t methyl isobutyl carbonyl (MIBC) as a frother agent. The tests were carried out with a solid content of 25%. The water used for the experiments was local water from the Mouteh gold mine. After conducting tests, the flotation concentrates and tailings were filtered and dried for gold assay and subsequent experiments.

2.3. Biooxidation experiments

Biooxidation experiments of the concentrate were carried out in 500 ml Erlenmeyer were located in shaking incubator. The volume of pulp was 200 ml that consisted of 10% solid content, 20% bacterial solution, 155 ml culture media (9K, Norris). The Norris culture media consist of 0.4g $(NH_4)_2SO_4$, 0.5g $MgSO_4$ and 0.4g $Ca(PO_4H_2)_2$ (Silverman & Lundgren, 1959). Culture media (9K, Norris) were prepared with distilled water. The residence time of the test was 28 days. The initial pH of the solution was adjusted to 1.6 using 2M sulfuric acid. Oxidation/reduction potential and pH of solutions were monitored daily and maintained in the range of 1.6-1.8 using 2M sulfuric acid or lime (20% solid). During the experiment, the evaporated solution was compensated with distilled water. In the end of the experiment, the contents of each Erlenmeyer were filtered separately, the rest solution for determination of iron content was maintained, and the rest solid content was washed and dried for performing the subsequent experiments. After these experiments, the effect of processing water of Mouteh gold mine on biooxidation was studied.

2.4. Cyanidation experiments

Non-biooxidized flotation concentrate and biooxidized concentrate with mesophilic and moderate thermophilic microorganisms were subjected to cyanidation testing for 48 hours for gold recovery. Experiments were conducted with a solid content of 25% and 4 g/l NaCN (NaCN 50%) by mechanical stirring method. lime (15% solid content) was used to adjust the pH in the range of 10.5-10.7. At the end of the experiment, the final solution for gold and cyanide analysis and the final solid were washed with hot water, dried, and sent for gold analysis. The initial cyanide concentration was 1410 ppm, which after 48 hours of cyanide leaching, reached 450, 240, and 330 ppm for the flotation concentrate, mesophilic biooxidized concentrate, and moderate thermophilic biooxidized concentrate, respectively.

3.   Results and discussion

3.1. Flotation

Flotation experiments were conducted with a solids content of 25% using PAX and MIBC collector and frother reagents, respectively. After conducting flotation tests, the gold content in the initial sample, flotation concentrate, and flotation tailings was determined to be 0.5, 3, and 0.2 g/t, respectively, using fire assay analysis. Gold recovery in these tests was 64%.

The primary feed, concentrate and tailing of flotation tests were characterized. The results of the elements analysis of the flotation concentrate are shown in **Error! Reference source not found.**.

Table 1. XRF analysis of the flotation concentrate

element	SiO_2	BaO	CaO	Fe_2O_3	K_2O	MgO	MnO	P	S	TiO_2
Content (%)	54.60	<0.05	1.69	13.65	1.64	2.13	<0.05	<0.05	8.60	0.73

XRD (X-ray diffraction) patterns of primary samples showed that the main mineral phases were quartz, albite, chlorite and muscovite. The XRD diagram of the flotation concentrate is shown in Figure 1. According to the SEM analysis of flotation concentrate (Figure 2), the irregular particles with sharp edges and varying size are crushed pyrite, resulting from sample preparation. According to the EDS diagram (Figure 3), the peaks related to iron and sulfur are clearly visible, which emphasizes that the main phase in this region could be pyrite.
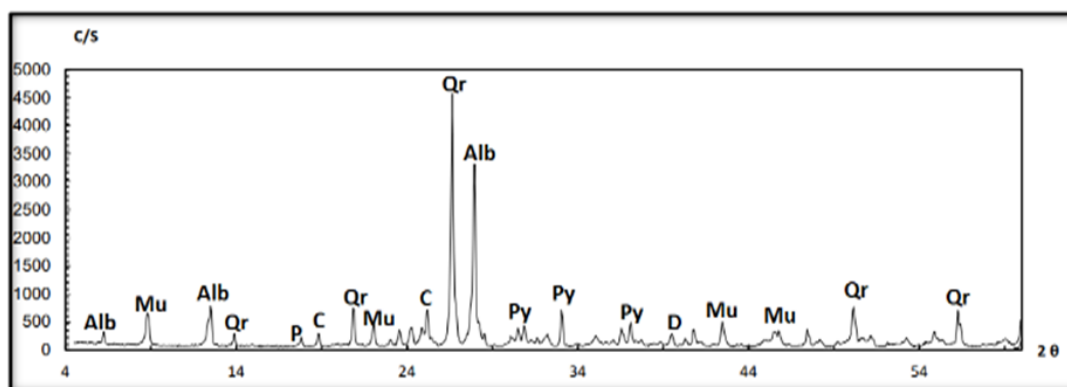
Figure 1. XRD diagram of the flotation concentrate (Alb: Albite, Mu: Muscovite, Qr: Quartz, P: Potassium Feldspar, C: Chlorite, Py: Pyrite, D: Dolomite)
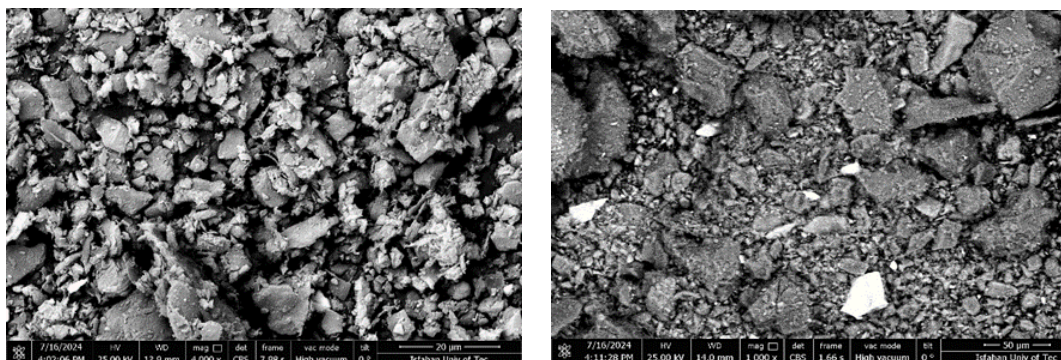
Figure 2. Scanning electron microscope (SEM) analysis of flotation concentrate
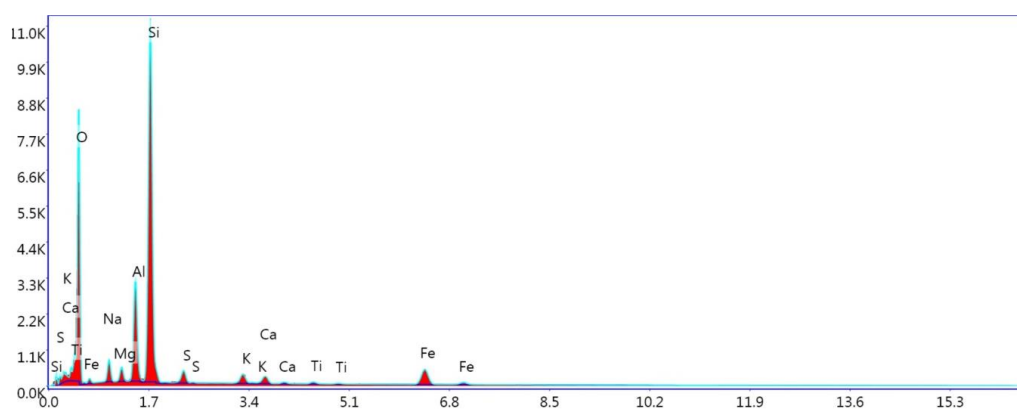
Figure 3. EDS analysis of flotation concentrate

3.2. Biooxidation

Concentrate biooxidation experiments were carried out with mesophilic and moderate thermophilic microorganisms and culture media prepared with distilled water. As can be seen from Figure 4 (a), For biooxidation with mesophilic microorganisms in Norris culture media, the pH increased from 1.5 to 2.4 within 1 day, and decreased to 1.7-1.8 after 16 days. The redox potential increased from about 408 mv in first day to 526 mv on the 9th day. The redox potential at the start of the experiment was higher than its value on the first day, which is due to the presence of ferric ions in the bacterial solution. On the first day of the process, due to the dissolution process, ferric iron ions are reduced to ferrous ions, which reduces the redox potential of the solution. After one day, the redox potential of the solution began to increase. The initial total iron concentration in sulfide flotation concentrate before biooxidation was 13.65% (w/w), which after biooxidation with mesophilic microorganisms in Norris culture media, reached 1.613 g/l on day 14 and 1.838 g/l on day 28.

For biooxidation with mesophilic microorganisms in 9K culture media (Figure 4 (b)), the pH increased from 1.6 to about 2 within 1 day, and decreased to 1.6-1.7 after 16 days. The redox potential was 424 mv on the first day of the experiment which increased to 600 mv on the 14th day. In this study, it was found that the lag phase of mesophilic microorganisms in 9K culture media was longer than their lag phase in Norris culture media. The total iron concentration after biooxidation with mesophilic microorganisms in 9K culture media, reached 1.849 g/l on day 14 and 2.103 g/l on day 28.

Biooxidation experiments of flotation concentrate were conducted using moderate thermophilic microorganisms in two culture media, Norris and 9K, under similar conditions. For biooxidation with moderate thermophilic microorganisms in Norris's culture media, as can be seen from Figure 4 (c), the pH increased from 1.6 to about 2 after 1 day. Then after 16 days, it was decreased to 1.6-1.7. The redox potential was 442 mv on first day of the experiment, began to increase on the 3rd day of the experiment. This increase continued until the 14th day, reaching to 520 mv. The total iron concentration after biooxidation with moderate thermophilic microorganisms in Norris culture media, reached 1.798 g/l on day 14 and 2.008 g/l on day 28.

(a)

(b)

(c)

(d)

Figure 4. pH and ORP of microorganisms in Norris and 9K culture media prepared with distilled water in biooxidation of flotation concentrate as a function of time

To investigate the effect of 9K culture media on the biooxidation with moderate thermophilic microorganisms, the biooxidation experiment was performed simultaneously and under the same conditions as in Norris medium. As can be seen from Figure 4 (d), the redox potential of the experiment on the first day was 434 mv, which increased to 585 mv by the 11th day. On the 3rd day of the experiment, the redox potential of the solution began to increase, and this increase continued until the 11th day. The pH increased from 1.6-2.2 after 1 day, and decreased to 1.5-1.6 after 16 days. By comparing the effect of culture media type on biooxidation of flotation concentrate with moderate thermophilic

microorganisms, it was found that by conducting experiments in 9K culture media, microorganisms have greater growth and activity than in Norris culture media, but their lag phase is the same in both types of culture medium. The total iron concentration after biooxidation with moderate thermophilic microorganisms in Norris culture media, reached 2.116 g/l on day 14 and 2.241 g/l on day 28.
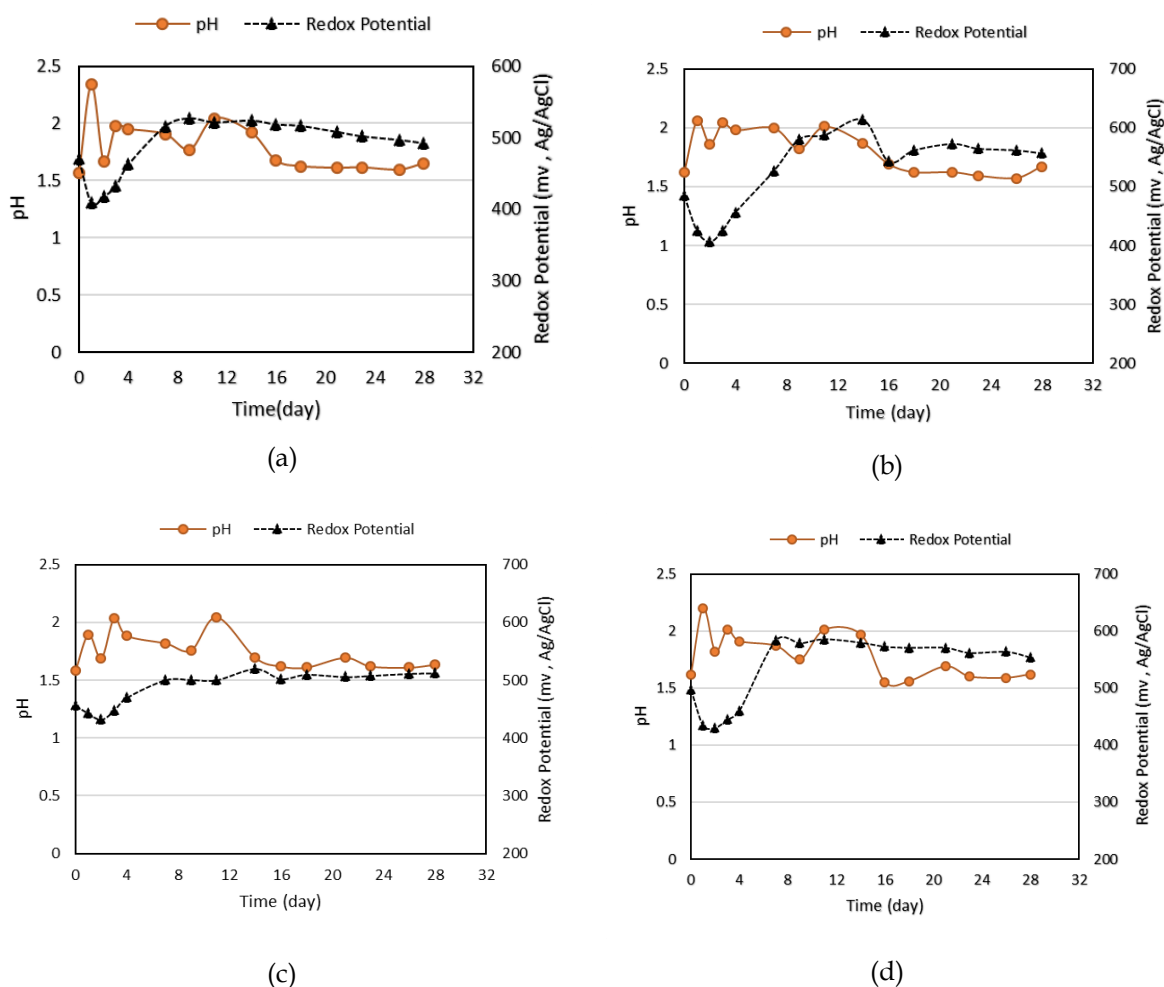
To investigate the effect of water type on concentrate biooxidation, experiments were carried out with mesophilic and moderate thermophilic microorganisms and culture media prepared with processing water of Mouteh gold mine. During the biooxidation with mesophilic microorganisms in Norris culture medium prepared with mine water (Figure 5 (a)), the pH increased from 2 to 2.5 within 1 day. Its value reached to 1.5-1.6 after 9 days. The redox potential was 395 mv on first day of the experiment. Its value increased to 589 mv after 16 days. The total iron concentration after biooxidation with mesophilic microorganisms in Norris culture media, reached 3.326 g/l on day 14 and 4.767 g/l on day 28.

For biooxidation with mesophilic microorganisms in 9K culture media, as can be seen from Figure 5 (b), The redox potential increased from about 397 mv on the first day to about 602 mv on the 14th day. On the 2nd day of the experiment, the redox potential began to increase, this increase continued until the 14th day. The pH increased from about 1.5 to 2.1 after 1 day, and decreased to 1.5-1.6 after 9 days. The total iron concentration after biooxidation with mesophilic microorganisms in 9K culture media, reached 4.213 g/l on day 14 and 5.554 g/l on day 28.

The biooxidation experiments of flotation concentrate were also repeated with moderate thermophilic microorganisms to investigate the type of water used in the preparation of the culture media. During biooxidation with moderate thermophilic microorganisms in Norris media (Figure 5 (c)), the pH increased from 1.5 to 1.7 within 1 day. Its value decreased to 1.5-1.6 after 9 days. The redox potential was 404 mv on first day. On the 2nd day of the experiment, the redox potential began to increase, this increase continued until the last day of the experiment (day 28) and increased to 603 mv. The total iron concentration after biooxidation with mesophilic microorganisms in Norris culture media, reached 2..882 g/l on day 14 and 3.548 g/l on day 28.

For biooxidation with moderate thermophilic microorganisms in 9K culture media, as can be seen from Figure 5 (d), the redox potential was 389 mv on first day of the experiment. Its value increased to 579 mv after 12 days. The pH increased from 1.7 to about 2.7 after 1 day, and decreased to 1.6-1.7 after 9 days. The total iron concentration after biooxidation with moderate thermophilic microorganisms in 9K culture media, reached 3.326 g/l on day 14 and 4.626 g/l on day 28.

(a)

(b)

(c)   (d)
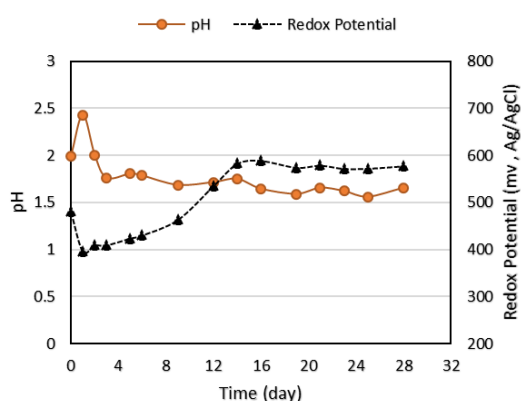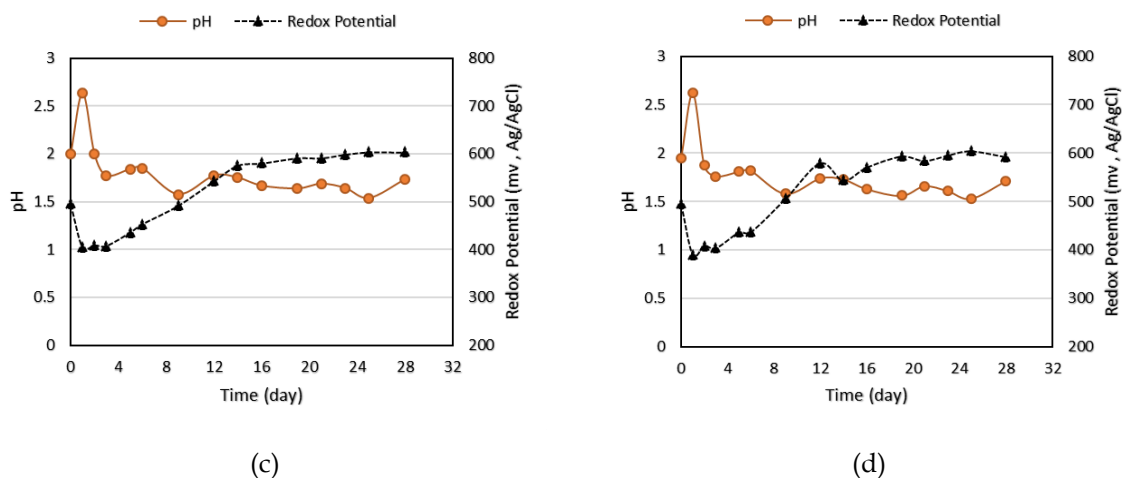
Figure 5. pH and ORP of microorganisms in Norris and 9K culture media prepared with local mine water in biooxidation of flotation concentrate as a function of time
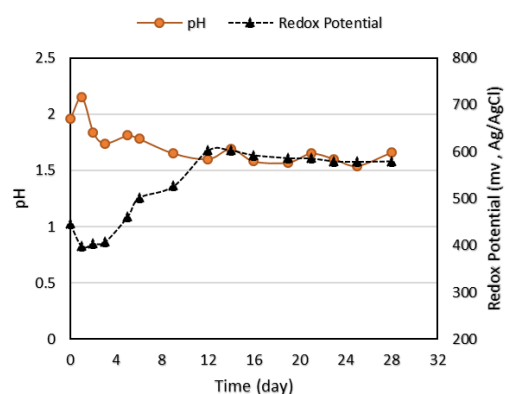
3.3. Cyanidation

After biooxidation experiments, the washed solid residue were subjected to cyanidation experiments. Experiments were conducted on non-biooxidized and biooxidized flotation concentrates with mesophilic and moderate thermophilic microorganisms. For further investigation, the biooxidized concentrate with mesophilic and moderate thermophilic microorganisms was cyanidated separately. Gold recovery from non-biooxidized flotation concentrate was 63.59%, while this value reached 80.21% after biooxidation with mesophilic microorganisms and 79.84% after biooxidation with moderate thermophilic microorganisms. As can be seen, biooxidation increased the gold recovery from the concentrate.

In the biooxidation of flotation concentrate using mesophilic and moderate thermophilic microorganisms, microorganisms grew and were more active in the 9K culture media prepared with mine water, also the rate of iron dissolution was higher using mesophiles, so gold recovery from biooxidized concentrate was higher with mesophiles, which indicate the better performance of mesophiles in this research. Janson investigated solid culture media for the isolation and enumeration of acidophilic bacteria, so observed that the growth of mesophilic bacteria were supported with the solid culture media that included ferrous iron (Johnson, 1995). Given the low gold recovery in the flotation experiments conducted, it is suggested that researchers conduct flotation experiments under optimal conditions and then perform the other steps. Figure 6 shown the used flowsheet for this research.
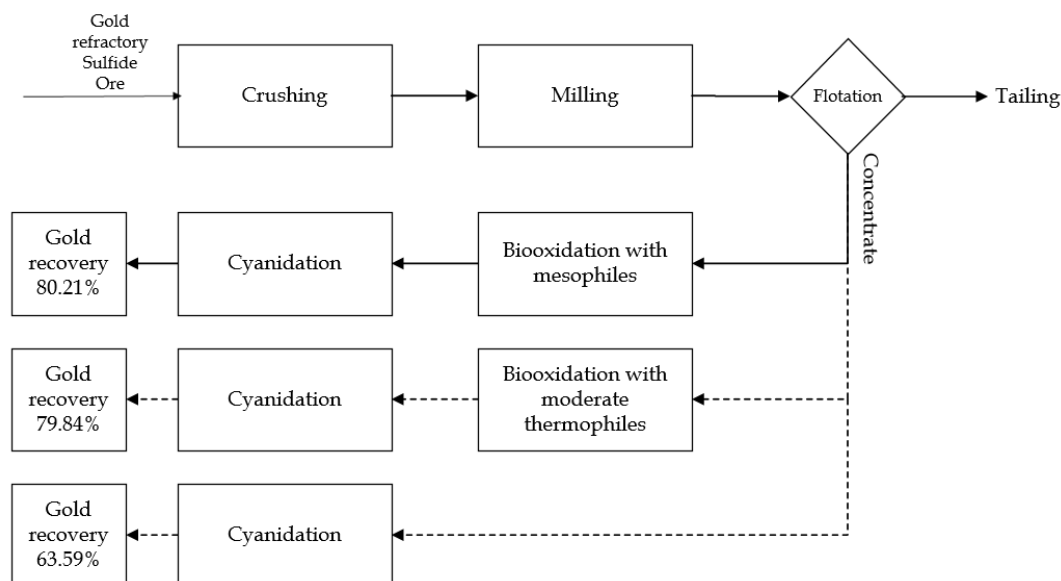
Figure 6.The flowsheet of flotation-biooxidation-cyanidation of gold refractory sulfide ore

4. Conclusion

The efficiency of flotation-biooxidation-cyanidation route to extract gold from the low-grade stock piles of Mouteh gold mine was investigated and the following results were obtained: Flotation experiments were conducted to prepare the required concentrate for biooxidation process. The gold grade for primary feed, concentrate, and flotation tailings were 0.5, 3, and 0.2, respectively. Gold recovery in flotation experiments was also 64%.

Results showed that both mesophillic and moderately thermophillic microorganisms had a good ability to oxidize pyrite at various cultures (nutrient media and water types) especially at local water and 9K nutrient medium.

Gold recovery by cyanidation from the non-biooxidized flotation concentrate was 63.59%, which increased to 80.21% and 79.84% after biooxidation with mesophilic and moderate thermophilic microorganisms, respectively. This increase was related to break down the sulfide network as a result of biooxidation.

It was found that flotation followed by biooxidation and conventional cyanidation could be an suitable processing route to extract gold from low grade and refractory gold ores and mine wastes.

References

Adams, M. D. (2005). *Advances in gold ore processing* (Vol. 15): Elsevier.

Anzoom, S. J., Bournival, G., & Ata, S. J. M. E. (2024). Coarse particle flotation: A review. *206*, 108499.

Asamoah, R., Amankwah, R., & Addai-Mensah, J. (2014). *Cyanidation of refractory gold ores: A review.* Paper presented at the 3rd UMaT Biennial International Mining and Mineral Conference.

Beiranvand, Z., Ahmadi, A., & Hosseini, M. R. J. M. E. (2023). Effect of mechanical activation on biooxidation and gold extraction of a high-grade flotation concentrate using mesophilic and moderately thermophilic microorganisms. *204*, 108394.

Fomchenko, N., Muravyov, M. J. A. B., & Microbiology. (2017). Chemical leaching of copper-zinc concentrate with ferric iron biosolution. *53*, 715-718.

Fomchenko, N. V., Kondrat'eva, T. F., & Muravyov, M. I. J. H. (2016). A new concept of the biohydrometallurgical technology for gold recovery from refractory sulfide concentrates. *164*, 78-82.

Han, J., Dai, S., Deng, J., Que, S., & Zhou, Y. J. S. (2024). Technology for Aiding the Cyanide Leaching of Gold Ores. *11*(8), 228.

Johnson, D. J. J. o. m. m. (1995). Selective solid media for isolating and enumerating acidophilic bacteria. *23*(2), 205-218.

Medina, D., & Anderson, C. G. J. M. (2020). A review of the cyanidation treatment of copper-gold ores and concentrates. *10*(7), 897.

Miller, P., & Brown, A. J. G. o. p. (2016). Bacterial oxidation of refractory gold concentrates. 359-372.

Muravyov, M. J. C. P. (2019). Two-step processing of refractory gold-containing sulfidic concentrate via biooxidation at two temperatures. *73*, 173-183.

Natal'ya, V. F., Muravyov, M. I., & Kondrat'eva, T. F. J. H. (2010). Two-stage bacterial–chemical oxidation of refractory gold-bearing sulfidic concentrates. *101*(1-2), 28-34.

Nouhi, E., & Ahmadi, A. J. E. E. S. (2025). Application of acid mine drainage for the biooxidation of a high-grade refractory sulfide gold ore. *84*(2), 67.

Olson, G. J. J. F. M. L. (1994). Microbial oxidation of gold ores and gold bioleaching. *119*(1-2), 1-6.

Seifi, M. (1402). *Processing gold ore by flotation method.* Sahand University of Technology,

Silverman, M. P., & Lundgren, D. G. J. J. o. b. (1959). Studies on the chemoautotrophic iron bacterium Ferrobacillus ferrooxidans II: Manometric Studies. *78*(3), 326-331.

Wang, G., Liu, X., Wu, Y., Zeng, T., Li, S., Liu, J., . . . Xie, S. J. H. (2020). Bio-oxidation of a high-sulfur refractory gold concentrate with a two-stage chemical-biological approach. *197*, 105421.

Wu, Z. L. (2018). *Sulfide Minerals Bio-Oxidation of a Low-Grade Refractory Gold Ore.* Paper presented at the Materials Science Forum.

Investigation of the Effect of Natural Salts on the Discharge Time of Remaining Voltage of Lithium-Ion Batteries During Crushing Stage

Mohammad Reza Vashadi Arani [1], Seyed Mohammad Razavian[2*]

[1]MSc of Mineral Processing Engineering, Department of Mining Engineering, Faculty of Engineering, University of Kashan, Kashan-Iran

[2]PhD of Mineral Processing Engineering, Department of Mining Engineering, Faculty of Engineering, University of Kashan, Kashan-Iran

*Corresponding author: razavian@kashanu.ac.ir (Seyed Mohammad Razavian)

Abstract:

The use of lithium-ion batteries has increased significantly in recent years due to their high energy density and the presence of valuable materials such as cobalt and nickel, making them an important source for secondary material recovery. However, recycling these batteries presents substantial safety risks, primarily from fire and explosion hazards caused by unwanted short circuits and high voltage components. These risks are especially pronounced during mechanical preparation, crushing, storage, and transportation, where damaged or improperly handled batteries can ignite or explode. To mitigate these hazards, rapid and controlled discharge of batteries before recycling is critical. Discharging using salt solutions is recognized as a simple, fast, and cost-effective method to reduce residual charge and minimize the risk of fire during subsequent handling. In this research, four different types of natural salts at various concentrations were tested, prioritizing the use of accessible, low-cost, and impure salts over pure laboratory-grade salts to enhance scalability and economic feasibility. Initial experiments involved direct immersion of batteries in salt solutions at concentrations of 10%, 15%, and 20% by weight. Among the complementary processes evaluated, the use of a high-speed magnetic stirrer, iron powder, and ultrasonic operations (ultrasonic bath and probe) were found to further reduce discharge time and help achieve target voltages more quickly. Notably, ultrasonic agitation at 28 kHz was particularly effective, significantly accelerating the discharge process and enabling the batteries to reach lower voltage thresholds such as 0.5 volts in a shorter time.

Keywords: Lithium-ion Batteries, Natural Salt, Discharge Voltage, Ultrasonic.

1. Introduction

The depletion of fossil fuels and environmental issues have paved the way for the use of renewable energy sources such as batteries. The current energy economy, based on fossil fuels, faces significant risks due to factors such as continuously increasing oil demand, depletion of non-renewable resources, and dependence on politically unstable oil-producing countries. Fossil fuels are a limited resource, and the world is facing an emerging energy crisis(Ojanen, Lundström, Santasalo-Aarnio, & Serna-Guerrero, 2018). It takes millions of years to produce the fossil fuels consumed in the past 200 years. Their consumption is the main cause of many environmental problems, including global warming, air pollution, and acid rain. Another concerning aspect of the current fossil fuel energy economy is the increasing level of carbon dioxide emissions, which have almost doubled in the past 30 years. Therefore, the use of renewable energy sources has grown. One of the most important renewable sources is batteries. Due to their rich composition of valuable materials such as cobalt, nickel, lithium, copper, and aluminum, batteries are used as sources of secondary raw materials. Batteries consist of one or more electrochemical cells capable of converting chemical energy into electrical energy and are a common energy source for many industrial and household applications.

Rapid technological advancement and the growing need for rechargeable batteries as energy sources have raised many concerns regarding the disposal of used batteries. Generally, batteries can be divided into primary batteries and rechargeable batteries, which mainly include lead-acid batteries, nickel-cadmium (Ni-Cd) batteries, nickel-metal hydride (Ni-MH) batteries, and lithium-ion batteries. Compared to other rechargeable batteries, some lithium batteries have higher energy density, higher cell voltage, less memory effect, lower self-discharge, longer cycle life, and are environmentally friendly, simple to charge, and maintain(Georgi-Maschler, Friedrich, Weyhe, Heegn, & Rutz, 2012). Various lithium-containing batteries first entered the market in the 1990s and are now widely used in modern equipment and life. Lithium-containing batteries are classified into rechargeable and non-rechargeable types, with primary lithium batteries being non-rechargeable and lithium-ion batteries (LIBs) considered a key technology enabling the transition to electric vehicles, thus replacing the traditional internal combustion engine design (J. Zhang, Zhang, Sun, & Wang, 2018).They are also the most suitable means for storing electrical energy. Renewable energies in electrical grids are currently the dominant power sources for various portable electronic devices. Lithium-ion batteries are noted for their high working voltage, low memory effects, and high energy density compared to traditional batteries (Doughty & Roth, 2012). As the use of alternative energy sources like solar and wind increases, the need for electrical energy storage becomes more pronounced. One of these storage methods is the use of lithium-ion batteries. The use of lithium-ion batteries is growing worldwide. This type of battery is increasingly being used in innovative applications, such as the aerospace industry, power transmission, consumer electronics, automotive industry, and renewable energy industry (Makuza, Tian, Guo, Chattopadhyay, & Yu, 2021). The increased use of personal electronic devices has led to a remarkable rise in lithium-ion battery waste. Meanwhile, electric vehicles are also on the rise, leading to the future production of large amounts of battery waste from vehicles. For instance, in 2019, about 50% of the cars sold in Norway were electric (Fujita et al., 2021; Karagiannopoulos & Solsvik, 2019). Thus, the issue of lithium-ion batteries used in electric vehicles has gained justified attention in recent years. Generally, electronic waste is one of the fastest-growing solid waste streams globally, posing significant challenges (Qiao, Wang, Gao, Wen, & Dai, 2021; Sattar, Ilyas, Bhatti, & Ghaffar, 2019).

1.1 Chemistry of Lithium-Ion Batteries and Materials

Since Sony first commercialized lithium-ion batteries using carbon as the anode and $LiCoO_2$ (LCO) as the cathode in 1991, billions of lithium-ion battery cells have been produced for portable electronic devices and other large electrical devices. The four main components of a lithium-ion battery are the cathode, electrolyte, separator, and anode. The anode stores lithium ions during charging, and lithium ions move towards the cathode during discharge to drive electrical applications. Therefore, the lithium-ion battery is also called a rocking-chair battery because lithium ions are exchanged between the cathode and anode. Common cathodes contain transition metal oxides such as LCO, $LiMn_2O_4$ (LMO), $Li(Ni_xCo_yAlz)O_2$ (NCA), and $Li(Ni_xCo_yMnz)O_2$ (NCM), which can be categorized accordingly. The crystal structures of LCO, NCA, and NCM are layered, with high specific energy and voltage, but cobalt is expensive, toxic, and thermally unstable. NCM contains less cobalt and is cheaper. LMO has high thermodynamic stability and high voltage but relatively low capacity. $LiFePO_4$ (LFP) cathode materials have a stable olivine structure and are safer than NCM and LCO, but they have low capacity and low charge/discharge rates (Ohzuku & Makimura, 2001). The demand for energy density and power density in lithium-ion batteries is continuously increasing. Many new high-capacity, high-voltage cathode materials have been identified, including nickel-rich, manganese-rich, and lithium-rich materials. Based on the nickel content, the ratio of nickel, cobalt, and manganese in commercial NCM cathodes varies, with different $Li(Ni_xCo_yMnz)O_2$ (NCM) compositions such as 8.5:0.75:0.75, 8:1:1, 7:1.5:1.5, 6:2:2, 5:2:3, 4:3:3, 1:1:1, etc. Increasing nickel and lithium contents can enhance the specific capacity of cathode materials but also lead to thermal instability. Nickel-rich commercial NCM materials such as $Li(Ni_{0.8}Co_{0.1}Mn_{0.1})O_2$ and $Li(Ni_{0.6}Co_{0.2}Mn_{0.2})O_2$ both exhibit higher specific capacities (specific capacity: 203 and 187 mAh/g respectively for $Li(Ni_{0.8}Co_{0.1}Mn_{0.1})O_2$ and $Li(Ni_{0.6}Co_{0.2}Mn_{0.2})O_2$ but lower thermal stability compared to low-nickel NCM materials like $Li(Ni_{0.5}Co_{0.2}Mn_{0.3})O_2$ or $Li(Ni_{0.33}Co_{0.33}Mn_{0.33})O_2$ (specific capacity: 175 and 163 mAh/g respectively for

$Li(Ni_{0.5}Co_{0.2}Mn_{0.3})O_2$ and $Li(Ni_{0.33}Co_{0.33}Mn_{0.33})O_2$ (Noh, Youn, Yoon, & Sun, 2013)).The common anode is made of graphite or $Li_4Ti_5O_{12}$ (LTO). The theoretical capacities for graphite and $Li_4Ti_5O_{12}$ are 372 and 175 mAh/g respectively (Z. Liu et al., 2019). The potential required for lithium insertion in $Li_4Ti_5O_{12}$ is 1.5 volts versus Li/Li^+, which is higher than the carbon-based anode, thus the full cell voltage with the $Li_4Ti_5O_{12}$ anode for a given cathode material decreases, and the energy density of the lithium-ion battery with $Li_4Ti_5O_{12}$ is lower compared to a graphite cell. However, the $Li_4Ti_5O_{12}$ anode has better cycle performance at high temperatures and better thermal stability compared to the graphite anode (Belharouak, Koenig Jr, & Amine, 2011). Similar to cathode materials, new high-capacity, high-voltage anode materials have also attracted special attention. These materials include silicon (approximately 4140 mAh/g, but with nearly 400% volume fluctuation during a cycle), tin (992 mAh/g), antimony sulfide (Sb_2S_3) (720 mAh/g, after 50 cycles at a current density of 250 mA/g), germanium (about 1200 mAh/g) (Choi et al., 2017; J. Liu, Kopold, van Aken, Maier, & Yu, 2015), and transition metal oxides (MO) where M is cobalt, nickel, copper, or iron, around 700 mAh/g), and silicon oxide. However, these new anode materials have yet to be commercialized. High volume expansion, low conductivity, instability of the solid electrolyte interphase (SEI) layer, and poor capacity retention are the main obstacles to the development of new anode materials(Wang, Jiang, Yu, & Sun, 2019).

1.2 Necessities of Recycling Lithium-Ion Batteries

The use of lithium-ion batteries in consumer electronics and electric vehicles is rapidly growing, leading to increased demand for resources such as cobalt and lithium. Therefore, recycling these batteries is essential not only to reduce energy consumption but also to address the scarcity of rare resources and eliminate the pollution of hazardous components, ensuring sustainability in industries related to consumer electronics and electric vehicles. Below are some main reasons for recycling these types of batteries: High number of consumed batteries, Environmental importance of consumed batteries, Resources available in consumed batteries, Protecting resources for future generations. This research examines the discharge process using chemical solutions containing four types of natural salts obtained from salt lakes and salt mountains, with these samples containing impurities. Advantages of using these types of salts include the use of natural, inexpensive, and readily available resources, reducing ongoing costs in the large-scale and industrial recycling process of lithium-ion batteries, shortening the discharge process time, and maintaining more stable voltage reduction in lithium-ion batteries.

2. Material and methods

2.1. Material

In this research, four different types of natural salts from Khur and Biabanak Playa (A), Aran and Bidgol Salt Lake (B), Urmia Salt Lake (C), and Garmsar-Semnan Salt Mountain (D) used. Sample A indirectly obtained with analysis from Khur Potash Complex. Samples B, C, and D directly collected from their locations through intermediaries residing near the salt sites.

2.2 XRD and XRF Analysis of Samples

To identify the elements and compounds present in the salt structures, XRD and XRF analyses were conducted at University of Kashan and and Mineral Exploration Organization's laboratories in Kerman, respectively. For sample A, since it indirectly obtained from a processing company, the exact analysis results provided with the sample. For the other three samples (B, C, and D), XRD and XRF analyses were performed. XRD provided qualitative information on the elements in the natural salt structures, while XRF measured the percentage of different elements quantitatively with an accuracy of hundredths. According to XRD results, halite (NaCl) and calcite (CaCO3) were present in sample B, only halite (NaCl) was in sample C, and halite (NaCl) and anhydrite (CaSO4) were in sample D. The elemental composition of each sample was then determined using XRF results (**Table 1**). The batteries

obtained from a battery recycling company in Tehran. The batteries were from smartphones of the Motorola brand and model BP6X; all used uniformly (Fig. 1). The salt solution in this case acted as a controlled short circuit or initial resistance to discharge the batteries. Using this approach allowed monitoring the evolution of the electrical potential of lithium-ion batteries solely due to discharge (i.e., not attributable to physical battery damage). The salts dissolved in ultra-pure and deionized water.

Table 1. Percentage of Elements and Compounds in Natural Salt Structures

Sample	Na (%)	K (%)	Ca (%)	Mg (%)	NaCl (%)	Ca(CO$_3$) (%)	Ca(SO$_4$) (%)	SiO$_2$ (%)	SO$_3$ (%)	Volatile Matters (%)
A	38.30	0.08	0.16	0.06	97.36	---	---	---	---	0.15
B	37.57	0.02	0.45	0.80	95.45	1.125	---	0.07	1.01	1.45
C	37.85	0.06	0.01	1.02	96.16	---	---	---	0.41	0.72
D	37.25	0.03	0.015	0.02	94.64	---	0.056	---	2.08	0.03

Fig. 1. Image of used batteries of Motorola brand and model (BP6X)

After examining indirect discharge and failing to achieve the research objectives, immersion testing adopted. According to previous research, 20% mass concentration was selected as the most effective for the discharge process, as it achieved the fastest voltage reduction without considering corrosion and water pollution. Therefore, the discharge process was tested with solutions containing salts A, B, C, D at 20% mass concentration, followed by tests at 10% and 15% concentrations. The 20% mass concentration showed the best performance for all solutions compared to other concentrations. Then, additional processes incorporated to shorten the discharge process duration. Complementary processes for discharging lithium-ion batteries in salt solutions included: discharge at 20% mass concentration with high-speed magnetic stirring, discharge with iron powder, discharge with iron and zinc powders, discharge using ultrasonic bath with 28 kHz ultrasonic waves, and discharge using ultrasonic probe (homogenizer) with 50 kHz ultrasonic waves in solutions containing salts A, B, C, D.

3. Results and Discussion

3.1 The Effect of the Type and Concentration of Natural Salts

Upon observing the test results, it found that the batteries in all solutions began to decrease voltage at a normal rate during the first hour, but a significant drop in voltage observed in the second hour.

From the third hour onward, the voltage drop returned to a normal rate. After one hour, the battery voltage in solutions A, B, C, D reached 3.38, 3.54, 3.52, and 3.61 volts, respectively. After a significant drop in the second hour, the battery voltage in solutions A, B, C, and D dropped to 0.63, 0.74, 0.64, and 0.69 volts, respectively. Following this second significant drop, the voltage reduction process normalized again, and the battery voltage in solutions A, B, C, and D reached 0.51, 0.51, 0.46, and 0.54 volts, respectively. The battery in solution A reached a voltage of 0.01 volts after 23 hours, the batteries in solutions B and C reached zero volts after 22 hours and 21.5 hours, and the battery in solution D reached its lowest voltage of 0.02 volts after 24 hours.

According to previous studies, one of the objectives of this research is to reduce battery voltage and reach voltage levels of approximately 1 volt and 0.5 volts. The main reason for using the 1-volt threshold is based on research indicating that this voltage level is considered safe for discharging lithium-ion battery recycling lines, and batteries below 1 volt are safer with minimized self-ignition risk . The 0.5-volt threshold is due to the duration of the process, requiring approximately 3 to 4 hours reducing the voltage from the initial level to 0.5 volts, whereas the reduction from 0.5 volts to zero takes 19 to 20 hours. In some salts, the voltage reduction to zero not achieved even after this time. In this series of tests, with a 20% concentration, the battery voltage in solutions containing salts A, B, C, D reached 1 volt after 80, 80, 70, and 95 minutes, respectively, and reached 0.5 volts after 185, 180, 150, and 245 minutes, respectively. It observed that the solution containing salt C performed better in achieving voltages of 1 and 0.5 volts (Fig. 2).

Fig. 2. Voltage-time ratio graphs for batteries directly in solutions containing salts A, B, C, D at a 20% mass concentration

3.2 The Effect of Using a High-Speed Magnetic Stirrer in the Battery Discharge Process

Based on better performance over time, the best concentration used considered 20% mass concentration, and all subsequent experiments aimed at examining various processes to reduce discharge time were prepared with this concentration. Unlike the indirect method, which halts battery voltage reduction, the direct method using appropriately concentrated solutions effectively reduced battery voltage to zero volts. However, aside from examining salt concentrations, another primary objective of this research is to reduce discharge time by considering various factors affecting this period. In the fourth step, to reduce discharge time, the battery discharge process was conducted in solutions containing salts A, B, C, D at a 20% concentration using a high-speed magnetic stirrer.

The results of this series of experiments showed that this series also follows the voltage reduction trend of previous tests. In this series, after one hour, the battery voltage in solutions A, B, C, D reached

3.69, 3.61, 3.71, and 3.60 volts, respectively. In the second hour, the battery voltage in solutions A, B, C, D reached 0.84, 0.71, 0.93, and 0.63 volts, respectively. In the third hour, the battery voltage in solutions A, B, C, D reached 0.60, 0.56, 0.58, and 0.48 volts, respectively. Achieving voltage levels of 1 volt and 0.5 volt considering the voltage ratio graphs, 1 volt and 0.5 volts can be equated to 0.26 and 0.13. It indicates 26% and 13% remaining battery voltage for solutions A, B, C, D took 105, 70, 115, and 65 minutes to reach 1 volt and 260, 240, 250, and 165 minutes to reach 0.5 volts, respectively. Comparing these results with the discharge process without using a magnetic stirrer, solution A performed poorly in reaching 1 volt and 0.5 volts. Solution B performed better in reaching 1 volt, reducing the time by 10 minutes, but performed poorly in reaching 0.5 volts, significantly increasing the time. Solution C showed poor performance in reaching both 1 volt and 0.5 volts, with significantly increased time. Solution D showed satisfactory performance in reaching 1 volt and 0.5 volts, improving the time by 30 minutes and 80 minutes, respectively. In this test, salt D reduced the battery voltage in a shorter time, making it the most suitable option for achieving the target voltage (Fig.3).
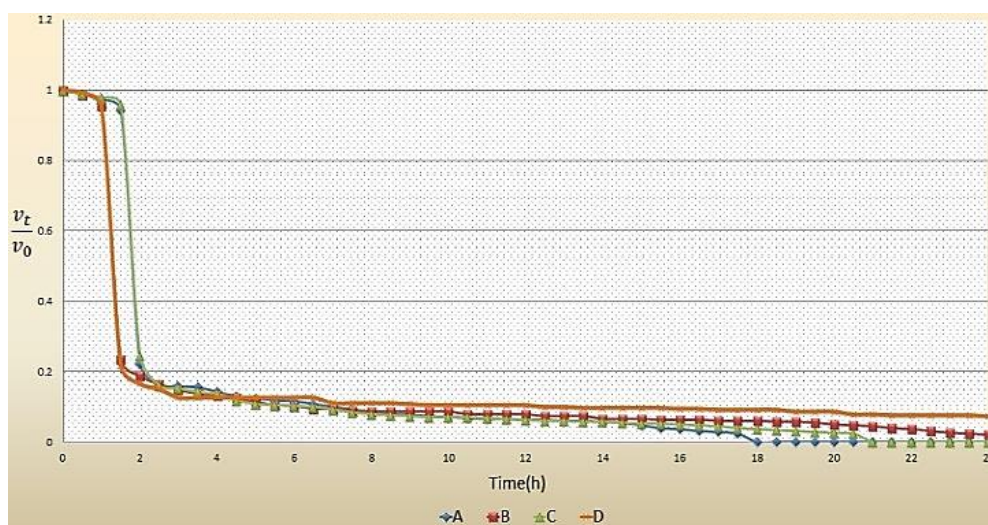
Fig. 3. Voltage-time ratio graphs for batteries discharging in solutions containing salts A, B, C, D at a 20% mass concentration using a high-speed magnetic stirrer

3.3 Discharge in the Presence of Metal Particles

3.3.1 The Effect of Iron Powder in the Battery Discharge Process

Based on the obtained results, the battery discharge trend follows the same trend as in other tests. Like other tests, the batteries in all solutions began to decrease voltage at a normal rate during the first hour, but a significant drop in voltage observed in the second hour, returning to a normal rate from the third hour onward. In the initial hour, the battery voltage in solutions A, B, C, D reached 3.64, 3.59, 3.70, and 3.58 volts, respectively. In the second hour, the battery voltage in solutions A, B, C, D reached 0.71, 0.71, 0.77, and 0.63 volts, respectively. In the third hour, the battery voltage in solutions A, B, C, D reached 0.50, 0.56, 0.64, and 0.48 volts, respectively. Achieving voltage levels of 1 volt and 0.5 volts (considering the voltage ratio graphs, 1 volt and 0.5 volts can be equated to 0.26 and 0.13) for solutions A, B, C, D took 95, 75, 110, and 70 minutes to reach 1 volt and 180, 240, 290, and 165 minutes to reach 0.5 volts, respectively. Comparing the 1 volt and 0.5 volt thresholds in this test with the base test without adding iron powder. Solution A showed positive feedback in reaching 0.5 volts, solution B in reaching 1 volt, and solution D in reaching both 1 volt and 0.5 volts, reducing the time, while other solutions performed similarly or worse, increasing the time to reach the target voltages (Fig. 4).
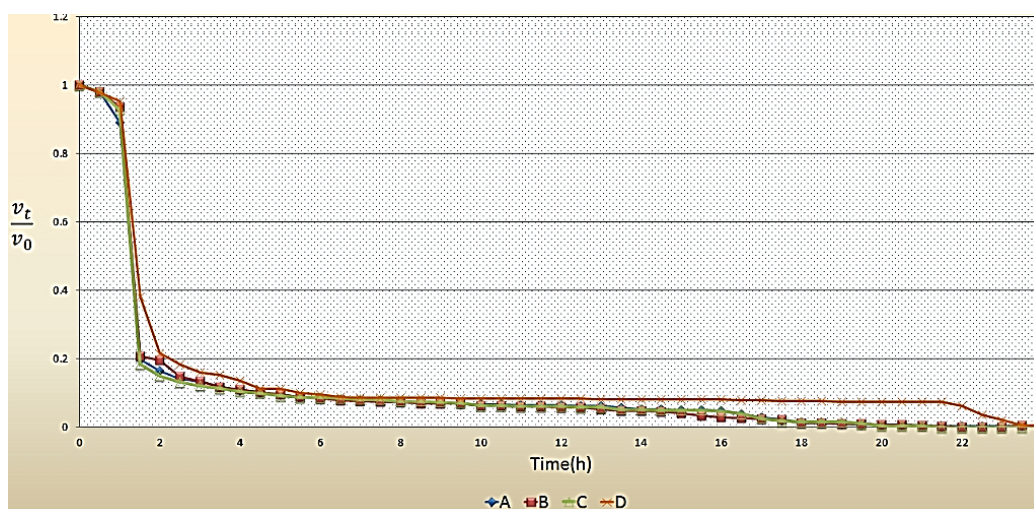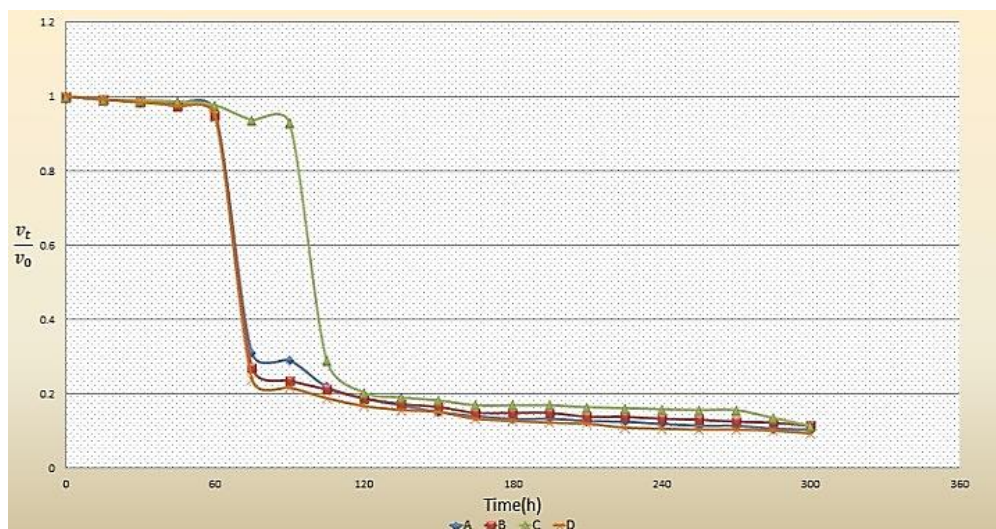
Fig. 4. Voltage-time ratio graphs for batteries discharging in solutions containing salts A, B, C, D at a 20% mass concentration with iron powder

3.3.2 The effect of iron and zinc powders in the Battery Discharge Process

After conducting the battery discharge process in solutions containing salts A, B, C, and D at a 20% mass concentration with the addition of iron powder, the results indicated no significant improvement in reducing discharge time. To further assess the impact of metal additives, pure iron and zinc powders (Merck brand) were also tested, and a magnetic stirrer was employed to enhance mixing during the experiments. In the solution containing salt B with iron powder, the battery voltage was recorded as 3.73 V after the first hour, 1.01 V after the second hour, and 0.72 V after the third hour. The battery reached target voltages of 1 V and 0.5 V after 122 minutes and 310 minutes, respectively. Similarly, in the solution with salt B and zinc powder, the voltage was 3.70 V after one hour, 0.97 V after two hours, and 0.76 V after three hours. The target voltages of 1 V and 0.5 V were achieved after 115 minutes and 470 minutes, respectively. When comparing these results to experiments without iron and zinc powder additives, no positive effect was observed in reducing the discharge time. In fact, the addition of pure iron and zinc powders did not enhance the battery discharge process, which is consistent with research indicating that the performance of metal powder additives is highly dependent on the electrolyte composition and the presence of specific additives or surfactants. While certain additives and optimized slurry compositions can improve discharge capacity in zinc-based systems, the simple addition of pure iron or zinc powder without further modification or the use of specialized additives does not necessarily yield better discharge performance. This highlights the importance of electrolyte engineering and the careful selection of additives to achieve meaningful improvements in battery discharge kinetics. (Fig. 5)

Fig. 5. Voltage ratio graph over battery discharge time in solutions containing salt B at a concentration of 20% by mass with the addition of iron and zinc powders

3.4 The effect of using an ultrasonic treatment in the Battery Discharge Process

After evaluating the effects of various physical and chemical processes-including magnetic stirring, the addition of iron and zinc powders, and the use of pure iron powder-on reducing the discharge time of lithium-ion batteries, the study progressed to explore the role of salt solutions and ultrasonic treatment. In this phase, batteries were discharged in 20% by mass salt solutions (salts A, B, C, and D), utilizing an ultrasonic bath operating at 28 kHz. The results demonstrated that the discharge profiles in these salt solutions, when combined with ultrasonic agitation, generally followed the decreasing voltage trends observed in earlier experiments. However, the timing and duration of normal, rapid, and resumed discharge phases varied between solutions. Notably, in all solutions except A, a sudden voltage drop occurred before the one-hour mark, indicating a more pronounced effect compared to previous methods. Specifically, after 6 minutes of ultrasonic treatment, the voltages of batteries in solutions A, B, C, and D dropped to 3, 1.36, 1.10, and 0.93 volts, respectively. At the 80-minute mark, all solutions reached the 1-volt threshold, with final voltages of 1, 0.76, 0.78, and 0.73 volts for solutions A, B, C, and D, respectively. The voltage reduction then returned to a normal trend. The time required for the voltage to reach approximately 1 volt was 80, 74, 70, and 66 minutes for solutions A, B, C, and D, respectively. To reach 0.5 volts, solutions A, B, C, and D required 112, 110, 118, and 106 minutes, respectively.Comparative analysis with baseline experiments (without ultrasonic treatment) revealed: Solution A: No change in reaching 1 volt, but a 73-minute reduction in reaching 0.5 volts. Solution B: Improved time to 1 volt, though not as effective as the best result with stirring; 70-minute reduction to 0.5 volts. Solution C: No change to 1 volt, but a 32-minute reduction to 0.5 volts. Solution D: Improved time to 1 volt (matching best performance with stirring) and a 139-minute reduction to 0.5 volts.

These findings indicate that ultrasonic agitation at 28 kHz significantly accelerates the discharge process, especially in reaching the lower voltage threshold of 0.5 volts. Among the tested salts, solution D was the most effective, achieving the fastest voltage reduction and making it the most suitable option for rapid battery discharge in this context. (Fig. 6)
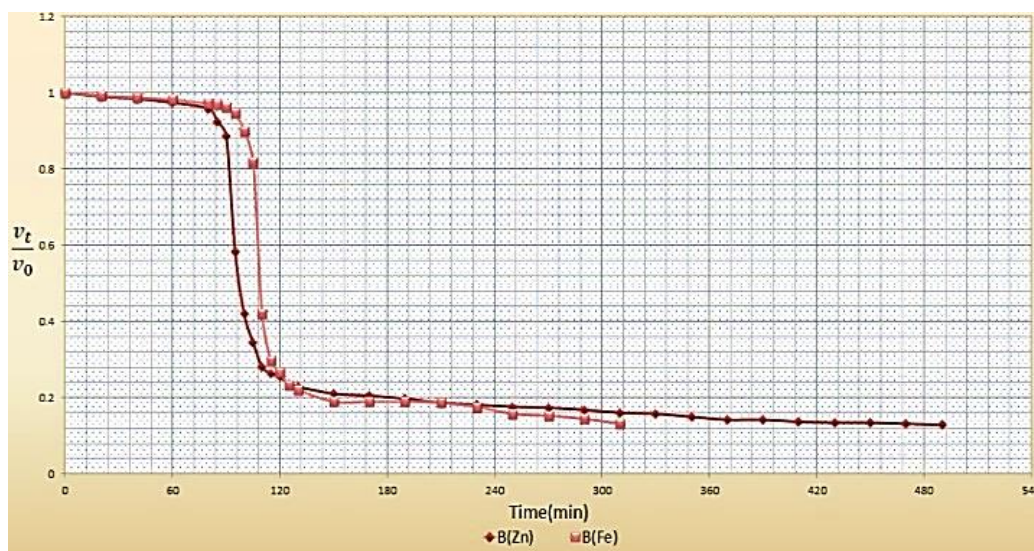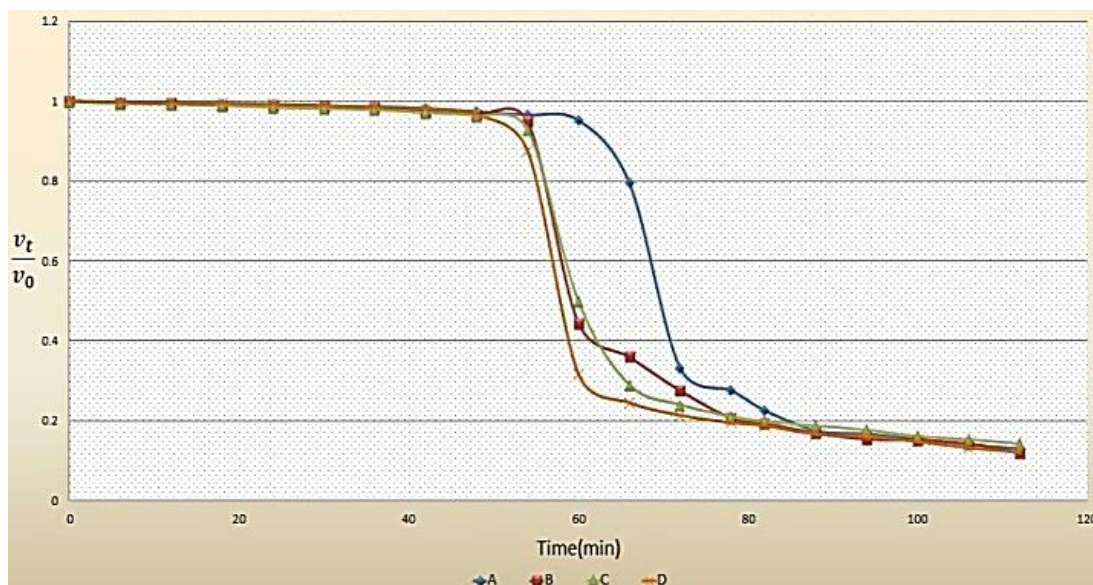
Fig. 6. Voltage ratio graph over battery discharge time in a solution containing salt A at a concentration of 20% by mass with the use of an ultrasonic bath with 28 kHz ultrasonic waves

4. Conclusion

According to the findings of this research, the most effective method for discharging lithium-ion batteries involves chemical processes and the direct immersion of the batteries in salt solutions. The primary objective was to identify the optimal salt concentration among the tested natural salt solutions for efficient battery discharge. Another aim was to achieve battery voltages at the thresholds of 1 and 0.5 volts. Initially, a series of experiments was conducted using salt solutions at concentrations of 10%, 15%, and 20% by mass. The results indicated that the 20% by mass salt solution provided superior performance in reducing battery voltage and achieving the target voltages compared to the lower concentrations. Among these, salt C enabled the fastest reduction in battery voltage, making it the most suitable option for reaching the desired voltage limits under standard conditions. Subsequently, the effect of enhanced mixing was examined by employing a high-speed stirrer in 20% by mass salt solutions. Under these conditions, salt D demonstrated the most rapid voltage reduction, indicating that mechanical agitation can influence the effectiveness of certain salts. The next phase involved the addition of iron powder to the 20% by mass salt solutions. When comparing the times required to reach 1 V and 0.5 V with and without iron powder, only solution A showed an improvement at the 0.5 V threshold, while solution B exhibited a slight improvement at the 1 V threshold. In most other cases, the addition of iron powder either had no effect or resulted in increased discharge times. Further experiments tested the impact of adding pure iron and zinc powders (Merck brand) to salt B solutions at 20% by mass. The results showed no positive effect on reducing discharge time compared to the base experiment without these metal powders. Finally, the discharge process was evaluated in 20% by mass salt solutions using an ultrasonic bath operating at 28 kHz. In this series of experiments, salt D facilitated the fastest reduction in battery voltage, establishing it as the most effective option for achieving the target voltages. In summary, the optimal battery discharge process identified in this study involves the direct immersion of batteries in a 20% by mass solution of salt D, particularly when combined with ultrasonic agitation. This method consistently achieved the most rapid and efficient reduction of battery voltage to the desired thresholds.

5. References

Belharouak, I., Koenig Jr, G. M., & Amine, K. (2011). Electrochemistry and safety of Li4Ti5O12 and graphite anodes paired with LiMn2O4 for hybrid electric vehicle Li-ion battery applications. *Journal of power sources, 196*(23), 10344-10350.

Choi, S., Cho, Y. G., Kim, J., Choi, N. S., Song, H. K., Wang, G., & Park, S. (2017). Mesoporous Germanium Anode Materials for Lithium-Ion Battery with Exceptional Cycling Stability in Wide Temperature Range. *Small, 13*(13), 1603045.

Clancy, R .Tesla Shares Fall after Car Fire and Rating Downgrade. (2018). Retrieved from https://www.telegraph.co.uk/finance/newsbysector/industry/10352809/Tesla-shares-fall-after-car-fire-and-rating-downgrade.html

Doughty, D. H., & Roth, E. P. (2012). A general discussion of Li ion battery safety. *The Electrochemical Society Interface, 21*(2), 37.

Fujita, T., Chen, H., Wang, K.-t., He, C.-l., Wang, Y.-b., Dodbiba, G., & Wei, Y.-z. (2021). Reduction, reuse and recycle of spent Li-ion batteries for automobiles: A review. *International Journal of Minerals, Metallurgy and Materials, 28*(2), 179-192.

Gao, W., Song, J., Cao, H., Lin, X., Zhang, X., Zheng, X., . . . Sun, Z. (2018). Selective recovery of valuable metals from spent lithium-ion batteries–process development and kinetics evaluation. *Journal of Cleaner Production, 178*, 833-845.

Georgi-Maschler, T., Friedrich, B., Weyhe, R., Heegn, H., & Rutz, M. (2012). Development of a recycling process for Li-ion batteries. *Journal of power sources, 207*, 173-182.

Karagiannopoulos, L., & Solsvik, T. (2019). Tesla boom lifts Norway's electric car sales to record market share. *Reuters Technology News, 1*.

Li, L., 2018. Flight Cabin Fire Sparks Online Debate. (2018). Retrieved from http://en.people.cn/n3/2018/0227/c90000-9430439.html

Liu, J., Kopold, P., van Aken, P. A., Maier, J., & Yu, Y. (2015). Energy storage materials from nature through nanotechnology: a sustainable route from reed plants to a silicon anode for lithium-ion batteries. *Angewandte Chemie, 127*(33), 9768-9772.

Liu, Z., Yu, Q., Zhao, Y., He, R., Xu, M., Feng, S., . . . Mai, L. (2019). Silicon oxides: a promising family of anode materials for lithium-ion batteries. *Chemical Society Reviews, 48*(1), 285-309.

Makuza, B., Tian, Q., Guo, X., Chattopadhyay, K., & Yu, D. (2021). Pyrometallurgical options for recycling spent lithium-ion batteries: A comprehensive review. *Journal of power sources, 491*, 229622.

Mozur, P . ; Lee, S.-h., 2018. Samsung to Recall 2.5 Million Galaxy Note 7s Over Battery Fires. (2018). Retrieved from https://www.nytimes.com/2016/09/03/business/samsung-galaxy-note-battery.html

Noh, H.-J., Youn, S., Yoon, C. S., & Sun, Y.-K. (2013). Comparison of the structural and electrochemical properties of layered Li [NixCoyMnz] O2 (x= 1/3, 0.5, 0.6, 0.7, 0.8 and 0.85) cathode material for lithium-ion batteries. *Journal of power sources, 233*, 121-130.

Ohzuku, T., & Makimura, Y. (2001). Layered lithium insertion material of LiCo1/3Ni1/3Mn1/3O2 for lithium-ion batteries. *Chemistry letters, 30*(7), 642-643.

Ojanen, S., Lundström, M., Santasalo-Aarnio, A., & Serna-Guerrero, R. (2018). Challenging the concept of electrochemical discharge using salt solutions for lithium-ion batteries recycling. *Waste management, 76*, 242-249.

Qiao, D., Wang, G., Gao, T., Wen, B., & Dai, T. (2021). Potential impact of the end-of-life batteries recycling of electric vehicles on lithium demand in China: 2010–2050. *Science of the Total Environment, 764*, 142835.

Sattar, R., Ilyas, S., Bhatti, H. N., & Ghaffar, A. (2019). Resource recovery of critically-rare metals by hydrometallurgical recycling of spent lithium ion batteries. *Separation and Purification Technology, 209*, 725-733.

Torabian, M. M., Jafari, M., & Bazargan, A. (2022). Discharge of lithium-ion batteries in salt solutions for safer storage, transport, and resource recovery. *Waste Management & Research, 40*(4), 402-409.

Wang, Q., Jiang, L., Yu, Y., & Sun, J. (2019). Progress of enhancing the safety of lithium ion battery from the electrolyte aspect. *Nano Energy, 55*, 93-114.

Wu, L., Zhang, F.-S., Zhang, Z.-Y., & Zhang, C.-C. (2023). Corrosion behavior and corrosion inhibition performance of spent lithium-ion battery during discharge. *Separation and Purification Technology, 306*, 122640.

Yao, L. P., Zeng, Q., Qi, T., & Li, J. (2020). An environmentally friendly discharge technology to pretreat spent lithium-ion batteries. *Journal of Cleaner Production, 245*, 118820.

Zeng, X., Li, J., & Singh, N. (2014). Recycling of spent lithium-ion battery: a critical review. *Critical Reviews in Environmental Science and Technology, 44*(10), 1129-1165.

Zhang, G., He, Y., Wang, H., Feng, Y., Xie, W., & Zhu, X. (2019). Application of mechanical crushing combined with pyrolysis-enhanced flotation technology to recover graphite and LiCoO2 from spent lithium-ion batteries. *Journal of Cleaner Production, 231*, 1418-1427.

Zhang, J., Zhang, L., Sun, F., & Wang, Z. (2018). An overview on thermal safety issues of lithium-ion batteries for electric vehicle application. *Ieee Access, 6*, 23848-23863.

A Conscious Lab-based approach for modeling and investigating the impact of influential parameters on feed rate and differential pressure in cement vertical roller mills

Rasoul Fatahi*, Hadi Abdollahi, Mohammad Noaparast, Mehdi Hadizadeh

School of Mining Engineering, College of Engineering, University of Tehran, Tehran, Iran

*Corresponding author: Rasoul.fatahi97@ut.ac.ir (Rasoul Fatahi)

Abstract:

Vertical Roller Mills (VRMs) are widely used in energy-intensive industries like cement, steel, and chemicals due to their efficiency in grinding, drying, and material transport. However, two critical aspects remain underexplored: the correlation between operational variables and differential pressure (dp) and the influence of key parameters, such as feed rate, on mill performance. To address these gaps, this study utilized advanced machine learning methods, including Random Forest (RF), LightGBM, and Shapley Additive Explanations (SHAP), integrated within a Conscious Lab-based (CL) framework. The study focused on modeling feed rate as a manipulated and dp as a controlled variable, with SHAP employed to analyze variable interactions. Findings identified operational factors such as working pressure, dp, counter pressure, and mill fan speed as significant determinants of feed rate setpoints. Working pressure emerged as the most influential variable impacting both dp and feed rate, establishing its critical role in stabilizing operations and regulating performance. Key variables, such as working pressure, mill fan speed, and feed rate, were also identified as primary contributors to dp, reflecting the principles of the CL framework for dynamic control. Validation tests revealed LightGBM as the best-performing algorithm, achieving the highest R^2 value(0.98 and 0.97) and lowest RMSE(1.34 and 0.16) for feed rate and dp prediction respectively, making it the optimal model for predicting feed rate and dp. This study highlighted the potential of combining machine learning with the CL framework to accurately model complex relationships among variables, optimize VRM operations, and advance sustainable energy-efficient practices in the cement industry.

Keywords: Vertical Roller Mill, Modeling, Differential Pressure

1. Introduction

The primary advantage of vertical roller mills (VRM) is their energy efficiency, which is crucial in mineral processing and cement production, where grinding consumes approximately 60% of total electrical energy (Fujimoto, 1993). Grinding processes account for approximately one-third of the total energy consumption in cement production, with an average of 57 kWh of electrical energy used per ton of cement for clinker grinding (Worrell et al., 2000). VRMs are high-capacity grinding equipment widely utilized in energy-intensive industries, including cement, steel, and chemicals (Zhu et al., 2020), combining grinding, drying, conveying, and powder separation functions within a single unit (Harder, 2010). VRMs have become preferred due to their superior grinding efficiency, lower energy consumption, and enhanced drying capabilities (Harder, 2010), offering benefits that can eliminate tertiary and even secondary crushing stages (Fahrland & Zysk, 2013; Schaefer, 2001). These multifunctional systems integrate grinding, drying, conveying, and powder separation (Altun et al., 2017; Harder, 2010), with operational parameters significantly influencing grinding outcomes, energy efficiency, and product quality (Altun et al., 2017). Conventional VRM operation relies heavily on

operator experience for manual parameter adjustment (Zhu et al., 2020), and most VRM studies remain theoretical or laboratory-based (Altun, 2017). Process control involves manipulating variables like working pressure, feed rate, and differential pressure (Little, 2021), leading to operational instability, increased energy consumption, and reduced grinding efficiency (Meng et al., 2015). The variation in operator experience poses risks to mechanical components and process stability. VRMs operate under negative pressure created by the mill fan to facilitate powder transportation. Enhancing classification efficiency and minimizing pressure differentials are crucial for reducing fan energy consumption. Various studies have examined variables affecting VRM grinding circuits (Liu et al., 2020), including material breakage behavior (Fatahi, Pournazari, et al., 2022), raw meal fineness prediction (Belmajdoub & Abderafi, 2023), material residence time (Barani et al., 2022), and energy consumption reduction (Altun et al., 2015). Research has advanced toward real-time cement fineness estimation (Stanišić et al., 2015), production index prediction (Lin & Zhang, 2016), and intelligent automatic control systems (Yan-yan et al., 2011). Mathematical and numerical modeling studies have analyzed flow field characteristics and blade parameters, revealing their significant impact on classification efficiency, differential pressure, and overall VRM performance (Hu et al., 2024; Liu et al., 2020). The Conscious Lab-based (CL) approach, an artificial intelligence-based framework, leverages operational data to develop dynamic AI systems that can reduce laboratory costs, address scale-up issues, save time, and make decisions based on actual factory conditions rather than theoretical concepts. This AI-based structure utilizes explainable AI algorithms based on control room monitoring data, optimizing production through operator training (Chelgani et al., 2024; Fatahi et al., 2025; Fatahi et al., 2021; Fatahi, Nasiri, et al., 2022; Fatahi et al., 2023). VRM stability depends significantly on differential pressure, discharged gas temperature, ventilation rate, and mill inlet negative pressure (Authenrieth et al., 2012; Yan-yan et al., 2011). Differential pressure, the difference between mill inlet and outlet pressure, reflects the material load inside the mill and correlates with other process variables (Fedoryshyn et al., 2012; Pareek & Sankhla, 2021). Despite extensive VRM research, two critical areas remain understudied: (1) the correlation between operational variables and differential pressure, and (2) the effects and correlation of key parameters like feed rate. This combined research employs machine learning methods, including Random Forest, LightGBM, and Shapley Additive Explanations (SHAP), to predict differential pressure and model feed rate as a manipulated variable and main drive power as a controlled variable. Understanding these complex interactions and relationships will guide optimal VRM operation, performance, and energy efficiency while enabling operators to make more rational decisions across various operational conditions.

2. Material and methods

2.1. Data set collection

The dataset for modeling vertical roller mill (VRM) processes was systematically gathered through continuous monitoring of operational parameters over an extended period. Data collection occurred in the central control room of Production Line 9 at Tehran Cement Plant (Tehran, Iran), one of Iran's largest cement production complexes with nine production lines and a production capacity of 13800 t/day. Monitoring spanned 1,026 hours under diverse operational conditions, representing actual industrial settings rather than laboratory conditions. The data collection process integrated scientific knowledge with operational expertise from experienced VRM operators. Process data was recorded by applying appropriate set points to manipulable variables and capturing the resulting responses from actuator systems. This comprehensive approach ensured that the dataset reflected real-world operational scenarios, including operator decisions and system responses to programmable logic controller (PLC) commands. Fig. 1 shows the schematic of data collection stages from the VRM cement grinding circuit.
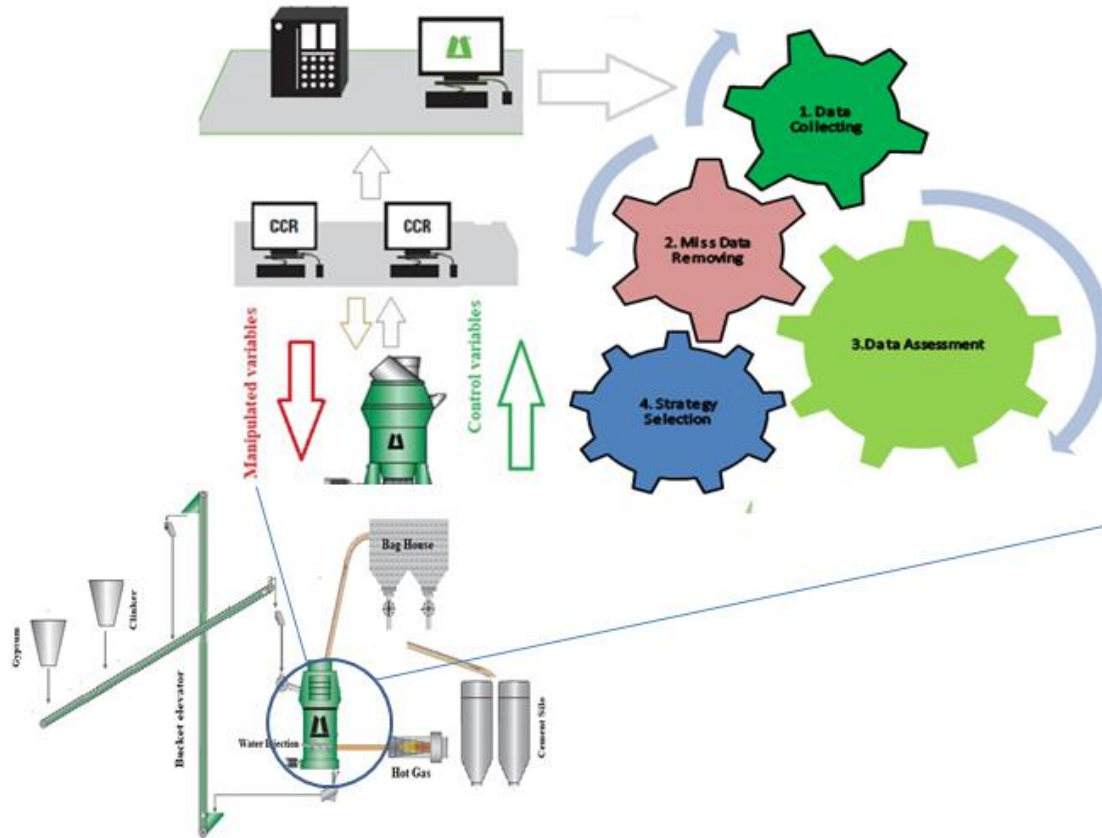
Fig. 1 Schematic of data set collection stages from the cement VRM grinding circuit.

2.2. Cement VRM grinding process

The cement VRM operates through a sophisticated grinding mechanism powered by a main drive connected via a vertical gearbox. Before the operation begins, a hydraulic system lifts the master and support rollers from the grinding table. The grinding process initiates when feed material, consisting primarily of clinker (with d_{80} approximately 32 mm) and gypsum in a 97:3 ratio, is introduced to the center of the rotating table. Centrifugal forces drive these materials toward the edges where they encounter significant pressure from the master rollers, resulting in grinding action between the rollers and the table surface. The VRM features a unique four-roller mechanism: two large master rollers responsible for grinding operations and two smaller support rollers that stabilize material layering on the grinding table. Bed breakage stability is maintained through both support roller action and water injection. After grinding, the processed material passes through a dam ring that regulates the height of the material layer before being collected by hot gas entering through a nozzle ring. This hot gas serves dual purposes-drying the materials and transporting finer particles to a dynamic separator above the mill. The cement powder exits with the gas stream and is collected in a bag house, while coarser particles return to the table for further additional grinding. Many modern VRMs incorporate external recirculation systems where coarse materials falling into the mill's gas ducts through the louver ring are reintroduced alongside fresh feed via conveyors or bucket elevators, achieving significant energy savings (Authenrieth et al., 2012; Fatahi, Pournazari, et al., 2022; Fedoryshyn et al., 2012; Pareek & Sankhla, 2021; Xu & Sun, 2020). The Process control parameters of cement VRM are shown in Table 1.

Table 1 Process control parameters of cement VRM grinding circuit.

Variables	Description of variables	Max	Min	Mean	STD
Mill output pressure	The outlet pressure of the mill	-27.95	-33.04	-29.33	0.61

Mill body vibrating (mm/s)	The vibration of the mill body due to operational parameters	8.84	2.31	4.12	0.89
Main Drive (Kw)	The power drawing of the main motor	1887.80	1005.10	1552.713	224.24
Mill fan power (Kw)	The power drawing of the motor mill fan	677.44	513.38	555.77	19.79
Water injection (m³/hr)	The rate of water spray for stabilization of bed breakage.	1.51	1.25	1.43	0.07
Differential pressure (mbar)	The differential pressure between the inlet and outlet of the mill	36.61	30.62	33.23	0.92
Mill body vibrating (mm/s)	The vibration of the mill body due to operational parameters	8.84	2.31	4.12	0.89
Counter pressure (bar)	The applied pressure for adjustment of the distance of the master roller from the table	16.90	14.35	15.29	0.61
Feed rate (t/h)	A load of mill feed	29.27	86.41	114.08	9.51
Silo Elevator (A)	The amper drawing of the main elevator motor	64.71	44.49	55.38	4.70
Bed Height(cm)	The thickness of the material bed	30	0.0	4.94	9.17
Mill fan speed (rpm)	The speed of the mill fan impeller	813.27	747.99	767.32	9.04

2.3. Shapley Additive exPlanations (SHAP)

Shapley Additive Explanations (SHAP) is an innovative approach introduced by Lundberg and Lee to enhance the interpretability of machine learning models (Lundberg & Lee, 2017). SHAP delivers local and global explanations by assigning feature importance at the instance level and across the dataset. It breaks down model outputs into feature-specific contributions, enabling tasks like debugging, feature engineering, and decision optimization (Mangalathu et al., 2021; Mao et al., 2021). Visualizing feature importance and prediction explanations enhances model interpretability and validation. Mathematically, outputs are expressed as the weighted sum of SHAP values for input features:

$$f(x) = \varphi_0 + \sum_{i=1}^{N} \varphi_i X_i' \qquad (1)$$

Here, f is the model's mapping function, N is the number of input features, φ_0 is the average prediction and φ_i is the SHAP value for the i-th feature. The coalition vector X_i' is computed from the original input X_i using a mapping function $X_i = h_x (X_i')$ (Bussmann et al., 2021; Mangalathu et al., 2021).

2.4. LightGBM

Gradient Boosting Decision Tree (GBDT) is highly efficient and reliable but faces challenges with big data as its scalability decreases due to the need to scan all instances (Friedman, 2001). LightGBM, introduced by Microsoft in 2017, addresses these issues (Ke et al., 2017). Unlike other algorithms, LightGBM builds trees focusing on leaves with the most loss, enhancing accuracy. Its speed benefits from Gradient-based One-Side Sampling (GOSS), and Exclusive Feature Bundling (EFB) (Ke et al.,

2017). It minimizes the loss function while adding weak learners, with the final prediction being the weighted sum of their forecasts (Liu et al., 2022).

loss function $= (y_i, \hat{y}_i)$ (2)

For each iteration (t), the negative gradient of the loss function relative to the predictions made by the previous model is calculated as:

$$g_i^{(t)} = -\frac{\partial L(y_i, \hat{y}_i^{(t-1)})}{\partial \hat{y}_i^{t-1}}$$ (3)

In LightGBM, the tree is constructed leaf-wise. For each node (m), the optimal split is determined in a way that minimizes the loss function. In this context, if (S) represents the set of samples that reach leaf node 'm', the optimal split point is found by:

$$\text{split}_m = \arg \min_{\text{split}} \sum_{i \in S} L(y_i, \hat{y}_i^{(t-1)} + \text{split})$$ (4)

Once the tree construction is completed, the output value for each leaf node 'm' is estimated by calculating a weighted sum of the negative gradient of the samples in that leaf:

$$\text{leaf\_output}_m = -\frac{\sum_{i \in S} g_i^{(t)}}{\sum_{i \in S} h_i^{(t)} + \lambda}$$ (5)

LightGBM uses histogram-based feature splitting and gradient-based one-side sampling, making it practical, especially for skewed datasets under similar parameters (Li et al., 2022).

2.5. Random Forest

Random Forest (RF), a tree-based predictive model renowned for handling high-dimensional data and not relying on parametric assumptions, was introduced by Breiman and utilizes ensemble learning techniques for tasks such as classification and regression (Matin et al., 2016). The Random Forest (RF) method builds upon Bootstrap aggregating (Bagging) by incorporating random variable selection at each node (Breiman, 1996). Essentially, it extends bagging by randomly selecting a subset of features within each data sample. RF modeling offers several advantages, including reduced overfitting, minimal tunable parameters, robustness to outliers, low bias, and decreased variance compared to traditional decision trees (DT) (Gong et al., 2018; Ouallouche et al., 2018) .Typically, RF generates an ensemble of N decision tree estimators, with the final prediction calculated as follows:

$$\hat{T}(X) = \frac{1}{N} \sum_{n=1}^{N} \hat{T}_n(X)$$ (6)

where x represents the input feature vector, and $\hat{T}_n(X)$ denotes the nth decision tree's prediction (Wager & Athey, 2018).

3. Results and discussion

3.1. Relationship of parameters assessments

The linear assessment results indicated the likelihood of multiple multivariable relationships among the operational variables in the cement VRM. Numerous studies have highlighted the potential for complex interactions between operational variables in the cement industry (Fatahi et al., 2021; Fatahi,

Nasiri, et al., 2022; Fatahi et al., 2023). Based on Fig. 2, when the target variable for modeling is the feed rate, it shows the highest correlation with the following parameters in descending order: working pressure (0.94), water injection (0.83), main drive (0.81), and dp (0.80). Similarly, the parameters with the strongest linear correlation to dp are working pressure (0.83), mill fan speed (0.82), and feed rate (0.80). In contrast, mill output (-0.592), counter pressure (-0.332), and bed height (-0.255) display negative correlations with dp, highlighting both positive and negative relationships among the operational variables.
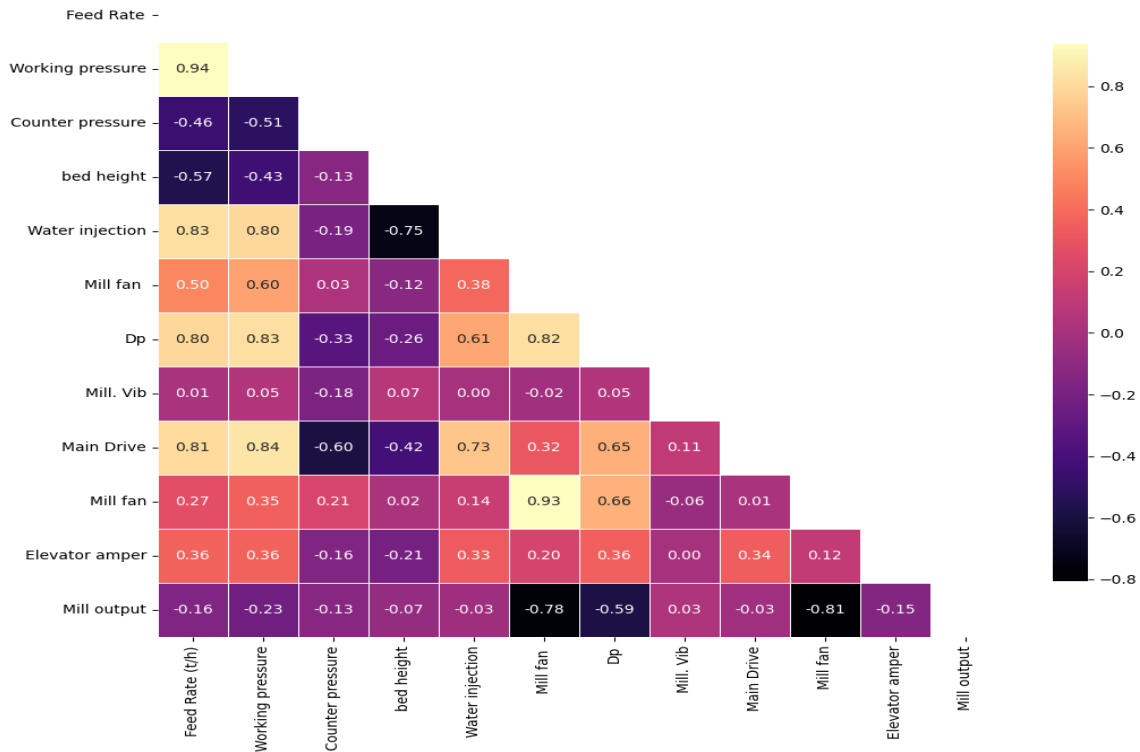
Fig. 2 Pearson correlation between process variables of cement VRM grinding circuit.

3.2. SHAP analyses of operational variables

SHAP is a highly effective technique for interpreting machine learning models, offering precise insights into the contribution of each variable to the model's predictions (Chelgani et al., 2021). Fig. 3 ranks variables based on importance, clearly illustrates their individual effects. The SHAP analysis revealed a ranking pattern similar to the Pearson correlation evaluation regarding parameter importance. For modeling with feed rate as the target variable, SHAP indicated that working pressure and dp have the most significant influence on the model, both showing a positive correlation on average. As the feed rate increases, operators raise the working pressure to enhance comminution efficiency, resulting in higher dp values (Yan-yan et al., 2011).
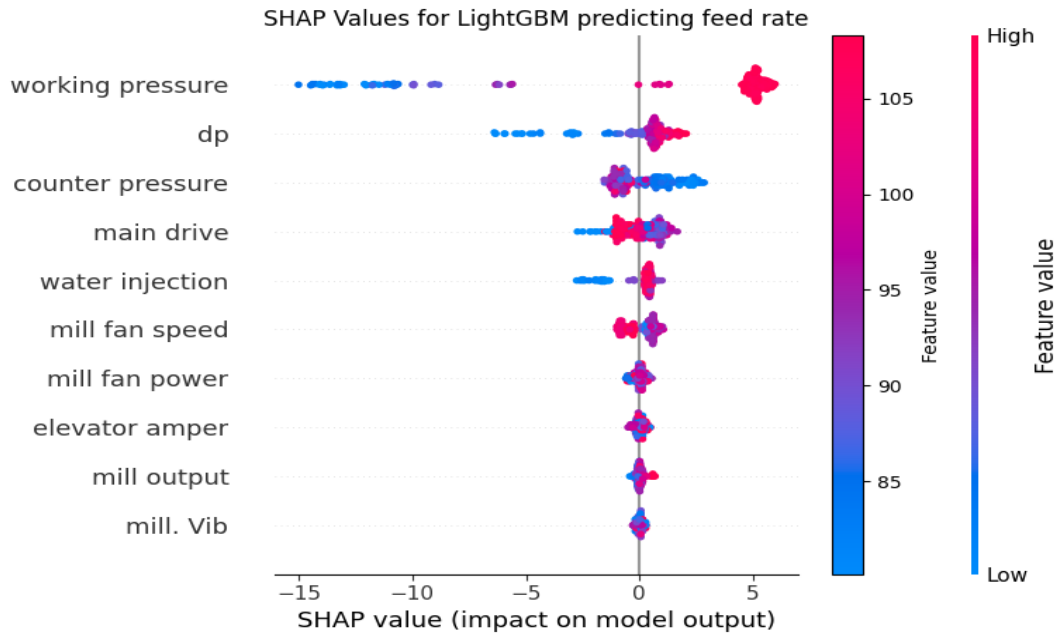
Fig. 3 Ranking variables based on their mean SHAP value for feed rate prediction.

Fig. 4 derived from SHAP analysis, identifies three key variables significantly influencing dp prediction in cement vertical roller mills. Their average impact on the model's output highlights that Dp is primarily affected by the material feed rate, the mill fan flow rate (or fan speed), and the working pressure (Pareek & Sankhla, 2021).
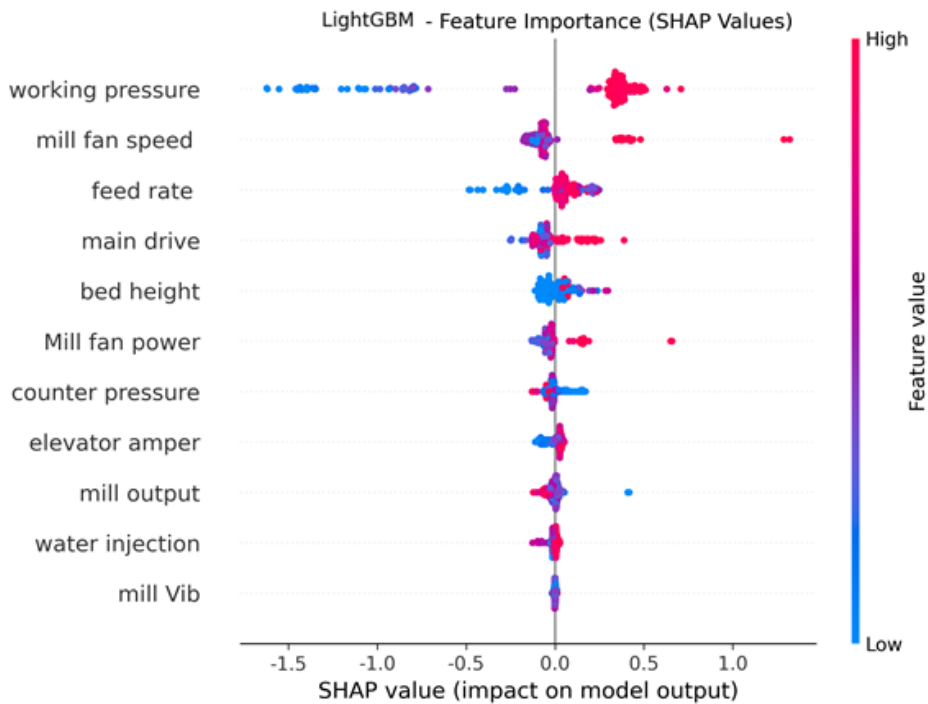
Fig. 4 Ranking variables based on their mean SHAP value for dp prediction.

125

 SHAP can identify and analyze multi-correlations and complex patterns among variables (Chelgani et al., 2023). Fig. 5 presents the SHAP analysis which highlights the multi-correlation between key parameters impacting feed rate modeling. The working pressure increases as operators raise the feed or product rate, as noted in (Altun et al., 2017). At lower feed rates, the working pressure remains minimal (blue points) whereas at higher feed rates, the pressure rises significantly (red points). DP which reflects the difference between the inlet and outlet pressures of the mill, indicates the mill's internal load and feed rate (Yan-yan et al., 2011). The inter-correlation between feed rate and dp shows that up to 115 t/h, increasing the feed rate leads to a sharp rise in dp, while beyond this threshold, the increase becomes more gradual. Feed rate variations during VRM operation influence the mill's load and, consequently, the dp. Adjusting the feed rate during operation requires increasing the working pressure which allows the rollers to apply greater force on the grinding bed for effective comminution. Counter pressure plays a role in this process by bringing the rollers closer to the table to optimize the application of working pressure.
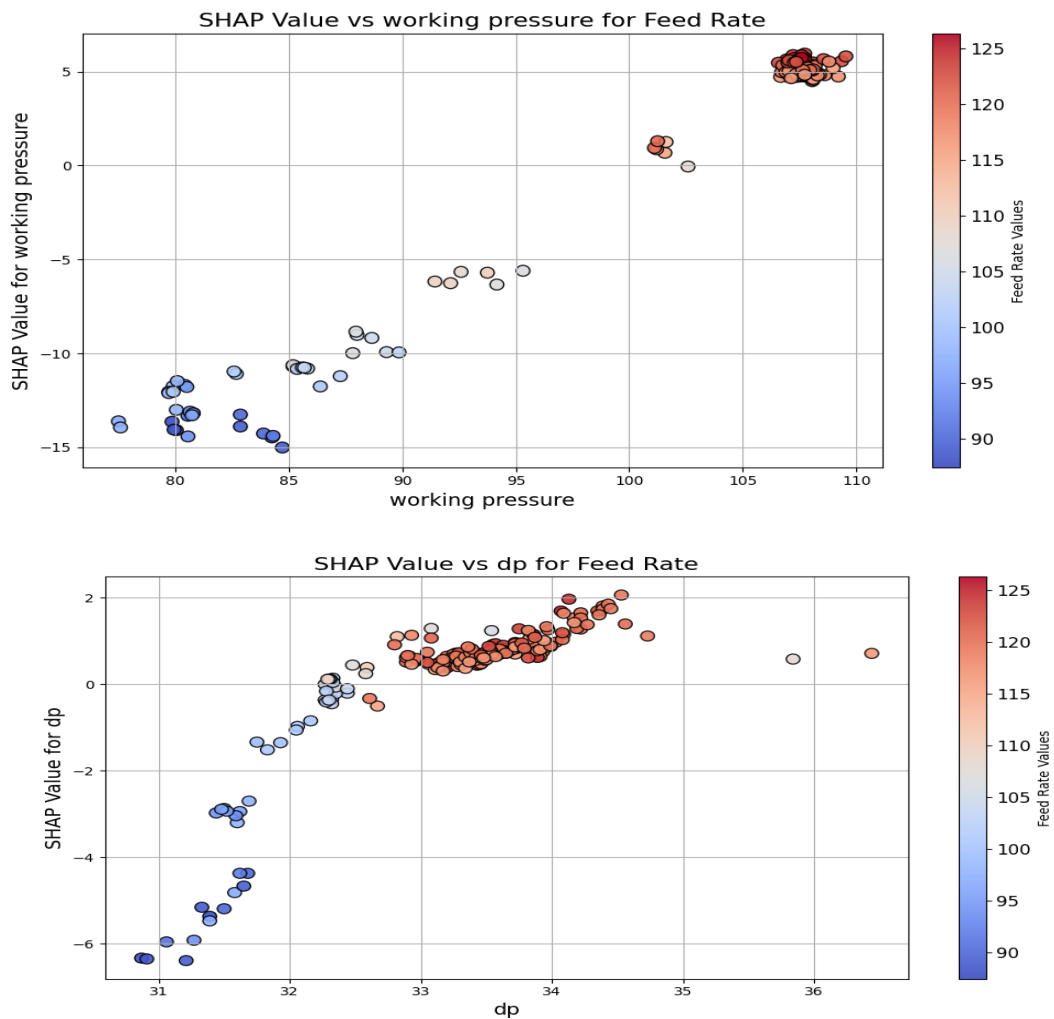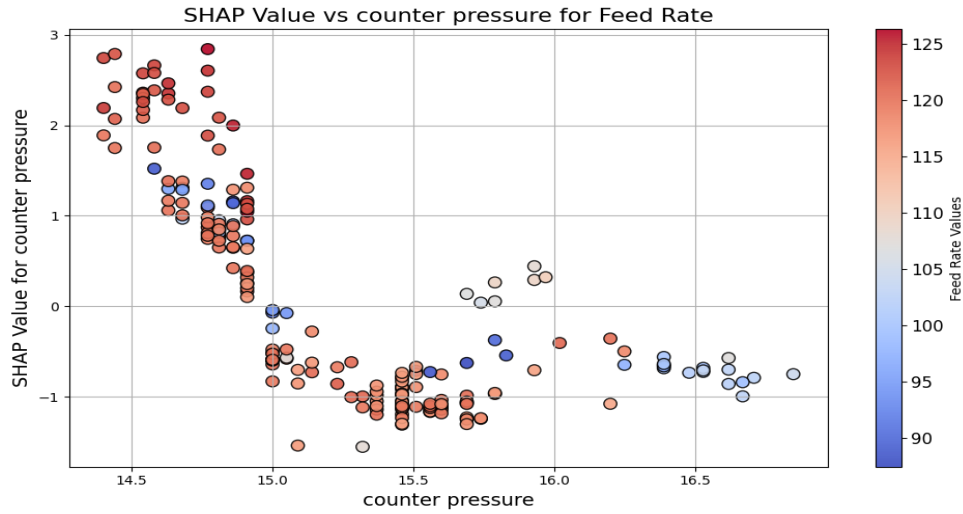
Fig. 5 SHAP values for multi-interactions dependent operational variables on feed rate prediction.

Fig. 6 shows the SHAP analysis reveals that mill fan speed significantly impacts on dp, with SHAP values transitioning from negative to positive as fan speed increases from 750 to 810 rpm. The highest dp values (around 36) are observed at 810–815 rpm fan speeds where the inlet-outlet pressure differential is maximized. Similarly, working pressure shows a positive, though non-linear, correlation with dp. At lower pressures (80–90), SHAP values are negative, improving as pressure rises to 110, with peak dp performance in the 105–110 range. Operators align higher working pressures with feed rate increases to maintain stable operation. Feed rate exhibits a more complex relationship. At lower feed rates (85–95), SHAP values are negative, becoming positive around 100–105. Data scatter in the middle range (100–115) suggests the influence of additional factors. At higher rates (115–125), SHAP values remain positive, with peak dp observed at feed rates of 110–115. Like fan speed, higher feed rates amplify the pressure differential. Maximum dp performance is achieved through high mill fan speed, elevated working pressure, and moderate to high feed rates. Working pressure shows the most linear and predictable relationship with dp, while fan speed and working pressure have more significant impacts than feed rate. Stabilizing dp and maintaining a consistent material bed under the rollers is essential, as a thick bed increases energy consumption, while a thin bed risks internal wear in the mill (Sahasrabudhe et al., 2006).
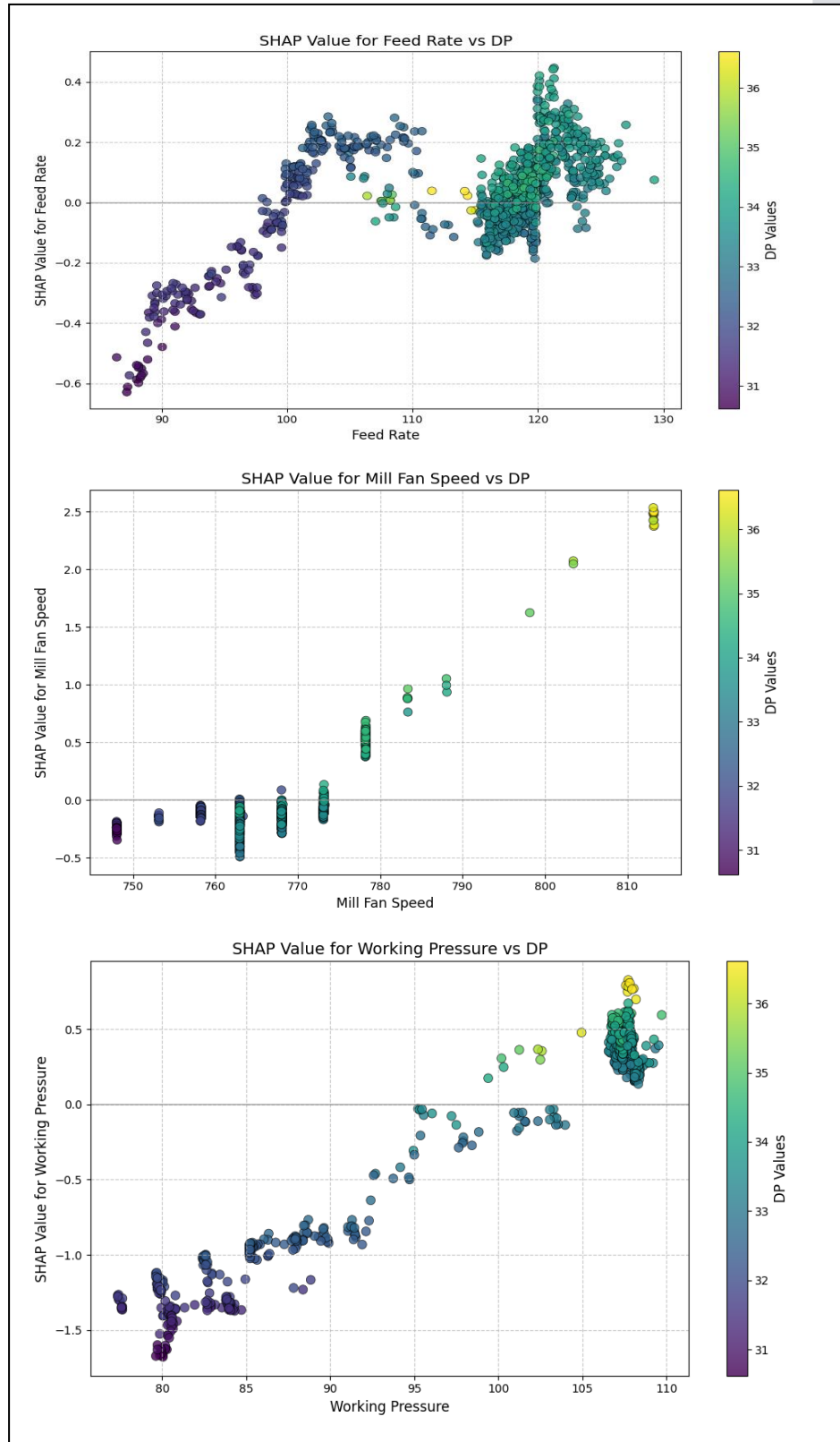
Fig. 6 SHAP values for multi-interactions dependent operational variables on dp prediction.

3.3. Feed rate and dp prediction

During the modeling process for predicting feed rate and dp, the dataset was randomly split into three parts: 70% was allocated for training. In contrast, two equal portions of 15% were designated for

testing and validation. Several hyperparameters were explored to optimize the model's performance using a randomized search strategy. This optimization process utilized the validation set to determine the best combination of parameters. The outcomes of this process are summarized in Table 2, which details the optimal values for the model's hyperparameters.

Table 2 Hyperparameters of models with Randomized Search CV and Model Performance Metrics.

Combined Machine Learning Model Hyperparameters						
Target	Model	Number of Trees	Max Features/ Num Leaves	Max Depth	Min Samples Split / Min Child Samples	Min Samples Leaf/ Learning Rate
Feed Rate	RandomForest	400	log2	10	2	1
	LightGBM	200	31	5	10	0.05
DP	RandomForest	200	None	15	2	1
	LightGBM	300	31	3	5	0.05

Model Performance Metrics					
Target	Model	Dataset	RMSE	MSE	R²
Feed Rate	RandomForest	Train	0.6490	0.4212	0.9753
		Validation	1.95	3.8025	0.9321
		Test	1.3896	1.9310	0.9478
	LightGBM	Train	0.6090	0.3709	0.9958
		Validation	1.3462	1.8122	0.9811
		Test	1.4009	1.9625	0.9775
Differential Pressure	RandomForest	Train	0.0599	0.0036	0.9656
		Validation	0.1825	0.033	0.9265
		Test	0.1656	0.0274	0.9480
	LightGBM	Train	0.0920	0.0085	0.9896
		Validation	0.1641	0.0269	0.9694
		Test	0.1798	0.0323	0.9623

Based on the cross-validation results shown in Table 2 and Fig. 7, both the LightGBM and RF algorithms successfully predicted the controlled variable "dp" and the adjustable variable "feed rate" with satisfactory accuracy. Among the tested algorithms, LightGBM outperformed RF in terms of predictive precision. In terms of performance metrics, LightGBM achieved the highest accuracy, with an R^2 of 0.98, an RMSE of 1.34 and 0.96, and an RMSE of 0.16 for feed rate and dp prediction, respectively, while RF performed slightly less effectively with an R^2 of 0.93 and an RMSE of 1.95 and 0.92 and an RMSE of 0.18. These findings underscore LightGBM's ability to predict mill feed rate set points and differential pressure efficiently.
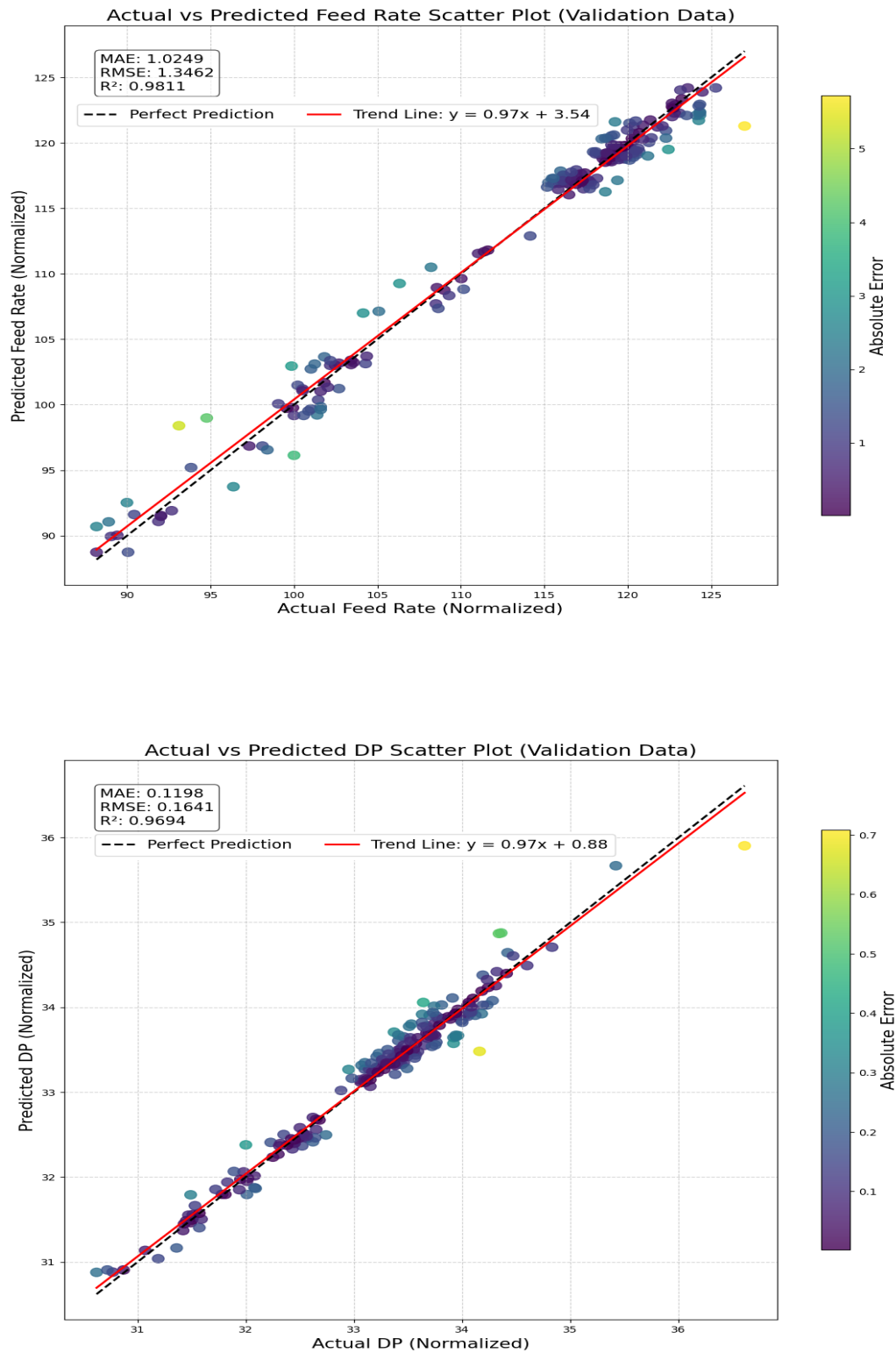
Fig. 7 Comparison between predicted and actual values by LightGBM in the validation step.

The results indicate that the SHAP-lightGBM model, as an advanced AI system, has successfully designed and implemented a CL system for Vertical Roller Mills (VRM). This model is capable of accurately modeling feed rates and main drive power. Furthermore, the SHAP analyses comprehensively reveal nonlinear relationships among various parameters. Studies show that this system can be utilized for modeling, controlling, and maintaining cement VRM circuits on an industrial scale. This capability enables operators to identify key parameters during operations, assess the effects of critical factors on feed rate increases (an essential operational parameter), optimize energy consumption by identifying factors influencing the main drive power, and take measures to enhance operational efficiency. The SHAP-lightGBM model is an effective tool for optimizing energy consumption and identifying key parameters in industrial processes.

4. Conclusions

This study investigated the variables influencing feed rate and dp in VRM, using machine learning algorithms such as RF and LightGBM. The developed models accurately reflected the feed rate's setpoint performance and the mill's subsequent dp while identifying linear and complex nonlinear relationships among operational variables. SHAP analyses highlighted the impact of variables such as working pressure, dp, and counter pressure on operators' determination of the feed rate setpoint. Furthermore, for dp, three key variables, working pressure, mill fan speed, and feed rate, were identified in order of significance, aligning with the operational principles under a CL approach. SHAP data also revealed that working pressure, a shared variable for predicting both feed rate and dp, had the most significant impact, establishing it as one of the critical operational parameters in VRM. This parameter is crucial in regulating mill feed rate and affects the mill's dp. Model evaluation via validation tests demonstrated the algorithms' stable performance and high generalization capacity. Among the models, LightGBM exhibited the highest R^2 value, equal to 0.98 and 0.97 for feed rate and dp prediction, respectively, and the lowest RMSE, equal to 1.34 and 0.16, positioning it as the best choice for predicting feed rate and dp. Overall, using the CL approach combined with machine learning algorithms demonstrated high-quality modeling in identifying complex relationships among operational variables, paving new paths for sustainable control and optimizing VRM performance in the cement industry.

Acknowledgments

References

Altun, D. (2017). Mathematical modelling of vertical roller mills.

Altun, D., Benzer, H., Aydogan, N., & Gerold, C. (2017). Operational parameters affecting the vertical roller mill performance. *Minerals Engineering*, *103*, 67-71.

Altun, D., Gerold, C., Benzer, H., Altun, O., & Aydogan, N. (2015). Copper ore grinding in a mobile vertical roller mill pilot plant. *International Journal of Mineral Processing*, *136*, 32-36.

Authenrieth, M., Hyttrek, T., Reintke, A., & McGarel, S. (2012). ILM-master for VRMs. *Int. Cement Rev.*

Barani, K., Azadi, M., & Fatahi, R. (2022). An approach to measuring and modelling the residence time distribution of cement clinker in vertical roller mills. *Mineral Processing and Extractive Metallurgy*, *131*(2), 158-165.

Belmajdoub, F., & Abderafi, S. (2023). Efficient machine learning model to predict fineness, in a vertical raw meal of Morocco cement plant. *Results in Engineering*, *17*, 100833.

Breiman, L. (1996). Bagging predictors. *Machine learning*, *24*, 123-140.

Bussmann, N., Giudici, P., Marinelli, D., & Papenbrock, J. (2021). Explainable machine learning in credit risk management. *Computational Economics*, *57*(1), 203-216.

Chelgani, S. C., Homafar, A., & Nasiri, H. (2024). CatBoost-SHAP for modeling industrial operational flotation variables–A "conscious lab" approach. *Minerals Engineering*, *213*, 108754.

Chelgani, S. C., Nasiri, H., & Tohry, A. (2021). Modeling of particle sizes for industrial HPGR products by a unique explainable AI tool-A "Conscious Lab" development. *Advanced Powder Technology*, *32*(11), 4141-4148.

Chelgani, S. C., Nasiri, H., Tohry, A., & Heidari, H. R. (2023). Modeling industrial hydrocyclone operational variables by SHAP-CatBoost-A "conscious lab" approach. *Powder technology*, *420*, 118416.

Fahrland, T., & Zysk, K. (2013). Cements ground in the vertical roller mill fulfil the quality requirements of the market. *Cement International*, *11*(2), 64-69.

Fatahi, R., Abdollahi, H., Noaparast, M., & Hadizadeh, M. (2025). Modeling the working pressure of a cement vertical roller mill using SHAP-XGBoost: A "conscious lab of grinding principle" approach. *Powder technology*, 120923.

Fatahi, R., Khosravi, R., Siavoshi, H., Yazdani, S., Hadavandi, E., & Chehreh Chelgani, S. (2021). Ventilation prediction for an industrial cement raw ball mill by bnn — a "conscious lab" approach. *Materials*, *14*(12), 3220.

Fatahi, R., Nasiri, H., Dadfar, E., & Chehreh Chelgani, S. (2022). Modeling of energy consumption factors for an industrial cement vertical roller mill by SHAP-XGBoost: a" conscious lab" approach. *Scientific Reports*, *12*(1), 7543.

Fatahi, R., Nasiri, H., Homafar, A., Khosravi, R., Siavoshi, H., & Chehreh Chelgani, S. (2023). Modeling operational cement rotary kiln variables with explainable artificial intelligence methods–a "conscious lab" development. *Particulate Science and Technology*, *41*(5), 715-724.

Fatahi, R., Pournazari, A., & Shah, M. P. (2022). A cement Vertical Roller Mill modeling based on the number of breakages. *Advanced Powder Technology*, *33*(10), 103750.

Fedoryshyn, R., Nykolyn, H., Zagraj, V., & Pistun, Y. (2012). The improved system for automation and optimization of solid material grinding by means of ball mills. Annals of DAAAM for 2012 & Proceedings of the 23rd International DAAAM Symposium,

Friedman, J. H. (2001). Greedy function approximation: a gradient boosting machine. *Annals of statistics*, 1189-1232.

Fujimoto, S. (1993). Reducing specific power usage in cement plants. *World Cement;(United Kingdom)*, *24*(7).

Gong, H., Sun, Y., Shu, X., & Huang, B. (2018). Use of random forests regression for predicting IRI of asphalt pavements. *Construction and Building Materials*, *189*, 890-897.

Harder, J. (2010). Grinding trends in the cement industry. *ZKG INTERNATIONAL*, *63*(4), 46-+.

Hu, H., Li, Y., Lu, Y., Li, Y., Song, G., & Wang, X. (2024). Numerical Study of Flow Field and Particle Motion Characteristics on Raw Coal Vertical Roller Mill Circuits. *Minerals Engineering*, *218*, 108997.

Ke, G., Meng, Q., Finley, T., Wang, T., Chen, W., Ma, W., Ye, Q., & Liu, T.-Y. (2017). Lightgbm: A highly efficient gradient boosting decision tree. *Advances in neural information processing systems*, *30*.

Li, B., Chen, G., Si, Y., Zhou, X., Li, P., Li, P., & Fadiji, T. (2022). GNSS/INS integration based on machine learning LightGBM model for vehicle navigation. *Applied sciences*, *12*(11), 5565.

Lin, X.-F., & Zhang, M.-Q. (2016). Modelling of the vertical raw cement mill grinding process based on the echo state network. 2016 12th World Congress on Intelligent Control and Automation (WCICA),

Little, W. (2021). Performance of the vertical roller mill in a mineral processing application when coupled with internal and external classifiers.

Liu, C., Chen, Z., Zhang, W., Yang, C., Mao, Y., Yu, Y., & Xie, Q. (2020). Effects of blade parameters on the flow field and classification performance of the vertical roller mill via numerical investigations. *Mathematical Problems in Engineering*, *2020*(1), 3290694.

Liu, H., Xiao, Q., Jin, Y., Mu, Y., Meng, J., Zhang, T., Jia, H., & Teodorescu, R. (2022). Improved LightGBM-based framework for electric vehicle lithium-ion battery remaining useful life prediction using multi health indicators. *Symmetry*, *14*(8), 1584.

Lundberg, S. M., & Lee, S.-I. (2017). A unified approach to interpreting model predictions. *Advances in neural information processing systems*, *30*.

Mangalathu, S., Shin, H., Choi, E., & Jeon, J.-S. (2021). Explainable machine learning models for punching shear strength estimation of flat slabs without transverse reinforcement. *Journal of Building Engineering*, *39*, 102300.

Mao, H., Deng, X., Jiang, H., Shi, L., Li, H., Tuo, L., Shi, D., & Guo, F. (2021). Driving safety assessment for ride-hailing drivers. *Accident Analysis & Prevention*, *149*, 105574.

Matin, S., Hower, J. C., Farahzadi, L., & Chelgani, S. C. (2016). Explaining relationships among various coal analyses with coal grindability index by Random Forest. *International Journal of Mineral Processing*, *155*, 140-146.

Meng, Q., Wang, Y., Xu, F., & Shi, X. (2015). Control strategy of cement mill based on bang-bang and fuzzy PID self-tuning. 2015 IEEE International Conference on Cyber Technology in Automation, Control, and Intelligent Systems (CYBER),

Ouallouche, F., Lazri, M., & Ameur, S. (2018). Improvement of rainfall estimation from MSG data using Random Forests classification and regression. *Atmospheric Research*, *211*, 62-72.

Pareek, P., & Sankhla, V. S. (2021). Increase productivity of vertical roller mill using seven QC tools. IOP Conference Series: Materials Science and Engineering,

Sahasrabudhe, R., Sistu, P., Sardar, G., & Gopinath, R. (2006). Control and optimization in cement plants. *IEEE Control Systems Magazine*, *26*(6), 56-63.

Schaefer, H. (2001). Loesche vertical roller mills for the comminution of ores and minerals. *Minerals Engineering*, *14*(10), 1155-1160.

Stanišić, D., Jorgovanović, N., Popov, N., & Čongradac, V. (2015). Soft sensor for real-time cement fineness estimation. *ISA transactions*, *55*, 250-259.

Wager, S., & Athey, S. (2018). Estimation and inference of heterogeneous treatment effects using random forests. *Journal of the American Statistical Association*, *113*(523), 1228-1242.

Worrell, E., Martin, N., & Price, L. (2000). Potentials for energy efficiency improvement in the US cement industry. *Energy*, *25*(12), 1189-1214.

Xu, B., & Sun, Y. (2020). On fault feature extraction and diagnosis of vertical mill. *Engineering Research Express*, *2*(4), 045006.

Yan-yan, N., Guang, Z., Ming-zhe, Y., & Zhuo, W. (2011). Design of intelligent control system for Vertical Roller Mill. 2011 2nd International Conference on Intelligent Control and Information Processing,

Zhu, M., Ji, Y., Zhang, Z., & Sun, Y. (2020). A data-driven decision-making framework for online control of vertical roller mill. *Computers & Industrial Engineering, 143*, 106441.

Application and limitations of element to mineral conversion to predict modal mineralogy: case study tailings of iron processing plant

Fatemeh Kazemi[1]*, Ali Akbar Abdollahzadeh[2]

[1]PhD of Mineral Processing, Department of Mining Engineering, Faculty of Engineering, University of Kurdistan, Sanandaj, Iran

[2]Associate Professor, Faculty of Mining Engineering, Amirkabir University of Technology, Tehran, Iran

*Corresponding author: fa.kazemi@uok.ac.ir (Fatemeh Kazemi)

Abstract:

Quantifying modal mineralogy is increasingly important in modern mining as mines exploit lower-grade and more complex ore deposits. The modal mineralogy of a deposit, which influences metal liberation, extraction, and concentration, is governed by the varying processing behaviors of different minerals. Element-to-mineral conversion (EMC) was used in this study to determine the modal mineralogy of iron processing plant tailings. The EMC approach involves measuring the bulk rock or mineral chemistry and textural properties of tailing piles. X-ray fluorescence determined chemical composition, while X-ray diffraction and light and electron microscopy determined mineralogy and texture. A framework has been developed to guide the decision-making process when applying the EMC approach for modal mineralogy quantification. Due to the imbalance between the number of minerals identified in mineralogical studies and the compositions measured in chemical analysis, the mineral grouping strategy has been used to determine the mineralogical modal. Based on EMC outputs, iron oxides, including magnetite and hematite and copper sulfide minerals are valuable minerals that can be extracted from the tailings. The highest magnetite grade is associated with the size fraction of -250 +106 microns (26%). The primary gangue minerals in the tailings are the diopside/calcite with an average grade of 35% and the garnet/quartz with an average grade of 26%, while pyrite and chalcopyrite are identified as minor minerals.

Keywords: Mineralogy studies, Ore texture, Chemical analysis, Grade of mineral, Magnetite

1. Introduction

The grade of ore deposits, irrespective of deposit type, has been steadily decreasing over the past century (Kazemi and Abdollahzadeh, 2024). In recent decades, active mines have been forced to mine lower-grade and mineralogically more complex parts of existing ore deposits (Norgate and Jahanshahi, 2010; Gordon et al., 2018), which have sufficiently low ore grades to challenge the financial viability of the mining activities. This introduces higher degrees of risk in the modern mining industry as a result of high ore variability due to increasing textural and mineralogical complexities. This situation has been exacerbated by the large production volumes required due to increased metal demand as well as stricter environmental regulations (Lishchuk and Pettersson, 2020). As a direct consequence, the importance of modal mineralogy quantification has increased, since the modal mineralogy of a deposit has a direct impact on the liberation, extraction and concentration of the valuable metals (Parian et al., 2015; Xie et al., 2021; Chen et al., 2017; Dehaine et al., 2021). This is particularly important for complex heterogeneous deposits where the valuable metal grade is not uniformly distributed throughout the deposit. The modal mineralogy of all minerals, including valuable and gangue minerals, needs to be known to ensure efficient ore processing (Dehaine et al., 2021; Parian et al., 2015; Schouwstra et al., 2013).

Historically, modal mineralogy was determined by optical microscopy and point counting (Gottlieb et al., 2000; Lund et al., 2013). However, this methodology is time consuming and the quality of the results is highly dependent on the skill of the mineralogist (Petruk, 2000). Mineral identification by optical microscopy relies on the interpretation by the mineralogist of the transmitted and reflected light behaviour of a mineral, an interpretation that could be very subjective depending on the skill of the mineralogist. Additionally, ore bodies can be highly complex, and manual mineralogy techniques cannot adequately quantify the mineralogical and textural variability of such ore deposits statistically robustly (Gottlieb et al., 2000). Furthermore, the use of optical microscopy and point counting to determine modal mineralogy is challenging, for example, in very fine-grained samples (Pirrie et al., 2011). The advent of improved analytical techniques for mineralogical analysis, particularly those that are automated, has significantly improved our ability to properly characterize the mineralogy of any ore deposit. These analytical developments fall into two instrument categories (both using x-ray analysis): those based on scanning electron microscopy (SEM) and those based on X-ray diffraction (XRD). Electron microprobes were historically used to determine accurate mineral compositions but were time consuming, expensive instruments that required a skilled operator. In recent decades, scanning electron microscopes have undergone significant improvements (particularly in their image optics), which has allowed the mineral identification and quantification process to be automated when combined with energy dispersive spectroscopy (EDS). Examples of automated mineralogy techniques based on SEM include QEMSCAN (Quantitative Evaluation of Minerals by Scanning Electron Microscopy) and MLA (Mineral Liberation Analyzer). These technologies identify minerals and quantify mineral proportions by scanning a sample in backscattered electron mode, measuring the EDS spectra, and comparing the measured EDS spectra with a database of minerals with known EDS spectra (Pirrie et al., 2011). Specific mineral compositions correspond with specific EDS spectra. Techniques of modal mineralogy characterization based on X-ray diffraction (XRD) work by measuring the X-ray diffraction pattern produced by X-rays interacting with the crystalline structure of a mineral. Mineral identification is done through comparison of the measured XRD pattern to a reference database of minerals with known XRD patterns. Characterization of mineralogy by XRD can either be qualitative (i.e, identification), semi-quantitative, or quantitative (Hupp et al., 2018). Thus, mineralogy characterization technologies based on SEM identify minerals using known mineral compositions, while mineralogy characterization technologies based on XRD identify minerals based on known mineral structures.

Element-to-mineral conversion (EMC) is a possible alternative approach to these analytical techniques for modal mineralogy determination. The EMC approach calculates modal mineral proportions by converting chemical assays to mineral proportions (Whiten, 2008). This conversion is feasible through the use of known mineral compositions applicable to the minerals to be calculated. The application and development of EMC as an alternative method is driven by gaining access to modal mineralogy at lower costs and earlier stages of the mining project (Mena Silva et al., 2018). Despite this, and being a known technique for decades, it is underused and very rarely applied in mining operations (Lund et al., 2013). This may be due to EMC's limitation to deposits with simple mineralogy, as the number of elements analyzed limits the number of minerals to be calculated (Parian et al., 2015). However, no definition of what characterizes an ore with "simple mineralogy" in the context of the EMC approach exists in the literature. Since the number of elements limits the number of minerals that can be calculated, minerals that have the same assigned element have been grouped to perform EMC on deposits where the number of minerals exceeds the number of elements (Lund et al., 2013; Ntlhabane et al., 2018). However, grouping minerals decreases the resolution of the modal mineralogy information produced. Another limitation of the EMC approach is that very few guidelines exist in the literature to aid the application of the EMC approach and this may also be a contributor to its under usage in the mining industry. The absence of these guidelines makes the application of the EMC approach a tedious process based on trial and error.

Although automated mineralogy provides faster quantitative analysis of mineral grades, there are limitations associated with its application (Moen, 2006; Lund et al., 2013). Some of these limitations result in difficulties with the identification of certain minerals (Lund et al., 2013), e.g, differentiating

between hematite and magnetite, minerals with almost identical chemical compositions and consequently similar grey levels (Moen, 2006; Gomes and Paciornik, 2012). Additionally, resolution becomes problematic in very fine-grained samples as the electron beam diameter approaches that of individual grains (Fandrich et al., 2007). Since EMC is based on the measured bulk chemistry and mineral chemistry, it may be advantageous in the quantification of the modal mineralogy of fine-grained samples. Although advances in X-ray-based automated mineralogy techniques such as XRD have allowed for the improvement of mineral proportion quantification, its accuracy is affected by factors such as crystallinity, preferred orientation of mineral phases and crystal size (Lund et al., 2013). XRD-based techniques also have less accurate detection limits than SEM-based techniques. Furthermore, the application of automated mineralogy requires extensive sample preparation and data processing, both of which can be time-consuming processes (Parian et al., 2015). For example, the initial automated dataset by QEMSCAN will include a very large number of categories of mineral compositional groupings, which then have to be validated, combined, or subdivided based on the required outputs of the individual mining project (Pirrie et al., 2011). Thus, there exists a need for a method to determine mineral grades that is relatively fast, cost effective and statistically reliable. The present study aims to determine the mineralogical modal of iron ore tailings using the EMC method. Considering the presence of various iron-containing minerals, including hematite and magnetite, in iron processing tailings, the use of the EMC approach is more efficient for determining their mineralogical modal composition.

2. Materials and methods

The study investigated tailings piles from lump iron ore processing plants in western Iran. These tailings result from low-intensity dry magnetic separation of magnetite iron ore. Sampling was conducted from various sections of the tailing piles, determined by their distribution over different production periods. With roughly one million tons of tailings, over 20 samples were extracted by digging trenches across different areas. Each trench provided approximately a 500 kg sample. These samples were then consolidated and thoroughly mixed in a designated area. Ultimately, a representative sample weighing around 500 kg was selected for further analysis. The sample with d_{80} = 6.5 mm (Figure 1) was crushed to <2 mm using a roll crusher. The crushed material was then sieved into the following size fractions: -2 +1, -1 +0.500, -0.500 +0.250, -0.250 +0.106, -0.106 +0.045, and -0.045 mm, to determine the mineralogical modal composition of the iron tailing piles.
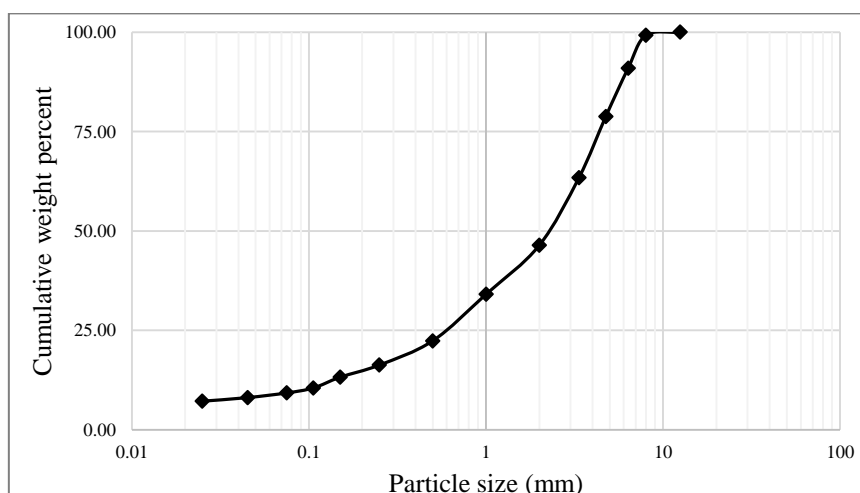
Fig. 1. Particle size distribution curve of iron tailing sample

2.1. Analysis and studies

Texture characteristics were determined using X-ray fluorescence, potentiometric titration (Redox), X-ray diffraction, optical image analysis (OIA), and scanning electron microscopy (SEM). Each size fraction was analyzed using XRD, XRF, OIA, and SEM. The resulting data provided insights such as the types and volume percentages of minerals, texture diversity, association indicators, mineral classification, alterations, hardness, size distribution of both valuable minerals and gangue, degree of liberation, and chemical composition. This information was crucial for calculating quantitative details and determining mineralogical modals.

The Zeiss SM-LUX-POL reflective polarizing microscope was employed for optical microscopy studies. To assess texture characteristics, three standard polished sections were prepared for each size fraction, with the mineral compositions meticulously evaluated through ore microscopy. Each section was examined at a magnification of 200X, resulting in the preparation of approximately 60 digital microscopic images. Since each image captures at least 80 particles, between 4800 and 5000 particles were counted per sample. Mineral characteristics were analyzed using ImageJ software (version 1.8.0_172). A grid pattern was applied to each corresponding image, and the count tool was used to determine the point count and volume of liberated and locked mineral grains. Finally, all data were transferred to Excel for calculating the average degree of liberation from different images. (Kazemi and Abdollahzadeh, 2024). To calculate the volume percentage of each mineral, multiple sections of each size fraction were analyzed. The average area of the mineral was measured across these sections. Assuming a constant and negligible third dimension, this area measurement represents the volume percentage of the mineral.

2.2. Element to mineral conversion

A straightforward method to estimate mineral grades is the Element-to-Mineral Conversion (EMC), which simultaneously solves a set of mass balance equations involving chemical elements and minerals. Chemical mass balance techniques rely on the principle that a rock's bulk chemistry is the sum of its minerals' chemistry weighted by their proportions (modal mineralogy).

To mineralogical modal determination, element-to-mineral conversion offers a potential alternative to analytical techniques (XRD and SEM). This study uses analysis and microscopy as reference data for each size fraction to determine mineralogical modal using the EMC method. The reference modal data or mineralogical studies data were prepared as follows:

1. XRF and titration data, initially in oxide form, were converted to elemental weight percentages.
2. Minerals identified through microscopy were grouped based on shared elements to meet the requirements of the EMC method, which necessitates that the number of chemical compounds equals the number of identified minerals.
3. Each mineral group was assigned a representative element.
4. The chemical composition of a representative mineral was assigned to its corresponding mineral group.

.

EMC has been semi-automated by the thermochemical software package, HSC Chemistry, created by Outotec. HSC Chemistry has an extensive mineral database and calculation modules for minerals processing and particle calculation. EMC is performed using HSC Chemistry's *Geo Module*, which was developed in 2006. The user has to manually input the bulk chemical assays and mineral chemistries of the deposit into the software and specify the EMC calculation routine. An appropriately formatted file of the bulk chemical assays can also be uploaded onto the software. Setting up an EMC routine

involves specifying the number of calculation rounds, the minerals calculated in each round, the elements assigned to minerals for calculation, and the specification of the estimation method to be used for the calculation round. The EMC routine refers to the order in which the mineral proportions will be quantified. The chemical analysis data for each size fraction and the mineral composition of the iron tailing piles were manually entered into the software. EMC calculations were then performed using linear least squares (LLS) and non-negative least squares (NNLS) estimations.

3. Results and discussion

To apply the EMC approach for modal mineralogy quantification, input data in the form of whole rock compositions and mineral chemistry data are required. XRF analysis results (Table 1) were converted to weight values for oxide compounds in each size fraction (Table 2).

Table 1. XRF analysis in each size fraction

Size fraction (mm)	SiO_2 (%)	Al_2O_3 (%)	CaO (%)	Fe (T) (%)	FeO (%)	K_2O (%)	MgO (%)	S (%)	Cu (%)
-2 +1	37.53	8.38	20.22	15.66	5.37	0.74	4.17	0.46	0.11
-1 +0.5	36.65	8.97	18.59	16.34	5.60	0.75	4.19	0.58	0.14
-0.5 +0.25	33.90	7.84	19.33	18.66	6.40	0.59	3.76	0.82	0.19
-0.25 +0.106	32.13	7.02	17.10	22.48	7.70	0.46	4.73	0.51	0.21
-0.106 +0.045	33.61	8.66	19.96	15.47	5.29	0.59	2.60	0.51	0.22
-0.045	31.26	6.98	18.90	25.03	8.58	0.65	5.89	0.31	0.25

Table 2. Weight percentage of elements in each size fraction of iron tailings

Size fraction (mm)	Si (%)	Al (%)	Ca (%)	Fe (%)	K (%)	Mg (%)	S (%)	Cu (%)
-2 +1	17.49	4.65	14.44	15.66	0.61	2.51	0.46	0.11
-1 +0.5	17.08	4.98	13.27	16.34	0.62	2.53	0.58	0.14
-0.5 +0.25	15.80	4.35	13.80	18.66	0.49	2.27	0.82	0.19
-0.25 +0.106	14.97	3.90	12.21	22.48	0.38	2.85	0.51	0.21
-0.106 +0.045	15.66	4.81	14.25	15.47	0.49	1.57	0.51	0.22
-0.045	14.57	3.87	13.49	25.03	0.54	3.55	0.31	0.25

Tailing piles are predominantly composed of non-metallic minerals (silicates and non-silicates) with a minor metallic mineral component, according to OIA and SEM analysis. The diverse non-metallic minerals include pyroxene, calcite, garnet, epidote, tremolite-actinolite amphibole, quartz, sphene, chlorite, and trace amounts of biotite, feldspar, and apatite. Metallic minerals are primarily oxides, with fewer sulfides. The volumetric percentage of magnetite and hematite, the main iron oxides, varies with particle size. Iron oxide content initially increases with decreasing particle size down to 45 microns, then decreases (Figure 2). Coarse fractions exhibit interlocks between iron oxides (mainly magnetite) and silicate/carbonate minerals, with gangue inclusions within iron oxides. Oxide mineral liberation increases with decreasing particle size, exceeding 85% in fractions smaller than 106 microns (Figure 2).
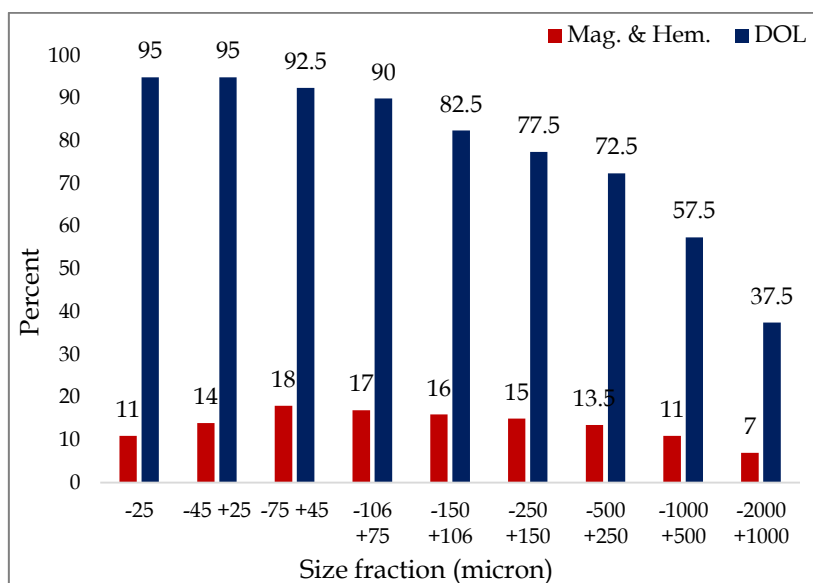
Fig. 2. Volumetric percentage and liberation degree of iron oxides in different size fractions of the tailings of lump iron ore processing plant

The most widely known and cited constraint of the EMC approach is that the number of elements limits the number of minerals that can be calculated. This constraint necessitates proper preliminary data preparation to enable the successful application of the EMC approach for any particular deposit. Preliminary input data preparation involves three main steps: the simplification of the mineral list, the assignment of elements for the calculation of minerals, and the assignment of mineral chemistry where minerals have been grouped. XRF analysis of each size fraction yielded values for 8 major oxide compounds (other compounds were below the 0.05% detection limit), while mineral identification in some fractions reached 20. To satisfy the EMC method's requirement for equal numbers of chemical compounds and identified minerals, minerals were grouped. Previous studies have employed three grouping approaches: common element (Lund et al., 2013), mineral group classification (e.g., grouping garnet and pyroxmangite as Manganese silicates), and shared chemical characteristics (e.g., pyrite and pyrrhotite sharing Fe and S) (Ntlhabane et al., 2018).

In this study, the grouping of minerals is based on their common element. The approach used in this study to determine the eligibility of a mineral set forms part of the Mineral Chemistry Designation Approach (MCDA) and involves the calculation of the standard deviation and average concentration of the assigned element for a mineral set. This method addresses the situation where a single element is the most suitable identifier for multiple minerals. This group of minerals, linked by a shared elemental designation conflict, constitutes a primary mineral set. For each mineral, the mass value of the designated element is then calculated based on its chemical formula. In the previous studies of the EMC method (Mena Silva et al., 2018; Parian, 2015; Cupido, 2021), the average and standard deviation of the element in each mineral group are calculated. If the difference between a mineral's element quantity and the average value is less than the standard deviation, the mineral stays in its group (Cupido, 2021). This method's key limitation is its failure to consider mineral weight within each size fraction. Furthermore, it struggles with two-mineral groups because elemental differences relative to the average are identical for both minerals, hindering accurate mineral identification. To address these shortcomings, this study incorporates mineral weight percentages within each size fraction. Specifically, volumetric percentages from microscopic analyses were converted to weight percentages using mineral-specific gravities (Table 3). Elemental content was then weighted by the corresponding mineral's weight percentage in each size fraction to determine elemental contribution per volume.

Next, weighted averages and standard deviations were calculated for each group. The difference between the element's abundance (element × weight) and the average weight of minerals was then

141

determined. If the absolute difference for a mineral or composition exceeded the standard deviation, it was considered a dominant phase of the element; otherwise, it was removed from the group and its elemental values were re-evaluated. Grouping minerals by weight percentage also identifies a representative mineral for each group, chosen based on the maximum weight percentage multiplied by elemental content. For example, Table 3 illustrates this process for Fe minerals in the -2 +1 mm size fraction. This methodology was applied to all minerals and elements in the iron tailings to identify representative minerals for each group. In the -2 +1 mm fraction, magnetite represents Fe-containing minerals, pyrite for S, chalcopyrite for Cu, diopside for Ca, chlorite for Al, biotite for Mn, feldspar for K, garnet for Si, and rutile for Ti. In Table 4, the representative minerals of each group are stated in different size fractions.

$$\bar{X}\,(element) = \frac{\sum V_i m_i}{\sum V_i} \tag{1}$$

$$\sigma = \sqrt{\frac{\sum m_i\,(x_i - \bar{x})}{\sum m_i}} \tag{2}$$

Table 3. Grouping for mineral set formation and mineral chemistry determination (size fraction: -2 +1 mm).

Minerals	Formula	Fe in mineral (%)	Volume (%)	S.G	Weight (%)	Weight * Fe (%)	Abs (W.Fe-Ave.)
Magnetite	Fe_3O_4	72.36	5.90	5.20	30.68	2220.00	1719.45
Hematite	Fe_2O_3	69.94	1.00	5.26	5.26	367.88	132.67
Geothite	$FeOOH$	62.86	0.05	4.30	0.22	13.51	487.04
Limonite	$FeOOH.nH_2O$	52.26	0.05	3.65	0.18	9.54	491.02
Pyrite	FeS_2	46.59	0.80	5.02	4.02	187.11	313.45
Chalcopyrite	$CuFeS_2$	30.48	0.80	4.25	3.40	103.63	396.92
Pyrrhotite	$Fe_{(1-x)}S$	63.57	0.10	4.00	0.40	25.43	475.13
Garnet	$Ca_3Fe_2(SiO_4)_3$	22.00	11.80	4.15	48.97	1077.34	576.78
Average			20.50		93.12	500.56	
Standard deviation						1077.94	

The HSC Chemistry-Geo module V.9.1 was used to solve a set of linear equations based on chemical analysis and mineral composition data (Table 4) for each size fraction, following user-specified parameters in the EMC routine. Two estimation methods were employed: Least Squares (LS) initially, and Non-Negative Least Squares (NNLS) when LS resulted in negative mineral proportions. The HSC Chemistry 100-sum tool was applied in the final EMC round for mineral proportions unresolved by elemental assignment. Figure 3 illustrates the EMC results, revealing that magnetite grade increases with decreasing particle size, peaking at 26% in the -250 +106 micron fraction and reaching its lowest grade in the coarse (+2 mm) fractions. The grade of chalcopyrite (representing chalcopyrite, covellite, and chalcocite) remains relatively constant across different size fractions (0.10% to 0.13%), with a maximum of 0.13% also observed in the -250 +106 micron fraction. Thus, both magnetite and chalcopyrite exhibit their highest grades in the -250 +106 micron size fraction.

Table 4. Represented minerals in different size fractions of iron tailings

Size (mm)	Si	Al	Ca	Fe	K	Mg	S	Cu	Ru
-2 +1	Garnet	Chlorite	Diopside	Magnetite	Feldspar	Biotite	Pyrite	Chalcopyrite	Rutile
-1 +0.5	Garnet	Chlorite	Diopside	Magnetite	Feldspar	Biotite	Pyrite	Chalcopyrite	Muscovite
-0.5 +0.25	Garnet	Chlorite	Diopside	Magnetite	Feldspar	Biotite	Pyrite	Chalcopyrite	-
-0.25 +0.106	Garnet	Chlorite	Diopside	Magnetite	Feldspar	Biotite	Pyrite	Chalcopyrite	Muscovite
-0.106 +0.045	Quartz	Chlorite	Diopside	Magnetite	Feldspar	Biotite	Pyrite	Chalcopyrite	Rutile
-0.045	Quartz	Chlorite	Calcite	Magnetite	Feldspar	Biotite	Pyrite	Chalcopyrite	-

The grade of calcite and diopside minerals (diopside group) is more than 34% in all size fractions. The grade of these minerals has increased with an increase in the particle size. The highest grade

, 38%, is in size fraction -500 +250 microns and is related to the diopside mineral. The group of quartz/garnet is the second major gangue mineral. In this group, the grade of minerals with the decrease in particle size has been increasing, and the highest grade of them is 27.14% related to the size fraction of -45 microns. The grade of chlorite increases with the increase in particle size. The highest grade calculated for chlorite is 8.94% in the -2 +1 mm size fraction. The grade variation of biotite and feldspar minerals is similar to the chlorite grade changes.
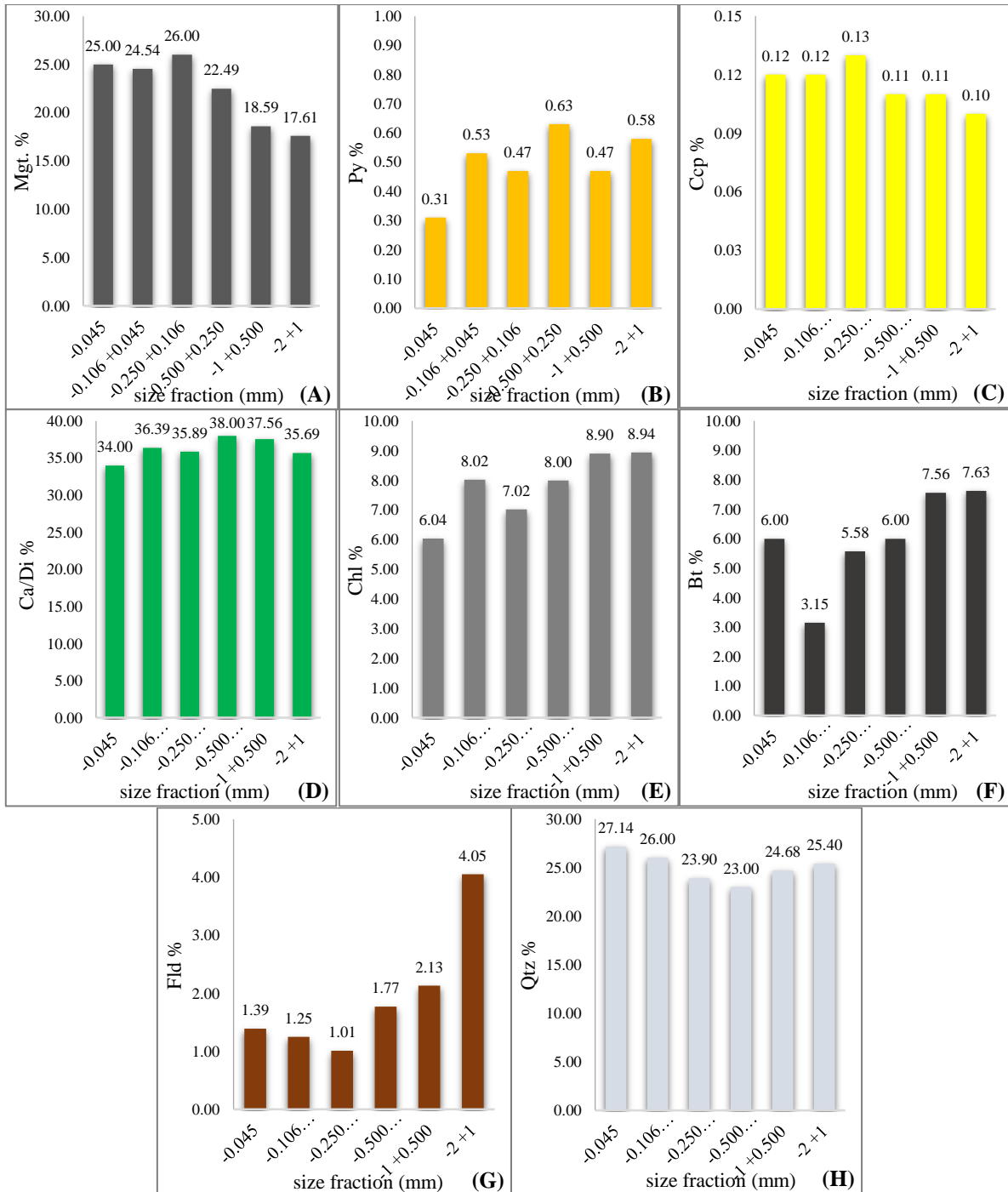
Fig. 3. Grade of A) Magnetite, B) Pyrite, C) Chalcopyrite, D) Diopside/Calcite, E) Chlorite, F) Biotite, G) Feldspar, H) Quartz, in each size fraction calculated by EMC method

4. Conclusions

The results of this study show that the element to mineral conversion (EMC) approach may serve as an alternative technique to determine the modal mineralogy of a deposit or resource. EMC may be valuable in the ore characterization stage, where not as much detail on individual mineral proportions is necessary to subdivide a deposit into ore types. The application of the EMC approach was not limited by the type of deposit, but rather whether or not all the minerals of a deposit could be assigned an element for calculation. Where a single element is deemed the most appropriate designation for multiple minerals, these minerals can be grouped. To increase the accuracy and detail produced by the EMC approach, the measured bulk chemistry can be supplemented by selective dissolution methodologies. The utilization of selective dissolution methodologies can be used to increase the number of components of a single element and thus increase the number of individual mineral proportions that can be calculated by EMC.

Using the element-to-mineral conversion method to determine the mineralogical modal of the tailings of the iron processing plant indicates that the majority of magnetite minerals stand in the -250 micron size range. The grades of main gangue minerals, calcite/diopside and quartz/garnet, have also increased with decreasing particle size. The most interlocked has been between the two iron oxide minerals magnetite and hematite, which is caused by the martitization of magnetite to hematite. This interlock is considered favorable from the point of view of magnetic separation and will lead to the recovery of hematite mineral to concentrate in low-intensity separators. In all size fractions, the major interlock of magnetite is with calcite/diopside phases, followed by the garnet/quartz phase.

References

Chen, W., Feng, Q., Zhang, G., Yang, Q., Zhang, C., & Xu, F. (2017). The flotation separation of scheelite from calcite and fluorite using dextran sulfate sodium as depressant. *International Journal of Mineral Processing*, *169*, pp.53-59. https://doi.org/10.1016/j.minpro.2017.10.005

Cupido I. (2021). Evaluating the application and limitations of element to mineral conversion to predict modal mineralogy: the development of a framework for its application. Doctoral dissertation, Stellenbosch: Stellenbosch University.

Dehaine, Q., Tijsseling, L.T., Glass, H.J., Törmänen, T., & Butcher, A.R. (2021). Geometallurgy of cobalt ores: A review. *Minerals Engineering*, *160*, p.106656. https://doi.org/10.1016/j.mineng.2020.106656

Fandrich, R., Gu, Y., Burrows, D., & Moeller, K. (2007). Modern SEM-based mineral liberation analysis. *International Journal of Mineral Processing*, *84*(1-4), pp.310-320. https://doi.org/10.1016/j.minpro.2006.07.018

Gomes, O.D.F.M., & Paciornik, S. (2012). Multimodal microscopy for ore characterization. In *Scanning Electron Microscopy*. In tech. Open.

Gordon, H.J.J., Miller, J.A., & Becker, M. (2018). Using Mineralogy for Early Stage Geometallurgical Domain Definition: a Case Study of the Swartberg Polymetallic Sulphide Deposit. *Proceedings of Geometallurgy 2018*, (August), pp.121–132.

Gottlieb, P., Wilkie, G., Sutherland, D., Ho-Tun, E., Suthers, S., Perera, K., Jenkins, B., Spencer, S., Butcher, A., & Rayner, J. (2000). Using quantitative electron microscopy for process mineralogy applications. *Jom*, *52*(4), pp.24-25. https://doi.org/10.1007/s11837-000-0126-9

Hupp, B.N., & Donovan, J.J. (2018). Quantitative mineralogy for facies definition in the Marcellus Shale (Appalachian Basin, USA) using XRD-XRF integration. *Sedimentary Geology*, *371*, pp.16-31. https://doi.org/10.1016/j.sedgeo.2018.04.007

Kazemi, F., & Abdollahzadeh, A.A. (2024). Valorisation of iron ore tailing piles: utilisation of element-to-mineral conversion and association index to building mineralogical modal. *Canadian Metallurgical Quarterly*, pp.1-14. https://doi.org/10.1080/00084433.2024.2306044

Lishchuk, V., & Pettersson, M. (2021). The mechanisms of decision-making when applying geometallurgical approach to the mining industry. *Mineral Economics*. 34, pp.71-80. https://doi.org/10.1007/s13563-020-00220-9

Lund, C., Lamberg, P., & Lindberg, T. (2013). Practical way to quantify minerals from chemical assays at Malmberget iron ore operations–An important tool for the geometallurgical program. *Minerals Engineering*, *49*, pp.7-16. https://doi.org/10.1016/j.mineng.2013.04.005

Mena Silva, C., Sørensen, B.E., Aasly, K., & Ellefmo, S.L. (2018). Geometallurgical approach to the element-to-mineral conversion for the Nabbaren nepheline syenite deposit. *Minerals*, *8*(8), p.325. https://doi.org/10.3390/min8080325

Moen, K. (2006). Quantitative Measurements of Mineral Microstructures: Development, implementation and use of methods in applied mineralogy. http://hdl.handle.net/11250/235833

Norgate, T., & Jahanshahi, S. (2011). Assessing the energy and greenhouse gas footprints of nickel laterite processing. *Minerals Engineering*. Elsevier Ltd, 24(7), pp.698–707. https://doi.org/10.1016/j.mineng.2010.10.002

Ntlhabane, S., Becker, M., Charikinya, E., Voigt, M., Schouwstra, R., & Bradshaw, D. (2018). Towards the development of an integrated modelling framework underpinned by mineralogy. *Minerals Engineering*, *116*, pp.123-131. https://doi.org/10.1016/j.mineng.2017.09.013

Parian, M., Lamberg, P., Möckel, R., & Rosenkranz, J. (2015). Analysis of mineral grades for geometallurgy: Combined element-to-mineral conversion and quantitative X-ray diffraction. Minerals Engineering. 15, pp: 82:25-35. https://doi.org/10.1016/j.mineng.2015.04.023

Petruk, W. (2000). *Applied mineralogy in the mining industry*. Elsevier

Pirrie, D., & Rollinson, G.K. (2011). Unlocking the applications of automated mineral analysis. *Geology Today*, *27*(6), pp.226-235. https://doi.org/10.1111/j.1365-2451.2011.00818.x

Schouwstra, R., De Vaux, D., Muzondo, T., & Prins, C. (2013). September. A geometallurgical approach at Anglo American Platinum's Mogalakwena operation. In *The Second AUSIMM International Geometallurgy Conference/Brisbane, QLD* (Vol. 30, pp. 85-92).

Whiten, B. (2008). Calculation of mineral composition from chemical assays. *Mineral Processing and Extractive Metallurgy Review*, 29(2), pp. 83–97. https://doi.org/10.1080/08827500701257860

Xie, H., Liu, Y., Rao, B., Gao, L., Chen, L., & Tian, X. (2021). Selective passivation behavior of galena surface by sulfuric acid and a novel flotation separation method for copper-lead sulfide ore without collector and inhibitor. *Separation and Purification Technology*, *267*, p.118621. https://doi.org/10.1016/j.seppur.2021.118621

Characterization of Polyglycol-Based Frothers: Investigation of Dynamic Froth Stability and Dynamic Frothability

Arefeh Zahab Nazoori, Bahram Rezai*, Aliakbar Abdolahzadeh

Department of Mining Engineering, Amirkabir University of Technology, Tehran, Iran

*Corresponding author: Rezai@aut.ac.ir (Bahram Rezai)

Abstract:

Assessing frother performance through various indices is crucial to understanding how their molecular structure affects functionality, as well as evaluating their effectiveness in floating both fine and coarse particles. This study investigates for the first time the frothing behavior and froth stability of PEG 300, DPG, and TEG and compares them with conventional frothers such as DF-250. The primary operational variables considered were air flow rate and frother concentration. Initially, the frothing behavior of the reagents was predicted using the HLB-M_W diagram, and then the frothing power of the desired frothers was examined using the dynamic frothability and dynamic froth stability indices. The results revealed that PEG300 exhibited the highest dynamic frothing index (13000 s.dm^3/mol) and high froth stability, which is suitable for the flotation of coarse particles. In contrast, DPG showed the lowest frothing power and froth stability, with a dynamic frothing index of 2500 s.dm^3/mol. TEG, with an intermediate frothing index of 5000 s.dm^3/mol, demonstrated moderate performance in both froth production and stability. DF-250, with an exceptionally high frothing index, outperformed all the other agents, providing both superior froth generation and stability. Froth stability was assessed using dynamic froth stability indices and dynamic frothing capability, providing meaningful insights into frother performance.

Keywords: Flotation Frother, Dynamic Frothability index, Dynamic Stability, Frothing index

1. Introduction

Flotation, which is widely used for the flotation of fine particles, is based on the adsorption of aqueous particles by air bubbles. In this process, surface-activating agents, such as frothers, are used to help produce fine air bubbles and stabilize the froth, which facilitates the transport of particles by adsorption at the air-water interface. Frothers are surface-active compounds that consist of a polar group (OH, COOH, C=O, OSO$_2$, and SO$_2$OH) and a hydrocarbon chain(Laskowski 1993; Bulatovic 2007). These compounds are active at the interface of liquid and gas; their connection mechanism is physical. The surface activity of a surfactant with a normal alkyl chain in its molecule increases by 3.2 times due to the addition of each -CH= group in the molecule(Finch, Nesset, and Acuña 2008; Somasundaran and Wang 2006). The frother molecules are oriented at the air-water interface in such a way that the polar or hydrophilic group is directed towards the liquid and the non-polar hydrocarbon chain is directed towards the air. Frothers not only create a relatively stable froth but also produce small bubbles, and in this way, the increase and dispersion of air bubbles on the surface of the pulp is the responsibility of the frother. Frothers also control the shape of the air bubble, and the air bubble in the presence of the frother is more spherical and has a slower rising speed(Bulatovic 2007; Edwards et al. 1991; Wang 2016; Tan and Finch 2016; Xue and Li 2024). The frothers have different structural groups, and the performance of frothers depends on their chemical structure. The use of frothers in

mineral flotation practice today is dominated by two nonionic surfactant families, alcohols (general formula: $C_nH_{2n+1}OH$) and polyglycols such as PEO (polyethylene oxide), PPO (polypropylene oxide), and PBO (polybutylene oxide). The compounds can be expressed using the general equation $R(X)_n OH$, where R is H or C_nH_{2n+1}, and X is ethylene oxide (EO), propylene oxide (PO), or butylene oxide (BO). The presence of ether oxygen and hydroxyl groups imparts hydrophilic characteristics, whereas the propylene and butylene segments exhibit hydrophobic properties. The equilibrium between the hydrophobic and hydrophilic components in these substances is regulated by modifying the number of units within the alkyl ether and by altering the number of ethylene oxide (EO), propylene oxide (PO), or butylene oxide (BO) groups within the poly(ethylene oxide) (PEO) chain(Bhattacharya and Dey 2008; Bulatovic 2007; Cho and Laskowski 2002; Khoshdast and Sam 2011; Gupta 2017; Laskowski 1993; Leonov et al. 1999; Pearse 2005; Rao 2013). Glycol-based frothers produce a relatively thick, stable froth with low selectivity, carry more water (i.e., are wet), and are less sensitive to pH changes(Dudenkov and Galikov 1969; Khoshdast and Sam 2011). This property of polyglycols is considered an advantage when recovering coarse particles. The molecular weight and hydrocarbon chain length of the polyglycol ethers determine their frothing ability. Frothers with higher molecular weight produce a more stable froth but with lower selectivity(Amidon, Yalkowsky, and Leung 1974; Bhattacharya and Dey 2008; CM et al. 2012; Dukhin, Kretzschmar, and Miller 1995; Finch, Nesset, and Acuña 2008). These surfactants rank among the most adaptable neutral frothers and are likely the second most prevalent category of commercial frothers currently in use. Based on these functions, frothers can be categorized into two distinct types: selective and powerful. The term "selective" pertains to the flotation of fine particles, while the term "powerful" refers to the frothing capability, which is crucial for the recovery and efficiency of flotation processes involving coarse particles. Consequently, by employing suitable indices, one can evaluate the performance of frothers according to their varying structural characteristics. Frothers belonging to the alcohol groups behave more selectively and are, therefore, more suitable for the flotation of fine particles, while polyglycerols have greater frothing power and are, therefore, suitable for the flotation of coarse particles(Laskowski 1993; Laskowski 2004; Crozier 1992; Gupta, Banerjee, and Mishra 2009; Khoshdast and Sam 2011; Leja and Leja 1982; Pan et al. 2025).

A prerequisite for choosing an evaluation index is that it must be structure-sensitive. The properties of any surfactant can be characterized by its hydrophilic-hydrophobic balance (HLB) number. Its value depends on the chemical groups present in the molecule. The amount of the molecular capacity of the polar and non-polar ends will be different, and the tendency of the frother to contact water or air. The magnitude of this tendency is expressed by comparing HLB(Griffin 1949; Tanaka and Igarashi 2016; Wang, Nguyen, and Farrokhpay 2016; Davies 1957). The critical role of froth stability in flotation is increasingly recognized, as it directly affects mineral grade determination and flotation recovery. The term froth stability is defined as the ability of froth bubbles to resist coalescence and collapse. In other words, a more stable froth has fewer coalescence and collapse events(Alsafasfeh, Alagha, and Al-Hanaktah 2024; Triffett and Cilliers 2004; Farrokhpay 2011). In this study, the Dynamic Frothability Index (DFI) and Dynamic Froth Stability Index (DFS) are used to investigate the stability of the froths of interest. DFI was described as a definitive measure of the stability of frother under dynamic conditions. DFI is used alongside static frothability as an acceptable criterion for measuring the properties of frothers. DFI is a characteristic of each frother. DFS, which is characterized by the ratio of froth volume to airflow in the system, serves as a metric for assessing froth stability in mineral flotation processes. (Elmahdy and Finch 2013; Moyo, Gomez, and Finch 2007; Neethling, Lee, and Cilliers 2003; Stevenson, Stevanov, and Jameson 2003; Zhang, Nesset, and Finch 2010; Zhang, Chen, and Peng 2020; Zheng, Johnson, and Franzidis 2006; Pawliszak et al. 2024; Zhao and Zhang 2024)In this study, the effect of the molecular structure of frothers on their performance is determined through the indices of HLB, DFI, and DFS using frothing indices; the selectivity or power of the frothers can be investigated.

2. Material and Methods

2.1. Material

The frothers tested are listed in Table 1, selected to cover a range of molecular weights. All were reagent grade from Sigma-Aldrich (identified as 99% purity or higher).

Table 1. Frothers used in the study(Laskowski 2004; Khoshdast et al. 2023; Zhang et al. 2012)

Frother Type	Chemical formula	Molecular weight (g/mol)	HLB
Tetraethylene Glycol	$H(C_2H_4O)_4OH$	194	12.1
PEG 300	$H(C_2H_4O)_{6.4}OH$	300	12.9
Dipropylene Glycol	$H(C_3H_6O)_2OH$	134	9.25
DF-250	$CH_3(C_3H_6O)_4OH$	264.37	7.8

2.2. Methods

2.2.1. Hydrophilic-Lipophilic Balance

Structural properties of frothers, such as hydrocarbon chain length, are related to flotation performance. The primary function of frothers is a reflection of their molecular structure, which affects flotation. For this reason, frothers characterization is of great importance. The HLB parameter was first proposed by Griffin in 1949. The HLB value calculated by this method will have a value between zero and 20. A value of zero belongs to a completely hydrophobic surfactant, and the number 20 indicates a completely hydrophilic surfactant(Griffin 1949; Tanaka and Igarashi 2016; Davies and Haydon 1959; Mittal and Shah 2013; Proverbio et al. 2003; Wu et al. 2004). After Griffin, many attempts were made to provide a simple and repeatable method for calculating HLB, among which the Davis method is still the most widely used. The HLB value for a particular frother can be ascertained by analyzing the types and quantities of functional groups present within the molecule, with each functional group corresponding to a designated group number(Davies 1957). In Davies' approach, the HLB is expressed by Equation 1.

HLB=7 +Σ (hydrophilic group numbers) +Σ (lipophilic group numbers)   (1)

The HLB value calculated by the Davis method for PEG 300, DPG, and TEG frothers is 12.9, 9.25, and 12.1, respectively. The surfactants with lower HLB values are more hydrophobic than those with higher HLB values. In other words, surfactants with higher HLB are of more water solubility.

2.2.2. Prediction of Frothing Behavior

The molecular weight (MW) of frothers plays a crucial role in flotation kinetics. Higher molecular weight frothers are known to produce more stable froth compared to their lower molecular weight counterparts. polyglycol-based frothers, which have larger molecular weights, are capable of floating larger particles and are more effective in floating a broader range of particle sizes, improving flotation recovery. Since higher molecular weight frothers reduce the rising bubble velocity more, it is predicted that the frothers studied in this study will have higher frothing power than MIBC (Chipfunhu et al. 2019; Dey, Pani, and Singh 2014; Gupta et al. 2007; Gupta, Banerjee, and Mishra 2009; Klimpel and Isherwood 1991; Kowalczuk and Drzymala 2017; Kracht, Orozco, and Acuña 2016; Laskowski 1993; Liu and Somasundaran 1994; Moreno, Bournival, and Ata 2022). The HLB-Mw diagram is an approach commonly used to characterize the selectivity and power of a frother. As seen, the frothers that fall on the left side of this diagram are known to be selective in flotation, while the

ones that are situated far to the right from this line are known to exhibit properties of strong flotation frothers(Laskowski 2004; Drzymala and Kowalczuk 2018; Gomez, Finch, and Muñoz-Cartes 2011; Laskowski et al. 2003; Xue and Li 2024). From the data given in Table 1, the position of PEG300, TEG, and DPG frothers in the HLB-Mw diagram can be drawn (Fig. 1). As seen in Fig, representative dotted for studied frothers is between Selective- and powerful lines, which means that may show an intermediate behavior in aqueous solution. It shows that all three frothers are more powerful than alcohol-based frothers and should give more frothing power. In contrast, 'they have less frothing power than DF-250 and would give lower frothability.

2.2.3. Dynamic Frothability Index

The frothability tests were carried out using a froth column meter of 50 mm interior diameter and a glass cylindrical tube of 1000 mm height. The froth was generated by aerating the surfactant solution using a fritted glass sparger through a semi-permeable mesh screen with a pore size of 85 mesh (160 microns) at the bottom of the froth measurement column (Fig.2). To start with the test, the froth column was filled with 200 mL of surfactant solution with concentrations of 5, 10, 15, 25, 50 and 100 ppm of frother. The flow meter was set to a determined air flow rate range of 1– 4 L/min, and when the froth height reached the equilibrium, it was recorded. Aqueous solutions of the tested frothers were prepared using Deionized water, and All the tests were conducted at room temperature (25±1 oC) and constant pH (pH: 7).
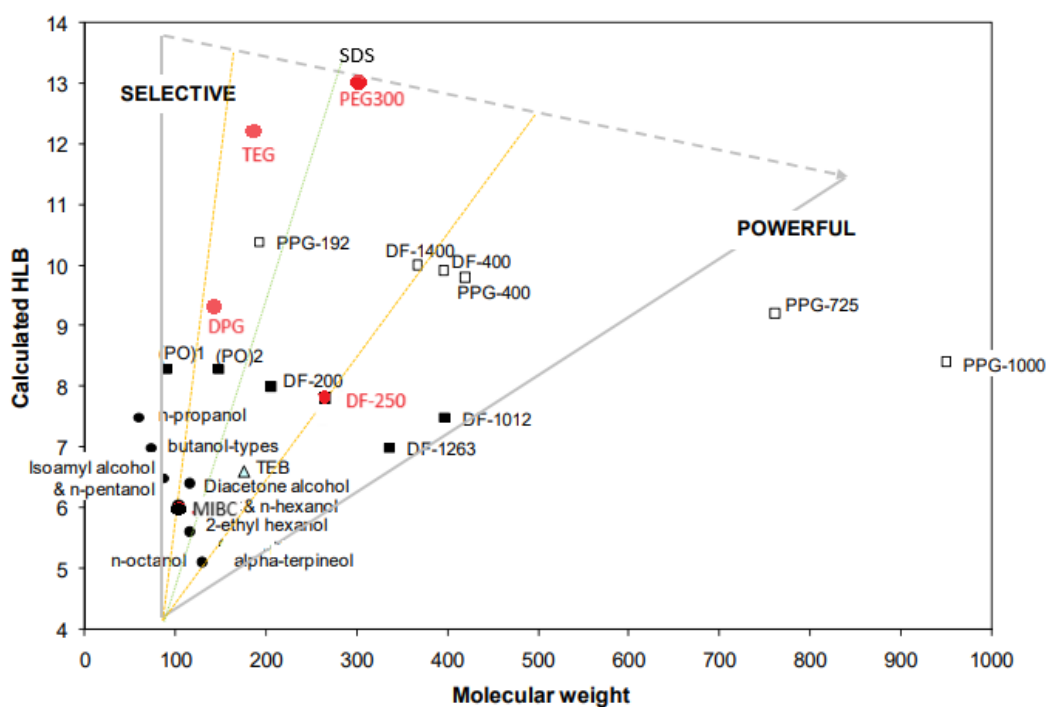
Fig1.The prediction of frothability using HLB-Mw diagram(Laskowski 2004)

Fig2. setup of a froth column

The calculation of the DFI for a given frother involves plotting froth volume against the aeration rate, where the slope of this graph indicates the retention time of the froth (equation 2).

$$rt = \frac{\Delta V}{\Delta Q}$$
(2)

Where rt is the froth retention time (s), V is the gas volume (in liquid and froth) (cm3), and Q is the Air flow rate (cm3 /s).

To calculate the DFI, the values of rt are plotted against the corresponding concentration, and the slope of the linear portion of the resulting graph is equal to the DFI which is calculated using the equation(3).

DFI $\qquad = \qquad \left(\frac{\partial rt}{\partial c}\right)_{c \to 0}$
(3)

Frother that has a higher DFI is capable of producing a more voluminous froth with greater stability(Khoshdast et al. 2023; Laskowski 2004; Miller and Ye 1989; Moreno, Bournival, and Ata 2021).

2.2.4. Dynamic Froth stability Index

Dynamic froth stability is closely related to DFI. The evaluation of dynamic froth stability involves measuring the froth growth rate and the maximum equilibrium height under different airflow velocities and varying concentrations of froth stabilizers. The dynamic stability index is affected by both the airflow rate and the concentration of the froth stabilizer(Barbian, Ventura-Medina, and Cilliers 2003; Bikerman 1973; Bikerman 2013). Equation (4) is the standard method originally proposed by Bikerman(Bikerman 1973).

$$\Sigma = \frac{V_f}{Q} = \frac{H_{max}A}{Q}$$
(4)

Where R is the dynamic froth stability, V_f is the froth volume, Q is the gas volumetric flow rate and H_{max}, and A is the total froth height and the cross-sectional area of the vessel, respectively.

3. Results and Discussion

3.1. The effect of frother structure

The molecular chain length is a crucial factor in determining the performance characteristics of frothers. In frothers with longer molecular chains, such as PEG 300, the molecules can more easily spread across the surface of the bubbles, forming protective layers that provide greater froth stability. This structure helps prevent the froth from collapsing quickly and makes it more resistant to environmental changes or agitation. In other words, longer chains can create a more organized structure on the surface of the bubbles, leading to increased stability. On the other hand, frothers like TEG, which have shorter molecular chains, are less capable of forming protective layers and stable structures. As a result, the foam produced by these frothers tends to be less stable and more sensitive to agitation and environmental conditions. Overall, the molecular chain length directly affects the froth's stability and its behavior under various conditions.

3.2. The effect of frother concentration on Frothability

The volume–air flow rate plots that were obtained for DF-250, PEG300, DPG, and TEG frothers procedure are shown in Fig 3. The steady-state froth height versus flow rate for the four different frothers is shown with varying frother concentrations. The figure clearly shows that the froth volume increases with increasing air flow rate and frother concentration for all the tested frothers. It may also be observed from the figure that DF-250 gives the highest froth volume, and DPG produces considerably low frothing. For the more powerful frothers, the volume–Air flow rate plots do not lend themselves to easy analysis. Therefore, determining DFI is very important.

The retention time values were plotted against the corresponding concentration for the desired frothers and obtained from the slope of the linear portion of the dynamic frothability index graph. (Fig4). The DFI values for the tested frothers are given in Table 2. The order of frothing power among the four frothers, in terms of the dynamic frothability index, is given below:

DF 250>PEG300>TEG>DPG

PEG 300 has a lower DFI than DF-250, which means it produces less froth, but what it does produce is more stable. DPG has not been able to provide long-term stability compared to other frothers due to the chemical characteristics of its structure that lead to faster froth degradation and TEG, which exhibits a behavior between the other two frothers.

In the evaluation of froth stability characteristics, a significant difference in the performance of frothers was observed. While frothers such as PEG300 produced relatively less foam, their more stable structure allowed for better froth retention under agitation. This may indicate the role of parameters such as the molecular chain length and the interaction between surfactants and bubbles. In contrast, frothers like DPG, due to their physicochemical properties, were unable to provide the required stability, and the froth they produced was mostly unstable.
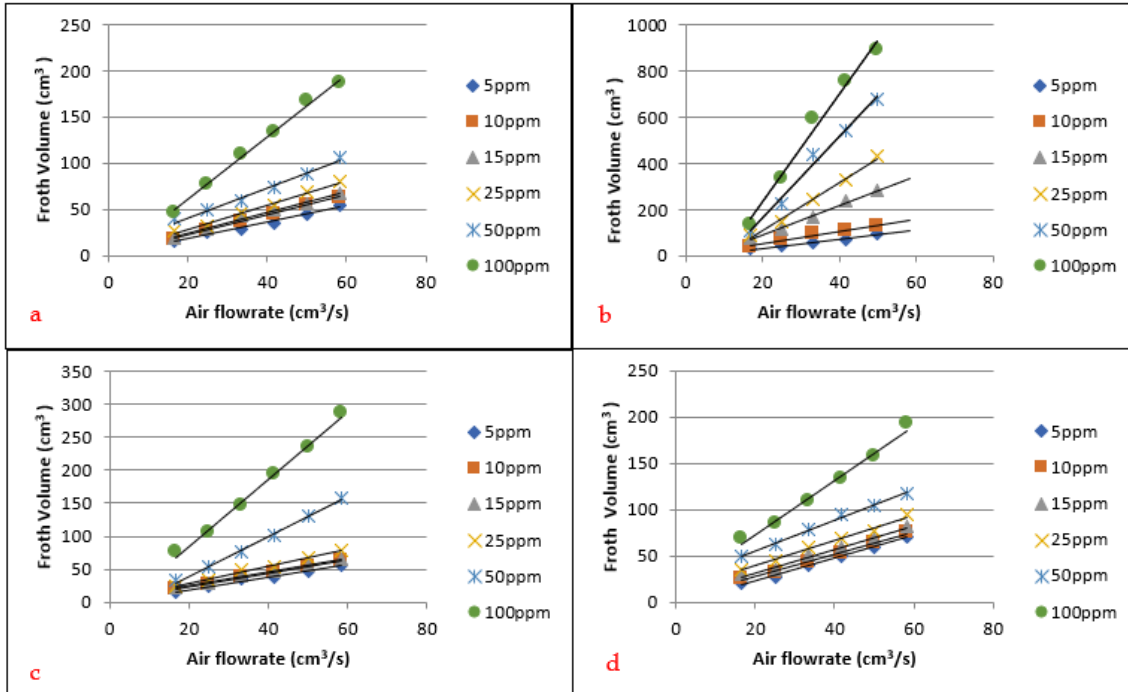
Fig3. Effect of frother concentration on retention time: : (a)TEG; (b) DF-250; (c) PEG300; (d) DPG.
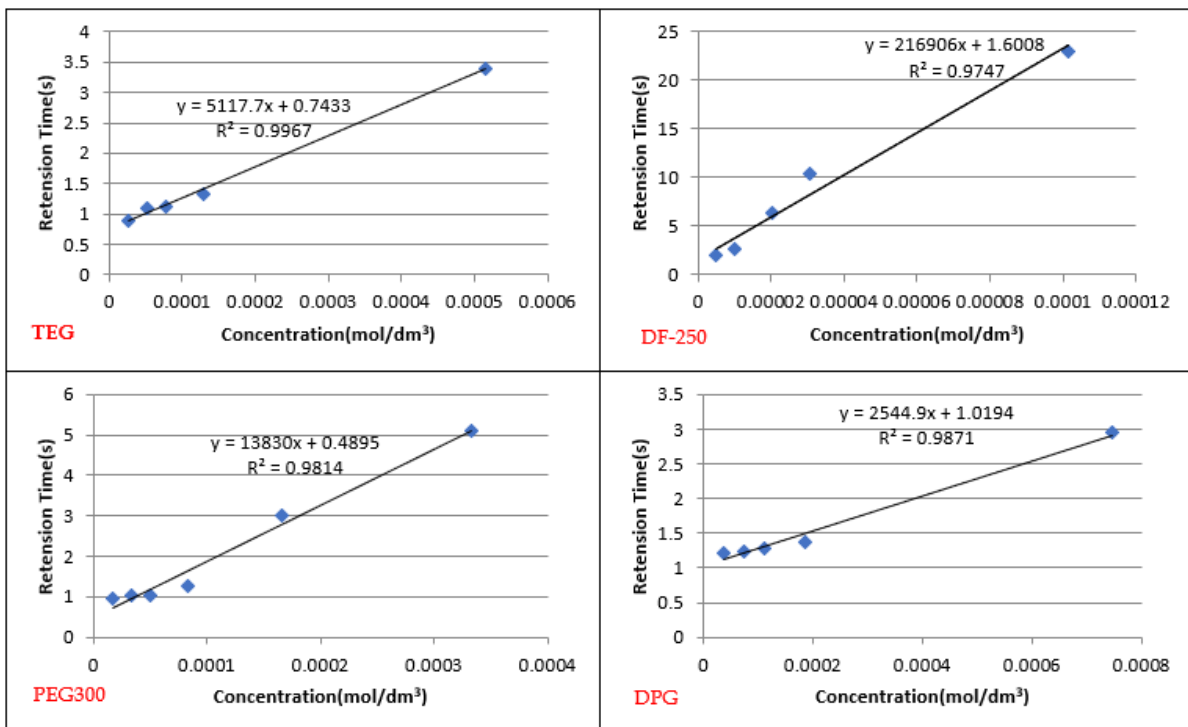
Fig4. Graphical determination of DFI for TEG; DF-250; PEG300; DPG frothers.

Table 2.Experimentally determined DFI values for the tested frother

Frother	DFI (s.dm³/mol)
Tetraethylene Glycol	5117.7
PEG 300	13657
Dipropylene Glycol	2544.9
DF-250	216906

3.3. The effect of frother concentration on equilibrium froth volume

Figure 5 illustrates the relationship between equilibrium froth volume and frother concentration at various airflow rates. It is evident that increasing the concentration of frothers significantly affects both the volume and the stability of the foam. At low concentrations, frothers are not sufficiently dispersed in the medium, leading to weak interaction with bubbles and the formation of unstable froths. As concentration increases, these frothers interact more effectively with the air-liquid interface, forming more cohesive and elastic films around bubbles, which contributes to higher foam volume and longer retention time. However, at very high concentrations, excessive surfactant accumulation can increase the viscosity of the system and amplify turbulence under high airflow rates, leading to faster foam collapse. This suggests that there is an optimal concentration range beyond which the benefits of increased frother presence may reverse. Additionally, the interplay between airflow intensity and frother concentration becomes critical, as stronger shear forces at high aeration can disrupt even stabilized foams. Thus, both the physicochemical properties of the frother and the operational parameters such as airflow must be carefully balanced to maintain stable froth characteristics.
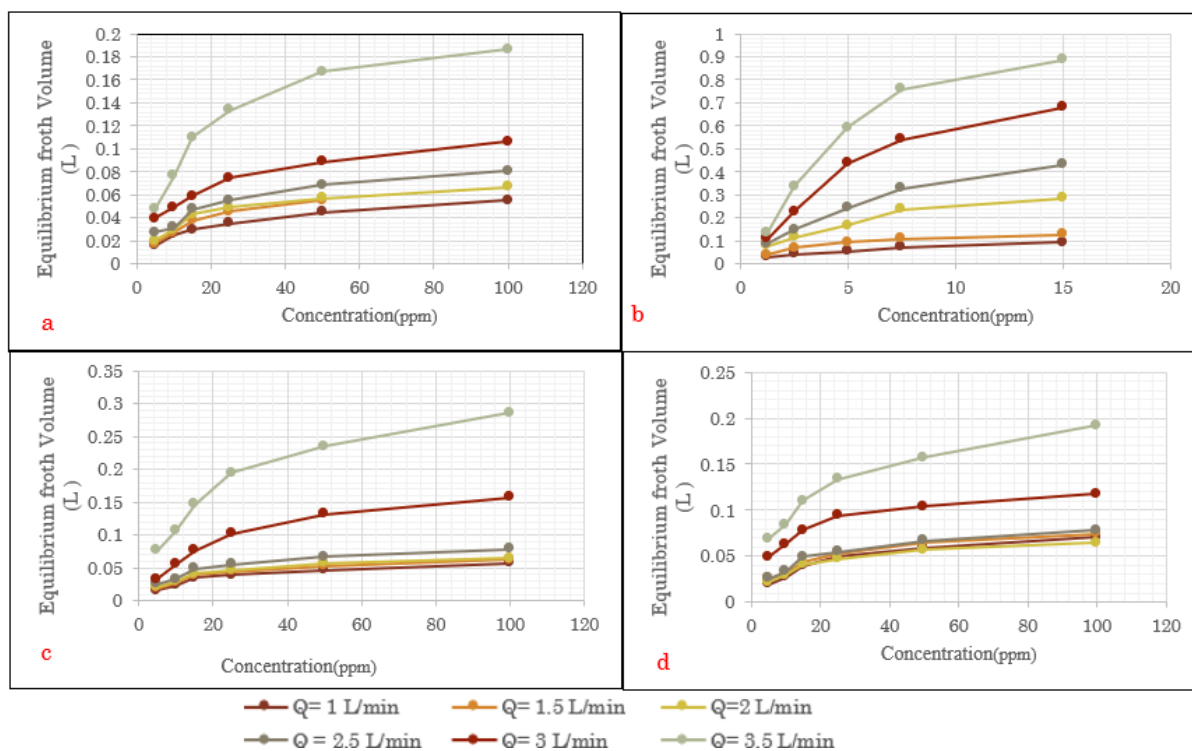
Fig5. Equilibrium froth volume as function of frother concentration for different air flowrates : (a)TEG; (b) DF-250; (c) PEG300; (d) DPG.

3.4. The effect of air flowrate on equilibrium froth volume

Fig. 5 shows the relationship between the equilibrium volume of the froth and the airflow rate at four different frother concentrations. It can be seen that at low surfactant concentrations, the equilibrium froth volume generally increases when the air flow rate is increased. The dynamic stability factor (Σ) corresponding to the previous results is shown in Fig. 6. DFS also showed similar results to the DFI. It is observed that the dynamic stability index initially increases with increasing aeration rate and then decreases due to turbulence at high aeration rates.
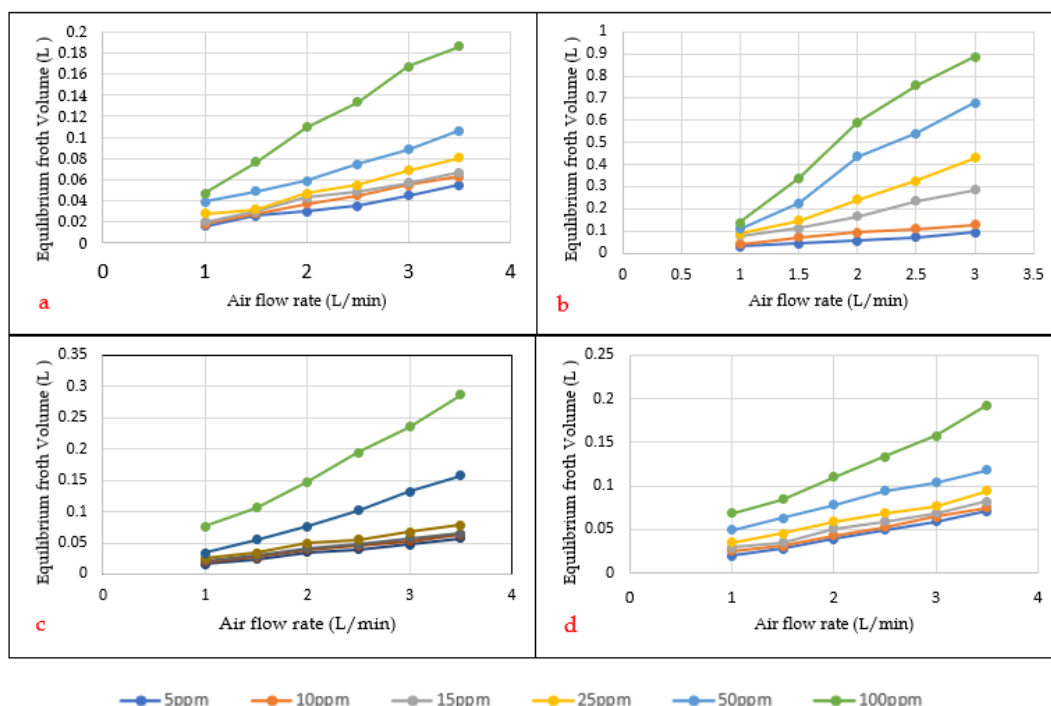
Fig5. Equilibrium froth volume as function of air flowrate for different frother concentrations : (a)TEG; (b) DF-250; (c) PEG300; (d) DPG.

Furthermore, increased aeration may lead to the formation of unstable froths that collapse immediately after formation. This can lead to reduced dynamic froth stability at higher aeration rates. PEG 300 has a lower DFI than DF-250, which means it produces less froth, but what it does produce is more stable. DPG has not been able to provide long-term stability compared to other frothers due to the chemical characteristics of its structure that lead to faster froth degradation, and TEG, which exhibits a behavior between the other two frothers, is less stable than PEG300 due to its shorter molecular chain length.

In addition to the chemical and physical properties of each frother, the type of variable and parameter used also affects its performance. For example, in high aeration systems, frothers with more resistant structures, such as PEG 300, will perform better. In contrast, in systems with lower aeration, frothers with higher surface activity but lower stability may still provide acceptable performance.
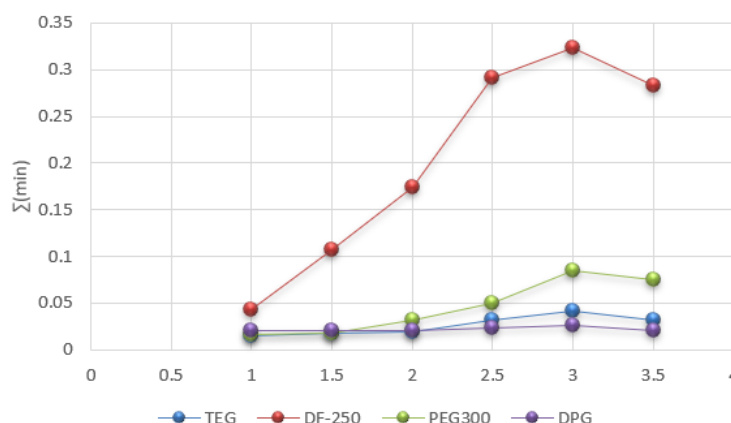
Fig6. Dynamic stability index as function of air flowrate for TEG; DF-250; PEG300; DPG frothers.

4.Conclusions

The effect of froth concentration and Air flow rate on froth height and retention time was investigated to characterize polyglycol-based froths. It is worth noting that these frothing properties are independent of bubble size. The frothers studied (PEG300, DPG, and TEG) were characterized based on the Hydrophilic- Lipophilic balance number, dynamic froth stability, and dynamic frothability of the frothers. DFI in this comparison showed that DF-250 showed significantly the highest froth production and stability. This could be due to its specific chemical structure, which produces stable froth and higher volume. In contrast, PEG300, despite its good frothing power, performed slightly worse than DF-250 in stability. This indicates the importance of molecular structure and chemical properties in froth stability. Based on the results of dynamic froth stability at low to medium air flow rates, good froth volume and stability can usually be achieved. However, at high, the froth volume may increase rapidly, but this increase in volume will be accompanied by a decrease in dynamic stability. The molecular structure of frothers and their chemical properties can also play an important role in maintaining sufficient stability against changes caused by increased air. This study showed that the molecular characteristics of three different frothers significantly affect their frothing power and dynamic froth stability. PEG300, with its long and linear structure, showed the highest frothing power and froth stability. On the other hand, DPG, with its branched structure, showed the lowest froth stability. TEG, with its medium-length linear structure, performs between the two in terms of frothing and stability. This study can help in the selection of polyglycol-based frothers for their efficiency in flotation of coarse and fine particles.

Acknowledgments

References

Alsafasfeh, Ashraf, Lana Alagha, and Amal Al-Hanaktah. 2024. 'The effect of methyl isobutyl carbinol "MIBC" on the froth stability and flotation performance of low-grade phosphate ore', *Mining, Metallurgy & Exploration*, 41: 353-61.

Amidon, GL, Samuel H Yalkowsky, and S Leung. 1974. 'Solubility of nonelectrolytes in polar solvents II: Solubility of aliphatic alcohols in water', *Journal of pharmaceutical sciences*, 63: 1858-66.

Barbian, N, E Ventura-Medina, and JJ Cilliers. 2003. 'Dynamic froth stability in froth flotation', *Minerals Engineering*, 16: 1111-16.

Bhattacharya, S, and Shobhana Dey. 2008. 'Evaluation of frother performance in coal flotation: A critical review of existing methodologies', *Mineral Processing & Extractive Metallurgy Review*, 29: 275-98.

Bikerman, Jacob Joseph. 2013. *Foams* (Springer Science & Business Media).

Bikerman, JJ, editor. 1973. 'General. Foam Films.' in, *Foams* (Springer).

Bulatovic, Srdjan M. 2007. *Handbook of flotation reagents: chemistry, theory and practice: Volume 1: flotation of sulfide ores* (Elsevier).

Chipfunhu, Daniel, Ghislain Bournival, Scott Dickie, and Seher Ata. 2019. 'Performance characterisation of new frothers for sulphide mineral flotation', *Minerals Engineering*, 131: 272-79.

Cho, Yoon-Seong, and JS Laskowski. 2002. 'Effect of flotation frothers on bubble size and foam stability', *International Journal of Mineral Processing*, 64: 69-80.

CM, Phan, H Nakahara, O Shibata, Y Moroi, Nguyen CV, and Deeptangshu Chaudhary. 2012. 'Surface potential of MIBC at air/water interface: A molecular dynamics study', *e-Journal of Surface Science and Nanotechnology*, 10: 437-40.

Crozier, Ronald D. 1992. 'Flotation: theory, reagents and ore testing'.

Davies, JT. 1957. "A quantitative kinetic theory of emulsion type, I. Physical chemistry of the emulsifying agent." In *Gas/Liquid and Liquid/Liquid Interface. Proceedings of the International Congress of Surface Activity*, 426-38. Citeseer.

Davies, JT, and F Haydon. 1959. "Proc. 2nd Int. Congr. Surface Activity." In.: Butterworths, London.

Dey, Shobhana, Santosh Pani, and Ratnakar Singh. 2014. 'Study of interactions of frother blends and its effect on coal flotation', *Powder Technology*, 260: 78-83.

Drzymala, Jan, and Przemyslaw B Kowalczuk. 2018. 'Classification of flotation frothers', *Minerals*, 8: 53.

Dudenkov, SV, and AA Galikov. 1969. 'Theory and practice of application of flotation reagents', *Nedra: Moscow, Russia*.

Dukhin, Stanislav Samuilovich, Günter Kretzschmar, and Reinhard Miller. 1995. *Dynamics of adsorption at liquid interfaces: theory, experiment, application* (Elsevier).

Edwards, DA, M Shapiro, H Brenner, and M Shapira. 1991. 'Dispersion of inert solutes in spatially periodic, two-dimensional model porous media', *Transport in Porous Media*, 6: 337-58.

Elmahdy, AM, and JA Finch. 2013. 'Effect of frother blends on hydrodynamic properties', *International Journal of Mineral Processing*, 123: 60-63.

Farrokhpay, Saeed. 2011. 'The significance of froth stability in mineral flotation—A review', *Advances in colloid and interface science*, 166: 1-7.

Finch, James A, Jan E Nesset, and Claudio Acuña. 2008. 'Role of frother on bubble production and behaviour in flotation', *Minerals Engineering*, 21: 949-57.

Gomez, Cesar O, James A Finch, and Daniela Muñoz-Cartes. 2011. "An approach to characterise frother roles in flotation." In *Proceedings of the 8th International Mineral Processing Seminar Procemin, Santiago, Chile*, 223-31.

Griffin, William C. 1949. 'Classification of surface-active agents by" HLB"', *J. Soc. Cosmet. Chem.*, 1: 311-25.

Gupta, Ashiwani Kumar, PK Banerjee, and Arun Mishra. 2009. 'Influence of chemical parameters on selectivity and recovery of fine coal through flotation', *International Journal of Mineral Processing*, 92: 1-6.

Gupta, Ashiwani Kumar, PK Banerjee, Arun Mishra, and P Satish. 2007. 'Effect of alcohol and polyglycol ether frothers on foam stability, bubble size and coal flotation', *International Journal of Mineral Processing*, 82: 126-37.

Gupta, Chiranjib Kumar. 2017. *Extractive metallurgy of molybdenum* (Routledge).

Khoshdast, Hamid, Ahmad Hassanzadeh, Przemyslaw B Kowalczuk, and Saeed Farrokhpay. 2023. 'Characterization techniques of flotation frothers-a review', *Mineral Processing and Extractive Metallurgy Review*, 44: 77-101.

Khoshdast, Hamid, and Abbas Sam. 2011. 'Flotation frothers: review of their classifications, properties and preparation', *The Open Mineral Processing Journal*, 4: 25-44.

Klimpel, RR, and Simon Isherwood. 1991. 'Some industrial implications of changing frother chemical structure', *International Journal of Mineral Processing*, 33: 369-81.

Kowalczuk, Przemyslaw B, and Jan Drzymala. 2017. 'Selectivity and power of frothers in copper ore flotation', *Physicochem. Probl. Miner. Process*, 53: 515-23.

Kracht, W, Y Orozco, and C Acuña. 2016. 'Effect of surfactant type on the entrainment factor and selectivity of flotation at laboratory scale', *Minerals Engineering*, 92: 216-20.

Laskowski, Janusz S. 2004. 'Testing flotation frothers', *Fizykochemiczne Problemy Mineralurgii/Physicochemical Problems of Mineral Processing*, 38: 13-22.

Laskowski, JS. 1993. 'Frothers and flotation froth', *Mineral Procesing and Extractive Metallurgy Review*, 12: 61-89.

Laskowski, JS, T Tlhone, P Williams, and K Ding. 2003. 'Fundamental properties of the polyoxypropylene alkyl ether flotation frothers', *International Journal of Mineral Processing*, 72: 289-99.

Leja, Jan, and Jan Leja. 1982. 'Flotation Froths and Foams', *Surface Chemistry of Froth Flotation*: 549-610.

Leonov, SB, ON Belkova, NV Kleimenova, BF Kukharev, VK Stankevich, GR Klimenko, NA Lobanova, and VA Kukhareva. 1999. 'Flotation activity of amino alcohols and their derivatives', *Journal of Mining Science*, 35: 434-38.

Liu, D, and P Somasundaran. 1994. 'Role of collector and frother, and of hydrophobicity/oleophilicity of pyrite on the separation of pyrite from coal by flotation', *International Journal of Mineral Processing*, 41: 227-38.

Miller, JD, and Yi Ye. 1989. 'Froth characteristics in air-sparged hydrocyclone flotation', *Mineral Procesing and Extractive Metallurgy Review*, 5: 307-27.

Mittal, Kashmiri Lal, and Dinesh Ochhavlal Shah. 2013. *Surfactants in Solution: Volume 11* (Springer Science & Business Media).

Moreno, Yesenia Saavedra, Ghislain Bournival, and Seher Ata. 2021. 'Foam stability of flotation frothers under dynamic and static conditions', *Separation and Purification Technology*, 274: 117822.

Moreno, Y.S., Bournival, G. and Ata, S., 2022. 'Classification of flotation frothers–A statistical approach', *Chemical Engineering Science*, 248: 117252.

Moyo, P, CO Gomez, and JA Finch. 2007. 'Characterizing frothers using water carrying rate', *Canadian Metallurgical Quarterly*, 46: 215-20.

Neethling, Stephen J, HT Lee, and JJ Cilliers. 2003. 'Simple relationships for predicting the recovery of liquid from flowing foams and froths', *Minerals Engineering*, 16: 1123-30.

Pan, Gaochao, Zhonglin Gao, Hongzheng Zhu, Jianqiang Yin, Qinhui Shi, and Yong Zhang. 2025. 'Effect of non-ionic frothers on bubble characteristics in flotation: a review', *Journal of Chemical Technology & Biotechnology*, 100: 493-507.

Pawliszak, Piotr, Bronwyn H Bradshaw-Hajek, William Skinner, David A Beattie, and Marta Krasowska. 2024. 'Frothers in flotation: A review of performance and function in the context of chemical classification', *Minerals Engineering*, 207: 108567.

Pearse, MJ. 2005. 'An overview of the use of chemical reagents in mineral processing', *Minerals Engineering*, 18: 139-49.

Proverbio, Zulema E, SM Bardavid, Eleuterio Luis Arancibia, and Pablo Carlos Schulz. 2003. 'Hydrophile–lipophile balance and solubility parameter of cationic surfactants', *Colloids and Surfaces A: Physicochemical and Engineering Aspects*, 214: 167-71.

Rao, S Ramachandra. 2013. *Surface chemistry of froth flotation: Volume 1: Fundamentals* (Springer Science & Business Media).

Somasundaran, Ponisseril, and Dianzuo Wang. 2006. *Solution chemistry: minerals and reagents* (Elsevier).

Stevenson, P, C Stevanov, and GJ Jameson. 2003. 'Liquid overflow from a column of rising aqueous froth', *Minerals Engineering*, 16: 1045-53.

Tan, Yue Hua, and James A Finch. 2016. 'Frother structure–property relationship: Effect of alkyl chain length in alcohols and polyglycol ethers on bubble rise velocity', *Minerals Engineering*, 95: 14-20.

Tanaka, Kosuke, and Akinori Igarashi. 2016. 'Determination of nonionic surfactants.' in, *Handbook Of Detergents, Part C* (CRC Press).

Triffett, BB, and JJ Cilliers. 2004. 'Measuring froth stability', *International Patent Application Number: PCT/AU2004/000331*.

Wang, Dianzuo. 2016. *Flotation reagents: applied surface chemistry on minerals flotation and energy resources beneficiation* (Springer).

Wang, Jianlong, Anh V Nguyen, and Saeed Farrokhpay. 2016. 'A critical review of the growth, drainage and collapse of foams', *Advances in colloid and interface science*, 228: 55-70.

Wu, Jiangying, Yuming Xu, Tadeusz Dabros, and Hassan Hamza. 2004. 'Development of a method for measurement of relative solubility of nonionic surfactants', *Colloids and Surfaces A: Physicochemical and Engineering Aspects*, 232: 229-37.

Xue, Yao, and Tengfei Li. 2024. 'The Significance of Flotation Frothers Chemical Structure and Fundamental Properties: A Review', *Open Journal of Applied Sciences*, 14: 2124-32.

Zhang, Na, Xumeng Chen, and Yongjun Peng. 2020. 'Effects of froth properties on dewatering of flotation products–A critical review', *Minerals Engineering*, 155: 106477.

Zhang, Wei, Jan E Nesset, Ramachandra Rao, and James A Finch. 2012. 'Characterizing frothers through critical coalescence concentration (CCC) 95-hydrophile-lipophile balance (HLB) relationship', *Minerals*, 2: 208-27.

Zhang, Wei, JE Nesset, and JA Finch. 2010. 'Water recovery and bubble surface area flux in flotation', *Canadian Metallurgical Quarterly*, 49: 353-62.

Zhao, Lina, and Qin Zhang. 2024. 'A significant review of froth stability in mineral flotation', *Chemical Engineering Science*: 120738.

Zheng, X, NW Johnson, and J-P Franzidis. 2006. 'Modelling of entrainment in industrial flotation cells: Water recovery and degree of entrainment', *Minerals Engineering*, 19: 1191-203.

Separation of Iron and Vanadium from Titanomagnetite by Thermal Treatment and Magnetic Separation

khadijeh Pariyan[1]*, Mohsen Fatahpour[1], Mohammad mehdi Ravanfar[1]

[1] Mineral Processing Department, Mobarakeh Steel Company, Isfahan, Iran

*Corresponding author: kh.pariyan@yahoo.com (khadijeh Pariyan)

Abstract:

In this paper, the extraction of iron and vanadium from titanomagnetite sources was studied by a reduction roasting process. Titanomagnetite has a spinel structure, and roasting facilitates its decomposition, making it easier to separate iron and titanium. In the roasting stage, several key parameters including temperature, particle size, and oxidation roasting were investigated on the iron separation, and a magnetic separator was used at a field intensity of 800 G to enrich the roasted product. For iron extraction, decreasing the particle size resulted in an increase in grade, and increasing temperature and oxidation did not have a positive effect on increasing in grade. The highest iron grade and recovery were 65.32% and 65.77%, respectively, were obtained with a particle size less than 38μm and a temperature of 550°C. The tailings from the magnetic separation stage contain titanium and vanadium, so the separation of vanadium was investigated using salt roasting at a temperature of 900°C and a roasting time of 2 h and leaching with water. The highest grade and recovery of vanadium oxide were obtained at 67.51 and 69.4%, respectively.

Keywords: Roasting, Titanomagnetite, Iron, Vanadium

1. Introduction

Today, with the increasing use of metals and their oxides in domestic industries, as well as the availability of rich metal resources in Iran, the need to achieve extraction technology and self-sufficiency in production is felt more than ever. Titanomagnetites are scattered resources that are usually a source of iron, titanium, and vanadium. The structure and composition of titanomagnetites vary, and this requires diverse methods for extracting metals from these sources(Chen et al., 2020; Zhang et al., 2019).

In addition to titanoferous deposits, titanomagnetite is found in coastal sands (placer) that are of volcanic origin and are economical to use due to their low cost of exploitation(Chen et al., 2011). The structure of titanomagnetite contains complex vanadium and has the chemical formula [$Fe_{0.23}$ ($Fe_{1.95}Ti_{0.42}$)O_4,Fe_2O_3.$FeTiO_3$] (Yang et al., 2020). Vanadium in titanomagnetite is isomorphous with iron minerals, with most of the vanadium present as spinel chalconite (FeV_2O_4) associated with magnetite(Han et al., 2021). Regardless of the type of feed, vanadium processing uses processes including physical concentration, salt roasting, leaching, solution purification, and precipitation(Li et al., 2019; Zhang et al., 2018). Salt roasting is carried out using sodium salts such as sodium carbonate, sodium sulfate, or sodium chloride, usually at temperatures of 800 to 1000°C. Based on the reaction 1 to 5, the vanadium produced in salt roasting reacts with added sodium salts such as sodium carbonate to form water-soluble sodium vanadate compounds such as sodium metavanadate ($NaVO_3$). Vanadium solubility and recovery are increased(Gilligan & Nikoloski, 2020; Yang et al., 2020).

$$FeO.V_2O_3 + 0.5O_2 \rightarrow Fe_2O_3.V_2O_3 \tag{1}$$

$$Fe_2O_3.V_2O_3 + 0.5O_2 \rightarrow Fe_2O_3.V_2O_4 \tag{2}$$

$$Fe_2O_4.V_2O_3 + 0.5O_2 \rightarrow Fe_2O_3.V_2O_5 \tag{3}$$

$$Fe_2O_3.V_2O_5 \rightarrow Fe_2O_3 + V_2O_5 \tag{4}$$

$$V_2O_5 + Na_2CO_3 \rightarrow 2NaVO_3 + CO_2 \tag{5}$$

Since titanomagnetites contain elements such as titanium, vanadium, and iron, studies have been conducted to separate these elements (Chen et al., 2011; Han et al., 2021; Yang et al., 2016). Safdar et al. (Safdar et al., 2020) developed a new method for extracting TiO₂-enriched materials from vanadium-titanomagnetite (VTM) concentrates, which combines partial carbon reduction and mild acid leaching. By optimizing the reduction at 1000°C for 3 h with 6% carbon and leaching with 0.2 mol/L H₂SO₄ at 80°C for 3–4 h, a rutile residue containing 72.2 wt% TiO₂ was obtained, which provides a valuable material for titanium extraction, while iron and vanadium were recovered from the leaching solution. Maldybayev et al.(Maldybayev et al., 2024) examines the processing of titanomagnetites using low-temperature treatment and magnetic separation, showing that with the use of a reducing agent, chloride additives, and calcium fluoride at 1200°C for 60 minutes, iron is effectively extracted, with the magnetic fraction yielding 75.5% and 97.8% iron extraction, while the titanium dioxide content in the non-magnetic fraction increases to 65%.

Processing, concentrating, and purifying placer titanomagnetite mines has a technical and economic justification, enabling the simultaneous extraction of strategic and high-value-added elements. The purpose of this project was to assess the feasibility of increasing the grade of placer minerals with the approach of simultaneous extraction of iron and vanadium. The use of the roasting method, especially at lower temperatures or under reducing conditions using reducing gases (such as CO or H₂), or under oxidizing conditions, is a less expensive and simpler process that can optimize the extraction process and achieve a more desirable result.

2. Material and methods

2.1. Material

The titanomagnetite used in this research was obtained from the placer deposits mine of Bazman (Sistan and Baluchestan, Iran). The chemical composition of the representative ore was characterized by X-ray diffraction (Asenware, AW/XDM 300, china), X-ray fluorescence (pw1410, Netherlands), thin section and polish section (Kaywa polarizing microscope) analyses. Also, the solutions taken from the leaching experiments, were analyzed by inductively coupled plasma spectrometry (ICP-OES, Perkin Elmer, Optima 7300DV, USA).

2.2. Method

In this process, the samples were first crushed to particles less than 500 μm. In the reductive roasting process, the parameters of temperature, particle size, and oxidation were investigated. Temperatures of 550 to 750 °C, oxidation temperatures of 700 to 1100 °C, and particle sizes of 38, 75, and 200 μm were investigated. It should be noted that the particle size entering the furnace was constant and the effect of particle size was investigated after reduction. Methane gas (0.5 L/min) was used along with a certain percentage of air (1-3%) and 2% nitrogen. After the reduction stage, re-crushing was performed and magnetic separation was performed using a Davis tube with an intensity of 800 G.

On the tailing of the magnetic separation step, a salt roasting step was performed using sodium chloride at a temperature of 900 °C for 2 hours. In a salt roasting, mix a 5 M sodium chloride solution

with a pulp density of 50% (W/W) and place it at a temperature of 80 °C for 2 hours until the water is completely evaporated, then place it in the oven and heat it. After the roasting process, it was leached in water at a temperature of 50 °C until the vanadium dissolved.

3. Results and discussion

3.1. Sample characterization

In order to characterize various properties of the titanomagnetite ore, several chemical and physical analyses were conducted. XRF analysis showed that the amount of Fe_2O_3 was 45.32% and V_2O_5 was 0.045% (Table 1).

Table 1. Chemical composition of the representative sample of the titanomagnetite ore

Element	Na_2O	K_2O	CaO	MgO	Al_2O_3	Fe_2O_3	MnO	SiO_2	SO_3	P_2O_5	TiO_2	V_2O_5	LOI
Content (% Wt)	2.34	0.98	3.36	3.98	6.89	45.32	0.21	25.62	0.56	0.23	6.95	0.045	2.99

Microscopic images related to thin sections were prepared using transmitted light with parallel (PPL) fibers. As can be seen in Fig. 1, they show that the sample contains magnetite, titanomagnetite, tremolite - actinolite. Degree of liberation studies showed that magnetite and titanomagnetite are seen in the higher fractions as inclusions. As the sample particle size decreases, the degree of freedom increases, so that in the fraction of -53+38 mµ, the degree of freedom reaches 80%.
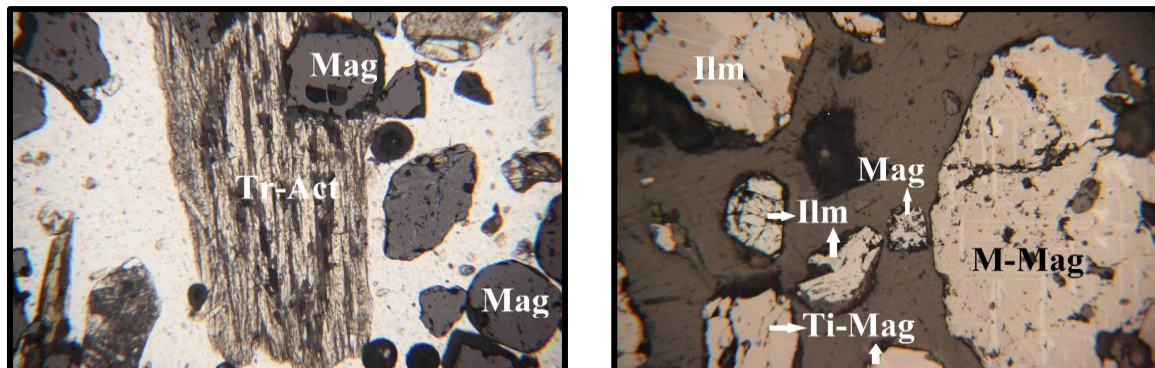
Fig. 1. Microscopic images of the titanomagnetite sample with polarizing microscope (Mag: magnetite, Ti-Mag: titanomagnetite, I: ilmenite, Tr-Act: tremolite – actinolite)

3.2. Effect of oxidation

One possible method to break the iron-titanium bond in titanomagnetite and ilmenite samples is oxidation at particle sizes less than 500 mµ. Therefore, all samples were oxidized by the fixed bed furnace at temperatures of 700, 800, 900, 1000, and 1100 °C with compressed air at a flow rate of 2 L/min, and then XRD analysis was performed on the obtained samples.

The results of XRD analysis of oxidation at different temperatures are shown in Fig. 2. The results indicate that at temperatures below 1000 °C, practically no significant change occurs in the sample and the phase is still hematite and titanomagnetite. The reason for the greater presence of hematite in these samples is due to the oxidation of magnetite to hematite at this temperature, although titanomagnetite remains unchanged at lower temperatures. As the temperature increases to 1000°C, almost no trace of titanomagnetite is seen in the XRD analysis, and iron is almost entirely in the hematite phase.

Studies have shown that magnetite is converted to weakly magnetic or non-magnetic phases such as hematite and maghemite, which reduces iron recovery during magnetic separation; furthermore, titanium is not effectively released from the iron phase, leading to a decrease in iron grade in the concentrate and overall process efficiency (Jena et al., 2015). Therefore, reduction roasting should be performed after this step. Oxidative roasting, by converting iron phases such as Fe_3O_4 to Fe_2O_3 and creating a uniform structure, allowed the next stage (gas reduction) to be reduced with H_2 and CO gases with higher efficiency and faster speed (Li et al., 2021).
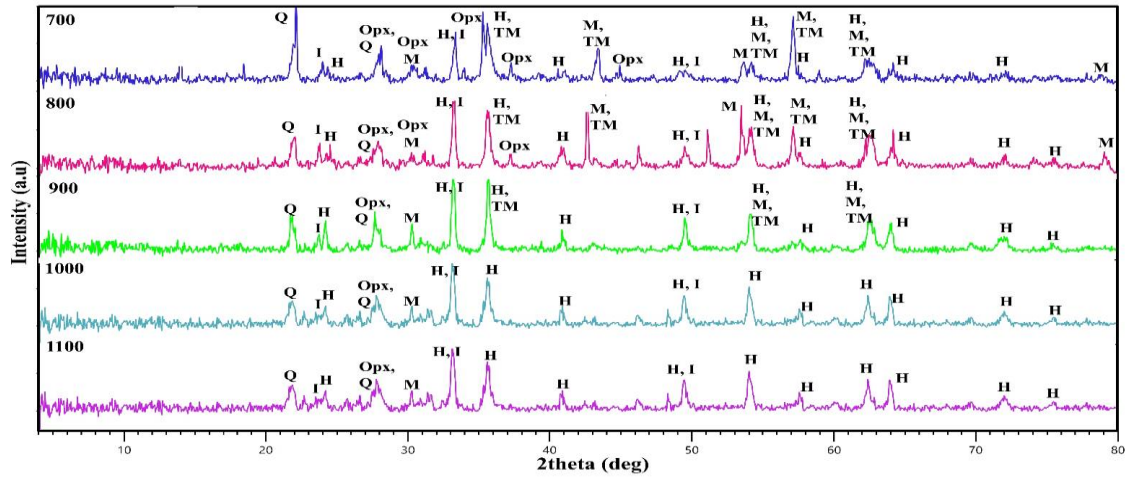
Fig. 2. XRD results of the sample after oxidation at different temperatures (M: magnetite, H: hematite, Q: quartz, TM: titanomagnetite, Opx: orthopyroxene, I: ilmenite)

After performing oxidation tests, the required amount of these samples was reduced by methane gas at 5 temperatures of 550, 600, 650, 700 and 750 °C. The results of sample reduction by methane showed that the hematite obtained at 600 °C was completely converted to magnetite (Fig. 3).
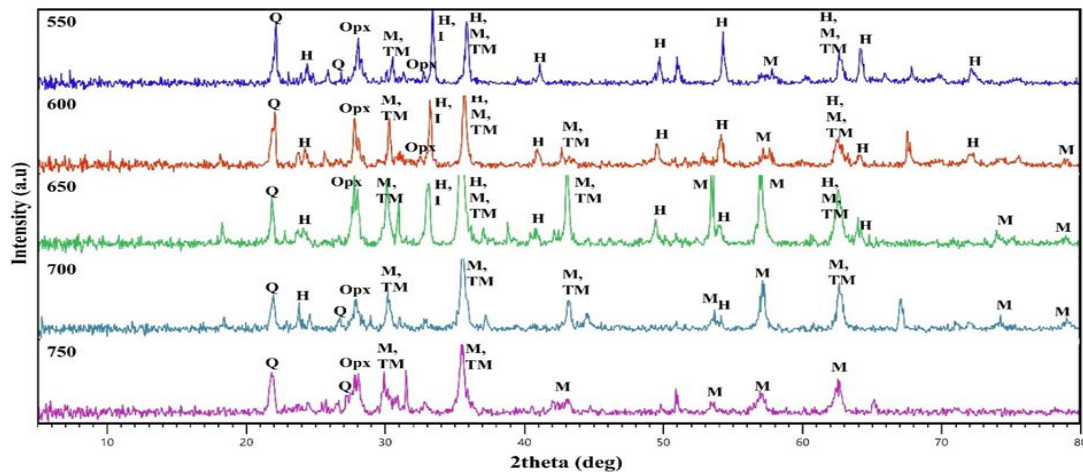
Fig. 3. XRD results of the sample after the reduction process at different temperatures with the oxidation process at 1000 °C (M: magnetite, H: hematite, Q: quartz, TM: titanomagnetite, Opx: orthopyroxene, I: ilmenite)

In Table 4, the results indicate an increase in iron content in the magnetic separation concentrate sample by more than 59%. The iron content in the concentrate did not change significantly with the increase in temperature reduction and remained approximately constant at 58-59%. The titanium content in the tailings at reduction temperatures of 550, 600, and 650°C was higher than the titanium content in the concentrate, indicating the relative separation of iron and titanium from each other.

However, with increasing reduction temperatures (700 and 750°C), the titanium content in the concentrate increased (more than 5%), which means that the iron and titanium bond did not separate at high reduction temperatures. At reduction temperatures of 750°C, the vanadium content in the concentrate increased and reached 0.25%. These results indicate the relative separation of iron in the concentrate phase and the accumulation of titanium in the tailings. However, the presence of vanadium in the concentrate indicates a correlation between iron and vanadium, which has not changed with oxidation and reduction. The correlation between iron and vanadium is consistent with previous studies (Yang et al., 2020). Iron recovery at temperatures of 550, 600, 650, 700 and 750°C was 86.92, 85.90, 86.10, 81.40 and 80.32%, respectively.

Pre-oxidation creates cracks and porous structures in the iron ore particles, which improves the permeability of the reducing gas (Zheng et al., 2021).

In previous studies, the effect of roasting temperature during suspension magnetic roasting of ores containing siderite and hematite was investigated. The results showed that at temperatures below 550°C, the phase transformation was incomplete, and the magnetic properties were poor. At around 610°C, the transformation of hematite and siderite to magnetite was almost complete, resulting in the highest iron recovery and grade. A further increase in temperature led to the formation of non-magnetic phases such as Fe_3O_4, which negatively affected the magnetic separation performance (Chen et al., 2022).

Table 2. XRF results of oxidized and reduced samples after magnetic separation

Element	Na$_2$O	K$_2$O	CaO	MgO	Al$_2$O$_3$	Fe[c]	MnO	SiO$_2$	SO$_3$	P$_2$O$_5$	TiO$_2$	V[d]	LOl
C[a] 550	0.08	0.09	0.78	1.84	2.36	58.67	0.44	3.5	ND	0.42	7.1	392	1.13
T[b] 550	0.99	0.56	2.75	6.63	5.65	33.41	0.47	25.81	0.11	0.31	10.43	211	1.64
C 600	0.07	0.08	0.71	1.74	2.25	59.24	0.45	3.05	ND	0.31	7.13	504	1.25
T 600	0.99	0.58	2.94	6.85	5.71	32.33	0.47	26.06	ND	0.32	10.56	241	0.96
C 650	0.08	0.07	0.7	1.76	2.25	59.38	0.45	3.14	ND	0.35	7.46	650	1.65
T 650	1.27	0.64	3.58	8.23	6.58	25.54	0.44	32.94	ND	0.39	9.39	261	0.15
C 700	0.09	0.07	0.7	1.77	2.23	58.69	0.47	3.3	0.09	0.3	9.03	1457	2.56
T 700	1.83	0.93	4.95	10.96	8.65	13.01	0.39	48.46	ND	0.36	3.95	204	0.88
C 750	0.08	0.08	0.62	1.87	2.34	59.26	0.47	3.29	ND	0.22	9.06	2431	3.26
T 750	1.95	0.9	5.35	10.75	8.84	12.14	0.42	48.55	ND	0.64	5.67	283	0.46

[a] Concentrate, [b] Tailing, [c] Analyzed by Titration, [d] Analyzed by ICP (ppm)

3.3. Effect of reductive temperature

Reduction tests were conducted directly at temperatures of 550, 600, 650, 700, and 750°C with methane gas to investigate the effect of the presence or absence of the oxidation process on factors such as iron recovery, titanium and vanadium recovery, and titanium separation from iron. The results obtained are shown in Fig. 4.
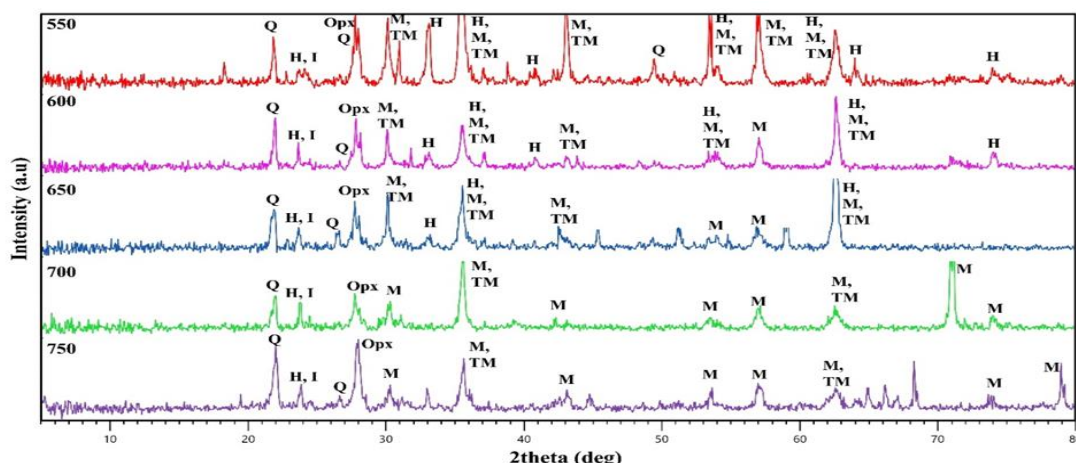
Fig. 4. XRD results of the sample after the reduction process with methane gas at different temperatures (M: magnetite, H: hematite, Q: quartz, TM: titanomagnetite, I: ilmenite)

In Table 3, an increase in iron grade of up to 59% can be seen. However, by comparing the results of these two tables, it can be seen that the oxidation process did not have much effect on increasing the iron grade in the magnetic separation concentrate sample. The iron content in the concentrate did not change significantly with the increase in temperature reduction and remained approximately constant at 58-59%. The titanium content in the concentrate is higher than its content in the tailings, indicating the effect of oxidation on breaking the bond between iron and titanium. The titanium grade in the concentrate at all reduction temperatures ultimately reached 5.5% and in the tailings it was below 3%. At reduction temperatures of 700 and 750 °C, the vanadium grade in the concentrate increased to more than 0.2%. These results indicate the relative separation of iron in the concentrate phase and the accumulation of titanium in the tailings. The presence of vanadium in the concentrate indicates a correlation between iron and vanadium, which has not changed with oxidation and reduction. Iron recovery at temperatures of 550, 600, 650, 700 and 750°C was 85.62, 87.47, 80.23, 84.31 and 78.32%, respectively.

The effect of roasting temperature on iron recovery and magnetic separation is discussed. The results show that at temperatures lower than 540°C, the roasting process is not able to fully convert hematite (Fe_2O_3) to magnetite (Fe_3O_4), leading to lower iron recovery. However, at 540°C, the conversion is complete, increasing the magnetic properties of the ore (Yu et al., 2018).

In the study by Chen et al. (Chen et al., 2020), the effect of roasting temperature on iron recovery from titanomagnetite was investigated. In this process, temperature plays a crucial role in the transformation of mineral phases and the improvement of the magnetic properties of iron ore. The results showed that increasing the temperature from 450°C to 550°C facilitates the reduction and transformation of hematite (Fe_2O_3) to magnetite (Fe_3O_4), improves magnetic properties, and accelerates the magnetic separation process.

Table 3. XRF results of the reduced samples after magnetic separation

Element	Na$_2$O	K$_2$O	CaO	MgO	Al$_2$O$_3$	Fe[c]	MnO	SiO$_2$	SO$_3$	P$_2$O$_5$	TiO$_2$	V[d]	LOl
C[a] 550	0.09	0.08	0.6	1.68	2.13	59.04	0.4	2.66	ND	0.31	9.27	1648	-2.04
T[b] 550	1.78	0.81	4.91	10.34	7.38	15.46	0.38	45.37	ND	0.57	5.05	236	0.74
C 600	0.09	0.07	0.56	1.67	2.13	59.03	0.39	2.67	ND	0.27	9.3	1924	-1.98
T 600	1.77	0.81	5.15	10.93	8.1	13.5	0.36	46.78	ND	0.52	4.19	200	1.92
C 650	0.09	0.07	0.55	1.77	2.19	59.18	`0.41	2.78	ND	0.24	9.36	1894	-2.5
T 650	1.67	0.78	4.68	9.76	7.86	18.05	0.35	42.3	ND	0.5	5.01	446	1.11
C 700	0.08	0.08	0.56	1.69	2.19	59.43	0.4	2.62	ND	0.25	9.41	2255	-2.68
T 700	1.93	0.88	5.24	11.4	8.42	12.45	0.36	50.55	ND	0.64	3.57	173	-0.88
C 750	0.09	0.09	0.56	1.77	2.23	59.19	0.4	2.81	ND	0.28	9.48	2674	-2.77
T 750	1.98	0.88	5.44	11.15	8.63	12.43	0.37	49.68	ND	0.56	3.81	212	-0.24

[a] Concentrate, [b] Tailing, [c] Analyzed by Titration, [d] Analyzed by ICP (ppm)

3.4. Effect of particle size

In order to investigate the effect of particle size on achieving proper separation of iron, titanium, and vanadium and breaking the correlation between them, a reduction test should be performed on different particle sizes and the effect of grinding the initial sample on the grade of the elements of interest should be studied. For this purpose, the unoxidized sample was reduced with methane gas at 550°C and the reduced sample was crushed with a planetary mill for specific times until 100% of the sample reached particle sizes below 200, 75, and 38 μm.

By examining the results obtained from Fig. 5, it can be concluded that particle size has a great impact on the iron and titanium content after the reduction process. When the particle size was reduced, the iron content in the tailings decreased, indicating the separation of the fine iron particles under a magnetic field. Regarding the silica impurity, it can be said that the separation has increased in the size fractions of 75, 200, and then 38 mμ, respectively. In general, the main goal, which was to eliminate the correlation of titanium and iron and increase their grade, is possible by changing the particle size. Iron recovery at particle sizes of 200, 75, and 38 μm was 72.25, 65.27 and 65.77%, respectively.

It was shown that reducing particle size through grinding enhances the recovery of iron and titanium during magnetic separation, as finer particles lead to better liberation of magnetic phases from non-magnetic ones. However, once an optimal grinding time is reached, further size reduction results in the formation of ultra-fine particles, which decreases separation efficiency because these fine particles are more difficult to recover in magnetic separation circuits (Liu et al., 2022).

Figure 5d shows the dissolution rate of V$_2$O$_5$ from tailings at different particle sizes, which reached 67.51% with a recovery of 69.4% after salt roasting and leaching at particle sizes less than 38 μm.

Reducing particle size increases grade and recovery because smaller particles roast better and dissolve more easily (Han et al., 2021).

Previous studies have shown that reducing particle size to below 74 µm helps to more effectively release vanadium-containing minerals. This leads to improved magnetic separation efficiency and increased iron and vanadium recovery and grade. Furthermore, the results show that the magnetic separation process reaches its maximum efficiency when more than 85.2% of the material is ground to below 74 µm. However, the authors caution that over-grinding may result in an increase in fines, which can reduce recovery in subsequent processing steps (Xu et al., 2017).
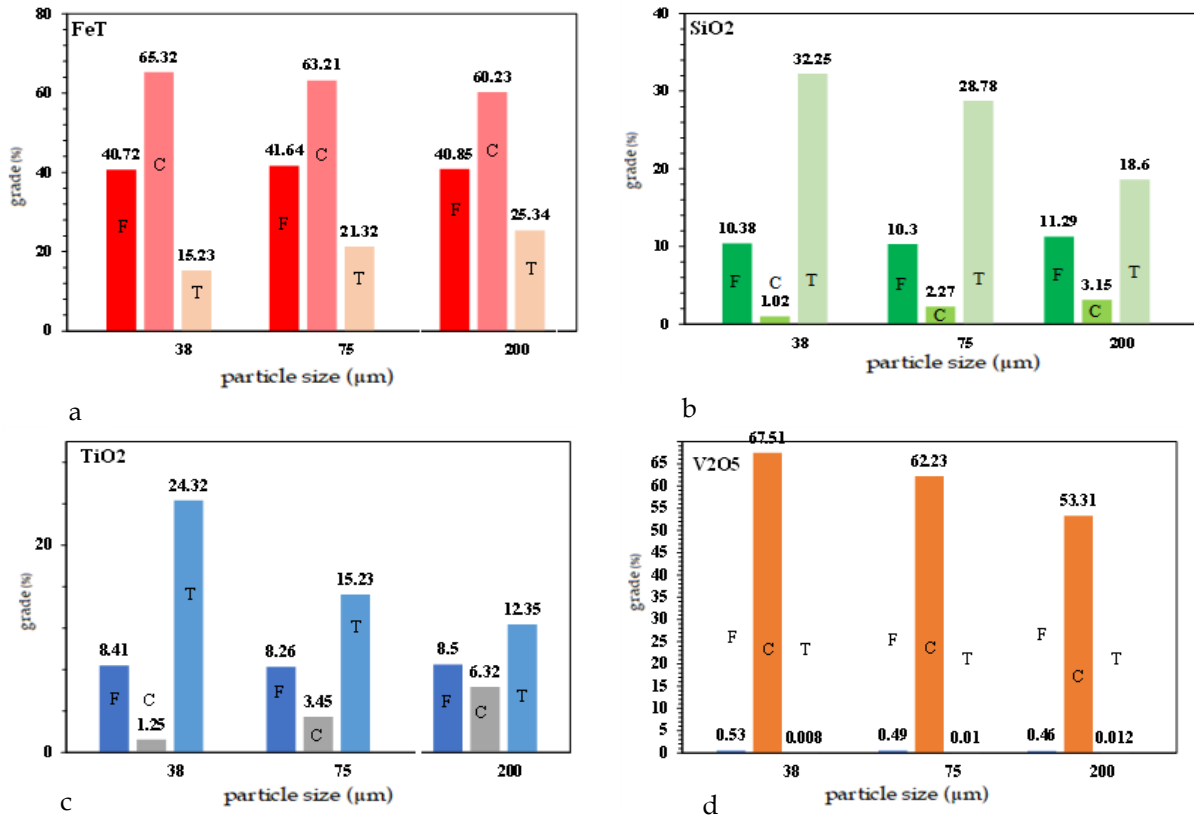
Fig. 5. The effect of particle size on a magnetic separation. a. Fe total b. SiO_2 c. TiO_2 d. V_2O_5 (F: Feed, C: Concentrate, T: Tailing)

4.   Conclusions

The development of innovative and sustainable technologies can contribute to mitigating existing challenges and optimizing the utilization of titanomagnetite resources. So, the extraction of iron and vanadium from titanomagnetite sources was investigated by a reduction roasting process and the following results were obtained:

- Increasing the temperature to 550°C has had a positive effect due to the conversion of hematite minerals to magnetite and the breaking of the iron-titanium bond.

- The reduction in particle size due to the low degree of liberation of the sample resulted in an increase in the grade.

- Oxidation roasting had no effect on iron grade and recovery, and the vanadium content decreased due to the high roasting temperature.

- The highest iron grade and recovery were 65.32% and 65.77%, respectively, obtained with a particle size less than 38μm and a temperature of 550°C.

- The highest grade and recovery of vanadium oxide, 67.51 and 69.4%, respectively, were obtained by salt roasting at 900°C and a roasting time of 2 h and leaching with water.

Acknowledgments

References

Chen, C., Han, Y., Zhang, Y., Liu, Y., & Liu, Y. (2022). Efficient Utilization of Siderite-and Hematite-Mixed Ore by Suspension Magnetization Roasting: A Pilot-Scale Study. *Sustainability*, *14*(16), 10353. doi: https://doi.org/10.3390/su141610353

Chen, D.-s., Song, B., Wang, L.-n., Qi, T., Wang, Y., & Wang, W.-j. (2011). Solid state reduction of Panzhihua titanomagnetite concentrates with pulverized coal. *Minerals Engineering*, *24*(8), 864-869. doi: https://doi.org/10.1016/j.mineng.2011.03.018

Chen, X., Wang, H., & Yan, B. (2020). Sulfuric acid leaching and recovery of vanadium from a spinel concentrate beneficiated from stone coal ore. *Hydrometallurgy*, *191*, 105239. doi: https://doi.org/10.1016/j.hydromet.2019.105239

Gilligan, R., & Nikoloski, A. N. (2020). The extraction of vanadium from titanomagnetites and other sources. *Minerals Engineering*, *146*, 106106. doi: https://doi.org/10.1016/j.mineng.2019.106106

Han, Y., Kim, S., Go, B., Lee, S., Park, S., & Jeon, H.-S. (2021). Optimized magnetic separation for efficient recovery of V and Ti enriched concentrates from vanadium-titanium magnetite ore: Effect of grinding and magnetic intensity. *Powder Technology*, *391*, 282-291. doi: https://doi.org/10.1016/j.powtec.2021.06.024

Jena, M. S., Tripathy, H., Mohanty, J., Mohanty, J., Das, S., & Reddy, P. (2015). Roasting followed by magnetic separation: A process for beneficiation of titano-magnetite ore. *Separation Science and Technology*, *50*(8), 1221-1229. doi: 10.1080/01496395.2014.965834

Li, W., Fu, G., Chu, M., & Zhu, M. (2021). An effective and cleaner process to recovery iron, titanium, vanadium, and chromium from Hongge vanadium titanomagnetite with hydrogen-rich gases. *Ironmaking & Steelmaking*, *48*(1), 33-39. doi: 10.1080/03019233.2020.1721955.

Li, W., Zhou, L., Han, Y., Zhu, Y., & Li, Y. (2019). Effect of carboxymethyl starch on fine-grained hematite recovery by high-intensity magnetic separation: Experimental investigation and theoretical analysis. *Powder Technology*, *343*, 270-278. doi: https://doi.org/10.1016/j.powtec.2018.11.024

Liu, J., Xing, Z., Cheng, G., Xue, X., & Ding, X. (2022). Study on the grinding kinetics and magnetic separation of low-grade vanadiferous titanomagnetite concentrate. *Metals*, *12*(4), 575. doi: https://doi.org/10.3390/met12040575

Maldybayev, G., Korabayev, A., Shayakhmetova, R., Khabiyev, A., Baigenzhenov, O., Sharipov, R., & Amirkhan, A. (2024). Separation of iron and titanium from titanium magnetite raw materials by low-temperature treatment and magnetic separation. *Case Studies in Chemical and Environmental Engineering*, 100848. doi: https://doi.org/10.1016/j.cscee.2024.100848.

Safdar, F., Zhang, Y., Zheng, S., Chen, X., Sun, P., Zhang, Y., & Li, P. (2020). Recovery of TiO2-enriched material from vanadium titano-magnetite concentrates by partial carbon reduction and mild acid leaching. *Hydrometallurgy*, *193*, 105324. doi: https://doi.org/10.1016/j.hydromet.2020.105324.

Xu, C., Zhang, Y., Liu, T., & Huang, J. (2017). Characterization and pre-concentration of low-grade vanadium-titanium magnetite ore. *Minerals*, *7*(8), 137. doi: https://doi.org/10.3390/min7080137.

Yang, B., He, J., Zhang, G., & Guo, J. (2020). *Vanadium: Extraction, Manufacturing and Applications*. Elsevier. https://books.google.com/books?id=cuTsDwAAQBAJ

Yang, S., Pan, R., Ma, L., Li, J., & Li, H. (2016). Investigation on Thermal Conductivity of Vanadium Titano-magnetite Concentrate Carbon-containing Pellets in Direct Reduction. 2016 International Forum on Energy, Environment and Sustainable Development, doi: 10.2991/ifeesd-16.2016.85.

fluidized magnetization roasting and magnetic separation. *Journal of Mining and Metallurgy, Section B: Metallurgy*, *54*(1), 21-27. doi: https://doi.org/10.1016/j.jhazmat.2019.02.081

Zhang, Y.-m., Wang, L.-n., Chen, D.-s., Wang, W.-j., Liu, Y.-h., Zhao, H.-x., & Qi, T. (2018). A method for recovery of iron, titanium, and vanadium from vanadium-bearing titanomagnetite. *International Journal of Minerals, Metallurgy, and Materials*, *25*, 131-144. doi: https://doi.org/10.1007/s12613-018-1556-0

Zhang, Y., Zhang, T.-A., Dreisinger, D., Lv, C., Lv, G., & Zhang, W. (2019). Recovery of vanadium from calcification roasted-acid leaching tailing by enhanced acid leaching. *Journal of hazardous materials*, *369*, 632-641. doi: https://doi.org/10.1016/j.jhazmat.2019.02.081

Possibility of Using Waelz Kiln Technology (Reduction Roasting) for Processing Chehel-Kureh Complex Sulfide Ore

Peiman Khakbaz[1], Kianoush Barani[*2], Shahab Romiani[3], Mohammad Mahmoudi Maymand[4]

[1]Ahangaran Mining Complex Manager, Sormak Company, Malayer, Iran

[2]Associate professor in Minerals Processing, Lorestan University, Khorramabad, Iran

[4]M.S in minerals processing, Canymes Engineering Company, Tehran, Iran

[4]M.S in minerals processing, Iran National Copper Industries Company, Kerman, Iran

*Corresponding author: barani.k@lu.ac.ir (Kianoush Barani)

Abstract:

The Chehel-Kureh copper deposit in southeastern Iran contains complex sulfide ores rich in copper, lead, and zinc, posing significant challenges for conventional flotation processing. Despite various flotation strategies, the plant has struggled to produce clean copper concentrates and separate lead and zinc products, resulting in low recoveries and environmental concerns due to metal losses in tailings. In this study, the application of Waelz kiln technology—a process commonly used for zinc recovery from metallurgical residues—was investigated as an alternative approach for metal recovery from Chehel-Kureh ore. Reduction roasting experiments were conducted on raw ore, as well as differential and bulk flotation concentrates, using coal as a reductant. The effects of roasting temperature, duration, and coal ratio on metal volatilization were examined. Under optimal conditions, volatilization of lead, copper, and zinc reached 89%, 84%, and 75% for the raw ore; 92%, 62%, and 74% for the differential concentrate; and 68%, 62%, and 43% for the bulk concentrate, respectively. These findings indicate that the Waelz process can achieve high metal volatilization efficiencies, particularly for lead and zinc, offering a promising alternative for pre-treatment and recovery of valuable metals from complex Cu–Pb–Zn ores while potentially minimizing environmental impacts.

Keywords: Chehel-Kureh , Walez technology, Complex ore, Roasting, Reduction

1. Introduction

The Chehell-Kureh mine, located in Sistan and Baluchestan province (in Iran), contains a complex sulfide ore of copper, lead, and zinc. The ore body exhibits a complex structure composed of veins, lenses, and irregular shapes, with mineralization including quartz, dolomite, ankerite, siderite, and calcite, alongside pyrrhotite, arsenopyrite, pyrite, chalcopyrite, marcasite, molybdenite, sphalerite, galena, ilmenite, and rutile. Among these, chalcopyrite, sphalerite, and galena are the economically valuable minerals, occurring in fine to medium grain sizes(Maanijou, Rasa and Lentz, 2008).

Initial metallurgical studies and processing experiments on drill core samples of Chehell-Kureh ore were conducted in 2012 by the Australian company AMMTEC. The results indicated that chalcopyrite, sphalerite, galena, and pyrite are the main sulfide minerals, with minor covellite. Sphalerite commonly occurs as inclusions within chalcopyrite, complicating separation. Efforts to float lead and zinc reduce copper recovery, making it difficult to produce a clean zinc concentrate.

Based on the results of the metallurgical tests and mineralogical studies, a plant flowsheet was designed, incorporating crushing, grinding, and flotation circuits. Mineralogical studies indicated that

valuable minerals are liberated up to 80% at a particle size of 25 µm. Consequently, in the first grinding stage, materials are ground to a D_{80} of 53 µm, followed by a second grinding stage to achieve a D_{80} of 25 µm. Figure 1 illustrates the grinding and flotation circuit of the Chehel-Kureh copper processing plant (Wong and Heyes, 2012).

The Chehel-Kureh processing plant, which began operations in March 2017, continues to face challenges after nearly eight years of operation, especially in producing separate copper, lead, and zinc concentrates. Metallurgical performance evaluations indicate that in differential flotation, approximately 9% of copper and over 80% of lead and zinc are lost to tailings, while in bulk flotation, nearly 10% of copper and 60% of lead and zinc are discarded. The concentrates in both flotation conditions exhibit low copper grades and significant lead and zinc content, complicating the smelting process. Additionally, significant amounts of lead and zinc (are sent to the tailings dam daily, posing environmental risks, especially due to lead's toxicity.
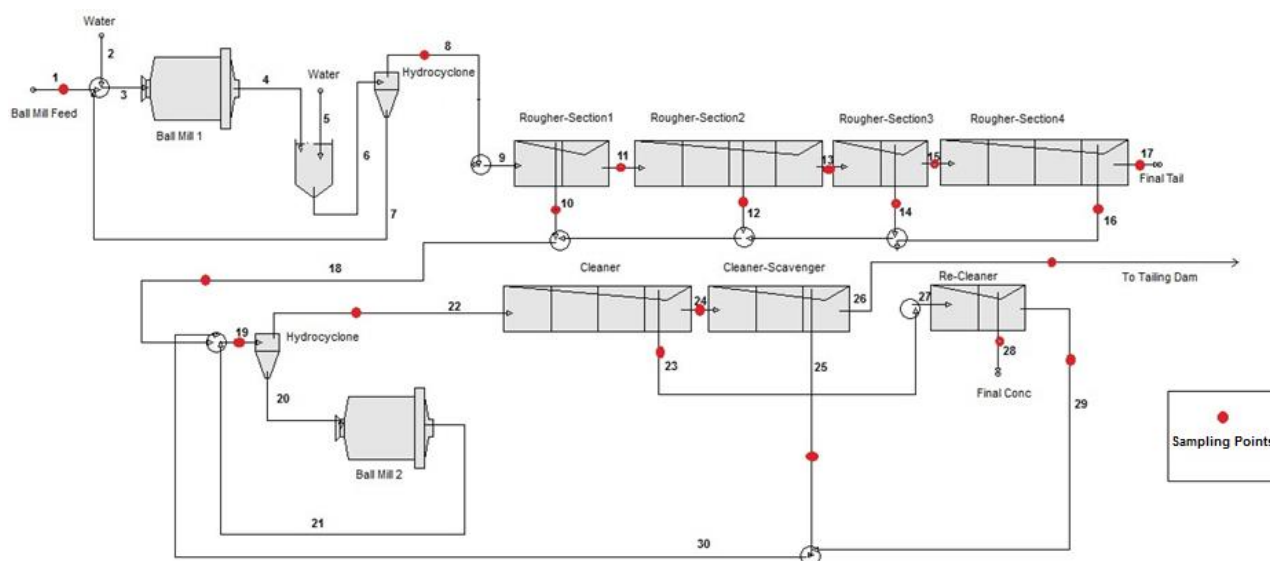
Fig 1. Flowsheet of the grinding and flotation circuit of the Chehell-Kureh copper processing plant

Several studies have been undertaken to address operational challenges at the Chehel-Kureh copper plant and to explore the recovery of lead and zinc from its copper ore. In one such study, conducted by Zarfaravar Company, various ore types from the Chehel-Kureh deposit as well as the plant's copper concentrate were examined using flotation, with the objective of producing separate copper and zinc concentrates(Zarfaravar Engineering Company, no date). The Research Center of the Sarcheshmeh Copper Complex conducted experiments on the Chehel-Kureh copper concentrate with the aim of increasing the copper grade in the copper concentrate and producing a separate zinc concentrate.The results of these studies showed that, despite the use of various depressant systems for lead and zinc, the successful production of a zinc concentrate was not achieved (Complex., 2021).

Despite significant advancements, flotation still faces challenges when processing complex copper-lead-zinc ores, as evidenced by the issues encountered with the Chehel-Kureh ore. A major difficulty is the similar behavior of copper sulfide, galena, and sphalerite, which complicates their separation (Bayraktar, Ipekoglu and Tolun, 1992). This problem is common to many complex copper-lead-zinc ores, where flotation often struggles to efficiently separate these metals. Hydrometallurgical methods are increasingly being explored a viable alternative to flotation for metal recovery. Techniques such as ferric and bioleaching, pressure leaching, roasting, chlorination, nitric-sulfuric acid leaching, glycine leaching, sodium metabisulfate leaching, and hydrogen peroxide leaching have been proposed for copper and zinc recovery (Lorenzo-Tallafigo et al., 2021).

One of the methods or technologies used alongside hydrometallurgy for metal recovery from ores, particularly oxidized ores and especially zinc ores, is Waelz kiln technology. The Waelz process is a

well-known method for recovering zinc and other volatile metals from metallurgical wastes such as electric arc furnace (EAF) dust, leaching residues, and recyclable materials. It uses a rotary kiln to reduce and volatilize metals, which are then recovered from the kiln dust. The process, first patented in 1910 and industrialized in Germany in the 1920s, has been recognized since 2000 as the *Best Available Technology* for EAF dust treatment (Maczek and Kola, 1980; Antuñano, Cambra and Arias, 2019).

The feed for the Waelz kiln can consist of either zinc ore or processed concentrates, and the ZnO grade in the kiln product is directly related to the feed grade. Before feeding, the zinc-bearing material (~74 wt%) is mixed with metallurgical coke or coal (~19 wt%) and lime (~7 wt%), then pelletized. The coal acts primarily as a reductant but also provides heat and promotes fluidization inside the rotating kiln, preventing agglomeration of fine zinc particles (Maczek and Kola, 1980; Antuñano, Cambra and Arias, 2019).

The Waelz process is a continuous high-temperature rotary kiln method (1000–1500°C) used for recovering zinc and other low-boiling-point metals. The key chemical reactions in the kiln include:

$$ZnO + C \rightarrow Zn \text{ (vapor)} + CO \tag{1}$$

$$Zn \text{ (vapor)} + CO + O_2 \rightarrow ZnO + CO_2 \tag{2}$$

$$ZnS + CaO + C \rightarrow Zn \text{ (vapor)} + CaS + CO \tag{3}$$

Zinc compounds in the feed are reduced, vaporized, and then condensed into zinc oxide powder using filters. The kiln achieves up to 97% recovery efficiency. Along with zinc, the oxide product may contain lead, cadmium, silver, and halogen compounds, which can be recovered by leaching.

In a review of the literature on the use of the Waelz process for the recovery of metals such as lead, zinc, and copper from ores or concentrates, limited research was found. Most of the available articles focused on the recovery of zinc from electric arc furnace dust, rather than from traditional lead-zinc-copper ores or concentrates. However, a study from a lead-zinc mine in South Africa presented an example where one of the plant's products is a silicate zinc concentrate (willemite) containing 45% zinc, produced at a rate of 3000 tons per month using flotation. Due to the fine particle size of this silicate zinc, significant amounts are not recoverable by flotation and are instead discarded as tailings, which still contain 18% zinc. In 1976, German researchers explored the recovery of zinc from both the concentrate and its tailings using the Waelz process on a pilot scale. The results showed that 90% of the zinc vaporized before reaching 1100°C, ultimately producing a zinc oxide product containing 63% zinc and 10% lead (Clay and Schoonraad, 1976).

In Hamadan Province, at the Ahangaran lead-zinc mine near Malayer, a Waelz kiln production line is in operation. The feed for this line consists of low-grade oxide ore from the mine. The process produces a product containing both zinc and lead, which is then subjected to leaching. Zinc is dissolved and separated through cementation, while lead remains in the final solid form. Both products are subsequently sold. According to the plant's data, the Waelz process at Ahangaran achieves 85-95% zinc recovery and approximately 90% lead recovery from the initial feed.

In this study, the potential of applying Waelz kiln technology for metal recovery from the Chehel-Kureh copper ore was investigated.

2. Materials and Methods

2.1. Sampling

Sampling was conducted from both the primary ball mill feed (raw ore) and the flotation concentrates. The plant initially operated under a differential flotation circuit (targeting copper flotation while suppressing lead and zinc) until June 15, 2023. After this date, the circuit was modified to implement bulk flotation of copper, lead, and zinc. However, in spring 2024, the plant returned to the differential flotation configuration. Accordingly, grid-based sampling was performed from both the differential

and bulk flotation concentrate stockpiles. Sampling of the plant feed was carried out over a 2h period, with samples taken every 15 mins and combined to form a representative sample.

The flotation concentrates had a particle size of d_{80} = 25 μm. The plant feed was also ground to d_{80}=25 μm. After homogenization, 30 g subsamples were prepared for reduction roasting experiments to evaluate the applicability of the Waelz kiln process.

2.2. Materials Characteristics

The chemical composition of the raw ore, the differential flotation concentrate, and the bulk flotation concentrate was determined. The concentrations of copper, lead, zinc, and iron were measured using wet chemistry methods. The results are presented in Table 1.

Table 1. Chemical analysis of the samples

Sample	Fe (%)	Cu (%)	Pb (%)	Zn (%)
Raw Ore	7.68	0.74	1.25	2.53
Differential Flotation Conc.	17.21	13.74	5.23	10.66
Bulk Flotation Conc.	18.90	11.65	6.32	11.48

2.3. Reduction Roasting Experiments

The reduction roasting experiments were carried out on the raw ore sample, bulk flotation concentrate, and differential flotation concentrate. In each experiment, a certain amount of powdered coal was mixed with 30g of the sample and heated in a programmable laboratory furnace capable of reaching temperatures up to 1200°C, for a specified time and temperature. The percentage of coal, roasting temperature, and roasting time were varied and studied to investigate their effects on the reduction roasting process. The weight of the sample was determined after the experiment was completed, and the roasted material was chemically analyzed by wet chemistry methods to measure copper, lead, zinc, and iron content. Based on the weight of the sample before and after roasting, as well as the chemical analysis before and after roasting, the evaporation percentages of copper, lead, zinc, and iron were calculated. All experiments and the chemical analyses were performed at the Ahangaran Lead and Zinc Complex in Malayer.

3. Results and Discussions

3. 1. Analysis of experiments on the raw ore sample

Fig 2 shows the effect of increasing the amount of coal on the evaporation of metals for the ore sample at a temperature of 950°C after 1h. It can be observed that with an increase in the amount of coal, the amount of metal evaporation increases. Generally, the metals lead, copper, zinc, and iron have the highest evaporation rates in that order. Given that the evaporation percentage of the metals is less than 80%, the reduction roasting temperature was increased in subsequent experiments.

Fig 3 shows the effect of increasing the amount of coal on the evaporation of metals for the ore sample at a temperature of 1100°C after 1h. It can be observed that with an increase in the amount of coal, the amount of metal evaporation did not significantly increase (except for zinc). Under the best conditions (20% by weight of coal, 1100°C, and one hour), 89% of lead, 84% of copper, and 74% of zinc entered the vapor phase. This indicates that, aside from economic considerations, the Wells furnace technology is feasible for the raw ore sample.

Fig 2. Effect of increasing the amount of coal on the evaporation of metals for the raw ore sample (temperature of 950°C and time of 1h)

Fig 3. Effect of increasing the amount of coal on the evaporation of metals for the raw ore sample (temperature of 1100°C and time of 1h)

3. 2. Analysis of experiments on the bulk flotation concentrate

Fig 4 illustrates the effect of increasing coal content on the extent of metal evaporation from the bulk flotation concentrate at 950°C and a duration of 1h. The results indicate generally low evaporation rates for all metals under these conditions. The highest evaporation occurred at 20 wt.% coal, where 20% of iron, 17% of copper, 12% of zinc, and 7% of lead transitioned into the vapor phase. These modest rates prompted further experiments with increased coal content and higher roasting temperatures.

Fig 5 presents the effect of coal addition on metal evaporation from the bulk flotation concentrate at an elevated temperature of 1100°C, also for 1h. It was observed that even at this higher temperature, the evaporation of copper, lead, and zinc remained below 40% across all conditions tested. The maximum evaporation was achieved at 40 wt.% coal, resulting in 60% of iron, 37% of copper, 37% of lead, and 30% of zinc being evaporated. Due to the still limited volatilization of the target metals, subsequent experiments focused on further increasing the coal content, roasting temperature, and duration.

Fig 6 demonstrates the impact of temperature on the evaporation of metals from the bulk flotation concentrate using 45 wt.% coal. At a temperature of 1150°C, the evaporation rates significantly improved, with 72% of iron, 68% of lead, 62% of copper, and 43% of zinc entering the vapor phase. These conditions yielded the most favorable results for the bulk concentrate. However, partial melting of the sample was observed at this temperature, leading to adhesion to the refractory brick surface. Additionally, increasing the roasting time to 2h at 1100°C did not result in further enhancement of metal evaporation.
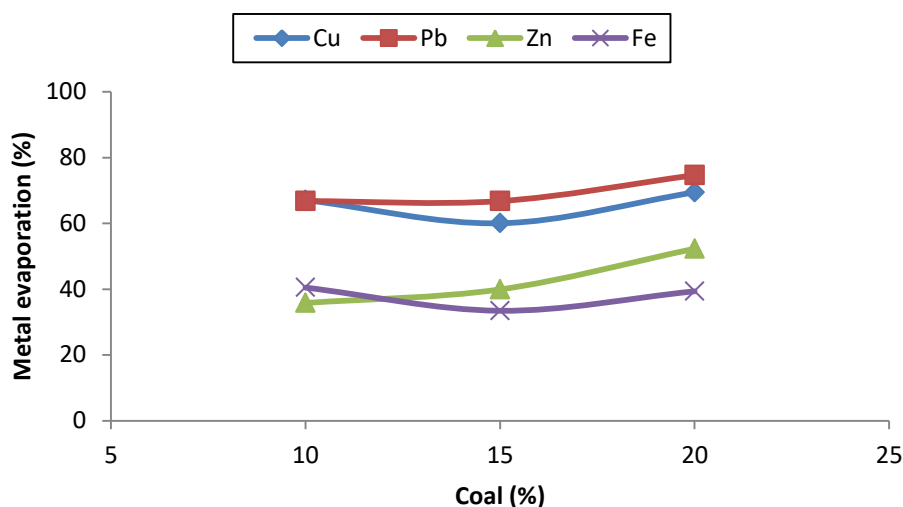

Fig 4. Effect of increasing the amount of coal on the evaporation of metals for the bulk concentrate sample (temperature of 950°C and time of 1h)
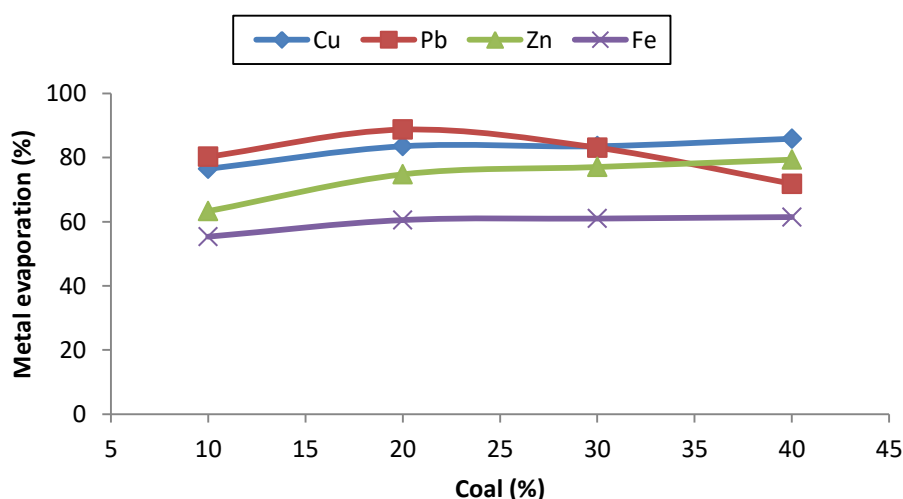

Fig 5. Effect of increasing the amount of coal on the evaporation of metals for the bulk concentrate sample (temperature of 1100°C and time of 1h)

Fig 6. Effect of increasing the amount of coal on the evaporation of metals for the bulk concentrate sample (different condition)

3. 3. Analysis of experiments on the differential flotation concentrate

Fig 7 illustrates the effect of increasing coal content on the evaporation of metals from the differential flotation concentrate at 950°C for 1h. As shown, metal evaporation remains low under all conditions tested. The maximum evaporation occurred at 20 wt.% coal, where 8% of iron, 21% of copper, 39% of zinc, and 19% of lead were volatilized. Based on these results, subsequent experiments were conducted at higher coal percentages and elevated roasting temperatures.

Fig 8 shows the effect of coal addition on metal evaporation from the differential flotation concentrate at 1100°C for 1h. The results indicate that increasing the coal content leads to enhanced metal evaporation. The highest evaporation values were observed in the order of lead > zinc > copper > iron. At 40 wt.% coal, 92% of lead, 74% of zinc, 62% of copper, and 58% of iron were transferred to the vapor phase. To further improve the volatilization of metals, later experiments involved increasing the coal content, temperature, and roasting time.

Fig 9 presents the effect of increasing temperature on metal evaporation from the differential flotation concentrate using 45 wt.% coal and a roasting time of 1.5 h. At 1150°C, 90% of lead, 55% of iron, 67% of zinc, and 66% of copper were evaporated. However, it was observed that at this temperature, the sample partially melted and adhered to the surface of the refractory brick.
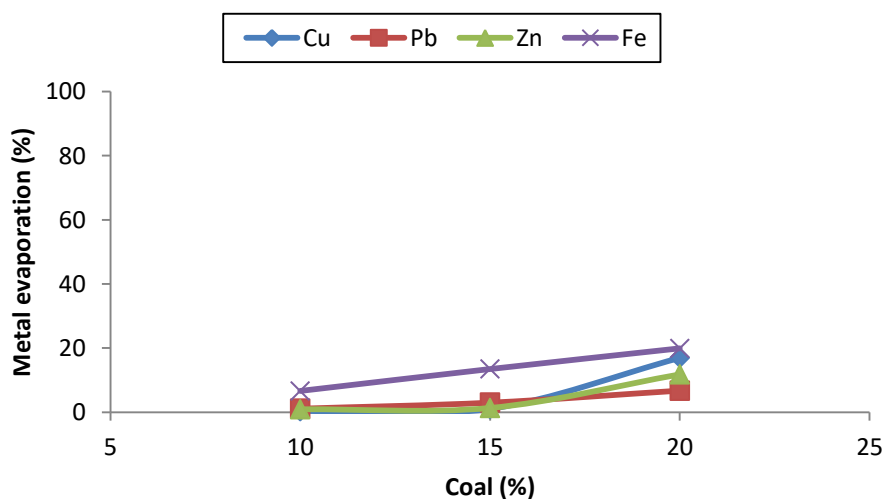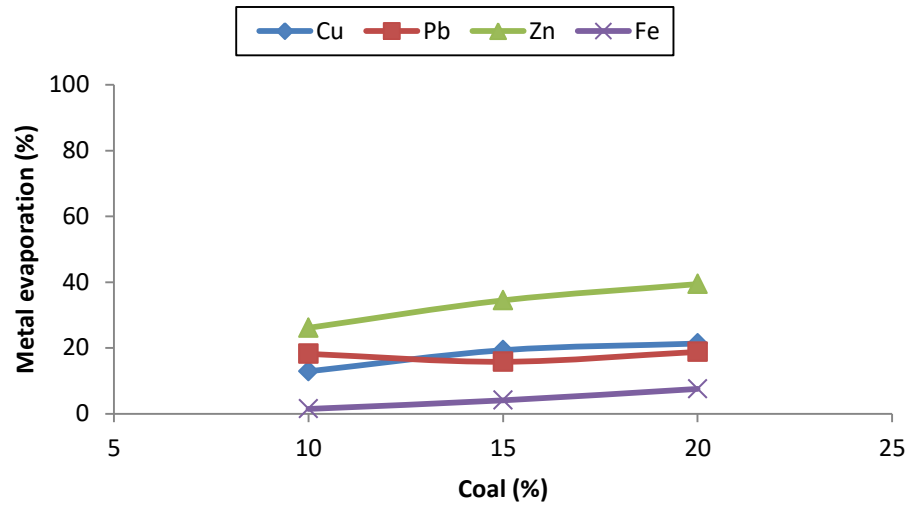
Fig 7. Effect of increasing the amount of coal on the evaporation of metals for the differential concentrate sample (temperature of 950°C and time of 1h)
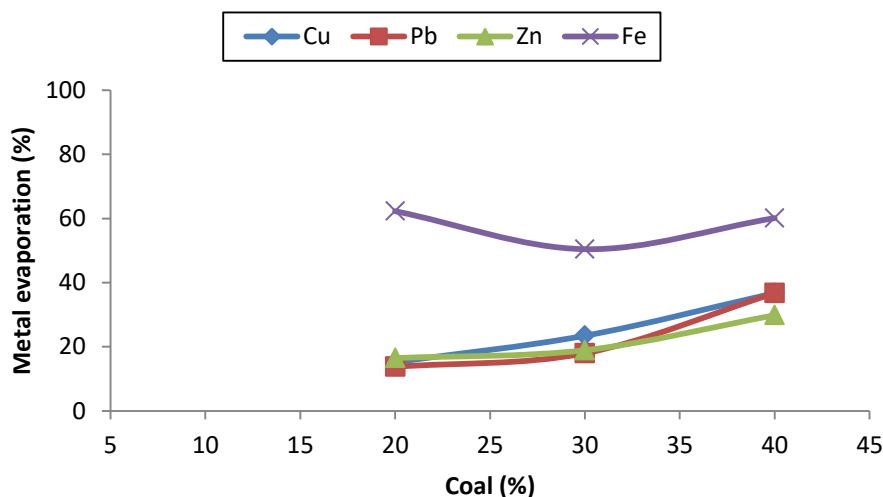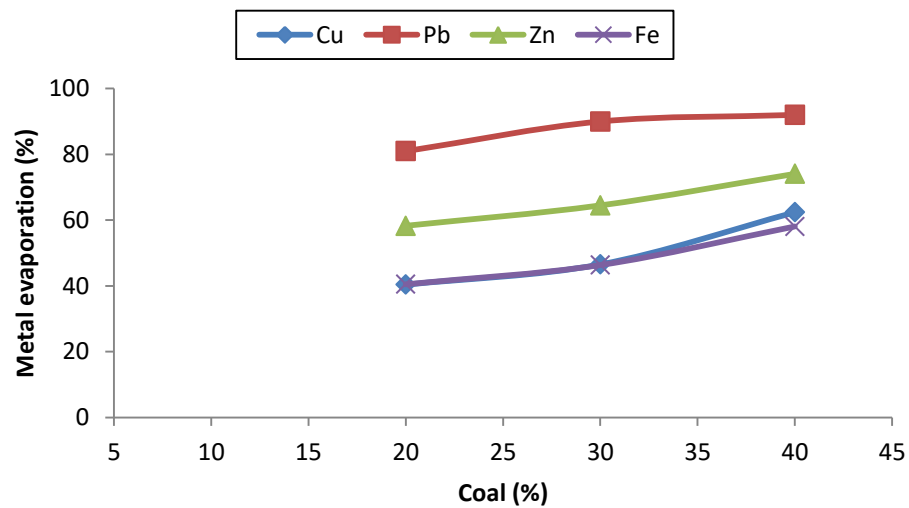

Fig 8. Effect of increasing the amount of coal on the evaporation of metals for the differential concentrate sample (temperature of 1100°C and time of 1h)
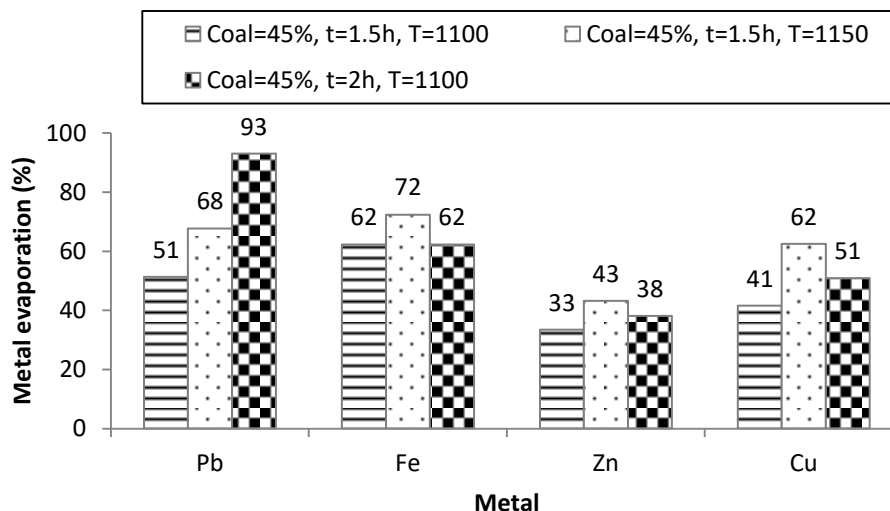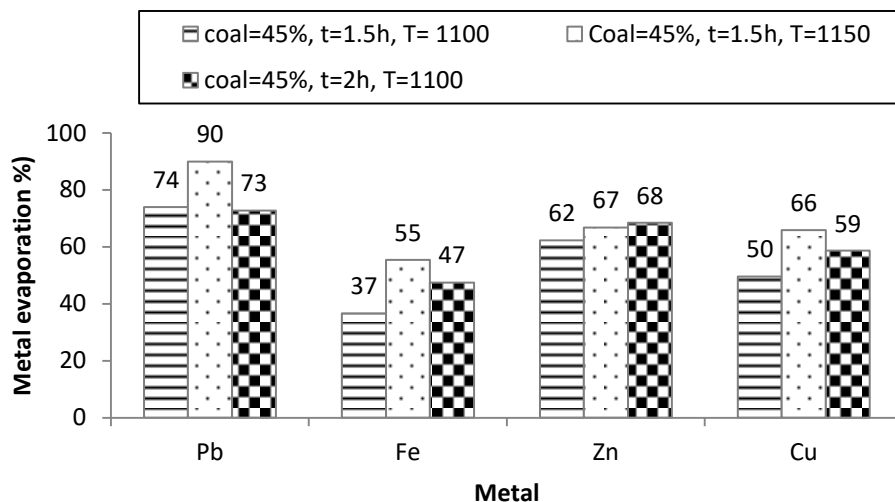
Fig 9. Effect of increasing the amount of coal on the evaporation of metals for the differential concentrate sample (different condition)

3. 4. The optimal conditions

Based on the highest metal vaporization percentages, the optimal conditions for the reduction roasting experiments of all three samples are presented in Table 2.

Table 2. Optimal reduction conditions for maximum metal vaporization

sample	Coal content (wt. %)	Roasting temp (℃)	Roasting time (h)	Metal evaporation (%)			
				Cu	Zn	Fe	Pb
Raw Ore	20	1100	1	83.55	74.78	60.52	88.74
Differential Flotation Conc	45	1150	1.5	62.44	43.19	72.35	67.66
Bulk Flotation Conc	40	1100	1	62.37	74.06	58.07	91.98

4. Conclusion

The results of the reduction roasting experiments demonstrated that metal volatilization efficiency is significantly influenced by sample type and roasting conditions, including coal content, temperature, and duration. For the raw ore, the highest metal evaporation was achieved at 20 wt% coal, 1100 °C, and 1 hour of roasting, with lead, copper, and zinc volatilization reaching 89%, 84%, and 75%, respectively. In the case of the bulk flotation concentrate, optimal results were obtained under more intense conditions—45 wt% coal, 1150 °C, and 1.5 hours—resulting in 68% lead, 62% copper, and 43% zinc vaporization. Meanwhile, the differential flotation concentrate showed the highest volatilization rates at 40 wt% coal, 1100 °C, and 1 hour, with 92% lead, 62% copper, and 74% zinc being evaporated.

These findings suggest that the differential concentrate is more responsive to reduction roasting under moderate conditions compared to the bulk concentrate, which required higher coal content and temperature to achieve acceptable volatilization levels. Furthermore, an inverse correlation was observed between the initial metal grade and its volatilization percentage, indicating that higher metal concentrations in the feed may inhibit efficient vapor-phase transfer during roasting. This trend was

particularly evident for copper, where increasing the feed grade from 0.4% to 6% reduced its volatilization from 83% to 62%, with minimal further reduction at grades above 6%.

Due to limitations in the laboratory-scale furnace setup, it was not possible to collect and condense the volatilized metals in the form of fume or dust, and therefore leaching experiments on the collected product were not conducted. However, for further research and better process evaluation, it is recommended to perform pilot-scale roasting tests under optimized conditions where dust collection systems are employed. Leaching experiments can then be carried out on the collected dust to assess metal recovery efficiency. Given that such fume products are typically oxide-rich in nature, it is expected that more than 90% of copper and zinc could be dissolved through acid leaching.

Finally, economic considerations must be taken into account to determine whether the combination of a Waelz kiln-based volatilization process followed by leaching of the collected dust is both energy-efficient and economically viable at industrial scale.

References:

Antuñano, N., Cambra, J.F. and Arias, P.L. (2019) 'Hydrometallurgical processes for Waelz oxide valorisation--An overview', *Process Safety and Environmental Protection*, 129, pp. 308–320.

Bayraktar, I., Ipekoglu, U.A. and Tolun, R. (1992) 'Features and flotation of complex Cu-Pb-Zn sulphides', pp. 307–330. Available at: https://doi.org/10.1007/978-94-011-2658-8_16.

Clay, J.E. and Schoonraad, G.P. (1976) 'Treatment of Zinc Silicates By the Waelz Process.', *Journal of The South African Institute of Mining and Metallurgy*, 77(1), pp. 11–14.

Complex., R.C. of S.C. (2021) *Separation of the Chehel-Kureh copper-zinc concentrate into copper concentrate and zinc concentrate*.

Lorenzo-Tallafigo, J. *et al.* (2021) 'A novel hydrometallurgical treatment for the recovery of copper, zinc, lead and silver from bulk concentrates', *Hydrometallurgy*, 200, p. 105548.

Maanijou, M., Rasa, I. and Lentz, D. (2008) 'Petrography and alteration of Chehelkureh copper deposit: Mass balance of elements and behavior of REE', *Journal of Geoscience*, 17(67), pp. 86–101.

Maczek, H. and Kola, R. (1980) 'Recovery of Zinc and Lead From Electric-Furnace Steelmaking Dust At Berzelius.', *Journal of Metals*, 32(1), pp. 53–58. Available at: https://doi.org/10.1007/bf03354543.

Wong, K.Y. and Heyes, G.W. (2012) *Chehel-Kureh copper mine metallurgical testing repor (AMMTEC Report)*.

Zarfaravar Engineering Company (no date) *Studies on the separation of lead and zinc from the Chehel-Kureh copper concentrate*.

Study on the Enrichment of Copper Oxide-Sulphide Ore Samples by Flotation Method

Hossein Hamedani[1], Arash Sobouti[2], Mohammad Baqaeifar [3], Bahram Rezai[4*], Fatemeh Sadat Hoseinian[5]

1- Msc student, Department of Mining Engineering, Amirkabir University of Technology, Tehran. hosien.hamadani@aut.ac.ir

2- Ph.D. Candidate, Department of Mining Engineering, Amirkabir University of Technology, Tehran. Arash.sobouti@aut.ac.ir

3- Msc student, Department of Mining Engineering, Amirkabir University of Technology, Tehran. mohammad.b@aut.ac.ir

4- Professor, Department of Mining Engineering, Amirkabir University of Technology, Tehran. Rezai@aut.ac.ir

5. Assistant professor, Department of Mining Engineering, Amirkabir University of Technology, Tehran. f_hoseinian@aut.ac.ir

*Corresponding author: e-mail (Rezai@aut.ac.ir)

Abstract:

In this study, a representative sample was initially prepared from exploratory drilling cores, followed by identification and characterization studies. Based on XRD analysis, the sample consists primarily of quartz, kaolinite, muscovite-illite, calcite, potassium feldspar, albite, dolomite, siderite, and chalcopyrite. Optical and scanning electron microscopy studies revealed that the sulfide minerals in the sample include chalcopyrite, chalcocite, and pyrite, with the most significant copper minerals primarily comprising chalcopyrite, chalcocite, and malachite. No free gold was observed, and gold mainly exists as a substitute within the structure of sulfide minerals. AAS analysis results indicated that the copper grade in the sample is 0.99%. To investigate the flotation of copper minerals, influential parameters such as pH, collector concentration, frother concentration, sodium sulfide concentration, and the effect of particle size were examined. The results demonstrated that under optimal conditions (pH = 11, collector concentration of 100 g/t potassium amyl xanthate (PAX), 100 g/t sodium isopropyl xanthate (SIPAX), 60 g/t frother methyl isobutyl carbinol (MIBC), and 1000 g/t Na2S at a particle size of d_{80}= 75μ), the total copper grade and recovery following two stages cleaner flotation were achieved at 21.2% and 60.2%, respectively.

Keywords: chalcopyrite, pH, flotation, collector concentration, Na_2S concentration.

1. Introduction

Copper is a strategic metal used in many industries, including electronics, construction, energy, and automotive. Given the growing demand for this metal, the extraction and processing of its mineral resources are of paramount importance. Copper occurs naturally in two forms: oxide ore and sulphide ore, each presenting unique characteristics and challenges. Sulphide ores, including minerals such as chalcocite and chalcopyrite, are more commonly processed using flotation methods, whereas oxide ores like malachite and azurite typically require hydrometallurgical processes. Due to the depletion of high-grade sulphide deposits and the increased extraction from oxide-sulphide sources, the development and optimization of concentration methods for these ores are essential (Yu et al. 2025; Sokolović et al. 2019; Bozhkov et al. 2024; Potysz et al. 2015).

The flotation process, which extensively concentrates sulphide minerals, is one of the most important methods for concentrating copper ores (Khoso et al. 2020; Geng, Han, and Wen 2024). This process operates based on the differences in the surface properties of valuable minerals and gangue, incorporating the use of chemicals like collectors, frothers, and other reagents to enhance mineral separation. Various factors such as the chemical composition of the ore, type and concentration of

collector, pH levels, and operational conditions have a direct impact on the efficiency of this method. For example, thiol-based collectors, such as xanthates, are effective for the flotation of sulphide minerals, while oxide minerals require pre-activation with sodium sulphide to become suitable for collector adsorption (Khoso et al. 2020; Zhang et al. 2025).

Lee et al. (2009) investigated the effect of n-octyl hydroxamate as a collector for the simultaneous recovery of copper sulphide and oxide minerals. Their results indicated that this collector enhanced the recovery of malachite and azurite (Lee et al. 2009). Additionally, Bulatović et al. (2010) demonstrated that the use of depressants, such as sodium silicate and sodium carbonate, significantly improved flotation selectivity and reduced the impact of gangue impurities (Srdjan 2007).

Further studies have shown that combining thiol and amine collectors can lead to higher copper recovery from oxide-sulphide ores. Fuerstenau et al. (2007) assessed how the oxidized or sulphide nature of copper ores affects flotation performance. They found that sulphide ores are typically well-flotated using xanthate collectors, whereas oxide ores require a pre-activation stage (Fuerstenau, Jameson, and Yoon 2007). Koleini et al. (2013) optimized the selective flotation process of chalcopyrite, sphalerite, and pyrite from the copper-zinc ore of the Taknar mine. The results indicated that the most effective parameter for copper and zinc recoveries in the copper concentrate was the type of collector mixture. The optimization results demonstrated that by maximizing copper recovery, the respective recoveries of copper, zinc, and pyrite were 89.04%, 25.3%, and 2.02%, achieved using a mixture of sodium isopropyl xanthate and sodium di-butyl dithiophosphate as collectors, dextrin as a pyrite depressant, 500 g/t of zinc sulfate, and a pH of 11.35 (Koleini, Soltani, and Abdollahy 2013). Ghodrati et al. (2013) optimized the concentration of chemical reagents used in the copper flotation process of the Shahre Babak complex through statistical design. The optimal conditions for achieving a maximum copper recovery of 91.31% were identified as follows: sodium isopropyl xanthate collector at 8.99 g/t, thionocarbamate collector at 22.8 g/t, dithiophosphate collector at 5.05 g/t, frother A65 at 12.52 g/t, and frother A70 at 7.68 g/t (M.A. Saeed Ghodrati 2013). Additionally, Wills and Finch (2015) studied the optimization of flotation process through precise control of operational parameters is crucial for improving efficiency and reducing processing costs (Wills and Finch 2015).

Marion et al. (2017) conducted a study investigating the effect of the structure of seven hydroxamic acid collectors on the flotation of malachite, finding that certain collectors, such as benzohydroxamic acid and C8 alkyl hydroxamate, demonstrated superior performance in flotation (Marion et al. 2017). Additionally, Zarei Varzeqan (2017) showed in a study that the use of potassium octyl hydroxamate at a dosage of 10 g/t could increase the recovery of oxide copper by up to 74.46%. Furthermore, the simultaneous use of ammonium sulphide and hydroxamates improved oxide copper recovery to 77.31% (Ahad Zare Varzeghan 2017).

Barfeyi and Paraspoor (2022) examined the effect of pH and chemical reagents on froth stability using a sample obtained from the copper processing plant in Mohammadabad Delijan, employing the Taguchi method. The results showed that the best froth stability happened at a pH of 11.2, using 20 g/t of sodium isopropyl xanthate collector, 15 g/t of di-thiophosphate collector, 20 g/t of the frother MIBC, and 15 g/t of the frother Dowfroth 250 (Barfaei and Parsapour 2022).

Recent studies indicate that the direct flotation method for recovering copper from copper smelting slag (CSS) faces limitations due to the high malleability of metallic copper and difficulties in grinding, often resulting in recovery rates of less than 90%. A study conducted by Jianjun et al. (2024) showed that combining gravity separation and flotation can more effectively recover copper from CSS and improve the overall process efficiency by reducing the copper grade in the tailings. These findings may also be beneficial in optimizing the concentration of oxide-sulphide copper ores (Sun et al. 2024).

Conventional collectors such as xanthates cannot directly flotate oxide minerals, which constitute a portion of copper deposits. In recent years, the sulphide-coating method for copper oxide minerals followed by flotation with xanthate collectors has gained attention, especially in areas like the Bouji region, which contains both sulphide and oxide copper minerals. The primary challenge in the processing and concentration of copper ores from this region lies in the presence of copper oxide

181

minerals that typically cannot be floated with conventional collectors like xanthates. As such, the processes for concentration and optimized methods for recovering copper from these minerals remain incompletely identified. Additionally, there isn't enough information about the exact details of the minerals, the characterization of waste minerals, and gold-containing minerals, especially using modern methods like scanning electron microscopy (SEM). The aim of this research is to first perform detailed identification and characterization from the perspective of mineral processing for samples from the Bouji region. In this study, SEM equipped with WDX was used, along with element distribution mapping, to accurately identify copper minerals, accompanying gangue minerals, and gold-bearing minerals. Subsequently, to achieve appropriate grade and recovery, flotation methods were applied, examining optimal levels of effective parameters such as pH, collector concentration, frother concentration, and Na_2S concentration.

2. Material and methods

2.1. Material

Approximately 120 kg of representative samples were obtained from the core drillings of the Bouji ore deposit, located 65 km east of Zanjan. The samples were crushed using jaw and roll crushers to a size of less than 2 mm. After homogenization, the samples were further ground in a ball mill according to liberation studies to a size of 80% passing 75 μm (d80) for flotation tests.

To identify the chemical composition of the sample, X-ray fluorescence (XRF) analysis was conducted using the X Unique II model from Philips. For identifying the present minerals, X-ray diffraction (XRD) analysis was performed using the X'Pert MPD model from Philips. The quantitative determination of the elements in the sample was carried out using Atomic Absorption Spectroscopy (AAS). Additionally, for more precise identification of minerals and calculating the degree of liberation of copper-bearing minerals, petrographic and mineralographic studies were conducted using optical and electron microscopy, utilizing polished and thin sections.

After preparing the polished sections, studies were continued with the XL 30 model scanning electron microscope from Philips, equipped with WDX, along with the preparation of element distribution maps. When using the Backscattered Electron (BSE) detector for imaging, heavier minerals stand out clearly, and the image gets dimmer as the average atomic number of the mineral decreases.

2.2. Chemicals Used

Various chemicals were utilized for the flotation experiments (Table 1).

Table 1 - Specifications of the chemicals used in flotation experiments

Chemical Reagent	Chemical Formula	Role and application
Potassium Amyl Xanthate (PAX)	$C_5H_{11}OCS_2K$	Collector
Sodium Isopropyl Xanthate (SIPAX)	$C_3H_5S_2Na$	Collector
Sodium Sulfide	Na_2S	Activator
Methyl Isobutyl Carbinol (MIBC)	$C_6H_{13}OH$	Frother
Calcium Carbonate	$CaCO_3$	pH Regulator
Sulfuric Acid	H_2SO_4	pH Regulator

2.3. Flotation Experiments

In all flotation experiments, 1 kg of sample were mixed with water to prepare a pulp with 30% solids, which was then transferred to a flotation cell in the Denver laboratory. Figure 1 shows a view of the flotation cell used in the Denver laboratory. Subsequently, chemicals including pH regulator,

activator, collector, and frother were added to the pulp. After a set preparation time, the aeration process was conducted. Finally, the froth collection was performed. The collected concentrate and the remaining tailings in the cell were weighed after filtration and drying. After each experiment, we determined the grades of the concentrate and tailings by sampling each using an atomic absorption device. With the grade and weight available, the recovery for each test was calculated using Equation (1). Additionally, all data were mass balanced, and tests with high mass balance errors were repeated.

$$R = \frac{C.c}{F.f} \times 100 \tag{1}$$

Where:

C: weight of the concentrate (g)

c: copper grade in the concentrate (%)

F: weight of the feed (g)

f: copper grade in the feed (%)

Figure 1 - Denver laboratory flotation cell used

Following crushing by jaw, cone, and cylindrical crushers, the ore underwent size analysis and grinding in a ball mill based on liberation studies. According to Table (2) and Figure (2), 80% of the particles are less than 75 microns (d_{80} = 75 µm).

Table 2 - Particle Size Analysis

Sieve Size (µm)	Weight Percent Retained (%)	Cumulative Percent Retained (%)	Cumulative Percent Passing (%)
+177	0.5	0.5	99.5
+149 –177	0.75	1.25	98.75

+105 –149	2.25	3.5	96.5
+74 –105	7.0	10.5	89.5
+53 –74	20.5	31.0	69.0
+44 –53	28.5	59.5	40.5
-44	40.5	100.0	0.0
Total	100	---	---
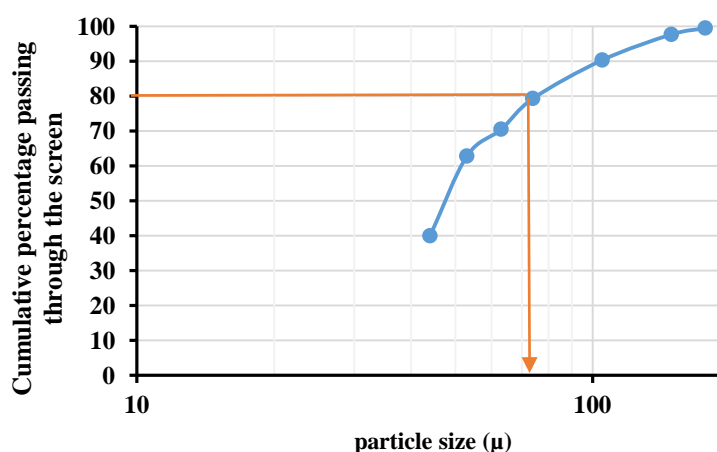
Figure 2: **Particle Size Analysis curve**

3. Results and discussions

3.1 Results of Optical Microscope Studies

According to Figure 3, the optical microscope studies showed that the copper minerals in the sample are mostly chalcopyrite and malachite. Some of the chalcopyrites are changing due to iron hydroxide, which is replacing them with malachite, chalcocite, and quartz. Some chalcopyrites are being replaced by malachite, chalcocite, and quartz due to iron hydroxide. Chalcopyrite alteration products have more iron hydroxide and malachite than the others, but chalcocite and quartz are much less. Bornite is also present in minimal amounts, mainly as minor intergrowths with chalcopyrite. Magnetite is primarily observed in semi-mafic volcanic rocks, where its occurrences are quite limited. Hematite is also present in low amounts, occurring as aggregates of platy-shaped crystals in a few samples.

The most common pairing of chalcopyrite grains, especially in the larger pieces, is with non-metallic gangue minerals. Due to the nature of the deposit, some chalcopyrite particles are being substituted by iron hydroxide; the most significant association of chalcopyrite occurs with gangue minerals and iron hydroxides, specifically limonite and goethite. In finer fractions (250–150 microns) and smaller fractions, the association of chalcopyrite is mainly with iron hydroxides. For malachite, it is mixed with non-metallic minerals, and in smaller sizes, it is found together with iron hydroxide. Overall, the abundance of chalcopyrite is approximately 2 to 2.5%, while the abundance of malachite is around 1%.
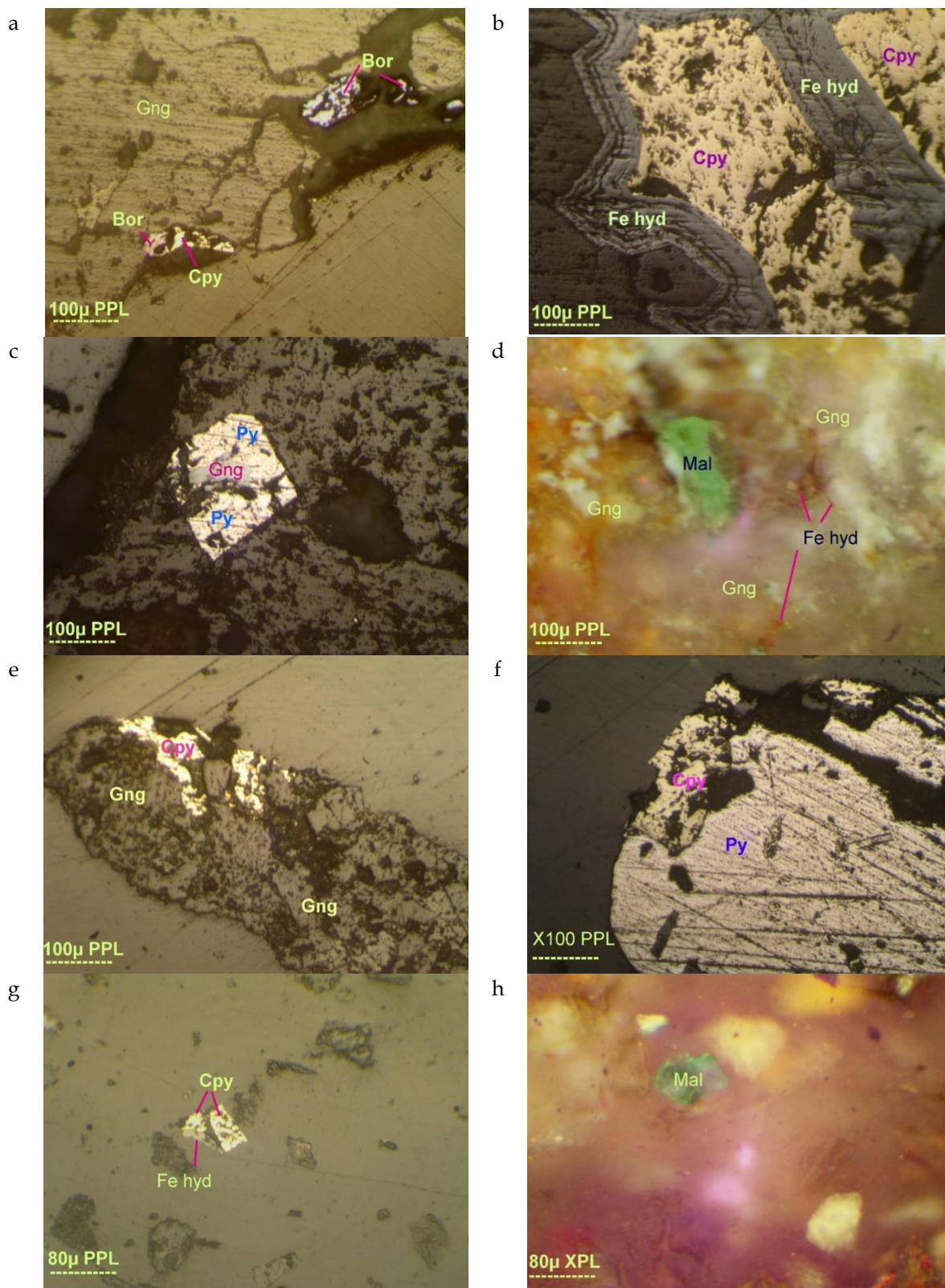
Figure 3 illustrates various associations within the studied fractions: (a) the association of chalcopyrite (Cpy) with bornite (Bor) and gangue, as well as the association of bornite with gangue (Gng) in the 2830+ micron fraction; (b) chalcopyrite (Cpy) undergoing substitution by iron hydroxide (Fe hyd) in the 2830+ micron fraction; (c) the association of pyrite (Py) crystals with gangue in the 2830+ micron

fraction; (d) the association of malachite (Mal) with gangue in the 2830+ micron fraction; (e) the association of chalcopyrite particles with gangue in the -500+350 micron fraction; (f) the association of chalcopyrite with pyrite in the -500+350 micron fraction; (g) the association of chalcopyrite and iron hydroxide in the -75+62 micron fraction; and (h) a free malachite particle in the -75+62 micron fraction.

3.2. XRD, XRF, and AAS Analysis

The results of the XRD analysis confirmed the findings from the microscopic studies. Figure 4 and Table 4 show that the main minerals in the sample are mostly quartz, kaolinite, muscovite-illite, calcite, potassium feldspar, albite, dolomite, siderite, and chalcopyrite. Additionally, the results of the XRF analysis are presented in Table 5, indicating a loss on ignition (L.O.I) of approximately 7.32%, which includes carbonates, sulphates, and water in the sample. The AAS analysis revealed that the copper and gold grades in the sample were 0.99% and 1616 ppb, respectively. The amount of oxidized copper in the sample was 0.43%. Due to the low gold content, identifying associated minerals through XRD analysis and optical microscopy was not feasible. Therefore, to identify gold-bearing minerals, SEM equipped with WDX was utilized.
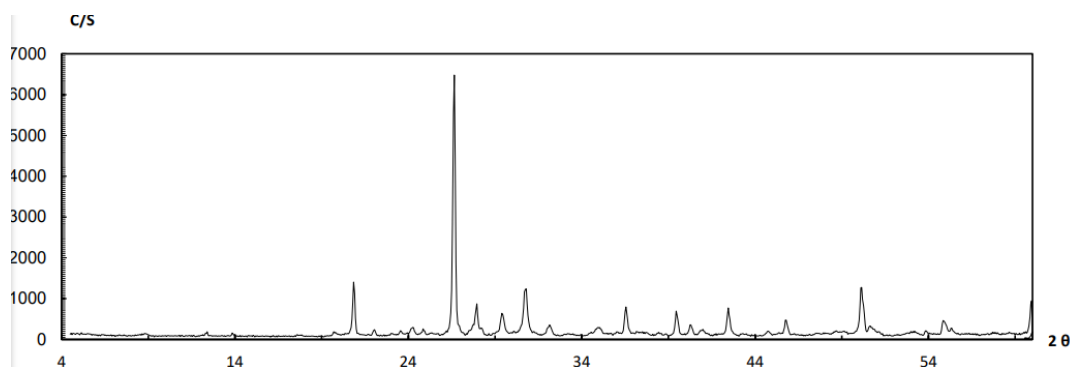
Figure 4 XRD of ore Sample

Table 4 - X-ray Diffraction Analysis

Mineral Name	Chemical Formula
Quartz	SiO_2
Albite	$NaAlSi_3O_8$
Muscovite	$KAl_2[(OHF)_2-AlSi_3O_{10}]$
Dolomite	$CaMg(CO_3)_2$
Siderite	$FeCO_3$
Calcite	$CaCO_3$
Kaolinite	$Al_2Si2O_5(OH)_4$
Calcite	$CaCO_3$
Orthoclase Feldspar	$KAlSi_3O_8$
Chalcopyrite	$CuFeS_2$

Table5 – Chemical composition of sample determined by XRF

SiO_2	Al_2O_3	CaO	Fe_2O_3	K_2O	MgO	MnO	Na_2O	P_2O_5	SO_3	TiO_2	Cu	LOI
62.74	8.95	4.66	7.44	1.8	1.58	0.45	1.38	0.13	2.15	0.46	0.99	7.32

3.3. SEM Studies

The findings from the scanning electron microscope studies of the sample are shown in element distribution maps in Figures 5, 6, and 7. Figure 5 shows the association of chalcocite and pyrite particles in the 150-105 micron size fraction. Analysis of these particles and the X-ray mapping of copper, iron, sulfur, and gold indicates that the light-colored mineral is chalcocite due to the simultaneous presence of copper and sulfur, while the dark portion is pyrite due to the simultaneous presence of iron and sulfur. It is evident that both minerals contain some gold in their structure. Figure 6 depicts the free and associated particles of valuable minerals and gangue in the 150-105 micron size fraction. The light-colored, free mineral in this image is chalcopyrite, which has copper and some gold in its structure. Figure 7 displays several free and associated heavy mineral particles and gangue together in the 75-62 micron size fraction. An analysis of some of the light-colored particles suggests the presence of two chalcopyrite particles along with one iron oxide particle. The brighter particles are identified as chalcopyrite containing copper, iron, and sulfur along with some gold in their structure, while the darker particle is due to the presence of iron without other elements, indicating iron oxide.
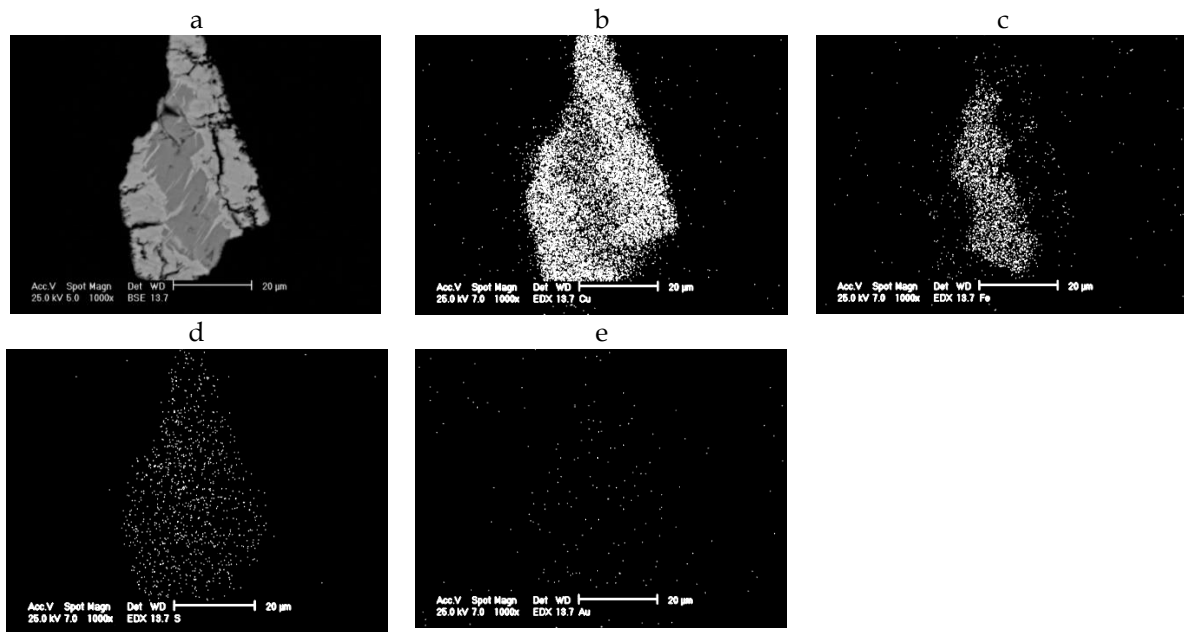
Figure 5: a) The interaction of chalcocite and pyrite within the particle size fraction of 105-150 microns. b) Distribution map of Cu in image a. c) Distribution map of Fe in image a. d) Distribution map of S in image a. e) Distribution map of Au in image a
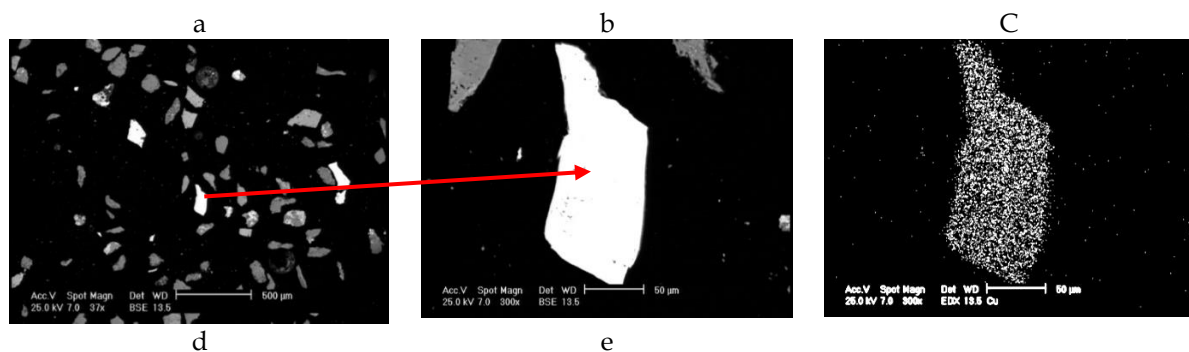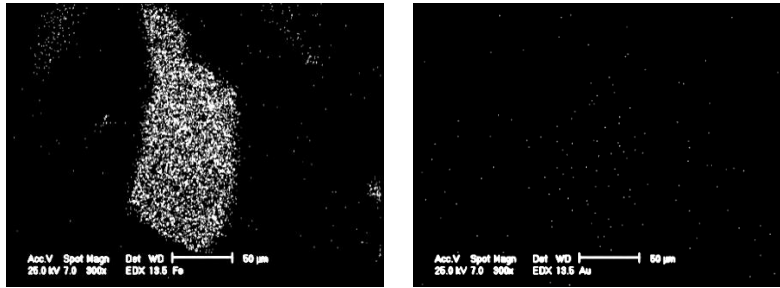
Figure 6: a) Free and locked particles of valuable minerals and gangue in the particle size fraction of 105-150 microns. b) An almost free particle of chalcopyrite. c) Distribution map of Cu in image b. d) Distribution map of Fe in image b. e) Distribution map of Au in image b
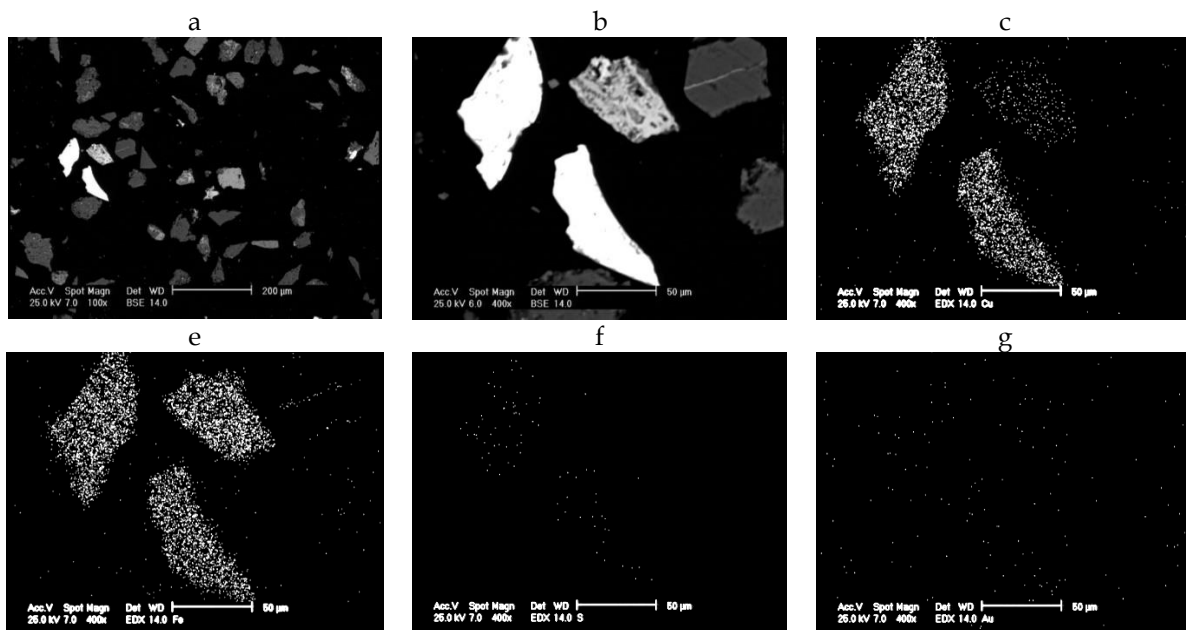
Figure 7: a) Free and locked particles of valuable minerals and gangue in the particle size fraction of 62-75 microns. b) Free particles of heavy minerals in image A with increased magnification. c) Distribution map of Cu in image b. d) Distribution map of Fe in image b. e) Distribution map of S in image b. f) Distribution map of Au in image b.

3.4. Effective Parameters

3.4.1. pH

pH is a key parameter in the flotation of sulphide and oxide minerals. In this study, the effect of pH was investigated by conducting flotation tests under similar conditions at three different pH levels, with the results presented in Figure 8. Figure 8(a) illustrates the copper recovery at three pH levels. Based on the results, increasing pH positively effects the recovery of both oxidized and total copper, but it has little effect on recovering sulphide copper. As pH increases from 9 to 10, the recovery of both oxidized and sulphide copper increases. As the pH increases from 10 to 11, the recovery of sulphide copper decreases. The reason for this is that raising the pH to higher levels requires a significant amount of lime. This quantity of lime leads to an increased precipitation of magnesium and calcium ions on the surface of valuable minerals, negatively impacting the flotation process. Additionally, the adsorption of $Mg(OH)_2$ and $CaCO_3$ precipitates on the surface of copper sulphide

minerals alters their surface characteristics, resulting in decreased recovery. Overall, these changes in surface properties lead to a reduction in the efficiency of the recovery and flotation process of sulphide copper (Suyantara et al. 2018). Whereas a further increase in pH from 10 to 11 results in a decrease in sulphide copper recovery, although oxidized copper recovery continues to rise at a slower rate. The increase in oxidized copper recovery with higher pH is attributed to improved sulfidization of oxide minerals. Additionally, the decrease in the recovery of sulphide minerals at pH 11 results from the depression of sulphide minerals such as pyrite and galena.

Figure 8(b) shows the grade versus pH chart. As depicted in Figure 8(b), with pH increasing from 9 to 11, the sulphide copper grade rises from 12.3% to 13.2%, indicating enhanced flotation performance. This grade increase is due to the depression of pyrite and galena in pH=11 and improved separation of chalcopyrite from the tailings (Maleki et al. 2023). Moreover, the oxidized copper grade increases from 5.8% at pH 9 to 6.2% at pH 11, indicating that a portion of oxidized copper is also entering the concentrate in alkaline environments. Ultimately, the total copper grade rises from 9.72% to 10.3%, reflecting improved concentrate quality, which may be attributed to optimized flotation conditions and increased selective separation of copper particles. At higher pH levels, the formation of hydroxide complexes for certain impurities, such as iron and silica, increases, leading to a reduced presence of these impurities in the concentrate and consequently enhancing the copper grade. The increase in oxidized copper recovery with rising pH is a result of improved sulfidization of oxide minerals. Since the goal during the rougher and scavenger stages is to achieve maximum recovery, pH=11 is considered the optimal value for determining other process parameters.

a)

b)

Figure 8: Effect of pH on copper a: recovery b: grade (collector concentration: 150 g/t, MIBC concentration: 45 g/t, and sodium sulphide concentration: 500 g/t).

3.4.2. Collector Concentration

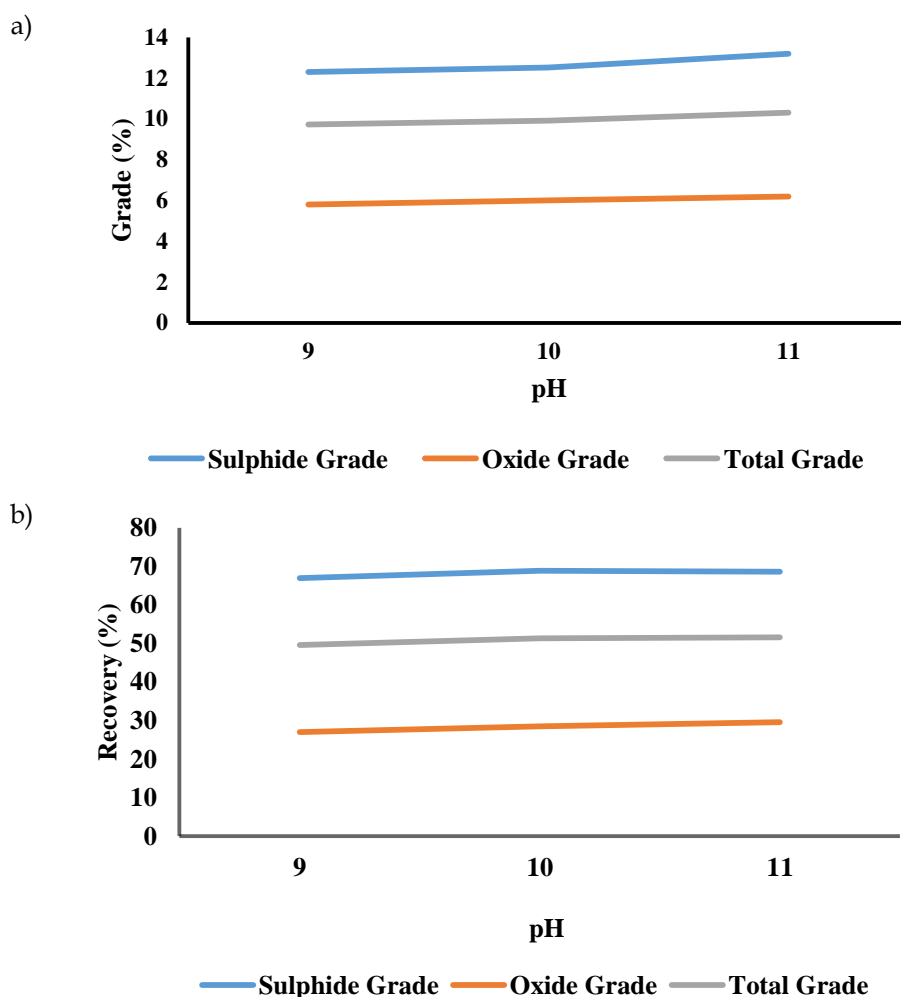In this study, two collectors—sodium isopropyl xanthate and potassium amyl xanthate—were used in equal weight ratios of 50%. The potassium amyl xanthate collector, because of its longer hydrocarbon chain, exhibits a powerful flotation compared to sodium isopropyl xanthate. To investigate the effect of collector concentration, flotation tests were conducted under similar conditions at four different levels of collector concentration, with the results illustrated in Figure 9. Figure 9(a) displays the impact of collector concentration on copper grades As shown in Figure 9(a), increasing the concentration of both sodium isopropyl xanthate and potassium amyl xanthate, in an equal weight ratio of 50%, from 100 to 200 g/t results in an increase in the sulphide copper grade from 12.3% to 13.3%, representing the maximum value within this range. However, further increasing the concentration to 250 g/t leads to a decrease back to 12.3%, indicating that the optimal collector amount for sulphide copper flotation is 200 g/t. The subsequent reduction in grade is attributed to surface saturation of the particles and decreased flotation recovery (Suyantara et al. 2018). On the other hand, the grade of oxide copper, which is 5% at 100 g/t, shows a slight increase at concentrations of 150 and 200 g/t, reaching 6.3%. However, at 250 g/t, the grade drops to 6%, suggesting that the collector has a minimal effect on oxide copper. The overall copper grade, starting at 9.12% at 100 g/t, rises to 10.12% at 150 g/t, but subsequently declines to 10.4% and 9.72% at 200 and 250 g/t, respectively. This data indicates that excessive collector addition can lead to a decrease in grade. Given that the objective in rougher and scavenger stages is to achieve maximum recovery, the best performance of the collector is noted at a concentration of 200 g/t, which is regarded as the optimal amount for determining other process parameters.

Figure 9(b) illustrates the effect of collector concentration on copper recovery. The recovery of sulphide copper exhibits an increasing trend with the rise in concentration of two collectors—sodium isopropyl xanthate and potassium amyl xanthate—in an equal weight ratio of 50%, ranging from 100 to 200 g/t, resulting in an increase from 59.3% to 71.25%. The increase in collector concentration enhances the surface coverage of the sulphide minerals present in the sample. This phenomenon increases the hydrophobicity of the surface, thereby improving their flotation. In this context, the collector is sufficiently available to cover the active sites of sulphide particles and facilitates bubble attachment by reducing interfacial energy. However, at a collector concentration of 250 g/t, it was observed that the recovery of sulphide copper decreased to 64.35% with increasing collector concentration. This is because the excess amount of collector can lead to increased foam stability due to micelle formation. In this situation, micelles cause a mix of minerals instead of separating the desired ones effectively, which lowers the recovery rate. Furthermore, the saturation of particle surfaces with the collector can lead to detrimental effects such as particle repulsion, increased froth buoyancy, and the mixing of valuable minerals with gangue (Lotter and Bradshaw 2010).

Conversely, the recovery of oxide copper initially increases with the concentration from 100 to 200 g/t, rising from 24.18% to 31.06%. However, it decreases at 250 g/t, reaching 28.18%, indicating that the optimal point for oxide copper recovery is also at 200 g/t. Finally, the overall copper recovery, which stands at 44.05% at 100 g/t, increases at 150 and 200 g/t to 51.04% and 53.79%, respectively. However, it drops to 48.64% at 250 g/t, showing that 200 g/t is the best amount for overall copper recovery; using too much of the collector reduces recovery.

a)

b)

Figure 9: Effect of collector concentration on copper a: recovery b: grade (pH= 11, MIBC concentration= 45 g/t, and sodium sulphide concentration= 500 g/t).

3.4.3. Frother Concentration

To determine the optimal concentration of frother, experiments were conducted at four levels: 30, 45, 60, and 75 g/t of MIBC frother under identical conditions. MIBC frother produces low-density bubbles, which can lead to lower recovery and increased transfer of water and slimes to the froth zone. Figure 10(a) demonstrates the effect of frother concentration on copper grade. According to Figure 10(a), the sulphide copper grade at a concentration of 30 g/t is 13.4%, and as the concentration of MIBC frother increases to 45 and 60 g/t, the sulphide copper grade slightly decreases from 13.3% to 13.2%, ultimately reaching 12.4% at 75 g/t. This indicates that excessive frother concentration negatively impacts the sulphide copper grade; an excessive amount of frother like MIBC can lead to the production of unstable froths or excessive froth stability. This results in the recovery of slimes or non-floatable particles, thereby reducing the selectivity of the flotation process and ultimately lowering the grade of the final concentrate (including the sulphide copper concentrate). Furthermore, highly stable froths can impede the effective separation of valuable particles from waste materials. On the other hand, the grade of oxide copper decreases from 6.4% to 6.1% when the

concentration of MIBC frother increases from 30 to 75 g/t. Flotation of oxide copper is more challenging due to its more hydrophilic surface compared to sulphide copper. The increased concentration of frother can hinder the effective attachment of oxide copper particles to air bubbles by thickening the froth layer and reducing the concentration of materials in the liquid phase, thus decreasing flotation recovery (Zhang 2016; Samiee Bayragh, Zakeri, and Bahri 2022). As a result, the frother has a lesser impact on the flotation of oxide copper, and increasing its amount does not lead to improved recovery. The overall copper grade at 30 g/t is 10.4% and remains relatively constant at 45 and 60 g/t, measuring 10.4% and 10.35%, respectively; however, it decreases at 75 g/t to 9.86%. This reduction indicates that an increase in frother concentration beyond the optimal amount leads to decreased flotation efficiency, thus showing that the best performance of the frother in this range occurs at 30 g/t, after which the increase in concentration results in a decline in recovery.

Based on Figure 10(b), the recovery of sulphide copper at a concentration of 30 g/t is 66.52%. With the increase in frother concentration from 45 to 60 g/t, the recovery of sulphide copper rose from 71.25% to 73.07%. However, at a concentration of 75 g/t, the recovery decreased to 70.85%, indicating that an increase in frother concentration up to 60 g/t improves sulphide copper recovery, while higher concentrations have a diminishing effect. At elevated concentrations, frothers can lead to excessively stable froths, which hinder the proper separation of valuable minerals from waste, resulting in a higher retention of gangue particles in the froth. Additionally, high frother concentrations increase the viscosity of the froth, and the bubbles can't move as easily, consequently decreasing flotation performance and leading to lower recovery rates. Conversely, the recovery of oxide copper, which is 30.95% at 30 g/t, increases to 31.06% and 31.25% at 45 and 60 g/t, respectively, but decreases to 30.5% at 75 g/t. This indicates that the effect of frother on oxide copper recovery is not significant and shows only slight variations. At higher frother concentrations, bubble size decreases, reducing the likelihood of oxide particles adhering to the bubbles (Finch, Nesset, and Acuña 2008). Furthermore, excessive frother concentration may preferentially adsorb onto the surfaces of gangue particles, disrupting the selectivity of the process [21]. Finally, the overall copper recovery at 30 g/t is 51.07%, and it increases to 53.79% and 54.9% at 45 and 60 g/t, respectively, but drops to 53.32% at 75 g/t. This trend indicates that optimal performance occurs at 60 g/t, after which flotation recovery declines.
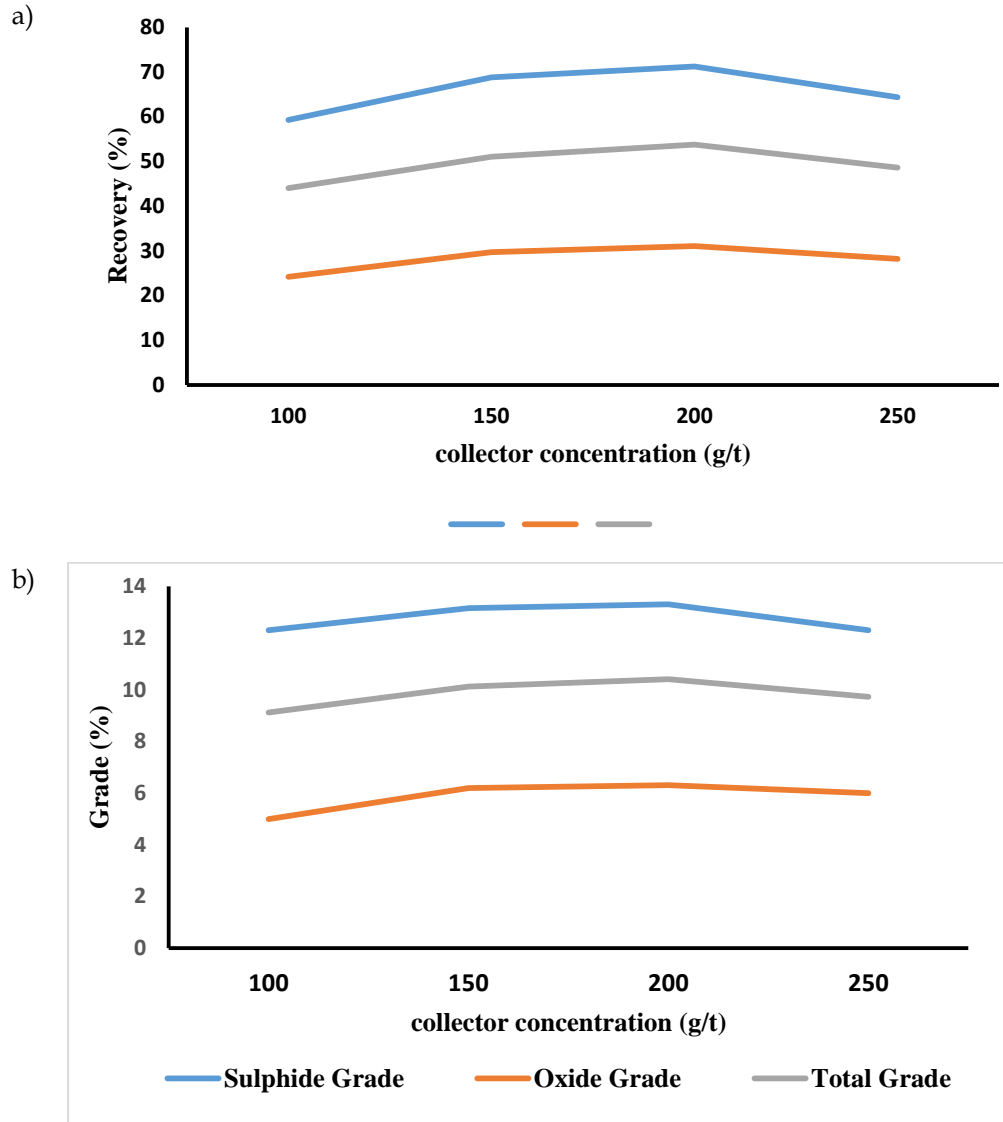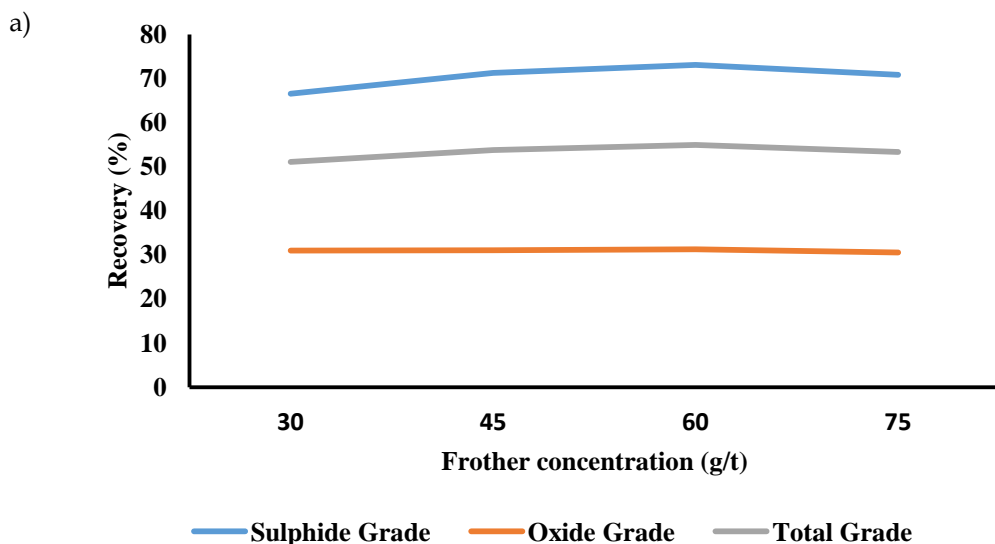

a)

b)

Figure 10: Effect of frother concentration on copper a: recovery b: grade. (pH= 11, collector concentration= 200 g/t, and sodium sulphide concentration= 500 g/t).

3.4.4. Sodium Sulfide Concentration

To investigate the effect of sodium sulphide (Na_2S) concentration, experiments were conducted at four levels: 500, 750, 1000, and 1250 g/t of Na_2S under identical conditions. According to Figure 11(a), increasing the concentration of Na_2S from 500 to 1250 g/t had no effect on the sulphide copper grade, which remained constant at 13.2%. In contrast, the oxide copper grade increased from 6.25% at 500 g/t to 8.1% at 750 g/t. Sulphide ions activated the oxide copper surface, making it more hydrophobic and improving its flotation, which may account for this increase. As the Na_2S concentration further increased to 1000 g/t, the oxide copper grade increased to 9.9%, indicating optimal activation conditions. However, when the Na_2S concentration reached 1250 g/t, the oxide copper grade decreased to 9.5%. This reduction could be due to excessive coverage of the particle surfaces by sulphide ions, leading to a reversion to a more hydrophilic nature. The overall copper grade also initially increased with rising Na_2S concentration, from 10.35% at 500 g/t to 11.02% and 11.68% at 750 and 1000 g/t, respectively, but decreased at a concentration of 1250 g/t to 11.54%. These changes suggest that the optimal Na_2S concentration for achieving maximum overall copper grade is around 1000 g/t, and exceeding this amount reduces process efficiency due to its negative effect on oxide copper flotation.

The optimal flotation performance observed at a dosage of 1000 g/t can be attributed to the effective activation of non-sulfide copper minerals, whereby their surfaces are sufficiently transformed into a sulfide-like state. This surface modification enhances their interaction with flotation collectors, thereby improving both copper recovery and concentrate grade. At this concentration, sodium sulfide appears adequate to induce the necessary surface changes that facilitate the selective flotation of valuable copper-bearing minerals.

According to Figure 11(b), the recovery of sulphide copper at a concentration of 500 g/t is 73.07%, and as the Na_2S concentration increases, the recovery of sulphide copper remains constant. This is because sulphide minerals inherently possess hydrophobic properties and float easily with common collectors such as xanthates. When Na_2S reacts with water, it creates sulphate compounds and elemental sulphur, which helps to improve the recovery of oxide copper. This increase in recovery is due to the formation of sulfur layers on the surface of oxide minerals. With the increase in Na_2S concentration,

the recovery of oxide copper rises from 31.25% at 500 g/t to 43.02% at 750 g/t, indicating a positive effect on oxide copper recovery within this range. The coating of oxide mineral surfaces with sulphide ions from Na$_2$S results in the formation of a layer of copper sulphides, which enhances the adsorption capacity for the collector xanthate. This process increases the hydrophobicity of the mineral surface and improves recovery in flotation. As Na$_2$S concentration increases to 1000 and 1250 g/t, oxide copper recovery reaches 60.32% and 55.23%, respectively, indicating that optimal performance occurs at 1000 g/t, after which recovery declines. At concentrations above 1000 g/t of Na$_2$S, oxide copper recovery decreases to 55.23%, indicating a negative effect of high Na$_2$S concentration on flotation process efficiency. At lower concentrations, Na$_2$S aids in increasing the hydrophobicity of mineral particle surfaces, facilitating their adhesion to air bubbles. However, as concentration increases, the likelihood of particle coverage by sulphide ions rises. This coverage can ultimately lead to a reversion to a hydrophilic nature in mineral particles, competing with the existing collectors and causing these ions to act as depressants. Therefore, increasing Na$_2$S concentration may reduce the ability of collectors to adsorb onto copper particle surfaces, resulting in lower recovery of oxide copper and potentially leading to the stability of weaker froths and decreased recovery (Maleki et al. 2023; Taheri et al. 2014). Ultimately, the optimal amount of Na$_2$S for achieving maximum overall copper recovery is around 1000 g/t, and any further increase results in a decline in recovery.
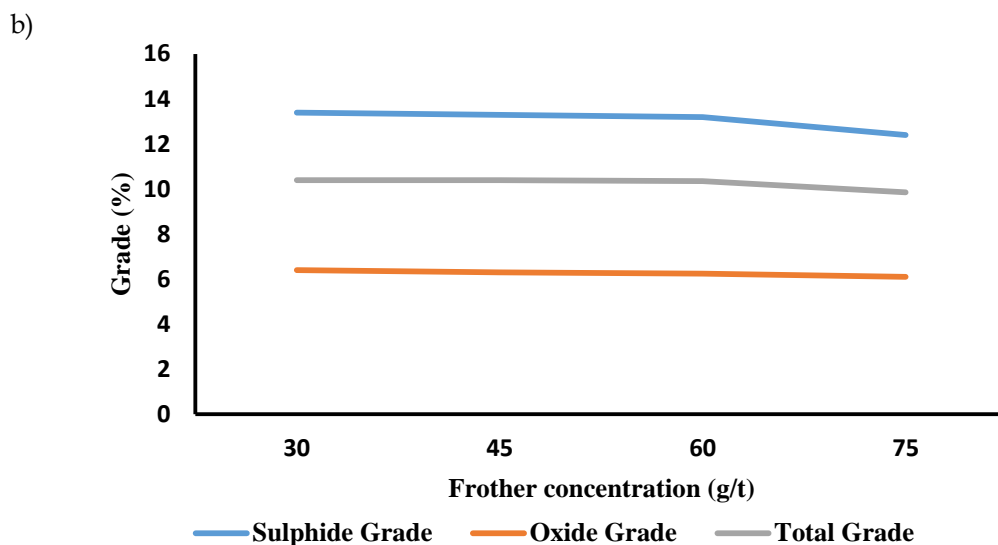
b)
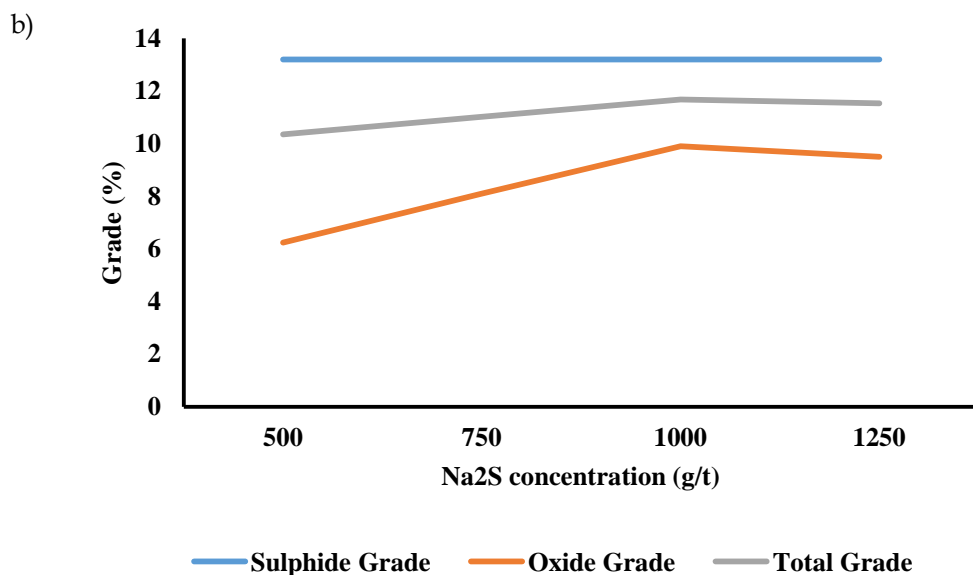
Figure 11: Effect of Na$_2$S concentration on copper a: recovery b: grade. (pH= 11, collector concentration= 200 g/t, and MIBC concentration= 60 g/t).

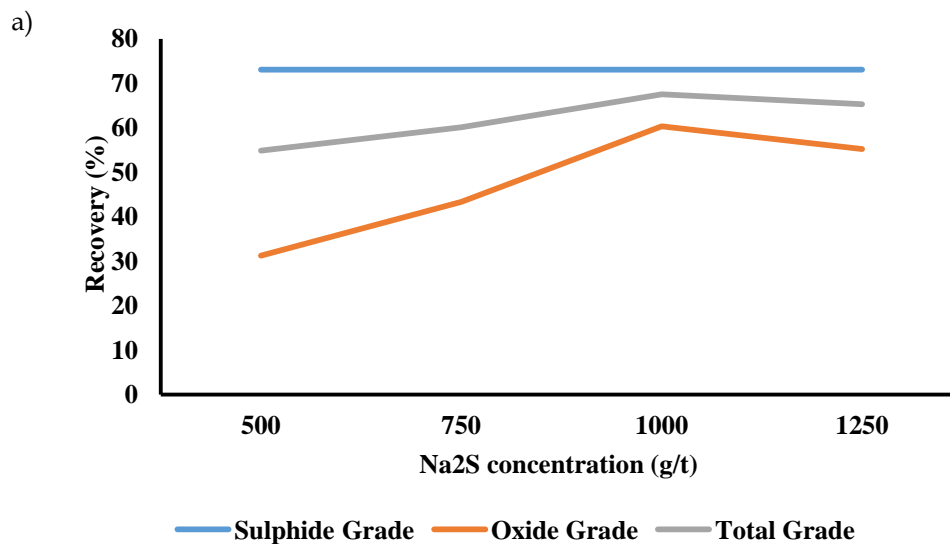### 3.5. Optimal Conditions

Based on the results of flotation experiments at various parameter levels, the optimal values for the parameters were determined. Under the optimal conditions of pH = 11, a concentration of 100 g/t of potassium amyl xanthate and 100 g/t of sodium isopropyl xanthate, a concentration of 60 g/t of MIBC frother, and a concentration of 1000 g/t of Na$_2$S, with a particle size of d$_{80}$= 75μ, the copper grade and recovery were obtained as 21.2% and 60.2%, respectively, after two stages of cleaner flotation.

4. Conclusion

This study investigated the flotation behavior of a complex copper ore from the Bouji region containing both sulphide (primarily chalcopyrite) and oxide (notably malachite) minerals, using a combination of mineralogical characterization and flotation parameter optimization. The mineralogical studies, including XRD, XRF, AAS, and SEM-WDX, confirmed the presence of copper-bearing minerals and their associations with gangue, revealing critical information about mineral liberation and intergrowths, which significantly influence flotation performance. Flotation experiments highlighted the importance of key operational parameters such as pH, collector concentration, frother concentration, and Na$_2$S concentration to achieving optimal recovery and grade. The results demonstrated that optimal flotation performance was achieved at pH 11, with a collector concentration of 200 g/t (equal parts potassium amyl xanthate and sodium isopropyl xanthate), 60 g/t MIBC frother, and 1000 g/t Na$_2$S. Under these optimized conditions, the final concentrate achieved a copper grade of 21.2% and a recovery of 60.2% after two stages of cleaner flotation. These results underscore the necessity of process customization based on ore mineralogy and confirm the potential for improving the recovery of mixed oxide-sulphide copper ores through integrated mineralogical analysis and flotation optimization. This approach not only enhances resource utilization but also provides a methodological framework for similar deposits facing processing challenges due to mineralogical complexity.

References

Ahad Zare Varzeghan, Mohammad Karamoozian, Asghar Azizi. 2017. 'Investigation on the effect of copper oxide minerals on flotation circuit recovery of the sungun copper complex concentration plant and introducing solutions to increase recovery', Shahrood University of Technology.

Barfaei, Mahmoud, and Gholamabbas Parsapour. 2022. 'Effect of pH and reagents on the froth stability in the copper flotation; Case study: Mohammadabad-E-Delijan copper company', *Journal of Separation Science and Engineering*, 13: 1-12.

Bozhkov, AI, Valentine V Bobkov, Tatiana P Osolodchenko, Oleg I Yurchenko, Vladimir Y Ganin, Evgen G Ivanov, Yevheniia D Batuieva, Valery V Minukhin, AV Goltvyanskiy, and VA Kozheshkurt. 2024. 'The antibacterial activity of the copper for Staphylococcus aureus 124 and Pseudomonas aeruginosa 18 depends on its state: metalized, chelated and ionic', *Heliyon*, 10.

Finch, James A, Jan E Nesset, and Claudio Acuña. 2008. 'Role of frother on bubble production and behaviour in flotation', *Minerals Engineering*, 21: 949-57.

Fuerstenau, Maurice C, Graeme J Jameson, and Roe-Hoan Yoon. 2007. *Froth flotation: a century of innovation* (SME).

Geng, Qing, Guang Han, and Shuming Wen. 2024. 'Flotation of Copper Sulfide Ore Using Ultra-Low Dosage of Combined Collectors', *Minerals*, 14: 1026.

Khoso, Sultan Ahmed, Zhiyong Gao, Mengjie Tian, Yuehua Hu, and Wei Sun. 2020. 'The synergistic depression phenomenon of an organic and inorganic reagent on FeS2 in CuS flotation scheme', *Journal of Molecular Liquids*, 299: 112198.

Koleini, SMJ, F Soltani, and M Abdollahy. 2013. 'Optimization of the reagent types and dosage in selective flotation of Cu-Zn Taknar mine by using D-Optimal method of statistical experiments design', *Journal of Mining Engineering*, 8: 1-11.

Lee, K, D Archibald, J McLean, and MA Reuter. 2009. 'Flotation of mixed copper oxide and sulphide minerals with xanthate and hydroxamate collectors', *Minerals Engineering*, 22: 395-401.

Lotter, NO, and DJ Bradshaw. 2010. 'The formulation and use of mixed collectors in sulphide flotation', *Minerals Engineering*, 23: 945-51.

M.A. Saeed Ghodrati, S. M. J. Koleini, M. Hekmati. 2013. 'Optimization of Reagent Dosages for Copper Flotation in Shahr-E-Babak Copper Complex Using Statistical Design', *Journal of Separation Science and Engineering*, 4: 17-27.

Maleki, Hassan, Mohammad Noparast, Sajjad Chehreghani, Mir Saleh Mirmohammadi, and Ali Rezaei. 2023. 'Optimization of flotation of the Qaleh Zari mine oxidized copper ore sample by the sequential sulfidation approach using the response surface method technique', *Rudarsko-geološko-naftni zbornik*, 38: 59-68.

Marion, Christopher, Adam Jordens, Ronghao Li, Martin Rudolph, and Kristian E Waters. 2017. 'An evaluation of hydroxamate collectors for malachite flotation', *Separation and Purification Technology*, 183: 258-69.

Potysz, Anna, Eric D van Hullebusch, Jakub Kierczak, Malgorzata Grybos, Piet NL Lens, and Gilles Guibaud. 2015. 'Copper metallurgical slags–current knowledge and fate: a review', *Critical Reviews in Environmental Science and Technology*, 45: 2424-88.

Samiee Bayragh, Abdoullah, Mehdi Zakeri, and Zahra Bahri. 2022. 'Estimation of copper grade from the flotation froth using image analysis and machine vision', *Amirkabir Journal of Civil Engineering*, 54: 869-84.

Sokolović, J, R Stanojlović, Lj Andrić, Z Štirbanović, and N Ćirić. 2019. 'Flotation studies of copper ore Majdanpek to enhance copper recovery and concentrate grade with different collectors', *J. Min. Metall. A Min*, 55: 53-65.

Srdjan, M Bulatovic. 2007. 'Handbook of Flotation Reagents Chemistry, Theory and Practice: Flotation of Sulfide Ores', *Elsevier Science & Technology Books*.

Sun, Jianjun, Liuyang Dong, Tianfu Zhang, Peilun Shen, and Dianwen Liu. 2024. 'Efficient recovery of copper from copper smelting slag by gravity separation combined with flotation', *Chemical Engineering Journal*, 494: 153159.

Suyantara, Gde Pandhe Wisnu, Tsuyoshi Hirajima, Hajime Miki, and Keiko Sasaki. 2018. 'Floatability of molybdenite and chalcopyrite in artificial seawater', *Minerals Engineering*, 115: 117-30.

Taheri, Bijan, Mahmoud Abdollahy, Sied Ziaedin Shafaei Tonkaboni, Soheyla Javadian, and Mohammadreza Yarahmadi. 2014. 'Dual effects of sodium sulfide on the flotation behavior of chalcopyrite: I. Effect of pulp potential', *International Journal of Minerals, Metallurgy, and Materials*, 21: 415-22.

Wills, Barry A, and James Finch. 2015. *Wills' mineral processing technology: an introduction to the practical aspects of ore treatment and mineral recovery* (Butterworth-heinemann).

Yu, Xingcai, Qicheng Feng, Han Wang, and Dianwen Liu. 2025. 'Surface sulfidization mechanism of difficult to enrich copper oxide in copper smelting slag and its response to recycling performance', *Applied Surface Science*, 684: 161825.

Zhang, Chonghui, Yihan Su, Tingshu He, Xianzhong Bu, He Wan, Sen Wang, and Jiwei Xue. 2025. 'The role of copper ions in improving the flotation of chalcopyrite at low temperatures', *Minerals Engineering*, 220: 109091.

Zhang, Wei. 2016. 'The effects of frothers and particles on the characteristics of pulp and froth properties in flotation—A critical review', *Journal of Minerals and Materials Characterization and Engineering*, 4: 251-69.

Sulfate Adsorption Mechanism Investigation from Acid Mine Drainage and Seawater Modification Method on Red Mud: Laboratory Studies and Molecular Simulation

Shima Rahimi [1*], Mehdi Irannajad[2], Mehdi Jamali[3]

[1*]**PhD at Amir Kabir University of Technology, Department of Mining Engineering, Tehran**

[2] **Professor at Amir Kabir University of Technology, Department of Mining Engineering, Tehran**

[3] **Head of Laboratory at OPSIM company**

*Corresponding author: sh.rahimi1983@gmail.com

Abstract:

In this study, Red Mud (RM) (byproduct in alumina production process from bauxite) was used as an adsorbent for sulfate contaminant adsorption from acid mine drainage (AMD). AMD discharge lead to the acidification of water which has detrimental effects on aquatic life and human health. Analytical methods, laboratory studies and molecular simulations were conducted to investigation of sulfate adsorption on RM. Thermodynamic calculations were performed after optimizing of existing metal oxide structure in RM with the Material Studio software using the dmol3 and DFT method. The adsorption energy results by Adsorption locator module were determined -819.09, -561.7, -268.8, -105.4, and -314.7 kcal/mol for Fe_2O_3, Al_2O_3, $CaCO_3$, TiO_2 and SiO_2, respectively. The most active compounds in RM (iron and aluminum oxides) account for 22.5% and 13.3% in the red mud structure, respectively. In addition, seawater washing was employed as RM modification method, and it could decrease high rates of pH and improve the sorption capacity of raw RM. The effect of this modification was investigated by solvent simulation in adsorption environment of sulfate on RM and the dielectric constant selection. For water as the primary solvent with a dielectric constant of 78.54, adsorption energy for RM was calculated to be -35.68 kcal/mol and it was increased to -56.69 kcal/mol for the seawater medium with a dielectric constant of 86. Therefore, RM can be considered as a potential sulfate adsorbent because of cost-effectiveness and alkaline pH that can lead to the neutralization of AMD.

Keywords: Sulfate, Adsorption, Red Mud, Seawater, Molecular Simulation.

1. **Introduction**

Acid mine drainage (AMD) is well-known as an important source of surface and underground water pollution all over the world that is produced specially from mining activities (Singh, et. Al. 2020 and Manisalidis, et al. 2020). AMD is released when sulfides are exposed to air and water (Alimohammadi, et al. 2017). Also, it often contains elevated levels of sulfate (500-2000 mg/L), and it is also produced from electroplating, steel pickling, nonferrous smelting, and other related materials or substances (Kitadai, et al. 2018). The high sulfate content causes low-pH water and sulfuric acid formation. This issue is due to the dissolution of toxic and heavy metals and creates unacceptable levels of these metals in water (Halajnia, et al. 2013). The production of AMD results in the death of vegetation and aquatic life, mineralization of water, corrosion of reinforced steel, scaling of equipment, damage to mammals and endangering human health, and corrosion of mine equipment (Baldwin and Mitchell, 2012).

Nonetheless, several methods have been employed to treatment of sulfate-containing wastewater, including chemical precipitation, crystallization (Silva, et al. 2012), ion exchange, biological treatment (Liang, et al. 2013), electro-dialysis (Lee, et al. 2003), nano-filtration (Galiana-Aleixandre, et al. 2005),

adsorption and reverse osmosis (Bodalo, et al. 2004). Most processes have significant disadvantages such as need for high energy and costly processes, low efficiency, production of high amounts of sludge, high levels of trace elements, and reclamation processes (Halajnia, et al. 2013). Among these processes, adsorption is commonly considered to be the most attractive and used technique due to its low cost, eco-friendliness, and high performance. An adsorbent can be assumed as low cost if it requires little processing, abundant in nature, or a by-product or waste material from another industry.

Red mud (RM) is produced as a by-product during the alkaline leaching of bauxite in the Bayer process. According to previous evidence, (He, et al. 2013 and Liu, et al. 2011), the production of 1 ton of alumina generally results in the creation of 0.3-2.5 t of RM strongly alkaline (pH = 12-13). High alkalinity, large amounts, and fine-grained nature (90% below the size of 75 μm) of RM cause serious environmental problems (Zhao, et al. 2012 and Ye, et al. 2015). It is also composed of a mixture of solid and metallic oxides. The red color arises from hematite, which can comprise up to 60% of the mass. The red mud is highly basic with a pH ranging from 10 to 13. In addition to iron, the other dominant components include silica, unleached residual aluminum compounds, and titanium oxide (Sutar, et al. 2014 and Burke, et al. 2013). On the other hand, RM is introduced as an unexpansive adsorbent for various contaminants due to its high metal oxide content and activated compound (He, et al. 2013, Palmer, et al. 2010). Further, various methods of surface modification have been implemented to improve the adsorption properties and enhance the adsorption amount of red mud and its pH reduction (Schwarz, et al. 2018). These methods are entailed sea water treatment, heat activation, acid washing, and granular with bentonite or fly ash and presence of different surfactants (Martins, et al. 2020). In this research, aimed to test RM as an alternate sulfate adsorbent and described the results of an investigation on the sulfate removing and seawater effects were studied as a natural, low-cost and available material on red mud treatment.

Molecular simulation methods were applied for microscopic analyses and physical phenomena investigation at molecular level. In these methods, the constituent species of a system such as: molecules and fine particles have been explored. One of the most important software which was applied for modeling, visualization, and analysis of material systems is Materials Studio. This software was utilized in advanced research about various materials such as: polymers, carbon nanotubes, catalysts, and metals. To investigate sulfate ions' adsorption energy and behavior on red mud, we studied a new approach for sulfate adsorption by performing theoretical calculations on metal oxides in the RM structure. It extends beyond the traditional static DFT (density functional theory) calculations, such as molecular quantum simulations, geometry optimization, and vibrational frequency calculations. Remarkably, Materials Studio was used for modelling, visualization, and analysis of material systems as one of the essential software and Fe_2O_3, Al_2O_3, $CaCO_3$, SiO_2, MgO, Na_2O and TiO_2 surfaces were used for these calculations (Rahimi and Irannajad, 2024 and Irannajad and Rahimi, 2024). In addition, calculations were performed to utilize the continuum solvation model, namely COSMO, to simulate modified methods and represent the local environments (water and seawater). Finally, the results of the adsorption energies for sulfate were reported and compared in diverse local environments. The research has expanded the experimentally reported effects such as sulfate removal, adsorption capacity, and computational modelling results.

2. Material and methods

2.1. Material

RM samples were provided by the Jajarm mine, which produces RM as a by-product during the alkaline leaching of bauxite in the Bayer process. RM was applied as the base material of the adsorbent from this mine that is located 5 km from Jajarm in north Khorasan province of Iran. The X-ray fluorescence (XRF) results and X-ray diffraction (XRD) studies of RM are provided in table 1 and its size distribution is shown in figure 1. Activated RM by seawater was used to improve the reactivity of

RM for the removal of sulfate ions in the solution. The sulfate solution was prepared by sodium sulfate (Na_2SO_4), and the solution of ionic strength was adjusted using NaCl (1M). HCl and sodium hydroxide (NaOH) were employed for adjusting the pH of the solution. Also, reagents were used for sulfate concentration measurement in solutions by UV-VIS spectrophotometers such as Glycerol and Isopropyl Alcohol. All reagents were supplied by Merck and were illustrated in table 2.

Table. 1. Chemical and mineralogical compositions of the red mud.

Chemical composition		Mineralogical composition	
Constituent	% (w/w)	Minerals	Formula
Fe_2O_3	22.5	Calcite	$Ca_{5.23}Mg_{0.77}C_6O_{18}$
Al_2O_3	13.3	Diopside	$Ca_{3.58}Mg_{3.55}K_{0.29}Al_{0.84}Si_{7.74}O_{24}$
SiO_2	15.2	Magnetite	$Fe_{24}O_{32}$
MgO	1.7	Vermiculite	$Si_{5.53}Al_{3.36}Fe_{0.41}Mg_{4.04}Ti_{0.08}O_{30.32}Ca_{0.86}$
K_2O	0.53	Ilmenite	$Fe_6Ti_6O_{18}$
TiO_2	6.7	Katoite	$Ca_{24}Al_{16}Si_{24}O_{96}$
MnO	0.104	hematite	Fe_2O_3
CaO	18.5	Rutile	TiO_2
P_2O_5	0.14	Sodalite	$Na_2O.Al_2O_{3.1.68}SiO_{2.1.73}H_2O$
Na_2O	2.57	Cancrinite	$3NaAlSiO_4.NaOH$
SO_3	0.47		
LOI	16.6		
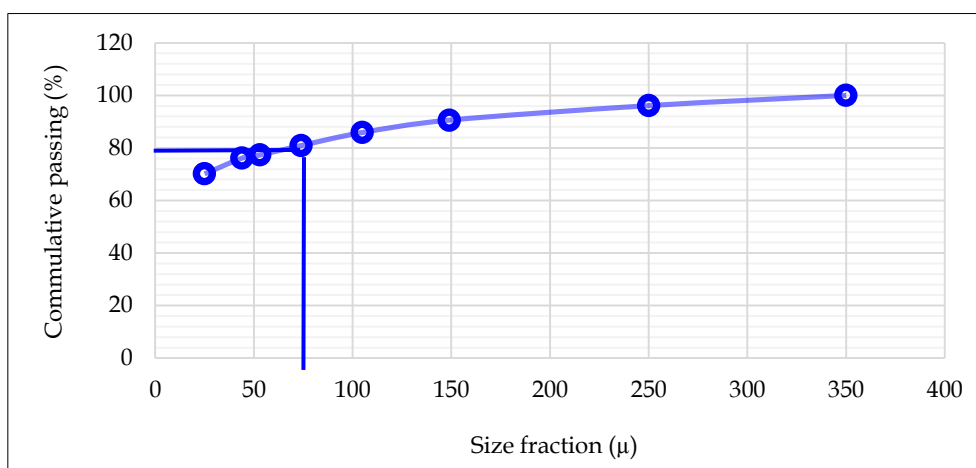
Fig.1. Size distribution plot of RM.

2.2. RM modification

Employing RM as adsorbent, it was micronized and then sieved through a 100-mesh screen to obtain D_{100} of less than 150 μm. Next RM was suspended in a solution of seawater with a 10% solid percentage for 1 hr (RMS) and mixed for 1 hr to decrease its pH. This can lead to the precipitation of hydroxide, carbonate or hydroxyl carbonate and a decrease in the pH rate to 8-8.5. Then, it was filtered and dried in the oven overnight (100 °C). Finally, RMS was ground and then sieved through a 75 μm screen (Rahimi and Irannajad, 2024).

Table. 2. Used chemical compositions in adsorption experiments.

Chemical compound name	Formula	Application	Purity (%)	Company
Distilled water	H_2O	Adsorption solution	-	Aryateb
Hydrochloric acid	HCl	Adjusting pH	37	Merk
Sodium hydroxide	NaOH	Adjusting pH	95	Merk
Sea water	-	RM modification	-	-
Sodium chloride	NaCl	Adjusting ionic strength	95	Merk
Sodium sulfate	Na_2SO_4	Adsorption solution	99	Merk
Glycerol	$C_3H_8O_3$	Sulfate reagent solution	99	Merk
Isopropyl Alcohol	C_3H_8O	Sulfate reagent solution	99	Merk

2.3. Batch adsorption studies.

The adsorption experiments were performed using the batch method in a 250 mL Erlenmeyer flask with a constant stirring rate of 420 rpm, at a temperature of 25 °C, and ionic strength of 0.01 M of NaCl. The sulfate solution with a desired concentration and contact time was prepared and placed in contact with raw and activated RM (0.5- 5 g /L) and underwent stirring. Then the sulfate solution was prepared with desired concentrations, followed by placing the raw and activated RM in contact with 100 mL sulfate solution and stirring. After equilibrium, the solution was filtered by Whatman filter paper No. 42 and a clear aliquot of the supernatant was taken accordingly. For sulfate ion measurement, by a UV-VIS spectrophotometer (model HITACHI U-2000), they were prepared standard and specific solution with 5, 10, 15 and 20 ppm sulfate concentration (Na_2SO_4) for instument calibration. According to previous research, the sulfate percentage in the solution was determined in 420 nm and adding sulfate reagents solution. This solution was included Isopropyl Alcohol, Glycerol, Hydrochloric acid and Sodium chloride which was added as identifier befor sulfate content measurment. Ultimately, the sulfate removal (R) and capacity adsorption of the adsorbent (q_e) were calculated using the following equation (1 and 2) (Irannajad and Rahimi 2024):

$$R = \frac{(C_0 - C_e)}{C_0} \times 100 \tag{1}$$

$$q_e = \frac{(C_0 - C_e)}{M} \times V \tag{2}$$

Where R is the sulfate removal percentage (%), and C_0 is the initial adsorbate concentration (mg/L). Furthermore, C_e and q_e represent the final adsorbate concentration in the solution after equilibrium adsorption (mg/L) and the amount of the adsorbed sulfate per unit of adsorbents (mg/g), respectively. Finally, M is the weight of the adsorbent (g), and V denotes the volume solution (L).

2.4. Equilibrium studies

For equilibrium isotherm investigation, 100 mL of the sulfate solution with various concentrations (250, 500, 750, 1000, 1500, and 2000 ppm) were stirred with 2 g of RM and RMS for 60 min (equilibrium time) at 420 rpm and at pH rate of 6.5-7. The equilibrium isotherms of sulfate adsorption were evaluated by Langmuir, Freundlich, Temkin, and Dubinin -Radushkevich models to study the removal amount of sulfate at equilibrium by the unit mass of the adsorbent from the solution at a

constant temperature. Equations, Linear expression, and parameters related to these models are presented in table 3 (Ye, et al. 2016).

2.5. Kinetic studies

The adsorption kinetics of sulfate onto RM, and RMS was evaluated by pseudo-first-order, pseudo-second-order, Elovich, and intraparticle diffusion kinetic models (table 4) to study the mechanism and rate-controlling step of adsorption. The kinetic model parameters were determined using the least-squares linear regression method. Additionally, the kinetic models of the pseudo-first-order and pseudo-second-order were investigated to determine the reaction mechanism (chemical or physical). To examine the kinetic isotherms, the sulfate solution with a concentration of 1000 ppm was stirred by 2 g of the adsorbent at 420 rpm and a pH rate of 6.5-7 for different times (10, 20, 30, 60, and 120 min), followed by calculating the parameters and validity of the kinetic models (correlation coefficients).

Table. 3. Isotherm models.

Isotherm models	Equations	Linear expression	Parameters
Langmuir	$q_e = q_m^{\frac{b\,C_e}{1+b\,C_e}}$	$\frac{C_e}{q_e} = \frac{1}{q_m}b + \frac{C_e}{q_m}$	q_m:(slope) −1, b: slope/intercept
Freundlich	$q_e = K_f C_e^{1/n}$	$\log q_e = \log K_f + \frac{1}{n}\log C_e$	K_f: exp(intercept), n:(slope) −1
Temkin	$q_e = \frac{RT}{B_T\,\ln A_T} + \frac{RT}{B_T\,\ln C_e}$	$q_e = \frac{RT}{B_T\,\ln A_T} + \frac{RT}{B_T\,\ln C_e}$	B_T: RT/slope, A_T:exp (intercept B_T/RT)
Dubinin–Radushkevich	$q_e = q_m\,\exp(-\beta\varepsilon^2)$	$\ln q_e = \ln q_m - \beta\,\varepsilon^2$	q_m: exp (intercept), β: - slope $\varepsilon = RT\ln(1+\frac{1}{C_e})$

Kinetic models	Equations	Linear expression	Parameters
Pseudo-first order	$q_t = q_e[1 - \exp(-k_{1p}\,t)]$	$\ln(q_e - q_t) = \ln q_e - k_{1p}t$	q_e=exp(intercept), k_{1p}=−(slope)
Pseudo-second order	$q_t = k_{2p}q_e^2\,t/(1+q_e k_{2p}t)$	$\frac{t}{q_t} = \frac{1}{k_{2p}q_e^2} + t/q_e$	q_e=slope−1, k_{2p}=(slope2)/ intercept
Elovich	$q_t = \beta\,\ln(\beta\alpha t)$	$q_t = \beta\ln(\alpha\beta) + \beta\ln t$	β=slope, α=(slope)−1exp (intercept /slope)
Intraparticle diffusion	$q_t = k_p t^{0.5}$	$\log q_t = \log k_p + 0.5\log t$	k_p =exp (intercept)

Table. 4. Kinetic models.

2.6. Thermodynamic studies

To calculate thermodynamic parameters such as Gibbs free energy (ΔG), entropy (ΔS) and enthalpy (ΔH), the 250 ml of sulfate solution with 1000 ppm concentration was prepared and stirred with 2 g/L adsorbent dosage and pH = 7 for 60 min in different temperatures. The stirring incubator was adjusted

to temperatures of 298, 303, 313, 323, and 333 K, with the constant stirring rate for ΔG, ΔS, and ΔH calculations (Equation 3, 4 and 5).

$$k_d = \frac{(C_0 - C_e)V}{C_e W} \tag{3}$$

$$ln\,k_d = \frac{\Delta S^0_{ads}}{R} - \frac{\Delta H^0_{ads}}{RT} \tag{4}$$

$$\Delta G^0_{ads} = \Delta H^0_{ads} - T\,\Delta S^0_{ads} \tag{5}$$

As can be observed in the above Equation, k_d is the distribution coefficient (mg/L) that was calculated in Equation 3 (Where C_0 is initial sulfate concentration (mg/L), and C_e is final sulfate concentration in the solution after equilibrium adsorption (mg/L). M and V represent the weight of the adsorbent (g), and volume solution (L), respectively. In Equation 4, T denotes solution temperature (K), and R is the universal gas constant (8.314 J/mol k). For thermodynamic parameters calculation, k_d was plotted on a 1/T curve and obtained $\frac{\Delta S^0_{ads}}{R}$ and $\frac{\Delta H^0_{ads}}{R}$ as intercept elevation and slop curve, respectively (Irannajad and Rahimi 2024), were calculated according to Equations 4 and 5.

2.7. Molecular simulation

Main oxides were simulated for molecular modeling of sulfate adsorption on RM surface. The main oxides in the RM structure were just considered (chemical composition amount > 5%) to simplify and minimize the calculation cost. The molecular modeling was applied to the adsorption mechanism of sulfate ions on red mud structure. Dmol3 module was used for DFT calculation in Material Studio software, version 2020. The iron, aluminum, calcium, silicon and titanium oxides were modeled by the generalized gradient functional of BLYP (Becke exchange plus Lee-Yang-Parr correlation). To achieve the best possible accuracy, a double numerical method was applied to all atoms, along with p-function polarization for hydrogen atoms (DNP). The most essential convergence for geometry optimization is summarized in table 5 (Zia, et al. 2019), This work's results were based on "all-electron relativistic" calculation without effective core potentials or pseudo-potentials.

Noteworthy, Fe_2O_3, Al_2O_3, $CaCO_3$, SiO_2, TiO_2, and Na_2O were built as crystal structures for adsorption energy calculation. The desired elements, the number of atoms, and the appropriate lattice parameters for each structure were selected. To investigate the adsorption of sulfate ions on red mud, we used the optimized crystal (with DMol3 module) as the basis of building models for red mud. Afterwards, the cleavage surface was created, and the 2×1 supercells were expanded. Finally, a vacuum slab was built with appropriate thickness for all species of crystals. In table 6, the lattice parameter, the cleavage surface, and the cutoff distance for each structure are illustrated. After that, the optimized sulfate ion was placed near the crystals' surface, and molecular simulations were performed with the DMol3 module. The details of the molecular simulations and our study's results are presented in the results section. The adsorption energy is calculated using Equation 6 (Wang, et al. 2018).

$$E_{adsorption} = E_{surf + adsorbate} - (E_{surf} + E_{adsorbate}) \tag{6}$$

Wherever $E_{adsorption}$ is the adsorption energy, $E_{surf + adsorbate}$ is the total energy of the surface with the adsorbed molecule, E_{surf} is the total energy of the clean surface, and $E_{adsorbate}$ is the total energy of the isolated adsorbate molecule.

Table. 5. Convergence tolerances for geometry optimization calculations.

Convergence tolerance parameters	
Energy	1×10^{-5} Hartree
Maximum force	2×10^{-3} Hartree/Å
Maximum displacement	5×10^{-3} Hartree
Maximum iterations	50
SCF tolerance	10^{-6} Hartree (fine)
Orbital cut-off	4.6 Å
Core treatment	All electron relativistic
Basis set	DNP
Basis File	4.4
Integration accuracy	Medium

Mineral name	Crystal system	Space group	Lattice constant	Cleave surface	Cutoff distance (Å)
Hematite	Hexagonal	R3_C	a=5.04, b=5.04, c=13.75, α=90, β=90 and γ=120	0 0 1	12.2
Corundum	Trigonal	R3_C	a=4.75, b=4.75, c=12.98, α=90, β=90 and γ=120	0 0 1	8.4
Calcite	Trigonal	R3_C	a=4.99, b=4.99, c=17.061, α=90, β=90 and γ=120	1 0 1	5.5
α-quartz	Trigonal	p3_221	a=4.91, b=5.405, c=4.916, α=90, β=90 and γ=120	0 1 1	12.5
Rutile	Tetragonal	p4_2/MNM	a=4.592, b=4.592, c=2.957, α=90, β=90 and γ=90	0 1 1	12.5

Table. 6. Lattice parameter, cleavage surface and cutoff distance of mineral structures.

As mentioned above, seawater washing was used in the experimental section for RM surface modification and improving adsorption. To simulate the modification methods and represent the local environment (water, and seawater), calculations were performed utilizing the continuum solvation model, namely COSMO (conductor-like screening model). The dielectric constants of the two solutions are composed of water, and seawater which were considered 78.54, and 84 respectively. The multipolar expansion was used to calculate the solvation energy for the whole model. The geometry optimization was validated based on the vibrational frequency analysis (Zia, et al. 2019).

3. Results and discussion

3.1. Effect of seawater modification method

The effect of RM dosage on sulfate removal from the aqueous solution at the pH of 6.5-7 is illustrated in figure 2. As shown, sulfate removal efficiency increases by increasing the RM dosage due to increasing the available surface of the adsorbent (Rahimi and Irannajad 2024). As can be seen, the maximum sulfate removal was 6.3, and 29.4% for RM, and RMS in 5 g/L adsorbent dosage. While sorption capacity almost decreases with increasing adsorbent dosage this can be due to a reduction in the number of sulfate ions in the solution compared to adsorbent sites and the maximum sorption capacity is obtained at 15.4 and 3.1 mg/g in 0.5, 2 and 4 g/L adsorbent dosage for RMS and RM, respectively. Further, figure 2 confirms that seawater washing rises sulfate adsorption onto the RM surface.
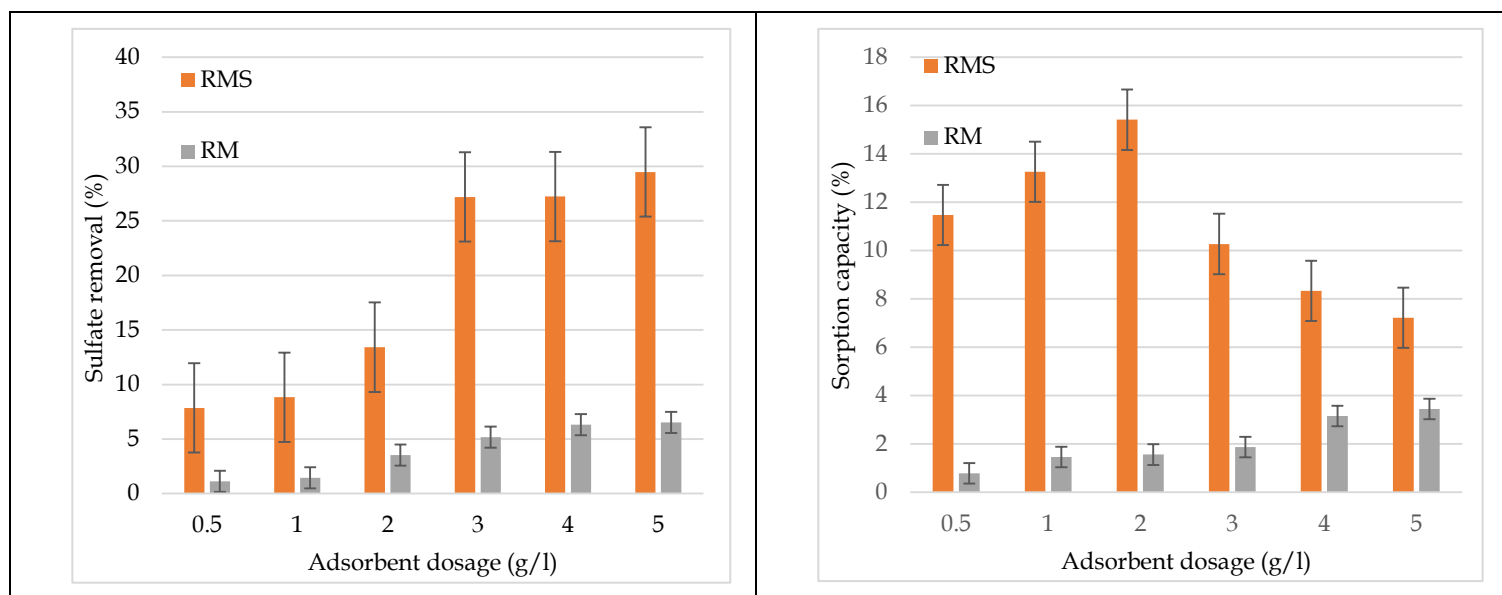
Fig. 2. Effect of adsorbent dosage on sulfate removal and sorption capacity by RM, and RMS (contact time of 60 min, sulfate concentration of 1000 ppm and temperature of 27 °C).

3.2. Adsorption isotherm and kinetic models

The obtained data from equilibrium tests, da were modeled using the linear regression method of least squares and correlation coefficient (R^2). The isotherm model parameters were determined by the solver add-in function in Microsoft Excel. Linear expressions, parameters and R^2 related to each model are listed in table 7.

According to the results of isotherm studies for RM, the order of the best model based on the R^2 values is Freundlich> Dubinin– Radushkevich> Temkin> Langmuir. For RMS, the matching of the sorption isotherm is almost the same as RM; the difference is that the matching of Langmuir is more than the Temkin model. There is more matching with the Freundlich model for RM and RMS with R^2 values 0.97 and 0.94. According to Freundlich isotherm results, maximum sorption capacity for RM and RMS are obtained at 0.88 and 2.45 mg/g. The Freundlich model indicates that the adsorbent surfaces are heterogeneous and the adsorption onto the adsorbent surface is multilayer. Moreover, adsorption is reversible. In this model, the favorable range of adsorption intensity (n) is $0 < 1/n < 1$, thus adsorption is desirable down. The Dubinin-Radushkevich model investigates maximum sorption capacity that it indicates 1.37 and 26.3 for RM and RMS. Also, this model determines the energy of adsorption and type of the adsorption process (physical adsorption (E < 8), chemical adsorption or ion exchange (E > 16), and particle diffusion that governs the reaction (E > 16)). Based on this model, the adsorption

205

process occurs with particle diffusion. In this model, it is assumed that the adsorbed amount for any adsorbate concentrations follows a Gaussian function of the Polanyi potential. The Temkin model evaluates the heat of adsorption and some indirect interactions of the adsorbate/adsorbate in the adsorption process. The increase of B_T for RMS rather than RM indicates that the seawater washing can improve the adsorption process of sulfate on the RM surface (Li, Et al. 2015). In compared to the other research for investigation of adsorption isotherm of RM, there was the most consistent with Freundlich isotherm (Deihimi, et al. 2019).

The adsorption kinetics of sulfate on RM, and RMS were evaluated by pseudo-first-order, pseudo-second-order, Elovich, and Intraparticle diffusion kinetic models (Table 8) to examine the mechanism and rate-controlling step of adsorption. The R^2 values (0.95 and 0.84 for RM, and RMS) demonstrated that the pseudo-second-order model outperformed the other kinetic models for the description of sulfate adsorption onto both RMS and RM. These results confirmed that the rate-controlling step in the sulfate adsorption process onto RM and RMS was a chemisorption interaction. According to this model, two reactions (series or in parallel) are proposed, including the fast reaction that quickly reaches equilibrium and the slow reaction that can continue for a long period (Deihimi, et al. 2018). The kinetics constants (K) of both pseudo-second-order and intraparticle diffusion models are more for RMS compared to RM, indicating a further absorption rate of sulfate onto the RMS surface. Contact time for adsorption equilibrium for other applied adsorbents in sulfate adsorption was 60-120 min, so obtained results for kinetic investigation is in good agreement with other results (Sadeghalvad, et al. 2011).

Table. 7. Isotherm model parameters for sulfate adsorption onto RM and RMS.

Isotherm Models	Parameters	RM	RMS
Langmuir	Linear expression	Y= -1.135X+755.57	Y= -0.4069X+414.6
	q_m	0.88	2.45
	b	-0.001	-0.005
	R^2	0.62	0.57
Freundlich	Linear expression	Y=2.3411X-5.6369	Y= 2.9026X-7.1636
	K_f	2.29×10-6	6.68×10-8
	N	2.34	2.9
	R^2	0.97	0.94
Temkin	Linear expression	Y= 5.4182X-26.981	Y=3.576X-5.5014
	B_T	468.2	709.4
	A_T	0.006	0.21
	R^2	0.69	0.32
Dubinin-Radushkevich	Linear expression	Y= -21.822X+76.301	Y= -0.0378X+3.27
	q_m	1.37	26.3
	β	21.8	0.03
	R^2	0.84	0.84

3.3. Thermodynamic properties

The simulation of single clusters in the RM structure include: Fe_2O_3, Al_2O_3, $CaCO_3$, SiO_2, and TiO_2 were conducted in water environment. DFT was applied for geometry optimization of these structures in the underground state. Figure 3. shows the optimized structure of these clusters and their bond

lengths and bond angles. Furthermore, the main thermodynamic properties were calculated for various structures in RM reaction with sulfate ion. The results of a vibrational analysis calculation were used to compute important thermodynamic properties such as enthalpy (H), entropy (S), free energy (G), total energy (E) and heat capacity at constant pressure (Cp) as a functions of temperature. DMol3 can be applied as a tool for the prediction of these thermodynamic properties of molecular systems and total energy yields. In this section, the thermodynamic properties of the main chemical composition of RM were calculated in separate documents. Table 9 indicates the calculation results of thermodynamic properties. In figure 4, the results of computed free energy in molecular simulation and obtained free energy from thermodynamic measurements were compared. Results indicated that there is a systematic conformity between the calculated free energy in molecular simulation and obtained free energy from thermodynamic measurements.

Table. 8. Kinetic model parameters for sulfate adsorption onto RM and RMS.

Isotherm Models	Parameters	BRM	RMH
Pseudo-first-order	Linear expression	Y= 0.0087X+1.8443	Y= 0.0106X+2.046
	q_e	6.32	7.73
	K_1	0.008	0.01
	R^2	0.51	0.42
Pseudo-second-order	Linear expression	Y= 0.0545X+1.3812	Y=0.0377X+1.2337
	q_e	18.34	26.52
	K_2	0.19	0.17
	R^2	0.95	0.84
Elovich	Linear expression	Y= 4.3641X-4.3701	Y= 6.8858X- 9.9079
	α	0.33	0.23
	β	0.22	0.14
	R^2	0.79	0.81
Intraparticle diffusion	Linear expression	Y= 1.6056X	Y=0.2365X
	Kp	1.6	0.23
	R^2	0.62	0.63

Fe_2O_3 Al_2O_3 $CaCO_3$ SiO_2 TiO_2
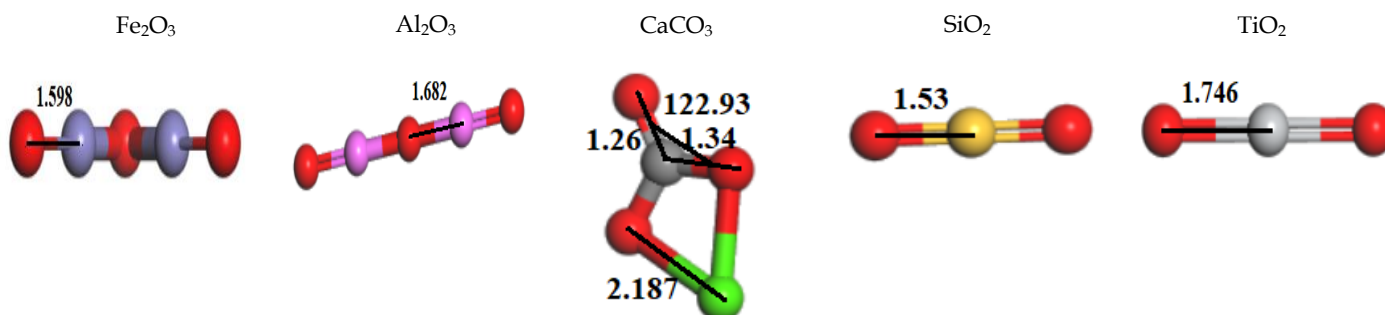
Fig. 3. Optimized structure of clusters and their bond lengths and angles.

Composition name	S (Cal/mol k)	Cp (Cal/mol k)	H (kcal/mol)	G (kcal/mol)
Al_2O_3	71.485	19.932	10.818	-10.495
Fe_2O_3	77.396	16.756	8.84	-14.236
$CaCO_3$	72.529	16.287	12.878	-8.746
SiO_2	57.433	11.066	6.725	-10.399
TiO_2	55.549	8.277	4.444	55.549
MgO	51.12	7.75	3.167	-12.075

Table. 9. Calculated thermodynamic properties of reactants and products.
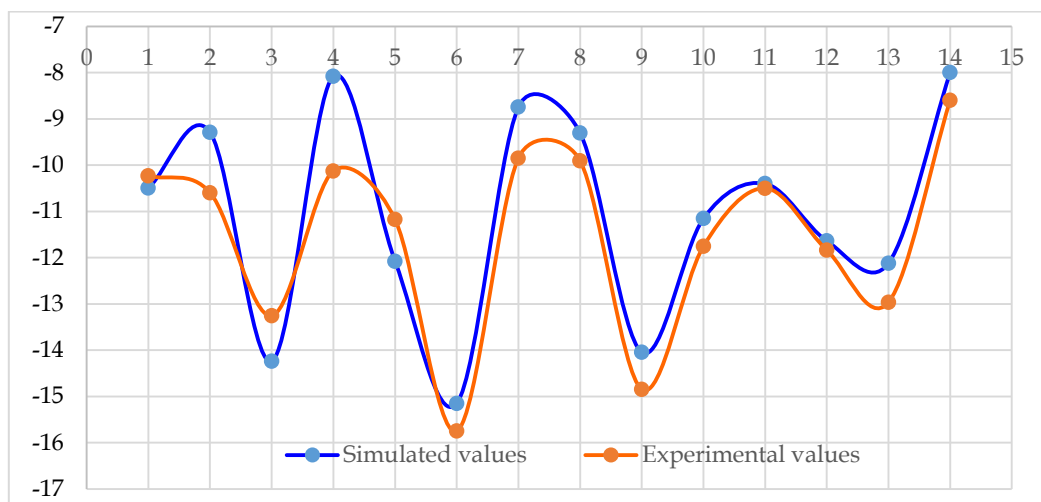
Fig. 4. Results of simulated free energy and obtained from thermodynamic measurements. (1:Al_2O_3, 2: Fe_2O_3, 3:$CaCO_3$, 4:SiO_2, 5: TiO_2, 6: MgO, 7: $Al_2 (SO_4)_3$, 8:$Fe_2 (SO_4)$, 9: $CaSO_4$, 10:$Si SO_4$, 11: $TiOSO_4$, 12: $MgSO_4$, 13: Na_2O, 14: Na_2SO_4).

3.4. Adsorption energy calculation

In the next step, after optimization of crystal oxide components existed in RM structure, $E_{surf + adsorbate}$, E_{surf} and $E_{adsorbate}$ were calculated for sulfate adsorption energy calculation. The optimized crystal components in RM structure after sulfate ion adsorption on their surface were demonstrated in figure 5. Adsorption bond lengths for each component were measured. The results illustrated that the shortest bond lengths which belonged to Fe_2O_3, Al_2O_3, TiO_2, $CaCO_3$ and SiO_2 and equal to 2.134, 2.745, 2.949, 3.194 and 18.229 Å, respectively. Therefore, the lowest bond length is related to Fe_2O_3, Al_2O_3 and TiO_2 that are main metal oxides and exist in RM structure. The results of adsorption energy calculation in water environment with dielectric constant =78.54 were brought in table 10. The results illustrated that all adsorption energies were negative. This issue showed that all main crystal components in RM structure had a great tendency to adsorption of sulfate ions. Among these crystal oxides, the highest adsorption energy belongs to Fe_2O_3, TiO_2, Al_2O_3, $CaCO_3$ and SiO_2, respectively. Whereas these

compounds were main oxides in RM structure, adsorption energy of RM was negative, too. The calculated adsorption energy for RM was equal to -35.68 kcal/mol.
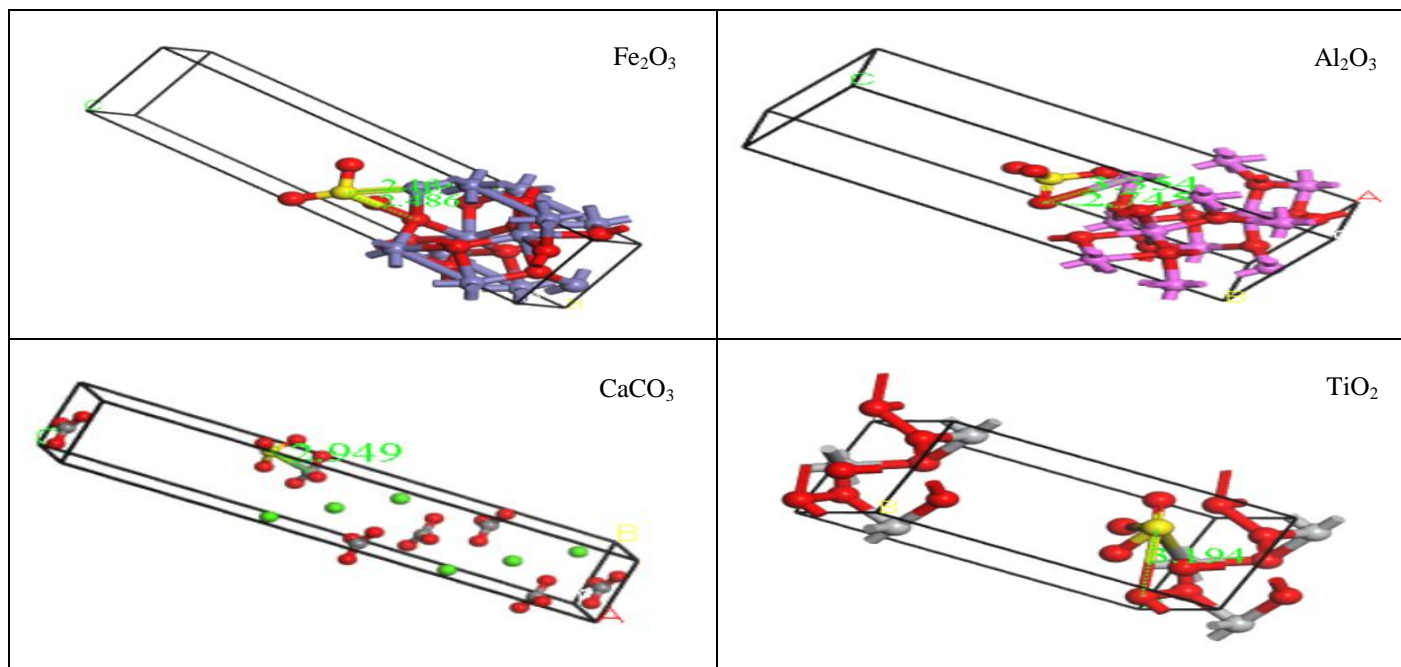
Fig. 5. Optimized crystal components in RM structure after sulfate ion adsorption.

Table. 10. Results of adsorption energy in water environment for different crystal oxide.

Mineral name	E surface or adsorbate	E SO_4^{2-} or adsorbent	E SO_4^{2-}/Surface or adsorbent/adsorbate	E Adsorption (Ha)	E Adsorption (kcal/mol)
Hematite	-8304.7	-700.69	-9008.22	-2.79	-64.33
Quartz	-2136.6	-700.69	-2837.97	-0.63	-14.52
Rutile	-5796.6	-700.69	-6497.7	-0.95	-21.9
Calcite	-5115.5	-700.69	-5817.4	-1.23	-28.36
Corundum	-2254.7	-700.69	-2956.8	-1.43	-32.97

There are various treatment methods for improving adsorption amount and surface modification of RM such as: seawater treatment, acid washing with different acids, heat activation, granular with bentonite or fly ash and presence of different surfactants (Rahimi and Irannajad, 2024). In this research, seawater treatment washing was applied for this aim. To simulate this environment (seawater) as solvent, calculations were performed using the continuum solvation model, namely COSMO. All simulation steps for main crystal oxides were repeated in seawater environment with 84 dielectric constants. The results are related to the calculations of simulation in seawater which has been brought in table 11. These results show that with increasing of dielectric constant, adsorption energies for all main crystal oxides existed in RM structure are raising. The adsorption energy for RM structures in seawater environment was equal to -56.69 kcal/mol. These results illustrate that applied modification method could improve the adsorption properties of raw RM. It is energetically favorable to transfer an ion from the liquid crystal layer with a lower dielectric constant to the alignment layer with a higher dielectric constant. So, with increasing the dielectric constant in adsorption

environment, it increases activated sites on surface layer of adsorbent. To increase ion adsorption on the alignment layer, an alignment layer with a higher dielectric constant is helpful. In the case of inorganic material (metal oxides), this issue is helpful in increasing ion adsorption on the alignment layer.

Mineral name	E surface or adsorbate	E SO_4^{2-} or adsorbent	E SO_4^{2-}/Surface or adsorbent/adsorbate	E Adsorption (Ha)	E Adsorption (kcal/mol)
Hematite	-8304.48	-700.58	-9009.15	-4.09	-94.31
Quartz	-2136.35	-700.58	-2838.05	-1.12	-25.82
Rutile	-5796.23	-700.58	-6498.75	-1.94	-44.73
Calcite	-5115.42	-700.58	-5817.67	-1.23	-38.51
Corundum	-2254.25	-700.58	-2957.47	-2.64	-60.87

Table. 11. Results of adsorption energy in seawater environment for different crystal oxide.

3.5. FTIR analyses

The FTIR spectra of RM, and SRM after sulfate adsorption are plotted in figure 6. The bands which appear at 1410-1470 cm^{-1} for adsorbents are related to carbonate bands. Besides, the peak at 1431 cm^{-1} and 1625 cm^{-1} for RM samples corresponds to C-O and C-C stretching vibration that could be attributed to the existence of cancrinite or calcite in RM structure (Ye, et al. 2015). In addition, the bands in the region of 460-590 and 680 cm^{-1} are the result of the stretching vibrations of the Fe-O bond that can be associated with hematite and magnetite as main composition of RM. Additionally, the bands at around 995 cm^{-1} may correspond to the Si-O-Si and Si-O-Al vibrations that could belong to alumina, Zhypsyt and Boehmite in RM (Deihimi, et al. 2018). The peak intensity of calcite (1431 cm^{-1}) in SRM spectra becomes sharper rather than other adsorbents and peak which can be related to OH^{-} (3420 cm^{-1}) reduction due to the neutralized OH^{-} ion with Mg, Al and Ca in seawater. As can be seen, there is a sharp intensity absorption around 1100 cm^{-1} that is related to SO_4^{2-} vibration band in RM, and SRM after sulfate adsorption. The intensity of this peak is sharper for SRM than RM, this issue shows more adsorption of sulfate on SRM.
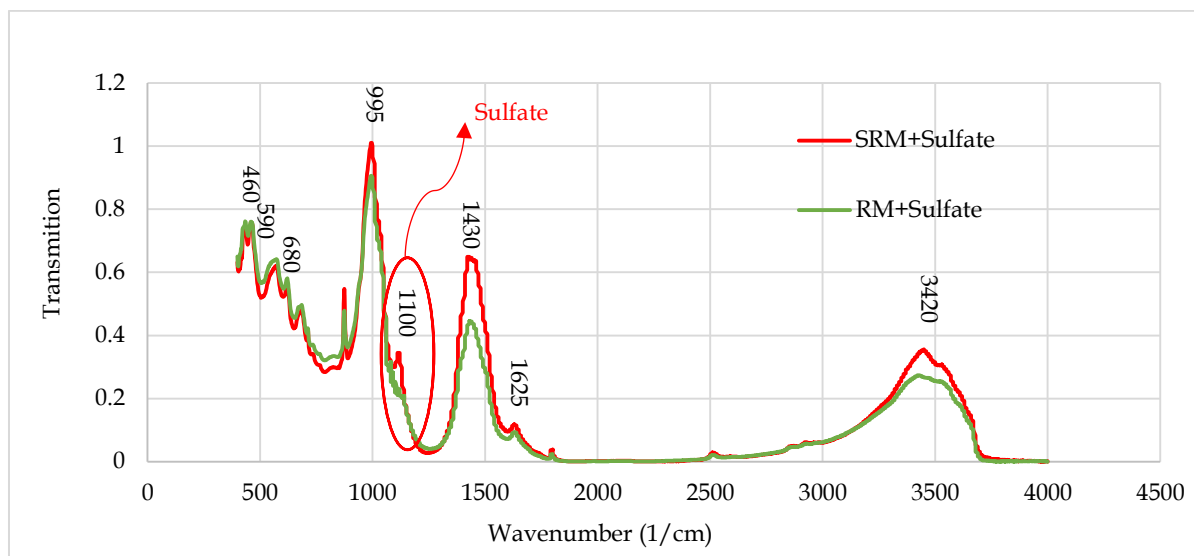
Fig. 6. The FTIR spectra of RM, and SRM after sulfate adsorption.

3.6. BET analyses

The specific surface area is an effective factor in the adsorption amount of adsorbents. Furthermore, the porosity volume per adsorbent mass indicates its specific surface area. For porosity analysis of RM samples, the nitrogen gas absorption and desorption in a range of relative pressure by a pore analysis device was profoundly investigated. Considerably, this device provides nitrogen gas absorption and desorption isotherms along with the dimensional distribution diagram of pores for samples. Moreover, it provides a summary for pore analysis report of samples, which includes information about specific surface area, surface area of micropores, total pore volume, pore volume of micropores and average pore diameter. The textural properties of RM and its modified shape are presented in table 12. According to the obtained results, the porosity volume of RMS is 0.034 cm^3/g that has decreased relative to raw RM (0.0686 cm^3/g). The reason may be the precipitation of various salts on the RMS surface from seawater. It can be the result of the existence of a positive layer on RMS surface and the precipitation of various salts on surface from seawater (Moldoveanu and Papangelakis 2012).

Adsorbent	Specific Surface Area (m²/g)	Dotted Special Surface (m²/g)	Size Particle (nm)	Volume Porosity (cm³ /g)
RM	28.7	26.5	78.6	0.0686
RMS	12.5	11.9	588.6	0.0345

Table. 12. Textural properties of RM and modified RM.

3.7. SEM and EDX results

Scanning electron microscopic pictures related to RM, and RMS are shown in figure 7. in a, and b sections, respectively. There are particles of various sizes and amorphous or crystalline structures. Metal oxide and primitive minerals especially iron have crystalline structures and large sizes and amorph minerals that were formed during the Bayer process including sodium and aluminum

minerals are smaller. EDX results in figure 8 illustrate the attendance of iron, calcium, titanium and silicon as main constituent elements in RM, and RMS structures. Comparing the EDX result of RMS with RM shows increasing calcium ions in RMS composition due to calcite and aragonite precipitation during seawater treatment.
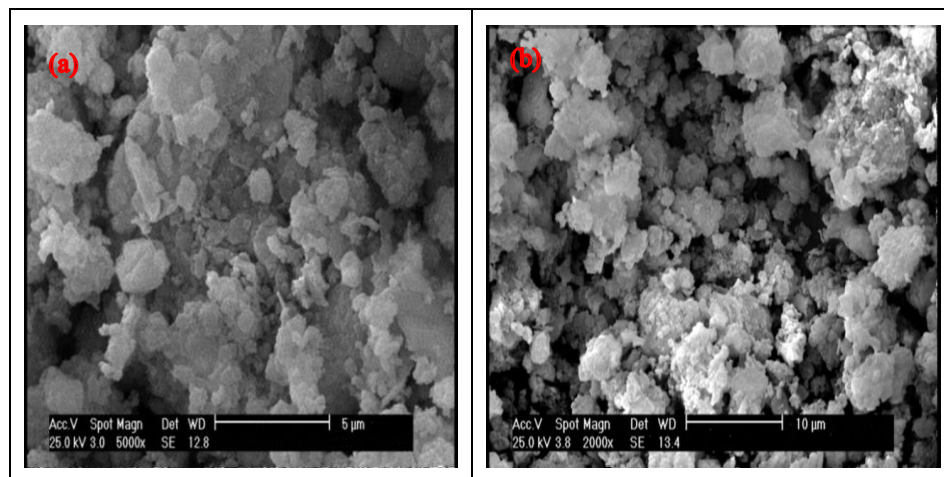
Fig. 7. Scanning electron microscopic of RM (a) and RMS (b).
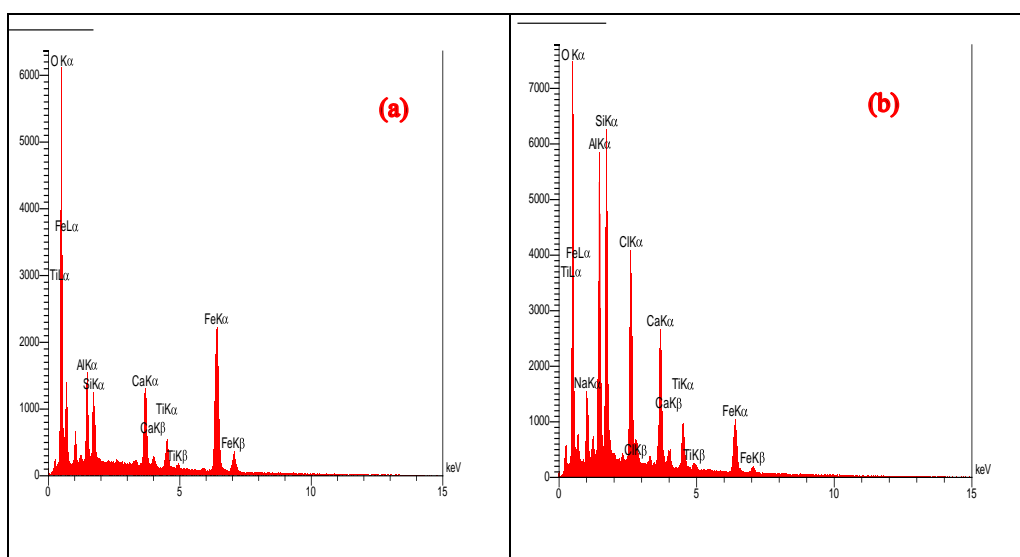
Fig. 8. Energy dispersive X-ray of RM (a) and RMS (b).

4. Conclusion

RM can introduce as an unexpansive adsorbent for sulfate removal from AMD due to its high metal oxides content and high level of pH that can increases low pH of this drainage. Experimental adsorption results illustrate that RM and its activated type by seawater can remove sulfate ions from AMD and sorption capacity by SRM was obtained 15.4 mg/g. Negative adsorption energies for main crystal components in RM structure shows that they have great tendency to the sulfate adsorption. Among these crystal oxides, the highest adsorption energy belonged to Fe_2O_3, TiO_2, Al_2O_3, $CaCO_3$ and SiO_2, respectively. Also, seawater treatment as a modification method was used for reducing pH and increasing adsorption capacity of RM. Seawater washing raises sulfate removal from 6.3% for RM to

29.4% for SRM. The adsorption energies for RM structure in water, and seawater using COSMO were calculated -35.68, and -56.69 kcal/mol. These results illustrate that applied modification method can improve the adsorption properties of raw RM. Comparing the EDX results show increasing calcium ions in RMS composition due to calcite and aragonite precipitation during seawater treatment. Also, there is a sharper intensity absorption related to SO_4^{2-} vibration band in FTIR analyses for SRM than RM after sulfate adsorption. Although RM and its activated type do not have high adsorption capacity and sulfate removal percentages, applying new activation methods include heating and combination with bio absorbent can increase adsorption amount and reduce destructive environmental effects of both RM and AMD. Regeneration study revealed the high reusability (>90%) and acceptable stability of RM even after five successive cycles. These findings indicate that RM use for pollutants removal from wastewater offers a green and environmentally sustainable approach. Although DFT and COSMO models are valuable tools for understanding the thermodynamics of sulfate adsorption, their lack of consideration for kinetics is a limitation.

Acknowledgments

References

Alimohammadi, V., Sedighi, M., Jabbari, E., (2017), Optimization of sulfate removal from wastewater using magnetic multi-walled carbon nanotubes by response surface methodology. *Water Sci Technol*, 76:(10) 2593–2602. https://doi.org/10.2166/wst.2017.424.

Baldwin, D. S., and Mitchell, A., (2012), Impact of sulfate pollution on anaerobic biogeochemical cycles in a wetland sediment. *Water research*, 46(4): 965-974. https://doi.org/10.1016/j.watres.2011.11.065.

Bodalo, A., Gomez, J. L., Gomez, E., Leon, G., Tejera, M., (2004), Reduction of sulphate content in aqueous solutions by reverse osmosis using cellulose acetate membranes, *Desalination*. 162(10): 55-60. https:// doi:10.1016/S0011-9164(04)00027-X.

Burke, I.T., Peacock, C.L., Lockwood, C.L., Stewart, D.I., Mortimer, R.J.G., Ward, M.B., Renforth, P., Gruiz, K., Mayes, W.M., (2013), Behavior of Aluminum, Arsenic, and Vanadium during the Neutralization of Red Mud Leachate by HCl, Gypsum, or Seawater, *Environmental Science Technology*. 47(12): 6527–6535. https://doi.org/10.1021/es4010834.

Deihimi, N., Irannajad, M., Rezai, B., (2018), Equilibrium and kinetic studies of ferricyanide adsorption from aqueous solution by activated red mud, *Journal of Environmental Management*. 227(1): 277–285. https://doi.org/10.1016/j.jenvman.2018.08.089.

Deihimi, N., Irannajad, M., Rezai, B., (2019), Removal of ferricyanide ions from aqueous solutions using modified red mud with cetyl trimethylammonium bromide. *Environmental earth sciences*. 78(6): 187-205. https://doi.org/10.1007/s12665-019-8173-8.

Deihimi, N., Irannajad, M., Rezai, B., (2018), Characterization studies of red mud modification processes as adsorbent for enhancing ferricyanide removal, *Journal of Environmental Management*, 206(1): 266-275. https://doi.org/10.1016/j.jenvman.2017.10.037.

Galiana-Aleixandre, M. V., Iborra-Clar, A., Bes-Pifi, A., Mendoza-Roca, J. A., Cuartas-Uribe, B., IborraClar, M. I., (2005), Nanofiltration for sulfate removal and water reuse of the pickling and tanning processes in a tannery, *Desalination*. 179(1-3): 307-313. https://doi.org/10.1016/j.desal.2004.11.076.

Halajnia, A., Oustan, S., Najafi, N., Lakzian, A.R. A., (2013), Adsorption–desorption characteristics of nitrate, phosphate and sulfate on Mg–Al layered double hydroxide. *Applied Clay Science*, 80(1): 305-312. https://doi.org/10.1016/j.clay.2013.05.002.

He, J., Jie, Y., Zhang, J., Yu, Y., Zhang, G., (2013), Synthesis and characterization of red mud and rice husk ash-based geopolymer composites, *Cement & Concrete Composites*, 37, 108-118. https://doi.org/10.1016/j.cemconcomp.2012.11.010.

Irannajad, M., Rahimi, Sh., (2024), Density Functional Theory Study of Adsorption Mechanism of Sulfate Contaminant on Red Mud Surfaces, *Environmental engineering science*. 32(5): 240416. http://dx.doi.org/10.1089/ees.2024.0077.

Irannajad, M**.**, Rahimi, Sh., (2024), Sulfate Adsorption Process from Acid Mine Drainage by Seawater and Acid-Activated Neutralized Red Mud. *Chemistry Africa,* 45: 1-10. http://dx.doi.org/10.1007/s42250-024-00984-5.

Kitadai, N., Nishiuchi, K., Tanaka, M., (2018), A comprehensive predictive model for sulfate adsorption on oxide minerals. *Geochimica et Cosmochimica Acta*, 238(1): 150-168. https://doi.org/10.1016/j.gca.2018.06.032.

Lee, H. J., Oh, S. J., moon, S. H., (2003), Recovery of ammonium sulfate from fermentation waste by electrodialysis, *Water Research*, 37(5): 1091-1099. http://dx.doi.org/10.1016/S0043-1354(02)00451-7.

Li, D., Ding, Y., Li, L., Chang, Z., Rao, Z., Lu, L., (2015), Removal of hexavalent chromium by using red mud activated with cetyl trimethylammonium bromide. *Environmental technology*, 36(9-12): 1084-1090. https://doi.org/10.1080/09593330.2014.975286.

Liang, F., Xiao, Y., Zhao, F., (2013), Effect of pH on sulfate removal from wastewater using a bioelectrochemical system. *Chemical engineering journal*, 218(1): 147-153. http://dx.doi.org/10.1016/j.cej.2012.12.021.

Liu, Y., Naidu, R., Ming, H., (2011), Red mud as an amendment for pollutants in solid and liquid phases, *Geoderma*, 163(1-2): 1-12. https://doi.org/10.1016/j.geoderma.2011.04.002.

Manisalidis, I., Stavropoulou, E., Stavropoulos, A., Bezirtzoglou, E., (2020), Environmental and Health Impacts of Air Pollution: A Review. *Front Public Health*, volume 8. https://doi.org/10.3389/fpubh.2020.00014.

Martins, Y. J. C., Almeida, A. C. M., Viegas, B. M., Nascimento, R. A., Ribeiro, N. F., (2020), Use of red mud from amazon region as an adsorbent for the removal of methylene blue: process optimization, isotherm and kinetic studies. *International Journal of Environmental Science and Technology*. 17: 4133–4148. http://dx.doi.org/10.1007/s13762-020-02757-2.

Moldoveanu, G.A., Papangelakis, V.G., (2012), Recovery of rare earth elements adsorbed on clay minerals: I. Desorption mechanism. *Hydrometallurgy*. 117(1): 71 – 7. http://dx.doi.org/10.1016/j.hydromet.2012.02.007.

Palmer, S. J., Nothling, M., Bakon, K. H., Frost, R. L., (2010), Thermally activated seawater neutralized red mud used for the removal of arsenate, vanadate and molybdate from aqueous solutions, *Journal of Colloid and Interface Science*, 342(1): 147–154. https://doi.org/10.1016/j.scitotenv.2018.06.272.

Rahimi, Sh., Irannajad, M., (2024), The molecular simulation of sulfate adsorption on hematite and other red mud clusters: Kinetic and thermodynamic modelling study. *Environmental engineering research.* 30(3): 240418. http://dx.doi.org/10.1061/JOEEDU.EEENG-7304.

Rahimi, Sh., Irannajad, M., (2024), Sulfate Removal from Acid Mine Drainage with Chitosan-Modified Red Mud Using Analytical Methods: Isotherm, Kinetic, and Thermodynamic Studies. *Journal of environmental engineering*. 150(10): 04024041-5. http://dx.doi.org/10.1061/JOEEDU.EEENG-7304.

Sadeghalvad, B., Khorshidi, N., Azadmehr, A., Sillanpa, M., (2011), Sorption, mechanism, and behavior of sulfate on various adsorbents: A critical review. *Chemosphere*. 263, 128064. https://doi.org/10.1016/j.chemosphere.2020.128064.

Schwarz, S., Schwarz, D., Ohmann, W., Neuber, S., (2018), Adsorption and desorption studies on reusing chitosan as an efficient adsorbent. *Proceedings of the 3rd World Congress on Civil. Structural and Environmental Engineering*, 8 – 10. http://dx.doi.org/10.11159/awspt18.128.

Silva, A. M., Lima, R., Leão, V., (2012), Mine water treatment with limestone for sulfate removal. *Journal of hazardous materials*, 221(1): 45-55. https://doi.org/10.1016/j.jhazmat.2012.03.066.

Singh, P., Yadav, A.K., Pal, Mishra, V., (2020). Water Pollutants: Origin and Status. *Sensors in Water Pollutants Monitoring: Role of Material*: 5–20. https://doi.org/10.1007/978-981-15-0671-0_2.

Sutar, H., Mishra, S.Ch., Sahoo, S., and Chakraverty, A. P., (2014), Progress of Red Mud Utilization: An Overview. *American Chemical Science Journal*, 4(3): 255–279.

Wang, R. B., and Hellman, A., (2018), Initial water adsorption on hematite (α-Fe2O3) (0001): A DFT + U study. *The journal of chemical physics*, 148: 094705-1. https://doi.org/10.1063/1.5020358.

Ye, J., Cong, X., Zhang, P., Zeng, G., Hoffmann, E., Wu, Y., Zhang, H., Fang, W., (2016), Operational parameter impact and back propagation artificial neural network modeling for phosphate adsorption onto acid-activated neutralized red mud, *Journal of Molecular Liquids*, 216(2): 35-41. https://doi.org/10.5004/dwt.2023.29958.

Ye, J., Cong, X., Zhang, P., Hoffmann, E., Zeng, G., Liu, Y., Fang, W., Wu, Y., Zhang, H., (2015), Interaction between phosphate and acid-activated neutralized red mud during adsorption process, *Applied Surface Science*, 356 (1): 128–134. http://dx.doi.org/doi:10.1016/j.apsusc.2015.08.053.

Zhao, Y., Yue, Q., Li, Q., Xu, X., Yang, Z., Wang, X., Gao, B., Yu, H., (2012), Characterization of red mud granular adsorbent (RMGA) and its performance on phosphate removal from aqueous solution, *Chemical Engineering Journal*, 193: 161-168. http://dx.doi.org/10.1016/j.cej.2012.04.040.

Zia, Y., Mohammadnejad, S., Abdollahy, M., (2019), Gold passivation by sulfur species: A molecular picture, *Minerals Engineering*, 134(6): 215-221. http://dx.doi.org/10.1016/j.mineng.2019.02.009.

Extraction of Alumina from Low-grade Jajarm's Bauxite by Lime Soda Sintering Method

Raheleh Hazrati Behnagh[1]*, Shahram Rostami[1], Sadegh Marahem[1]

1 *Minerals Application Research Centre in the West of Country, Azarshahr, Iran*

*Corresponding author: e-mail (Raheleh Hazrati Behnagh): rh_hazrati@yahoo.com

Abstract:

The components of low-grade bauxite are 28.4% silica, 34.9% alumina, 16.1% iron oxide as ferric oxide and 11.26% loss on ignition. Due to the high silica content of this type of bauxite, it cannot be processed by Bayer method. Therefore, a sintering method with limestone and sodium carbonate was used for selective extraction of alumina. Experimental design was performed by surface response method (RSM) using central composite design. Selected parameters are temperature, soaking time, mole ratio of sodium oxide to alumina, mole ratio of calcium oxide to silica. The maximum amount of extraction of alumina from low-grade Jajarm bauxite by sintering method is 74.2%, which is obtained in the optimal values of the parameters as follows: A temperature of 1157°C, a soaking time of 35 minutes, a mole ratio of alkaline oxide ($K_2O + Na_2O$) of 1.25 and a mole ratio of calcium oxide to silica of 1.99. In 31 run experiments, the mixture of materials powder was transferred to an alumina crucible and heated in a muffle furnace at temperatures and soaking times determined by the experimental design. The sintered material was pulverized. The resulting powder was leached by 150 mL of a boiling alkaline solution (20 g/L NaOH + 20g/L Na_2CO_3) for 30 minutes at a stirring speed of 300rpm. Extracted aluminum from the leaching stage was analyzed by atomic absorption spectrometry.

Keywords: Sintering, Alumina, Low Grade Bauxite, Central Composition Design.

1. Introduction

The worldwide requirement for alumina, an essential precursor in the aluminum manufacturing process, has experienced a remarkable increase in recent years. As of the year 2024, the global output of aluminum has attained 67 million metric tons, with a projected annual growth rate of 3.3% (International Aluminum Institute, 2024). This escalation in the demand for aluminum has directly impacted the necessity for augmented alumina production, given that it constitutes the principal raw material utilized in the aluminum refining process. Nonetheless, one of the most critical obstacles faced by the alumina sector is its dependence on high-grade bauxite ores, which are becoming progressively scarce in terms of both availability and quality. Low-grade bauxite, characterized by a substantial presence of impurities such as silica, iron oxides, and various other minerals, presents formidable challenges in extraction methodologies. In light of these challenges, the Lime Soda Sintering Method has garnered attention as a viable alternative to conventional techniques for the extraction of alumina from low-grade bauxite ores (Ghaemmaghami et al., 2022).

The significance of addressing the challenge associated with low-grade bauxite extraction is paramount. As high-grade bauxite resources become increasingly depleted, a substantial proportion of the world's bauxite reserves is now categorized as low-grade (Sampaio et al., 2023). This transition towards low-grade ores has engendered a heightened demand for extraction methodologies that are not only more efficient and cost-effective but also environmentally sustainable (Shamroukh et al.,

2025). The traditional Bayer process, which is extensively employed for the extraction of alumina from high-grade bauxite, encounters considerable limitations when applied to low-grade ores, attributable to their elevated impurity levels, diminished alumina content, and more intricate chemical compositions (Jha et al., 2021). The challenges associated with the efficient processing of low-grade bauxite ores underscore the necessity for the development of alternative methodologies, which would mitigate dependence on high-grade bauxite and assist in fulfilling the escalating global demand for aluminum.

The Lime Soda Sintering Method presents a potential solution to these challenges. This method involves the use of lime and soda to sinter low-grade bauxite at high temperatures, allowing for the separation of alumina from the gangue minerals through a series of complex chemical reactions (Shen et al., 2022). Several studies have explored the potential of this method, including investigations into the optimum temperature conditions, the types and quantities of additives, and the overall efficiency of the process. For example, research by Yang et al. (2020) demonstrated the feasibility of the Lime Soda Sintering Method in extracting alumina from low-grade bauxite, yielding alumina at high purity levels with relatively low energy consumption. Other studies have focused on the effects of different sintering parameters on alumina extraction efficiency, such as the influence of sintering time, temperature, and chemical additives on the recovery rates (Patel et al., 2021). Despite these advances, challenges remain in optimizing the process for a wide range of low-grade bauxite ores, which vary significantly in mineral composition.

While research into the Lime Soda Sintering Method has provided valuable insights, there remain notable gaps in the current body of knowledge. The predominant focus of current research has been confined to particular bauxite ores, and there exists a deficiency of thorough investigations that assess the method's efficacy across a more extensive array of low-grade bauxite resources (Zhou et al., 2023). Moreover, the environmental ramifications of this methodology, especially concerning waste management and energy utilization, have not been adequately explored. There is an imperative for additional research to refine the sintering process, aimed not only at enhancing alumina extraction efficiency but also at reducing its ecological footprint. Furthermore, a substantial portion of the prevailing literature is concentrated on laboratory-scale investigations, with insufficient attention paid to industrial-scale implementations, which are essential for the successful commercialization of this approach (Sampaio et al., 2023).

The purpose of the current research is to investigate the feasibility of the Lime Soda Sintering Method for extracting alumina from a variety of low-grade bauxite ores, with a particular focus on improving the efficiency of the process and minimizing its environmental footprint. This study aims to optimize the sintering parameters and evaluate the economic and environmental implications of the process, contributing to the development of more sustainable extraction techniques. The primary research question guiding this study is: "How can the Lime Soda Sintering Method be optimized to improve the efficiency of alumina extraction from low-grade bauxite ores while minimizing environmental impact?"

The structure of this paper is organized as follows: in the next section, we outline the methodology employed in this study, including the selection of bauxite ores, experimental design, sintering conditions, and analytical techniques. The results of the experimental work will be presented in the subsequent section, followed by a discussion of the findings, which will include a comparison with existing extraction methods and an evaluation of the environmental and economic feasibility of the optimized Lime Soda Sintering Method. Finally, the paper will conclude with recommendations for future research and practical implications for the alumina industry.

2. Materials and Methods

2.1. Materials

Bauxite and limestone were received from Iran Alumina Company located in North Khorasan province (Jajarm County). Table 1 shows the chemical composition of these two minerals.

Table 1. Chemical composition of minerals

	$Al_2O_3\%$	$SiO_2\%$	$CaO\%$	$K_2O\%$	$Na_2O\%$	$Fe_2O_3\%$	$MgO\%$	LOI
Bauxite	34.9	28.4	1.27	0.90	0.18	16.1	0.024	11.26
Limestone	0.15	0.77	52.8	0.024	0.36	0.087	1.39	43.03

Industrial grade sodium carbonate with a purity of 99% was used in this research work.

2.2. Instruments

Atomic absorption spectrometry analysis (Varian 220 Atomic Absorption Spectrometer, Australia) was used to determine the aluminium in the pregnant solution resulting from the leaching of sintered material.

Sintering of the dry powder mixture of materials was carried out in an electric furnace with a capacity of 60 dm^3 manufactured by Sanat Ceram Company (Iran).

Roller crusher and disc mill manufactured by Danesh Faravaran Company (Iran) were used to crush

2.3. Experimental design

The design of experiments was carried out using the response surface methodology (RSM) and the Central Composition Design (CCD) technique using version 19 of Minitab software. Four parameters affecting the process (the number of factors, k = 4) were defined as RSM factors: sintering temperature, soaking time of the reactants at the sintering temperature, the mole ratio of alkaline oxide (K2O + Na2O) to alumina and the mole ratio of calcium oxide to silica. In all experiments, 5 g of bauxite were used. The yield of alumina leached was selected as the response of the model.

The evaluation of the obtained model was carried out by analysis of variance (ANOVA). The modality of the polynomial equation was assessed statistically by the determination coefficient (R^2), and its statistical importance was evaluated by F-test. Table 2 shows Actual and coded values of independent factors. Table 3 shows the design of the experiments.

Factor	Symbol	-α	-1	0	+1	+α
Temperature	A	1100°C	1150°C	1200°C	1250°C	1300°C
Soaking time	B	0 min	15 min	30 min	45 min	60 min
mole ratio of alkaline oxides to alumina	C	0.6	0.8	1	1.2	1.4
mole ratio of calcium oxide to silica	D	1	1.5	2	2.5	3

Table 2. Actual and coded values of independent factors

Table 3. Design of the experiments

Run	A (T°C)	B (min)	C	D	R%
1	1150	15	0.8	1.5	26.08
2	1250	15	0.8	1.5	15.07
3	1150	45	0.8	1.5	27.64
4	1250	45	0.8	1.5	8.68
5	1150	15	1.2	1.5	55.07
6	1250	15	1.2	1.5	39.81
7	1150	45	1.2	1.5	57.38
8	1250	45	1.2	1.5	16.53
9	1150	15	0.8	2.5	42.23
10	1250	15	0.8	2.5	56.71
11	1150	45	0.8	2.5	52.76
12	1250	45	0.8	2.5	49.55
13	1150	15	1.2	2.5	54.36
14	1250	15	1.2	2.5	47.56
15	1150	45	1.2	2.5	64.12
16	1250	45	1.2	2.5	25.13

17	1100	30	1.0	2.0	52.71
18	1300	30	1.0	2.0	5.45
19	1200	0	1.0	2.0	56.05
20	1200	60	1.0	2.0	66.31
21	1200	30	0.6	2.0	28.42
22	1200	30	1.4	2.0	73.67
23	1200	30	1.0	1.0	16.23
24	1200	30	1.0	3.0	55.68
25	1200	30	1.0	2.0	64.47
26	1200	30	1.0	2.0	63.07
27	1200	30	1.0	2.0	63.26
28	1200	30	1.0	2.0	73.31
29	1200	30	1.0	2.0	69.25
30	1200	30	1.0	2.0	65.91
31	1200	30	1.0	2.0	62.88

2.4. Processing procedure

Bauxite powder, limestone powder and industrial sodium carbonate were mixed according to the experimental design (table3). 5 grams of bauxite were used in each experiment. The powder mixture of materials was transferred to ceramic crucibles (Figure 1) and the materials were sintered (Figure 2) in an electric furnace at the temperatures and times specified in the experimental design (table3).

Fig. 1. Mixed materials before sintering

Fig. 2. Sintered materials

After sintering, the sintered materials were powdered to dimensions below 100 μm and subsequently leached. To perform leaching, a leachant solution was first prepared by dissolving industrial sodium hydroxide (20 g/L) and industrial sodium carbonate (20 g/L). Each sintered powder sample was leached with 150 ml of the leachant solution. The alumina in the leaching solution was determined by atomic absorption spectrometry method and the alumina extraction from bauxite was calculated.

3. RESULTS AND DISCUSSION

Response surface methods are very useful for quantifying and internalizing the relationship between parameters and response. The experimental model resulting from these methods consists of second-order polynomials in the parameters. When the experimenter is relatively close to the optimum point, it is usually necessary to approximate the response with a model that has curvature. In most cases, a second-order model is obtained by the equation below, where y is the response value of the parameter x.

In the extraction of alumina from any of the alumina-bearing minerals (in this case bauxite) by sintering with limestone and sodium carbonate, the parameters affecting the process are: sintering temperature, soaking time of the reactants at the sintering temperature, the mole ratio of sodium oxide

to alumina and the mole ratio of calcium oxide to silica. In the CCD (full factorial two-level design) experimental design method, the number of experiments is obtained from the equation1:

$$N = 2^K + 2K + C \qquad (1)$$

Where N is the number of experiments, K is the number of parameters, and C is the number of central point's repetition.

3.1. Statistical analysis

The factor's levels and the experimental conditions are presented in Table 3. In column R%, the amount of alumina extracted by leaching the sintered material is entered as the response (experimental result). The effects of factors affecting response, including sintering temperature, soaking time of the reactants at the sintering temperature, the mole ratio of alkaline oxide (K_2O + Na_2O) to alumina and the mole ratio of calcium oxide to silica by the surface response method using the Central Composition Design. Data analysis by RSM provides the following model for the amount of alumina extracted (equation 2):

$$R\% = -6488 + 9.86\,A + 9.22\,B + 1030\,C + 55.3\,D - 0.003987\,A^2 - 0.00864\,B^2 - 111.9\,C^2 - 33.00\,D^2 - 0.00695\,A{\times}B - 0.520\,A{\times}C + 0.1289\,A{\times}D - 0.670\,B{\times}C + 0.137\,B{\times}D - 63.4\,C{\times}D \qquad (2)$$

where A, B, C, and D, are sintering temperature (°C), soaking time of the reactants at the sintering temperature (min), the mole ratio of alkaline oxide (K2O + Na2O) to alumina and the mole ratio of calcium oxide to silica, respectively.

ANOVA was used to evaluate the significance and quality of the obtained model. The p-values smaller than 0.05 at the significance level of 95% indicate the significance of the regression model. For the model of alumina extraction, the p-value was equal to 0.000, which is less than 0.05.

The residual plots (Figure 3) indicate the Gaussian distribution of the residuals and the absence of significant bias in the residuals. The maximum amount of extraction of alumina from low-grade Jajarm bauxite by sintering method was predicted to be 74.2% The model predicts that the maximum amount of alumina extraction will be happened at a temperature of 1157 °C, a soaking time of 35 minutes, a mole ratio of alkaline oxide (K2O + Na2O) to alumina of 1.25, and a mole ratio of calcium oxide to silica of 1.99 (Figure 4). Plotting the predicted alumina extraction versus the actual values (Figure 5) is linear (R^2 predicted = 0.938). Contour plots (Figure 6) and surface plots (Figure 7) show changes in the alumina extraction as a function of factors values.
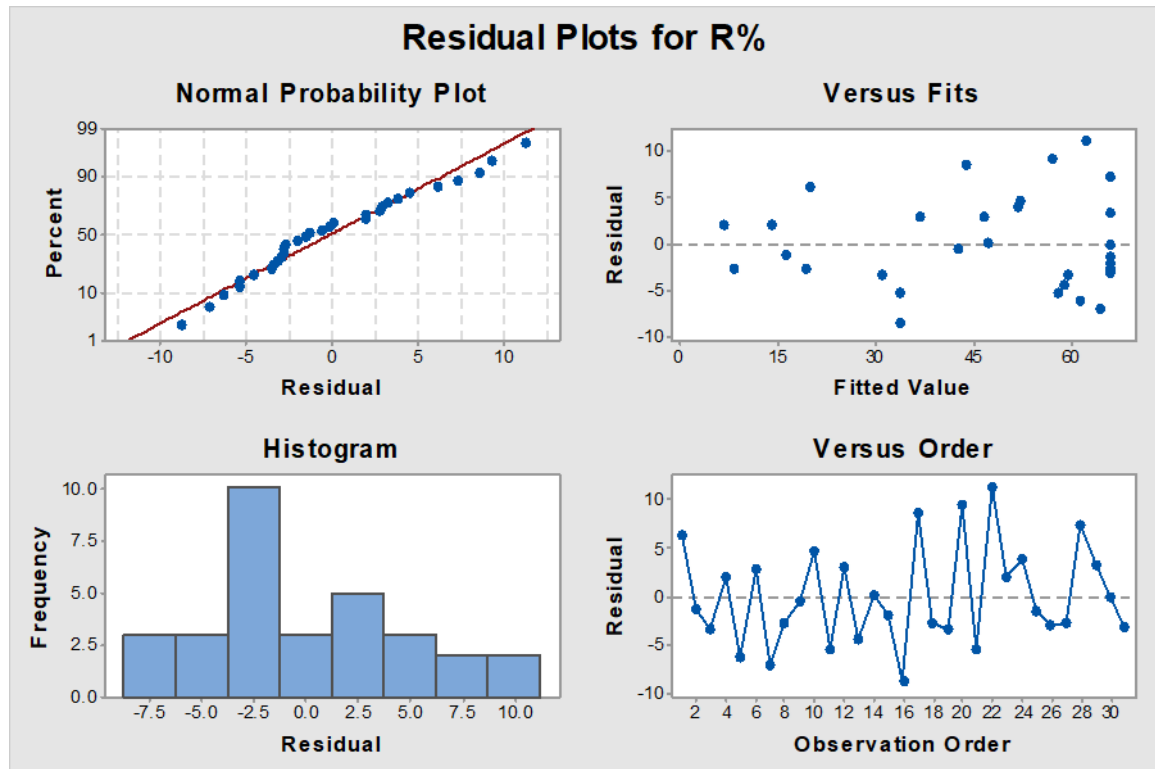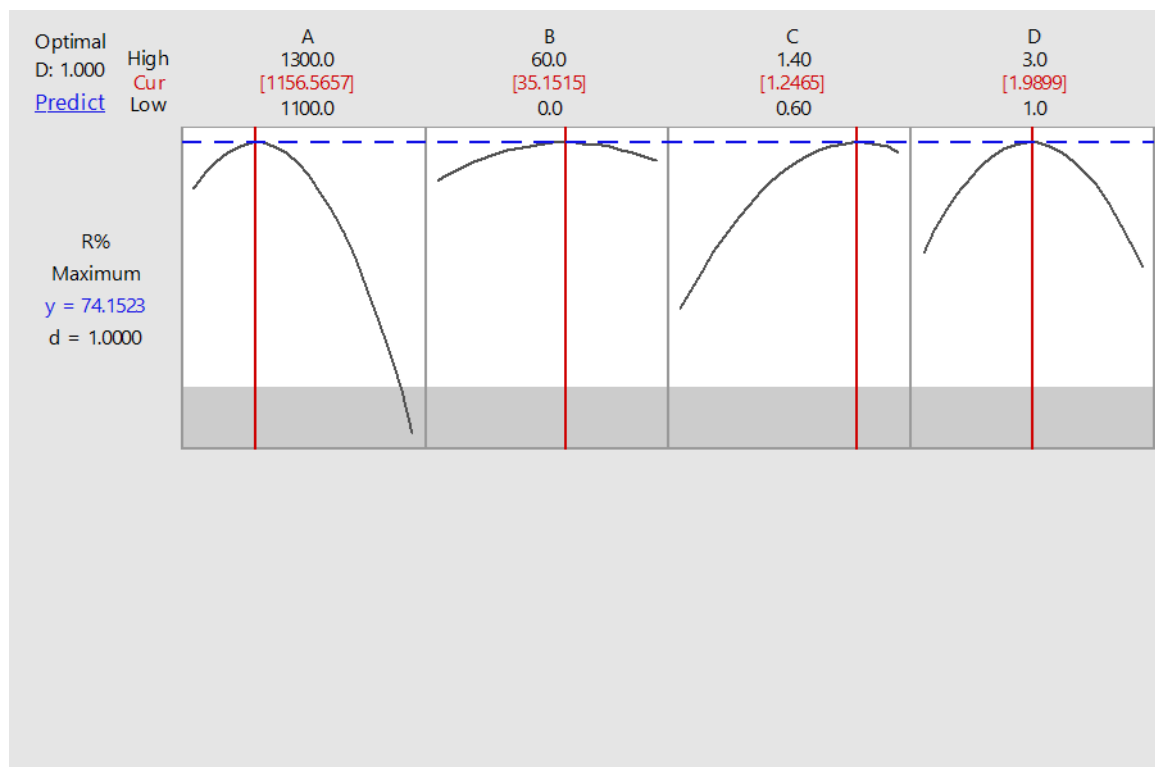
Fig. 3. The residual plots

Fig. 4. Factor's levels at maximum extraction of alumina
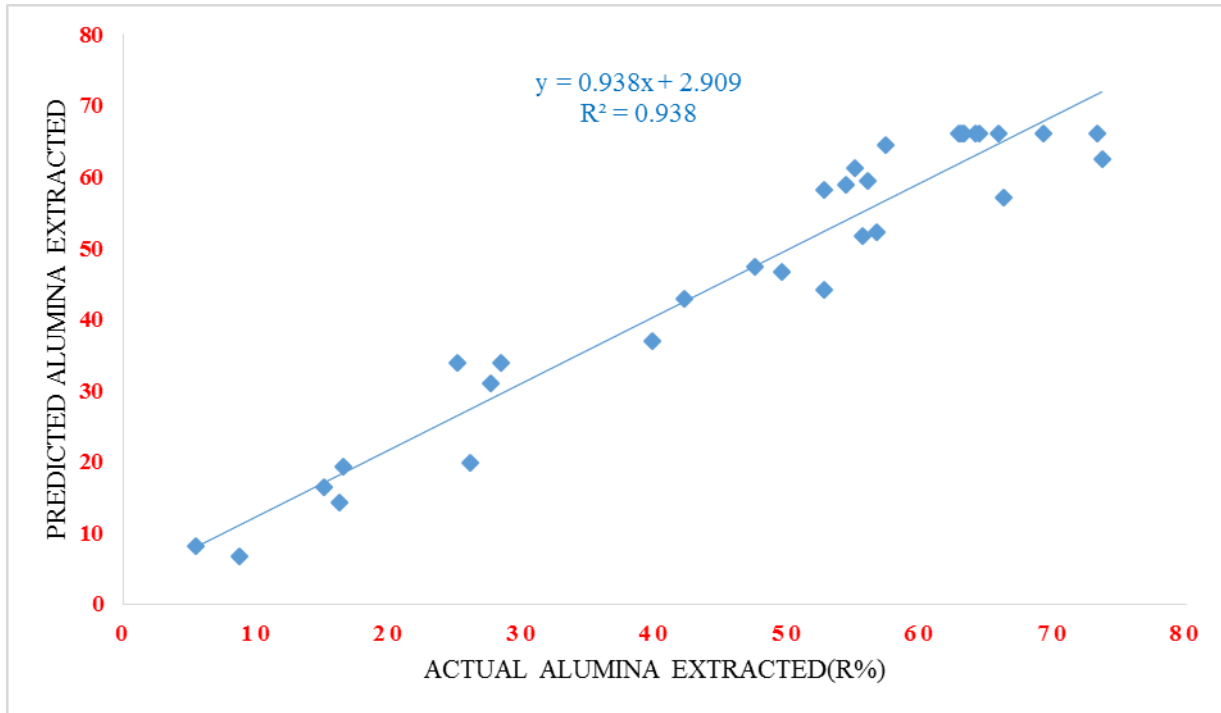
Fig. 5. Predicted alumina extraction versus the actual values
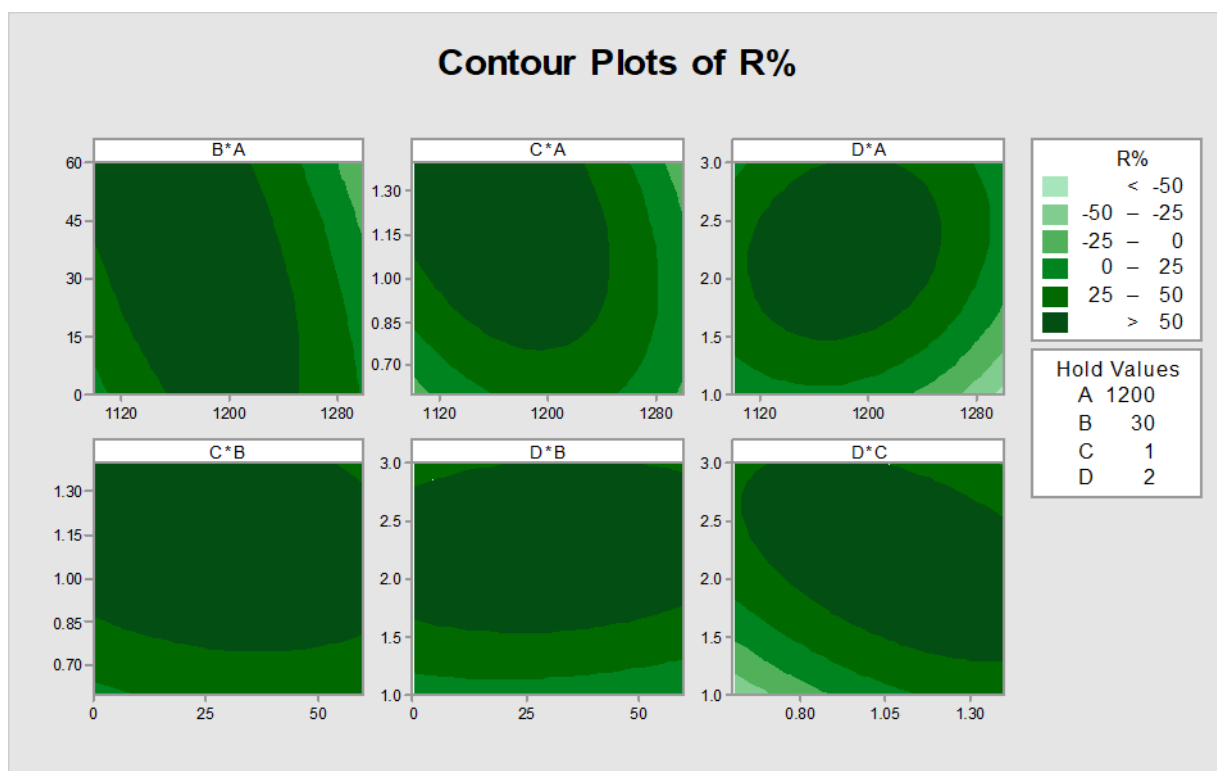
Fig. 6. The contour plots
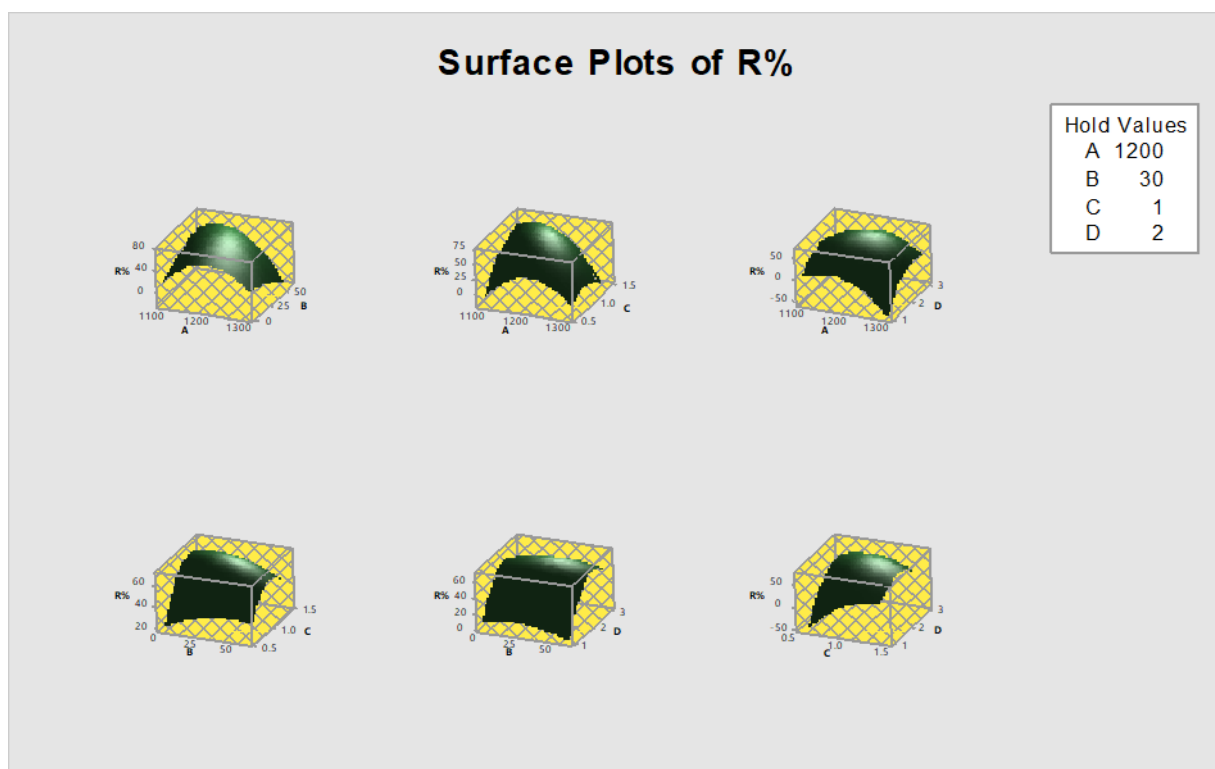
Fig. 7. The Surface plots

225

3.2. Comparison of the Bayer Process and Lime-Soda Sintering for Alumina Extraction

The Bayer process and lime-soda sintering are two main methods for alumina extraction, each suited to different ore types.

Bayer Process:

This method uses caustic soda to digest bauxite under high pressure and temperature. It is efficient for low-silica, high-grade bauxites.

Advantages: High alumina recovery, industrially mature, lower energy requirement.

Disadvantages: Ineffective for high-silica ores due to sodalite formation, red mud generation, high-pressure equipment needed.

Lime-Soda Sintering:

In this method, ore is mixed with Na_2CO_3 and $CaCO_3$ and sintered at 1100–1300°C. Alumina forms soluble sodium aluminate, while silica is fixed as inert calcium silicates.

Advantages: Suitable for high-silica or low-grade ores, minimizes alumina loss, enables recovery of by-products.

Disadvantages: High energy consumption, more complex and costly, produces lime-rich solid waste.

Accordingly, the Bayer process is optimal for high-grade ores with low silica, while sintering is preferred for silica-rich aluminosilicates. Selection depends on ore composition and economic factors.

4. Conclusions

This study successfully demonstrated the feasibility and efficiency of the Lime Soda Sintering Method for extracting alumina from low-grade Jajarm bauxite, which contains high levels of silica (28.4%) and is not amenable to the conventional Bayer process. Through response surface methodology and central composite design, the optimal conditions for maximum alumina extraction (74.2%) were identified as a sintering temperature of 1157°C, a soaking time of 35 minutes, a mole ratio of alkaline oxides ($K_2O + Na_2O$) to alumina of 1.25, and a mole ratio of calcium oxide to silica of 1.99. The strong statistical significance of the model ($p < 0.05$) and a high predicted R^2 value of 0.938 affirm the model's reliability. These findings confirm that sintering with lime and soda is a technically viable and promising alternative for alumina recovery from bauxites with high silica content.

Laboratory-scale studies on the extraction of alumina from low-grade Jajarm bauxite via the lime-soda sintering route have demonstrated promising results. To enable the transition from bench-scale experimentation to semi-industrial application, a structured scale-up strategy is essential.

The transition from laboratory to semi-industrial scale requires an integrated approach encompassing process engineering, material science, energy optimization, and environmental stewardship. The successful implementation of a pilot-scale operation will be a critical milestone toward the industrialization of alumina production from low-grade Jajarm bauxite.

Acknowledgments

References

International Aluminum Institute. (2024). Global aluminum production report.

Ghaemmaghami, E., Samadzadeh Yazdi, M. R., Darvishi, M. A., Sadati, A. A., & Najafi, A. (2022). Alumina extraction by lime-soda sinter process from low-grade bauxite soil of Semirom mine. Journal of mining and environment, 13(4), 1159-1169.

Jha, A., Kumar, S., & Mishra, A. (2021). Challenges in the extraction of alumina from low-grade bauxite. Hydrometallurgy, 107, 45-53.

Li, H., Zhang, J., & Zhao, F. (2021). Optimization of carbon-assisted sintering for alumina extraction. Journal of Cleaner Production, 279, 123567.

Patel, R., Zhang, J., & Chen, Y. (2021). Energy-efficient methods for alumina extraction from low-grade bauxite ores. Minerals Engineering, 156, 147-155.

Sampaio, S. P., & Oliveira, S. F. (2023). The role of carbon-assisted sintering in sustainable alumina production. Minerals Processing and Extractive Metallurgy, 45(2), 180-189.

Shamroukh, A. M. M., Eldeeb, A. B., Salman, S. A., & Farghly, M. G. (2025, March). Sustainable Green Application of Kaolin Ore for Alumina Recovery Based on Lower Temperatures Sintering Process. In TMS Annual Meeting & Exhibition (pp. 24-32). Cham: Springer Nature Switzerland.

Shen, Y., Xu, J., & Li, Z. (2022). Application of carbon-assisted sintering in alumina extraction from low-grade bauxite. Metallurgical and Materials Transactions B, 53(8), 1603-1610.

Yang, X., Zhao, L., & Lu, W. (2020). Carbon-assisted sintering for alumina extraction from diasporic bauxite. Minerals Processing and Extractive Metallurgy Review, 41(5), 314-323.

Zhang, Y., Wang, Z., & Liu, M. (2022). Carbon-assisted sintering for enhanced alumina extraction from low-grade bauxite. Journal of Hazardous Materials, 413, 125463.

Zhou, H., Zhang, T., & Li, P. (2023). Environmental and economic analysis of carbon-assisted sintering for alumina extraction. Journal of Cleaner Production, 319, 128115.

Electrochemical Study Of Pyrite Oxidation In The Presence Of Ozone

Marzieh Sadeghizade[1]*, Ebrahim Azimi[2], Mohammad Raouf Hosseini [3], Mehdi Khandel[4]

[1]PhD Candidate at Department of Mining Engineering, Isfahan University of Technology, Isfahan, Iran

[2]Associate Professor at Department of Mining Engineering, Isfahan University of Technology, Isfahan, Iran

[3]Associate Professor at Department of Mining Engineering, Isfahan University of Technology, Isfahan, Iran

[4]Expert in mineral processing laboratory at Department of Mining Engineering, Isfahan University of Technology

*Corresponding author: **marzieh.sadeghi@mi.iut.ac.**ir (Marzieh Sadeghizade)

Abstract:

Ozone is an environment-friendly and effective oxidant in oxidizing resistant minerals. Studies show its favorable effect on pyrite leaching. However, the effect of ozone from the electrochemical perspective is not known. This study aims to investigate the impact of ozone on pyrite oxidation from an electrochemical perspective. OCP increased when oxidizing species were present. This increase may be attributed to a rise in the concentration of the oxidizing agent in the electrolyte. CV shows the formation of a weak anodic peak in the potential range of 0.3 to 0.5 V, indicating incomplete surface oxidation in the absence of oxidant. Also, the increase in the intensity of anodic peaks in the pyrite oxidation condition and the presence of ozone compared to the absence of oxidant confirms the improvement of oxidation conditions. In the absence of ozone, the presence of two cathodic peaks C_1 and C_2 at potentials of 0.45 and -0.3 V, respectively, indicates the reduction of oxidation products, and it is expected that intermediate species such as FeS and H_2S are formed. In the conditions of acidic solution saturated with ozone, the cathodic peak C_2 is attributed to the reduction of ozone and oxygen adsorbed on the pyrite surface. Because ozone and saturated oxygen in the solution are more prone to accept electrons compared to oxidation products and intermediate species. Finally, the morphology of the pyrite surface remaining from the electrochemical test was examined by FESEM analysis, which confirmed the effect of ozone on the corrosion of the pyrite surface.

Keywords: ozone, pyrite, oxidation, electrochemical, cyclic voltammetry

1. Introduction

Pyrite is the most abundant sulfide mineral and is frequently found as gangue with other sulfide minerals such as chalcopyrite, sphalerite, galena, and cobalt. Pyrite ordinarily contains precious metals such as gold and silver[1, 2]. Primary sulfide minerals such as pyrite require the presence of oxidants for effective dissolution[3]. Many studies have investigated the oxidation of pyrite and observed its behavior in the presence of various oxidants. It has appeared that the oxidation of pyrite in acidic media is related to both chemical and electrochemical properties[4, 5]. The nature and extent of the reaction between pyrite and oxidants in aqueous media are highly related to the potential and pH of the solution, and electrochemical studies can determine the surface properties and the extent of dissolution or formation of a passive layer on the surface[4]. Some researchers reported that at a potential of less than 0.5 V (vs. SCE), the electrode surface is covered with elemental sulfur and $Fe(OH)_3$, which leads to limited penetration of the oxidizing agent to the surface, and by increasing the potential to 0.6 V (vs. SCE), the amorphous sulfur-rich layer on the surface is converted to S8, which improves the oxidation conditions. Also, increasing the potential to values higher than 0.7 V (vs. SCE) leads to the formation of $Fe(OH)_3$ and $SO4^{-2}$ species, along with polysulfides and an iron-rich layer in the form of FeO and Fe_2O_3 on the surface [6, 7]. In a study, it was reported that at low anodic

potential (0.4 to 0.6 V SCE), $Fe_{1-x}S_2$ and $Fe(OH)3$ species and a layer rich in elemental sulfur were formed on the mineral surface, which controlled the diffusion process, and by increasing the potential to over 0.7 V, sufficient potential was provided to completely oxidize pyrite and the inhibitory species that had already formed on it. At potentials higher than 0.9 V (vs SCE), extensive oxidation of pyrite also occurred [8]. Several oxidants have been investigated to provide the potential and improve the oxidation conditions of pyrite, the most important of which is Fe III. Fe III can increase the rate of the oxidation process, on the other hand, its reaction with sulfide minerals can lead to the formation of an inhibitory layer containing polysulfides and elemental sulfur that prevents the penetration of the reactant species on the surface and slows or stops the process [2, 8, 9]. Subsequently, the utilization of an oxidant with high effectiveness, reasonable energy, and negligible environmental problems is essential. Ozone, with its unique properties such as a potential of 2.07 V in acidic medium, may be a promising oxidant in the acidic dissolution of pyrite, which can be produced in situ, has suitable kinetics, and minimal environmental impacts [3, 10]. Due to its high oxidation power, ozone is thermodynamically capable of dissolving pyrite in a sulfuric acid medium and at temperatures close to ambient temperature according to equation (1):

$$FeS_2 + 2/5O_3 + 0/5H_2O \rightarrow Fe^{3+} + 2SO_4^{2-} + H^+ \tag{1}$$
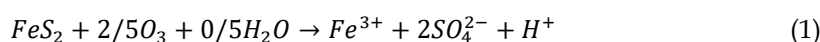
In this paper, the oxidizing behavior of ozone on the dissolution of pyrite surface is investigated using electrochemical techniques. For this purpose, the ozone utilized was present as saturated micro-nanobubbles within an aqueous solution. Cyclic voltammetry is used to detect the reduction reactions and possible products formed. In addition, Eh-pH diagrams of pyrite can predict the products formed during the oxidation-reduction process at a given temperature and pressure. To better understand the oxidation of the mineral, experiments performed with an ozone-saturated solution were compared with oxygen-saturated solution and blank solution. Also, to observe the changes of pyrite after oxidation, the surface of the mineral was investigated using FESEM analysis.

2. Material and methods

2.1. Material

The samples used in this research were high-purity pyrite crystals, which were obtained from the Chah Firouze mine in Kerman. Phase identification was performed using X-ray diffraction (XRD) from Philips, Netherlands, and analyzed using HighScore Plus software. The XRD results in Fig. 1 indicated the high purity of the sample. The amount of minerals in the sample was 96.3% pyrite and 3.6% calcite. Chemical analysis was also performed using an XRF device from Bruker, Germany, and the results are listed in Table 1.
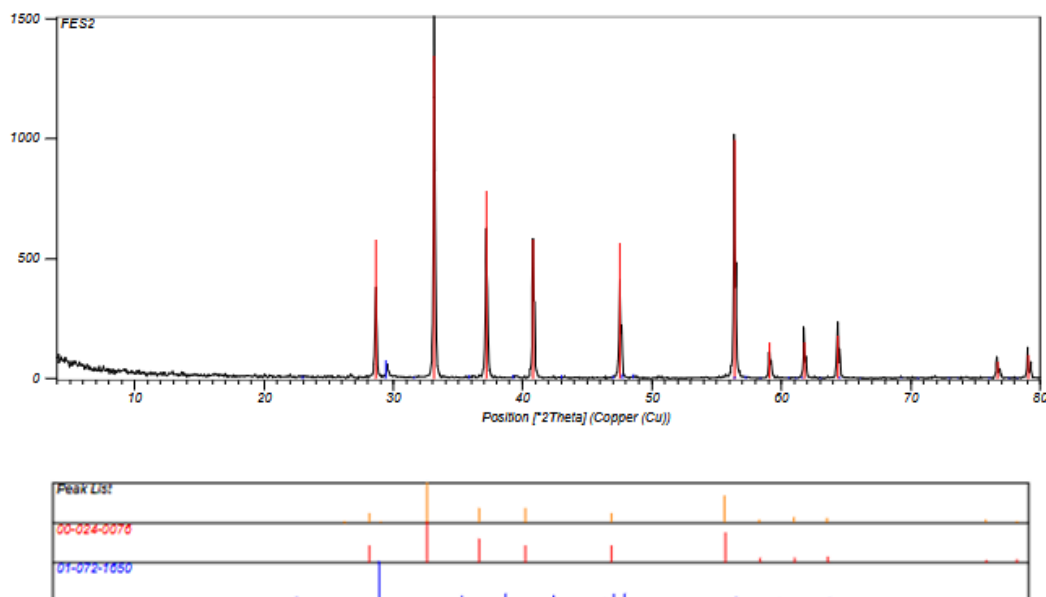
Fig. 1. X-ray diffraction pattern of the chalcopyrite electrode.

Table. 1. Chemical analysis of the chalcopyrite sample (%wt)

Composition	SO_3	Fe_2O_3	CaO	SiO_2	MgO	CoO	Al_2O_3	CuO	NiO	LOI	Total
%wt	46.71	21.46	2.96	0.618	0.209	0.055	0.048	0.029	0.027	27.76	99.88

2.2. Electrode preparation

To make the working electrode (WE), intact and cubic pyrite pieces were used. According to Fig. 2, the crystal surface was smooth and without defects. To remove impurities and further polish the pyrite surface, it was polished on a rotating disc for ten minutes. To prepare the electrode, a copper wire with silver soldered at its end was connected to the pyrite by electric welding.

Fig. 2. Preparation steps of pyrite (WE) working electrode

To make the working electrode (WE), intact and cubic pyrite pieces were used. According to Fig. 2, the crystal surface was smooth and without defects. To remove impurities and further polish the pyrite

surface, it was polished on a rotating disc for ten minutes. To prepare the electrode, a copper wire with silver soldered at its end was connected to the pyrite by electric welding.

2.3. Method

All the tests were carried out with a potentiostat (Model PARSTAT 2273, USA). This device is connected to Power Suite. All tests were performed in a 300 ml cell containing three silver/silver chloride (Ag/AgCl) electrodes as reference electrodes, a platinum electrode with a thickness of 1 mm and a length of 10 mm as an auxiliary electrode, and a pyrite electrode as a working electrode. Two reference electrodes (RE) and a counter electrode (CE) were manufactured by Azar Electrode Co., Iran. Ozone was produced by pure oxygen with a flow rate of 2 liters per minute connected to a corona discharge ozone generator manufactured by Dantek Iran Company, and the ozone flow rate was obtained as 0.2-0.3 liters per minute. The ozone produced by the two-phase vortex pump was in the form of ozone micro-nanobubbles, and after 30 minutes of water circulation, the ozone nanobubbles in the solution reached a saturated state. To perform electrochemical tests, the open circuit potential (OCP) was first recorded for 600 seconds or more until the potential reached a stable state. The tests were performed in such a way that the pyrite electrode was placed in an acid solution, an oxygen-saturated solution, and an ozone-saturated solution, and the open circuit potential and cyclic voltammetry results were recorded.

2.4. Results and Discussion

2.4.1. Eh-pH diagram

The Eh-pH diagram is used for thermodynamic studies and stable species in solution or surface corrosion analysis in potentials and acidic/alkaline environments. Fig. 3 shows the thermodynamic stability range of iron and sulfur components in the pyrite system in solution. The diagram was drawn with the HSC.V6 software. According to the diagram, pyrite is stable in a wide range of pH from 1 to 13 [11, 12]. In a highly acidic environment (pH less than 2), with a decrease in potential from 1 to 0.5 V, iron oxidation is possible. The stability potential range of pyrite is in the range of -0.6 V to +0.3 V [13]. On the other hand, with an increase in potential to more than 0.7 V, pyrite oxidation will be accompanied by the production of Fe III and sulfate.
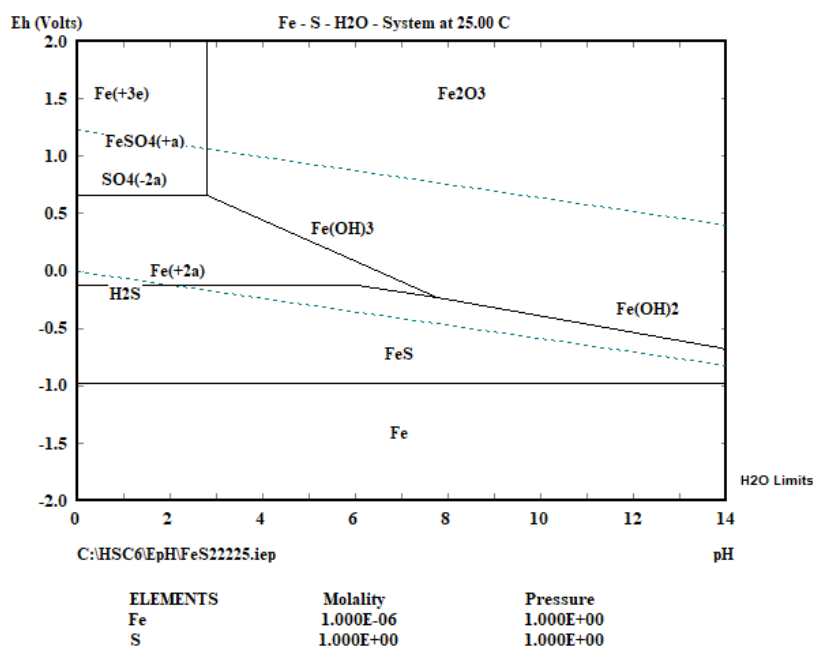
Fig. 3. Eh-pH diagram of pyrite at ambient temperature and pressure

2.4.2. Open Circuit Potential (OCP)

Open circuit potential is a parameter that indicates a surface's resistance to corrosion. Decreasing OCP to lower values indicates that the surface of the material is more easily corroded, and increasing OCP to higher values creates greater resistance to surface corrosion. Fig. 4 shows that the OCP of pyrite in acidic solution increases in the first few minutes and then reaches a steady state.
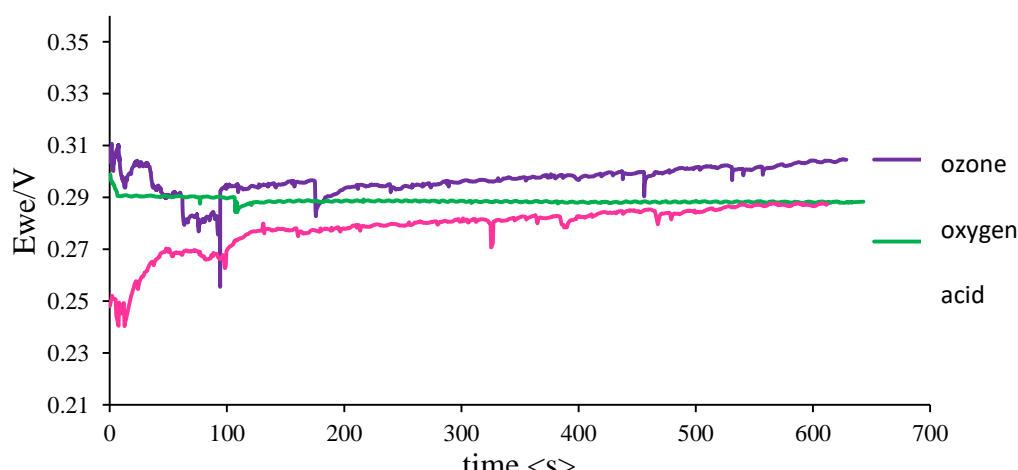
Fig. 4: Open circuit potential of pyrite electrode in sulfuric acid solution, acid and oxygen-saturated solution, and acid and ozone-saturated solution

The open circuit potential of a surface changes when exposed to an electrolyte because, in the initial moments of contact with the solution, the surface is further protected from corrosion by the spontaneous growth of an oxide layer on the surface, and the OCP increases. Over time, the value of the potential becomes stable. The time to reach a steady state depends on factors such as the type of mineral and its chemical composition, and the electrolyte resistance. The control potential (sulfuric

acid solution) reached a steady state of 0.28 V in 10 minutes. Within the case where the electrolyte solution was saturated with nano-ozone, the steady state potential increased to 0.3 V, which could be due to the increase in the concentration of the oxidizing agent (ozone or oxygen) in the electrolyte. According to the Nernst equation, the solution potential is directly related to the concentration of the oxidizing agent [14].

2.4.3. Cyclic voltammetry (CV)

When the electrode reached a steady state, the open circuit potential was measured, and cyclic voltammetry was performed based on the open circuit potential. The voltammetric scan started from the negative side to re-identify the species that had previously formed during oxidation. Fig. 5 shows the voltammetric curve of pyrite in acidic solution and ozone-saturated acidic solution. In this study, the potential sweep was from -500 mV to +900 mV at a scan rate of 10 mV/s within the anodic current direction, and then the reverse scan was applied in the cathodic current direction. Each curve was scanned in three consecutive cycles, and finally, the results of the last scan cycle, which had less noise, were presented. As is clear from Fig. 5, three anodic peaks A_1, A_2, and A_3 were identified in the anodic (oxidation) section, and two peaks C_1 and C_2 were identified in the cathodic (reduction) section. The potential values throughout this report are expressed in terms of the silver chloride reference electrode. It should be noted that to express the potential in terms of the standard hydrogen reference electrode (SHE), the measured values are summed with 222 mV. Also, the saturated electrolyte and the control electrolyte were not stirred during the process.
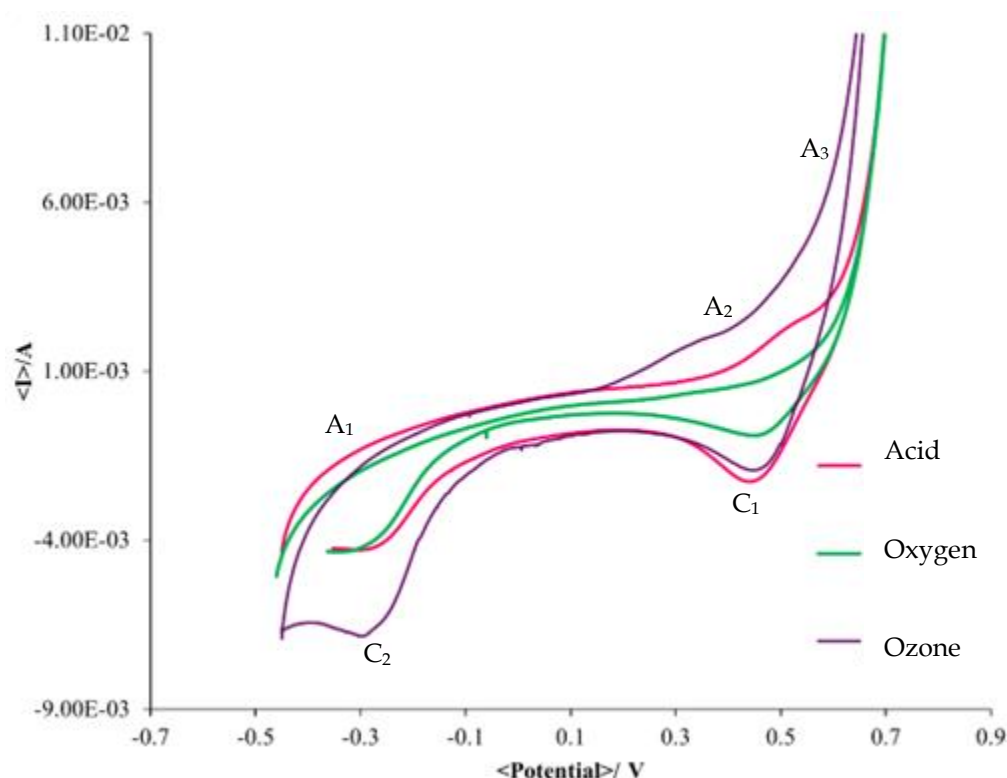
Fig. 5: Cyclic voltammetry of pyrite electrode in sulfuric acid solution and ozone-saturated sulfuric acid solution and scan rate mV/s10

The cathodic peak C_1 of the curve according to equation (1 and 2) in the potential range of 0.45 V is attributed to the reduction of Fe III and $Fe(OH)_3$ to Fe^{2+}:

233

$$Fe^{3+} + 3H^+ + e^- \rightarrow Fe^{2+} + 3H_2O \tag{2}$$

$$Fe(OH)_3 + 3H^+ + e^- \rightarrow Fe^{2+} + 3H_2O \tag{3}$$

In the cathode peak of C_2, according to equation (4) in the potential range of 0.05 to -0.35 V, it is expected to see the reduction of pyrite and the formation of FeS and H_2S species.

$$FeS_2 + 2H^+ + e^- \rightarrow FeS + H_2S \tag{4}$$

The cathodic peak C_2 is observed to be relatively wider, which could indicate multicomponent systems and multi-step charge transfer, or be associated with a combination of processes such as the reduction of thiosulfate and metal-deficient polysulfides. In this range, the peak intensity is relatively low. According to Timoury et al., the produced H_2S gas disperses relatively quickly, resulting in a low concentration around the surface[15]. On the other hand, according to equation (5), the C_2 peak can be attributed to elemental sulfur, which itself leads to the formation of H_2S and is thermodynamically feasible[16]:

$$S^° + 2H^+ + 2e^- \rightarrow H_2S \tag{5}$$

At the end of the cathodic scan, the curve at the potential of -0.45 V has a reverse scan to the positive side. A mild anodic current peak is observed in region A_1. According to Liu et al., the oxidation of H_2S, which was produced in the C_2 region, probably occurs in this region[9]. In the A_2 region, oxidation of FeII occurs, and ferric hydrate is formed. According to Chen et al., peak A_2 is related to the oxidation of pyrite and the formation of a sulfur layer on the electrode surface [17]. The anodic peaks were not as prominent as the cathodic peaks, which could be due to the low concentration of the oxidized species in the solution. The range of cathodic peaks in sulfuric acid solution was between 0.2 to 0.6 V and -0.45 to -0.05 V [6].

By increasing the potential from 0.05 V, partial oxidation of pyrite can lead to the production of intermediate sulfur-rich species such as polysulfides. The accumulation of these species on the surface of the electrode can lead to the formation of a penetration layer, which according to equations (6 and 7) can only be removed at higher potentials or favorable oxidation conditions the penetration layer [15].

$$FeS_2 + 3H_2O \rightarrow Fe(OH)_3 + 2S^° + 3H^+ + 3e^- \tag{6}$$

$$FeS_2 \rightarrow Fe^{2+} + 2S^° + 2e^- \tag{7}$$

In the curve related to acid solution saturated with ozone, the cathodic peak of C_2 is attributed to the reduction reaction of ozone and oxygen absorbed on the surface of pyrite and with equation (9 and 8). Ozone and saturated oxygen in solution are more prone to accept electrons compared to the products and intermediate species [2]:

$$4H^+ + O_2 + 4e^- \rightarrow 2H_2O \tag{8}$$

$$O_3 + 2H^+ + 2e \rightarrow O_2 + H_2O \tag{9}$$

Peak C_2 for pyrite electrode in acidic solution saturated with ozone and oxygen is broader than in acidic solution without oxidant. In other words, this peak can be attributed to the difference in the increase of ozone and dissolved oxygen concentration on pyrite surface. It has been reported that ozone and dissolved oxygen are more effective on pyrite oxidation than intermediate products[2].

Anodic current peaks A_1 and A_2 were proposed for pyrite oxidation and the activation of intermediate surface products. The current increased exponentially during anodic scanning towards the potential of 0.7 V. At higher potentials, with a slight increase in potential, the current value increased exponentially (peak A3); according to studies and examination of the Eh-pH diagram, complete oxidation of FeS_2 to $Fe(OH)_3$ and SO_2^{-4} occurs. Additionally, species such as iron-deficient sulfides ($Fe_{1-x}S_2$), which were previously formed during the partial oxidation of pyrite at a potential of 0.05 V, are also extensively oxidized in this potential range according to equations. (10 and 11).

$$Fe_{1-x}S_2 + 8H_2O \rightarrow (1-x)Fe^{3+} + 2SO_4^- + 16H^+ + 3(5-x)e^- \tag{10}$$

$$S^\circ + 4H_2O \rightarrow SO_4^{2-} + 8H^+ + 6e^- \tag{11}$$

After several stages of CV scanning, a dark layer was visually observed on the surface of the pyrite electrode, which can be evidence of the formation of iron hydroxide $Fe(OH)_3$ according to equation (12) [6, 16]

$$FeS_2 + 11H_2O \rightarrow Fe(OH)_3 + 2SO_4^{2-} + 19H^+ + 15e^- \tag{12}$$
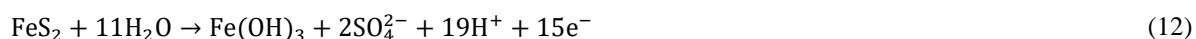
The anodic peaks of the ozone-saturated acid curve show higher values compared to the acid curve, which could be due to the activation of intermediate products on the pyrite surface. In other words, the higher the concentration of species, the higher the voltage in the anodic direction, leading to the oxidation of intermediate products and a greater electron current is exchanged between the surface and the ions. Similarly, in the case of the cathodic current, due to the higher concentration of dissolved species, a greater electron current intensity is observed for the reduction of species such as ferric ions on the pyrite surface [9].

2.4.4. FESEM-EDS analysis

The morphology of the pyrite surface remaining from the electrochemical test was examined by FESEM analysis. According to Fig. 6, the pyrite surface was smooth and clean before the electrochemical test, and no roughness or species were observed on its surface. After pyrite was exposed to 0.5 M acidic solution, species were observed on its surface that can be attributed to the formation of intermediate species. Of course, it cannot be properly discussed whether the formed layers are inhibitory [3]. The formed surface could be elemental sulfur or metal-free polysulfide. In the Fig, roughness and small holes are observed on the pyrite surface, which could be due to surface corrosion of the electrode in the ozone-saturated solution.
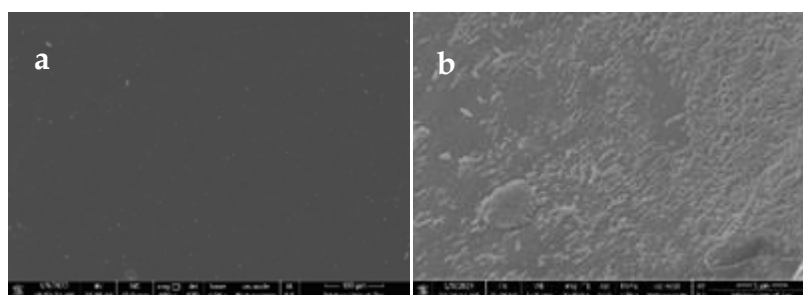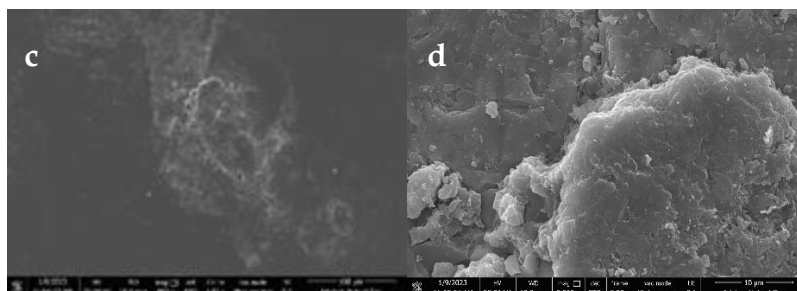
Fig. 6: Results of FESEM analysis of pyrite surface before (a) and after exposure to sulfuric acid solution (b) and ozone-saturated acidic solution (c) and (d)

3. Conclusions

Ozone (O_3) appears as a strong candidate with several advantages, including fast reaction kinetics even at near-ambient temperatures, in situ generation, and minimal secondary pollution. Its ability to decompose passive layers and promote complete pyrite oxidation under mild conditions makes it especially promising for industrial hydrometallurgical applications. In this article, the effect of ozone on pyrite oxidation was investigated by electrochemical test. Due to its high oxidation power, ozone in a sulfuric acid environment and at a temperature close to ambient temperature is thermodynamically capable of proper oxidation of pyrite and proper removal of intermediate species and products on its surface. The increase in the intensity of anodic peaks in the pyrite oxidation condition and the presence of ozone compared 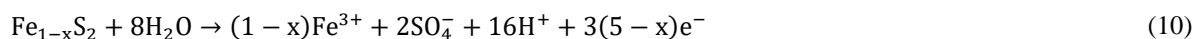to the absence of oxidant confirms the improvement of oxidation conditions. In the conditions of acidic solution saturated with ozone, the cathodic peak is attributed to the reduction of ozone and oxygen adsorbed on the pyrite surface. Because ozone and saturated oxygen in the solution are more prone to accept electrons compared to oxidation products and intermediate species. By comparing the curves obtained from the voltametric and FESEM tests, the positive effect of ozone on the oxidation of pyrite in an acidic medium can be realized. Ozone can improve the performance of gold extraction from sulfide deposits by breaking the pyrite crystal lattice.

References

[1]   A. Chandra and A. R. Gerson, "The mechanisms of pyrite oxidation and leaching: A fundamental perspective," *Surface Science Reports,* vol. 65, no. 9, pp. 293-315, 2010.

[2]   G. Chen, "Electrochemical study on Surface Oxidation of Natural Pyrite in Ferric Sulfate Solution," *International Journal of Electrochemical Science,* vol. 14, pp. 7047-7061, 08/01 2019.

Influence of Complete Gas Dispersion and Critical Impeller Speed on the Flotation Kinetics

Hossna Darabi[1], Faraz Soltani[2*]

[1] Department of Mineral Processing, Tarbiat Modares University, Tehran, 14115-11, Iran

[2] Department of Mining Engineering, Arak University of Technology, Arak, Iran

*Corresponding author: faraz.soltani@arakut.ac.ir (Faraz Soltani)

Abstract:

The main characteristic of mechanical flotation cells is to have an impeller, which is responsible for creating particles suspension, gas dispersion and producing turbulence necessary to create effective bubble-particle interactions. For this purpose, in this paper, the conditions for complete gas dispersion in a Denver laboratory flotation cell have been investigated. Then, the critical impeller speed has been investigated for quartz particles with different size fractions. The effect of complete dispersion of introduced gas and critical impeller speed on the flotation rate constant (k) of particles was investigated. The results showed that k was the minimum value at impeller speed of 700 rpm in the superficial gas velocity of 0.041- 0.125cm/s for all size fractions. The impeller speed of 700 rpm was sufficient to keep -106μm quartz particles suspended, but at all superficial gas velocities, the minimum impeller speed required for complete gas dispersion was 850 rpm. Therefore, it can be stated that the reason for the low k value at a stirring speed of 700 rpm is the incomplete distribution of bubbles and particles (+106μm), resulting in a reduced probability of air bubbles colliding with solid particles. By increasing the impeller speed to values greater than 700 rpm, the k value increased which is due to the complete distribution of particles and air bubbles in the flotation cell (increased probability of particles -air bubbles collision). Therefore, it is necessary to provide suitable operating conditions for complete dispersion of air bubbles and also to keep solid particles suspended.

Keywords: Mechanical flotation cell, Critical impeller speed, Flotation kinetics, Complete gas dispersion

1. Introduction

Mechanical flotation cells are one of the most common flotation cells in mineral processing. For this reason, any inefficiency in the flotation process leads to significant financial losses in mineral processing plants. Therefore, many researchers are seeking to increase their knowledge and understanding of the flotation process. Since the flotation process occurs in an aqueous environment, the interaction between particles and bubbles is strongly influenced by the hydrodynamic forces generated by the surrounding liquid and the relative motion between bubbles and particles. Although advances in the understanding of flotation chemistry have improved the flotation process, especially the flotation of fine particles, optimizing the flotation hydrodynamic environment can also significantly improve the flotation process. The flow regime in mechanical flotation cells is turbulent. Turbulence generated by the impeller affects the flotation process in the mechanical cell by affecting macroprocesses (particle suspension and gas dispersion) and microprocesses (bubble-particle collision, attachment and stability) (Schubert 1999, Darabi et al. 2019, Darabi et al. 2020a). As a result, optimizing flotation performance requires a detailed understanding of the effect of turbulence on

hydrodynamics, particle suspension, gas dispersion and bubble-particle interactions (Darabi et al. 2017, Darabi et al. 2020b, Shen, Z. 2021, Darabi et al. 2024). Therefore, the first step in properly conducting a flotation experiment is to create suitable agitation conditions for complete dispersion of air bubbles and complete suspension of mineral particles in the flotation cell, so that the necessary conditions for bubble-particle interactions (bubble-particle collision, bubble-particle attachment and stability) and, consequently, flotation process are provided. If the bubbles and particles are not completely distributed in the flotation cell, the probability of particle collection is reduced. For this purpose, in this paper, the conditions for complete gas dispersion in a Denver laboratory flotation cell were investigated. The critical impeller speed (the lowest impeller speed required to keep all solid particles suspended at the bottom of the cell) was investigated to ensure proper agitator conditions for particle suspension. Then, the effect of complete gas dispersion conditions and critical impeller speed on the flotation rate constant using pure quartz particles at different size fractions was investigated.

1.1 Complete gas dispersion condition

In a mechanical flotation cell, air is introduced either by the rotor-stator in a self-aerating system or through an external aeration system and is collected in low-pressure cavities behind the agitator blades. As the agitator rotates and shears these air cavities, small and large bubbles are produced. High turbulence in the impeller zone causes the large bubbles to break into small bubbles. The bubbles are then dispersed throughout the cell by the impeller pumping action and fluid circulation. The upward movement of the air bubbles causes the turbulence in the cell to change. Energy is introduced into the flotation cell in the form of kinetic energy through the impeller. Initially, energy is transferred through the primary eddies in the system. As the size of the eddies decreases, the number of eddies increases, but the total energy of the eddies decreases. Large scale eddies are known as macroturbulence. The energy of these eddies is used to suspend and transport particles and bubbles. Smaller eddies, i.e., eddies in the inertial subrange and dissipation subrange, are known as microturbulence. The energy of these eddies is used to disperse the air into small bubbles, and to cause bubble-particle collisions, attachment, and detachment [1]. The bubbles formed in the area near the impeller are carried along with the radial flow generated by the impeller and are dispersed throughout the pulp in the flotation cell. The bubbles then rise in the cell due to buoyancy force but are randomly dragged around by the turbulence in the cell. In flotation cells, the aeration number and the ratio of power consumption under non-aerated to aerated conditions can be used to describe gas dispersion and mixing efficiency(Harris 1974, Harris and Mensah-Biney 1977).

As air bubbles enter the cell with a radial flow impeller, three types of flow patterns are created due to the way the bubbles disperse, depending on the impeller speed and the superficial gas velocity. The impeller is considered flooded when there is an axial flow of gas through the impeller plane that reaches the surface of the free liquid (as shown in Figure 1A). By increasing the impeller speed beyond the critical threshold N_f, the impeller is loaded (refer to Figure 1B), with gas moving across the entire area above the impeller. If the impeller speed is further raised above the critical level N_{CD}, a greater dispersion of gas and liquid occurs both above and below the impeller plane (illustrated in Figure 1C) (Paglianti 2002, Lins Barros et al. 2022). Determining the minimum impeller speed necessary for complete gas dispersion (N_{CD}) is crucial for gaining insights into the flow pattern in a flotation cell (Nienow 1977). The ratio of power input under aerated conditions (P_g) to un-aerated (P_u) conditions states typically falls within the range of 30% to 100%, depending on the impeller type and the superficial gas velocities applied. This ratio not only indicates actual power input but also sheds light on the characteristics of gas dispersion [6]. Analyzing the ratio of unaerated to aerated power input (P_g/P_u) in relation to the Aeration number (N_Q) is vital for identifying the minimum impeller speed needed for complete gas dispersion in the cell. Specifically, at a certain superficial gas velocity, the impeller speed that minimizes this ratio is referred to as the N_{CD}. These conditions of complete gas dispersion are marked by a bubbly fluid flow pattern, ensuring that there is no flooding around the impeller (Yawalkar et al. 2002).
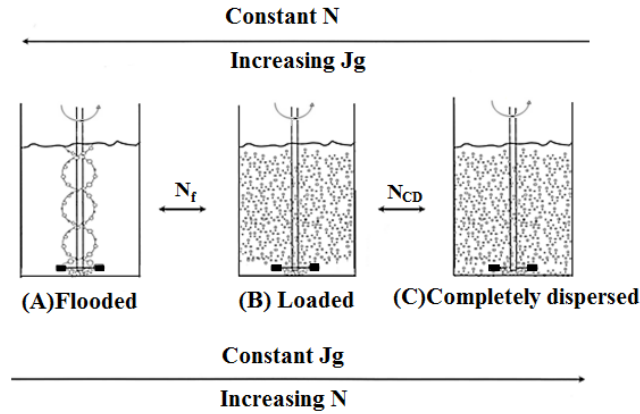
Constant N

Increasing Jg

N_f N_{CD}

(A)Flooded   (B) Loaded   (C)Completely dispersed

Constant Jg

Increasing N

Fig. 1. Schematic picture of the bulk flow patterns.

Aeration number (N_Q) can be calculated using following equation: $N_Q = Q_g/ND^3$, where Q_g denotes the total volumetric gas flow rate, N represents the impeller speed, and D is the impeller diameter(Harris and Mensah-Biney 1977).

1.2 Critical impeller speed (N_{js})

Achieving effective solids suspension is crucial for particles collection and depends greatly on the hydrodynamic conditions within the cell (Schubert and Bischofberger 1998, Darabi et al. 2017). This process consists of two main stages: the first involves lifting solids off the bottom and the second involves spreading and distributing them evenly throughout the cell (Arbiter et al. 1969, Harris and Mensah-Biney 1977, Shen, Z. 2021,). Consequently, methods for evaluating solids suspension typically focus on either the conditions for off-bottom suspension (e.g., the critical impeller speed) or the conditions for solids distribution (e.g., the suspension height). In the literature, the critical impeller speed, denoted as N_{js}, is frequently referenced as the primary criterion for assessing the effectiveness of solids suspension. This speed is defined as the minimum impeller speed required to fully lift all solids off the bottom of the cell (Zwietering 1958, Van der Westhuizen and Deglon 2007, Van der Westhuizen and Deglon 2008).

2. Materials and methods

The tests were conducted using a Denver flotation cell with a capacity of 10.5 L. The cell bottom's square shape was created by its 20 cm by 20 cm dimensions. The stator consisted of 12 blades with a diameter of 12 cm, while the impeller was composed of 8 blades with a diameter of 9 cm. Additionally, the impeller and cell bottom were separated by 2 cm (off-bottom clearance). The impeller's rotational speed, N, was fixed at 700, 850, and 1000 revolutions per minute. The superficial gas velocity was 0.041, 0.083 and 0.125cm/s. Studies were conducted on pure quartz particles (particle density 2.65 g/cm³). The pure quartz sample was prepared from Technosilis Corporation (Tehran, Iran). The sample was screened to obtain seven size classes containing -300+212 and -212+150 µm (coarse particles), -106+75 and -150+106 µm (medium particles), -75+53, -53+38, and -38 µm (fine particles). All samples were rinsed by distilled water to prevent any coated fine quartz particles. The pulp density was considered to be 5%. Under a pH of 9, pure quartz exhibits a robust negative charge and achieves complete dispersion. Consequently, quartz suspensions exhibit no yield stresses at low solid concentrations (<10% solids by volume) (Ndlovu et al. 2011, Ndlovu et al. 2011). In flotation cells, conditions resembling an ideal suspension may be approximately met only when volume fractions of solids are below 0.05 to 0.1. Under these circumstances, the impact of particles on turbulence can be disregarded (Schubert 1999). The frother concentration of 22.4 ppm (C/CCC = 2) methyl isobutyl carbinol (MIBC) was employed. Additionally, dodecyl amine was utilized as the collector at a concentration of 2.837×10^{-5} mol/L at pH =9. Concentrates were collected at consistent intervals of 30, 60, 120, 180, 240, 360, and 480 seconds, each collected into separate containers. Throughout the process, water was added to sustain the pulp level within the flotation cell. The

concentrates and tailings were subjected to drying and subsequent weighing. Following this, the recovery (R_i) was calculated as a function of time. It has been established that the lab-scale flotation process operates as a first-order rate process (Jameson et al. 1977, Ralston 1992). Hence, the flotation rate constant was determined by the following equation:

$$R_i = R_{max}(1 - e^{-kt}) \tag{1}$$

where k is the flotation rate constant (1/min), t is time (min) and R_{max} is recovery (%) at time infinity (ultimate recovery). Non-linear least square regression method was used to calculate k and R_{max} for each particle size range using Eq. (1).

2.1 Power input

In order to finding the ratio of unaerated to aerated power input (P_g/P_u), the torque was measured under both unaerated and aerated conditions. Each measurement was repeated three times and the average power consumption and standard deviation were determined for each set of test conditions. The power input (P) by the impeller at both conditions was calculated as follows (Gui et al. 2013),

$$P = \frac{2\pi TN}{60} \tag{2}$$

where T is the stirring shaft torque.

2.2 Critical impeller speed (N_{js})

The critical impeller speed necessary for complete suspension, denoted as N_{js}, was established by incrementally raising the impeller speed starting from 300 rpm while observing the bottom of the flotation cell through an inclined mirror illuminated by a light source (Figure 2). The 1s-criterion, introduced by Zwietering in 1958 (Zwietering 1958) and widely adopted by other researchers (Van der Westhuizen and Deglon 2007, Van der Westhuizen and Deglon 2008, Lima et al. 2009), was utilized to visually assess the just-suspended state.
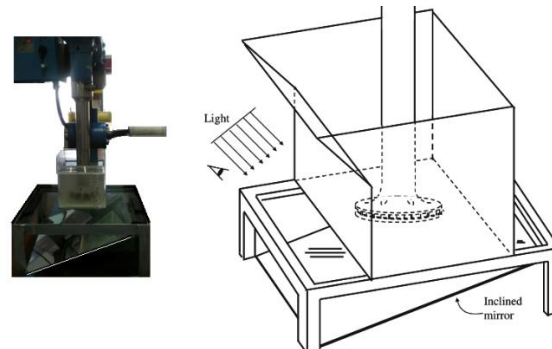
Fig 2. Experimental scheme used to measure the critical impeller speed.

3. RESULTS AND DISCUSSION

3.1 Critical impeller speed (N_{js})

The results of the critical impeller speed measurements are presented in Table 1. The minimum required impeller speed for particles of -106+74 μm at an aeration rate of 0.041 cm/s is 705 rpm and the maximum required impeller speed for particles of -300+212 μm at the superficial gas velocity of 0.125 cm/s is 1010 rpm. Therefore, the impeller speed range between 700-1000 rpm was selected for the experiments. Since the other size classes selected for the flotation experiments are smaller than the -106+74 μm particles, it can be stated that this impeller speed range is suitable for all selected size classes.

Table 1. Critical impeller speed (N_{js}) for particles with different size classes at different superficial gas velocities

Superficial gas velocity (cm/s)	Particle size (μm)	N_{js} (rpm)
0	-106+74	660
0.041	-106+74	705
0.083	-106+74	765
0.125	-106+74	880
0	-150+106	740
0.041	-150+106	805
0.083	-150+106	825
0.125	-150+106	920
0	-212+150	775
0.041	-212+150	855
0.083	-212+150	915
0.125	-212+150	985
0	-300+212	935
0.041	-300+212	970
0.083	-300+212	985
0.125	-300+212	1010

3.2 Complete dispersion of introduced gas

In Figure 3, the ratio of power consumption under aerated conditions to power consumption under non-aerated conditions (Pg/Pu) is plotted as a function of the Aeration number (NQ) at different impeller speeds. The Pg/Pu ratio was 0.82 to 1. In this figure, the minimum speed required for complete dispersion of introduced gas (N_{CD}) is presented as the impeller speed at which the Pg/Pu ratio is minimum at a given superficial gas velocity. At all superficial gas velocities, the N_{CD} was equal to 850 rpm. It can be stated that in the superficial gas velocity range of 0.125-0.041 cm/s, impeller speed of 700 rpm is not sufficient for complete gas dispersion in the cell. Therefore, flotation experiments need to be performed at impeller speeds higher than 850 rpm.
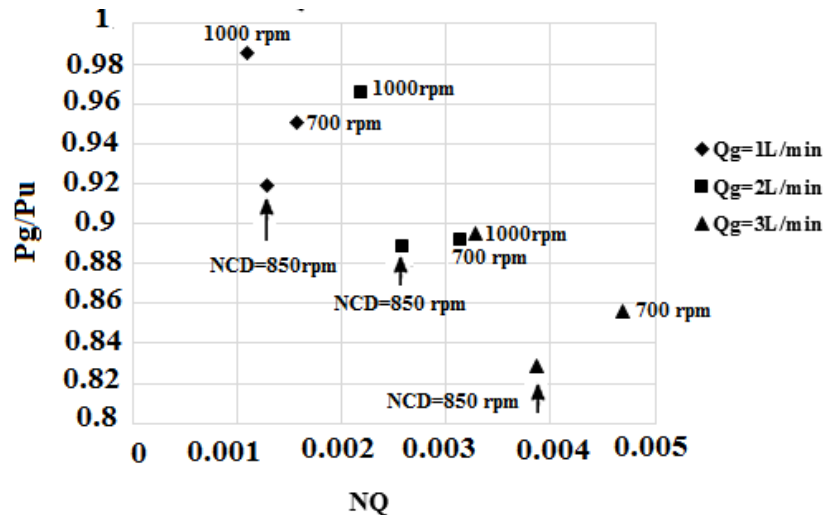
Fig. 3. The relationship between N_Q and P_g/P_u

3.3 Influence of Complete dispersion of introduced gas and Critical impeller speed on the Flotation Kinetics

In order to investigate the relationship between flotation rate constant (k), N_{js} and N_{CD}, for each of the size classes of quartz particles studied in this paper, the flotation rate constant for impeller speeds of 700, 850 and 1000 rpm at the superficial gas velocities of 0.125-0.041 cm/s is investigated in Figure 4.
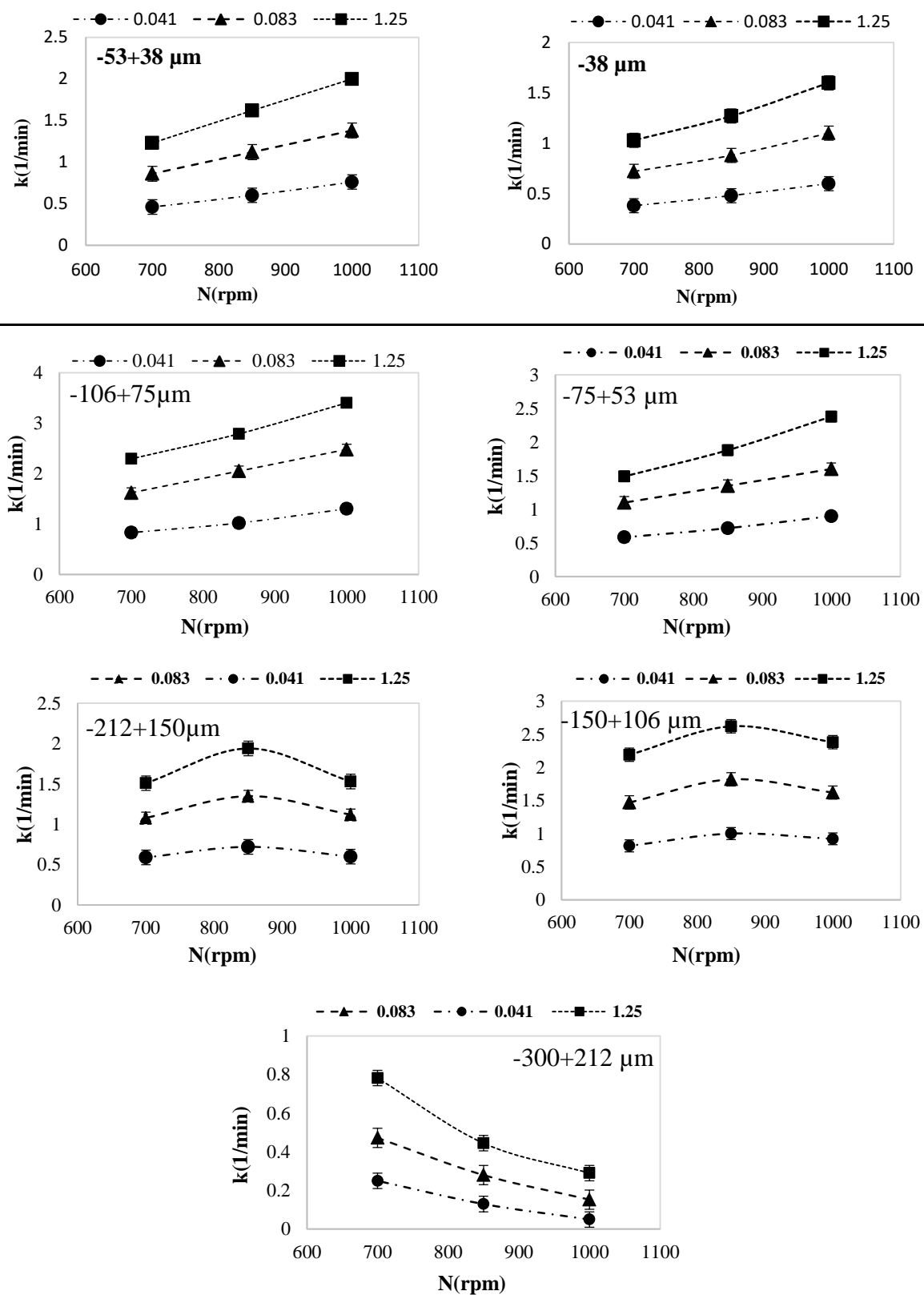
Fig. 4. The relationship between impeller speed and flotation rate constant at different particle sizes and superficial gas velocities

The results show that , k has the minimum value at the impeller speed of 700 rpm and the superficial gas velocities of 0.125-0.041 cm/s for all size classes. According to the results, the impeller speed of 700 rpm is sufficient to keep quartz particles smaller than 106 µms in suspension, but at all superficial gas velocities, the N_{CD} obtained to be equal to 850 rpm. Therefore, it can be stated that the reason for the low k value at the impeller speed of 700 rpm is the lack of complete distribution of air and particles (larger than 106µm) in the flotation cell, resulting in a decrease in the bubbles- particles collision probability. As can be seen in Figure 4, at impeller speeds of 850 rpm (equivalent to N_{CD} 1.2 N_{js}) to 1000 rpm (equivalent to 1.5 N_{js}), the flotation rate kinetics of particles smaller than 106 µm increased beacuse particles have a more uniform spatial distribution in the flotation cell at impeller speeds of 1.2 to 1.5 N_{js} (Darabi et al. 2017). On the other hand, the N_{CD} obtained to be equal to 850 rpm. Accordingly, we can say that k values increase because bubbles and particles are uniformly distributed throughout the flotation cell, increasing the likelihood of collisions between the two when the impeller speed is between 850 and 1000 rpm (Darabi et al. 2019). However, k for particles larger than 106µm decreases as the impeller speed increases above 850 rpm because particles and air bubbles are more likely to separate from one another, even though the particles and bubbles are still evenly distributed (Darabi et al. 2020a). Therefore, it is necessary to provide suitable operating conditions for complete dispersion of air bubbles and also to keep solid particles suspended in order to provide optimal flotation conditions.

4. CONCLUSIONS

This paper investigated the conditions for complete gas dispersion in a Denver laboratory flotation cell. The critical impeller speed was investigated to ensure the creation of suitable agitation conditions for particle suspension. Then, the effect of complete gas dispersion conditions and critical impeller speed on the flotation rate constant using pure quartz particles was investigated. The results of the investigation of the conditions for complete gas dispersion showed that in the range of the superficial gas velocities of 0.125-0.041 cm/s, the impeller speed of 700 rpm is not sufficient for complete gas dispersion in the cell. Therefore, it is necessary to conduct flotation experiments at impeller speeds higher than 850 rpm. The minimum critical impeller speed for particles of -106+74 µm at the superficial gas velocity of 0.041 cm/s was 705 rpm, and the maximum required impeller speed for particles of -300+212 µm at the superficial gas velocity of 0.125 cm/s was 1010 rpm. Since the other size classes selected for flotation experiments are smaller than the -106+74 µm particles, it can be stated with certainty that this impeller speed range of 700-1000 rpm is suitable for all selected size classes. For a impeller speed of 700 rpm in the range of the superficial gas velocity of 0.125-0.041 cm/s for all size classes, k has the minimum value. According to the results of the critical impeller speed determination experiments, the impeller speed of 700 rpm was sufficient to keep quartz particles smaller than 106 µms in suspension, but at all the superficial gas velocities, N_{CD} (the minimum impeller speed required for complete gas dispersion) was obtained 850 rpm. Therefore, it can be stated that the reason for the low k value at the impeller speed of 700 rpm is the lack of complete distribution of bubbles and particles (larger than 106 µms) in the flotation cell, and as a result, the probability of bubbles- particles collision is reduced. The flotation rate kinetics of particles smaller than 106µm changed at impeller speeds of 850 to 1000 due to the full distribution of air and the more uniform spatial distribution of particles in the flotation cell. The likelihood of a bubble-particle collision then increased. Despite the overall particle and bubble distribution, K for particles larger than 106µm was decreased by increasing the impeller speed to values greater than 850 rpm. The higher detachment efficiency of particles and air bubbles may be the cause of this. There fore, it is essential to provide suitable operating conditions for complete dispersion of air bubbles and also to keep solid particles suspended in order to provide optimal flotation conditions.

REFERENCES

Arbiter, N., Harris, C. and Yap, R. (1969). "Hydrodynamics of flotation cells. *SME Transactions,* 244: 134-148.

Darabi, H., Koleini, S. M. J., Rezai, B., & Abdollahy, M. (2017). "The Investigation of Critical Impeller Speed in a Laboratory Mechanical Flotation Cell. *Nashrieh Shimi va Mohandesi Shimi Iran*, 36(3), 211-223.

Darabi, H., Koleini, S. J., Deglon, D., Rezai, B. and Abdollahy, M. (2019). "Investigation of bubble-particle interactions in a mechanical flotation cell, part 1: Collision frequencies and efficiencies. *Minerals Engineering,* 134: 54-64.

Darabi, H., Koleini, S. J., Deglon, D., Rezai, B. and Abdollahy, M. (2020a). "Investigation of bubble-particle attachment, detachment and collection efficiencies in a mechanical flotation cell. *Powder Technology,* 375: 109-123.

Darabi, H., Koleini, S. M. J., Soltani, F., Abdollahy, M., & Ghadiri, M. (2020b). "Turbulence characteristics and flotation performance using particle image velocimetry technique. *Powder Technology*, 376, 458-467.

Darabi, H., Soltani, F., and Deglon, D. (2024). "Enhancing flotation kinetics: Investigating hydrodynamic impact for improved predictive modeling. *Minerals Engineering*, 215, 108832.

Gui, X., Cheng, G., Liu, J., Cao, Y., Li, S. and He, Q. (2013). "Effects of energy consumption on the separation performance of fine coal flotation. *Fuel Processing Technology,* 115: 192-200.

Harris, C. (1974). "Impeller speed, air, and power requirements in flotation machine scale-up. *International Journal of Mineral Processing,* 1(1): 51-64.

Harris, C. and Mensah-Biney, R. (1977). "Aeration characteristics of laboratory flotation machine impellers. *International Journal of Mineral Processing,* 4(1): 51-67.

Jameson, G., Nam, S. and Young, M. M. (1977). "Physical factors affecting recovery rates in flotation. *Miner. Sci. Eng.;(South Africa),* 9(3).

Lima, O. A. d., Deglon, D. A. and Leal Filho, L. d. S. (2009). "A comparison of the critical impeller speed for solids suspension in a bench-scale and a pilot-scale mechanical flotation cell. *Minerals Engineering,* 22(13): 1147-1153.

Lins Barros, P., Ein-Mozaffari, F., & Lohi, A. (2022). "Gas dispersion in non-Newtonian fluids with mechanically agitated systems: A review. *Processes*, 10(2), 275.

Ndlovu, B., Becker, M., Forbes, E., Deglon, D. and Franzidis, J.-P. (2011). "The influence of phyllosilicate mineralogy on the rheology of mineral slurries. *Minerals engineering,* 24(12): 1314-1322.

Ndlovu, B., Forbes, E., Becker, M., Deglon, D., Franzidis, J. and Laskowski, J. (2011). "The effects of chrysotile mineralogical properties on the rheology of chrysotile suspensions. *Minerals Engineering,* 24(9): 1004-1009.

Nienow, A. (1977). Effect of scale and geometry on flooding, recirculation and power in gassed stirred vessels. 2nd Euro, Conf. Mixing, Cambridge, England.

Paglianti, A. (2002). "Simple model to evaluate loading/flooding transition in aerated vessels stirred by Rushton disc turbines. *The Canadian Journal of Chemical Engineering,* 80(4): 1-5.

Ralston, J. (1992). The influence of particle size and contact angle in flotation. Developments in mineral processing, Elsevier. **12:** 203-224.

Schubert, H. (1999). "On the turbulence-controlled microprocesses in flotation machines. *International journal of mineral processing,* 56(1-4): 257-276.

Schubert, H. and Bischofberger, C. (1998). "On the microprocesses air dispersion and particle-bubble attachment in flotation machines as well as consequences for the scale-up of macroprocesses. *International journal of mineral processing,* 52(4): 245-259.

Shen, Z. (2021). "Dynamic Characteristics and Evaluation of Flotation Machines. Principles and Technologies of Flotation Machines, 59-83.

Van der Westhuizen, A. and Deglon, D. (2007). "Evaluation of solids suspension in a pilot-scale mechanical flotation cell: The critical impeller speed. *Minerals Engineering,* 20(3): 233-240.

Van der Westhuizen, A. and Deglon, D. (2008). "Solids suspension in a pilot-scale mechanical flotation cell: A critical impeller speed correlation. *Minerals Engineering,* 21(8): 621-629.

Yawalkar, A. A., Heesink, A. B., Versteeg, G. F. and Pangarkar, V. G. (2002). "Gas−liquid mass transfer coefficient in stirred tank reactors. *The Canadian Journal of Chemical Engineering,* 80(5): 840-848.

Zwietering, T. N. (1958). "Suspending of solid particles in liquid by agitators. *Chemical engineering science,* 8(3-4): 244-253.

Enhancing Flotation Performance of Zinc-Oxide Minerals Using a Mixed Collector System

Amir Mabudi[1]

[1] Assistant Prof. of Mineral Processing, Department of Mining Engineering, Sahand University of Technology, Tabriz, Iran.

Orcid ID: https://orcid.org/0000-0002-4377-9929

*Corresponding author: E-mail: mabudi@sut.ac.ir (Amir Mabudi)

Abstract:

The flotation of zinc oxide ores presents significant technical challenges due to their complex surface chemistry and fine particle size. This study investigates the flotation behavior of a zinc oxide ore (13–14% Zn, 3–4% Pb) from the Barmalek deposit using different collector systems—potassium amyl xanthate (KAX), cocoalkylamine acetate (Armac C), and a mixed collector system. Comprehensive mineralogical and liberation analyses confirmed the oxide-dominated nature of the ore and the presence of slime-generating fractions, which negatively affect flotation performance. Systematic flotation experiments were conducted using Taguchi design arrays (L8, L12, L18) to evaluate the effects of various parameters, including reagent dosages, pH, and flotation time, both with and without desliming. Results showed that KAX or Armac C alone provided limited recovery and selectivity. In contrast, the mixed collector system significantly enhanced zinc recovery and concentrate grade, particularly when combined with desliming. ANOVA and model optimization predicted a maximum Zn recovery of 84.3% and Zn grade of 42.1%, with calcium recovery minimized to 13.8%. Validation experiments confirmed the model predictions, although actual recoveries slightly decreased after accounting for slime losses. The findings demonstrate the synergistic potential of mixed collectors and highlight the critical role of desliming and reagent optimization in improving the flotation of refractory zinc oxide ores.

Keywords: *Zinc oxide flotation, Mixed collectors, Xanthate, Armac C, Desliming, Taguchi design, Reagent optimization*

1. Introduction

Zinc is a critical industrial metal with extensive applications in galvanization, alloy production, battery manufacturing, and pharmaceuticals, primarily due to its excellent corrosion resistance and favorable electrochemical properties {Nayak, 2022 #5}. Traditionally, the global zinc supply has been derived mainly from sulfide ores, particularly Sphalerite (ZnS) {Mukherjee, 2024 #2}. However, non-sulfide zinc-bearing minerals, including Smithsonite ($ZnCO_3$) and Hemimorphite ($Zn_4Si_2O_7(OH_2).H_2O$), have gained increased attention in recent years due to the gradual depletion of high-grade sulfide reserves {Maghfouri, 2018 #3}. Despite their abundance, zinc oxide ores are often considered complex and less attractive for conventional beneficiation because of their fine particle size, intricate mineralogy, and inherently poor floatability {Ejtemaei, 2014 #4}. The recovery of zinc from oxide ores presents notable technical challenges. These ores are typically of low grade and often associated with high concentrations of gangue minerals such as calcite and dolomite, which interfere with separation processes {Nayak, 2022 #5}. Their surface chemistry is significantly different from that of sulfides, leading to poor attachment to conventional flotation collectors. As a result, developing

efficient and economically viable processing strategies for zinc oxide minerals is crucial for ensuring the long-term sustainability of zinc production {Nayak, 2022 #5}.

Several concentration techniques have been employed for zinc minerals, including gravity separation, hydrometallurgical leaching, and froth flotation {Moradi, 2011 #6}. Among these, flotation remains the most commonly used method due to its selectivity and scalability. For sulfide ores, flotation using xanthate collectors under alkaline conditions is well established. However, oxide minerals resist conventional flotation owing to their hydrophilic nature {Abkhoshk, 2014 #7}. To address this, sulfidization using sodium sulfide (Na_2S) is often applied to convert oxide surfaces into sulfide-like phases, making them more amenable to xanthate flotation {Önal, 2005 #8}. While this method is widely practiced, it often suffers from variable performance, surface passivation, and excessive reagent consumption. Alternative approaches, such as direct flotation using amine collectors, have also been explored {Önal, 2005 #8}. Nevertheless, these techniques are frequently hampered by poor mineral selectivity and the need for high reagent dosages, leading to increased operational costs. In recent years, attention has shifted towards innovative reagent schemes—particularly the use of mixed collectors—to improve recovery and grade in challenging ore systems. Mixed collectors offer the potential to exploit the synergistic interactions between different reagent types, thereby enhancing surface hydrophobicity, improving froth stability, and optimizing mineral separation {Javdantabar, 2025 #9}.

The application of mixed collector systems has shown promising results in both sulfide and oxide mineral flotation {Chen, 2024 #10}. In sulfide flotation, combining thiol and non-thiol collectors often leads to improved performance by targeting different mineral surface sites {Miao, 2021 #11}. Similarly, for oxide systems, integrating anionic collectors such as xanthates with cationic agents like amines has been reported to enhance collector adsorption and surface activation. Specifically for zinc oxide minerals, mixed collector systems such as potassium amyl xanthate (KAX) and Armac C (a cationic collector) can produce a more robust hydrophobic layer on the mineral surface, reducing calcite entrainment and improving selectivity {Yipeng, 2022 #12}. These systems also allow for reduced reagent usage and lower operating costs, which is particularly important when processing low-grade ores.

Building on these developments, this manuscript investigates the synergistic effects of using mixed collectors—specifically KAX and Armac C—for the flotation of zinc oxide ore from the Barmalek deposit in Iran. The study systematically examines the limitations of single-collector systems and demonstrates that a combined approach significantly enhances zinc recovery and selectivity. Furthermore, the roles of critical pre-treatment steps such as de-sliming and the use of auxiliary reagents (e.g., Na_2S for sulfidization, sodium silicate for gangue depression, and other depressants) are evaluated to optimize overall flotation performance. The findings offer practical insights into the design of more effective reagent schemes for complex oxide ores and contribute to the sustainable development of secondary zinc resources in the face of declining sulfide reserves.

2. Material and methods

2.1. Sample Preparation and Characterization

A representative sample of zinc-lead oxide ore was carefully homogenized and subjected to sieve analysis to evaluate its particle size distribution. The ore, with an average assay of 13–14% Zn and 3–4% Pb, was dry-sieved using standard ASTM meshes (10 to −200 mesh), and the weight percentage retained on each sieve was recorded (Table 1). To assess the distribution of valuable metals across different size fractions, each fraction was chemically analyzed for Zn and Pb content using atomic absorption spectroscopy (AAS). The results demonstrated a relatively uniform distribution of metals, as evidenced by low coefficients of variation (0.074 for Zn and 0.259 for Pb), indicating that grade fluctuations were statistically insignificant across the size classes.

To further characterize, X-ray diffraction (XRD) analysis was performed (Table 2). The XRD results identified calcite ($CaCO_3$, 40.1%) as the predominant gangue mineral, followed by zinc-bearing phases such as Hemimorphite ($Zn_4Si_2O_7(OH)_2.H_2O$, 17.5%) and Smithsonite ($ZnCO_3$, 14.8%). Non-sulfide gangue minerals included Magnesite (($Mg,Fe)CO_3$, 17.1%) and quartz (SiO_2, 3.5%). This mineralogical profile confirmed the oxide-dominant nature of the ore, with calcite posing a key challenge due to its floatability interference and similar physicochemical properties to zinc carbonate minerals. The presence of Hemimorphite, a zinc silicate, further highlighted the ore's complexity, necessitating tailored beneficiation strategies to address both carbonate and silicate-hosted zinc.

Table 1. Particle size distribution and Pb/Zn grade variation across sieve fractions of the oxide ore

Size (µm)	Remain Mass (gr)	Remain Mass (%)	Cumulative passed (%)	Zn (%)	Pb (%)
+2000	44.15	2.23	97.77	23.5	0.7
+1000	400.82	20.27	77.5	24.79	0.84
+500	544.84	27.55	49.95	22.96	0.97
+297	290.83	14.71	35.24	21.1	1.22
+177	481.38	24.34	10.9	20.35	1.39
+149	161.94	8.19	2.71	20.58	1.42
+75	38.46	1.95	0.76	20.68	1.43
-75	14.98	0.76	0	22.85	1.5
Bulk S.				21.52	0.98

Table 2. XRD analysis results

Mineral name	Mineral phase	(%)
Calcite	$CaCO_3$	40.1
Hemimorphite	$Zn_4Si_2O_7(OH)_2.H_2O$	17.5
Magnesite	$(Mg,Fe)CO_3$	17.1
Smithsonite	$ZnCO_3$	14.8
Hemimorphite	$Zn_2(SiO_4).H_2O.2ZnO(SiO_2).H_2O$	7.0
Quartz	SiO_2	3.5

2.2. Degree of Liberation

Liberation analysis was conducted through a comprehensive mineralogical assessment using reflected and transmitted light microscopy on thin and polished sections prepared from the sieved size fractions (−212+150, −150+125, and −125+75 µm). Given the heterogeneous texture and complex mineral associations typical of oxidized zinc ores, the liberation degree was quantified for each fraction using particle counting methods under 200× magnification. The results revealed that smithsonite, the primary zinc-bearing mineral, required grinding to a particle size of ≤75 µm to achieve 80% liberation from the gangue matrix (predominantly calcite and quartz). However, this degree of comminution risked generating excessive slimes (−20 µm), which could adversely affect downstream flotation performance through increased reagent consumption and reduced selectivity.

Detailed microscopic examination further identified intricate mineral intergrowths, particularly smithsonite grains encapsulated within Cerussite ($PbCO_3$) (Figure 1), as well as complex boundaries between hemimorphite and iron oxides. These textural relationships indicated that complete liberation would require ultra-fine grinding to 20–40 µm, which was deemed impractical for industrial flotation due to high energy costs and exacerbated slime-related challenges. Back-scattered electron (BSE) imaging coupled with energy-dispersive X-ray spectroscopy (EDS) confirmed these mineral associations and provided quantitative phase distribution data. The liberation analysis underscored a

critical trade-off: while finer grinding improved zinc mineral exposure, it simultaneously increased slime generation and operational costs. This finding highlighted the need for alternative beneficiation strategies, such as staged grinding or slime rejection, to optimize the liberation-flotation efficiency balance for this refractory ore type.
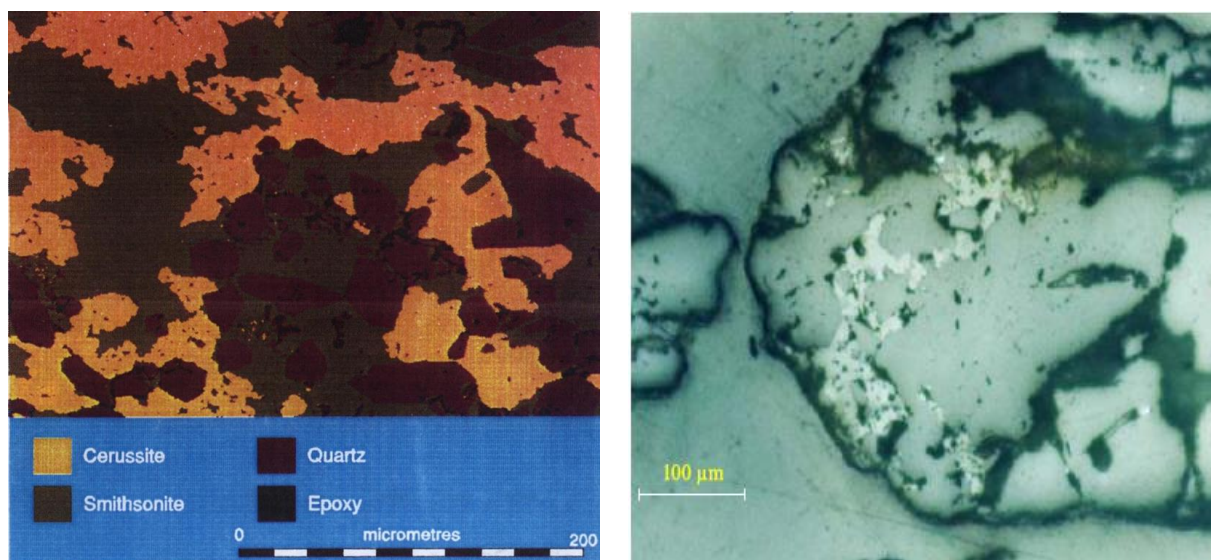
Figure 1. Entrapment of Smithsonite particles within Cerussite.

2.3. Bond Work Index Determination

The grindability of the ore sample was quantitatively evaluated through determination of the Bond work index (W_i) using the standardized Bond ball mill test procedure (ASTM G408-93). The calculated Bond work index of 10.76 kWh/short ton (equivalent to W_i = 10.76 ($\frac{kWh}{sh.t}$)) indicates moderately hard grinding characteristics, comparable to values reported for similar oxidized zinc ores. This result suggests the ore requires approximately 15-20% more energy for comminution than typical sulfide zinc ores ($\approx$ 9-10($\frac{kWh}{sh.t}$)). The relatively high work index can be attributed to the presence of hard, abrasive gangue minerals (quartz and magnesite) identified in the mineralogical analysis.

2.4. Flotation Reagents and Conditions

The flotation tests employed potassium amyl xanthate (KAX), cocoalkylamine acetate (Armac C), and their mixed system, with Na_2S as a sulfurizing agent. Sodium silicate (dispersant), Calgon (depressant), and starch were used to mitigate slime interference. De-sliming was incorporated to enhance selectivity.

3. Results and Discussion

3.1. Flotation Using Xanthate Collectors

Xanthates, particularly potassium amyl xanthate (KAX), are among the most widely used collectors in the flotation of sulfide minerals. Due to their established efficacy, their application has also been explored for oxide zinc ores, despite the significant differences in surface chemistry. The hydrolysis of xanthates in aqueous systems results in several decomposition products, including xanthate ions (AX^-), monothiocarbonates, xanthic acid, carbon disulfide (CS_2), and dixanthogen, each contributing to the complex chemistry of flotation pulp. In sphalerite-KAX systems, AX^- is the dominant phase at

pH values between 8 and 10, while lower pH values favor the formation of other species. Prior to designing full-scale flotation tests, a series of preliminary experiments was conducted to assess the general flotation behavior of zinc oxide ore using KAX as the primary collector. These trials helped determine feasible reagent ranges and minimized the number of tests required by identifying critical factors influencing flotation. An L8 Taguchi design was implemented to evaluate seven factors, each at two levels, affecting zinc recovery and grade. These factors included pH, KAX dosage, sulfidization using Na_2S, and auxiliary reagents such as Calgon, sodium silicate, $CuSO_4$, and flotation time.

The results (Table 3) revealed that Na_2S concentration had the most significant impact on both zinc grade and recovery. According to the analysis, Na_2S, $CuSO_4$, and Calgon concentrations, along with flotation time, significantly affected flotation responses. For concentrate grade, pH was also a notable factor. Regression plots (Figure 2 and Figure 3) show strong agreement between experimental and predicted values ($R^2 = 0.99$ for Zn grade, $R^2 = 0.96$ for recovery), confirming the reliability of the developed models.

Table 3. Zinc grade and recovery results from flotation experiments using a xanthate collector (KAX)

| N	Calgon (ppm)	Sodium Silicate (ppm)	Na_2S (ppm)	$CuSO_4$ (ppm)	pH	KAX (ppm)	Flotation time(min)	Grade (Zn)%	Recovery (Zn) %
1	500	400	800	200	8	300	2	29.3	31.26
2	500	400	800	400	10	600	4	28.66	36.43
3	500	800	1600	200	8	600	4	34.26	40.27
4	500	800	1600	400	10	300	2	31.68	42.16
5	1000	400	1600	200	10	300	4	30.71	42.64
6	1000	400	1600	400	8	600	2	33.84	41.83
7	1000	800	800	200	10	600	2	26.35	34.59
8	1000	800	800	400	8	300	4	29.59	39.22
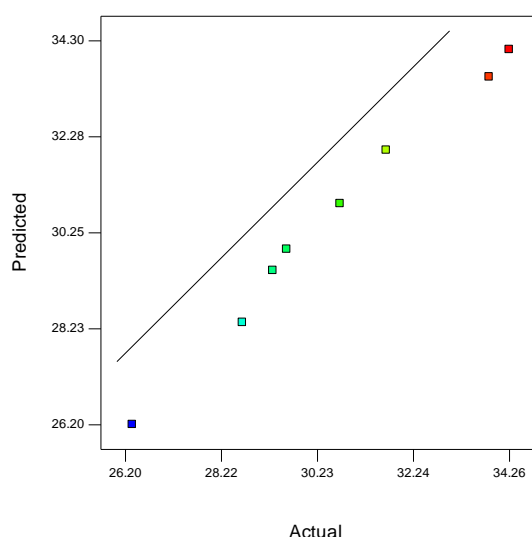
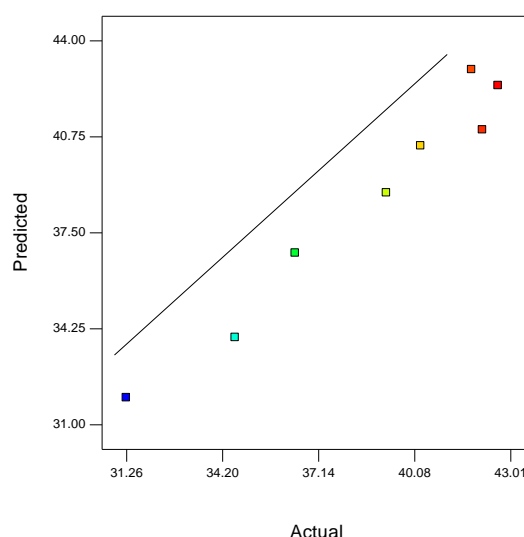*Figure 2. Regression plot of actual versus predicted values for zinc grade (R² = 0.99).*

Figure 3. Regression plot of actual versus predicted values for zinc recovery (R² = 0.96).

Despite optimization efforts, the overall zinc recovery using KAX was relatively low, suggesting the limited suitability of xanthates for oxidized zinc ores. This limitation is attributed to the instability of Zn–xanthate surface complexes and the poor froth stability observed during tests. The froth generated was short-lived, rapidly collapsing and releasing attached particles back into the pulp. Notably, froth volume appeared unaffected by variations in frother concentration, collector dosage, or sulfidizing reagents, implying that collector–mineral interactions are the primary control mechanism. Although the presence of slimes negatively impacted flotation efficiency, their effect in xanthate-based flotation of oxidized zinc ore was not significant enough to account for the poor performance. Overall, the findings confirm that xanthates, while effective for sulfide minerals, are not suitable collectors for the flotation of zinc oxide ores. Their poor interaction with oxide surfaces and unstable froth behavior necessitate the exploration of alternative or synergistic reagent systems for enhanced flotation performance.

3.2. Flotation Using Cationic Collectors

Unlike xanthates, which function via chemisorption, cationic collectors such as amines rely primarily on electrostatic attraction between their polar head groups and the electrical double layer at the mineral surface. These interactions are generally weaker than the covalent bonding observed with xanthates, resulting in less robust surface hydrophobization. Cationic collectors are particularly suited for the flotation of oxidized, carbonate, and silicate ores, as well as alkaline earth minerals like barite, carnallite, and sylvite. Among cationic collectors, primary amines, amine salts, and quaternary ammonium compounds are commonly used. Their flotation performance is highly sensitive to the pH of the pulp. These reagents tend to be most active in mildly acidic to neutral environments, while strong acidic or alkaline conditions can significantly reduce their effectiveness. For instance, dodecylamine, a well-studied cationic collector, exhibits solubility and phase behavior highly dependent on pH. At neutral pH, the un-ionized amine species predominates, whereas at pH 10.6 and above, the equilibrium shifts toward protonated and dimeric forms, reducing collector availability.

In the present study, the cationic collector cocoalkyl amine acetate, commercially known as Armac C with the chemical formula $[R-NH_2] \cdot [CH_3COOH]$, was used. Armac C is widely applied in industrial-scale flotation of oxidized zinc ores. Adsorption of the collector onto smithsonite surfaces, particularly after sulfidization with sodium sulfide (Na_2S), is a crucial step in promoting hydrophobicity and flotation. To evaluate the influence of various process parameters, a Taguchi L8 orthogonal array design was employed, considering seven variables at two levels. These tests assessed the impact of Calgon, sodium silicate, Na_2S, $CuSO_4$, pH, Armac C concentration, and flotation time on the grade and recovery of zinc. Outcomes (Table 4) clearly show that Na_2S concentration had the most significant positive impact on both grade and recovery. Increasing flotation time improved zinc recovery but simultaneously reduced concentrate grade, likely due to entrainment effects. Among the reagents tested, sodium silicate, sodium sulfide, copper sulfate, and Armac C all showed a synergistic effect: as their dosage increased, both grade and recovery improved.

Table 4. Zinc grade and recovery results from flotation experiments using a amine collector (armac c)

N	Calgon (ppm)	Sodium silicate (ppm)	Na_2S (ppm)	$CuSO_4$ (ppm)	pH	Armac C (ppm)	Flotation time (min)	Grade Zn (%)	Recovery Zn (%)
1	500	400	800	200	8	300	2	33.61	34.29
2	500	400	800	400	10	600	4	31.29	42.32
3	500	800	1600	200	8	600	4	37.56	44.68
4	500	800	1600	400	10	300	2	39.98	46.09
5	1000	400	1600	200	10	300	4	31.01	43.63
6	1000	400	1600	400	8	600	2	38.52	45.44
7	1000	800	800	200	10	600	2	32.73	39.67
8	1000	800	800	400	8	300	4	33.26	43.58

All flotation tests were conducted without de-sliming. Although recovery and grade were generally better with Armac C compared to xanthate-based flotation, the overall performance still fell short of industrially acceptable levels. This suggests that while cationic collectors offer some advantages, particularly in oxide ore flotation, further optimization—potentially through reagent combinations or surface modification strategies—is necessary to achieve satisfactory results.

3.3. Mixed Collectors

3.3.1. Without Desliming

To better understand the flotation behavior of zinc oxide ore with mixed cationic and anionic collectors and reduce the number of full-scale experiments, a preliminary series of tests was conducted using a Taguchi L12 orthogonal array design. This design included 11 process variables, each evaluated at two levels. The selected parameters encompassed pH, reagent dosages, conditioning times, and flotation durations, with their roles in the flotation process summarized in Table 5.

Table 5. Key Factors in the Taguchi L12 Design with 11 Two-Level Factors

N.	Factors	Unit	Low level	High level
1	pH	-	9	11
2	Sodium Silicate Concentration 1	ppm	500	1000
3	Starch	ppm	400	800
4	Na_2S concentration 1	ppm	1500	3000
5	Conditioning time	min.	5	10
6	Xanthate concentration 1	ppm	300	600
7	Flotation time	min.	3	6
8	Sodium silicate concentration 2	ppm	2000	4000
9	Na_2S concentration 2	ppm	800	1600
10	Armac C concentration	ppm	100	200
11	Xanthate concentration 2	ppm	200	400

Twelve experimental runs were performed based on the L12 matrix, with each test repeated twice to enhance statistical reliability and enable calculation of signal-to-noise (S/N) ratios. The flotation process was conducted in two sequential stages. In the first stage, starch and sodium silicate were introduced into the pulp and mixed thoroughly, followed by sodium sulfide addition and pH adjustment. Xanthate was then added and conditioned prior to flotation. In the second stage, following froth removal, additional sodium sulfide was added and pH adjusted before sequential addition of Armac C and xanthate. Air flow was initiated two minutes later to commence the second flotation stage. No frother was used in the second stage. Observations during testing revealed that froth characteristics were highly dependent on Armac C concentration. Interestingly, lower Armac dosages tended to yield better flotation responses, potentially due to reduced surface tension and improved selectivity. The two main response variables were zinc recovery and calcium recovery in the

concentrate. Since high calcium content increases acid consumption during downstream leaching, minimizing calcium recovery while maximizing zinc recovery was targeted. The combined concentrates from both flotation stages were analyzed, and the results are presented in Table 6.

Analysis of variance (ANOVA) for zinc recovery indicated that flotation time, the dosages of sodium silicate and sodium sulfide in the first stage, Armac C dosage, and pulp pH had significant effects. Calcium recovery ANOVA also revealed notable influences from conditioning time, starch dosage, and xanthate addition, particularly in the first stage. Optimization was carried out using Statistical method, assigning higher importance to zinc recovery than calcium recovery. The optimal process conditions included: pH 10.8, sodium silicate (Stage 1: 997 ppm, Stage 2: 4000 ppm), starch 400 ppm, Na_2S (Stage 1: 2193 ppm, Stage 2: 1090 ppm), conditioning time 5 min, xanthate (Stage 1: 434 ppm, Stage 2: 375 ppm), Armac C 100 ppm, and flotation time 6 min. Model predictions under these conditions yielded a zinc recovery of 63.5% and calcium recovery of 19.1%. Validation tests confirmed the general trend, with zinc recovery ranging from 53.2% to 54.4%, and calcium recovery between 21.8% and 22.7%. The lower-than-expected zinc recovery is likely due to the negative effect of slimes and ultra-fine particles in the feed, which were not removed prior to flotation.

Table 6. Experimental Results Using the Taguchi L12 Method for Cationic Collectors without Desliming

Experiment N.	Zn recovery %		Ca recovery %	
	Response 1	Response 2	Response 1	Response 2
1	39.28	43.51	6.57	8.26
2	52.66	61.18	17.93	19.92
3	53.18	54.97	19.03	24.11
4	63.53	68.44	22.42	20.09
5	55.83	58.57	20.27	21.49
6	57.16	55.14	20.87	23.51
7	63.46	69.73	22.13	27.84
8	53.91	52.38	20.05	19.02
9	46.45	50.27	11.64	18.37
10	52.75	60.12	14.38	15.64
11	58.33	64.26	19.17	23.46
12	66.49	62.49	26.52	25.34

3.3.2. With Desliming

To improve flotation performance and reduce interference from ultra-fine particles, desliming was carried out by removing particles smaller than 20 µm from the feed prior to flotation. The flotation tests were then conducted using mixed collectors under the experimental design of a Taguchi L8 ($2^1 \times 3^7$) orthogonal array. This design incorporated eight factors, one at two levels and the rest at three levels, as detailed in Table 7.

Table 7. Key Factors and Their Levels for Flotation Experiments with Desliming

N.	Factors	Unit	Level 1	Level 2	Level 3
1	pH	-	9	10	11
2	Sodium silicate concentration	ppm	400	800	1200
3	Starch	ppm	400	700	1000
4	Na_2S concentration	ppm	800	1800	2800
5	Xanthate concentration 1	ppm	250	500	750
6	Flotation time	min	2	4	6
7	Xanthate concentration 2	ppm	200	400	-
8	Armac C concentration	ppm	100	200	300

Eighteen experiments were conducted based on the L18 matrix, with a randomized test order to minimize systematic error. The factors studied included pulp pH, concentrations of sodium silicate, starch, sodium sulfide, xanthate (at two stages), Armac C dosage, and flotation time. The responses analyzed were zinc recovery, zinc grade in the concentrate, and calcium recovery in the concentrate. The experimental results are summarized in Table 8. To evaluate the influence of each parameter on the flotation performance, marginal means and signal-to-noise (S/N) ratio plots were generated for each response. Analysis of variance (ANOVA) show that for zinc grade in the concentrate, Na_2S concentration was the most significant factor ($p = 0.009$), followed by xanthate dosage in the second stage ($p = 0.034$). The overall model was statistically significant ($F = 4.54$, $p = 0.038$), with a good match between predicted and experimental data. Regarding calcium recovery, starch concentration showed a strong effect ($p = 0.010$), with additional contributions from xanthate 1, flotation time, and Armac C ($p < 0.1$). The model was significant ($F = 4.52$, $p = 0.038$), and the predicted vs. actual calcium recovery values confirmed the model's validity.

Table 8. Experimental Responses for Each Flotation Test with Desliming

Experiment	Zn recovery %		Zn grade%		Ca recovery %	
N.	Response 1	Response 2	Response 1	Response 2	Response 1	Response 2
1	73.80	74.58	31.59	30.29	29.69	20.29
2	74.86	71.09	29.49	28.39	19.29	21.19
3	82.19	80.78	41.08	40.78	13.19	15.28
4	81.94	82.39	34.79	35.58	24.89	14.39
5	76.34	77.58	39.89	38.49	30.59	24.39
6	75.60	71.98	34.79	35.28	19.89	15.98
7	76.16	79.29	34.18	36.69	25.78	22.09
8	76.57	74.68	32.59	33.09	18.08	16.88
9	80.11	80.58	36.59	35.19	28.48	28.49
10	76.19	75.19	41.69	41.18	16.89	15.19
11	71.57	71.79	36.29	32.89	34.19	34.98
12	80.27	79.88	39.98	38.98	24.28	26.59
13	78.64	77.89	40.89	36.58	28.09	21.69
14	83.74	82.58	34.49	38.29	20.09	23.29
15	72.16	72.59	36.18	36.58	27.98	25.89
16	80.13	81.29	39.19	34.39	22.58	26.68
17	82.46	82.69	37.48	36.18	26.29	15.79
18	77.38	77.88	35.69	35.94	20.29	19.88

Overall, desliming significantly improved flotation performance, yielding zinc recoveries above 80% and higher zinc grades, while maintaining acceptable levels of calcium recovery in the concentrate.

These results highlight the importance of proper feed preparation and optimization of reagent dosages in flotation of zinc oxide ores.

3.4. Optimized condition

The flotation process was optimized to maximize zinc recovery and grade and minimize calcium recovery in the concentrate. Using design constraints within selected factor ranges and assigning importance levels to each parameter, the software predicted 10 optimal conditions (

Table 9), all leading to improved Zn recovery and grade while reducing Ca contamination. Case 1 was identified as the most optimal, with predicted Zn recovery of 84.27%, Zn grade of 41.52%, and Ca recovery of 13.85%. Confidence intervals confirmed the reliability of the predictions. Experimental tests under these optimal conditions confirmed the model's accuracy, although actual recoveries were slightly lower after adjusting for desliming losses. Corrected values accounted for the loss of fine particles, which contained significant amounts of zinc and calcium. After correction, Zn recovery ranged from 64.7% to 74.2%, indicating a trade-off between desliming benefits and overall recovery.

Table 9. Ten Predicted Optimal Conditions

	Xanthate 2	pH	Sodium silicate.	Starch	Na2S	Xanthate 1	Flotation time	Armac C
1	400	11	400	1000	2800	500	4	300
2	400	11	1200	1000	2800	500	4	300
3	400	10	400	1000	2800	500	6	300
4	400	11	400	1000	2800	500	6	300
5	400	10	1200	1000	2800	500	6	300
6	400	11	1200	1000	2800	500	6	300
7	400	10	400	1000	2800	500	4	300
8	400	10	1200	1000	2800	500	4	300
9	400	9	400	1000	2800	500	6	300
10	400	9	1200	1000	2800	500	6	300

Table 10. Ten Predicted Optimal responses and Their Corresponding real Responses

Number	Predicted			Test Result		
	Zn recovery	Zn grade	Ca recovery	Zn recovery	Zn grade	Ca recovery
1	84.27	41.52	13.85	81.87	38.24	13.09
2	84.27	42.05	13.85	79.30	39.46	14.32
3	84.91	41.52	14.65	77.29	40.16	16.19
4	86.23	41.52	14.65	80.19	41.08	13.64
5	84.91	42.05	14.65	81.43	38.97	14.08
6	86.23	42.05	14.65	80.74	39.37	12.93
7	82.96	41.52	13.85	72.38	40.60	14.57
8	82.96	42.05	13.85	74.85	41.53	15.94
9	83.14	41.52	14.65	81.26	40.03	15.69
10	83.14	42.05	14.65	77.47	42.19	15.38

4. Conculding Remarks

This study evaluated the flotation performance of a complex zinc oxide ore using single and mixed collector systems under various operational conditions. Key findings include:

- **Single Collectors Underperform:** Both xanthate (KAX) and amine (Armac C) collectors alone failed to deliver satisfactory zinc recoveries and selectivity due to limited interaction with oxide surfaces and unstable froth behavior.
- **Mixed Collector System Enhances Performance:** Combining KAX and Armac C significantly improved zinc recovery and concentrate quality. The mixed system provided a more robust and stable hydrophobic layer on mineral surfaces, enhancing flotation efficiency.
- **Desliming is Crucial:** Removing slimes (<20 μm) prior to flotation improved both zinc recovery and grade, minimizing the adverse effects of fine particles on reagent interaction and froth stability.
- **Optimization Validated:** Statistical modeling using Taguchi and ANOVA techniques identified optimal flotation conditions. Predicted results closely matched experimental values, with Zn recovery reaching up to 84.3% and Zn grade above 42% under optimal conditions. Adjusting for slime losses, real recoveries ranged between 64.7% and 74.2%.
- **Practical Implications:** The combined use of desliming and mixed collector strategies presents a viable solution for processing refractory zinc oxide ores. These findings are especially relevant for complex ores with high gangue content and could guide future reagent scheme development in industrial applications.

References:

1. Raju L, Deviga G, Mariappan M, Rajkumar E. Zinc in Industry. Zinc: CRC Press; 2024. p. 136-53.

2. Mukherjee R, Pattanaik JK, Purushothaman P. Understanding Zinc: Its Genesis, Distribution and Uses. Zinc: CRC Press; 2024. p. 1-13.

3. Maghfouri S, Hosseinzadeh MR, Rajabi A, Choulet F. A review of major non-sulfide zinc deposits in Iran. Geoscience Frontiers. 2018;9(1):249-72.

4. Ejtemaei M, Gharabaghi M, Irannajad M. A review of zinc oxide mineral beneficiation using flotation method. advances in Colloid and Interface Science. 2014;206:68-78.

5. Nayak A, Jena M, Mandre N. Beneficiation of lead-zinc ores–a review. Mineral Processing and Extractive Metallurgy Review. 2022;43(5):564-83.

6.   Moradi S, Monhemius A. Mixed sulphide–oxide lead and zinc ores: Problems and solutions. Minerals engineering. 2011;24(10):1062-76.

7.   Abkhoshk E, Jorjani E, Al-Harahsheh M, Rashchi F, Naazeri M. Review of the hydrometallurgical processing of non-sulfide zinc ores. Hydrometallurgy. 2014;149:153-67.

8.   Önal G, Bulut G, Gül A, Kangal O, Perek K, Arslan F. Flotation of Aladag oxide lead–zinc ores. Minerals engineering. 2005;18(2):279-82.

9.   Javdantabar K, Gharabaghi M, Abdollahi H, Mabudi A, Ojaghi Shirmard M. Mixed anionic/cationic collectors for pyrite flotation: An experimental and theoretical study. Mineral Processing and Extractive Metallurgy Review. 2025;46(1):116-28.

10.   Chen Y, Sun Y, Han Y. Efficient flotation separation of lead–zinc oxide ores using mineral sulfidation reconstruction technology: A review. Green and Smart Mining Engineering. 2024.

11.   Miao Y, Long T, Wang J, Lai F, Zuo W, Guo B. The Inadvertent Activation of Silicate Minerals Flotation and Their Depression in Molybdenite Beneficiation. Minerals. 2021;11(11):1296.

12.   Yipeng Z. Recovery valuable metals from processing gangue minerals. REPOSITORIO NACIONAL CONACYT. 2022.

Recovery of Rare Earth Elements and Titanium Using Direct Atmospheric Leaching and Digestion Methods from Low-Grade Monazite Sources

Seyed Javad Mousavi[1]*, Hasan Sedigi[1], Yousef NejadAzar[2], Alireza Parvizi[1], Mohsen Mirzaee[1]

[1]Iran Mineral Processing Research Center

[2] Iranian Mines and Mining Industries Development and Renovation Organization

*Corresponding author: s.javad.mousavi.c@gmail.com (Seyed Javad Mousavi)

Abstract:

Rare earth elements (REEs) have an increasingly wide range of applications in various industries. This study investigates the dissolution of REEs using two methods: direct atmospheric leaching and digesting with sulfuric acid, aiming to compare the efficiency of both approaches. Prior to leaching experiments, magnetic and gravity pre-concentration processes were applied to the sample to enhance the grade of rare earth elements. The total concentrations of REEs, titanium, and iron in the monazite low-grade sample were 0.88%, 3.88%, and 8.25%, respectively. In the direct leaching method, the effects of various parameters such as temperature, time, acid concentration, and the liquid-to-solid ratio on the recovery of REEs and associated metals were examined. Based on the experiments, the optimal conditions for these parameters were found to be an acid-to-solid ratio of 1.5, a liquid-to-solid ratio of 1.5, a temperature of 125°C, and a duration of 3 hours. Under these optimal conditions, the recovery rates for REEs, titanium, and iron were 80.1%, 89%, and 81.2%, respectively. For the digesting method using sulfuric acid, influential factors such as digesting temperature, sulfuric acid-to-solid ratio, water leaching time, water leaching-to-solid ratio, water leaching temperature, and water leaching duration were investigated. The optimal conditions for digesting and subsequent leaching were determined to be a sulfuric acid-to-solid ratio of 1.2, a digesting temperature of 220°C, a digesting time of 1 hour, a water-to-solid ratio of 1.5 during leaching, a leaching time of 1 hour, and a leaching temperature of 30°C. Under these optimal conditions, the recovery rates for REEs, titanium, and iron were 91.4%, 88.2%, and 72.4%, respectively.

Keywords: Rare earth elements (REEs), leaching, digesting, sulfuric acid, titanium

1. Introduction

Rare earth elements (REEs) are a group of 17 metallic elements, including the lanthanides, scandium, and yttrium that play a crucial role in modern technologies (Echeverry-Vargas & Ocampo-Carmona, 2022). Their unique electronic, magnetic, and optical properties make them essential in high-performance magnets, electric vehicle batteries, wind turbines, catalysts, and advanced electronic devices (Mwewa et al., 2022). The increasing global demand for REEs, particularly in clean energy and high-tech industries, has intensified research efforts to develop efficient and sustainable extraction and recovery methods. However, REE extraction presents significant challenges due to their complex mineral associations and the environmental concerns associated with traditional processing techniques (Julapong et al., 2023; Kusrini et al., 2018).

Monazite is one of the primary sources of REEs and is commonly processed using sulfuric acid digestion or direct atmospheric leaching. However, other REE-bearing minerals, such as bastnäsite,

xenotime, loparite, allanite, parisite, apatite, and gadolinite, have also been studied for their potential in REE extraction (Kumari et al., 2015). Among these, monazite is widely utilized due to its relatively high REE content and established processing methods. However, the presence of radioactive elements such as thorium and uranium in monazite complicates its processing and requires careful waste management strategies (Alves et al., 2021).

Several studies have focused on improving the efficiency and environmental sustainability of REE extraction from monazite. Sulfuric acid digestion, one of the most widely used methods, involves treating monazite with concentrated sulfuric acid at high temperatures (200–300°C) to convert REEs into soluble sulfates. However, this method presents challenges such as incomplete REE conversion and the generation of hazardous waste. Alternative leaching techniques, including direct leaching with sulfuric acid, have been explored to enhance dissolution rates and reduce processing temperatures, thereby improving both efficiency and safety. Additionally, hydrometallurgical processes, such as sulfuric acid baking and alkaline digestion, have been compared to determine the most effective method for different grades of monazite. Studies indicate that lower-grade monazite concentrates are often processed using sulfuric acid digestion, whereas alkaline digestion is more suitable for higher-grade materials (Berry et al., 2018; Demol et al., 2018).
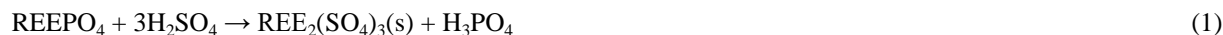
In sulfuric acid digestion, after monazite reacts with sulfuric acid, the resulting rare earth sulfates must be separated from impurities through a water leaching step. Water leaching plays a critical role in REE recovery by dissolving the REE sulfates into solution while leaving insoluble residues, such as thorium and iron, behind (Sadri et al., 2017). The efficiency of this step depends on factors such as the water-to-solid ratio, leaching temperature, and leaching duration, which influence REE recovery and impurity separation. Optimizing these conditions enhances overall REE extraction efficiency and reduces contamination from non-REE elements (Jha et al., 2016).

Another method for REE recovery is direct atmospheric leaching, in which monazite is treated with sulfuric acid under atmospheric pressure conditions to dissolve REEs selectively while minimizing impurity dissolution (Al Sheidi et al., 2024). The direct leaching reaction with sulfuric acid can be represented as follows (Equation 1):

$$REEPO_4 + 3H_2SO_4 \rightarrow REE_2(SO_4)_3(aq) + H_3PO_4 \tag{1}$$

This reaction indicates that monazite's phosphate structure is broken down under acidic conditions, releasing REEs into solution while phosphoric acid (H_3PO_4) is generated as a byproduct. The efficiency of this process depends on various factors, including acid concentration, temperature, leaching time, and the liquid-to-solid ratio (Hou et al., 2025; Peelman et al., 2016).

The chemical reactions involved in sulfuric acid digestion and subsequent water leaching include the breakdown of the phosphate structure in monazite to form rare earth sulfates and phosphoric acid (Equation 1, 2 and 3):

$$REEPO_4 + 3H_2SO_4 \rightarrow REE_2(SO_4)_3(s) + H_3PO_4 \tag{1}$$

$$ThPO4 + 3H_2SO_4 \rightarrow Th(SO_4)_2(s) + H_3PO_4 \tag{2}$$

$$REE2(SO_4)_3(s) + H_2O \rightarrow REE_2(SO_4)_3(aq) \tag{3}$$

To enhance REE recovery, key parameters such as the acid-to-solid ratio, reaction temperature, reaction time, and water leaching conditions must be optimized. Higher temperatures generally improve digestion efficiency, but excessive heating can lead to unwanted byproducts. Similarly, the choice of water leaching parameters affects the final recovery rates of REEs and the purity of the extracted solution (Berry et al., 2018; Zhang et al., 2016).

This study investigates and compares direct atmospheric leaching and sulfuric acid digestion for REE recovery from low-grade monazite sources. By systematically optimizing key processing parameters, the research aims to enhance REE extraction efficiency, reduce environmental impact, and contribute to the development of more sustainable and economically viable REE recovery technologies.

2. Material and methods

2.1. Mineralogical Studies and Sample Analysis

To conduct mineralogical studies, polish and thin sections of a low-grade monazite ore sample from Central Iran (Saghand) were prepared and examined using a ZEISS Axioplan 2 polarized light microscope with transmitted and reflected light (Figure 1). Prior to these studies, magnetic and gravity pre-concentration processes were applied to the sample to enhance the grade of rare earth elements. The studies revealed that plagioclase, accompanied by tremolite and phlogopite, is the most significant mineral in the sample. Other observed minerals include chlorite, titanite, quartz, pyrite, and dolomite. Ilmenite and magnetite are the primary metallic minerals, comprising approximately 2% to 4% of the sample. The ilmenite mineral was predominantly found interlocked with titanite. Trace elements such as cerium, lanthanum, and yttrium were present in very small amounts and appeared as bright zones within the ilmenite and titanite.
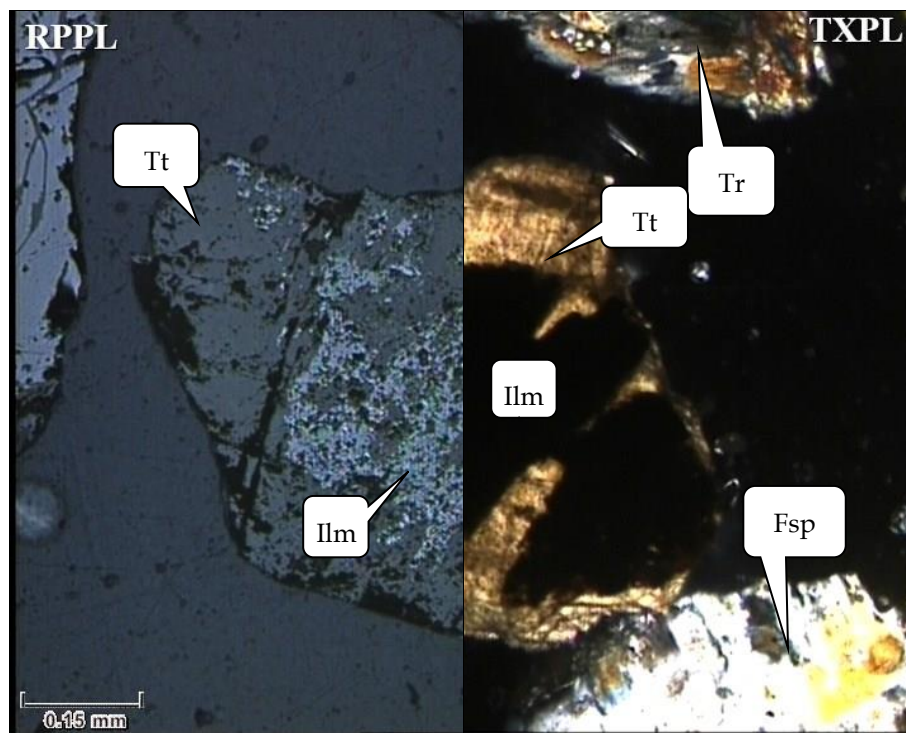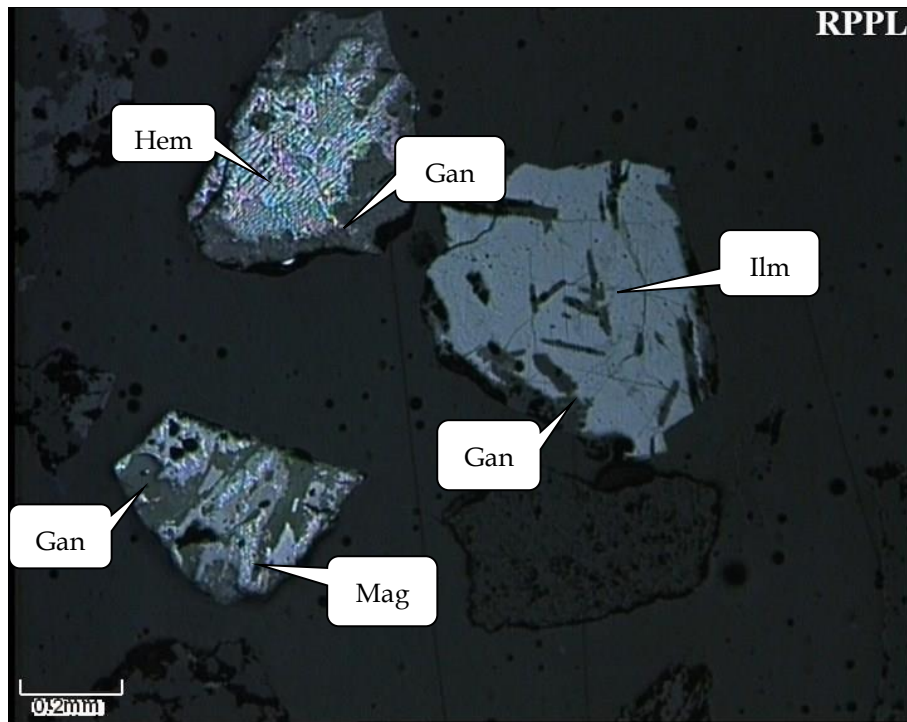
Figure 1. Microscopic images depicting the interlocking of magnetite, hematite, ilmenite, and titanite with gangue minerals

Further analyses were conducted using a scanning electron microscope (SEM) and SEM/EDX analysis, revealing that rare earth elements (REEs) occur as monazite minerals in extremely fine particles (smaller than 5 microns), interlocked with titanite and ilmenite.

EDS1- Ce, La, Y

EDS2-Ce, La, Y, U

EDS3-Ilmenite

EDS4-Titanite
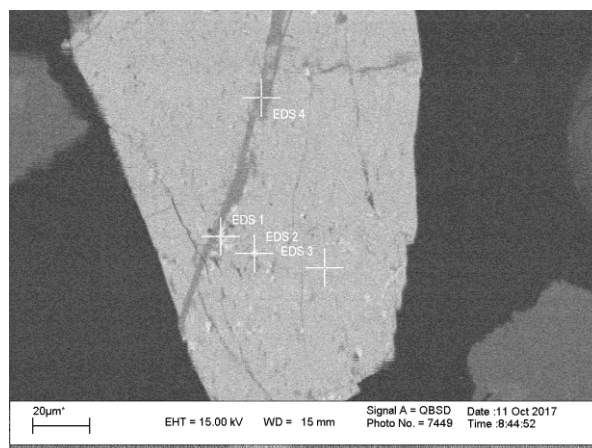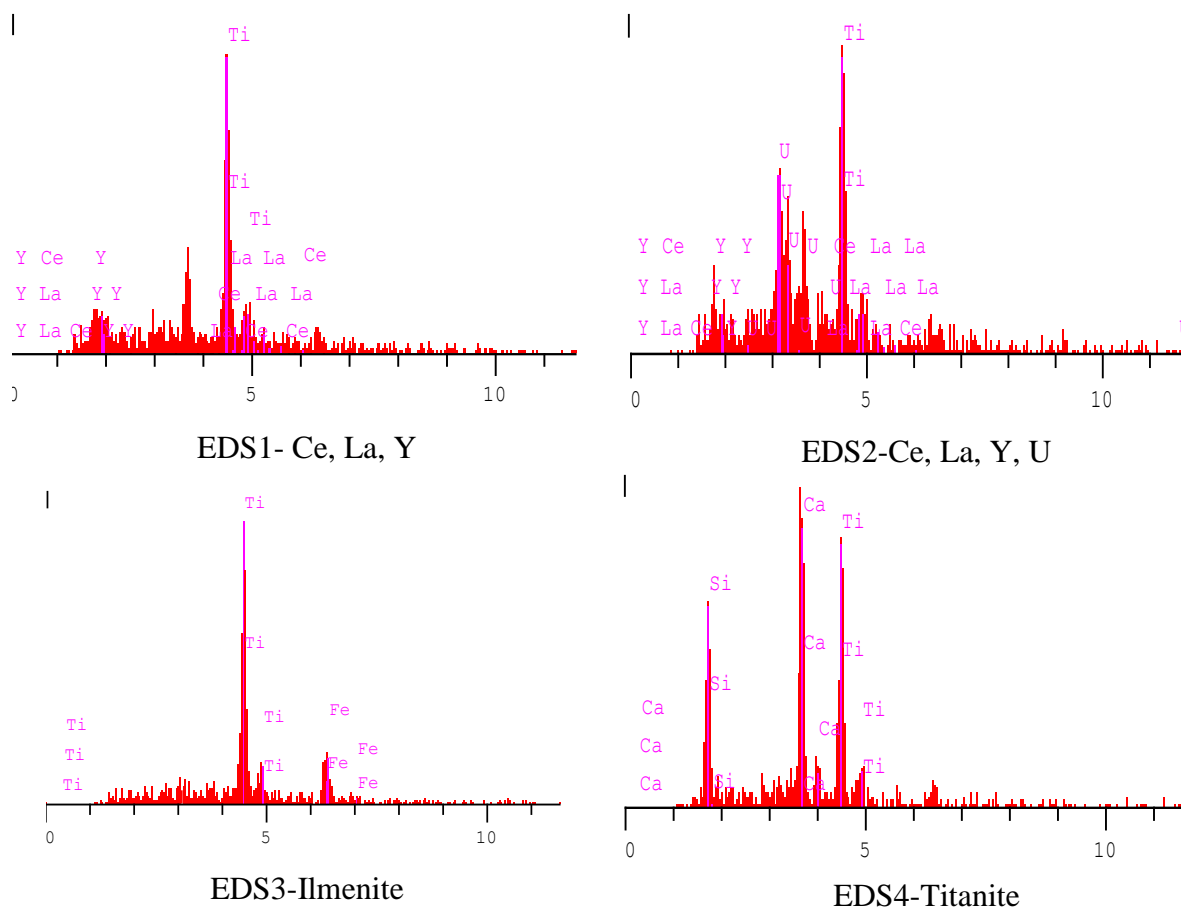
Figure 2. SEM image and SEM/EDX results of Ilmenite, Titanite and Monazite ores

The sample, labeled as LP12, was analyzed using an ICP-OES device to determine the grade of rare earth elements and other metals. The total REE and other metal contents in sample LP12 are shown in Table 1.

Table 1. The total grade of rare earth elements and the metals titanium and iron in sample LP12

Sample	∑REE(ppm)	Ti(%)	Fe(%)
LP12	8837	3.875	8.25

After grinding, the sample had a d_{80} particle size of 23 microns, which was used for leaching and digestion experiments. The particle size distribution analysis of sample LP12 is depicted in Figure 3.

d(10%): 1.082 μm   d(50%): 6.196 μm   d(80%): 23.023 μm   d(90%): 35.793 μm

Figure 3. The particle size distribution of sample LP12 using a Laser Diffraction Particle Size Analyzer.

2.2. Direct Leaching Method

The direct leaching of REEs from the sample was conducted using sulfuric acid under stirring conditions. After leaching, the pregnant leach solution (PLS) was separated from the solid using vacuum filtration, followed by washing the solid 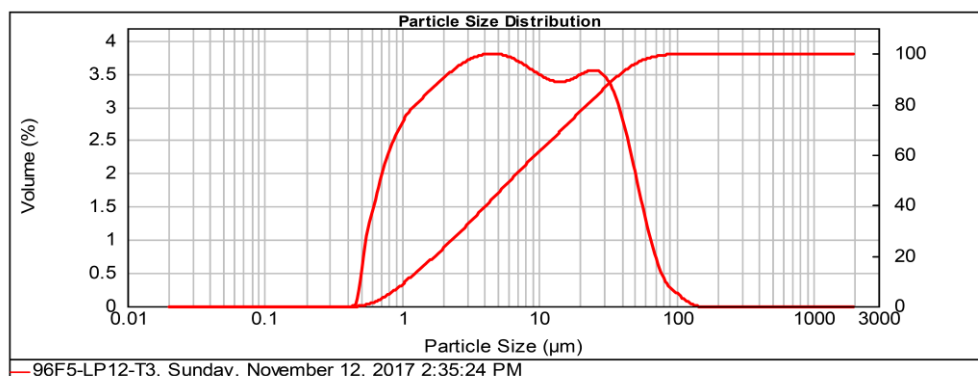residue with water. The leach residue and the volume-adjusted PLS were sent for chemical analysis to calculate the recovery rates. The leaching experiments were carried out in 500 mL Erlenmeyer flasks with condensers to prevent water evaporation.

The effects of key factors, such as leaching time, temperature, solid-to-liquid ratio, and sulfuric acid concentration, were investigated using the Taguchi experimental design method. The leaching test conditions and their results are summarized in Table 2.

Table 2. The direct leaching test conditions and their results

Num	Acid Concentration (M)	Temperature (°C)	Time (h)	Solid to Liquid (mL/g) ratio	∑REE Recovery (%)	Ti Recovery (%)
L11	8	90	3	5	62.1	68.9
L12	4	60	3	5	12.7	16
L13	4	60	3	2.5	11.3	13.5
L14	8	60	6	5	24.2	28
L15	8	60	6	2.5	17.3	20
L16	8	90	3	2.5	71.7	80.8
L17	4	90	6	2.5	61.3	66.5
L18	4	90	6	5	72.4	75

2.3. The digestion method using sulfuric acid and leaching.

Unlike leaching, which is a single-step process, the digestion of rare earth elements involves two distinct stages. In the first stage, the sample is thoroughly mixed with concentrated sulfuric acid at room temperature. Then, the temperature is increased to promote the digestion process. After the digestion is completed, the second stage involves water leaching of the digested material to transfer the rare earth elements into the aqueous phase. To evaluate the efficiency of digestion using sulfuric acid, various digestion experiments were conducted on the sample using sulfuric acid. The key factors influencing the digestion process were examined, including digestion temperature, leaching time, sulfuric acid-to-solid ratio, water leaching-to-solid ratio, water leaching temperature, and water leaching time.

The experimental conditions for digestion and the values for each factor are presented in Table 3. The experiments were designed using the Taguchi experimental design method.

Table 3. The conditions for conducting digestion experiments using the Taguchi experimental design method.

Num	Acid to Solid (gr/gr) ratio	Digestion Time (h)	Digestion Temperature	Water to Solid ratio in Leaching (ml/gr)	Leaching Temperature	Leaching Time (h)
1	1	5	220	6	50	3
2	1.2	1	260	6	50	1
3	1	3	180	8	50	1
4	1	3	180	6	30	3
5	0.8	1	220	8	50	5
6	1	1	180	6	70	5
7	1.2	1	220	4	70	3
8	0.8	3	220	6	70	1
9	1	3	220	4	30	5
10	1.2	5	180	4	50	5
11	0.8	5	180	8	70	3
12	1	1	260	8	30	3
13	0.8	5	260	6	30	5
14	0.8	3	260	4	50	3
15	1.2	3	260	8	70	5
16	1.2	5	220	8	30	1
17	0.8	1	180	4	30	1
18	1	5	260	4	70	1

3. Results and Discussion

3.1. Direct Leaching Method

In Figure 4, the average effect of each factor is shown while keeping other factors at their average levels. Based on the average effects, it is determined that temperature has the greatest impact on the recovery of rare earth elements. Additionally, after temperature, acid concentration has a greater influence on the recovery of rare earth elements compared to other factors.
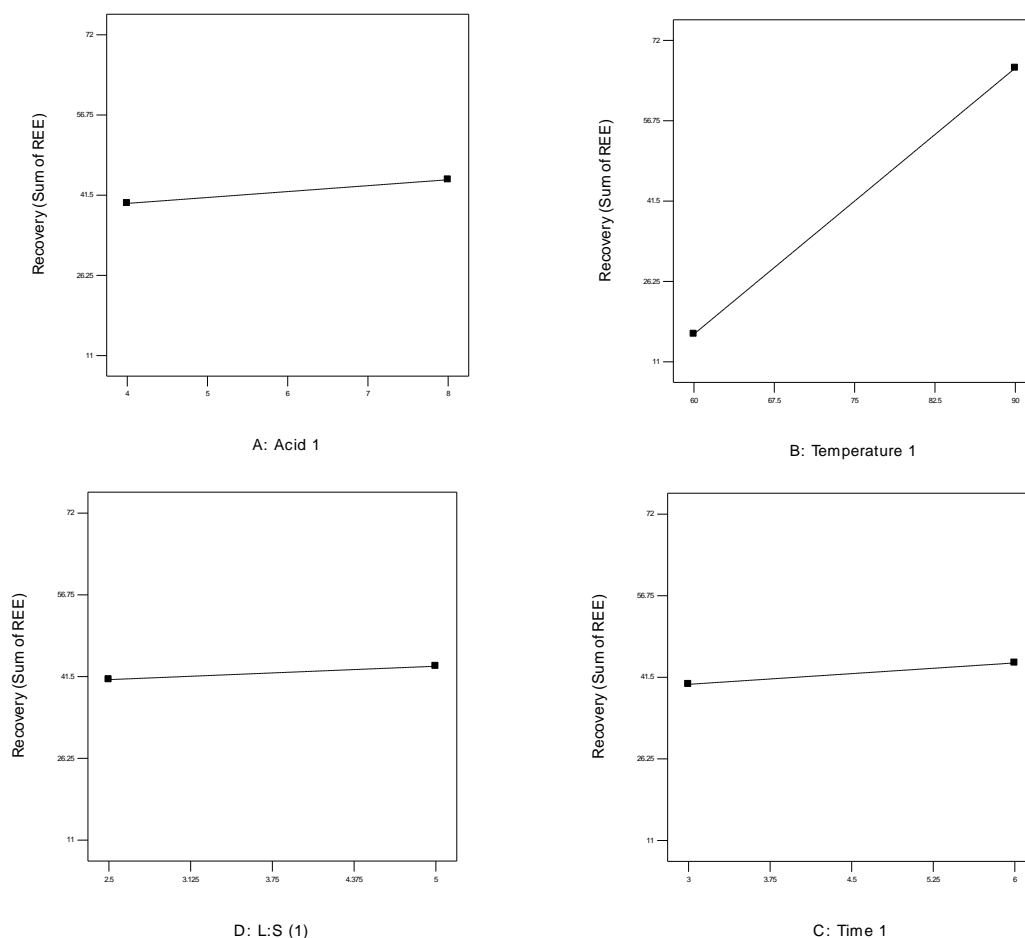
Figure 4. The average effect of leaching factors on the recovery of rare earth elements

Based on the results obtained from laboratory activities, it was determined that temperature is the most influential factor in the recovery of rare earth elements. Therefore, for subsequent experiments, an increase in temperature to higher levels was examined.

The results also indicate that increasing the temperature from 90°C to 125°C under identical conditions enhances the recovery of rare earth elements from 72% to an average recovery of 81%. Based on the conducted leaching experiments, it was determined that temperature has the most significant impact on the recovery of rare earth elements. The highest recovery was observed at the boiling point of the solution (110–125°C). Additionally, factors such as acid concentration, liquid-to-solid ratio, and leaching time also influence the recovery process.

According to the experiments, the optimal conditions for these factors were found to be an acid-to-solid ratio of 1.5, a liquid-to-solid ratio of 1.5, and a leaching time of 3 hours at 125°C. Under these optimal conditions, the recovery rates for rare earth elements, titanium, and iron were 80.1%, 89%, and 81.2%, respectively.

## 3.2. Direct Leaching Method

The results of the digestion experiments conducted (Table 3) are presented in Table 4. This table includes the recovery rates of rare earth elements, titanium, and iron.

Table 4. The results of the digestion experiments designed using the Taguchi experimental design method.

Num	∑REE Recovery (%)	Ti Recovery (%)	Fe Recovery (%)
1	84.6	83.8	73.6
2	87.0	88.0	75.2
3	83.7	85.7	83.7
4	88.2	85.3	85.2
5	66.3	62.0	61.3
6	67.0	63.4	69.6
7	53.8	51.1	58.1
8	64.7	60.9	68.3
9	75.7	72.2	75.6
10	84.6	89.8	84.9
11	77.7	38.4	69.5
12	69.8	62.4	65.9
13	70.5	61.4	69.9
14	59.0	53.8	62.2
15	85.6	79.3	80.9
16	64.8	46.1	55.5
17	43.1	28.1	43.4
18	86.8	84.4	77.0

The results obtained from the digestion and leaching experiments, analyzed using Dx7 software, indicate that the absence of a condenser and the drying of the pulp have the greatest impact on the recovery of rare earth elements, leading to an increase in their recovery. After the effect of the condenser, the sulfuric acid-to-solid ratio has the next highest impact, where increasing the acid ratio enhances the recovery of rare earth elements. The effect of each factor on the recovery of rare earth elements is shown in Figure 7. Other factors have a lesser impact on the recovery rate, with their effects summarized as follows:

- Increasing the digestion time slightly increases the recovery of rare earth elements.
- Increasing the digestion temperature also slightly increases the recovery of rare earth elements.
- Increasing the leaching time does not affect the recovery of rare earth elements within the selected time range.
- Leaching temperature has an inverse effect, where increasing the temperature slightly reduces the recovery.
- Increasing the water-to-solid ratio during leaching slightly increases the recovery of rare earth elements.
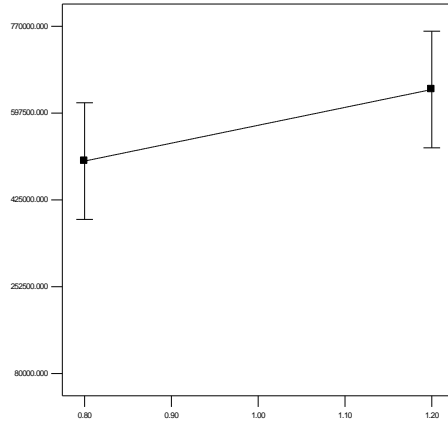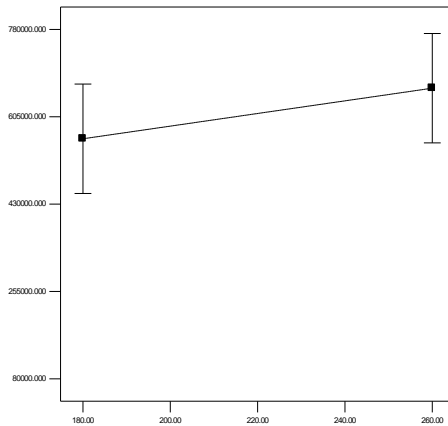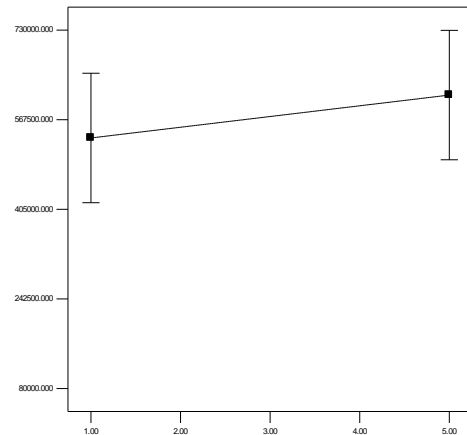

C: Acid ratio

B: Condenser

.١,١
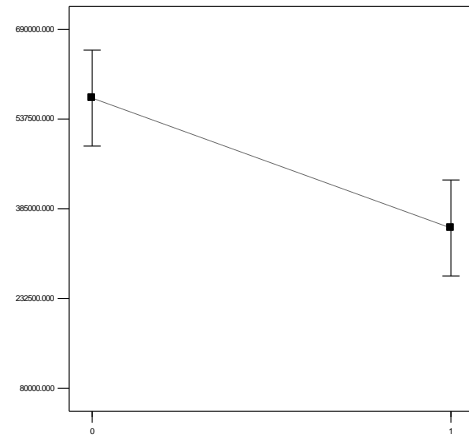
E: Digest Temperature

D: Digest Time

G: Leaching Temperature
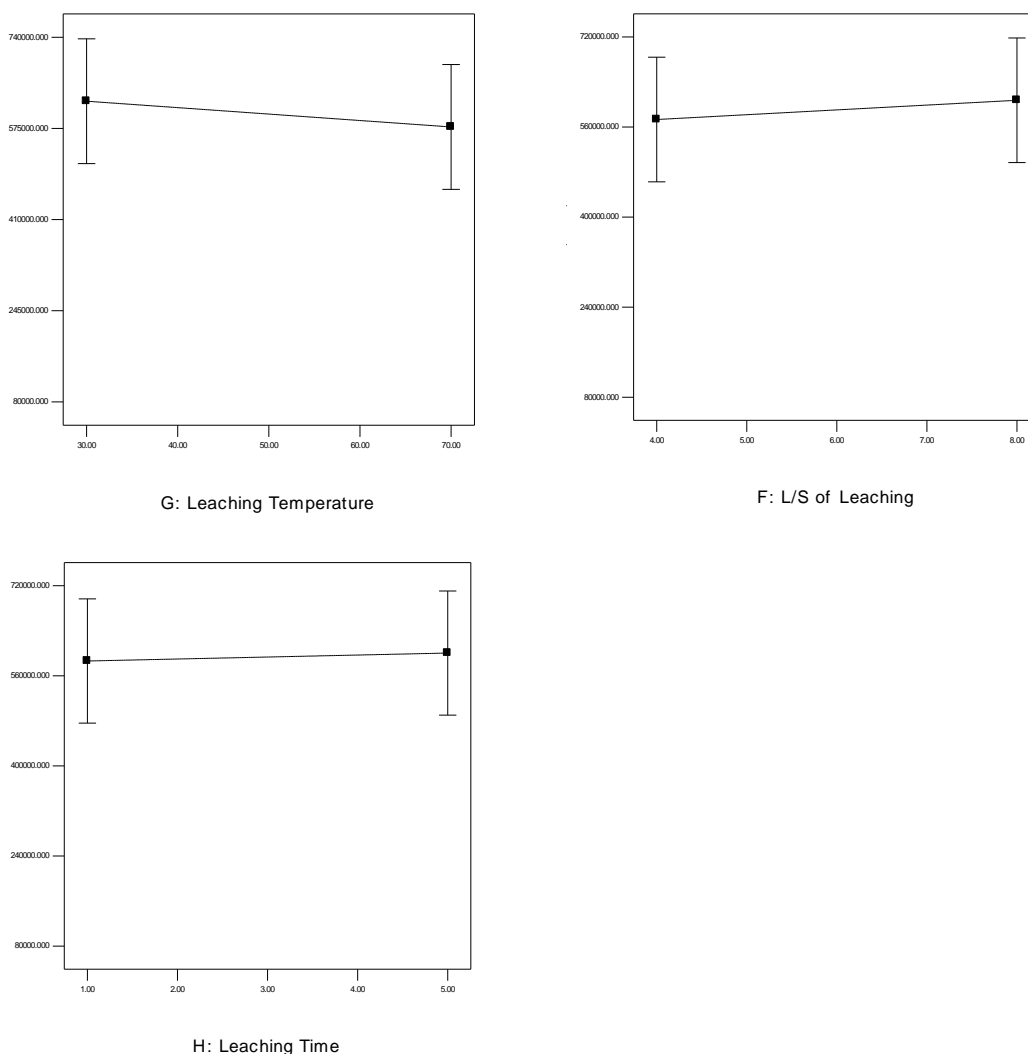

F: L/S of Leaching

H: Leaching Time

Figure 5. the effect of digestion and leaching factors on the recovery of rare earth elements.

Based on the analysis of the digestion experiment results, the conditions for maximum recovery of rare earth elements were determined. The optimal experimental conditions include a digestion temperature, a leaching time of 1 hour, a sulfuric acid-to-solid ratio of 1.2, a water leaching-to-solid ratio of 4, a water leaching temperature of 30°C, and a leaching time of 1 hour.

For further investigation, the effects of digestion temperature and the sulfuric acid-to-solid ratio were examined. In these experiments, temperatures of 220°C and 260°C and acid-to-solid ratios of 1.2 and 1.5 were evaluated. Additionally, in another experiment, the effect of increasing the digestion time from 1 hour to 2 hours was assessed.

The results of these experiments, comparing digestion and leaching conditions with the optimal conditions, showed that increasing the temperature from 200°C to 260°C and increasing the sulfuric acid-to-solid ratio from 1.2 to 1.5 did not enhance the recovery of rare earth elements. Furthermore, the results indicated that extending the digestion time from 1 to 2 hours had no effect on the recovery of rare earth elements.

The effect of reducing the water-to-solid ratio in leaching and the sulfuric acid-to-solid ratio was also investigated in other experiments. In these tests, water-to-solid ratios of 4 and 1.5 in leaching and acid-to-solid ratios of 1.2 and 1 were examined.

The results indicate that reducing the acid ratio from 1.2 to 1 leads to a decrease in the recovery of rare earth elements and titanium. However, it was also found that reducing the water-to-solid ratio in leaching does not reduce the recovery of rare earth elements. Therefore, to increase the concentration of rare earth elements in the PLS (Pregnant Leach Solution), the water-to-solid ratio can be reduced.

In another experiment, the effect of increasing the digestion temperature was investigated, where the digestion temperature was set at 400°C. The other conditions for digestion and leaching remained the same as the optimal conditions.

The results show that increasing the temperature to 400°C does not result in a significant increase in the recovery of rare earth elements, and the optimal digestion temperature can be considered 220°C. However, increasing the digestion temperature reduces the recovery of iron.

The results of the digestion experiments show that not using a condenser and allowing the pulp to dry has the greatest impact on increasing the recovery of rare earth elements. Following the effect of the condenser, the sulfuric acid-to-solid ratio has the next highest influence, where increasing the acid ratio improves the recovery of rare earth elements.

4.   Conclusions

Based on the experiments conducted at this stage, the optimal conditions for digestion and subsequent leaching were identified. These conditions include a sulfuric acid-to-solid ratio of 1.2, a digestion temperature of 220°C, a digestion time of 1 hour, a minimum water-to-solid ratio of 1.5 during leaching, a leaching time of 1 hour, and a leaching temperature of 30°C. Under this optimal digestion and leaching conditions, the recovery rates of rare earth elements, titanium, and iron are 91.4%, 88.2%, and 72.4%, respectively.

For direct leaching, the optimal conditions include a sulfuric acid-to-solid ratio of 1.5, a liquid-to-solid ratio of 1.5, and a leaching time of 3 hours at 130°C. Under these conditions, the recovery rates of rare earth elements, titanium, and iron are 80.1%, 89%, and 81.2%, respectively.

The recovery achieved using the digestion and leaching method is higher than that obtained through sulfuric acid leaching at high temperatures. Moreover, the digestion method consumes less acid compared to high-temperature sulfuric acid leaching. Therefore, the digestion and leaching method has been identified as a more suitable approach for the dissolution of rare earth elements and titanium.

Acknowledgments

References

Al Sheidi, A. S., Dyer, L. G., & Tadesse, B. (2024). Leaching Efficacy of Ethylenediaminetetraacetic Acid (EDTA) to Extract Rare-Earth Elements from Monazite Concentrate. *Crystals*, *14*(10), 829.

Alves, R. C., Nascimento, M., Paulino, J. F., & Afonso, J. C. (2021). Selection of a hydrometallurgical process for rare earths extraction from a Brazilian monazite. *Hydrometallurgy*, *200*, 105556.

Berry, L., Agarwal, V., Galvin, J., & Safarzadeh, M. S. (2018). Decomposition of monazite concentrate in sulphuric acid. *Canadian Metallurgical Quarterly*, *57*(4), 422-433.

Demol, J., Ho, E., & Senanayake, G. (2018). Sulfuric acid baking and leaching of rare earth elements, thorium and phosphate from a monazite concentrate: Effect of bake temperature from 200 to 800 C. *Hydrometallurgy*, *179*, 254-267.

Echeverry-Vargas, L., & Ocampo-Carmona, L. M. (2022). Recovery of rare earth elements from mining tailings: A case study for generating wealth from waste. *Minerals*, *12*(8), 948.

Hou, S., Huang, W., Liu, Y., Zhang, B., & Liu, C. (2025). Effect of phosphoric acid on leaching of monazite during low-temperature sulfuric acid cyclic leaching process. *Journal of Rare Earths*, *43*(4), 784-793.

Jha, M. K., Kumari, A., Panda, R., Kumar, J. R., Yoo, K., & Lee, J. Y. (2016). Review on hydrometallurgical recovery of rare earth metals. *Hydrometallurgy*, *165*, 2-26.

Julapong, P., Numprasanthai, A., Tangwattananukul, L., Juntarasakul, O., Srichonphaisarn, P., Aikawa, K., Park, I., Ito, M., Tabelin, C. B., & Phengsaart, T. (2023). Rare earth elements recovery from primary and secondary resources using flotation: A systematic review. *Applied Sciences*, *13*(14), 8364.

Kumari, A., Panda, R., Jha, M. K., Kumar, J. R., & Lee, J. Y. (2015). Process development to recover rare earth metals from monazite mineral: A review. *Minerals engineering*, *79*, 102-115.

Kusrini, E., Nurani, Y., & Bahari, Z. (2018). Extraction of rare earth elements from low-grade Bauxite via precipitation reaction. IOP Conference Series: Materials Science and Engineering,

Mwewa, B., Tadie, M., Ndlovu, S., Simate, G. S., & Matinde, E. (2022). Recovery of rare earth elements from acid mine drainage: A review of the extraction methods. *Journal of environmental chemical engineering*, *10*(3), 107704.

Peelman, S., Sun, Z. H., Sietsma, J., & Yang, Y. (2016). Leaching of rare earth elements: review of past and present technologies. *Rare earths industry*, 319-334.

Sadri, F., Rashchi, F., & Amini, A. (2017). Hydrometallurgical digestion and leaching of Iranian monazite concentrate containing rare earth elements Th, Ce, La and Nd. *International Journal of Mineral Processing*, *159*, 7-15.

Zhang, J., Zhao, B., & Schreiner, B. (2016). *Separation hydrometallurgy of rare earth elements* (Vol. 449). Springer.

Feasibility Study of Vanadium Extraction from Steelmaking Slag of Mobarakeh Steel Company at laboratory and semi-industrial scales

Dorna Pirouzan[1*], Reza Parvareh[1], Ziaeddin Pourkarimi[1], Mehdi Rahimi[1], Seyyed Javad Mousavi1, Hossein Habibi[1],

[1] Iran mineral processing research center

*d.piruzan@gmail.com (Dorna Pirouzan)

Abstract:

In our country, a massive volume of slag is generated annually from steel production facilities, amounting to about 20 percent of the total steel produced. This slag is an important and valuable source for extracting vanadium, with 67 percent of the world's vanadium production sourced from slag. Iran ranks among the top five countries that possess this vital metal; however, vanadium extraction from slag has not been carried out to date. Moreover, due to the unstable quality of the slag, its utilization in other industries has not been feasible. To prevent the environmentally harmful effects of accumulating slag and the inability to utilize it in various industries, it is essential to implement an economic solution for recovering the components present in steel-making slag. In the present project, after sampling from the stored slag deposits at Mobarakeh Steel Company, comprehensive laboratory and pilot-scale studies were conducted on the representative samples. Through processes involving roasting with sodium carbonate, acid leaching with 2 M sulfuric acid, iron cementation, solvent extraction using DEHPA, stripping, and scrubbing, we successfully extracted pentoxide vanadium with high purity suitable for producing ferrovanadium.

Keywords: slag of steel production, Vanadium oxidation in stripping, pentoxide vanadium

1. Introduction

Vanadium holds significant importance in the steel manufacturing industry. It is a crucial alloying element in many types of steel, particularly in high-strength low-alloy steels. The impact of increasing vanadium content leads to improved hardness and wear resistance. Iron alloys containing vanadium are harder and stronger than regular iron, exhibiting greater resistance to rust and corrosion. Furthermore, vanadium is utilized in non-ferrous alloys, especially in titanium-vanadium alloys and nickel-based superalloys, which are essential for the aerospace industry. Another application of vanadium is its role as a catalyst, which plays a special position in the chemical industries. One of the compounds used for this purpose is vanadium pentoxide (V_2O_5), which is employed in processes such as the oxidation of SO_2 to SO_3 in sulfuric acid production, the removal of sulfur from crude oil, and in the dye and ink manufacturing industries (Lindvall M., 2017; Diao J and et al., 2009; Coetsee T and Pistorius C, 2000; Zhang Y L and et al.,2011).

Vanadium extraction from steel plant slag is generally carried out by two methods: hydrometallurgy and pyrometallurgy. The pyrometallurgical method typically has higher energy consumption and economic capacity compared to the hydrometallurgical method. In this process, ferrovanadium (FeV) is produced directly through smelting. However, the ferrovanadium produced by this method has a lower grade (40 to 50 percent), resulting in a lower vanadium recovery rate compared to hydrometallurgy. Additionally, the pyrometallurgical method requires higher investment than

hydrometallurgy and is less environmentally friendly due to the generation of toxic gases as byproducts (Howard. R.L. and et al., 1992; Xiao.Y. and et al, 2010).

The hydrometallurgical method is more environmentally friendly with lower investment costs. One advantage of the hydrometallurgical method for extracting vanadium from slag is that it allows for the production of high-grade vanadium pentoxide, which can then be reduced with aluminum in combination with scrap and lime to obtain high-grade ferrovanadium (around 80 percent). In hydrometallurgy, if the vanadium content in the slag changes, it offers better flexibility compared to pyrometallurgy. Hydrometallurgical methods include salt roasting and aqueous, acidic, or alkaline leaching. The elements constituting the slag content from steel plants determine the effective hydrometallurgical method for extracting vanadium from iron slag (Tavakolikhaledi, M.R., 2014; Gupta C.K. and Krishnamurphy N., 1992).

The calcium content present in the iron slag plays a significant role in process selection (Fang, H. X. and et al., 2015). The salt roasting-leaching with water method is applicable when the calcium content in the slag is very low. For every one percent increase in CaO, the percentage of V_2O_5 extraction significantly decreases. In 2012, Mr. Sheng Li and Bing Zhi, and also in 2015, Mr. Zhao Manyan and colleagues conducted hydrometallurgical studies to extract vanadium from iron slag. The slag contained a lot of calcium, so they recovered vanadium in the leaching solution by direct roasting without adding salt and then alkaline leaching(Xiao-Man Yan, and et al.,2015 ; Xin-sheng and Bing Xie, 2012).

As mentioned, depending on the elements in the vanadium feed, either acidic or alkaline leaching can be used to extract vanadium. Mr. Deng studied the sample in the year of 2010 which used acidic leaching applying sulfuric acid (Deng, Z., Wei and et al., 2010).

Furthermore, In 2017, research by Mr. Jiang et al. (Rare Metal Technology, 2017) focused on recovering vanadium using acid leaching after the roasting process. Acid leaching dissolves complex vanadium compounds formed during roasting, improving leaching efficiency. The research optimized the parameters of this acid leaching process to enhance vanadium recovery from the leaching solution, as also supported by other studies involving acid leaching and solvent extraction for vanadium recovery from various sources like clay vanadium ore and oil-fired boiler slag. This approach addresses the challenge of extracting valuable vanadium from complex matrices.

Following the leaching process, solvent extraction process is vital to transfer vanadium from aqueous phase to organic phase. Depending on the associated elements and primary leaching, various types of solvent extractors can be used (Bal Y., and et al, 2004; El-Nadi, Y.A., and et al, 2009; Biswas R.K. and Mondal M.G.K., 2003; Hughes M.A., 1991)

In 2021, Liu Y. and his colleagues obtained a new aproach of stripping process via transferring vanadium from the organic phase to the aqueous phase using only the vanadium oxidation method (Liu Y., and et al., 2021)

In our country, a huge volume of slag is obtained annually from steel manufacturing plants. The amount of slag is approximately 20 percent of the steel produced and is the most important valuable source for the extraction of vanadium, accounting for 67 percent of the world's vanadium production. Despite having significant vanadium reserves, Iran is classified among the top five countries possessing this vital metal; however, vanadium extraction has not been carried out so far. Furthermore, due to the unstable quality of the slag, its use in other industries has not been feasible. Therefore, the aim of this project is to enable the production of vanadium pentoxide from slag as a valuable source of vanadium under optimal technical and economic conditions. Additionally, the

waste generated from the processes of this project contains minimal harmful materials and can be utilized in other industries.

2. Material and methods

2.1. Sample preparation and comminution

In order to study the slag of the Isfahan Steel Plant, samples were first taken from the slag depot. The slag generated from several years of steel production has been collected in multiple depots at the Mobarakeh Steel Company site. Sampling from the depots was carried out to select a representative sample, in consultation with colleagues from Mobarakeh Steel Company, as follows: Initially, three samples, each weighing approximately 100 tons on average, were selected under the careful supervision of IMPRC experts from different points within the new slag depots. These samples were then transferred to another location using specialized machinery. After several rounds of division and homogenization of the samples, approximately 15 tons of the sample were sent to the Iran Mineral Processing Research Center as the representative sample.

The sent slag sample was crushed to under one inch using a jaw crusher. After homogenizing the sample manually, a control sample was selected and stored using a conical method in a single step. The remaining sample was crushed using a cone crusher with an output aperture size of 3 millimeters in a closed circuit with a 3-millimeter sieve for control. The sample was then divided into 1-kilogram representative sample packages using a rotary splitter.

2.2. Sample Identification

complete chemical analysis and XRF studies were conducted on the representative sample. Mineralogical studies were also performed on it. These mineralogical studies included X-ray diffraction (XRD), microscopic studies, and SEM. The results of the complete chemical analysis are presented in Table 1. Additionally, the results of the XRF studies are provided in Table 2.

Table 1. Results of the full Chemical Analysis of the Mobarakeh Steel Slag Sample

Ag (ppm)	Al (%)	As (ppm)	Be (ppm)	Bi (ppm)	Ca (%)	Cd (ppm)	Ce (ppm)	Co (ppm)	Cr (ppm)
<1	1.51	<10	<2	<20	14.93	<1	101	8	119
Cu (ppm)	Fe (%)	K (%)	La (ppm)	Mg (%)	Mn (ppm)	Mo (ppm)	Na (%)	Ni (ppm)	P (%)
8	27.93	0.16	71	4.41	1325	<2	0.47	<10	0.2
Pb (ppm)	S (%)	Sb (ppm)	Sc (ppm)	Sr (ppm)	Ti (%)	V (ppm)	Y (ppm)	Zn (ppm)	
36	<0.1	<20	<5	86	0.47	6037	27	39	

Table 2. XRF study results of the Mobarakeh Steel Slag Sample

SiO2 (%)	Al2O3 (%)	CaO (%)	MgO (%)	TiO2 (%)	Fe2O3 (%)	MnO (%)	SO3 (%)
17.03	3.65	27.65	5.49	.78	39.93	0.32	0.06
P2O5 (%)	Na2O (%)	K2O (%)	V2O5 (%)	SrO (%)	Cl (%)	L.O.I (%)	
0.32	0.59	0.18	1.08	<.1	<.1	-	

-XRD studies result

XRD studies were conducted on several different samples taken from various slag deposition areas, and it was determined that the majority of the contained minerals include merwinite, wuestite, fayalite, gehlenite, perovskite, and magnetite. Quartz, calcite, hedenbergite, monticellite, dolomite, grossular, diopside, anorthite, hematite, and akermanite were identified as minor minerals in some samples. Figure 1 shows the results of the XRD study.
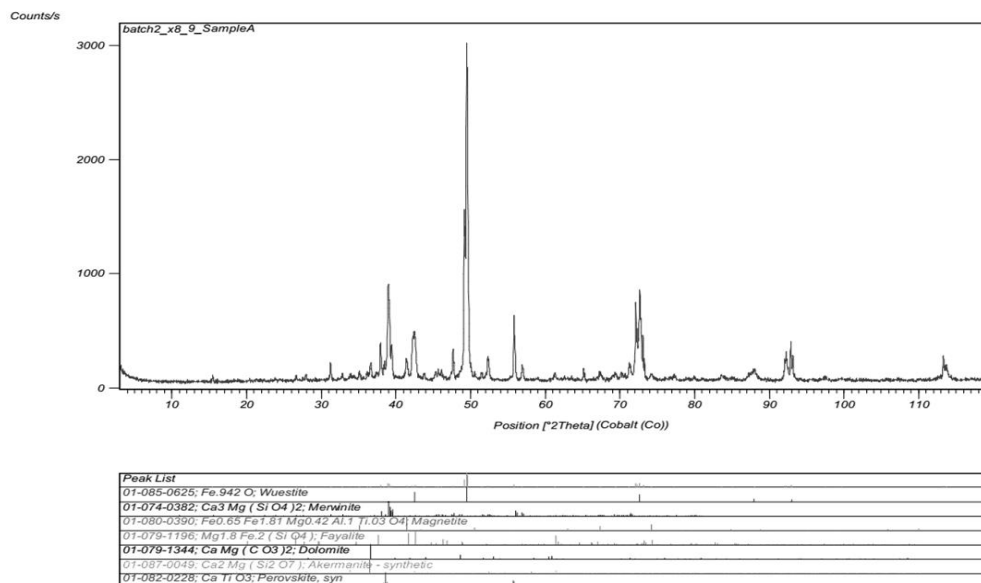

Fig1. XRD studies on the slag sample

-Microscopic studies result

The results of microscopic studies on the reference sample also indicated that the sample is composed of two phases: metallic and silicate. The metallic phase of the sample is predominantly made up of iron metal and both divalent and trivalent iron oxides. The silicate phase consists mainly of quartz (high-temperature silica), cristobalite, fayalite, which is the most significant constituent of the silicate in the slag, and pyroxene (mainly diopside). The texture of most slag particles is flow-like, sometimes displaying a glassy and shiny texture. Porosity is observed on the surface of most grains. The iron present in the sample is seen in the form of wuestite, a divalent iron oxide, which is the final reduction product of iron. However, in most cases, trivalent iron (magnetite) is also observed, exhibiting idiomorphic and dendritic textures. The approximate abundance of magnetite can be estimated at 10 to 15 percent. Magnetite is fully embedded within the silicate phases (quartz, fayalite, and pyroxene). Magnetite has been oxidized to hematite and, in some cases, to goethite, which is observed in the sample. Other minerals present in the sample, estimated at approximately 3 to 5 percent in crystalline form, include calcite and dolomite.

-SEM studies result

SEM studies were conducted on samples with fractionation (0.106+0.031-), (0.038+0.075-), and (0.075+0.106-). The results of the SEM studies indicated a significant amount of iron oxides (primarily magnetite and occasionally hematite) present in the sample, with the interaction of magnetite with perovskite and pyroxene observable in various parts of the sample. The ragged texture of magnetite is evident in the sample. Some dendritic iron formations are also present in the sample, which are, in some areas, associated with magnetite and pyroxene. Additionally, several phases containing iron,

titanium, vanadium, and aluminum were identified. The identified minerals in the sample include some calcite, minor chalcopyrite, chlorite, quartz, albite, and diaspor.

2.3. Processing studies

The following processes were carried out to extract vanadium from slag; which includes roasting with sault, Acid Leaching, solvent extraction, stripping and precipitation.

2.3.1. Roasting and Acid Leaching

In the roasting processes, sodium carbonate (Na_2CO_3) was used. It is worth mentioning that, in addition to this salt, other salts such as sodium sulfate (Na_2SO_4) and sodium chloride (NaCl) were also tested. However, nowadays, the use of sodium carbonate is more common due to its environmental compatibility, and the recovery of vanadium using sodium carbonate is greater than that achieved with the other mentioned salts.

Roasting with salt leads to the formation of sodium vanadate ($NaVO_3$), which is soluble in water. In the next stage, the sodium vanadate obtained from the roasting process can be recovered using a leaching process. Leaching has been studied in both acidic and alkaline forms. In both cases, the investigated parameters were optimized, and it was found that the vanadium recovery from the roasting and alkaline leaching process was lower than that from the roasting and acidic leaching process. Therefore, acidic leaching was selected, and the factors under investigation and optimization will be described further.

-The Effect of Salt Weight Percentage in the Roasting Process on Vanadium Recovery

The effect of Na_2CO_3 salt at weight percentages of 0, 10, 15, 20 and 30 on vanadium extraction from slag was evaluated during the roasting process. Since sodium vanadate begins to form at temperatures above 500 degrees, the initial roasting temperature was set at 600 degrees for 150 minutes for all experiments. The conditions for the roasting and acidic leaching processes are presented in Table 3. Except for the weight percentage, the other parameters were kept constant. Figure 2 illustrates the vanadium recovery as a function of the salt weight percentage in the roasting process. It can be observed that as the percentage of sodium carbonate salt increases from 0 to 15 percent during the roasting process, the percentage of vanadium recovery in the leaching solution increases from 86.4 percent to 95.6 percent. However, when the weight percentage of sodium carbonate salt in the roasting process was raised to 30%, the vanadium recovery stabilized and even experienced a slight decrease. Therefore, a weight percentage of 15 percent was selected as the optimal percentage for subsequent stages. Additionally, in examining the effect of Na_2CO_3 salt in the roasting and acidic leaching processes on iron dissolution, it was observed that at a salt weight percentage of 15 percent, the maximum iron dissolution reached 87.6%.

Table3. Conditions of conducted experiments to evaluate the effect of sault additive

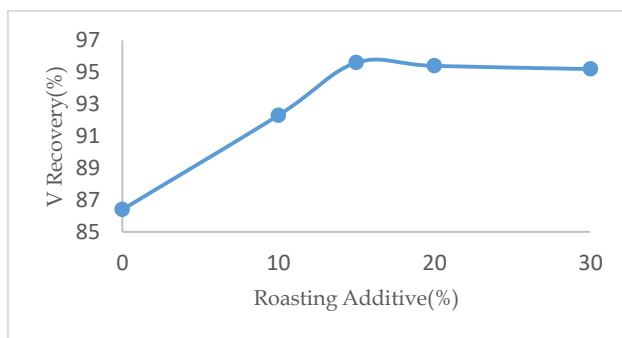| Particle size (d$_{80}$ μm)	Roasting Condition			Leaching Condition				
	Additive (%W)	Temp (°C)	Time (min)	Agent Name	Agent (Molarity)	S/L	Time (min)	Temp (°C)
75	0,10,15,20	600	150	H_2SO_4	2	1/10	150	90

Fig2. The effect of sault additive on vanadium recovery

-The Effect of Roasting Temperature on Vanadium Recovery

The roasting temperature was evaluated at four levels: 600, 800, 1000, and 1100 degrees Celsius for vanadium extraction from slag, according to the experimental conditions outlined in Table 4. Figure 3 shows the vanadium recovery as a function of roasting temperature. It can be observed that as the roasting temperature increases from 600 degrees Celsius to 1000 degrees Celsius, the percentage of vanadium recovery in the leaching solution increases; however, beyond this, at 1100 $^\circ$C, it decreases from 95 percent to 88 percent. Therefore, a roasting temperature of 1000 $^\circ$C was selected as the optimal roasting temperature for subsequent stages. It is noting that at the roasting temperature of 1000 $^\circ$C, where vanadium recovery is maximized, the iron dissolution is also maximized.

Table 4.the conditions of conducted experiments to evaluate the effect of roasting temperature

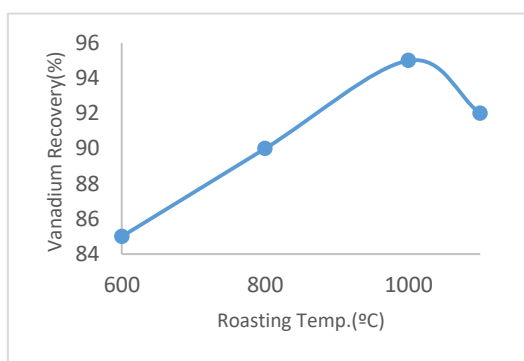| Particle size (d$_{80}$ μm)	Roasting Condition			Leaching Condition				
	Additive (%W)	Temp (°C)	Time (min)	Agent Name	Agent (Molarity)	S/L	Time (min)	Temp (°C)
75	15	600,800,1000,1100	150	H$_2$SO$_4$	2	1/10	150	90

Fig3. The effect of roasting temperature on vanadium recovery

-The Effect of Roasting Time on Vanadium Recovery

The effect of roasting time on vanadium extraction from slag was evaluated according to the experimental conditions outlined in Table 5. Figure 4 illustrates the vanadium recovery as a function of roasting time. In Figure 4, it can be observed that as the roasting time increases from 45 minutes to 90 minutes, the percentage of vanadium recovery in the leaching solution remains relatively stable at about 92 percent. However, as the roasting time increases from 90 minutes to 150 minutes, the percentage of vanadium recovery in the leaching solution increases from 92 percent to 95.73 percent.

Therefore, a roasting time of 150 minutes was selected as the optimal roasting time for subsequent stages.

Table5. the condition of conducted experiments to evaluate the effect of the roasting time

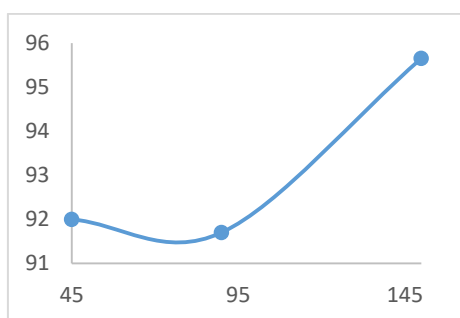| Particle size (d$_{80}$ μm)	Roasting Condition			Leaching Condition				
	Additive (%W)	Temp (°C)	Time (min)	Agent Name	Agent (Molarity)	S/L	Time (min)	Temp (°C)
75	15	1000	45,90,150	H$_2$SO$_4$	2	1/10	150	90

Fig4. The effect of roasting time duration on vanadium recovery

-The effect of sulfuric acid concentration on vanadium extraction

The effect of sulfuric acid concentration on the extraction of vanadium from slag was evaluated according to the experimental conditions stated in Table 6. Figure 5 shows the vanadium recovery curve relative to acid concentration. It can be observed that as the concentration of sulfuric acid increases from 1 molar to 2 molar, the percentage of vanadium extraction in the leaching pregnant solution increases from 62% to 95.6%. However, with a further increase in acid concentration from 2 molar to 3 molar, the percentage of vanadium extraction in the leaching pregnant solution remains almost constant, with only a slight increase from 95.73% to 96%. Therefore, the 2 molar acid concentration was selected as the optimal concentration for subsequent stages. Additionally, at a 3 molar sulfuric acid concentration, where the dissolution of vanadium is maximized, the dissolution of iron is also at its maximum, equal to 93.83%. In contrast, at a 2-molar sulfuric acid concentration, the dissolution of iron is lower, at 87.7%.

Table 6. the condition of conducted experiments to evaluate the effect of acid molarity in leaching process

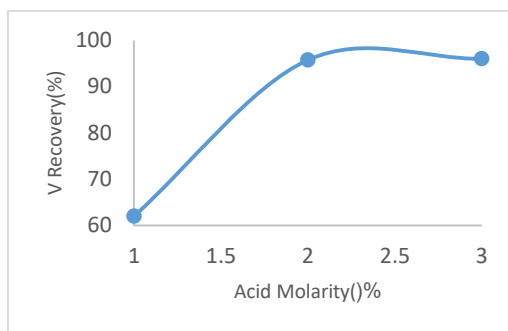| Particle size (d$_{80}$ μm)	Roasting Condition			Leaching Condition				
	Additive (%W)	Temp (°C)	Time (min)	Agent Name	Agent (Molarity)	S/L	Time (min)	Temp (°C)
75	15	1000	150	H$_2$SO$_4$	1,2,3	1/10	150	90

Fig5. The effect of acid molarity in leaching process on vanadium recovery

-The effect of the liquid-to-solid ratio on vanadium extraction

The effect of the liquid-to-solid ratio at ratios of (5, 10, 15) in the leaching process on the extraction of vanadium from slag was evaluated according to the experimental conditions stated in Table 7. Figure 6 shows the vanadium recovery curve relative to the liquid-to-solid ratio in the leaching process. As seen in Figure 6, with an increase in the liquid-to-solid ratio from 5 to 10, the percentage of vanadium extraction in the leaching pregnant solution increases from 68% to 95.6%. However, with a further increase in the liquid-to-solid ratio from 10 to 15, the percentage of vanadium extraction in the leaching pregnant solution remains constant. Therefore, a liquid-to-solid ratio of 10 was selected as the optimal ratio for subsequent stages.

Table7. the condition of conducted experiments to evaluate the effect of L/S in leaching process

Particle size (d_{80} μm)	Roasting Condition			Leaching Condition				
	Additive (%W)	Temp (°C)	Time (min)	Agent Name	Agent (Molarity)	L/S	Time (min)	Temp (°C)
75	15	1000	150	H_2SO_4	2	5,10,15	150	90
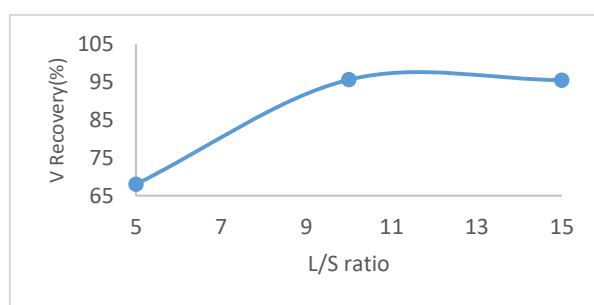
Fig6. The effect of L/S ratio in leaching process on vanadium recovery

-The effect of acid leaching time on vanadium recovery

The effect of acid leaching time on vanadium recovery was examined according to Table 8. The results are presented in Figure 7. As shown in Figure 7, with an increase in leaching time from 60 to 90 minutes, the vanadium extraction in the leaching pregnant solution increases from 89.79% to 92%. Furthermore, with an increase in leaching time from 90 to 150 minutes, the percentage of vanadium

extraction in the leaching pregnant solution rises from 92% to 95.6%. Furthermore, at a leaching time of 150 minutes, where the dissolution of vanadium is maximized, the dissolution of iron is also at its maximum, equal to 87.87%.

Table 8. the condition of conducted experiments to evaluate the effect of leaching time duration

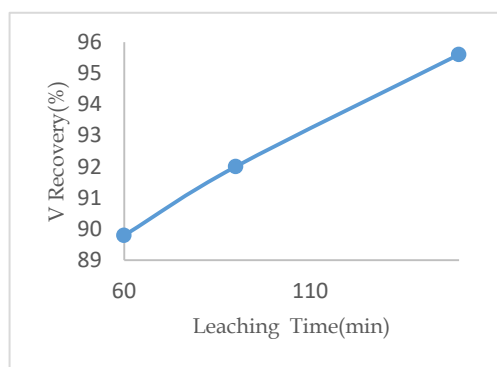| Particle size (d$_{80}$ μm)	Roasting Condition			Leaching Condition				
	Additive (%W)	Temp (°C)	Time (min)	Agent Name	Agent (Molarity)	S/L	Time (min)	Temp (°C)
75	15	1000	150	H$_2$SO$_4$	2	1/10	60,90,150	90

Fig7. The effect of leaching time duration on vanadium recovery

-Optimized condition

The optimal conditions for roasting with sodium carbonate and leaching with sulfuric acid, as well as the amount of vanadium recovery in the leaching solution, are shown in Table 9.

Table 9. the optimized condition of roasting and leaching processes

Particle size (d$_{80}$ μm)	Roasting Condition			Leaching Condition					V-Recovery (%)
	Additive (%W)	Temp (°C)	Time (min)	Agent Name	Agent (Mollar)	S/L	Time (min)	Temp (°C)	
75	15	1000	150	H$_2$SO$_4$	2	1/10	150	90	95.6

After vanadium has entered the leaching solution, it must be transferred from the aqueous phase to the organic phase using a solvent extraction process.

2.3.2. Iron cementation process and its necessity before solvent extraction with D2EHPA

The leaching solution content is mostly in the form of ferric ions (Fe^{3+}), which compete with vanadium for transfer to the organic phase. To prevent iron from entering the organic phase, Fe^{3+} should be converted to Fe^{2+} as much as possible. Using the cementation process, ferric iron can be converted to ferrous iron by adding iron powder (reaction 1) under the following conditions as shown in Table 10.

$$Fe^0 + 2Fe^{3+} = 3Fe^{2+} \tag{1}$$

Table 10. condition of Fe cementation process

Temperature	Ambient Temp.
Time duration	1 hour
Deoxygenation	15 minutes of argon gas blowing into the solution before adding metallic iron – 0.5 liters/minute of argon gas blowing during the test
The amount of Fe powder	Iron powder – 1.2 times the stoichiometric amount of total iron in the leaching solution

2.3.3. Solvent extraction process

After the cementation process and the conversion of ferric ions to ferrous, the solvent extraction process was carried out with a ratio of organic phase to aqueous phase of one to one under optimal conditions. By using an organic phase containing 10% D2EHPA and a kerosene diluent, it was possible to transfer about 96% of the vanadium content to the organic phase and only 2% of the iron to the organic phase. It is noted that the suitable pH for leach solution in solvent extraction is 1; therefore, some amount of NaOH was added before that.

2.3.4. Investigation of the effect of vanadium concentration in the organic phase on the extraction rate of vanadium

In order to investigate the effect of vanadium concentration in the organic phase on the extraction rate of vanadium, solvent extraction experiments were conducted in several stages. In the first stage, the leaching solution after cementation was contacted with the fresh organic phase (Step1). In the second stage, the leaching solution after cementation was contacted with the fresh organic phase of the first stage (Step2). These stages continue until the crud is formed. The experiments showed that the crud was formed after three stages. In the first stage, 95% of vanadium was extracted from the leaching

solution; in the second stage, 56%; and finally, in the third stage, only 11% of vanadium was extracted (Fig8).
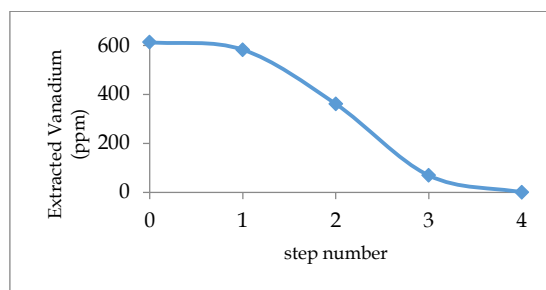

Fig8. the effect of vanadium concentration in the organic phase on the extraction rate of vanadium

Since it is difficult to separate the valuable material from the organic phase, it is necessary to transfer the valuable material back to the aqueous phase. Therefore, in the stripping process, the aqueous phase is contacted with a charged organic phase to allow the transfer of vanadium metal from the organic phase to the aqueous phase.

2.3.5. Stripping process

The stripping process often takes longer than the solvent extraction process because the kinetics of the stripping process are slower than that of solvent extraction.

Different aqueous phases were evaluated for the stripping process.

First, acid was used in the aqueous phase. The recovery of vanadium was very low when using hydrochloric and sulfuric acids. In the case of nitric acid (in aqueous phase conditions of 4M, V_O/V_A = 4.1), the recovery was about 50%, and in the saturated state, the vanadium content was only 1 g/l, and during the precipitation stage, vanadium was not precipitated.

In the second study, alkali was also used in the organic phase. In the first stage (in aqueous phase conditions of 4M, V_O/V_A = 4.1), the recovery was about 50%, but in the concentration stage, a huge volume of viscous precipitate was formed in the aqueous phase, which could not be separated.

Direct precipitation from the organic phase was also investigated. In this method, a solution of ammonium sulfate in water is selected as the aqueous phase. The amount of ammonium sulfate is 2 times the stoichiometry of the vanadium content in the organic phase. The stripping process was carried out for 4 hours at a temperature of 50 ° C with a ratio of organic phase to aqueous phase of 3 to 1. After separating the two phases from each other, it was determined that no precipitation had occurred.

But in the end, the solution to the vanadium stripping process was obtained; That was the oxidation of vanadium. In this way, the aqueous phase consists of water with a pH of about 6.5 to 8 and 2% by

volume of hydrogen peroxide. The ratio of organic phase to aqueous phase is 3 to 1 and the duration of its execution is less than 2 minutes. In order to concentrate vanadium in the aqueous phase, a three-step stripping process is performed with fresh organic phase. Then, the color of the aqueous phase solution becomes ochre, containing 8 g/L of vanadium (Figure 9).

Fig9. the aqueous phase containing 8 g/L vanadium

2.3.6. Precipitation process

At this stage, the stripped solution is kept around 90°C for 6 hours and then under 60°C for 24 hours with a condenser. After filtering, 75% of the vanadium in the solution has precipitated. The results of this experiment show that heat and time duration of heating are an important and effective factors in the precipitation of vanadium. After calcination at 550°C for 2 hours, V_2O_5 containing 75% vanadium with the purity of 86.2% was obtained

3. Result and Disscution

3.1. Operational flowsheet

After doing full study at laboratory scale, the flowsheet for the process of extracting vanadium from steel plant slag is obtained which is shown in the figure 10. By performing a set of effective technical processes, vanadium extraction from steel plant slag under optimal conditions has become possible which leads to vanadium pentoxide production with a grade of 86.2%.
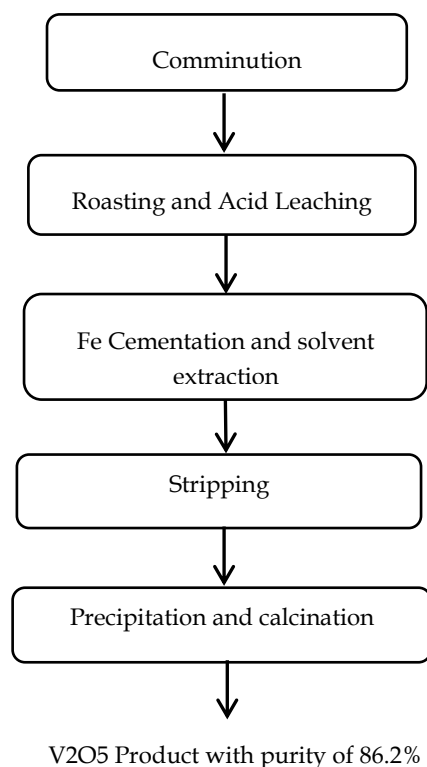
```
┌─────────────────────────────┐
│        Comminution          │
└─────────────────────────────┘
              │
              ▼
┌─────────────────────────────┐
│   Roasting and Acid Leaching │
└─────────────────────────────┘
              │
              ▼
┌─────────────────────────────┐
│   Fe Cementation and solvent │
│          extraction          │
└─────────────────────────────┘
              │
              ▼
┌─────────────────────────────┐
│          Stripping          │
└─────────────────────────────┘
              │
              ▼
┌─────────────────────────────┐
│  Precipitation and calcination │
└─────────────────────────────┘
              │
              ▼
```

V2O5 Product with purity of 86.2%

Fig10. flowsheet of processes to product V2O5 from slag

3.2. Semi-industrial implementation

Vanadium pentoxide flowsheet was implemented on pilot scale thorough these processes:

-100 kg of steel slag sample was crushed to less than one inch by jaw crusher. It was then crushed by a cone crusher with an outlet size of 3 mm in a closed circuit with a 3 mm control screen. Then it was milled in a closed circuit to a size of d80=75 mμ.

-Roasting and acid leaching process was performed on 100 kg of material. To avoid adding NaOH solution to adjust pH, the sodium carbonate salt was increased by 30% in the roasting process to bring the pH of the leaching solution to approximately 1, thus preventing its dilution. Roasting conditions included temperature of 1000 degrees for 150 minutes with addition of 30% by weight of sodium carbonate salt. Acid leaching was also performed under temperature conditions of 90 $^\circ$C, solid to liquid ratio of 1 to 10, for 150 minutes with 2 molar sulfuric acid.

-The solvent extraction, stripping and scrubbing processes were carried out in a continuous circuit as follows: The organic phase consists of 10% D2EHPA and kerosene diluent. The solvent extraction process was carried out with a ratio of aqueous to organic phase of 1:1 for 40 minutes. After the solvent extraction process was completed and stabilized, the stripping process was carried out. In the stripping process, the aqueous phase consists of water (pH=6-8) and 2% by volume of H_2O_2. The stripping process was performed in 6 steps with a ratio of aqueous to organic phase of 1:1 for 2

minutes. The organic phase was scrubbed with 2 molar sulfuric acid for 20 minutes after loading, and then 70% of it was mixed with 30% of the organic phase of the carpet and returned to the beginning of the circuit.

-The aqueous phase containing vanadium from the stripping process was heated at 90°C for 6 hours, then at 60°C for 48 hours. After filtration, the calcination process was carried out at 550°C for 2 hours, and vanadium pentoxide was obtained with a purity of 86.2%.

The final product of vanadium pentoxide is shown in Figure 11, and its full analysis is also given in Table 11.A semi-industrial scale operational flowsheet along with a mass balance is illustrated in figure 12. The overall recovery of the processes is 70%.

Fig11. Pentaoxide vanadium product

Table11. Full analysis of Pentaoxide vanadium product

Ag(ppm)	Al(%)	As(ppm)	Be(ppm)	Bi(ppm)	Ca(%)	Cd(ppm)	Ce(ppm)	Co(ppm)	Cr(ppm)
<1	0.09	15	<1	<20	0.62	<1	31	15	16
Cu(ppm)	Fe(%)	K(%)	La(ppm)	Mg(%)	Mn(ppm)	Mo(ppm)	Na(%)	Ni(ppm)	P(%)
779	0.26	0.08	11	0.23	85	498	1.2	116	2.01
Pb(ppm)	S(%)	Sb(ppm)	Sc(ppm)	Sr(ppm)	Ti(%)	V(%)	Y(ppm)	Zn(ppm)	
80	<0.1	<20	<5	106	0.1	48.29	7	526	

3.3. Environmental study on leaching waste

After acid leaching and filtering, leaching cake (waste) is produced. (About 900 grams of waste per kilogram of leaching feed). According to the information of Table12, the levels of iron, magnesium, and other interfering elements in the leach cake are minimized (Environmental Protection Agency,2023). Concequently, The waste is free of harmful heavy metal elements in nature and it is unobstucted in terms of water pollution standards.
By adding appropriate additives and without the need for crushing, it is possible to use the waste in the cement and road construction industries

Table12. Environmental study of waste generated from the acid leaching process

	Ag (ppm)	As (ppm)	Cd (ppm)	Co (ppm)	Cr (ppm)	Cu (ppm)	Mo (ppm)	Ni (ppm)	Pb (ppm)	Sb (ppm)	V (ppm)	Zn (ppm)
Leaching waste	2	14	1>	5	76	157	28	38	32	20	208	19
Soil Pollution Standard Values -Environmental Protection	20	17	3.9	20	64	63	4	50	300	20	130	200

Soil Contamination Standard Values -Groundwater Protection	100	100	20	1000	3000	1500	100	600	300	12	500	3000

4. Conclusions

The extraction of vanadium from the steelmaking slag of the Isfahan Steel Company has been studied at laboratory and semi-industrial scales under optimized conditions. The slag from the Isfahan Steel Company contains 0.6% vanadium and 28% iron. In this study, a combination of mineral processing methods such as roasting with salt, acid leaching, solvent extraction, stripping, and precipitation was employed to obtain vanadium pentoxide (V_2O_5) concentrate with a grade of 86.2%. Furthermore, the vanadium recovery after the entire process was 70%.

It is noteworthy that in the stripping stage, nearly complete extraction of vanadium from the organic phase was achieved solely using an oxidation process in a neutral pH aqueous phase. Another important point is that after acid leaching in this process, the levels of iron, magnesium, and other interfering elements in the leach cake are minimized, allowing for its utilization in other industries, such as the cement industry.

Acknowledgments

V Grade: (ppm, %)
V Recovery(%)

100 Kg Feed

G=0.6%

Comminution to d_{80}=75 μm

42.8 kg Na_2CO_3

Roasting with 30% Na_2CO_3

139.23 kg roasted sample   G=0.43%   139 kg cake

Acid leaching with 2M sulfuric acid, 90°C, for 150 minutes, solid to liquid ratio 1/10,

G=208 ppm
R=4.8%

1400 L Leaching solution   G=407 ppm, R=95.2%

Fe cementation

pH=1   420 L of organic phase

Aqueous phase

Scrubbing

Solvent extraction, D2EHPA 10%

G=5 ppm
R=1.3%

980 L scrubbed organic phase

G=402 ppm, R=98.7%

1400 L

Stripping   Unloaded organic phase

Unloaded aqueous phase

1166.67 L   1400 L

G=2412 ppm,
R=99.8%

233.33 L +2% H_2O_2

233.33 L loaded aqueous phase

aqueous phase

0.96 kg Vanadium   0.87 kg V_2O_5

Precipitation   Calcination

R=75% .G=43.8% R_{total}=70% .G=86.2%
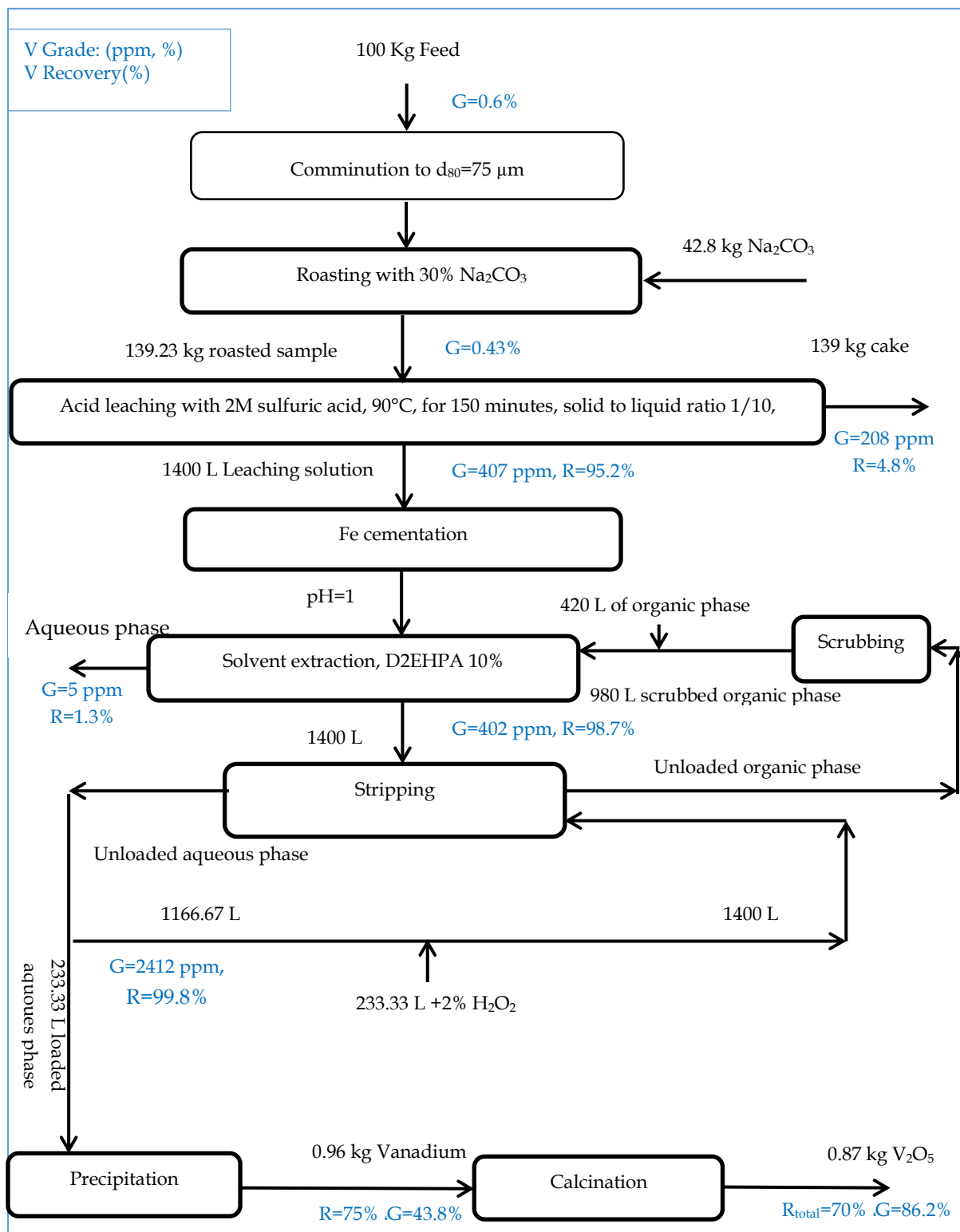
Fig12. Semi-industrial implementation with mass balance

References

Bal, Y., Bal, K.E., Cote, G. and Lallam, A., 2004. Characterization of the solid third phases that precipitate from the organic solutions of Aliquat 336 after extraction of molybdenum(VI) and vanadium(V). Hydrometallurgy, 75(1-4): 123-134.

Biswas, R.K. and Mondal, M.G.K., 2003. Kinetics of VO2+ extraction by D2EHPA. Hydrometallurgy, 69(1-3): 117-133.

Coetsee T and Pistorius C, 2000, Preliminary observations on phase relations in the "V2O3 FeO" and V2O3-TiO2 systems from 1400°C to 1600°C in reducing atmospheres. J. Am. Ceram. Soc. 83(6):1485-1488.

Environmental Protection Agency (Deputy of Human Environment, Water and Soil Office), 2023, Permissible limits of soil contamination and pollutants entering it for various uses.

Deng, Z., Wei, C., Fan, G., Li. M., Li, C. and Li, X., 2010. Extracting vanadium from stone-coal by oxygen pressure acid leaching and solvent extraction. Transactions of Nonferrous Metals Society of China, 20(Supplement 1): s118-s122.

Diao J, Xie B, Wang Y, Ji C Q, 2009, Mineralogical characterization of vanadium slag under different treatment conditions. Ironmak. and Steelmak, 36 (6):476-480.

El-Nadi, Y.A., Awwad, N.S. and Nayl, A.A., 2009. A comparative study of vanadium extraction by Aliquat-336 from acidic and alkaline media with application to spent catalyst. International Journal of Mineral Processing, 92(3-4): 115-120.

Fang H. X., Li, H. Y., Zhang T., Liu B S, Xie B, 2015, Influence of CaO on Existence form of Vanadium-containing Phase in Vanadium Slag. ISIJ Int. 55:200-206.

Gupta, C. K. and Krishnamurphy, N., 1992. Extractive metallurgy of vanadium (Process Metallurgy). Elsevier Science, Netherland.

Howard. R.L.,Richards. S.R., Welch. S.J., and Moore. J.J.,1992, Pyrolllctallurgical processing of vanadiferous slag using plasma/induction heating. INFACON 6. Proceedings of the 6th International ferroalloys Congress, Cape Town. Volume l. Johannesburg, SAlMM. 1992. pp. 225-231.

Hughes, M.A. and Biswas, R.K., 1991. The kinetics of vanadium (IV) extraction in the acidic sulphate-D2EHPA-n-hexane system using the rotating diffusion cell technique. Hydrometallurgy, 26(3): 281-297.

Jiang, J., et al. (2017). "Study on Acid Leaching Process of Vanadium from Roasted Vanadium Titanomagnetite." Rare Metal Technology.

Lindvall M., 2017, A Study on Vanadium Extraction from Fe-V-P Melts Derived from Primary and Secondary Sources, PhD Thesis, KTH Royal Institute of Technology.

Liu, Y., Li, Q., Zhang, T., Wu, X., Du, J., Zhang, G., Zeng, L., 2021, New process condsisting of oxidative stripping of vanadium from loaded D2EHPA organic solution with H2O2 and direct precipitation with sulphuric acid, Hydrometallurgy 203,105611.

Tavakolikhaledi, M.R., 2014 , Leaching and Solvent Extraction, The Faculty of Graduate and Postdoctoral Studies (Materials Engineering), THE UNIVERSITY OF BRITISH COLUMBIA (Vancouver).

Xiao-Man Yan, Bing Xie, Lu Jiang, Hai-Peng Guo, Hong-Yi Li, 2015, Leaching of Vanadium from the roasted vanadium slag with high calcium content by direct roasting and soda leaching, Rare Metal Technology (Book), Publisher: Springer, pp. 209-216.

Xin-sheng Li and Bing Xie, 2012, Extraction of vanadium from high calcium vanadium slag using direct roasting and soda leaching, International Journal of Minerals, Metallurgy and Materials, Volume 19, Number 7, , Page 595-600.

Xiao Y., Jalkanen H. , Mambote C. R. , Boom R., 2010, Ferrovanadium production from petroleum fly ash and BOF flue dust, Minerals Engineering, Pages 1155-1157.

Zhang Y L, Zhao F, Wang Y G, 2011, Effects of influencing factors on distribution behaviors of vanadium between hot metal and FeO-SiO2-MnO (-TiO2) slag system. Steel Res. Int. 82:940-950.

Optimization of iron (III) extraction by leaching process from tailings produced in iron ore concentration process

Hamid Bouriabadi¹*

¹PhD student in inorganic chemistry and Iron Ore Laboratory Specialist 1

*Chem.hamid@yahoo.com (Hamid Bouriabadi)

Abstract:

Mining is crucial for the development of human society. A significant amount of iron ore tailings, a key secondary mineral resource, is generated globally. This study investigated the liquid-liquid extraction of iron (III) from tailings produced by the Sangan Khorasan Steel Mining Industries Company's concentration process, using hydrochloric acid leaching combined with a tributyl phosphate (TBP)-methyl isobutyl ketone (MIBK) mixture in kerosene. The effects of parameters such as contact time, hydrochloric acid concentration, and TBP-MIBK concentration on extraction efficiency were examined. Under optimized conditions – a 3:1 TBP-MIBK ratio, 9 M hydrochloric acid, and a 3-minute contact time at 20 °C – the extraction efficiency of iron (III) exceeded 98%."

Keywords: *Liquid-liquid extraction, Leaching process, Iron Ore Tailings, Tributyl Phosphate, Methyl Isobutyl Ketone*

1. Introduction

Iron ore processing involves operations to modify the particle size distribution and increase the iron content, without changing the chemical or physical identity of the minerals (Lima and Abreu, 2020). During mining, iron ore tailings are produced. The production of iron ore tailings (coarse or fine tailings) is estimated to be 20–40% of the total mining weight (Lima and Abreu, 2020). Iron ore tailings occupy huge areas of land and cause environmental pollution, therefore, the recovery and utilization of the iron remaining in iron ore tailings is very important to save iron resources (Dauce et al., 2019).

The solvent extraction technique is known as an excellent separation method due to its ease, simplicity, speed, and wide scope (Morrison, 1950). The solvent extraction method is more effective and attractive for the separation of metals than the precipitation method, because in this method, the separation is almost complete and the operation time is much shorter compared to the precipitation method. The iron ore tailings can be used to recover pure iron by the liquid-liquid extraction process. The use of hydrochloric acid to dissolve iron ore generally results in a solution with a high iron concentration (Alafara et al., 2005). Iron (III) has a high tendency to form complexes that can be selectively extracted by TBP-MIBK (Saji et al., 1998).

In this study, iron (III) in iron ore tailings produced in the concentration process of Sangan Khorasan Steel Mining Industries Company was separated by liquid-liquid extraction and the effect of various factors including contact time, hydrochloric acid concentration, and tributyl phosphate methyl isobutyl ketone concentration on the extraction efficiency was investigated.

2. Material and methods

2.1. Material

2.1.1. Commercial extractant tributyl phosphate (TBP)

2.1.2. Methyl isobutyl ketone (MIBK)

2.1.3. Kerosene

2.1.4. Distilled water

2.1.5. Hydrochloric acid (HCl)

2.2. Laboratory Equipment

2.2.1. Laboratory shaker

2.2.2. decanter funnel

2.2.3. spectrophotometer

2.2.4. common laboratory glassware

2.3. Methods

First, a tailings sample was obtained from the iron ore tailings dam of the Khorasan Sangan Steel Mining Industries Company and prepared according to the ISO 3082 standard (ISO 3082, 2017). Then, 10 grams of the tailings sample were dissolved via hydrochloric acid leaching at 100°C, and the iron(III) concentration in the resulting solution was determined. The extraction experiments were performed by mixing equal volumes (25 mL) of the aqueous phase (leaching liquid) with the organic phase containing TBP-MIBK. The TBP-MIBK was prepared at molar ratios of 1:1, 2:1, 3:1, and 4:1, diluted in kerosene, and added to the reaction medium. The mixture was then stirred mechanically (300 rpm) for 4 minutes at 20°C. After phase separation, the iron(III) concentration in the aqueous phase was determined spectrophotometrically by measuring the absorbance at 465 nm. The concentration of iron(III) in the organic phase was calculated from the mass balance. The extraction percentage (%E) was calculated using Equation (1):

$$\%E = 100D/(D + Vaq/Vorg) \tag{1}$$

Where V represents the volume of the two aqueous and organic phases and D is the distribution ratio of iron (III) in the organic and aqueous phases, which can be calculated based on equation (2).

$$D = [Fe]org/[Fe]aq \tag{2}$$

3. Results and Discussion

A chemical analysis of iron ore tailings was performed, and the results are summarized in Table 1. Ten grams of iron ore tailings were mixed with 90 mL of hydrochloric acid in an oil bath at 373 K for 2 hours while stirring at 200 rpm to extract iron species. After the process was completed, the cooled solution was filtered to separate it from the remaining sediment. The filtered solution contained ferric chloride ($FeCl_3$) with an iron concentration of 0.025 M and achieved an extraction efficiency of 94%.

Table 1. Chemical properties of iron ore tailings

Parameter	Value
Fe (%)	21.07
FeO (%)	10.74
SiO_2 (%)	25.73
CaO (%)	18.70
MgO (%)	3.70
Al_2O_3 (%)	7.43

3.1. Effect of Time on Iron (III) Extraction

To evaluate the effect of time, all other parameters were held constant. The specific conditions were as follows: iron (III) concentration of 0.025 M, hydrochloric acid concentration of 5 M, TBP to MIBK ratio of 3:1, aqueous to organic phase ratio of 1:1, stirring speed of 300 rpm, and a reaction temperature of 20 °C. The results of time's effect on extraction are depicted in Figure 1. As shown, increasing the contact time from 10 seconds to 60 seconds resulted in a rapid increase in iron extraction from 43% to 84%. Beyond this point, the extraction rate plateaued. Therefore, a reaction time of 3 minutes was selected for all subsequent experiments.
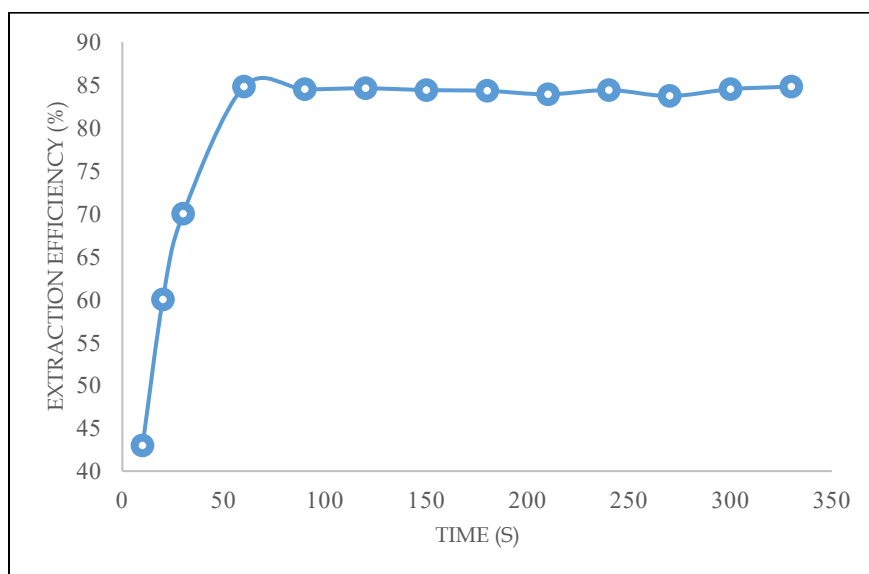
Fig. 1. Effect of time on iron (III) extraction

3.2. Effect of Hydrochloric Acid Concentration on Iron (III) Extraction

The concentration of hydrochloric acid plays a crucial role in iron extraction. It has been reported that $FeCl_3$, in the presence of HCl, aids in the formation of $HFeCl_4$, which can then interact with TBP-MIBK in the extraction complex, facilitating the extraction reaction (Saji and Reddy, 2001). The effect of HCl concentration, ranging from 1 M to 11 M, on iron (III) extraction was examined, as illustrated in Figure 2. The data reveal that the percentage of iron (III) extraction increases with higher HCl concentrations. Hence, Hcl 9 M was determined to be the optimal concentration, resulting in an extraction efficiency of approximately 89.40%.
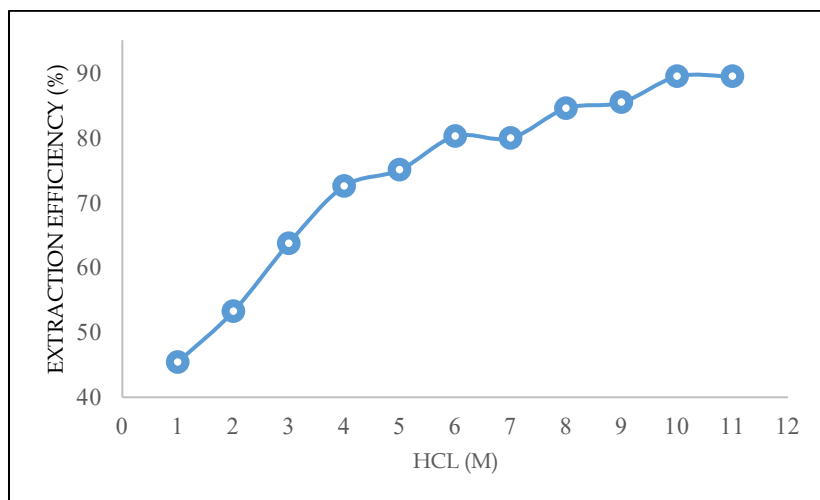
Fig. 2. Effect of hydrochloric acid concentration on iron (III) extraction

3.3. Effect of TBP and MIBK Ratio on Iron (III) Extraction

The influence of the TBP to MIBK ratio (1:1, 2:1, 3:1, and 4:1) on iron (III) extraction was assessed under conditions of 3 minutes stirring time, 0.025 M iron (III), an aqueous to organic phase ratio of 1:1, stirring speed of 300 rpm, and a temperature of 20 °C. The results are presented in Figure 3. It was observed that the percentage of iron (III) extracted increased significantly, from 85.37% to 98.12%, with the rising TBP to MIBK ratio.
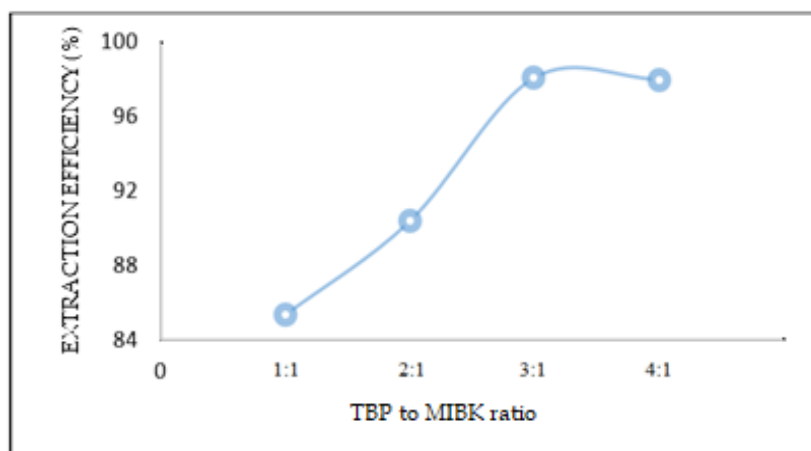
Fig. 3. Effect of TBP and MIBK ratio on iron (III) extraction

4. Conclusions

The solvent extraction technique is recognized as an excellent separation method due to its ease of use, simplicity, speed, and versatility. Given the gradual depletion of high-grade iron ore reserves, there is an increasing interest in utilizing the vast resources of low-grade iron ore and iron ore tailings generated during the concentration process as a secondary source of iron. Iron (III) was successfully separated from the tailings produced in the concentration process of the Sangan Khorasan Steel Mining Industries Company using a liquid-liquid extraction method. This method involved a mixture of tributyl phosphate (TBP) and methyl isobutyl ketone (MIBK) in kerosene. Various parameters, including contact time, hydrochloric acid concentration, and the TBP-MIBK ratio, were investigated to optimize extraction efficiency. Under the optimized conditions of a TBP-MIBK ratio of 3:1, 9 M hydrochloric acid, and a contact time of 3 minutes at 20 °C, the extraction efficiency for iron (III) exceeded 98%. This process

demonstrates a valuable method for extracting iron (III) from low-grade iron ore and iron ore tailings, serving as a sustainable source of iron.

Acknowledgments

References

Alafara, A. B., Adekola, F. A., Folashade, A. O., (2005). Quantitative leaching of a Nigerian iron ore in hydrochloric acid. *Journal of Applied Sciences and Environmental Management*, *9* (3) 15-20. doi: 10.4314/jasem.v9i3.17346

Dauce, P. D., de Castro, G. B., M. Lima, Lima, R., (2019). Characterisation and magnetic concentration of an iron ore tailings. *Journal of Materials Research and Technology*, *8* (1) 1052-1059. doi: 10.1016/j.jmrt.2018.07.015

ISO 3082, (2017). Iron ores, Sampling and sample preparation procedures. *International Organization for Standardization.*

Lima, R. M. F., Abreu, F. P. V. F., (2020). Characterization and concentration by selective flocculation/magnetic separation of iron ore slimes from a dam of quadrilátero Ferrifero - Brazil. *Journal of Materials Research and Technology*, *9* (2) 2021-2027. doi: 10.1016/j.jmrt.2019.12.034

Morrison, G. H., (1950). Role in Extraction in Analytical Chemistry. *Journal of Analytical Chemistry*, *22* (11) 1388–1393. doi: 10.1021/ac60047a011

Saji, J., Prasada, RT., Iyer, C. S. P., Reddy, M. L. P., (1998), "Extraction of iron (III) from acidic chloride solutions by Cyanex 923", *Journal of Hydrometallurgy*, *49* (3) 289-296. doi: 10.1016/S0304-386X(98)00030-9

Saji, J., Reddy, M. L., (2001). Liquid–liquid extraction separation of iron(III) from titania wastes using TBP–MIBK mixed solvent system. *Journal of Hydrometallurgy*, *61* (2) 81–87. doi: 10.1016/S0304-386X(01)00146-3

Milling Circuit Optimization Study For Ehya Sepahan No. 2 Iron Concentrator

Reza Zolfaghari[1]*, Iman Ameri 2[2], Mohammad Reza Javadian3[2], Daryoush Pakgohar 4[2], Seyyed Mehdi Hashemi 5[2].

[1,2] Ehya Sepahan Iron Mine Company 1

*Corresponding author: Reza_zolfaqari@yahoo.com (Reza Zolfaghari)

Abstract:

A comprehensive sampling campaign was carried out to minimize particle size, enhance product fineness to meet mill requirements, and evaluate capacity expansion opportunities. To ensure process continuity during 2nd ballmill maintenance activities, such as liner, gearbox, and pinion replacements, a bypass route for 2nd ballmill was introduced. This innovation stabilized the process, preventing declines in both concentrate quality (Fe=67%) and production rates.

The project also focused on optimizing the circulating load, establishing the mass balance for breaking the largest feed particles, and calculating the energy needed to gain the target comminution size (P80=100 Micron). Trommel performance and operational conditions were thoroughly analyzed, leading to optimized circulating load and changing liner/lifter size for enhanced efficiency.

These measures ensured uninterrupted concentrate production during repairs while maintaining product output and quality. Additionally, modifications in the milling circuit improved charge behavior without compromising mill capacity.

The average availability of the production line was 78%, highlighting challenges in production stability due to equipment aging and maintenance demands. However, in 2024, the implementation of key process improvements—specifically optimizing the 2nd mill bypass and upgrading mechanical systems—resulted in a significant increase in availability, reaching 84%.

The introduction of the bypass route and milling circuit optimization increased the circulating load from 80% to 110%, unlocking the potential for simultaneous production growth. Consequently, annual concentrate production rose by over 30,000 tons. Furthermore, grinding circuit optimization boosted throughput from 60 tons per hour to 90 tons per hour, with final product quality consistently maintained.

Keywords: *Milling, optimization, bypass route**, **circulating load, mass balance.*

1. Introduction

Despite its well-documented inefficiency, the ballmill remains the most widely used milling equipment. However, its versatility allows it to be adjusted to achieve various outcomes. For any designer, the goal is to optimize returns while working within given constraints. This doesn't guarantee that the optimal answer will always be achieved, nor does it ensure that today's best answer will remain ideal in the future, as factors such as ballmill feed or outcome specifications may change over time (Chimwani et al., 2020)

Liners and lifters significantly influence the load trajectory and, consequently, the mill's breakage efficiency (Toor et al., 2013). Their size, form, and amount play a crucial role in determining the tumbling motion of the mill's contents (King, 2001). Additionally, the way they transfer energy to the comminution media directly affects the breakage rate due to the mechanical interaction between the liners and the load (Makokha et al., 2006). Considerable research has focused on optimizing liner profiles, with various operational configurations offer to enhance ballmill efficiency (Rezaeizadeh et

al., 2010). the holistic approach to mill liner management, incorporating wear monitoring, operational efficiency, and cost optimization to enhance mill performance, extend liner life, and improve maintenance strategies (Powell et al., 2012)

In this paper, Due to design and manufacturing process improvements, we have been able to simultaneously maintain concentrate production and significantly increase the plant's production capacity despite increased access to the Phase 2 iron concentrate plant line. Improvements such as changing the 2nd mill Bypass and optimizing the liner of the 1st ballmills have allowed the plant to continue production without interruption during times when some equipment was out of service for repairs or overhauls.

This study integrates these techniques to develop an initial practical tool aimed at aiding milling circuit optimization and selection, considering both liner lifespan and mill performance.

2.   Material and methods

EHYA, a mine company in Khorasan Razavi that is involved in research has lately been exploring a milling circuit optimization that can elevate ball comminution.

The Phase 2 iron concentrate plant, operated by EHYA Iron, materials are poured from under the stockpile and through feeders onto conveyor belts that direct the materials to the inlet chute of the 1st ballmill. The first crushing stage is carried out in the ballmill, where particles are crushed from 7 mm to 0.5 mm in size. The output of the 1st ballmill enters the magnetic separation stage, which includes two parallel medium-intensity magnetic separators (Cubber). The concentrate from the Cubber magnetic separator enters the classification circuit (two clusters of 6 hydrocyclone) and is classified into two size ranges. The coarse-grained portion is returned to the 2nd ballmill as circulating load, and the fine-grained portion enters the two-stage magnetic separation stage. The flowsheet is shown in Figure 1.
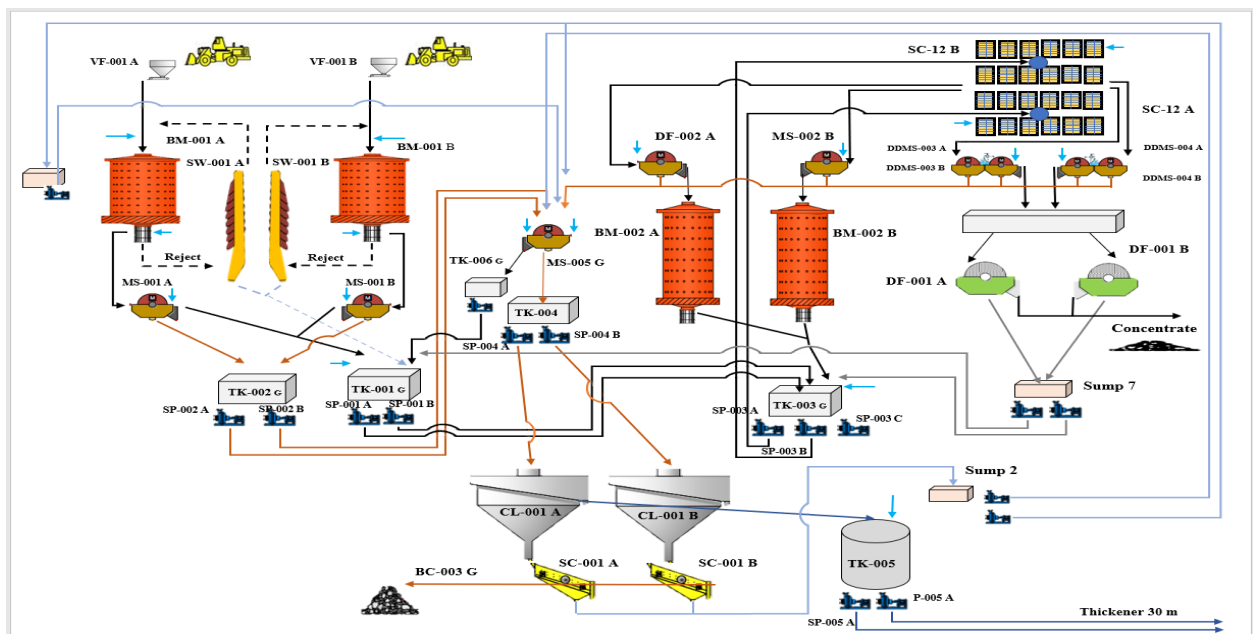

Figure 1 - General diagram of the processing circuit of the Phase 2 iron concentrate plant

The concentrator team conducted a sampling campaign in late June 2024, by which time the mill circuit load had been reverted to 65% of the critical level. Another sampling campaign took place from late May to early June 2024. Although the ballmill continued operating iron, its output was lower compared to when the circuit load was at 79%.

The main milling circuit plan for the Phase 2 iron concentrate plant was based on the following:

➤ 1st milling outflow of 27% passing 75 μm

➤ 2nd milling outflow of 60–65% passing 75 μm.

the Phase 2 iron concentrate plant consists of two 1st ballmills, which operate simultaneously and 2nd ballmills. The main and 2nd ballmills are lined with steel liners. Figure 1 shows the milling circuit, Along with the measurement locations during the Phase 2 iron concentrate plant sampling campaign indicated.

Initially, after a detailed review of the current situation and process requirements by the engineering team, a preliminary diversion route fellowship was prepared (Figure 1-b). The principal goal of this design was to create another system that would allow the feed flow to be directed smoothly and without disruption to the 1st production ballmill during shutdown or overhaul of the 2nd ballmills. This plan was designed using modern equipment and technologies and in accordance with industrial safety and efficiency standards, so that in the event of any breakdown or repair operations of the 2nd ballmills, the production process would continue without interruption.

Table 1: the Phase 2 iron concentrate plant

Ballmill Description	1st ballmill	2nd ballmill
diameter (*mm*)	2400	2400
length (*mm*)	4500	7000
filling (% of mill volume)	30	33
critical speed (%)	79.25	81.2
power available (*kW*)	475	570
Top size of the ball (*mm*)	80	40
Discharge type	diaphragm	overflow
Top size of the feed (*mm*)	7800	450

To find out the status of the solid percentage of important circuit flows, solid percentage monitoring was carried out. The solid percentage monitoring of all lines was carried out for 6 consecutive days. The monitoring was carried out through the local method (scale and 1 liter container). To calculate the solid percentage using the local method, there are preset formulas or tables. Since the density of various flows was not available in the tables, it was obtained through calculations. The equipment required to measure the solid percentage on site is a scale along with a 1-liter container (Figure 2).

Figure 2 - Manual measurement of pulp solids percentage in situ.

The operating parameters and performance of the milling circuit were evaluated to identify necessary plan or working modifications for achieving the desired improvements. Simulations were performed to analyze load behavior and the trajectory of balls and charge within the mill, utilizing LSD's MillTraj software. MillTraj employs trajectory plans to follow the outermost ball path for choosed ball sizes that interact with the lifterbar and shellplate (Royston, 2001). Additionally, the software forecasts the probable situation of the charge toe and estimates the shellplate expanse to subjected lifterbar height ratio, known as the S/H ratio. The effects of various S/H ratio spans on throughput and specific energy, as documented by Brough and Moller (1989), are presented in Figure 3.
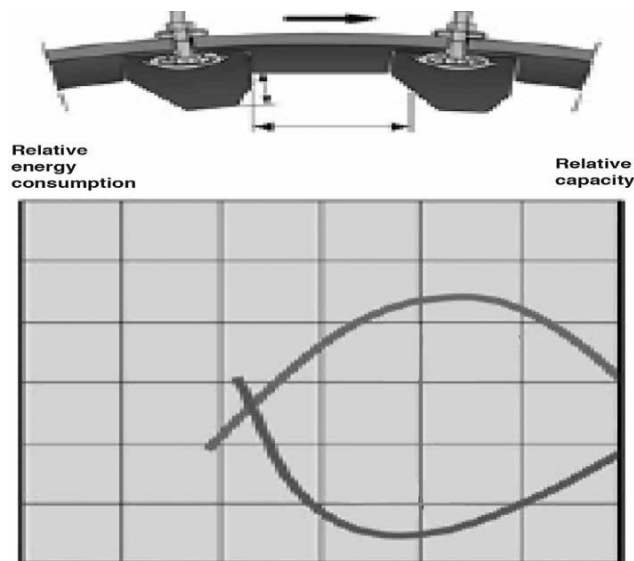

Figure 3—General ratio of shellplate wideness to the exposed lifterbar height ($S/H\ ratio$) (Brough and Moller, 1989; Powell et al., 2006).

Figure 4 illustrates the lifters currently seated in both the 1st and 2nd mills. The lifterbars are 218 mm in width, with heights of 165 mm for the 1st mill and 170 mm for the 2nd mill. The 1st mill has a lifter height-to-angle ($H2A$, defined as the distance from the base of the lifter to the front face angle) of 82 mm, whereas the 2nd mill's $H2A$ is 88 mm.
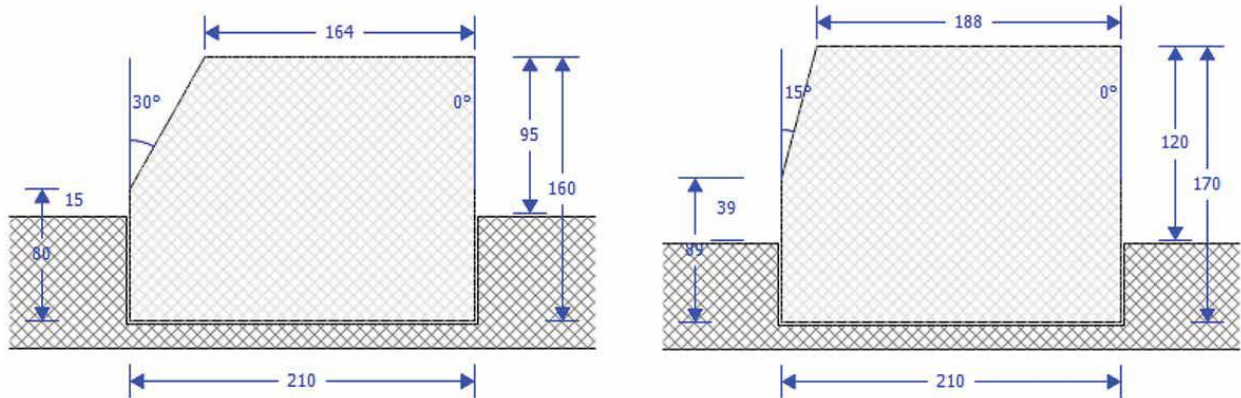
Figure 4—Present lifterbar forms for 1st ballmill (left) and 2nd ballmill (right) declined into the shellplate.

As mentioned in the introduction, the gearbox was replaced twice: first to grow the 1st ballmill speed from 67% to 77% of critical speed, and then to return it to 67% of critical speed. Consequently, the parsing of the present lifterbars considered both speed settings.

From Figure 4, it is evident that the S/H ratio of the liners, at 1.97, was significantly less than the recommended plan ratio of approximately 2.6, which is the minimum required to balance ballmill efficiency and liner lifespan. This discrepancy called for a replan of the liners to reduce the effect on comminution efficiency.
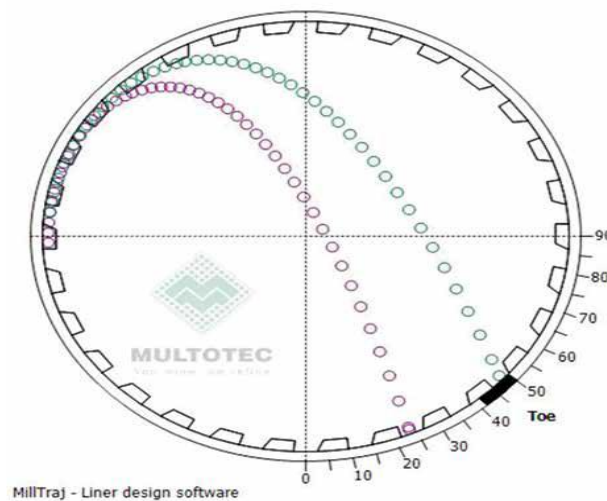

Figure 5−The simulation of the MillTraj of the outermost ball layer in the 1st ballmill at ballmill critical speeds of 67% (purple) and 77% (green).

The imagery (Figure 5 and 6) indicated that growing the ballmill speed from 67% to 77% of critical caused the outermost balls to shift external toward the toe situation of the charge. According to Royston (2007), growing ballmill speed can enhance both ball effects at the toe and charge turnover, leading to improved mill efficiency by growing ball-charge interaction. However, when ballmill speeds exceed 77-79% of critical, lifterbar performance may decrease, potentially impacting ballmill efficiency.
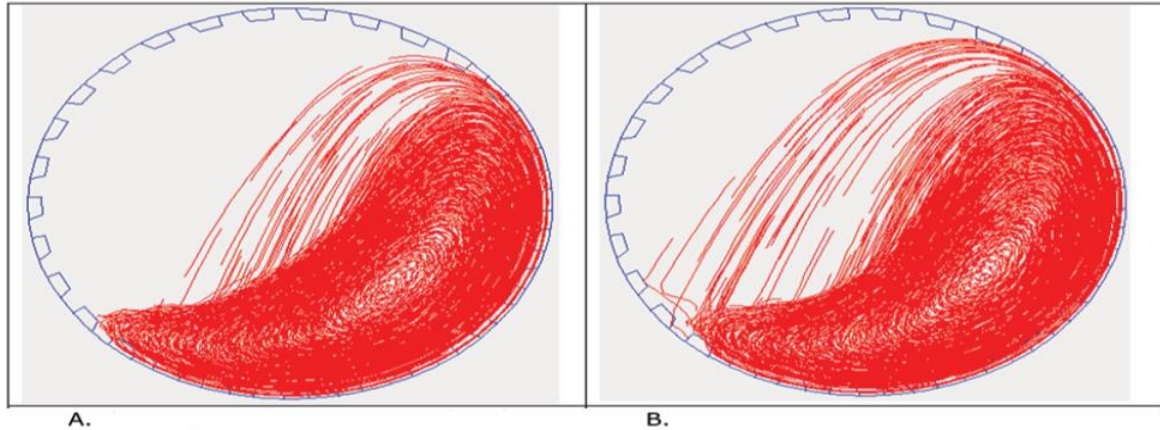
A: 1st mill load behavior at 68% of critical speed   B: 1st mill load behavior at 78% of critical speed

Figure 6−$PFC - DEM$ imagery of the installed 1st ballmill lifterbars

Although growing mill speeds beyond 77-79% of critical speed may reduce lifterbar performance and negatively impact on overall ballmill efficiency, ball effect on the toe situation is crucial for effective size scale down. However, when balls fall on the shell above the toe situation, they can cause failure to both the shellplate and the balls. Typically, growing the ballmill speed would be expected to enhance impact breakage for material in the size span closer to the -35 mm top size of the feed.

To estimate the theoretic make-up size of the ball and the energy needed to gain the aim grind, the ore hardness, plant stream flow rates, and size distribution of the particle (*PSD*) were characterized. Bond Ball Work Index (*BBWI*) experiments were performed on the *DMS* sample of the feed and 1st ballmill conveyor belt cuts to assess ore hardness. The *BBWI* values for the *DMS* feed and 1st ballmill conveyor belt cut samples were 17.14 kWh/t and 13.4 kWh/t, respectively. The stream flow rates and *PSDs* were determined using data from the sampling campaign and historical plant records. Samples were collected from the locations shown in Figure 7.
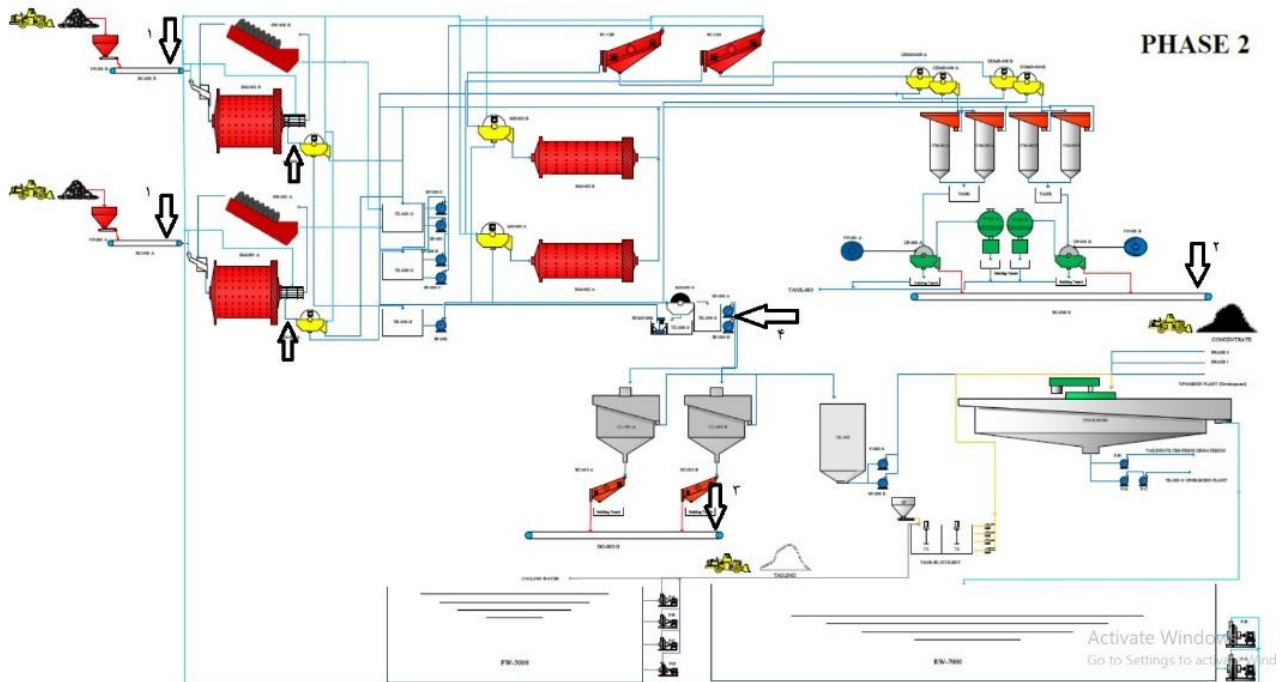

Figure 7−flowsheet of the ballmilling flow, stating sample points (specified arrow).
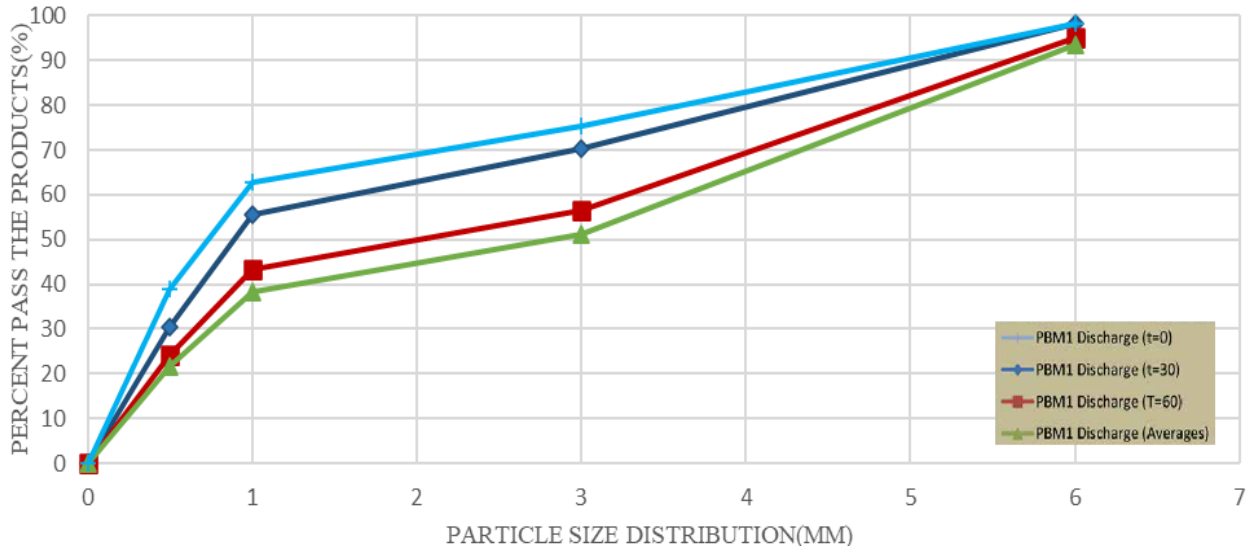
Figure 8—1st ballmill no. 1 discharge distribution of the particle size.

Figure 8 illustrates the difference in PSD for four sets of samples taken from the discharge of 1st ballmill. A basic mean of the sample sections gathered at $t = 0$, $t = 30$, and $t = 60$ minutes was used to show the flow PSD . The flow PSD_s for 1st ballmill no. 1 are presented in Figure 6. From these stream PSD_s, the F_{80} and P_{80} values were derived and used to express the mill feed and outcome PSD .
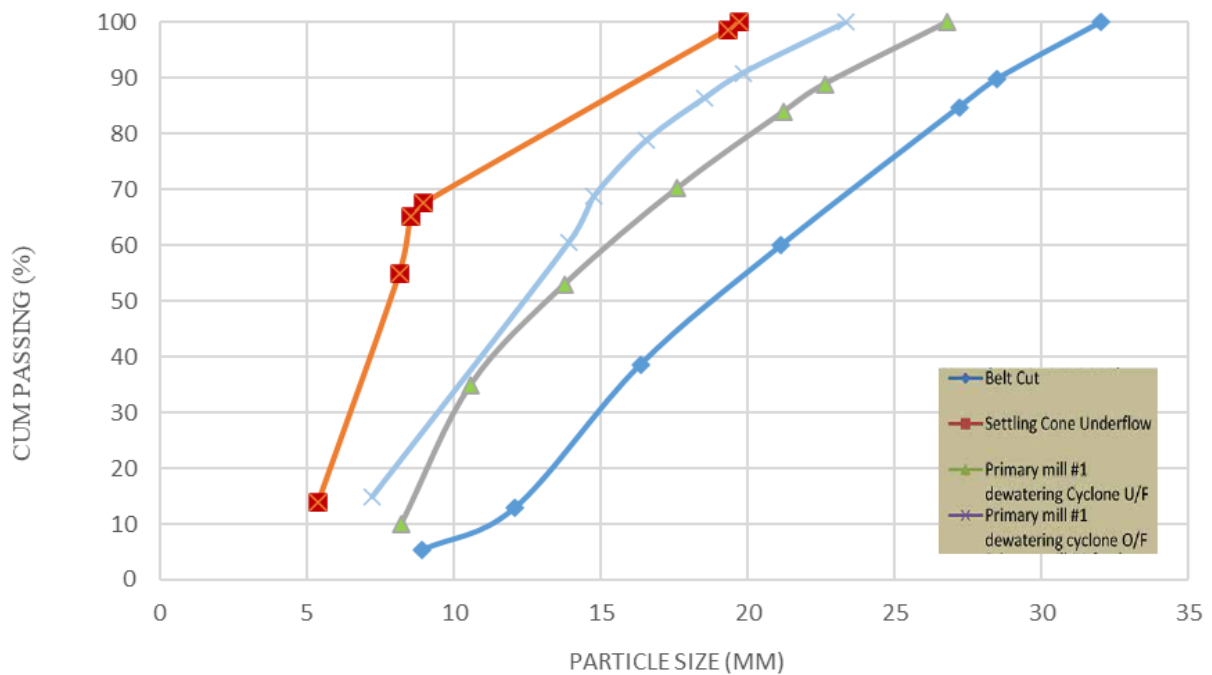

Figure 9—1st ballmill averaged of the stream distributions of the particle size.

The sizes of the make-up balls were determined using the ball size formula developed by Bond. (1957) (Equation [1]), and the outcomes are presented in Table 2. The ball sizes selected were determined to satisfy or surpass the required specifications, suggesting they were not responsible for the generation of scats.

Table 2: Current lifter profile and lifter profile options presented to the KP1 for consideration

Profile	Width (mm)	Height (mm)	Angle of face (")	Effective H2A (mm)	Critical speed (%)	Shellplate thickness (mm)
Current	212	162	25	15	80	75
Option 1	212	160	20	25	72	75
Option 2	165	160	20	25	72	75
Option 3	210	160	35	25	72	75

$$B = \left[\left(\sqrt{\frac{F_{80}}{K}} * \sqrt[3]{\frac{SG*W_i}{N\sqrt{3,281*D_i}}}\right)\right] * 25,4 \tag{1}$$

where B is the optimum top-up ball size (mm), F_{80} is the new feed 80% passing size (μm), SG is specific gravity of the ore being milled, N is the percentage of critical speed, W_i is work index of the feed material, D_i is ballmill diameter inside liners (m), and K is a constant with a value of 350.

Energy estimation was aimed at distinguishing the energy demand for the current ballmill feed and outcome size, and this was connected to the mill power available. To establish the energy demanded, the population balance model (PBM) using the sampling campaign PSD as well as $BBWI$ test results were used. The specific selection function (Fuerstaneu and Herbst, 1973) that incorporate the specific energy (P/m_p) was used, *i.e.*:

$$S_i = S_i^E \left(\frac{p}{m_p}\right) \tag{2}$$

where S_i^E is the specific selection function, independent of ballmill working conditions, P is the industrial ballmill power drawn, and m_p is the industrial ballmill hold-up. S_i is the proportionality constant known as the specific rate of breakage per unit time.

Table 3: Top ball size demands for the ballmill feed sizes

Description	1st ballmill no. 1		1st ballmill no. 2		2nd ballmill
F_{80}, mm	7854		7451		245
Speed %	70	72	70	72	79
Ball size, mm	80	80	80	80	40

The wear plan can be utilized to test various liner sections in order to identify those that offer the longest wear life. The challenge with this method is that a new *DEM* imagery must be conducted each time the liner profile is altered enough to notably impact the distribution of impacts. This could need 3 to 4 simulations for each liner profile being tested.

3. Conclusions

The analysis of the current position and optimization process enabled the determination of a lifterbar profile that would achieve the desired load behavior for optimal grinding. A methodology for fitting and predicting liner wear evolvement in ballmill is introduced and tested using actual data from three measured liner section of a 4.5-meter diameter ballmill. The wear plan can predict the evolution of the liner profile over time using an initial section and a fitted wear constant, as long as the liner material and the ore type remain unchanged. However, it was found that the wear 'constant' is influenced by the liner's angle, which needs further research.

DEM simulations can calculate the impact energy spectra and collision rates of balls in a large industrial mill. Simplified models are then used to estimate breakage and wear rates. Combining predictions of liner profile evolution and grinding rate offers a powerful tool for advanced mill liner design, allowing for a balance between liner life and mill performance throughout the liner's lifespan during the design phase.

A comprehensive optimization campaign enhanced milling efficiency, stabilized production, and improved product quality. Implementing a 2nd ball mill bypass ensured process continuity during maintenance, preventing quality and production declines. Key improvements, including circulating load optimization and liner adjustments, increased efficiency without reducing capacity. These efforts raised production line availability from 78% to 84% in 2024. Milling circuit enhancements boosted the circulating load from 80% to 110%, increasing annual concentrate production by over 30,000 tons and throughput from 60 to 90 tons per hour while maintaining quality.

Acknowledgments

References

Show the cited publication in alphabetical order without numbers in the front. Show all the authors. Follow the examples:

For jorunal article:

Bond, F.C., 1958. Grinding ball size selection. Mining Eng., 10, pp.592-595.

Herbst, J.A. and Fuerstenau, D.W., 1973. Mathematical simulation of dry ball milling using specific power information. Trans. AIME, 254, p.343.

Austin, L.G., Klimpel, R.R. and Luckie, P.T., 1984. Process engineering of size reduction: ball milling. Society of Mining Engineers of the AIME.

Moller, T.K. and Brough, R., 1989. Optimizing the performance of a rubber-lined mill. Mining engineering, 41(8), pp.849-853.

Royston, D., 2001, September. Interpretation of charge throw and impact using multiple trajectory models. In Proceedings of the International Conference on Autogenous and Semi-autogenous Grinding Technology (SAG2001) (pp. 115-123).

Eriksson, K.G. and Schaeffer, L., 2006. Selection and design of mill liners. Advances in Comminution, 331.

Royston, D., 2007. Semi-autogenous grinding (SAG) mill liner design and development. Mining, Metallurgy & Exploration, 24(3), pp.121-132.

Powell, M.S., Hilden, M.M., Weerasekara, N., Yahyaei, M., Toor, P., Franke, J. and Bird, M., 2012, January. A more holistic view of mill liner management. In 11th AusIMM Mill Operators'

Chimwani, N. and Bwalya, M.M., 2020. Using DEM to investigate how shell liner can induce ball segregation in a ball mill. Minerals Engineering, 151, p.106311.

Simulation of a coal gasification unit with the aim of using the produced synthesis gas in the sponge iron production unit.

Mohsen Bahoosh, Eslam Kashi*

Department of Chemical Technologies, Iranian Research Organization for Science and Technology (IROST), P.O. Box 33535111, Tehran, Iran

*Corresponding author: Kashi@irost.ir (Eslam Kashi)

Abstract:

Due to the irregular availability of natural gas and its challenges in maintaining a sustainable supply, coal has been proposed as an alternative source for the production of synthesis gas in steel plants. In this research, a simulation of a coal gasification unit aimed at producing synthesis gas was performed. Initially, the simulation was carried out using available data from a reference study, and its results were compared with actual data. After confirming the accuracy of the simulation model, Tabas coal data were introduced as the feedstock, and the gasification process was simulated using an entrained-flow gasifier in Aspen Plus software.

A sensitivity analysis was conducted on the type of coal as well as on the water-to-coal and oxygen-to-coal ratios to identify the key factors affecting the process. The results showed that both the type of coal used and the ratios of water and oxygen to coal are critical factors in the gasification process, influencing the quality and quantity of the produced synthesis gas. This research can serve as a valuable guide for improving the efficiency and productivity of coal gasification units in the steel industry. By offering practical suggestions regarding the selection of coal type and the adjustment of water and oxygen to coal ratios, the optimization of the gasification process becomes achievable. Overall, the findings of this study indicate that using coal as a source for synthesis gas production has great potential in meeting energy demands and enhancing productivity in the steel industry.

Keywords: Coal gasification, Tabas coal, Steel, simulation, Aspen Plus

1. Introduction

The iron and steel industry, which plays a crucial role in stabilizing growth and employment, is vital for the development of a country's national economy. Moreover, the steel industry is one of the most energy-intensive sectors, accounting for the largest share of energy consumption among industrial sectors.

In order to reduce CO_2 emissions and address the high energy consumption in the steel industry, Direct Reduction Iron (DRI) technology has been developed and has rapidly advanced. DRI is a process that converts iron ore into sponge iron at temperatures below the melting point. This method offers several advantages such as lower pollution, reduced energy consumption, and immunity to the limitations caused by a shortage of coking coal compared to the traditional rotary kiln method for iron production. Furthermore, the sponge iron produced via the DRI process is characterized by low levels of impurities like sulfur, phosphorus, silicon, and other harmful contaminants, making it an essential raw material for manufacturing high-grade steel. Various methods exist for producing sponge iron by direct reduction. For example, in India — one of the world's largest producers of DRI sponge iron — two primary DRI production methods are employed: one uses small-scale rotary kilns that rely on coal and iron ore, while the other utilizes large-scale shaft furnaces that operate with natural gas and iron oxide

pellets. Since the capacity of rotary kilns is limited and cannot fully meet the requirements of steel plants, the use of natural gas has become more common. However, when natural gas availability also becomes constrained, coal gasification emerges as a suitable alternative. Coal gasification itself encompasses various types—such as fixed-bed, fluidized-bed, and others—and all these processes rely on the partial oxidation of carbon-containing feedstocks (*Gasifipedia*, n.d.; Hasanbeigi et al., 2013).

Subsequent studies on the simulation of the coal gasification process have examined the units used to define the gasifier, the parameters influencing the process, and the expected results.

Nayak et al. (Nayak & Mewada, 2011) used Aspen Plus to simulate coal gasification in a fluidized bed, integrating pyrolysis, combustion, and steam gasification. They found that increasing the steam-to-coal ratio lowered CO and CH_4 while raising H_2 and CO_2, highlighting the importance of operating conditions in gasification.

Liu et al. (Liu et al., 2012) developed a simulation model for a pressurized fluidized bed gasifier with an ash agglomerator using a sequential modular method with recycle loops. Their model, which incorporated both hydrodynamic and kinetic parameters computed via the PR–BM equation, matched experimental data well and demonstrated that optimizing oxygen-to-coal and steam-to-coal ratios can control the H_2/CO ratio.

Hu et al. (Hou & Zhang, 2017) optimized the effective syngas fraction (H_2 + CO) in an entrained-flow gasifier using the Taguchi method, RSM, and the Nelder–Mead algorithm. Their study showed that the oxygen-to-coal ratio is key to maintaining stable syngas composition, with pressure also playing a regulatory role.

Rudra Paol et al. (Rudra Paul et al., 2019) simulated gasification of high-ash Indian coal in a fluidized bed, varying the steam-to-coal ratio and temperature while keeping the feed rate and air-to-coal ratio constant. Their results demonstrated that hydrogen production increases with steam-to-coal ratio up to a certain temperature, whereas CO, CH_4, and CO_2 respond differently to changes in temperature and steam-to-coal ratio, affecting overall carbon conversion.

Dang et al. (Dong et al., 2020) simulated Shenmu coal gasification by dividing the process into pyrolysis and gasification stages. Their model, which included preheating, mixing, heat exchange, separation, and cooling (with both direct and indirect heat transfer), showed that higher water-to-coal ratios at lower temperatures boost hydrogen production and reduce CO and CO_2, with a novel quench loop improving water recycling and process stability.

Zhang et al. (Zhang et al., 2024) created a five-unit thermodynamic equilibrium model for SNG production from coal gasification in Aspen Plus (V10), considering both dry and slurry feed as well as bituminous and lignite coals. Sensitivity analysis revealed that the $O_2/coal$ ratio is critical—an optimal value of 6/0 yields high-quality SNG—while CO_2 flow and water-to-coal ratios also significantly influence the higher heating value and overall gas quality.

Notably, all these studies employ several reactors and separators to define the gasifier. This is due to the absence of a dedicated gasifier process unit in the Aspen software. Consequently, in simulating the unit, various processes occurring throughout the gasifier (such as dehydration, pyrolysis, gasification, separation of volatile materials, etc.—as shown in Fig. 1) have been simulated using different equipment.
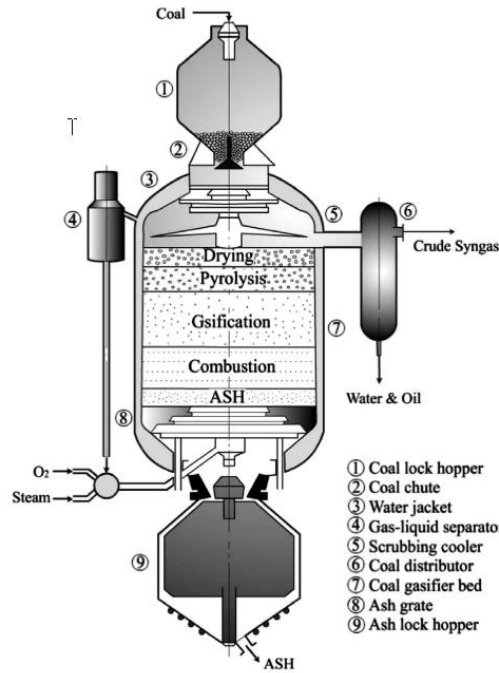
Fig. 1. Schematic of the Lurgi gasifier along with the various processes within the gasifier (He et al., 2013)

In this study, for the first time, all the operational units required for converting coal into synthesis gas for a steel plant have been simulated by using Aspen Plus V14. Moreover, unlike previous research, the rapid quenching process in the gasifier has been fully modeled to allow for a more precise calculation of the process water amount.

2. Material and methods

2.1. Base simulation

In this section, the initial simulation was performed as a reference and compared with experimental data and other models to verify the simulation method and input data. The simulation describes a Gibbs free energy-based model for Texaco entrained-flow gasifiers and follows the modeling approach proposed by Wen and Chang (Wen, 1968; Wen & Chaung, 1979). Key features of the model include:

- Steady-State Operation: The model is carried out under steady-state conditions.
- Comprehensive Process Representation: It captures the main physical and chemical processes within the gasifier, including coal pyrolysis, volatile combustion, and coke gasification.
- Instantaneous Mixing: It is assumed that the gaseous phase is instantly and completely mixed with the solid phase.
- Negligible Pressure Drop: The pressure drop in the gasifier is disregarded.

2.1.1. Material Specifications

During the gasification process, various materials and compounds are produced. This section presents their corresponding chemical components (Table 1).

Table 1. Chemical Components Used in the Model(Wen, 1968; Wen & Chaung, 1979)

ID	Type	Name	Formula
O_2	CONV	OXYGEN	O_2
CO	CONV	CARBON-MONOXIDE	CO

H_2	CONV	HYDROGEN	H_2
CO_2	CONV	CARBON-DIOXIDE	CO_2
H_2O	CONV	WATER	H_2O
H_2S	CONV	HYDROGEN-SULFIDE	H_2S
N_2	CONV	NITROGEN	N_2
CH_4	CONV	METHANE	CH_4
C_6H_6*	CONV	BENZENE	C_6H_6
C	SOLID	CARBON-GRAPHITE	C
S	SOLID	SULFUR	S
COAL	NC	------	------
CHAR1*	NC	------	------
CHAR2*	NC	------	------
ASH	NC	------	------

2.1.2. Pilot Gasifier Process Description

The pilot gasifier, whose data is used to evaluate the simulation in this project, is briefly reviewed here. The Texaco gasifier is an entrained-flow design. This steel vessel—with a diameter of 5.1 meters and a length of 1.6 meters—is internally divided into two sections (Fig. 2). The upper section is lined with a special refractory material designed to withstand harsh operating conditions and is dedicated to coal gasification. In this process, powdered coal (with particle sizes smaller than 500 μm) is mixed with water to form a coal-water slurry, which, together with oxygen, is fed into the upper section. Here, coal pyrolysis, volatile combustion, and coke gasification occur to produce synthesis gas under operating pressures of 20–50 atmospheres and temperatures exceeding 1000°C (Wen, 1968; Wen & Chaung, 1979). The lower section serves as a cooling chamber. A water reservoir continuously supplies cooling water at the bottom, where ash and synthesis gas exit from the upper section. The ash remains in the water and is later removed, while the saturated synthesis gas is drawn from above the water. Although commercial petroleum-based gasifiers are designed to operate at pressures up to 80 atmospheres, the coal-based pilot unit is designed for a maximum pressure of 28 atmospheres (Robin, 1976).
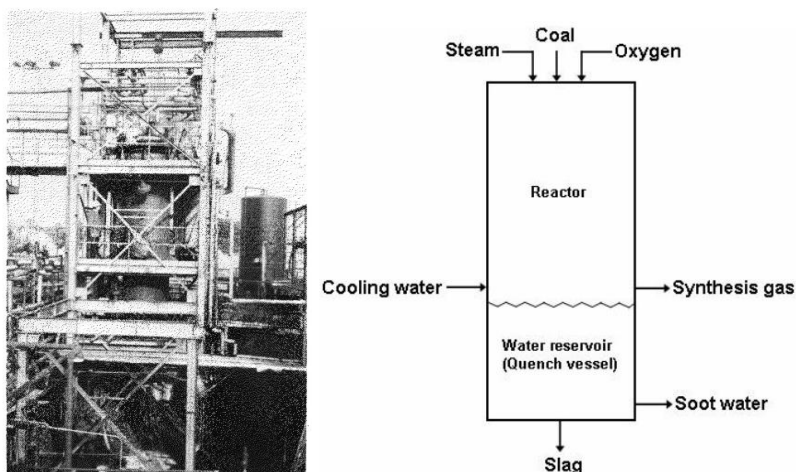

Fig. 2. Schematic of the Texaco Gasifier (Breault, 2010; Robin, 1976)

2.1.3. Physical Properties and Feed Specifications

n this project, the RK-SOAVE method is used to calculate the physical properties of conventional mixture components as well as CISOLID components. To evaluate the unconventional components, the HCOALGEN and DCOALIGT models are employed for determining enthalpy and density, respectively. The HCOALGEN model requires three key analyses for the unconventional components:

- Proximate Analysis (PROXANAL): Provides the weight fractions of moisture, fixed carbon, volatile matter, and ash.
- Ultimate Analysis (ULTANAL): Gives the weight percentages of ash, carbon, hydrogen, nitrogen, chlorine, sulfur, and oxygen.
- Sulfur Analysis (SULFANAL): Breaks down the sulfur content into pyritic, sulfate, and organic sulfur fractions.

Table 2 presents the characteristics of the coal component used in our base model, adopted from the modeling work of Wen and Chuang (Wen, 1968; Wen & Chaung, 1979). Based on these specifications, the coal's enthalpy and density are calculated. The same procedure is applied to the char and ash produced during coal conversion; their enthalpy and density are determined using the same models, with analysis results obtained from a mass balance based on the original coal analysis data and the amount of gasified product. Since Aspen Plus does not offer a dedicated graphical block for a gasifier, several reactors are used for the simulation. For example, when coal enters the gasifier, it first undergoes pyrolysis to convert into volatile products and char. The corresponding chemical reaction is shown in Equation (1):
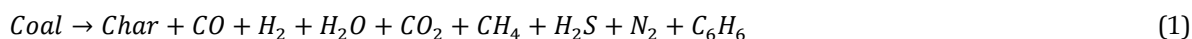
$$Coal \rightarrow Char + CO + H_2 + H_2O + CO_2 + CH_4 + H_2S + N_2 + C_6H_6 \tag{1}$$

Table 2. Feed Coal Specifications (Wen, 1968; Wen & Chaung, 1979)

Proximate analysis		Ultimate analysis		Sulfur analysis	
Element	Value (wt.%)	Element	Value (wt.%, dry basis)	Element	Value (wt.%, dry basis)
Moisture (wet basis)	0.2	C	74.05	Pyritic	0.59
Fixed carbon (dry basis)	58.01	H	6.25	Sulfate	0.59
Volatile matter (dry basis)	26.46	N	0.71	Organic	0.59
Ash (dry basis)	15.53	Cl	0.37		
		S	1.77		
		O	1.32		
		Ash	15.53		

In our model, the volatile components include CO, H_2, H_2O, CO_2, CH_4, H_2S, N_2, and C_6H_6. A separate reactor is designated for these reactions, and the yield of coal conversion into char and volatiles is presented in Table 3 based on laboratory results by Wen and Chuang. For a more precise outcome, Equation (2) can be employed and the conversion yield adjusted according to the reactor's operating pressure (24 atm) (Wen, 1968; Wen & Chaung, 1979).

Table 3. Coal Conversion Yield to Char and Volatiles at 1 atm (Wen, 1968; Wen & Chaung, 1979)

Components	Yield (mass basis on original coal)
CO	0.0059
H2	0.0084
CO2	0.003
H2O	0.0079
H2S	0.0094
N2	0.0035
CH4	0.1637
C6H6	0.071
Char	0.7272
Total	1

$$V_2 = V_1(1 - \alpha ln P_t)$$ (2)

$V1$ = total yield of volatiles at 1atm, $V2$ = total yield of volatiles at the pressure of the real gasifier.

Pt= pressure in real gasifier, atm., α = constant. In this model, α = 0.066.

2.1.4. Unit Flow Sheet

Fig. 3 presents the overall flow of the coal gasification process. In this model, the cooling section for the hot gas is not simulated. The function of each block is detailed in Table 4, while additional feed specifications are provided in Table 5. Blocks B1 and B2 are used for simulating coal pyrolysis, Block B3 models the volatile combustion process, and Block B7 is dedicated to coke gasification. The remaining blocks assist in simulating these three main processes. As shown in Table 5, the coal is preheated to a temperature range of 100–300°C, which facilitates easier transfer and improves gasification efficiency (Wen, 1968; Wen & Chaung, 1979).
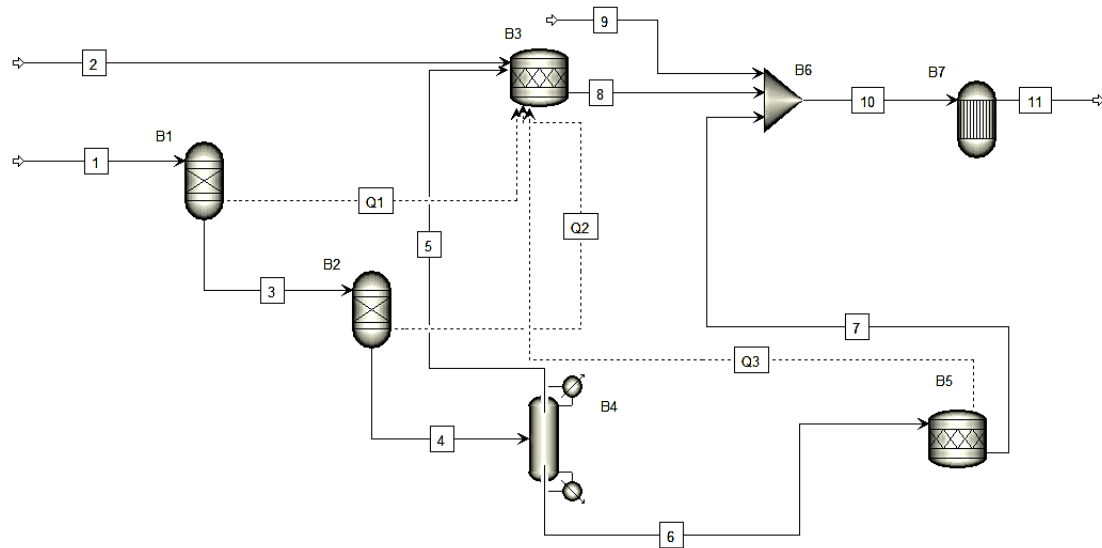

Fig. 3. Base Simulation Flow Sheet

Table 4. Explanation of the Base Simulation Blocks

Block	Model	Function
B1	RYield	Simulation of coal pyrolysis based on pyrolysis test results at 1 atm pressure.
B2	RYield	Adjustment of each product's yield from the pyrolysis test pressure (i.e., 1 atm) to the actual gasifier pressure.
B3	RStoic	Stoichiometric modeling of volatile gas combustion.
B4	Sep2	Separation of gases and char.
B5	RStoic	Conversion of char into C, H_2, O_2, N_2, S, and ash.
B6	Mixer	Mixing of the feed and steam.
B7	RGibs	Gasification of the feed mixture.

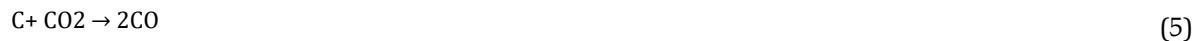Table 5. Specifications of Feed Streams in the Base Simulation

Feedstock	Stream ID	Parameter	Value	Unit
Coal	1	Flow rate	76.66	g/s
		Temperature	505.22	K
		Pressure	24	atm

		Diameter of particle	350	μm
		Velocity entering into gasifier	3	m/s
Oxygen	2	Ratio of oxygen to coal flow rates	0.866	dimensionless
		Temperature	298	K
		Pressure	24	atm
Steam	9	Ratio of steam to coal flow rates	0.241	dimensionless
		Temperature	696.67	K
		Pressure	24	atm

2.1.5. Examination of the Base Simulation Results

Based on the input conditions provided in the previous section, the gasifier output results were obtained and are presented in Table 6 as the Aspen Plus model. For comparison, the results from Wen and Chaung's work are also shown in the table. It is evident that Wen and Chaung's results more closely match the experimental data. In our base simulation, the CO flow rate and carbon conversion are slightly higher than the experimental values, while the CO_2 flow rate is somewhat lower.

The discrepancies in the CO and CO_2 flow rates and carbon conversion may stem from several factors: the use of Gibbs free energy instead of stoichiometric relations, the lack of direct consideration of reactor dimensions and residence time, and the higher gasifier outlet temperature calculated by our base model. In our model, the outlet temperature is 1766 K compared to around 1422 K in the Wen and Chaung model. The higher temperature accelerates the reactions between solid carbon and gases (i.e., reactions (3)–(6)), resulting in a higher carbon conversion than observed experimentally. Additionally, differences in the CO and CO_2 flow rates are linked to reaction (7), an exothermic reaction. A temperature increase causes this reaction to shift in the reverse direction—leading to a higher production of CO and a lower production of CO_2. Consequently, the elevated temperature reduces the simulated CO_2 flow rate while increasing the simulated CO flow rate.

$$C + \frac{1}{\varphi}O2 \rightarrow 2\left(1 - \frac{1}{\varphi}\right)CO + (\frac{2}{\varphi} - 1)\,CO2 \tag{3}$$

$$C + H2O \rightarrow CO + H2 \tag{4}$$

$$C + CO2 \rightarrow 2CO \tag{5}$$

$$C + 2H2 \rightarrow CH4 \tag{6}$$

$$CO + H2O \rightarrow CO2 + H2 \tag{7}$$

φ is a coefficient that depends on the diameter of the coal particles. There are two reasons why the base simulation produces a higher gasifier temperature. The first reason is the coal combustion heat (HCOMB). In the base model, the HCOMB of the coal is calculated using the Boie correlation in Aspen Plus due to the lack of precise experimental data. However, HCOMB has a significant impact on the coal's enthalpy; an inaccurate value for HCOMB may lead to an incorrect coal enthalpy, and consequently, a substantial deviation in the gasifier temperature. The second reason is the amount of heat loss in the gasifier. In the base simulation, the model is simulated under adiabatic conditions, whereas in Wen and Chaung's model, heat loss to the environment is considered. Therefore, the combination of these two factors may result in a higher gasifier temperature in the base model.

To further investigate the above explanation— which leads to differences in the CO and CO_2 flow rates and carbon conversion due to the higher temperature in the base model— in case b, HCOMB for the coal is manually entered so that the gasifier outlet temperature from the base simulation matches that of Wen and Chaung's work.

Table 6. Comparison of Base Simulation Results, Experimental Data, and Wen & Chang's Model [9,10]

Parameters	Experimental		Wen and Chaung's model		Aspen Plus model a		Aspen Plus model b	
	Flow rate (g/s)	Mole fraction (%, dry basis)	Flow rate (g/s)	Mole fraction (%, dry basis)	Flow rate (g/s)	Mole fraction (%, dry basis)	Flow rate (g/s)	Mole fraction (%, dry basis)
CO	123.77	57.57	123.94	56.60	127.7	58.69	124.57	57.55
H_2	6.01	39.13	6.23	39.84	6.02	38.48	5.94	38.16
CO_2	9.985	2.95	10.04	2.92	6.92	2.02	10.16	2.98
CH_4	0.15	0.12	0.20	0.16	0.013	0.010	0.62	0.499
H_2S	0.133	0.06	0.726	0.27	1.44	0.54	1.44	0.54
N_2	0.53	0.12	0.454	0.208	0.54	0.25	0.54	0.25
Carbon conv. (%)	98.64		98.88		100		100	
Temp. (K)	------		1421.9		1766.25		1416.47	

**In model a, the coal combustion heat (HCOMB) is calculated using the Boie correlation; whereas in model b, the coal HCOMB is manually set to 13,416 Btu/lb.

When the coal combustion heat (HCOMB) is manually set to 13,416 Btu/lb (compared to the coal HCOMB calculated as 83/14080 Btu/lb using the Boie correlation), the gasifier outlet temperature becomes 1416 K, which is in good agreement with the 1422 K reported in Wen and Chaung's work. Under these conditions, the flow rates of CO and CO_2 also closely match the experimental data. These observations indicate that the product gas composition and carbon conversion are highly dependent on the gasifier temperature, and that both the coal HCOMB and heat loss are key parameters in determining the gasifier temperature.

2.2. Simulation of the Gasification Unit

In this section, based on the model derived from the base simulation and incorporating information from other studies, first, some existing issues are examined before the simulation of the gasification unit is carried out.

2.2.1. Feed Specifications for Tabas Coal

Comparison of the analysis results presented in various studies ((Toloue Farrokh et al., 2017) (Rajabzadeh et al., 2016) (Raygan et al., 2010))shows that coal analysis can vary depending on the location, stratum, and sampling conditions. For instance, the moisture content reported in the study by Talakoub and Rajabzadeh is about 1%, whereas in the report by Rāyegān and Eskandari it is 9%. Considering the more comprehensive report by Rajabzadeh et al. (Rajabzadeh et al., 2016) an adjusted average of the data from this report has been used as the reference analysis for the simulation, as shown in Table 7.

Table 7. Proximate and Ultimate Analysis of Tabas Anthracite Coal According to Rajabzadeh et al. [18]

Proximate analysis (% by wt)				Ultimate analysis (% by wt)					Forms of sulfur		
FC (d)	M (ad)	V (daf)	A (d)	O (daf)	H (daf)	N (daf)	C (daf)	St (d)	Sp (d)	Ss (d)	So (d)
54.075	0.8	22.475	23.45	6.34	15.8	7.38	64.64	5.84	4.46	0.17	1.21

** FC, fixed carbon, M, moisture; VM, volatile matter; Ash, ash yield; O, Oxygen H, hydrogen; N, nitrogen; C, carbon; St, total sulfur; Sp, pyritic sulfur; Ss, sulfatic sulfur; So, organic sulfur; ad, air-dry basis; d, dry basis; daf, dry and ash-free basis.

The specifications of Tabas coal, which serve as the input data for the software, are ultimately presented in Table 8.

Table 8. The specifications of Tabas coal, which serve as the input data for the software

Proximate analysis		Ultimate analysis		Sulfur analysis	
Element	Value (wt.%)	Element	Value (wt.%, dry basis)	Element	Value (wt.%, dry basis)
Moisture	0.8	ASH	23.45	Pyritic	3.41
Fixed carbon (dry basis)	54.075	CARBON	49.48	Sulfate	0.14
Volatile matter (dry basis)	22.475	HYDROGEN	12.1	Organic	0.92
Ash (dry basis)	23.45	NITROGEN	5.65		
		CHLORINE	0		
		SULFUR	4.47		
		OXYGEN	4.85		

2.2.2. Block Diagram

The block diagram of the target unit is shown in Fig. 4 (Lacson et al., 2015). In this process, the processed coal is first combined in the gasifier with the required oxygen obtained from the air separation unit. The synthesis gas produced at this stage is impure and must be purified—and, if necessary, its temperature, pressure, and H_2/CO ratio adjusted—before entering the sponge iron production unit.
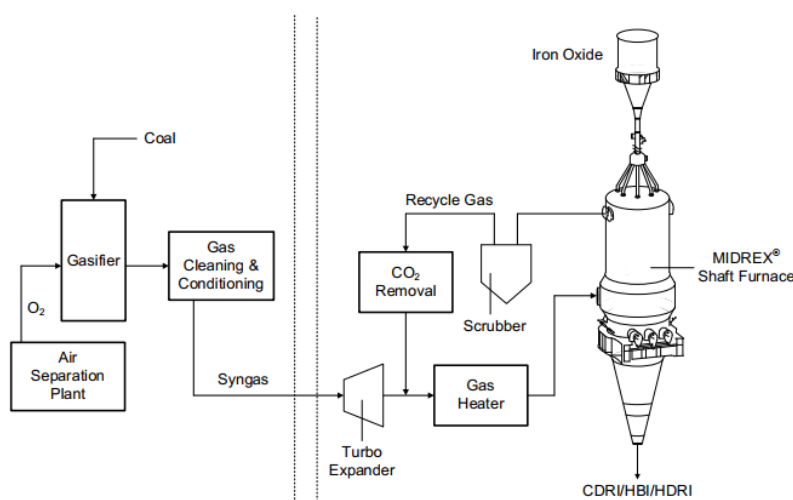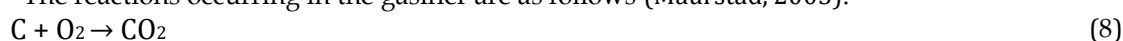

Fig. 4. Flow Sheet of the Combined Gasification Unit and Sponge Iron Production Unit According to the Processes of Lurgi and Midrex (Lacson et al., 2015)

2.2.3. Simulation Assumptions

In the simulation, the following assumptions have been applied:

- This process is carried out under steady-state conditions.
- Ash is considered an inert material with no catalytic activity and does not participate in the gasification process.
- Heat and pressure losses are neglected.
- All reactions are assumed to reach equilibrium, and reaction kinetics are not taken into account.

- Drying and pyrolysis occur simultaneously, with the volatile products consisting of H_2, CO, CO_2, CH_4, and H_2O.
- The operating conditions are based on an Entrained Flow gasifier (with a pressure range of 20 to 50 atmospheres and temperatures above 1000°C).
- In this model, the RK-SOAVE method is used to calculate the physical properties of conventional components and CISOLID components. The HCOALGEN and DCOALIGT models are used, respectively, to calculate the enthalpy and density of the unconventional components.
- Since Aspen Plus does not provide a dedicated graphical block for a gasifier unit, several different reactors are used to simulate the gasifier.
- The air separation unit and feed preparation unit are not simulated; in this modeling, oxygen and coal are directly fed into the gasifier.
- The reactions occurring in the gasifier are as follows (Maurstad, 2005):

$$C + O_2 \rightarrow CO_2 \tag{8}$$

$$C + \tfrac{1}{2} O_2 \rightarrow CO \tag{9}$$

$$H_2 + \tfrac{1}{2} O_2 \rightarrow H_2O \tag{10}$$

$$C + H_2O \rightarrow CO + H_2 \tag{11}$$

$$C + 2H_2O \rightarrow CO_2 + 2 H_2 \tag{12}$$

$$C + CO_2 \rightarrow 2CO \tag{13}$$

$$C + 2H_2 \rightarrow CH_4 \tag{14}$$

$$CO + H_2O \rightarrow CO_2 + H_2 \tag{15}$$

$$CO + 3H_2 \rightarrow CH_4 + H_2O \tag{16}$$

$$C + H_2O \rightarrow \tfrac{1}{2} CH_4 + \tfrac{1}{2} CO_2 \tag{17}$$

- Most of the oxygen injected into the gasifier is consumed in reactions (8) to (10) to supply the required heat for drying the fuel, breaking chemical bonds, and raising the reactor temperature to achieve the gasification reactions (reactions (11) to (17)).
- An oxygen-to-coal ratio of 0.8 and a steam-to-coal ratio of 0.3 have been considered (Gungor et al., 2011; Mrakin et al., 2020).
- The total coal feed is calculated based on PFD of the Ghaenat Steel Complex South Khorasan and is designed for an inlet synthesis gas flow rate of approximately 174.6 m³/hr to the DRI furnace for the production of 110 tons per hour of sponge iron.

2.2.4. Operational Units

2.2.4.1. Water-Gas Shift Unit

The synthesis gas produced in the gasifier must be reprocessed before it can be utilized in downstream units. The water-gas shift reaction (WGSR) is employed to adjust the chemical composition of the synthesis gas and increase the hydrogen to carbon monoxide ratio. In fact, the water-gas shift reaction is a vital step in coal gasification, where the synthesis gas is passed over a fixed-bed reactor containing shift catalysts, converting carbon monoxide (CO) and water (H_2O) into carbon dioxide (CO_2) and hydrogen (H_2) (Lacson et al., 2015):

$$CO + H_2O \rightarrow CO_2 + H_2 \tag{18}$$

This reaction is typically catalyzed by various materials depending on the operating temperature (Baraj et al., 2022; Ebrahimi et al., 2020; Smith R J et al., 2010).

High-temperature synthesis gas from the gasifier can be processed in one of two ways:

- Direct Water Quenching: The gas is rapidly cooled through direct water contact, saturating it with steam and eliminating the need for additional steam in the water-gas shift reaction. This method is commonly used in hydrogen and ammonia production facilities (Robin, 1976).
- Gas Cooling via a Gas Cooler: The gas is cooled using a gas cooler, which generates a separate high-pressure steam stream.

Furthermore, the water-gas shift (WGS) reactor can be placed either before sulfur removal (acid shift) or after it (sweet shift). In the acid shift, operating at 232–260°C with a cobalt–molybdenum catalyst, the water-saturated gas converts CO and H_2O into CO_2 and H_2 while also transforming COS into H_2S, thus easing subsequent sulfur removal. Although the sweet shift can operate at higher temperatures (HT: 288–482°C) with iron-based catalysts or at lower temperatures (LT: 204–260°C) with copper-zinc-alumina catalysts, it often demands additional steam injection. For coal gasification, the acid shift is generally preferred because the moisture recovered from the water scrubber effectively drives the reaction to achieve the desired H_2/CO ratio (*Gasifipedia*, n.d.).

2.2.4.1. Acid Gas Separation

Acid gas separation units using amine gas treating are employed to remove acid gases, such as hydrogen sulfide (H_2S) and carbon dioxide (CO_2), from gas streams (e.g., natural gas or synthesis gas). This process operates on the principle of chemically absorbing the acid gases into amine solutions (Kohl & Nielsen, 1997a; Mandal et al., 2004; Roshdi et al., 2023; Rozanska et al., 2023). In Iran, companies like SAZEH, PIDEK, ODCC, and EIED are active in constructing petrochemical facilities, and the domestic technology and capability now exist to build both water-gas shift and acid gas separation units.

2.2.4.1. Dehydration Unit

The dehydration unit in the coal gasification process plays a critical role in removing moisture and water vapor from the synthesis gas (syngas) exiting the gasifier reactor (Table 9). This operation is essential to prevent problems such as corrosion, gas hydrate formation, and disruptions in downstream processes (e.g., chemical synthesis or combustion). Triethylene glycol (TEG) is the most commonly used glycol for syngas dehydration due to its non-corrosive properties, high boiling point, anti-foaming characteristics, low vapor pressure, low cost, and the ability to regenerate up to 98% (GANDHIDASAN, 2003; Higman & van der Burgt, 2008; Jamekhorshid et al., 2021; Kohl & Nielsen, 1997b, 1997c). In this project, based on the process requirements, the glycol dehydration method was selected.

Table 9. Comparison of Dehydration Methods (GANDHIDASAN, 2003; Higman & van der Burgt, 2008; Jamekhorshid et al., 2021; Kohl & Nielsen, 1997b, 1997c)

Parameter	Glycol (TEG)	Molecular Sieve	Condensation
Moisture Output	~0.1% volume	~0.001% volume	~5% volume
Capital Cost	Medium	High	Low
Energy Consumption	Medium (reboiler)	High (high-temp regen)	Low (cooling only)
Application	Natural Gas/Syngas	Petrochemical Industry	Pre-treatment

2.2.4.1. Pressure Regulation Unit

To reduce the pressure of the synthesis gas stream from 24 bar to 1.5 bar, several technical options are available. These options differ in terms of installation cost, maintenance cost, energy efficiency, and operational considerations. A comparative outlining these options is provided in Table 10:

Table 10. Overall Comparison of Pressure Regulation Methods

Option	Installation Cost	Maintenance Cost	Energy Efficiency	Recommended Application
PRV (Pressure Relief Valve)	Low	Low	Low	Low-capacity systems / Budget-limited setups
Expander Turbine	Very High	High	Very High	High-capacity systems / Energy recovery needs
Flow Control Valve	Very Low	Very Low	Very Low	Temporary / Emergency pressure reduction
Multi-Stage System	Medium	Medium	Medium	Pressure reduction with minimal noise/vibration

Based on the considerations outlined in Table, an expander turbine will be used in this project for regulating the pressure of the synthesis gas.

3. Results and discussion

The blocks in the simulated PFD of the gasification unit are depicted in Fig. 5. The corresponding block naming conventions are provided in Table 11, while the simulation results are presented in Table S.1 (Supplementary).

Table 11. Specifications of Simulation Blocks

| Block	Model	Function
B1	RYield	Simulates coal pyrolysis.
B2	Sep2	Separates ash from other pyrolysis products.
B3	Mixer	Mixes feed, steam, and oxygen.
B4	RGibs	Gasifies the feed mixture.
B5	Mixer	Combines raw syngas and water to achieve 200°C (quench simulation).
B6	RStoic	Water-gas shift unit to adjust the H_2/CO ratio.
B7	HEX	Heat exchanger to reduce temperature to 50°C.
B8	Sep	Separates syngas and liquids.
B9	Sep	Removes acid gases in the amine tower.
B10	Sep	Dehydrates syngas by removing moisture.
B11	Heater	Raises syngas temperature before entering the pressure regulation unit to prevent condensation.
B12	Turbine	Regulates syngas pressure.
B13	Heater	Adjusts syngas temperature.
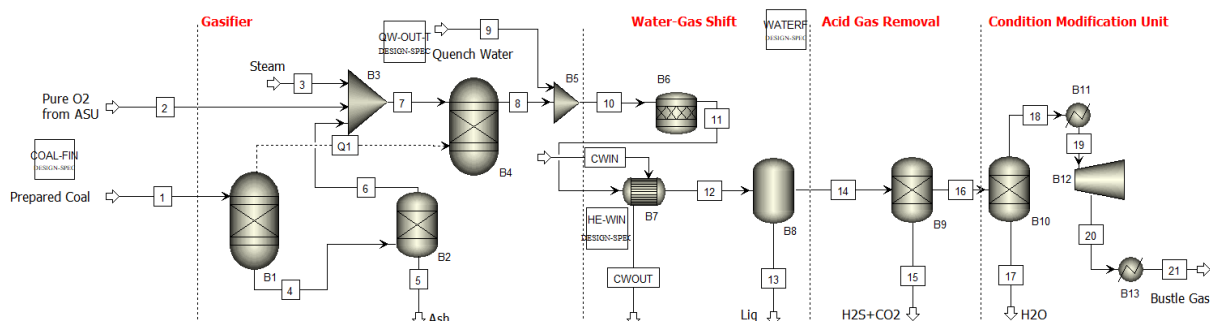
Fig. 5. PFD of the Gasification Unit

3.1. Sensitivity Analysis

3.1.1. Oxygen-to-Coal and Water-to-Coal Ratios

As discussed in the literature review, the H_2/CO ratio in the syngas produced from coal gasification is influenced by several factors, including the $O_2/Coal$ and Water/Coal ratios:

- **O_2/Coal Ratio:** Increasing the oxygen-to-coal ratio typically results in greater production of carbon monoxide (CO) and hydrogen (H_2). However, the CO increase is generally more significant, which may reduce the H_2/CO ratio (Shahabuddin & Bhattacharya, 2021).

- **Water/Coal Ratio:** Raising the water-to-coal ratio enhances the water-gas shift reaction, producing more hydrogen. This leads to an increased H_2/CO ratio, as more hydrogen is generated relative to carbon monoxide (Cao et al., 2008; Ravaghi-ardebili et al., 2014).

The effect of increased oxygen input is illustrated in Fig. 6, while the impact of increased water input on the H_2/CO ratio in the gasifier outlet stream is shown in Fig. 7. Variations in these parameters alter the H_2/CO ratio, and the results align with previous research findings (Cao et al., 2008; Ravaghi-ardebili et al., 2014; Shahabuddin & Bhattacharya, 2021).
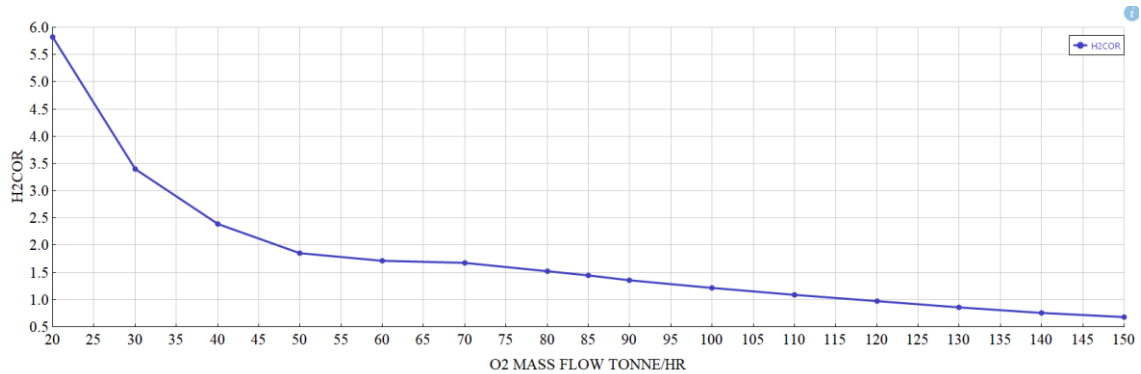
Fig. 6. Effect of Increased Oxygen Input on the H_2/CO Ratio in the Gasifier Outlet
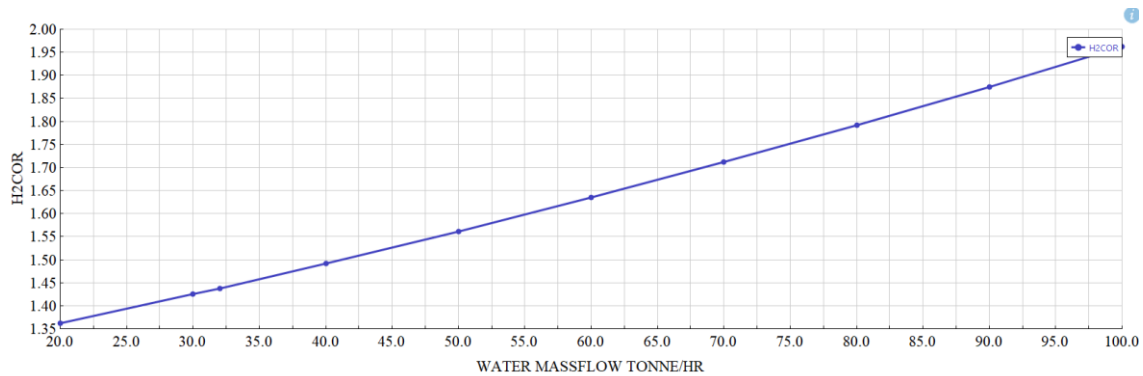
Fig. 7. Effect of Increased Water Input on the H_2/CO Ratio in the Gasifier Outlet

3.1.2. Effect of Coal Type

The type and quality of coal, as the primary feedstock in the process, have a significant impact on the amount of water required to achieve the desired H_2/CO ratio. For instance, simulation have been conducted based on the coal used in the Lurgi project and Jindal company (Lacson et al., 2015) (Table 12, Fig. 8).

315

Table 12. Analysis of Indian Coal in the Lurgi Project and Jindal Company (Lacson et al., 2015)

Attribute ID	PROXANAL	
Element	Value	
MOISTURE	7	
FC	34.4	
VM	27.96	
ASH	37.63	

Attribute ID	ULTANAL	
Element	Value	
ASH	37.63	
CARBON	48.02	
HYDROGEN	3.12	
NITROGEN	0.94	
CHLORINE	0	
SULFUR	0.62	
OXYGEN	9.67	

Attribute ID	SULFANAL	
Element	Value	
PYRITIC	0.62	
SULFATE	0	
ORGANIC	0	
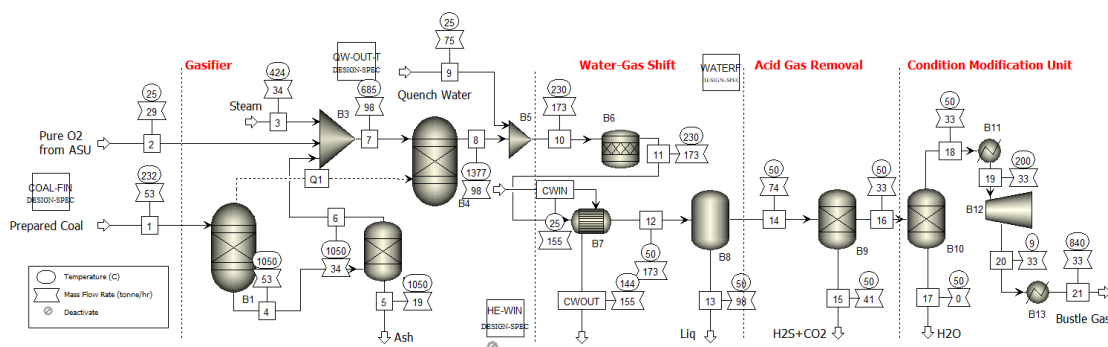
Fig. 8. PFD of the Indian Coal Gasification Unit (This process flow diagram (PFD) illustrates the Indian coal gasification unit, including mass flow rates (tons/hour), temperatures, and volumetric flow rates.)

The simulation results indicate that, assuming similar conditions at the gasifier outlet to meet volumetric and operational requirements (temperature of 839°C and pressure of 1.4 kg/cm² gauge) for Ghaenat Steel Complex South Khorasan PFD, approximately 53 tons per hour of Indian coal are required. This amount is roughly double the quantity of Tabas coal needed to achieve similar conditions.

It is essential to note that comparing two systems solely by changing the type of coal is not sufficient. For a stable process (particularly in terms of temperature in the gasifier), other parameters, such as the steam-to-coal and oxygen-to-coal ratios, must also be adjusted. It should be noted that, apart from the type of gasifier, the quality of the input coal significantly influences the amounts of water and oxygen required. Lower-quality coals generally demand higher quantities of both water and oxygen (Bell et al., 2010; Rezaiyan & Cheremisinoff, 2005). Consequently, the use of lower-quality coal leads to an increase in water consumption.

4. Conclusions

This study successfully simulated the complete coal gasification unit required for syngas production at the Ghaenat Steel Complex South Khorasan using Aspen Plus V14 software. The findings demonstrated the following:

- Coal Input: Approximately 29 tons per hour of coal is required under the operational conditions (839°C and 1.4 kg/cm² gauge pressure) to produce 174.6 m³/h of syngas feeding the DRI furnace, resulting in the production of 110 tons/hour of sponge iron.

- Process Water Consumption: The process water consumption is around 0.3 times the coal input in the gasifier, excluding utility and auxiliary water.

- Cooling and Quenching Water: For cooling and quenching syngas, the water-to-coal ratio is approximately 1.7, with most of the water being treated and reused within the system.

- Water-Gas Shift Reaction: Additional water input is not required for the water-gas shift reaction due to syngas quenching in the gasifier.

- Coal Quality: High-quality Tabas coal demands lower amounts of oxygen and water for syngas production compared to lower-grade coals, making it a more efficient feedstock.

Acknowledgments

References

Baraj, E., Ciahotný, K., & Hlinčík, T. (2022). Advanced Catalysts for the Water Gas Shift Reaction. *Crystals*, *12*(4), 509. https://doi.org/10.3390/cryst12040509

Bell, D. A., Towler, B. F., & Fan, M. (2010). *Coal gasification and its applications*. William Andrew.

Breault, R. W. (2010). Gasification Processes Old and New: A Basic Review of the Major Technologies. *Energies*, *3*(2), 216–240. https://doi.org/10.3390/en3020216

Cao, Y., Gao, Z., Jin, J., Zhou, H., Cohron, M., Zhao, H., Liu, H., & Pan, W. (2008). Synthesis Gas Production with an Adjustable H2 /CO Ratio through the Coal Gasification Process: Effects of Coal Ranks and Methane Addition. *Energy & Fuels*, *22*(3), 1720–1730. https://doi.org/10.1021/ef7005707

Dong, K., Rong, Q., Li, M., Lin, J., Xiao, R., & Li, Y. (2020). A novel simulation for gasification of Shenmu Coal in an entrained flow gasifier. *Chemical Engineering Research and Design*, *160*, 454–464. https://doi.org/10.1016/j.cherd.2020.06.015

Ebrahimi, P., Kumar, A., & Khraisheh, M. (2020). A review of recent advances in water-gas shift catalysis for hydrogen production. *Emergent Materials*, *3*(6), 881–917. https://doi.org/10.1007/s42247-020-00116-y

GANDHIDASAN, P. (2003). Parametric Analysis of Natural Gas Dehydration by a Triethylene Glycol Solution. *Energy Sources*, *25*(3), 189–201. https://doi.org/10.1080/00908310390142235

Gasifipedia. (n.d.). The National Energy Technology Laboratory (NETL) of USA. https://netl.doe.gov/carbon-management/energy-systems/gasification/gasifipedia

Gungor, H., Ozbayoglu, Kasnakoglu, Biyikoglu, & Uysal. (2011). *Determination of Air/Fuel and Steam/Fuel Ratio for Coal Gasification Process to Produce Synthesis Gas*. https://api.semanticscholar.org/CorpusID:137210361

Hasanbeigi, A., Price, L., & Arens, M. (2013). *Emerging Energy-efficiency and Carbon Dioxide Emissions-reduction Technologies for the Iron and Steel Industry*. https://escholarship.org/uc/item/5sw966f9

He, C., Feng, X., & Chu, K. H. (2013). Process modeling and thermodynamic analysis of Lurgi fixed-bed coal gasifier in an SNG plant. *Applied Energy*, *111*, 742–757. https://doi.org/10.1016/j.apenergy.2013.05.045

Higman, C., & van der Burgt, M. (2008). *Gasification*. Elsevier. https://doi.org/10.1016/B978-0-7506-8528-3.X0001-6

Hou, J., & Zhang, J. (2017). Robust optimization of the efficient syngas fractions in entrained flow coal gasification using Taguchi method and response surface methodology. *International Journal of Hydrogen Energy*, *42*(8), 4908–4921. https://doi.org/10.1016/j.ijhydene.2017.01.027

Jamekhorshid, A., Karimi Davani, Z., Salehi, A., & Khosravi, A. (2021). Gas sweetening simulation and its optimization by two typical amine solutions: An industrial case study in Persian Gulf region. *Natural Gas Industry B*, *8*(3), 309–316. https://doi.org/10.1016/j.ngib.2021.04.006

Kohl, A. L., & Nielsen, R. (1997a). *Gas Purification*. Elsevier. https://doi.org/10.1016/B978-0-88415-220-0.X5000-9

Kohl, A. L., & Nielsen, R. B. (1997b). Gas Dehydration and Purification by Adsorption. In *Gas Purification* (pp. 1022–1135). Elsevier. https://doi.org/10.1016/B978-088415220-0/50012-4

Kohl, A. L., & Nielsen, R. B. (1997c). Sulfur Recovery Processes. In *Gas Purification* (pp. 670–730). Elsevier. https://doi.org/10.1016/B978-088415220-0/50008-2

Lacson, J., Goyal, J., & Agrawal, A. (2015). *PEP Report 148D-Synthesis Gas Production from Chinese Gasifiers* (Issue December). ihs.com

Liu, Z., Fang, Y., Deng, S., Huang, J., Zhao, J., & Cheng, Z. (2012). Simulation of Pressurized Ash Agglomerating Fluidized Bed Gasifier Using Aspen Plus. *Energy & Fuels*, *26*(2), 1237–1245. https://doi.org/10.1021/ef201620t

Mandal, B. ., Biswas, A. ., & Bandyopadhyay, S. . (2004). Selective absorption of H2S from gas streams containing H2S and CO2 into aqueous solutions of N-methyldiethanolamine and 2-amino-2-methyl-1-propanol. *Separation and Purification Technology*, *35*(3), 191–202. https://doi.org/10.1016/S1383-5866(03)00139-4

Maurstad, O. (2005). An Overview of Coal Based Integrated Gasification Combined Cycle (IGCC) Technology. *MIT, Laboratory for Energy and the Environment*, 44. https://doi.org/10.1533/9780857096180.129

Mrakin, A. N., Selivanov, A. A., Satonin, A. V., Minervina, T. V., Batrakov, P. A., & Ermolaev, D. V. (2020). *Calculation study of the coal gasification process with steam*. 020013. https://doi.org/10.1063/5.0027713

Nayak, R., & Mewada, R. R. K. (2011). Simulation of Coal Gasification Process using Aspen Plus. *International Conference of Current Trends in Technology*, 8–10. https://masters.donntu.ru/2017/feht/chumarina/library/article10.pdf

Rajabzadeh, M. A., Ghorbani, Z., & Keshavarzi, B. (2016). Chemistry, mineralogy and distribution of selected trace-elements in the Parvadeh coals, Tabas, Iran. *Fuel*, *174*, 216–224. https://doi.org/10.1016/j.fuel.2016.02.004

Ravaghi-ardebili, Z., Manenti, F., Pirola, C., & Soares, F. (2014). Influence of the effective parameters on H2:CO Ratio of Syngas at Low-Temperature Gasification. *Chemical Engineering Transactions*, *37*, 253–258. https://doi.org/http://dx.doi.org/10.3303/CET1437043

Raygan, S., Abdizadeh, H., & Rizi, A. E. (2010). Evaluation of Four Coals for Blast Furnace Pulverized Coal Injection. *Journal of Iron and Steel Research International*, *17*(3), 8-12,20. https://doi.org/10.1016/S1006-706X(10)60065-9

Rezaiyan, J., & Cheremisinoff, N. P. (2005). *Gasification technologies: a primer for engineers and scientists*. CRC press.

Robin, A. M. (1976). *Hydrogen production from coal liquefaction residues. Final report* (Vol. 233, Issue December). https://doi.org/10.2172/7117259

Roshdi, S., Bairami, A., & Abbasi, I. (2023). Screening Gas Sweetening Process and Optimizing its Parameters with MDEA-PZ Solvent using Plackett-Burman Approach. *Iranian Journal of Chemical Engineering*, *20*(3), 70–89. https://doi.org/10.22034/ijche.2023.402335.1494

Rozanska, X., Valtz, A., Riva, M., Coquelet, C., Wimmer, E., Gonzalez-Tovar, K., & de Meyer, F. (2023). Selective H2S Absorption in Aqueous Tertiary Alkanolamine Solvents: Experimental Measurements and Quantitative Kinetic Model. *Industrial & Engineering Chemistry Research*, *62*(29), 11480–11490. https://doi.org/10.1021/acs.iecr.3c00888

Rudra Paul, T., Nath, H., Chauhan, V., & Sahoo, A. (2019). Gasification studies of high ash Indian coals using Aspen plus simulation. *Materials Today: Proceedings*, *46*(xxxx), 6149–6155. https://doi.org/10.1016/j.matpr.2020.04.033

Shahabuddin, M., & Bhattacharya, S. (2021). Co-Gasification Characteristics of Coal and Biomass Using CO2 Reactant under Thermodynamic Equilibrium Modelling. *Energies*, *14*(21), 7384. https://doi.org/10.3390/en14217384

Smith R J, B., Loganathan, M., & Shantha, M. S. (2010). A Review of the Water Gas Shift Reaction Kinetics. *International Journal of Chemical Reactor Engineering*, *8*(1). https://doi.org/10.2202/1542-6580.2238

Toloue Farrokh, N., Askari, M., & Fabritius, T. (2017). Investigation of Tabas anthracite coal devolatilization: Kinetics, char structure and major evolved species. *Thermochimica Acta*, *654*(March), 74–80. https://doi.org/10.1016/j.tca.2017.05.015

Wen, C. Y. (1968). Noncatalytic heterogeneous solid-fluid reaction models. *Industrial & Engineering Chemistry*, *60*(9), 34–54.

Wen, C. Y., & Chaung, T. Z. (1979). Entrainment coal gasification modeling. *Industrial & Engineering Chemistry Process Design and Development*, *18*(4), 684–695.

Zhang, Y., Takyi, S. A., & Chen, Q. (2024). Coal conversion to SNG: Thermochemical insights through kinetic-free modeling in entrained flow gasifier. *Case Studies in Thermal Engineering*, *56*(March), 104266. https://doi.org/10.1016/j.csite.2024.104266

Supplementary

Table S.1. Simulation Stream Information

	Units	1	2	3	4	5	6	7	8	9	10	11	12
From					B1	B2	B2	B3	B4		B5	B6	B7
To		B1	B3	B3	B2		B3	B4	B5	B5	B6	B7	B8
Temperature	C	232.07	24.85	423.52	1050	1050	1050	799.02	1393.3	25.00	230.00	230.00	50.00
Pressure	kg/sqcm	24.80	24.80	24.80	24.80	24.8	24.80	24.80	24.80	24.80	24.80	24.80	24.80
Mass Vapor Fraction			1.00	1.00	0.28		0.36	0.74	1.00		1.00	1.00	0.41
Mass Liquid Fraction										1.00			0.59
Mass Solid Fraction		1.00			0.72	1.00	0.64	0.26					
Mass Flows	tonne/hr	29.14	23.31	8.74	29.14	6.78	22.36	54.41	54.41	49.48	103.90	103.90	103.9
Mass Fractions (%)													
COAL		100											
ASH					23.26	100							
C					49.08		63.96	26.29					
H2					12.00		15.64	6.43	5.52		2.89	2.94	2.9
N2					5.60		7.30	3.00	3.00		1.57	1.57	1.5
CL2													
S					4.43		5.78	2.37	0.00		0.00	0.00	0.0
O2			100		4.81		6.27	45.42	0.00		0.00	0.00	0.00
CO									53.52		28.03	27.41	27.41
CO2									12.20		6.39	7.37	7.37
METHANE									0.01		0.00	0.00	0.00
WATER				100	0.80		1.04	16.49	23.22	100	59.79	59.39	59.39
H2S									2.52		1.32	1.32	1.32
Volume Flow	cum/hr		728	1117	8582		8582	11423	19906		10384	10387	3115

	Units	13	14	15	16	17	18	19	20	21	CWIN	CWOUT
From		B8	B8	B9	B9	B10	B10	B11	B12	B13		B7
To			B9		B10		B11	B12	B13		B7	
Temperature	C	50.00	50.00	50.00	50.00	50.00	50.00	200.00	9.31	840.00	25.00	144.32
Pressure	kg/sqcm	24.80	24.80	24.80	24.80	24.80	24.80	24.80	1.40	1.40	4.08	4.08
Mass Vapor Fraction				1.00	1.00	1.00		1.00	1.00	1.00	1.00	0.45
Mass Liquid Fraction		1.00			0.00	1.00					1.00	0.55
Mass Solid Fraction												
Mass Flows	tonne/hr	61.47	42.43	9.01	33.43	0.26	33.17	33.17	33.17	33.17	120	120
Mass Fractions (%)												
COAL												
ASH												
C												
H2		0.00009	7.19		9.13		9.20	9.20	9.20	9.20		
N2		0.00001	3.85		4.89		4.92	4.92	4.92	4.92		
CL2												
S		0.00003	0.00									
O2		0.00000	0.00		0.00		0.00	0.00	0.00	0.00		
CO		0.00025	67.11		85.20		85.86	85.86	85.86	85.86		

CO2		0.00637	18.03	84.94								
METHANE		0.00000	0.01		0.01		0.01	0.01	0.01	0.01		
WATER		99.96582	0.61		0.78	100.00					100.00	100.00
H2S		0.02743	3.20	15.06								
Volume Flow	**cum/hr**		3115	209	2890		2877	4224	44299	174611		25589

Beneficiation of Low-Grade Manganese Ore Using Wet High Intensity Magnetic Separator (WHIMS)

Hadi Sharifidarabad[1]*, Alireza Farazmand[1], Vahid Moradi[1]

[1]Sepanta Tose'e Sorin Company, Research and Development Department, Tehran, Iran

*Corresponding author: Sharifi@stsorin.ir (Hadi Sharifidarabad)

Abstract:

Manganese is mainly used in the form of ferromanganese (FeMn) and ferrosilicomanganese (FeSiMn) for steel production and non-ferrous alloy production. The increasing demand for steel has consequently led to an increasing need for FeMn and FeSiMn, which has had a significant impact on the manganese ore market. In Iran, the manganese ore required for FeMn and FeSiMn production is mainly imported due to its low manganese content and high content of gangue materials, particularly silica. Therefore, processing low-grade manganese ores to a product with a manganese content above 25% can play a crucial role in ensuring a stable domestic supply for ferroalloy production. Sepanta Tose'e Sorin Company has designed and manufactured a wet high intensity magnetic separator (WHIMS) which is mainly used to process hematite ores to produce a high quality manganese concentrate suitable for the production of FeMn and FeSiMn. In this study, magnetic separation experiments were conducted at four different magnetic field intensities in a single-stage process as well as in a two-stage process (rougher-cleaner) through three series of high intensity magnetic separation experiments on manganese ore from a manganese Mine in Fars province containing 7% manganese and 40% silica. Under optimal conditions, the two-stage rougher-cleaner process, carried out at magnetic field intensities of 8000 and 6500 gauss, produced a final product containing 32% manganese and 18% silica.

1. Introduction

Manganese, as one of the key elements in the iron and steel production chain and ferroalloys, plays a crucial role in enhancing the mechanical and metallurgical properties of alloys. The primary application of this element is in the form of ferromanganese and silicomanganese for the production of crude steel, tool steel, and stainless steel. Additionally, non-ferrous alloys also utilize manganese compounds. The growing global steel production has significantly increased the demand for manganese-bearing ferroalloys, which has directly impacted the manganese ore supply market [1,2]. Notably, approximately 90–95% of manganese is consumed in the steel industry, while it is also used in the production of dry batteries and dietary supplements [3,4].

China is the largest producer of low-grade manganese ore (containing less than 30% Mn), while South Africa leads in the production of medium-grade manganese ore. On the other hand, countries such as Gabon, South Africa, Australia, and Brazil are the primary producers of high-grade manganese ore (containing more than 44% Mn). The global distribution of manganese resources has a direct impact on the price and availability of this raw material in international markets. In Iran, the available manganese ores are generally low-grade and contain significant impurities, such as silica, which pose challenges for the economic exploitation of these mines. Consequently, a major portion of the domestic demand for ferromanganese and silicomanganese is met through imports. Therefore, developing efficient

methods for pre-processing domestic manganese ores to increase their grade is a crucial and strategic necessity.

Rehman et al. [5] employed wet high intensity magnetic separator (WHIMS) for the beneficiation of manganese ore (pyrolusite). In this study, with a magnetic field intensity of 8500 Gauss, the manganese content increased from 27% to 45%, while the recovery rate was only 23%. Additionally, the silica content was reduced to 30%. According to this study this method can produce a higher-grade manganese product compared to other beneficiation techniques but it results in lower recovery rates due to the incomplete liberation of fine manganese particles from silica in the non-magnetic fraction.

In another study [6], the issue of depleting high-grade manganese ore reserves was investigated for the Abu Shaar manganese ore in northwestern Hurghada, Egypt. In this research, the manganese grade of pyrolusite ore was increased from 30.58% to 44.12% using a dry high intensity dry magnetic separation process. The recovery rate varied depending on particle size, with larger particles exhibiting lower recovery. This study demonstrated that dry high intensity dry magnetic separation can significantly enhance the quality of low-grade manganese ore.

The Sepanta Tose'e Sorin Company (STS) has designed and built a wet high intensity magnetic separator (WHIMS), which is commonly used for processing weakly magnetic ores such as hematite iron ore, manganese (pyrolusite), chromite, garnet, and others (Fig. 1). This system has successfully produced a high-grade manganese product that can be used in final product manufacturing. This technology enables the extraction of a high-grade product from low-grade domestic ores, significantly reducing the need for imports.

Fig. 1. WHIMS used in this study built by Sepanta Tose'e Sorin (STS)

In this study, high intensity magnetic separation experiments were conducted to evaluate the efficiency of the wet high intensity magnetic separation process in obtaining a suitable product and to assess the impact of various process parameters on separation performance, with the aim of increasing manganese grade and reducing impurities in low-grade manganese ore.

2. Material and methods

2.1. Material

More than 100 kg of representative samples were collected from the Fars manganese mine, with the specifications listed in Table 1. As indicated, the manganese grade of this mine is 7.85%, while its primary impurity is silica, which constitutes 42.74% of the ore.

Table 1. Detailed Analysis of Fars Manganese Ore

MgO	Al_2O_3	CaO	Fe_2O_3	SiO_2	MnO
1.33	3.25	18.16	9.78	42.74	7.85

2.2. Methods

For conducting the high-intensity magnetic separation (HIMS) experiments, the representative sample was initially crushed using a jaw crusher and a roll crusher. After homogenization and preparation, the sample was split into two portions using a laboratory riffle. One portion was archived as a reference sample, while the other was subjected to high-intensity magnetic separation experiments.

The sample designated for separation tests was ground in a laboratory rod mill to achieve a particle size below 300 microns. Subsequently, the ground sample was divided into 10 kg batches for the magnetic separation experiments. These tests were conducted under high intensity magnetic field conditions of 10,000, 8,000, 6,500, and 5,000 Gauss, following the constant parameters listed in Table 2.

Table 2. Fixed Conditions for Wet High-Intensity Magnetic Separation Tests

Rod diameter (mm)	Matrix Type	Number of pulses (#/min)	Ring rotation speed (rpm)	Inlet flow (lit/h)	Size (μm)	Solidity(%)
2.5	Rod	290	4	420	0-300	22

For the two-stage rougher-cleaner separation experiments, 20 kg of sample was prepared for each test and subjected to wet high intensity magnetic separation (WHIMS) under rougher-cleaner conditions at magnetic field intensities of 10,000-8,000, 10,000-6,500, and 8,000-6,500 Gauss, following the fixed conditions outlined in Table 2.

Finally, all samples were dewatered, dried, and weighed before being analyzed using X-ray fluorescence (XRF) for grade assessment. The experimental procedure is illustrated in the flowchart shown in Figure 2.
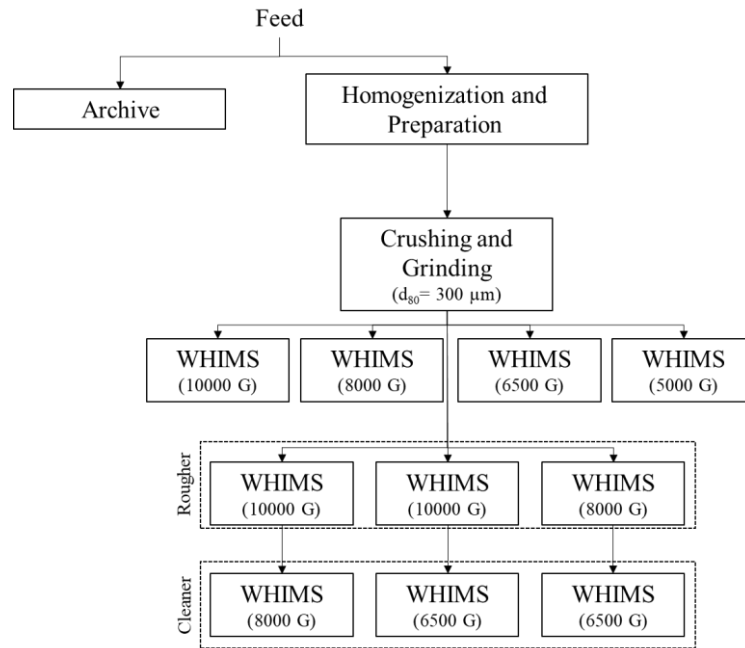
Figure 2. Flowchart of experimental procedure

3. Results and Discussion

This study aimed to obtain a product with a manganese grade higher than 30%, while also achieving a low silica content and high recovery. Since the primary goal was to enhance the manganese content of the product compared to the feed, experiments at lower magnetic field intensities (5,000 and 6,500 Gauss) were prioritized, along with two-stage rougher-cleaner tests.

Additionally, the middling was analyzed separately to evaluate different approaches for improving overall recovery if a suitable grade could be achieved.

3.1. Results of Single-Stage Tests

As mentioned earlier, single-stage tests were conducted at magnetic field intensities of 10,000, 8,000, 6,500, and 5,000 Gauss, yielding the results presented in Table 3.

Table 3. Result of single-stage wet high intensity magnetic separation tests

Test Number	Magnetic Intensity (Gauss)	Sample	Mn Grade (%)	Recovery (%)
1	10,000	Product	16.54	33.98
		Middling	3.55	13.58
		Tail	3.37	52.44
2	8,000	Product	22.13	22.48
		Middling	4.89	8.31
		Tail	3.22	69.21
3	6,500	Product	24.98	17.25
		Middling	4.83	16.63
		Tail	4.70	66.12
4	5,000	Product	28.24	10.08
		Middling	5.37	15.35
		Tail	5.13	74.57

Based on the results presented in Table 3, none of the conducted tests achieved a manganese grade of 30%, and there remains a significant gap between the obtained grades and the target value. One of the

key observations is the relatively minor change in manganese grade with decreasing magnetic field intensity, which could be attributed to insufficient comminution to the required liberation degree. Given that the manganese ore feed grade under investigation is approximately 8%, grinding it to full liberation would be highly cost-intensive. Therefore, regardless of the obtained results, additional fine grinding was not considered, and the grade enhancement was pursued within the existing particle size distribution of $d_{80} = 300$ μm.

On the other hand, the increase in iron-bearing phase grade and the reduction in recovery (at an appropriate ratio) with decreasing magnetic field intensity indicate the proper performance of the equipment. Another important aspect is the extremely low grade of the tailings, confirming that the separation process in these tests was effective. According to the results, the manganese recovery was depended on the intensity of the magnetic separation, demonstrating the efficiency of the magnetic separation. Additionally, the middling grade suggests that it can be directly added to the tailings. Therefore, based on these findings, two-stage rougher-cleaner tests were considered as the next step to achieve a manganese concentrate with a grade exceeding 30%.

3.2. Results of Two-Stage (Rougher-Cleaner) Tests

The two-stage rougher-cleaner tests were performed at magnetic field intensities of 10,000–8,000 Gauss, 10,000–6,500 Gauss, and 8,000–6,500 Gauss. The detailed results of these experiments are presented in Table 4.

Table 4. Results of two-stage wet high intensity magnetic separation tests

Test Number	Stage	Sample	Mn Grade	Recovery (%)	Mn Recovery (%)
		Rougher-Cleaner (10,000-8,000 Gauss)			
5	Rougher	Product	16.63	33.83	71.04
		Middling	4.05	13.52	19.18
		Tail	3.31	53.65	6.92
	Cleaner	Product	23.30	50.03	66.83
		Middling	12.19	11.61	20.51
		Tail	9.52	38.36	6.34
		Rougher-Cleaner (10,000-6,500 Gauss)			
6	Rougher	Product	16.64	33.37	71.08
		Middling	3.96	13.36	19.40
		Tail	3.24	53.27	6.77
	Cleaner	Product	27.88	42.73	66.57
		Middling	10.70	12.88	22.35
		Tail	9.54	44.39	6.86
		Rougher-Cleaner (8,000-6,500 Gauss)			
7	Rougher	Product	22.03	22.53	69.31
		Middling	4.67	8.57	25.51
		Tail	3.59	68.90	5.10
	Cleaner	Product	31.86	45.05	64.91
		Middling	14.66	11.18	24.64
		Tail	12.02	43.77	6.08

As shown in Table 4, the grades of the middling product and the tailings were consistently similar at both the rougher and cleaner stages across all experiments, allowing for their effective combination. The outcomes of the final product from all three two-stage tests are presented in Table 5.

Table 5. Results of the final product from all three two-stage tests

Test Number	Magnetic Intensity (Rougher-Cleaner)	Sample	Mn Grade	Total Recovery (%)
5	10,000 – 8,000 Gauss	Final Product	23.30	16.92
		Tail of Rougher	3.46	66.17
		Tail of Cleaner	11.57	49.97
6	10,000 – 6,500 Gauss	Final Product	27.88	14.26
		Tail of Rougher	3.39	66.63
		Tail of Cleaner	10.44	57.27
7	8,000 – 6,500 Gauss	Final Product	31.86	10.11
		Tail of Rougher	3.71	77.47
		Tail of Cleaner	14.12	54.95

It is evident from that the highest manganese grade, 31.86%, was achieved in the 8,000–6,500 Gauss rougher-cleaner test, marking the best performance in this study. Notably, a key observation was the exceptional reproducibility of the tests when compared to single-stage experiments, underscoring the stable and reliable operation of the WHIMS equipment.

Moreover, during the cleaner stage, the tailings grade was significantly higher than that observed in the rougher stage and the feed. This suggests that recirculating the cleaner tailings to the rougher stage could increase the feed grade for the rougher step, thereby improving both equipment efficiency and overall recovery. This strategy not only boosts the final recovery but also results in a higher-grade of final product.

Based on these findings, the proposed processing flowchart for manganese ore from the Fars manganese mine is illustrated in Figure 3.
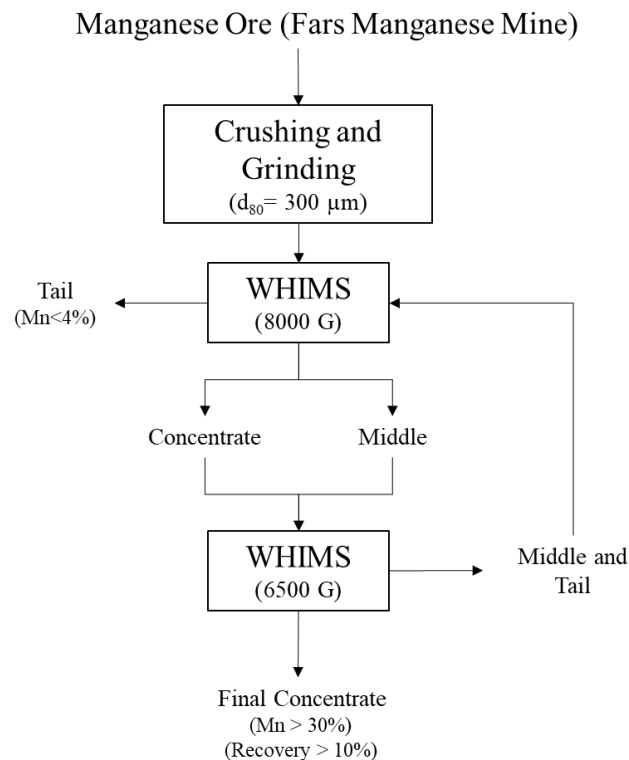
Figure 3. Proposed flowchart for manganese ore processing in Fars Manganese Mine

4. Conclusions

In this study, the beneficiation of low-grade manganese ore was investigated using wet high-intensity magnetic separator (WHIMS). Given the increasing global demand for manganese-based ferroalloys and the challenge of securing high-grade manganese ore in Iran, the development of pre-processing methods is essential. The experimental results demonstrated that the two-stage separation process (rougher-cleaner) at magnetic field intensities of 8000 and 6500 Gauss successfully produced a concentrate with 32% Mn and 18% SiO2. These results highlight the high efficiency of the proposed method in upgrading domestic manganese ores.

Implementing this approach can reduce dependence on imports and serve as a significant step toward securing raw materials for the country's ferroalloy industries. Additionally, the findings suggest that further process optimization is possible by recycling tailings, which could enhance overall recovery. Therefore, the development and optimization of wet high-intensity magnetic separator (WHIMS) represent a viable and effective strategy for the economic utilization of low-grade manganese resources in Iran.**Acknowledgments**

References

[1] Luo, Z., Shu, J., Chen, M., Wang, R., Zeng, X., Yang, Y., Wang, R., Chen, S., Liu, R., Liu, Z., Sun, Z., Yu, K., & Deng, Y. (2021). Enhanced leaching of manganese from low-grade pyrolusite using ball milling and electric field. *Ecotoxicology and Environmental Safety, Volume 211*, Page 111893. doi: https://doi.org/10.1016/j.ecoenv.2021.111893

[2] Tukaram bai, M., Srivani, P., Noothana, P., & Nageswara rao, V. (2019). Beneficiation of Manganese Ore Using Froth Flotation Technique. *Mater. Today Proc., Volume 18*, Pages 2279–2287. doi: https://doi.org/10.1016/j.matpr.2019.07.010

[3] Pereira, M. J., Lima, M. M. F., & Lima, R. M. F. (2014). Calcination and characterisation studies of a Brazilian manganese ore tailing. *International Journal of Mineral Processing*, V*olume 131*, Pages 26–30. doi: https://doi.org/10.1016/j.minpro.2014.08.003

[4] Liu, B., Zhang, Y., Lu, M., Su, Z., Li, G., & Jiang, T. (2019). Extraction and separation of manganese and iron from ferruginous manganese ores: A review. *Minerals Engineering*, *Volume 131*, Pages 286–303. doi: https://doi.org/10.1016/j.mineng.2018.11.016

[5] Rehman, W. U., Rehman, A. U., Khan, F., Muhammad, A., & Younas, M. (2020). Studies on Beneficiation of Manganese Ore through High Intensity Magnetic Separator. *Advances in Sciences and Engineering, Volume 12 (1)*, Pages 21–27. doi: https://doi.org/10.32732/ase.2020.12.1.21

[6] Xiong, S., Li, X., Liu, P., Hao, S., Hao, F., Yin, Z., & Liu, J. (2018). Recovery of manganese from low-grade pyrolusite ore by reductively acid leaching process using lignin as a low cost reductant. *Minerals Engineering, Volume 125*, Pages 126–132. doi: https://doi.org/10.1016/j.mineng.2018.06.003

Evaluation of the Performance of the Pilot-Scale Paste Thickener

Amir Firouzi [1]*, Maryam Khosravi [1], Mohsen Mirzaei [1], Ziaeddin Pourkarimi [1], Ali Ghafari [1],

[1]Iran Mineral Processing Research Center

*Corresponding author: a.firouzi2018@gmail.com (Amir Firouzi)

Abstract:

Considering the high cost of water supply for large mineral processing plants in desert areas, the treatment and recovery of wastewater from these plants is essential. One common method for solid-liquid separation on a large scale is the use of paste thickeners. The most important advantages of paste thickeners are increased water recovery, maximized underflow density, and enhanced tailings dam capacity. Therefore, to investigate this matter, a pilot-scale paste thickener was designed with a dry feed rate of 530 kilograms per hour and an input solid percentage of 10%. The pulp flow rate entering the feedwell was set at 4920 liters per hour, and the flocculant consumption for this thickener was considered 50 grams per ton of dry solids. The flocculant was prepared as a solution with a concentration of 0.16 grams per liter in the flocculant preparation tank before it was injected into the feedwell. The results of the study indicated that the solid settling rate using flocculant AN905 (Polyacrylamide) was higher than that of flocculant A26 (Polyacrylamide), while the overflow water clarity was satisfactory for both flocculants. The average bed formation rate over time was approximately 0.26 meters per hour. After feeding the thickener, when the bed height increased to 3 meters, the underflow solid percentage of the paste thickener reached 65%. The concentration profile results revealed that at greater heights, the solid percentage of the sample approached the feed solid percentage, while at lower heights, the solid percentage aligned more closely with the underflow solid percentage.

Keywords: *paste thickener, flocculant, underflow solid percentage, overflow turbidity*

1. Introduction

Solid-liquid separation in large settling tanks is widely used in the mineral processing and water treatment industries (Rudman et al. 2010). Thickening is the process of separating suspended solid particles from water through gravitational settling to increase the solid percentage. Nowadays, the industry focuses on issues such as water recovery, environmental management, and the production and storage of tailings with higher solid content (Henriksson. 2005). Deep cone thickeners were developed in the British coal industry during the 1960s and 1970s. Several years later, with advancements in flocculant technology, feedwell design, and improvements in tank and underflow system design, modern deep cone paste thickeners emerged. These thickeners have a height-to-diameter ratio greater than one, whereas conventional and high-rate thickeners have a much lower ratio. The combination of a high height-to-diameter ratio and a steep cone angle facilitates easier discharge of the paste underflow. Since the effect of gravity on paste tailings is governed by the yield stress of the paste, it is considered a key parameter in paste thickener design. The paste must flow through the thickener, reach the pumping system, and then be transported to the designated

discharge point. By correctly interpreting the operating range of paste thickeners, the yield stress curve can be used to determine the maximum underflow concentration and the minimum overflow concentration, which are directly related to slurry settling behavior (September and Kirkwood. 2010). The bed depth of paste thickeners distinguishes them from other types of thickeners. In deep cone paste thickeners, the bed depth can reach 10 meters or more. Reducing the surface area relative to depth increases compressive forces, which in turn enhances the underflow solid percentage (September and Kirkwood. 2010). Flocculation occurs through polymer bridging, charge compensation or neutralization, surface polymer complex formation and depletion, and/or a combination of these mechanisms (Onen et al. 2018). For the flocculant A-130 (5 g/t), the research results indicated that an underflow solid percentage of 70% was achieved at a height of 2 meters, with a retention time of 5 hours and a settling flux of 2 t/h/m² (Moosakazemi et al. 2020). The research results showed that the maximum underflow solid percentage of 55.6% can be achieved using the laboratory-scale paste thickener (Olcay et al. 2009).

2. Material and methods

With the construction of a pilot-scale paste thickener, the cold commissioning of this thickener was carried out. After ensuring the functionality of all equipment, the hot commissioning was performed in the presence of the consulting team and the client on the tailings sample from the Golgohar processing plant. Similar to the bench-scale thickener experiments, the appropriate flocculant type and its concentration should first be determined at the laboratory scale. Here, due to the required flocculant volume (which is greater than the amounts used in the bench-scale thickener startup), two types of flocculants, A26 and AN905, were examined. Afterward, based on the optimized experimental conditions, tests were conducted at the pilot scale. The goal of these experiments was to determine the minimum thickener surface area required to achieve the maximum underflow solid percentage, which aligns with the values observed in the industrial thickener. In addition to the above, this thickener can be used to determine the bed formation rate at different fluxes and the concentration profile. All of these factors will help determine the sedimentation and consolidation characteristics of the minerals in the paste thickener, which will assist in the design and optimization of the industrial thickener.

2.1. Components of the Pilot Thickener

The various components of this thickener are as follows:

Feed tank, Flocculant preparation tank, Peristaltic feed pump, Flocculant dosing pump, Peristaltic dilution water pump, Pilot paste thickener (including main parts such as the header box, overflow, feedwell, rake, and its mechanism), Peristaltic underflow pump, Recirculation pump.

The Gol Gohar Sirjan tailings, which had been used at the bench scale, were also selected as the basis for pilot-scale tests. For this purpose, the sample was prepared in the feed tank, which is equipped with an agitator, at a solids percentage of 30%. It was then transferred into the feed sump using a peristaltic pump and a hose. This pump allows for feed flow rate control during experiments by adjusting its frequency. At the pilot scale, feed dilution takes place in the feed sump, simulating the conditions of an industrial-scale paste thickener. In this experiment, the dilution was carried out to 10% by weight.

The flocculant tank is used for the preparation and storage of the flocculant solution. This tank is equipped with an agitator. The flocculant pump, located beneath the flocculant tank, delivers the flocculant solution into the feed sump via a hose. This pump is also a peristaltic type, with an adjustable flow rate. In these experiments, the flocculant solution was prepared at a concentration of 0.16 g/L. To mitigate the risk of flocculant shortage, two tanks were used for flocculant preparation, allowing the second tank to replace the first one when depleted.

The pilot-scale paste thickener has an internal diameter of 1.5 meters and a height of 5 meters. Sampling valves were installed at half-meter intervals along the height, facilitating easy sampling at various thickener heights and enabling the creation of a concentration profile. This thickener is equipped with a small header box at the top to minimize initial feed turbulence and facilitate proper flocculation. Additionally, Similar to industrial thickeners, the feedwell was used for feed circulation and guidance inside the thickener. For optimal flocculation, four injection points for the flocculant solution were designated—two in the header box and two on the pipe connecting the header box to the feedwell.

The dilution of the incoming feed is also carried out in the header box using overflow water. A V-notch section was designed inside the thickener for the transfer of overflow water, allowing it to be directed out of the thickener after reaching this section. The discharged water is collected in a tank, and a portion of it is recirculated back into the header box using a peristaltic pump for feed dilution. Additionally, an underflow pump is used to discharge the thickened slurry. Similar to the feed pump, this pump has a controllable and adjustable flow rate.

Since the thickener is made of metal, two transparent acrylic panels, each 1.7 meters in height, were installed on opposite sides of the thickener body to provide a clear view of its interior. This allows for the observation and recording of the bed level, sedimentation behavior, and material compaction inside the thickener. Additionally, The thickener was also equipped with a recirculation pump to facilitate material flow in case of underflow clogging. This pump increased flowability by reducing paste viscosity without lowering the solid percentage. Figure 1 presents images of various sections of the thickener from different perspectives.

Figure 1 - Different parts of the pilot scale paste thickener

2.2. Experimental Procedure

At this stage, the flocculant solution was prepared at a concentration of 0.16 g/L. As mentioned earlier, two tanks were used for flocculant preparation to minimize the risk of shortages, allowing for

the replacement of one tank with the other when depleted. Simultaneously, the feed was prepared with a solids percentage of 30%. Before starting the experiment, the paste thickener was filled with water. The flocculant pump was then started, and its flow rate was adjusted. Next, the dilution pump was activated, followed by the feed pump, with their respective flow rates also being adjusted. Initially, the experiment was conducted in batch mode to reach the desired bed height. During this phase, the underflow pump remained off until the bed height reached the target level (3 meters in this case). Once the desired bed height was achieved, the underflow pump was started.

The bed formation rate can be determined by measuring the time required to reach different heights. Once the bed height reaches approximately 3 meters, the underflow pump is started. The underflow flow rate must be adjusted to maintain the bed height at 3 meters. Therefore, the underflow rate is entirely dependent on the bed height, and adjustments continue until the bed height stabilizes.

At a constant flux and a stable bed height, a fixed paste density is achieved. Additionally, to analyze the sedimentation and consolidation behavior of the target mineral, samples can be collected from the thickener wall, and a concentration profile can be plotted.

Based on these principles, experiments were conducted on the iron tailings sample from the Gol Gohar processing plant. The operational conditions of the thickener and flocculant preparation during the experiment are provided in Table 1 and 2.

Table 1 - Operational Conditions of the Pilot Paste Thickener

Flocculant	Preparation Concentration (g/L)	Consumption Rate (g/t)	Solution Flow Rate (L/h)
AN905	0.16	50	165.5

Table 2 - Operational Conditions of the Pilot Paste Thickener

Pulp	Solid Flux (t/m²/h)	Feed Solid percentage(Before Dilution)	Feed Solid percentage (After Dilution)	Feed Flow Rate Before Dilution (L/h)
	0.3	30	10	1387.3

Based on the solid flux and thickener surface area, the dry feed tonnage was 530 kg/h. Given a 10% solid percentage in the feed, the pulp flow rate to the feedwell was approximately 4920 L/h, requiring 3533 L/h of dilution water.

3. Experimental Results

3.1. Flocculant Selection

Similar to the bench-scale thickener setup tests, the appropriate type and concentration of flocculant must first be determined at the laboratory scale for pilot-scale experiments. Given the larger volume of flocculant required at the pilot scale (compared to the bench scale), two types of flocculants, A26 and AN905, were evaluated. The experiments were conducted at a solids percentage of 10% with a flocculant dosage of 50 g/ton. The results of these tests are presented in Figure 2.
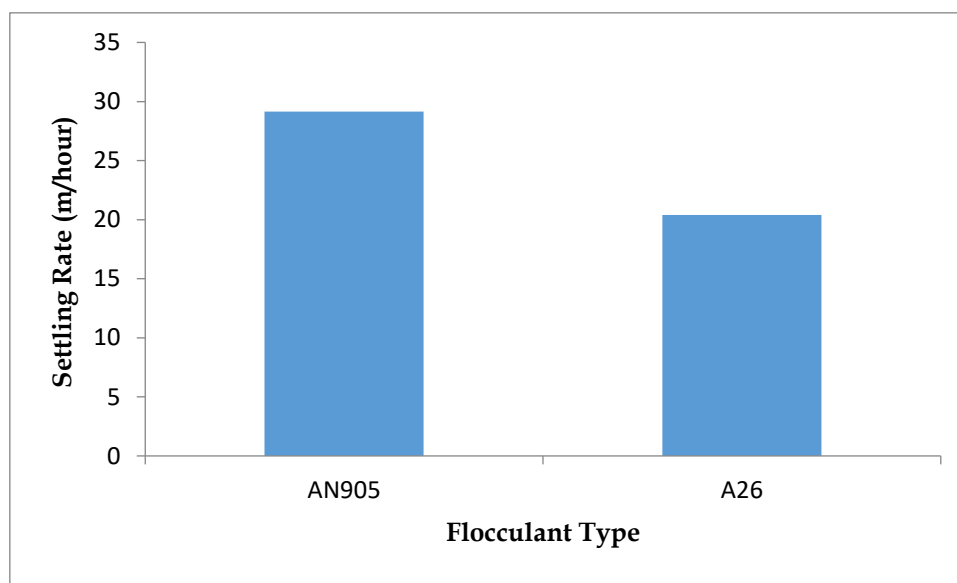
Figure 2 – Initial settling rate of different flocculants

As observed, the settling rate of flocculant AN905 is higher than that of A26. However, the turbidity of the overflow water was also examined, and the water clarity was found to be suitable for both types of flocculants. Therefore, flocculant AN905 was selected for use in the experiments.

3.2. Bed Formation Rate

After starting the experiment and filling the conical section of the thickener, with the bed level reaching the eye sight level, the bed formation process was recorded over time in batch conditions. In this case, the zero time for bed formation was considered at a height of 30 centimeters above the bottom of the thickener cylinder. The bed height values over time are shown in Figure 3. According to this graph, the average bed formation rate over time was approximately 0.26 meters per hour, which is about 0.24 meters per hour lower than the bench-scale experiment (0.50 meters per hour).

This decrease in the bed formation rate compared to the bench-scale is due to the presence of paddles and the pickets on them. The pickets create vertical channels in the bed of materials, which leads to the release of trapped water within the bed. As a result, the bed compaction is much higher than in the bench-scale conditions, and a more uniform bed is formed. Therefore, the paddles play a crucial role in paste thickeners, and special attention should be given to their design in thickener systems.
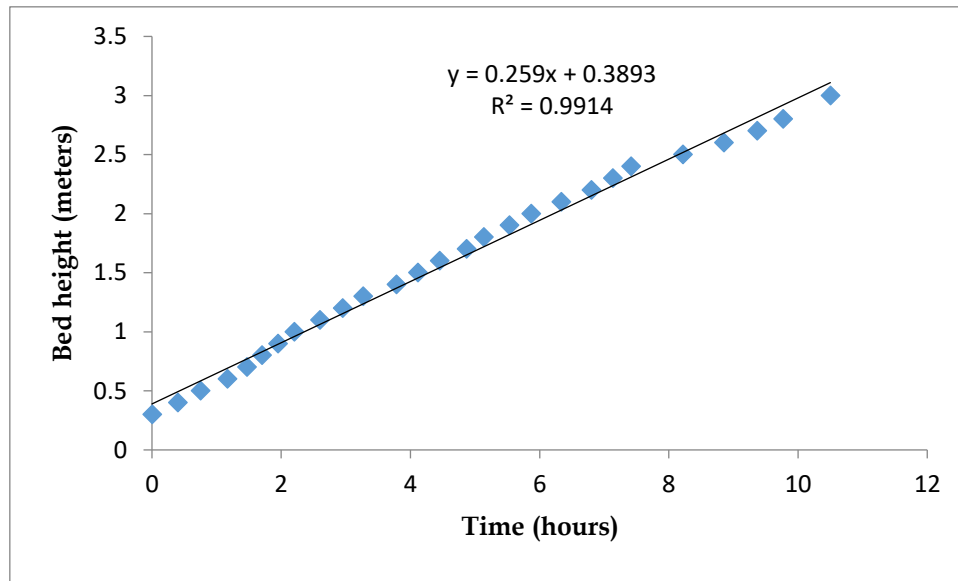
Figure 3 – Bed height values over time

3.3. Underflow Solid Percentage

As the bed height increased to 3 meters, the underflow pump was started. As mentioned earlier, the underflow flow rate must be adjusted so that no decrease in bed height occurs. In other words, the underflow flow rate must be varied to keep the bed height constant at 3 meters. Afterward, samples were taken from the underflow at different time intervals. The results of several sampling stages, taken at the start of the underflow pump and after 1 hour of operation, are shown in Figure 4.

As observed, the average final solids percentage of the underflow varied at the start of the underflow pump, but after 1 hour of discharge and the establishment of stable conditions, the underflow solids percentage reached approximately 65%. Therefore, at a flux of 0.3 tons per square meter per hour, the solids percentage of the underflow in an industrial-scale paste thickener will be around 65%.
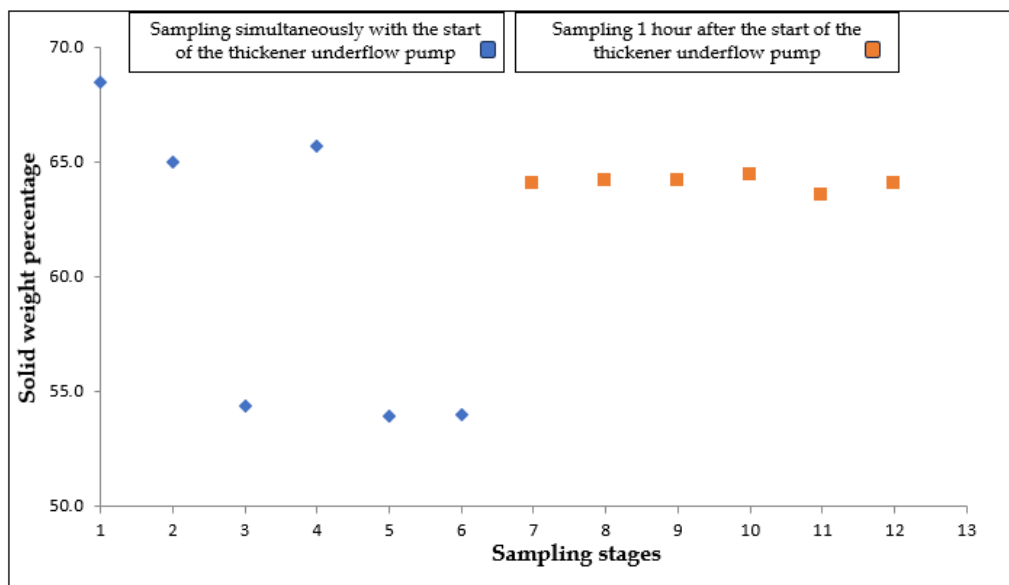
Figure 4 - Underflow solid percentage at different sampling stages

3.4. Concentration Profile

By sampling from the sample valves on the thickener body, the concentration profile related to this experiment is shown in Figure 5. In this figure, the zero height refers to the thickener underflow. As observed, as the graph approaches higher heights, the solid percentage of the sample gets closer to the solid percentage of the feed. Conversely, as it moves towards lower heights, the solid percentage approaches that of the underflow.
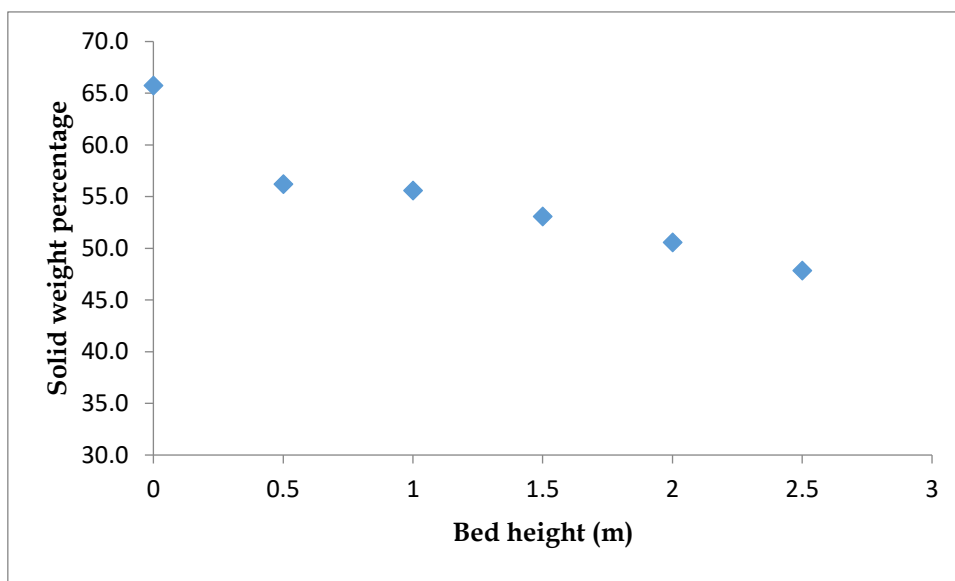
Figure 5 - Solid percentage profile at different heights of the pilot-scale paste thickener

4. Conclusion

Based on the conducted experiments, the following results were obtained:

Predicting the final solid percentage of a paste thickener at an industrial scale is feasible using a pilot-scale paste thickener. The sedimentation and consolidation behavior can be fully monitored at this scale. However, tests at this scale should be conducted at different flux rates to determine the most optimal and efficient thickener performance. For the iron tailings sample from the Gol Gohar processing plant, at a flux of 0.3 tons per square meter per hour, the industrial-scale solid percentage is expected to be around 65%.

The bed formation rate at this scale is lower compared to the bench-scale thickener under similar conditions, due to the presence of rakes and pickets (0.26 meters per hour in the pilot scale compared to 0.5 meters per hour in the bench scale). The pickets create channels within the material bed, facilitating water release between particles and increasing compression in the thickener. Additionally, since this water release occurs simultaneously with thickening, the bed formation rate becomes more uniform.

References

Rudman, M., Paterson, D.A. and Simic, K., 2010. Efficiency of raking in gravity thickeners. International Journal of Mineral Processing, 95(1-4), pp.30-39.

Henriksson, B., 2005. Mining: the evolution of thickening rake mechanisms. *Filtration & Separation*, *42*(10), pp.26-27.

September, N. and Kirkwood, R., 2010. Clermont Coal Mine Project Selection of Tailings Paste Thickener AusIMM–Technical Meeting. Rio Tinto, p.10.

Onen, V., Beyazyuz, P. and Yel, E., 2018. Removal of turbidity from travertine processing wastewaters by coagulants, flocculants and natural materials. *Mine Water and the Environment*, *37*(3), pp.482-492.

Moosakazemi, F., Hayati, M., Tavakoli Mohammadi, M.R., Tajvidi Asr, E. and Koleini, S.M.J., 2020. A novel procedure for performance assessment of paste thickeners. *Mineral Processing and Extractive Metallurgy Review*, *41*(6), pp.396-404.

Olcay Barreda, R.H., de Araujo, A.C., Valadão, G.E.S. and Hernández, C.A., 2009, April. Development and testing of a laboratory scale paste thickener. In *Paste 2009: Proceedings of the Twelfth International Seminar on Paste and Thickened Tailings* (pp. 119-128). Australian Centre for Geomechanics.

Magnesium Oxide Production from Dolomite Ore

Hasan Vafaei Jirsarai[1]*, Ziaeddin Purkarimi [2] , Reza Parvareh[3], Behrouz Karimi Shahraki[4], Seyed Ramin Bani Hashemi[5], Morteza Dehghani[6]

1.Iranian Mineral Processing Research Center (IMPRC)

*Corresponding author: e-mail (hasan.vafaei@ shahroodut.ac.ir)

Abstract:

In this study, the production of magnesium oxide (MgO) from dolomite ore ($CaMg(CO_3)_2$) from a mine in the southern region of the country was investigated. After sampling from the dolomite mine, the samples were transferred to the Iranian Mineral Processing Research Center for XRF, ICP, XRD, and TGA-DTA analyses. The results of mineralogical and chemical analyses indicated that the main minerals in these samples were dolomite and calcite, which are significant for magnesium production. The calcination process at a particle size of 3 mm and a temperature of 800°C led to the conversion of dolomite into an oxide phase. Magnesium oxide was produced through acid leaching with HCl at a concentration of 2 M and a solid-to-liquid ratio of 5:15 at 70°C for 3 hours. The precipitation process using NaOH at a pH of 8–9 resulted in the formation of magnesium hydroxide, which was further heated at 600°C to convert it into magnesium oxide (MgO).The results demonstrated that the complete production of magnesium oxide is feasible at the Iranian Mineral Processing Research Center. This study highlights the high potential of the dolomite mine in the southern region as a source of raw material for MgO production and emphasizes the need to develop industrial infrastructure to complete the value chain of this strategic metal.

Keywords: Magnesium, Dolomite, Calcination, Acid Leaching

1. Introduction

Magnesium, the eighth most abundant element in the Earth's crust, plays a vital role in various industries due to its unique properties, including low density, high strength, excellent formability, and good electrical and thermal conductivity. Dolomite ore is one of the most important sources for magnesium extraction. Composed of calcite and magnesite, dolomite is widely regarded as an ideal raw material for producing magnesium and its compounds. Formed primarily through regional metamorphism, this rock typically contains at least 45% magnesium carbonate and appears naturally white, though impurities may introduce gray, pink, green, or black hues. Dolomite has a specific gravity of approximately 2.6 g/cm³, a hardness of 3.5–4 on the Mohs scale, and a vitreous to pearly luster. Significant dolomite deposits exist worldwide, particularly in regions such as Indonesia.This study explores hydrometallurgical techniques for extracting magnesium from dolomite ore, which are among the most efficient methods for producing magnesium and its derivatives. The research focuses on magnesium oxide production from dolomite sourced from a southern region of the country, analyzing a composite reserve sampled from multiple stations with varying compositions. The experimental procedures and results are presented in detail, offering insights into optimizing magnesium extraction and production from mineral resources.

2. Material and methods

This research investigated dolomite sourced from a mine in southern Iran. Composite samples were prepared by blending material from five sampling stations with equal weight percentages from different areas of the mine. The results of XRF and XRD analyses are presented in Table 1 and Figure 1. XRF data revealed that the dolomite samples contained Caro, MgO, Na_2O, SiO_2, Al_2O_3, P_2O_5, SO_3, K_2O, and Fe_2O_3, with CaO and MgO as the predominant compounds and the others as minor constituents. XRD analysis confirmed that most peaks corresponded to dolomite, with additional minor peaks attributed to $CaCO_3$ and SiO_2 impurities.The composite dolomite samples were crushed to ≤3 mm using jaw and roller crushers at the Iran Mineral Processing Research Center. This particle size was selected to minimize fines (preventing agglomeration during calcination) while ensuring complete calcination. The crushed samples were then calcined at 800°C for 5 hours, decomposing the dolomite into calcium oxide (CaO) and magnesium oxide (MgO).Subsequent leaching was performed using 37% hydrochloric acid (2 M concentration) at a solid-to-liquid ratio of 1:3 and 70°C for 3 hours to solubilize the primary dolomite components, magnesium and calcium. After leaching, the solution was filtered to remove the negligible insoluble residue. The filtrate was then treated with 10 M sodium hydroxide to adjust the pH to 8.5–9.5, precipitating magnesium hydroxide ($Mg(OH)_2$). Due to the temperature sensitivity of $Mg(OH)_2$, precipitation was conducted below 60°C. The precipitated $Mg(OH)_2$ was collected via filtration and subsequently calcined at 600°C for 1 hour to produce magnesium oxide (MgO). The complete process flow is illustrated in Figure 2.

Table 1: XRF Analysis Results of the Composite Sample from 5 Sampling Stations

Element	P_2O_5 (%)	SO_3 (%)	TiO_2 (%)	MgO (%)	CaO (%)	Al_2O_3 (%)
Composition (wt. %)	0.01	0.46	0.01	19.08	33.19	0.1
Element	L.O.I (%)	Fe_2O_3 (%)	SiO_2 (%)	SrO (%)	K_2O (%)	Na_2O (%)
Composition (wt. %)	46.38	0.1	0.57	0.01	0.17	0.1
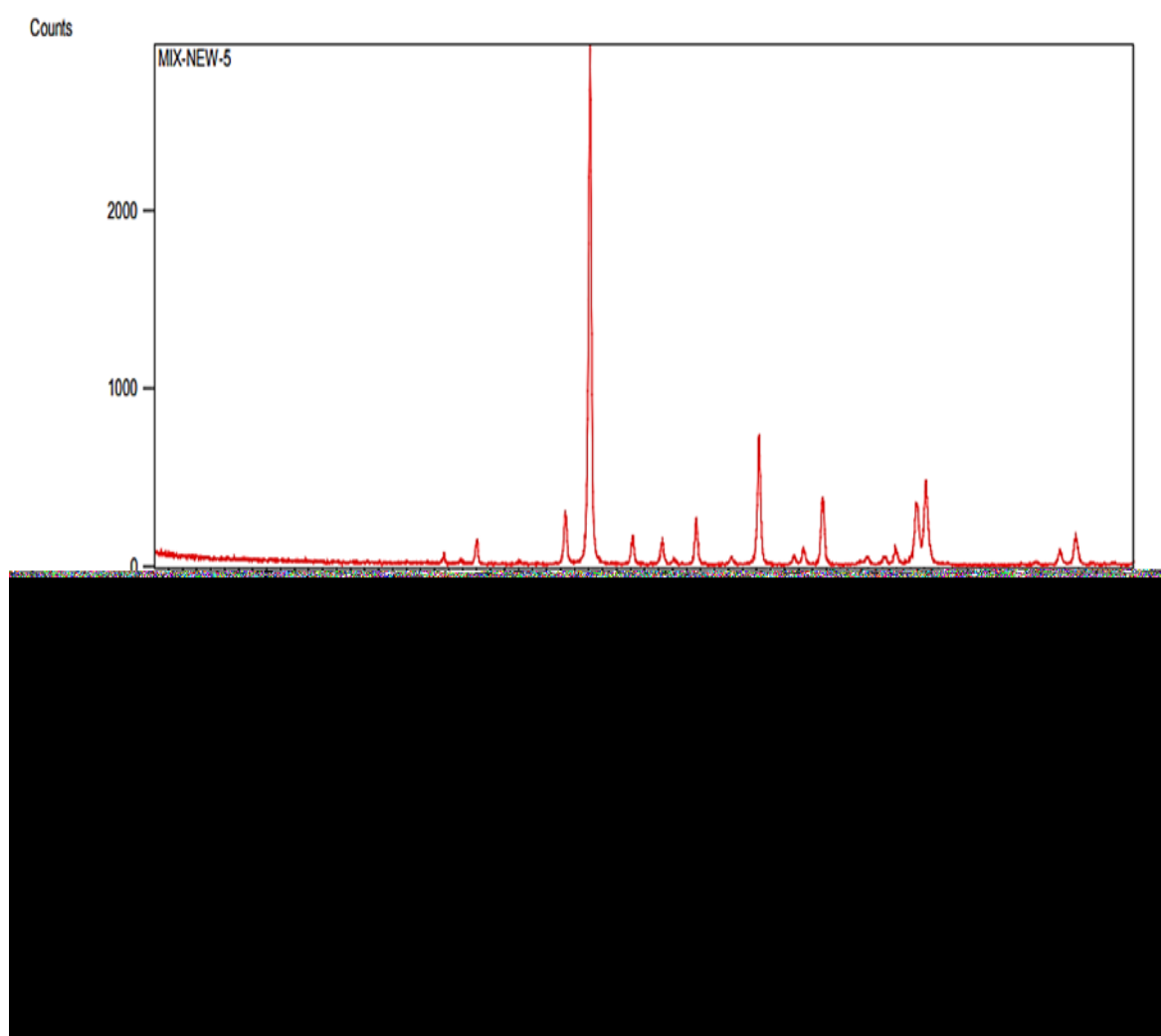
Figure 1 – XRD diagram of the combined sample of 5 sampling stations
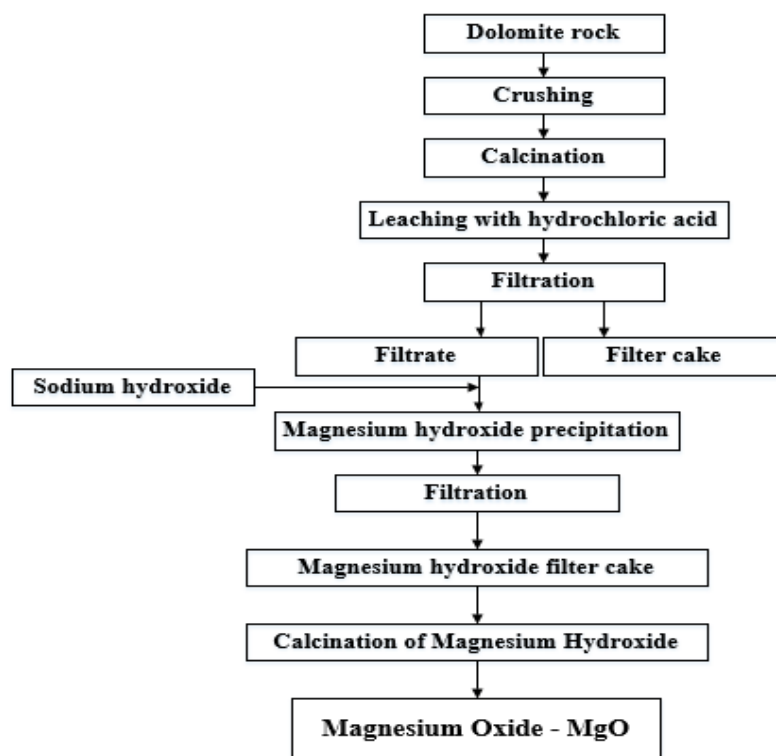
Figure 2 – Flowchart of Magnesium Oxide Production Test Procedures

3. Results and Discussion
3.1. The Effect of Heat on Dolomite Calcination

The thermogravimetric (TGA) and differential thermal analysis (DTA) results presented in Figure 3 demonstrate the thermal behavior of composite dolomite samples within the 750-900°C temperature range, which was investigated to determine the optimal calcination conditions. Our analysis revealed two distinct decomposition events at 798.52°C and 915.38°C, corresponding to dolomite and calcite decomposition respectively, accompanied by a total mass loss of 19.47%. Systematic calcination experiments conducted at 750, 800, 850, and 900°C for 5 hours enabled observation of the thermal decomposition process following Reaction 1:

$$CaMg(CO_3)_2 \rightarrow CaO + MgO + 2CO_2 \qquad\qquad (1)$$

XRD analysis of the calcination products showed complete dolomite decomposition at 800°C, with well-defined CaO and MgO phases of high purity. These findings, supported by the data in Figure 4, establish 800°C as the optimal calcination temperature, while Figure 5 provides clear visual evidence of the pronounced structural transformations occurring during calcination at this temperature.
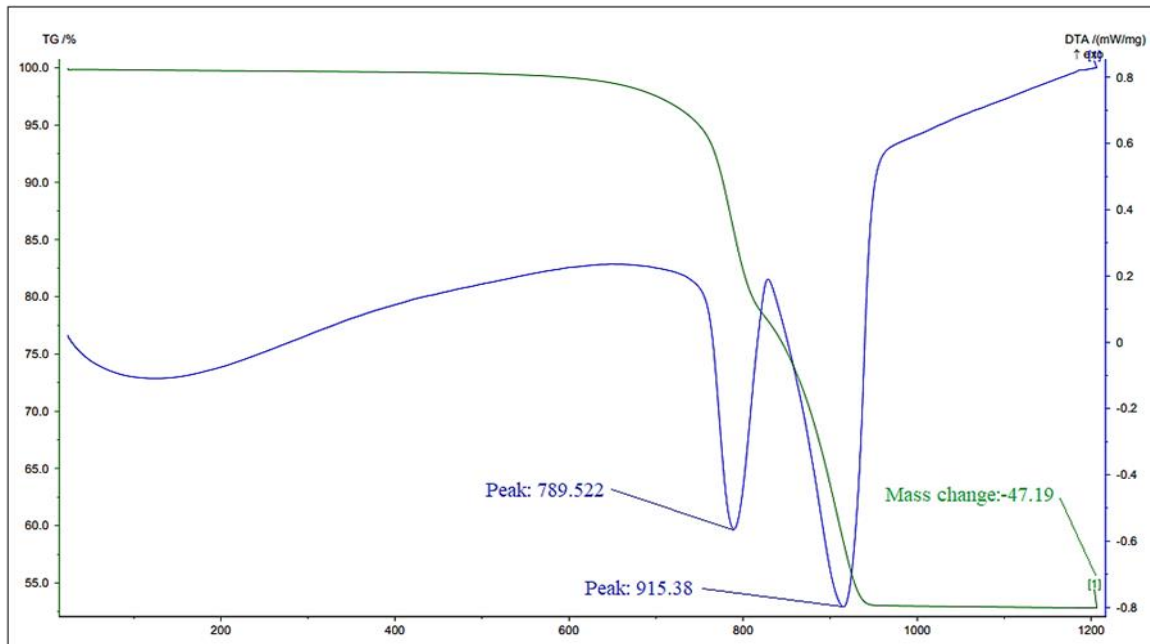
Figure 3 - TGA-DTA diagram of the combined sample of 5 sampling stations
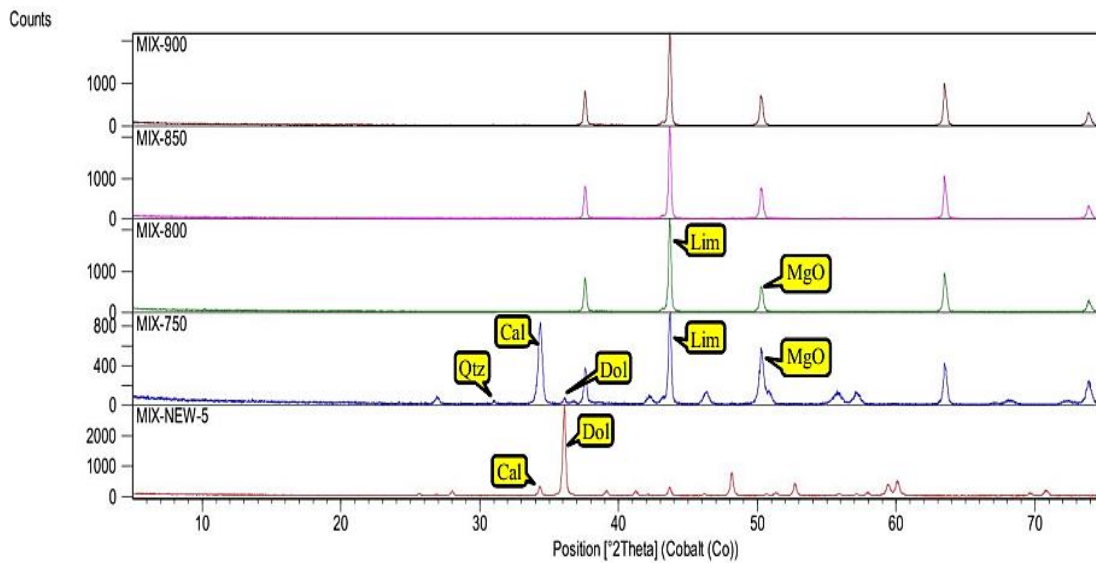
Figure 4 - XRD pattern of the calcination of the composite sample at different temperatures

Figure 5 - Comparative images of the composite sample (right) pre-calcination state and (left) post-calcination state at 800°C.

3.2. The Effect of Hydrochloric Acid Concentration on Leaching of Calcined Dolomite

In the leaching experiments conducted at 70°C with a liquid-to-solid ratio of 3, the concentration of hydrochloric acid (HCl) varied from 0.5 to 2 M. The results indicated that magnesium extraction increased with rising HCl concentration. Over a 3-hour leaching period, increasing the HCl concentration from 0.5 M to 2 M enhanced the dissolution of calcined dolomite from 2.4% to 99.07%. Images of the hydrochloric acid leaching process and the filtration of the leaching solution are shown in Figures 6 and 7, respectively.

Figure 6 – Hydrochloric Acid Leaching of Calcined Dolomite

Figure 7 - Filtration of the Hydrochloric Acid Leaching Solution

3.3. The Effect of Sodium Hydroxide Addition on Magnesium Hydroxide Precipitation

The hydrochloric acid leaching solution has a pH of 2.5, and sodium hydroxide must be added to precipitate magnesium oxide. The pH rapidly increases from 2.5 to 8 upon NaOH addition, but the rise from 8 to 9 occurs slowly, during which magnesium hydroxide gradually appears as a white precipitate at pH 8, with complete precipitation achieved at pH 9. After filtration, magnesium hydroxide can be separated from the solution. The XRD analysis results of the precipitated magnesium hydroxide, the precipitation solution, and the solid magnesium hydroxide are shown in Figures 8, 9, and 10, respectively. Note that the precipitation temperature must be set at 60°C due to the low solubility of magnesium hydroxide at higher temperatures.
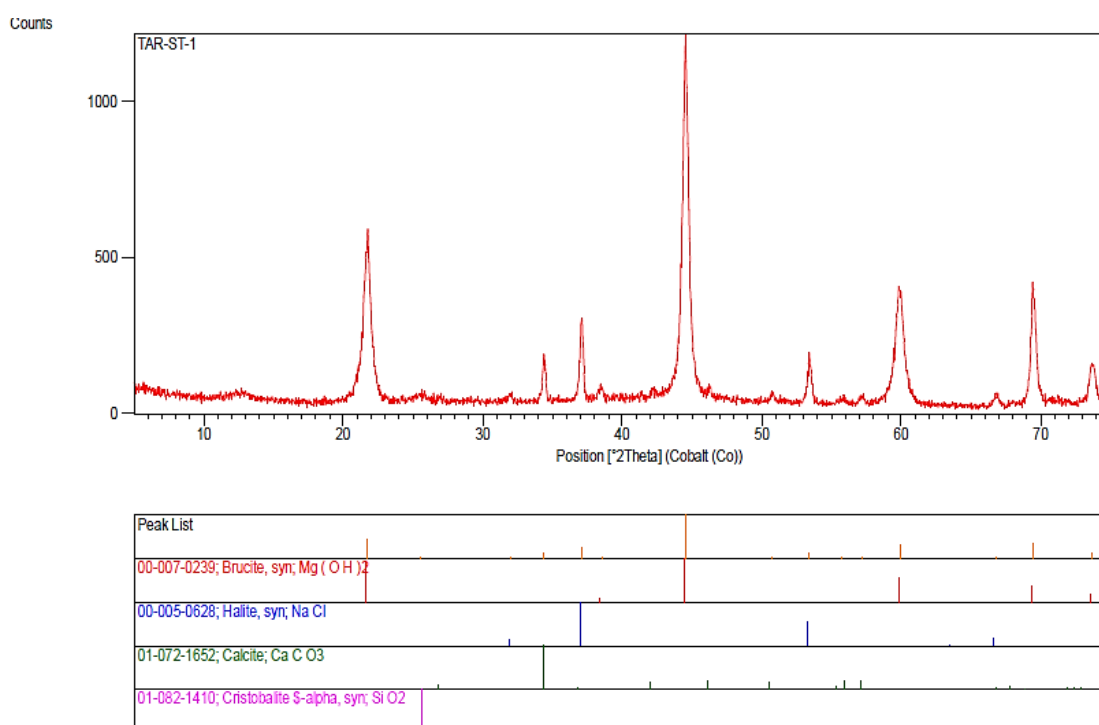
Figure 8 - XRD analysis results of the precipitated magnesium hydroxide

Figure 9 - Precipitation solution of magnesium hydroxide
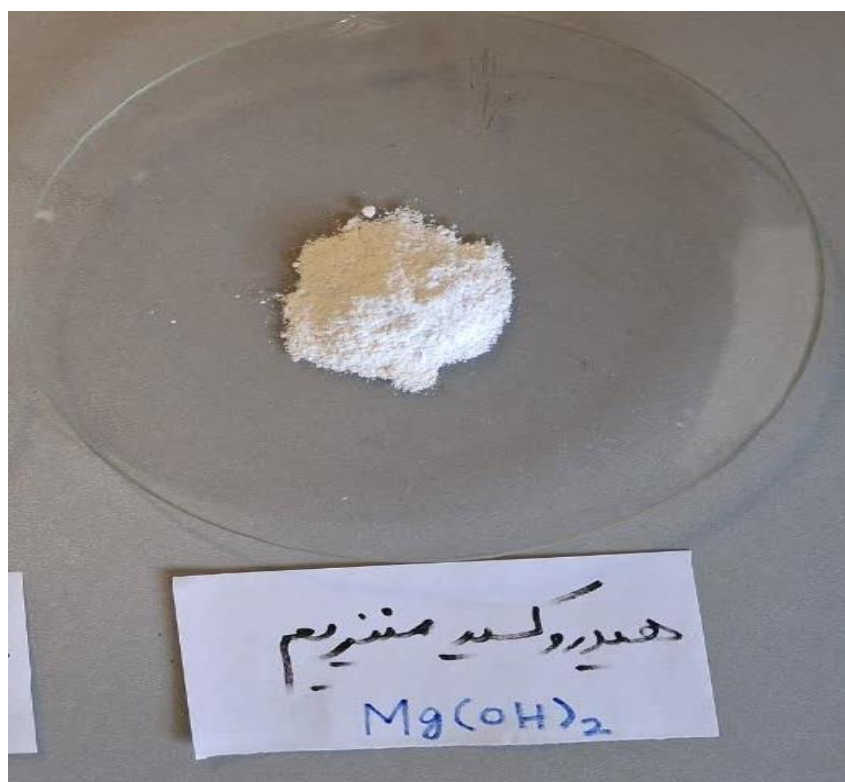
Figure 10 - Solid magnesium hydroxide

3.4.The effect of heat on the conversion of magnesium dioxide to magnesium oxide

To produce magnesium oxide (MgO), the thermal decomposition of magnesium hydroxide (Mg(OH)$_2$) was carried out at 600°C for 1 hour. To optimize the decomposition temperature, Mg(OH)$_2$ was heated at 500°C, 600°C, and 650°C for 1 hour each. Based on the results, 600°C was selected as the optimal temperature due to a 36% weight loss. The XRF results and XRD analysis of the thermally decomposed magnesium oxide are presented in Table 2 and Figure 11, respectively.

Table 2 - the XRF analysis results of magnesium oxide

P$_2$O$_5$ (%)	SO$_3$ (%)	TiO$_2$ (%)	MgO (%)	CaO (%)	Al$_2$O$_3$ (%)
0.01	0.32	0.01>	75.81	5.77	0.99
L.O.I (%)	Fe$_2$O$_3$ (%)	SiO$_2$ (%)	SrO (%)	K$_2$O (%)	Na$_2$O (%)
12.41	0.94	0.64	0.01	0. 1>	3.01
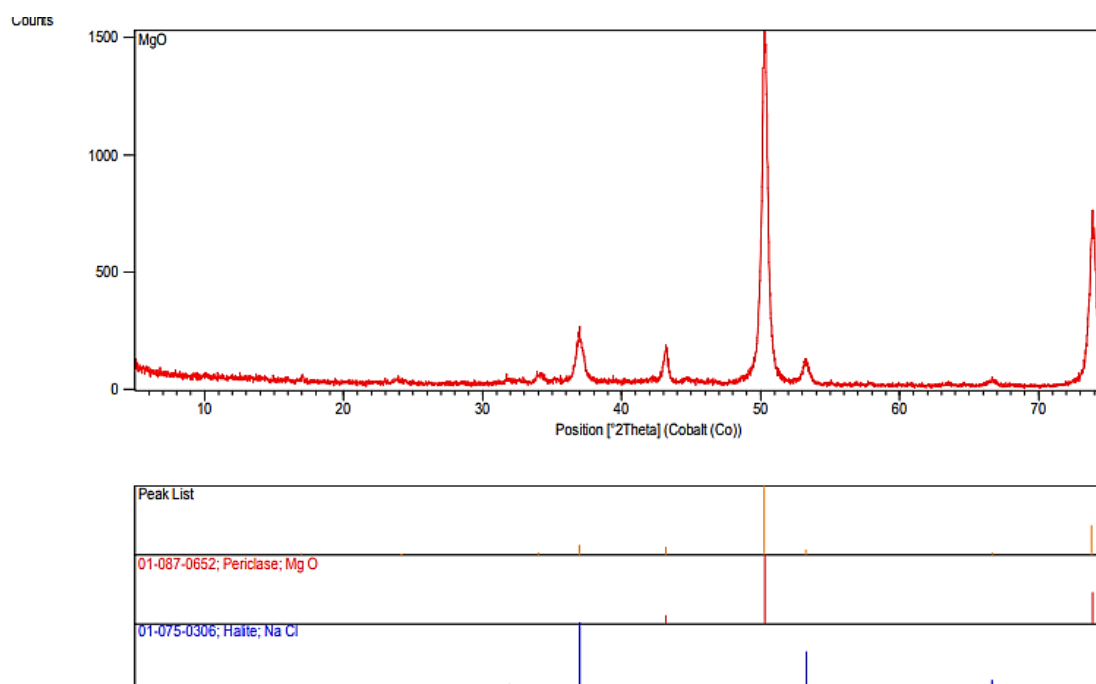
Figure 11 -the XRD patterns of magnesium oxide

4.Conclusion

A hydrochloric acid leaching process for magnesium extraction and magnesium oxide production from calcined dolomite ore was successfully demonstrated. Results showed that magnesium extraction efficiency increased with both rising hydrochloric acid concentration and higher liquid-to-solid ratio. The addition of sodium hydroxide proved crucial for pH adjustment to 8-9 to precipitate magnesium hydroxide (Mg(OH)$_2$), which is essential for optimal conversion to magnesium oxide (MgO). The optimized conditions included: dolomite calcination at 800°C, leaching with 2 M hydrochloric acid at 70°C with a 15:5 liquid-to-solid ratio for 3 hours, and pH maintenance at 8 -9 for hydroxide precipitation. Thermal decomposition at 600°C was identified as the optimal temperature for converting magnesium hydroxide to magnesium oxide.

References

1. Akhmedov, M., Dadakhodzhaev, A., & Guro, V. (2018). Technology of Processing of Navbakhore Dolomite on Magnesium Compounds. Open Access Journal of Chemistry, *2*(1), 1-6.

2. Amer, A. (1996). A contribution to hydrometallurgical processing of low-grade Egyptian dolomite deposits. Hydrometallurgy, *43*(1-3), 345-356.

3. *Azizi, A., & Jafarnejad, M.* (2017). Leaching of magnesium from dolomite ore in nitric acid solutions. International Journal of Mineral Processing, *166*, 45-51.

4. El-Naggar, M. R., El-Kamash, A. M., & El-Dessouky, M. I. (2009). Extraction of magnesium from hydrometallurgical tailings by hydrochloric acid leaching. Journal of Hazardous Materials, *168*(2-3), 832-837.

5. Kipouros, G. J., & Sadoway, D. R. (2001). Toward greener processes for the production of magnesium: An overview. Journal of Metals, *53*(5), 34-37.

6. Liu, Y., & Li, J. (2015). A novel process for the extraction of magnesium from dolomite by vacuum aluminothermic reduction. Journal of Alloys and Compounds, *619*, 634-638.

7. Royani, A., Sulistiyono, E., Prasetiyo, A., & Subagja, R. (2018). Extraction of magnesium from calcined dolomite ore using hydrochloric acid leaching. AIP Conference Proceedings, *1964*(1), 020030.

8. Warren, J. K. (2016). Evaporites: A geological compendium (2nd ed.). Springer.

9. Yildirim, M. (2008). Dissolution kinetics of Icel-Aydincik dolomite in hydrochloric acid. *Journal of the Southern African Institute of Mining and Metallurgy*, *108*(2), 127-132.

10. Yildirim, M., & Akarsu, H. (2010). Preparation of magnesium oxide (MgO) from dolomite by leach-precipitation-pyrohydrolysis process. Physicochemical Problems of Mineral Processing, *44*, 257-272

Magnetic Roasting of Hematite Ore and Enrichment by Magnetic Separation Method

khadijeh Pariyan[1]*, Mohsen Fatahpour[1], Mohammad mehdi Ravanfar[1]

[1] Mineral Processing Department, Mobarakeh Steel Company, Isfahan, Iran

*Corresponding author: kh.pariyan@yahoo.com (khadijeh Pariyan)

Abstract:

Hematite deposits and concentrate production from them can make a significant contribution to the steel production supply chain. The hematite/goethite reduction roasting method followed by enrichment with low-intensity magnetic separation is one of the new and high-potential solutions. In this study, the effect of temperature, reaction time, particle size, and ratio of reducing agent (coal) on roasting and the effect of field intensity on magnetic separation were investigated. Increasing the reaction time, temperature, and coal ratio in the roasting process and decreasing the magnetic field intensity in the Davis tube increased the grade. The highest iron grade (65.62%) was obtained at a temperature of 850°C, a reaction time of 2 h, and a coal ratio of 5%.

Keywords: *Roasting, Hematite, Iron, Magnetite*

1. Introduction

Some of the most important iron-bearing minerals include magnetite (Fe_3O_4), hematite (Fe_2O_3), goethite ($Fe_2O_3.H_2O$), siderite ($FeCO_3$), and limonite ($Fe_2O_3.nH_2O$) (Cornell & Schwertmann, 2003). Among the main iron ores, producing concentrate from magnetite is more cost-effective, easier, and the processing methods for magnetite ore have seen significant advancements due to its ferromagnetic properties (Lu, 2015). High-grade resources have been steadily decreasing over the years, and on the other hand, with the increasing demand for this metal, it is necessary to produce iron from the tailings of mines containing significant amounts of hematite and goethite, as well as from low-grade deposits, which also present many challenges(Li et al., 2010). The methods for producing concentrate from hematite deposits include gravity separation, flotation, separation high-intensity magnetic, and magnetic reduction. Concentrate production from high-grade deposits is typically carried out using gravity separation, flotation, and high-intensity magnetic separation methods (Cornell & Schwertmann, 2003). The magnetite reduction process is the only method capable of producing magnetite concentrate from low-grade hematite/goethite deposits (Li et al., 2010). Roasting is the process of heating materials at a temperature below their melting point to induce a chemical change that improves subsequent stages. Types of roasting processes include oxidative, evaporative, sulfatic, chloridic, and reductive roasting (Sohn & Wadsworth, 2013). The reduction process takes place in a furnace and in a reducing environment. If the product of the reduction process has magnetic properties, the process is referred to as magnetite reduction. In the next stage, after magnetite reduction, a crushing step is required, followed by separation using a low-intensity magnetic separator (Jang et al., 2014). Given the significant impact of parameters on the product of the magnetite reduction process, controlling these parameters is crucial and plays an important role in the environmental and economic assessments of the process. Important parameters of the process include temperature, time, particle size of the sample, amount of reducing agent used, and ... (Uwadiale, 1992). Magnetite reduction, compared to flotation, gravity separation, and high-intensity magnetic separation methods, is an effective and successful process for producing

concentrate from low-grade hematite/goethite ores (Uwadiale, 1992). Countries that use this method for concentrate production include China, India, and Australia (Cornell & Schwertmann, 2003). The mechanism of reductive roasting for hematite, considering that the reducing gas is CO, is as follows: The first stage is the diffusion of the reducing gas into the diffusion layer and its arrival at the surface of the particles. The second stage is the entry of the reducing gas into the pores and micropores within the particles. The third stage is the reduction process occurring at the surface of the hematite particles. The fourth stage is the exit of CO_2 from the pores and its movement to the diffusion layer. The fifth stage is the exit of the gas from the diffusion layer (Peng et al., 2017). Among the five stages, only the third stage is where the chemical reaction occurs, and the reduction takes place. In this stage, CO reaches the surface, removes oxygen from it, and produces two electrons along with CO_2 gas, as shown in reaction 1. The carbon dioxide gas is then removed from the particle through stages four and five. The separated electrons, according to reaction 2, reduce ferric iron (Fe^{3+}) to ferrous iron (Fe^{2+}). The ferrous ion (Fe^{2+}) present, according to reaction 3, reacts with the surface hematite and undergoes a transformation, leading to the formation of magnetite (Chen et al., 2017).

$$CO + O^{2-} \rightarrow CO_2 + 2e^- \tag{1}$$
$$Fe^{3+} + e^- \rightarrow Fe^{2+} \tag{2}$$
$$Fe_2O_3 + FeO \rightarrow Fe_3O_4 \tag{3}$$
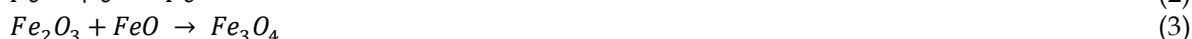
Studies on the processing of hematite using the roasting method have been conducted (Chen et al., 2017; Peng et al., 2017). Yu et al. (Yu et al., 2017) carried out the magnetite reduction process using coal as a reducing agent and low-intensity magnetic separation, achieving a grade of 65.4%. Nayak et al. (Nayak et al., 2019) investigated the reduction process using coconut shell as a reducing agent. Yuan et al. (Yuan et al., 2020) also examined reductive roasting and magnetic separation.

The aim of this research was to investigate the impact of parameters affecting the magnetite reduction method, such as particle size, temperature, reaction time, reducing agent, and others, in producing a product that can be used in the steel industry.

2. Material and methods

2.1. Material

The hematite used in this research was obtained from a hematite mine (Kerman, Iran). The chemical composition of the representative ore was characterized by X-ray diffraction (Asenware, AW/XDM300, China), X-ray fluorescence (pw1410, Netherlands), Differential thermal analysis (STA409PC), thin section and polish section (Kaywa polarizing microscope) analyses.

2.2. Method

Reductive roasting experiments were done using coal in a tube furnace (Azar furnace 1200, Iran), which was initially purged with nitrogen gas at a flow rate of 0.4 L per min for 20 min. After that, the inlet gas was closed and the furnace was set for 1 h to reach the desired temperature, and it was kept at this temperature for a certain period of time. After finishing the roasting, the furnace was turned off until reaching room temperature without air or oxygen purging the sample.

For this purpose, the prepared sample was first crushed to sizes smaller than 10 mm and subjected to magnetite roasting tests under various conditions of temperature, reaction time, and coal-to-ore ratio. Based on previous studies, the roasting temperature was examined in the range of 750 to 850°C, coal content between 3 to 5%, roasting time between 0.5 to 2 h, and particle sizes of 10 and 1 mm. After reduction roasting under different conditions, the samples were grind in a planetary mill for 10 min at

250 rpm, reaching a particle size of less than 45 mμ. Subsequently, magnetic separation was performed using a Davis tube with an intensity of 900 G.

3. Results and discussion

3.1. Sample characterization

In order to characterize the various properties of the raw hematite ore, several chemical, physical and thermal analyses were conducted. According to the XRD analysis, the main phases of the representative sample were quartz, hematite, gothite and dolomite (Fig. 1). Also, XRF analysis showed that the amount of Fe_2O_3 was 47.15% and SiO_2 was 18.90% (Table 1).
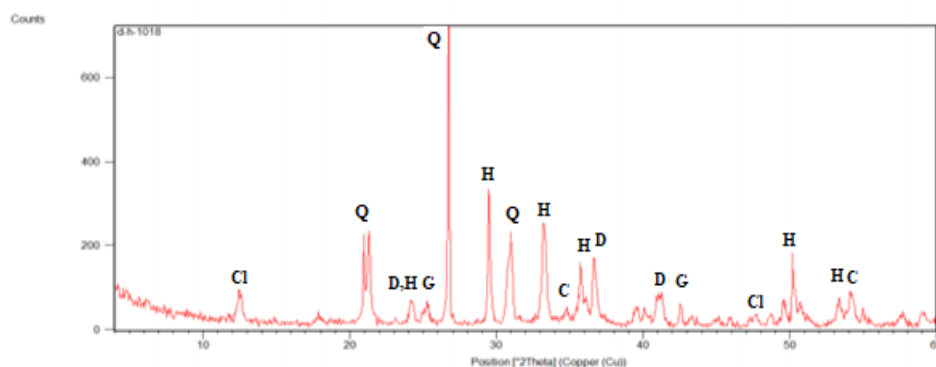
Fig. 1. X-ray diffraction pattern of the representative sample of the hematite ore (H: Hematite, Q: Quartz, D: Dolomite, G: Goethite, C: Calcite, Cl: Chlorite).

Table 1. Chemical composition of the representative sample of the hematite ore

Element	SiO_2	K_2O	CaO	MgO	Al_2O_3	Fe_2O_3	MnO	Na_2O	SO_3	P_2O_5	TiO_2	LOI
Content (% Wt)	18.90	0.14	8.58	3.67	2.81	47.15	2.05	0.11	0.1	0.08	0.33	16.04

In order to investigate the changes in the sample during the roasting process, such as the change of the crystal structure, the loss of molecular water, chemical decomposition and determining the temperature of the dehydration and reaction stages, thermogravimetry (TG) and differential thermal analysis (DTA) with a thermal gradient of 10 °C per min in atmospheric environment was done (Fig. 2).

By studying the behavior of the TG and DTA curves, it is observed that the DTA/TG analysis shows two endothermic peaks at temperatures around 320°C and 850°C, which are due to the reaction and structural transformation of the sample and are attributed to the release of adsorbed water. The 2% weight loss at 320°C is attributed to the transformation of goethite (FeOOH) to hematite (Fe_2O_3), as shown in the following equation 4. The 8% weight loss at the roasting temperature of 850°C is attributed to the decomposition of dolomite, as shown in equation 5.

$$2FeO.OH \rightarrow Fe_2O_3 + H_2O \tag{4}$$
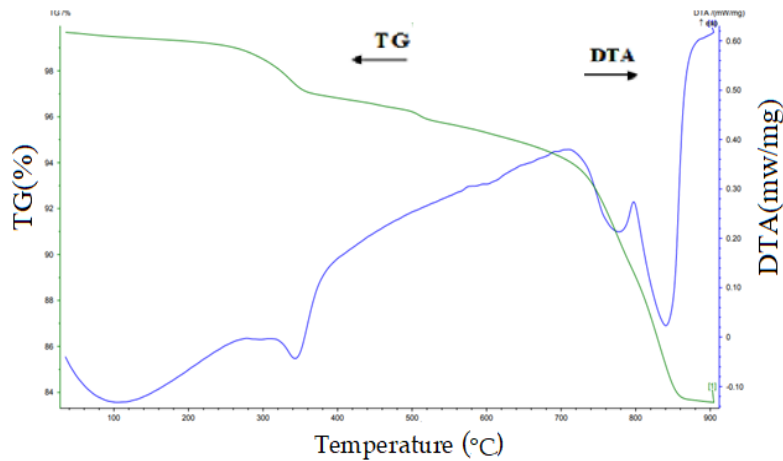$$CaMg(CO_3)_2 \rightarrow MgO + CaO + 2CO_2 \tag{5}$$

Fig. 2. Thermogravimetry (TG) and differential thermal analysis (DTA) curves for the hematite.

Microscopic images related to thin sections were prepared using transmitted light with parallel (PPL) and crossed (XPL) fibers. As can be seen in Fig. 3, they show that the sample contains mainly hematite and goethite exists in a dispersed and fine-grained form. The substitution of dolomite by iron oxides as a result of reaction with hydrothermal iron-bearing waters is observable.
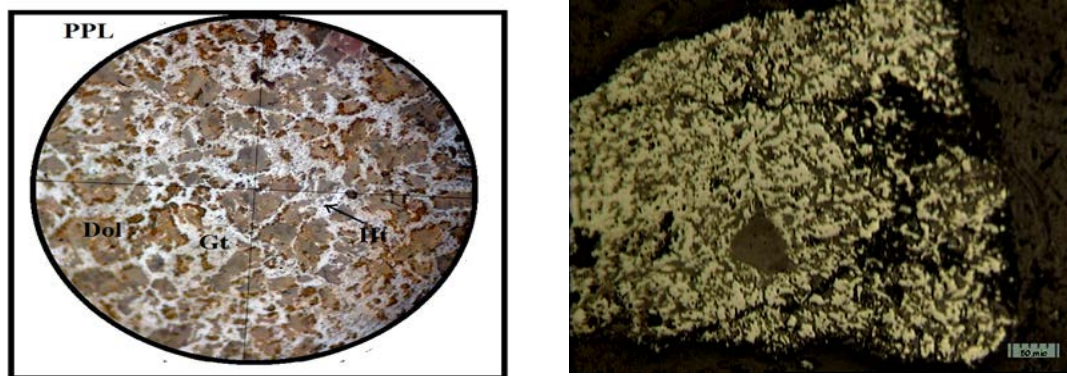

Fig. 3. Microscopic images of the hematite sample with polarizing microscope (Ht: Hematite, Gt: Goethite, Dol: Dolomite).

3.2. Effect of reductive temperature

In order to investigate the effect of temperature on the roasting process, experiments were conducted for reaction time of 1 h, particle size less than 10 mm, coal ratio of 5%, and temperatures of 750, 800, and 850°C. According to Fig. 4, with increasing roasting temperature, recovery decreased and grade increased. The reducing agent in these experiments is coal, and the coal reaction is completed by roasting at temperatures above 850°C (Pariyan et al., 2023). Therefore, magnetization is better at higher temperatures and increases the grade, which reaches 58.64%.
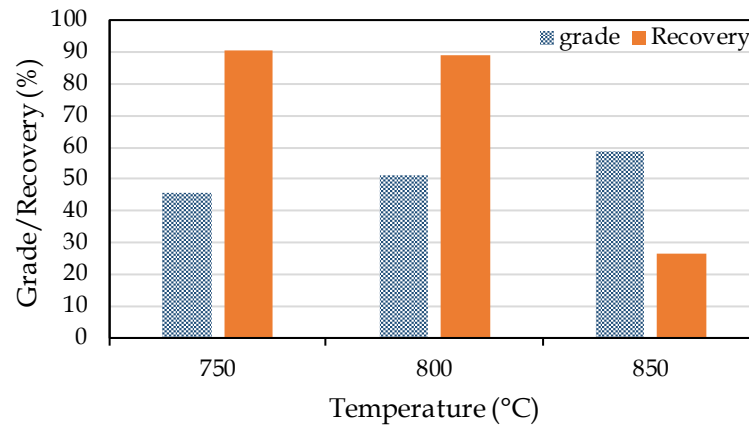
Fig. 4. Effect of roasting temperature on the grade and recovery iron

3.3. Effect of reaction time

The time parameter is very important in all engineering processes. This parameter shows itself well in process kinetics. The effect of reaction time on the roasting process was investigated at a temperature of 850°C, particle size less than 10 mm, coal ratio of 5%, times of 0.5, 1, and 2 h. Increasing the roasting time increased the grade and decreased the recovery. Increasing the roasting time, the more time the particles have to undergo the magnetization reaction. Considering that the particle size in these tests is less than 10 mm, the penetration of heat and the reducing agent into the particles takes time, and this reaction occurs faster in smaller particle sizes. Previous studies also show this trend (Ravisankar et al., 2019).
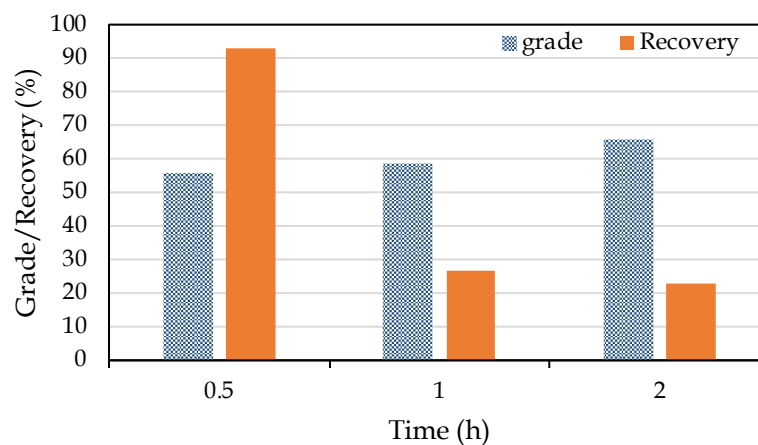
Fig. 5. Effect of reaction time on the grade and recovery iron

3.4. Effect of coal ratio

The effect of the coal ratio in the roasting process was investigated under the conditions of reaction time of 1 h, particle sizes smaller than 10 mm, a temperature of 850°C, and coal ratios of 3.5 and 5%. When less coal was used, the grade and recovery were 56.68 and 25.16%, respectively, which showed a difference of less than 2% compared to the 5% coal ratio. Since temperature is inversely related to the amount of reducing agent, it means that as the temperature increases, the amount of reducing agent required for the reduction process decreases (Sharma & Sharma, 2014). In this experiment, due to the high roasting temperature, the effect of the reducing agent amount is not significant.

3.5. Effect of particles size

In order to investigate the effect of particle size, particle sizes less than 1 mm were investigated. Roasting was carried out at a temperature of 850°C, 5% coal, and a roasting time of 1 h. The iron grade in Davis Tube concentrate reached 64.26%, resulting in iron recovery of 76.29%. The results of XRF and XRD analyses show that silica is the most important impurity present in the concentrate. When the particle is 10 mm, the heat cannot penetrate well inside the coarse particles, and the reaction occurs only in the upper layers, so gride was decresing (Pariyan et al., 2023).

Table 2. Chemical composition of the hematite ore after roasting

Element	SiO₂	K₂O	CaO	MgO	Al₂O₃	Fe₂O₃	MnO	Na₂O	SO₃	P₂O₅	TiO₂	LOI
Content (% Wt)	5.18	0.14	1.6	1.06	0.8	91.8	1.15	0.05	0.07	0.05	0.07	-2.24
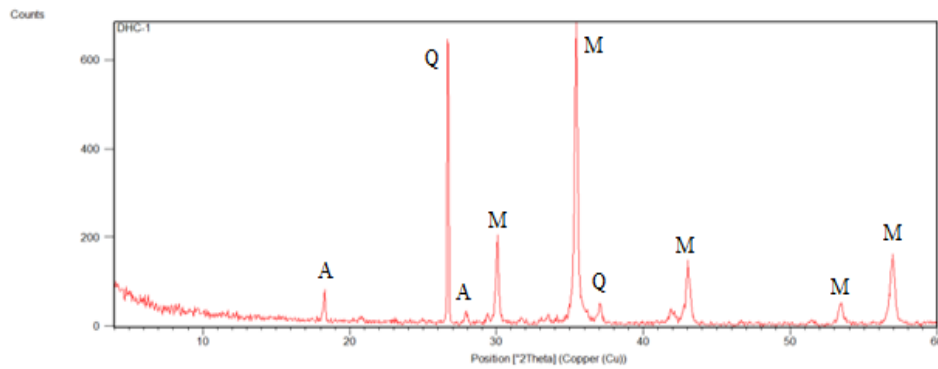
Fig. 6. X-ray diffraction pattern of the representative sample of the hematite ore after roasting (M: Magnetite, Q: Quartz, A: Albite).

3.6. Effect of magnetic field intensity

The effect of magnetic field intensity under roasting conditions of 850°C, reaction time of 1 h, particle size smaller than 10 mm, and 5% coal content was investigated, with magnetic field intensities of 700, 800, and 900 G examined. The highest iron grade was 64.22% at a magnetic field intensity of 700 G. As the magnetic field intensity increased, most of the intermediate particles, which include both magnetic and non-magnetic particles, entered the concentrate. As a result, the recovery increased, but the grade decreased.
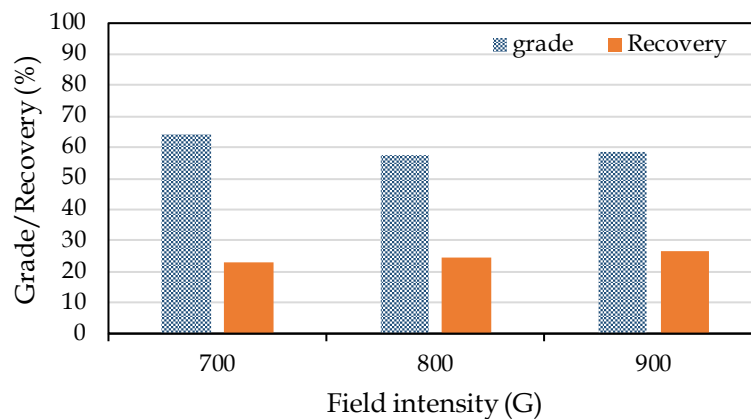

Fig. 7. Effect of magnetic field intensity on the grade and recovery iron

351

4. Conclusions

Magnetic roasting of hematite ore was carried out using a coal reductant, and then magnetic separation was carried out using a Davis tube, which yielded the following results:

- Increasing roasting time and temperature increased the grade and decreased the recovery.

- By reducing the particle size, the grade increased due to the faster particle diffusion reaction.

- The highest iron content (65.62%) was obtained at a temperature of 850°C, a reaction time of 2 h, and a coal ratio of 5%.

- Increasing the magnetic field intensity caused a decrease in grade because locked non-magnetic particles also found their way into the concentrate.

Acknowledgments

References

Chen, H., Zheng, Z., Chen, Z., & Bi, X. T. (2017). Reduction of hematite (Fe_2O_3) to metallic iron (Fe) by CO in a micro fluidized bed reaction analyzer: A multistep kinetics study. *Powder Technology*, *316*, 410-420. doi: https://doi.org/10.1016/j.powtec.2017.02.067

Cornell, R. M., & Schwertmann, U. (2003). *The iron oxides: structure, properties, reactions, occurrences, and uses* (Vol. 664). Wiley-vch Weinheim.

Jang, K.-o., Nunna, V. R., Hapugoda, S., Nguyen, A. V., & Bruckard, W. J. (2014). Chemical and mineral transformation of a low grade goethite ore by dehydroxylation, reduction roasting and magnetic separation. *Minerals Engineering*, *60*, 14-22. doi: https://doi.org/10.1016/j.mineng.2014.01.021

Li, C., Sun, H., Bai, J., & Li, L. (2010). Innovative methodology for comprehensive utilization of iron ore tailings: Part 1. The recovery of iron from iron ore tailings using magnetic separation after magnetizing roasting. *Journal of hazardous materials*, *174*(1-3), 71-77. doi: https://doi.org/10.1016/j.jhazmat.2009.09.018

Lu, L. (2015). *Iron ore: mineralogy, processing and environmental sustainability*. Elsevier.

Nayak, D., Dash, N., Ray, N., & Rath, S. S. (2019). Utilization of waste coconut shells in the reduction roasting of overburden from iron ore mines. *Powder Technology*, *353*, 450-458. doi: https://doi.org/10.1016/j.powtec.2019.05.053

Pariyan, K., Ahmadi, A., & Hosseini, M. R. (2023). Effect of thermal pretreatment on the two-stage extraction of aluminum, sulfur and potassium from a fine-quartz bearing alunite. *Minerals Engineering*, *204*, 108430. doi: https://doi.org/10.1016/j.mineng.2023.108430

Peng, T., Gao, X., Li, Q., Xu, L., Luo, L., & Xu, L. (2017). Phase transformation during roasting process and magnetic beneficiation of oolitic-iron ores. *Vacuum*, *146*, 63-73. doi: https://doi.org/10.1016/j.vacuum.2017.09.029

Ravisankar, V., Venugopal, R., & Bhat, H. (2019). Investigation on beneficiation of goethite-rich iron ores using reduction roasting followed by magnetic separation. *Mineral Processing and Extractive Metallurgy*, 128(3), 175-182. doi: https://doi.org/10.1080/03719553.2017.1412876

Sharma, J., & Sharma, T. (2014). Beneficiation of low grade iron ore fines by magnetizing roasting. *Int. J. Engineering. Research. & Science. & Technology*, *3*(2), 59-64.

Sohn, H. Y., & Wadsworth, M. E. (2013). *Rate processes of extractive metallurgy*. Springer Science & Business Media.

Uwadiale, G. (1992). Magnetizing reduction of iron ores. *Mineral Processing and Extractive Metullargy Review*, *11*(1-2), 1-19. doi: https://doi.org/10.1080/08827509208914211

Yu, J., Han, Y., Li, Y., & Gao, P. (2017). Beneficiation of an iron ore fines by magnetization roasting and magnetic separation. *International journal of mineral processing*, *168*, 102-108. doi: https://doi.org/10.1016/j.minpro.2017.09.012

Yuan, S., Zhou, W., Han, Y., & Li, Y. (2020). Selective enrichment of iron particles from complex refractory hematite-goethite ore by coal-based reduction and magnetic separation. *Powder Technology*, *367*, 305-316. doi: https://doi.org/10.1016/j.powtec.2020.04.004

Iron grade increasing possibility of concentrate at Opal Parsian Sangan Industrial and Mining: Statistical study, Waste minerals characterization and Chemicals in flotation.

Shima Rahimi[1]*, Jafar Nikmanesh poor[2], Omid Alimohammadi[3], Atiyeh Eslamian[4]

Reza Arjmand[5].

[1] Research and development manager in OPSIM company

[2] Head of Production in OPSIM company

[3] Head of Production Technical Office in OPSIM company

[4] Control quality manager in OPSIM company

[5] Technology manager in OPSIM company

*Corresponding author: Sh.rahimi1983@gmail.com (Shima Rahimi)

Abstract:

One of the most important indicators in the target market of iron concentrate is grade factor and low grade of concentrate will cause to numerous problems throughout the steelmaking chain. In this research, after initial characterization of different mines in the Sangan region, different kinds of feed compositions entering to the concentrate unit, using XRD, XRF and mineralogy methods to identifying the type of gangue minerals into concentrate. With statistical investigation of affective factors on iron grade, solutions have been presented regarding to the removal of these gangue minerals. The initial characterization results of various mines showed that the main minerals in the Baghak anomaly were Pyrite and carbonate minerals; CN anomaly, Pyrite, Pyrrhotite, Biotite and Clay minerals; Dardvay anomaly, Pyrite, Chlorite, and Biotite; B anomaly, Calcite and A anomaly, Pyroxene. Statistical studies demonstrated that excluding lowest grade level (65-65.3%), sulfur amounts in concentrate are approximately constant (0.3-0.35%). While, consequences disclose when the total amount of oxide impurities reduce from 6.8% to 5.6%, concentrate grade rises from 65 to 66. Also, investigating of main factors including of feed grade, iron oxide, sulfur content and percentage of impurities and concentrate size distribution, show a significant correlation coefficient (0.1-0.4) with the concentrate grade. Also, by adjusting the feed composite, three main compositions from different mines were fed to the concentrate unit, and the mineralogical analysis of their concentrates showed that the main gangue minerals present are included silicate and carbonate minerals of aluminum, silicon, magnesium and calcium. To remove these minerals, mixing of sodium isopropyl xanthate (SIPX) and dodecyl ammine (DDA) collectors and adjusting the pH of pulp were used. Finally, the results showed an increase in the concentrate grade from 66.2 to 66.65%.

Keywords: Iron grade, Statistical study, Characterization, Gangue minerals, Flotation.

Introduction

First product obtained from iron rock is concentrate during the steel production chain. Iron concentrate have quality characteristics that the most important are included Fe, FeO and sulfur content, moisture and blain number. Among them Fe content (Fe grade) has a particular importance and effects quantity and quality of pellets, sponge iron and steel. Therefore, maintaining iron grade in permitted range for customers has exclusive significance. Due to fluctuations of input feed during

recent years for instance feed iron content, process plants have faced with iron grade decreasing in final concentrate. For this reason, efforts and studies continue to achieve higher iron grade.

One of the most important iron deposit in Iran is sangan iron ore mines that is located in the Khorasan-Razavi Province, Middle East of Iran with an iron ore reserve more than 1.2 billion tons. Opal Parsian Sangan Industrial and Mining (OPSIM) Company, located at 18 km north-east of Sangan, started its activity on 2012. OPSIM is the first iron ore processing plant in Sangan region annually produces 2.6 million tons of concentrate with an iron grade of more than 66% (Ghasemi, et al. 2019). Products are included iron concentrate and pellets where nominal capacity of beneficiation plant is 3.1 million tons per year and pelletizing plant is 5 million tons per year. Also, the 2.4 million-ton concentrate factory is in the stage of equipment installation and ready for operation in 2025. Pellets production is used to complete the steel production chain. In the OPSIM plant, the processing circuit consists of four sequential steps of low-intensity magnetic separation and flotation cells. The drum type magnetic separators have a diameter of 1220 mm, a length of 2400 mm, and a magnetic intensity of 1300 Gauss. The flotation process is consisting of conditioner, rougher, cleaner and scavenger stages that its purpose is removing sulphur present in the iron ore concentrate as pyrites (Nikmanesh poor, et al. 2015).

Nowadays, by decreasing the ore grades, ordinary methods do not have good efficiency for processing of iron ores. In the recent years, iron grade and liberation degree of valuable minerals in raw materials deal to extreme reduction (Rahimi, et al. 2017). Since, design of plant equipment were conducted based on rock with higher grade and quality, production grade reach to lower amounts. It seems, optimization and modification for upgrading circuit of concentrate production is essential in these conditions. The froth flotation always introduces as an effective method for beneficiation of iron concentrates (Corathers, et al. 2006 and Mishra, et al. 2009). Also, collectors as surfactant agents play the most important role in the flotation of minerals (Mehdilo, et al. 2014 and Rahimi, et al. 2017). Anionic collectors especially xanthate groups are common in iron and sulfur flotation. Also, these collectors have high efficiency and availability, they aren't effective about other impurities. The cationic collectors are commonly used in the flotation of oxide and silicate minerals (Bulatovic, et al. 2010, Fen, et al. 2009, Fuerstenau, et al. 2005 and Gao, et al. 2017). Since, impurities present in the iron concentrate classified in the silicate oxide minerals, so the cationic collectors can play an important role in their removal.

In this research, one of the most important problem in iron beneficiation plant as iron grade was investigated. Firstly, different samples from various anomalies at sangan ore deposit were studied and main impurities present were recognized. Then, different influential factors on grade reduction were monitored and it was identified one of the most effective parameters on grade concentrate using statistical methods. In the final stage, appropriate methods have suggested in chemical reagents and flotation process for upgrading of concentrate.

1. Material and methods

1.1. Iron ore sample

The Sangan iron ore mine is located in the Khorasan-Razavi Province, east of Iran. It is one of the largest iron mines in Iran and in the Middle East with an iron ore reserve more than 1.2 billion tons. The most important anomalies in this area are known by the names of Northern Crooks (CN), Baghak (BG), Dardvay (DV), A and B. These anomalies have had different physicochemical properties and different composition of them effect on concentrate quality especially iron grade. The samples used in this work was taken from the all anomalies as representative. For this purpose, total samples were taken in a one-month period and then, the samples were communicated, separated, homogenized and used for characterization methods. These samples with the size of -150+45 μm were prepared by grinding and sieving taken from the deposit. Also, by adjusting of feed composite, three main

compositions from different mines were fed to the concentrate plant, and were conducted the mineralogical analysis of feed and concentrate samples.

1.2. Statistical methods

By statistical methods including of histogram, fish-bone, rout-cause analysis and scatter plots, different impressive parameters and its impact coefficient were investigated using Minitab 2022 software. The main categories including of raw material, equipment and process and sub-factors are influenced on grade fluctuations. Based on root-cause analysis forms; fish-bone diagram was prepared. It became clear that, various parameters including of iron grade, iron oxide and sulfur content of feed, size distribution of concentrate and other impurities are decisive about product quality and iron content.

1.3. Characterization methods

The mineralogical composition of the anomaly samples was determined by Philips-Xpert Pro X-ray diffraction (XRD) analyzer. Philips PW 1400 X-ray Fluorescence (XRF) analyzer was used for determining the chemical composition of the sample. The Fe and FeO contents of the sample were chemically determined by titration with potassium dichromate according to the ASTM E246 and ASTM D3872 standard test methods, respectively. The sulfur content of the sample was determined by Leco instrument. Different phases of the samples were determined through high-resolution imaging using mineralogy by Zeiss transmitted polarizing optical microscope in Iran mineral processing research center in Alborz province; with production of thin and polished sections.

1.4. Flotation experiment

The flotation experiments were carried out on 300 g of ore sample with a -150µm size fraction in a 1l Denver cell with a solid percentage of 25% (wt.%). After mixing and agitating the pulp for 4 min, the pH of the pulp was adjusted in a range of 7-7.5. Then the collector agents including of DDA and SIPX were added (100 g/t) and the suspension was conditioned for 5 min for each of them. Finally, MIBC (70 g/t) as frother agent was added with a conditioning time of 2 min. The froth phase was collected for 4 min. The flotation concentrate and tailing were filtered, dried and weighed, and analyzed by titration.

2. Results and discussion

2.1. Characterization results

The samples used in this work were taken from different anomalies were analyzed by XRF and the mineralogical compositions were determined using X-ray Diffraction (XRD) analysis. The result of semi-quantitative mineralogy was shown in Table 1 and presented in Fig.1 A-C section (A, B and C are related to BG, CN and DV, respectively). The results showed that the most amount of sulfur as the known main disturbing element; there is as Pyrrhotite and Pyrite minerals in BG, CN, D and A anomaly, respectively. It is noteworthy that, sulfur in Pyrrhotite form is exist in BG and CN anomaly. Also, there is the highest amount carbonate minerals and calcite in BG and A, B anomalies, respectively. Clay minerals and biotite are present at CN and DV anomalies.

According to XRD and XRF analysis, there are Al_2O_3, SiO_2, MgO and CaO as main impurities besides sulfur in all anomaly samples (Khaphaje, 2019). Since, there isn't any suitable reagent for their removing, presence of oxide impurities up to the flotation stage and failure of elimination in the various magnetic separation can lead to a reduction of final concentrate product grade. Therefore, it was investigated detecting an appropriate technique for removing these impurities in the next step.

Table 1. Result of semi- quantitative analysis of XRD and XRF.

Minerals name	Chemical formulas	Anomaly name				
		BG	CN	DV	B	A
Pyrite	FeS2	55	40-45	35	-	10
Carbonate minerals	(Ca,Mg,Fe)(CO3)2	25-30	-	-	-	-
Pyrrhotite	Fe1-xS	5-8	10-15	3	-	5
Magnetite	Fe3O4	5	-	15-20	70	55
Pyroxene	XY(Si,Al)2O6	5	5	-	5	10-15
Chalcopyrite	CuFeS2	< 2	< 2	-	-	-
Hematite	Fe2O3	-	-	-	10	5
calcite	CaCO3	-	-	-	15	5-10
Biotite	K(Mg,Fe)3AlSi3O10(F,OH)2	-	15	25	-	-
Clay minerals	-	-	5-10	5	-	5
Chlorite	(Mg,Fe)3(Si,Al)4O10	-	10-15	-	-	-
Amphibole	NaCa2(Mg,Fe,Al)5(Al,Si)8O22(OH)2	-	-	10	-	-
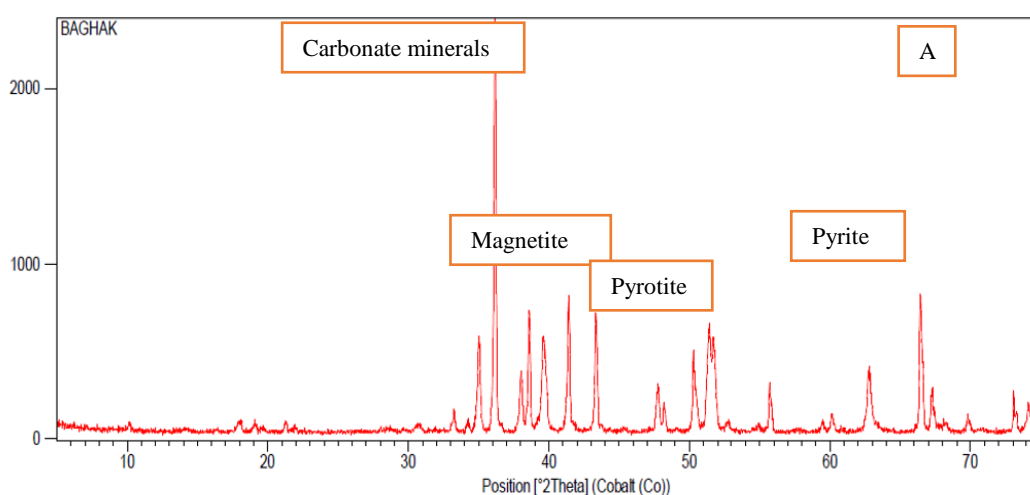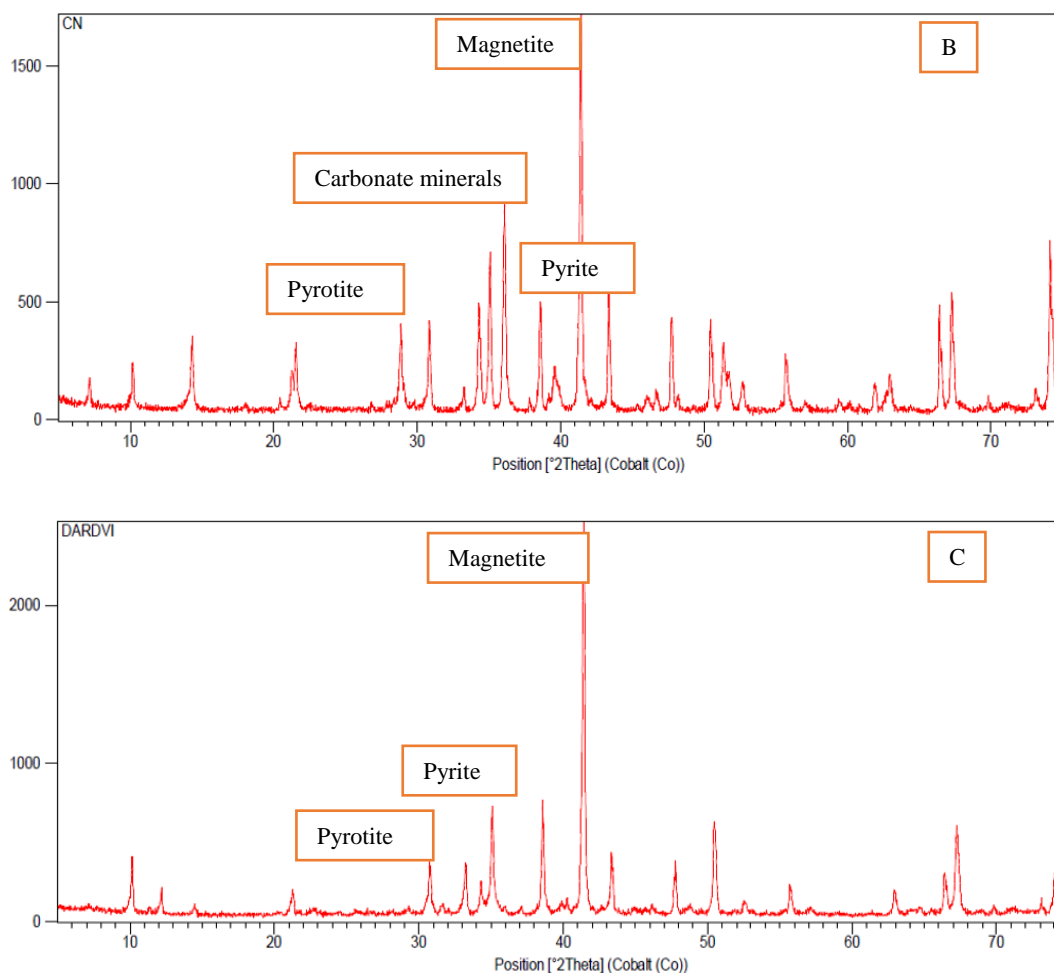
Fig.1 XRD results of different anomalies (A, B and C are BG, CN and DV, respectively).

In this phase, the samples related to main feed, flotation feed and flotation product were studied in 278 days of one working year. These data were categorized in different grade levels of concentrate and were brought in Table 2. The results demonstrated that excluding lowest grade level (65-65.3%), sulfur amounts are approximately constant (0.3-0.35%). Thus, sulfur content couldn't be an influential factor on grade of iron concentrate. Consequences disclose, when the total amount of oxide impurities reduce from 6.8% to 5.6%, concentrate grade rises from 65 to 66. Therefore, one of the most important elements in maintaining the concentrate grade in the acceptable district is related to the amount of impurity removal. Consequently, it should be used adequate chemical reagents for impurity removal in flotation as final upgrading process.

Table 2. Sulfur and other impurities content at grade levels of concentrate.

Grade levels	Concentrate sulfur (%)	Feed impurities (%)	Concentrate Impurities (%)
65-65.3	0.63	31.12	6.8
65.3-65.5	0.35	27.93	6.41
65.5-65.8	0.33	26.27	6.09
65.8-66	0.3	25.74	5.9
> 66	0.3	25.18	5.63

2.2. Statistical study results

Iron grade is the most important qualitative indicator of concentrate for the market supply. The results of investigating obtained data from 278 days in Fig. 2, showed that the highest frequency data are in the range of 66-66.3%. These data constitute 45% of total data, approximately. Mean grade and standard deviation of the results are 66% and 0.316, respectively. Also, skew the normal histogram graph is toward to the right and higher than 66.3%.

Three main categories including of raw material, equipment and process are influenced on grade fluctuations. In this part, divers reasons are introduced as sub-factors and subset of main reasons. Based on the frequency of these causes in different days in root-cause analysis forms; fish-bone diagram was prepared in Fig. 3. Survey show the factors inclusive of feed iron content, feed iron oxide content, feed sulfur percentage, percentage of other impurities and concentrate size distribution are the most conspicuous.
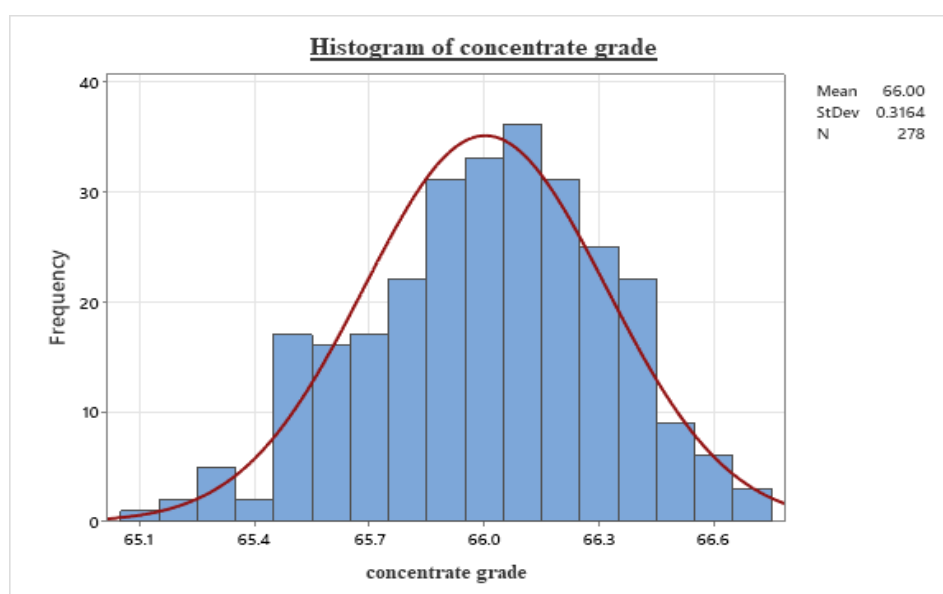
Fig .2 Normal histogram for concentrate grade in 278 working days.

In the next step, were plotted diagram of relationship between main effective factors and grade indicator (Fig. 4 A to F) and correlation amount was calculated. Results of correlation number for various factors were brought in Table 3. These results illustrate that Fe content of concentrate increase with increments of Fe, sulfur and FeO content in raw materials. This issue show that rocks with higher sulfur content for instance BG, CN and DV anomalies produce better grade of concentrate. Also, Fe grade rise with reduction of tonnage and impurity content of feed and d_{80} of concentrate. Therefore, feed tonnage increase maybe leads to lack of control on size distribution and d_{80} in production and decline of grade content. Among the examined parameters, the most relevant factors are d80 of concentrate, tonnage, Fe and sulfur content, impurity and FeO content of input feed, with -0.479, -0.319, +0.19, +0.138, +0.094 and -0.09 correlation coefficients, respectively.
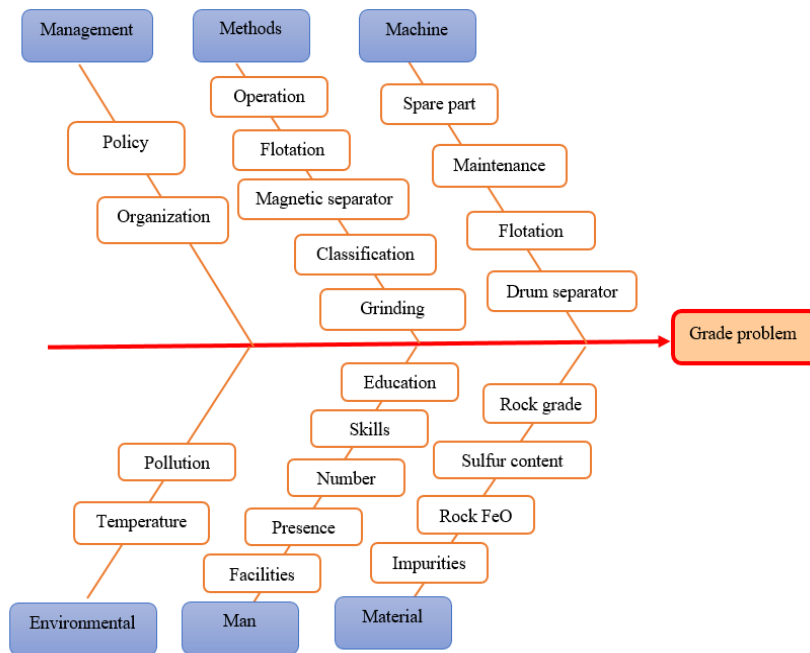
Fig .3 Fish-bone diagram for grade problem based on root-cause analysis forms.

The interesting point is that among the impurities present, increasing sulfur content in raw material causes to Fe grade rising. While, other impurities content has destructive effect on product grade. It seems, there is appropriate solution for sulfur removal in flotation process when other impurities exist in small quantities, but with other impurities rise there aren't suitable reagent for their removing. Therefore, suitable reagents in flotation process for impurities reduction were experimented in the next step.
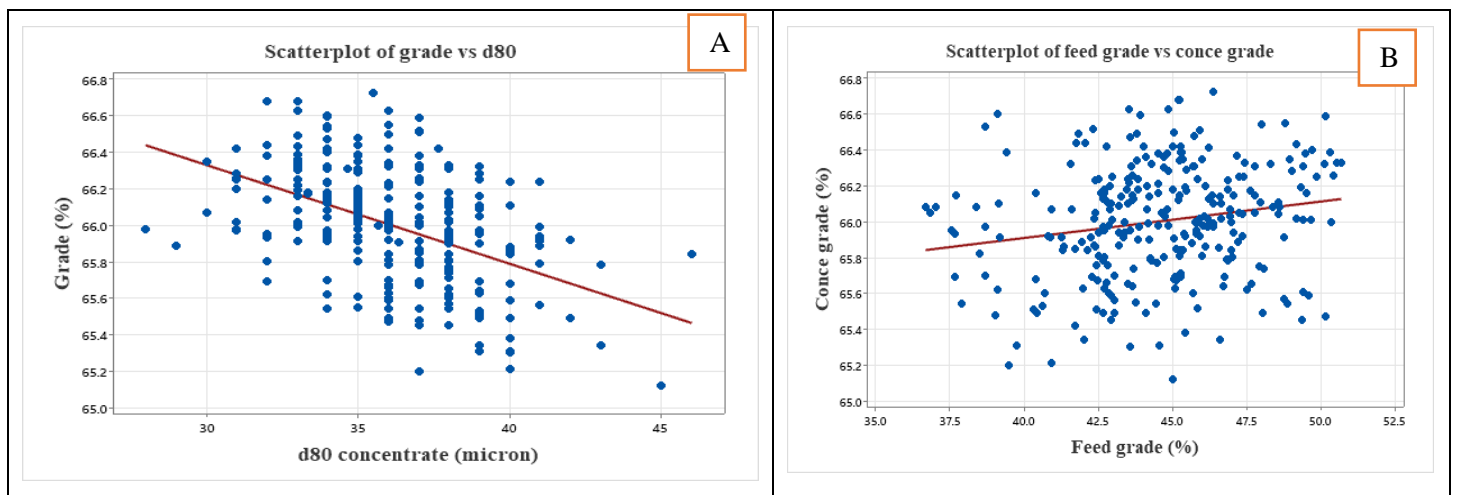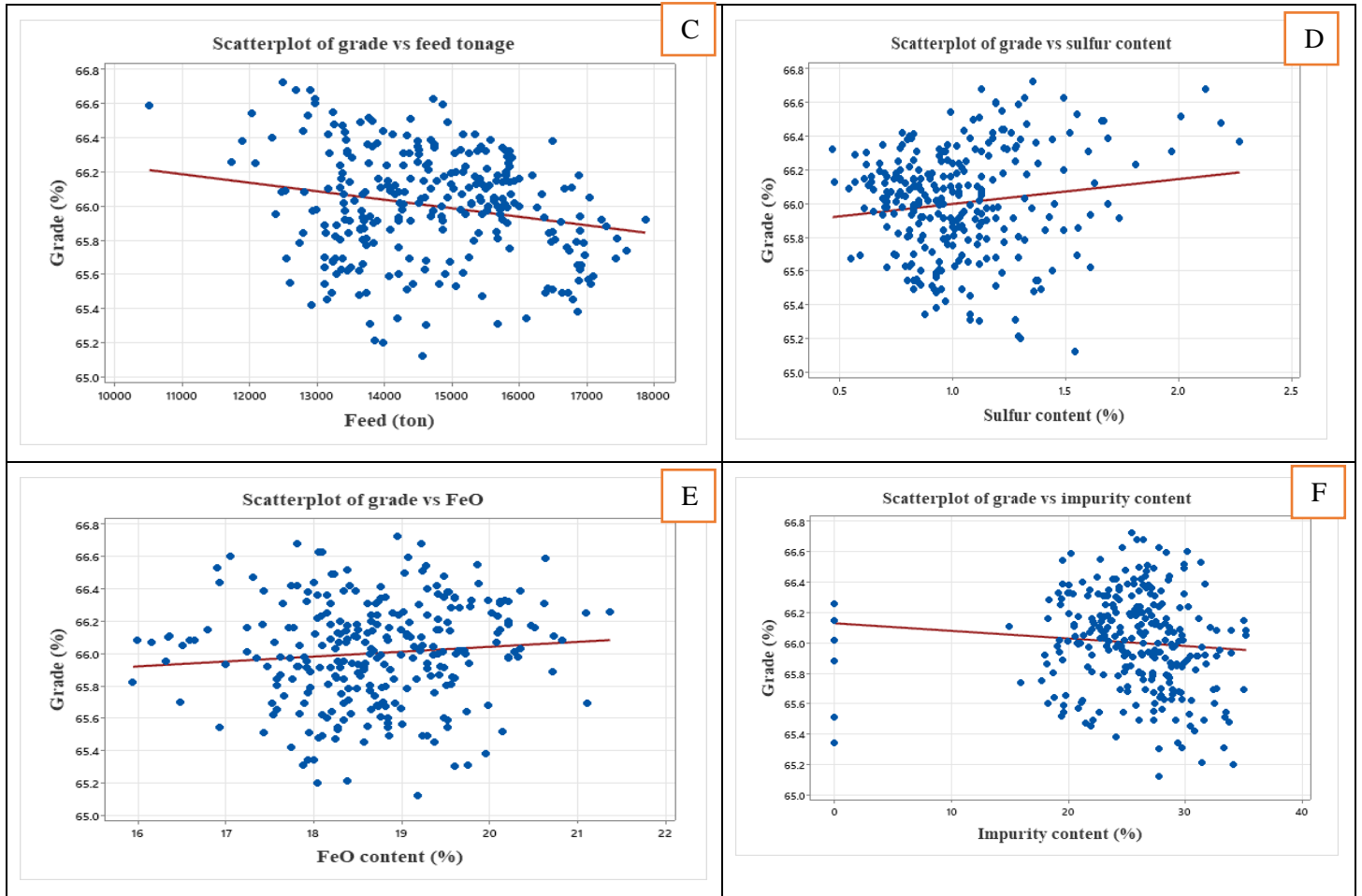
Fig 4. Scatterplots for main effective factors on concentrate grade.

Table 3. Correlation coefficient for main effective factors on concentrate grade.

Factors name	units	Correlation coefficient
D80 concentrate	Micron	-0.479
Feed Fe grade	%	+0.19
Feed tonnage	Ton	-0.319
Feed sulfur content	%	+0.138
Feed FeO content	%	+0.094
Feed impurity content	%	-0.09

2.3. Flotation results

In this phase, for determining the chemical and mineralogical composition of feed and concentrate; three main probable combinations from different anomalies were fed to the concentrate plant, and were taken samples from feed and production. Amount of each anomaly in these three composite were given in Table 4. Phase composition related to these three main compositions were shown in Fig 5. A to C. Results illustrate that in composition 1 with 70% from A and B anomalies, main impurities in input feed are Calcite and Diopside that there are both of them in concentrate composition as major

minerals. Although CN constitutes the main part of the structure in composition 2, the main phases of impurities are Calcite, Diopside and Phlogopite in concentrate product. In the case of composition 3 with higher amount of BG and DV, in addition to Diopside, Pyrrhotite adds as main impurity to concentrate composition too. Consequently, silicate and carbonate minerals of aluminum, silicon, magnesium and calcium are the most important groups which are present with the concentrate as interfering compounds.

Table 4. Anomaly amounts in three main composite of feed.

Composition name	Contribution of anomalies (%)				
	CN	BG	DV	A	B
Composition 1	20	5	5	35	35
Composition 2	48	8	8	18	18
Composition 3	35	20	15	20	10

Since, there aren't any used suitable reagent in flotation process for other impurities removing, in this research, individual chemicals were suggested for reduction of identified impurities in ore characterization instead of ordinary reagent in iron ore flotation. The flotation experiments carried out at conventional conditions of concentrate plant and with identical consumption (100 gr/ton collector and 70 gr/ton frother). Based on the previous literatures, cationic collectors can froth oxide mineral such as calcite and quartz (Rahimi, et al. 2017). In this research, it was applied DDA as cationic collector. The flotation tests were carried out at pH=7.5 using different dosages of DDA and SIPX. The optimal results are presented in Table 5. The Fe content concentrates and Fe recovery produced using mixing both collectors and each collector alone was reported in the Table 5. The results show that using DDA and SIPX as mixing can increase Fe content from 66 to 66.6%. Obtained Fe recovery in the concentrates by mixing collectors is a little less than SIPX. These results show that a final concentrate containing almost 66.6% Fe with 97.5% recovery can be produced by the combination of anionic and cationic collectors in flotation process.
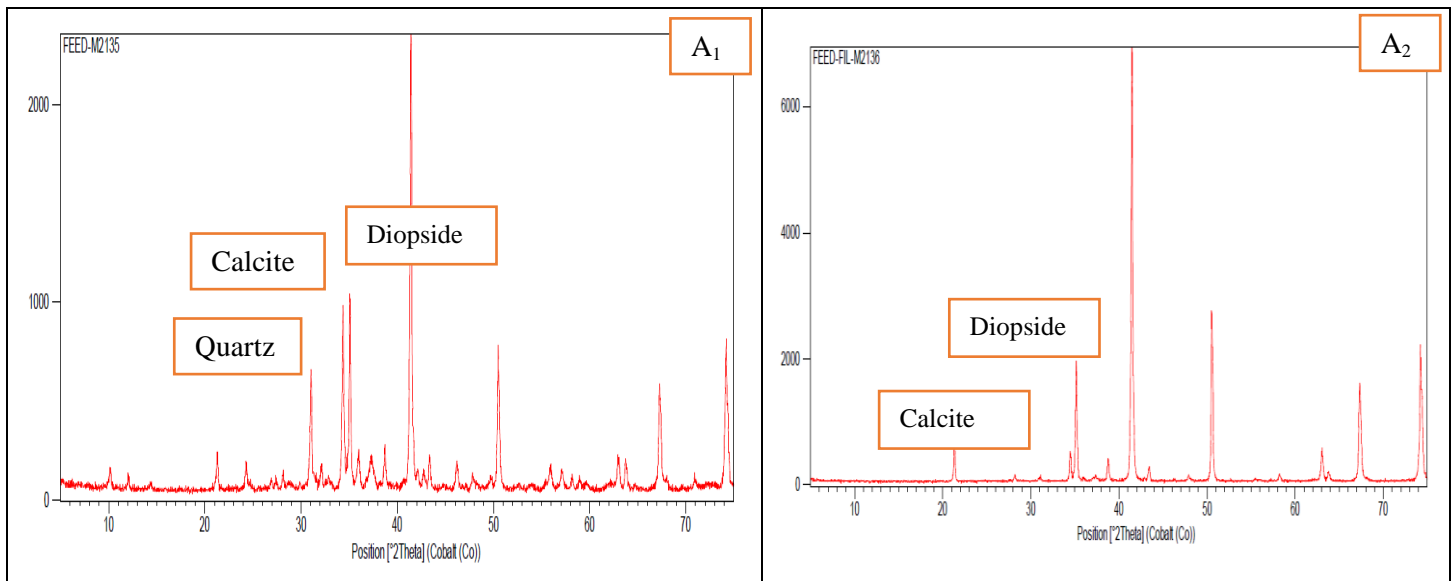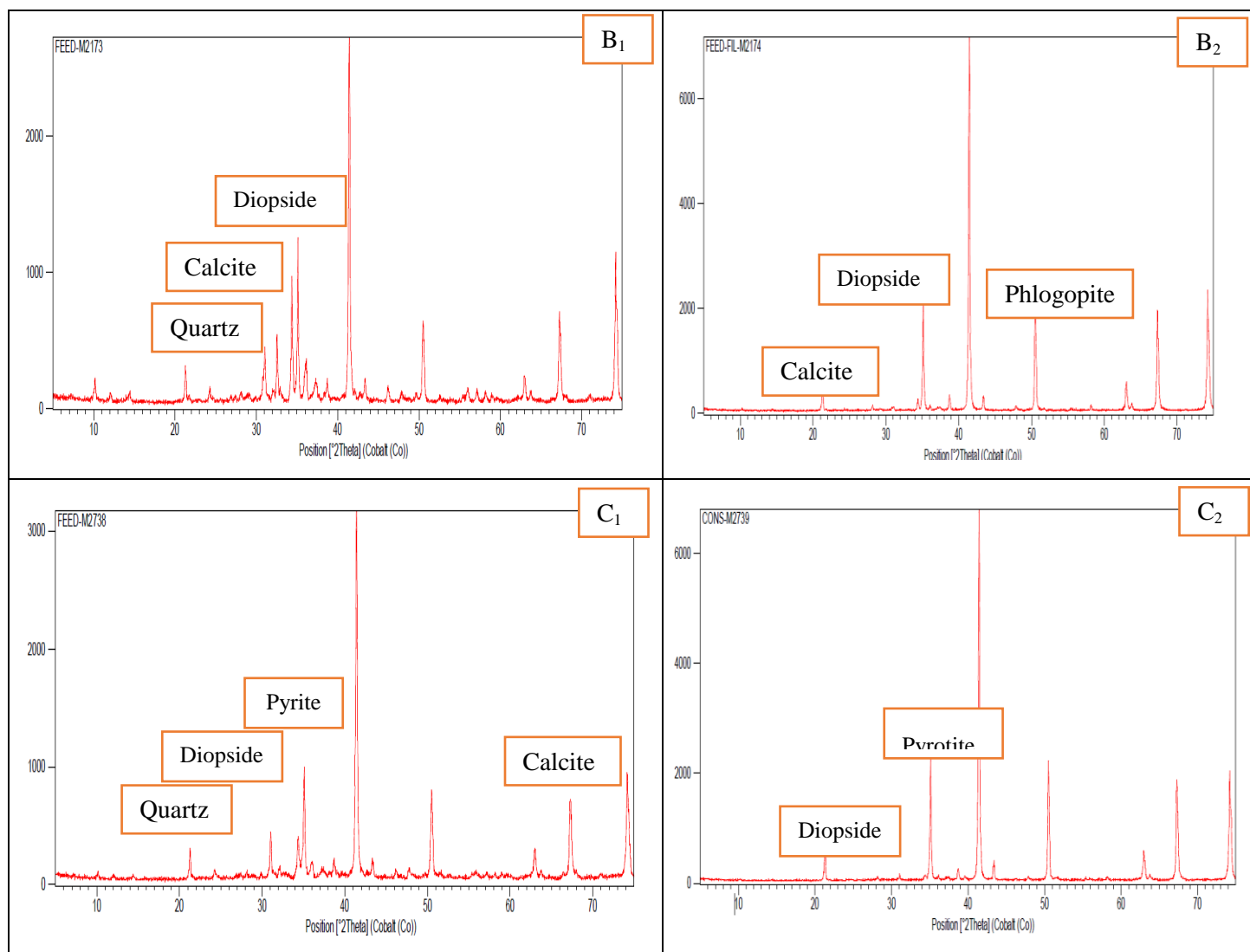
Fig 5. Phase composition of three main compositions (A_1, A_2: feed and concentrate of composite 1, B_1, B_2: feed and concentrate of composite 2 and C_1, C_2: feed and concentrate of composite 3).

Table 5. Fe content and Fe recovery produced by mixing collectors in flotation tests.

Composition name	Fe (feed)	Fe (concentrate)	Fe (tail)	Weight recovery	Fe recovery	S (feed)	S (concentrate)
SIPX							
Composition 1	65.82	66.18	35.8	98.8	99.35	0.388	0.118
Composition 2	65.95	66.23	35.18	98.5	99.5	0.558	0.282
Composition 3	65.89	66.2	35.5	98.9	99.45	0.554	0.322
SIPX + DDA							
Composition 1	65.82	66.58	36.87	97.4	98.56	0.388	0.115
Composition 2	65.95	66.65	37.06	97.63	98.66	0.558	0.275
Composition 3	65.89	66.63	36.9	97.51	98.6	0.554	0.35

3. **Conclusion**

- The most amount of sulfur; there is as Pyrrhotite and Pyrite minerals in BG, CN, DV and A anomaly, respectively, but sulfur in Pyrrhotite form is exist in BG and CN anomaly.

- There is the highest amount carbonate minerals and calcite at BG and A, B anomalies, respectively. Clay minerals and biotite are present at CN and DV anomalies.

- Survey show the factors inclusive of iron, iron oxide, sulfur and other impurities percentage in raw materials, and size distribution of concentrate are the most effective factors on iron grade.

- Silicate and carbonate minerals of aluminum, silicon, magnesium and calcium are the other most important groups which are present with the concentrate as interfering compounds.

- Among the examined parameters, the most relevant factors are concentrate size distribution, feed tonnage, Fe and sulfur content, impurity and FeO content of raw material, respectively.

- Increasing sulfur content of feed causes to Fe grade rising, and, other impurities content has destructive effect on product grade. So, one of the most important factors maintaining the concentrate grade is amount of other impurity removal.

- The final concentrate containing almost 66.6% Fe with 97.5% recovery can be produced by the combination of anionic and cationic collectors in flotation process

References

Bulatovic, S., Srdjan, M. (2010). *Handbook of flotation reagents: chemistry, theory and practice.* (Vol. 2): Flotation of Gold, Pgm and Oxide Minerals.

Corathers, L. A, Machamer, J. F. (2006). Manganese, in: Edited by Jessica Elzea Kogel, Nikhil C. Trivedi, James M. Barker and Stanley T. Krukowski. *Industrial Minerals and Rocks*, pp 631-637.

Feng, G., Hong, Z., Guang-yi, L., Sheng-gui, Z., & Liu-yin, X. (2009). Flotation of aluminosilicate minerals using alkylguanidine collectors. *Trans. Nonferrous Met. Soc. China*. *19*(1), 228-234. DOI: 10.1016/S1003-6326(08).

Fuerstenau, D.W., Pradip, T. (2005). Zeta potentials in the flotation of oxide and silicate minerals. *Adv. Colloid Interface Sci*. 114-115, 9-26. doi.org/10.1016/j.cis.2004.08.006.

Gao, Z., Li, C., Sun, W., & Hu, Y., (2017). Anisotropic surface properties of calcite: A consideration of surface broken bonds. *Colloids Surf A Physicochem Eng Asp*. 520, 53-21. DOI:10.1016/S1003-6326(11)61306-X.

Ghasemi, S., Behnamfard, A., & Arjmand, R. (2019). Reprocessing of Sangan iron ore tailings by flotation. *Journal of Mining and Environment (JME), 10*(3), 729-745. *DOI: 10.22044/jme.2019.8137.1682.*

Khaphaje, E., & Behnamfard, A. (2019). Characterization of Sangan low-grade iron ore and its processing by dry low-intensity magnetic separation. *Int. J. Min. & Geo-Eng. (IJMGE)*, *53* (2), 111-116. DOI: 10.22059/ijmge.2019.261398.594748

Mehdilo, A., & Irannajad, M. (2014). Evaluation of pyrolusite flotation behavior using a cationic collector. *J. Min. Sci. 50*(5), 982-993. DOI:10.1134/S1062739114050184.

Mishra, P.P., Mohapatra, B.K., & Mahanta, K. (2009). Upgradation of low-grade siliceous manganese ore from bonai-keonjhar belt, Orissa, India. *Journal of Minerals & Materials Characterization & Engineering. 8*(1), 47-56. DOI:10.4236/jmmce.2009.81005.

 Nikmanesh poor, J., Karamoozian, M., Rahimi. sh. (2015). Investigating the possibility of reducing the sulfur content of iron concentrate in the Sangan flotation circuit. *International Specialized Congress of Earth Sciences.*

Rahimi, Sh., Irannajad, M., & Mehdilo, A. (2017). Comparative studies of two cationic collectors in the flotation of pyrolusite and calcite. *International Journal of Mineral Processing*, *167*(3), 103-112. DOI: 10.1016/j.minpro.2017.07.016

Rahimi, Sh., Irannajad, M., & Mehdilo, A. (2017). Effects of sodium carbonate and calcium chloride on calcite depression in cationic flotation of pyrolusite. *Trans. Nonferrous Met. Soc. China, 27*(4): 1831−1840. DOI: 10.1016/S1003-6326(17)60206-1

An efficient approach to chlorine removal in the zinc hydrometallurgical process

Matin Najafi[1], Bahram Behnajady[2]*, Saeid Karimi[3]

[1]Bachelor of Science, Research Centre of Advanced Materials, Faculty of Materials Engineering, Sahand University of Technology, Sahand New Town, Iran

[2]Assistant professor, Research Centre of Advanced Materials, Faculty of Materials Engineering, Sahand University of Technology, Sahand New Town, Iran

[3]Assistant professor, Department of Metallurgy and Materials Engineering, Hamedan University of Technology, Hamedan, Iran

*Corresponding author: b_behnajady@sut.ac.ir (Bahram Behnajady)

Abstract:

Nowadays, most of the metallic zinc is produced through hydrometallurgical processes. In order to attain high-purity zinc through electrowinning, the concentration of chlorine ions in the electrolyte should not exceed 0.5 g/L due to its negative consequences. One in particular is the corrosion of non-consumable lead anodes, which is responsible for the dissolution of Pb that causes impurity in the produced zinc metal. Moreover, chlorine emission in the work environment could be a danger to the health of staff, which stems from the oxidation of chlorine ions on the non-consumable Pb anodes. In this research, a potential alternative procedure is employed to significantly reduce chlorine in zinc concentrate. The results showed that under the appropriate conditions of T=60 °C and 1 h of experiment, two-step dichlorination using water along with 20 g/L Na_2CO_3 had a salient efficiency of 98% and the lowest amount of 0.48 g/L chlorine remaining in the leaching solution. Compared to traditional dichlorination methods of zinc, the employed procedure had satisfying dichlorination efficiency, considering the economic aspects of the produced zinc, particularly on the industrial scale.

Keywords: Dichlorination, Zinc, Electrowinning, Leaching, Chlorine

1. Introduction

Recently, the importance of zinc continues to increase in the metallurgical industry and particularly, in the galvanization industry. Zinc is produced from both sulphide and oxide-based ores, but the zinc hydrometallurgical process is of paramount importance due to its numerous advantages compared to pyrometallurgy, such as low energy consumption and air pollution (Behnajady & Moghaddam, 2017a; Dai et al., 2018). With regard to its invaluable advantages, in recent years, most of the metallic zinc is produced through the hydrometallurgical process. The zinc hydrometallurgical production process usually involves grinding, acidic leaching, neutralizing, purification, and electrowinning. In the leaching process, sulphuric acid (H_2SO_4) is employed in a solid/liquid = 250 g/L. In the neutralizing step, in order to remove some impurities such as Arsenic, Germanium, and Iron in its hydroxide form, calcium hydroxide is used to increase the pH and adjust it around 4 (Dongxia et al., 2023; Hu et al., 2018). As the next step, the solution undergoes the Hot Purification process after filtration. According to its name, this process takes place at T=70-80 °C, where $KMnO_4$ and $[Ca(OH)_2]$ are used to oxidize Co, Mn and remaining Fe and remove them in their oxide and hydroxide forms (Behnajady & Moghaddam, 2017b, 2023, 2024; Nusen et al., 2015). After removing the mentioned impurities, the final pH of the solution will be 3-3.5. In order to remove the other remaining impurities, such as Cu,

Cd, and Ni, the solution is subjected to the next step, which is the Cold Purification process (Ashtari & Pourghahramani, 2015; Balesini Aghdam et al., 2020; Behnajady et al., 2024). To remove Cadmium, the best temperature is 50 °C, but Ni requires higher purification temperatures. In this stage, the pH of the solution is 4 – 4.5, and zinc powder is used for purification due to its higher oxidative potential (Dai et al., 2018; Su & Chen, 2013; Yin et al., 2011). After these steps, the pregnant leach solution is ready to be electrowin and produce metallic zinc.

Hydrometallurgical zinc production industries deal with the chloride ion, which enters the pregnant leaching solution before moving on to the electrowinning section. Before the electrowinning process, the concentration of chlorine ions in the electrolyte should not exceed 0.5 g/L due to its negative consequences. Chlorine emission in the work environment could be a danger to the health of staff, which stems from the oxidation of chlorine ions on the non-consumable lead anodes. Moreover, $HClO_4$ which is formed as a result of the oxidation of chlorine ions could cause corrosion in non-consumable lead anodes and consequently, since it is more active compared to zinc and easily deposits on the aluminum cathode, the negligible amount of the dissolved Pb could be responsible for possible impurity in produced zinc through electrowinning process (Antuñano et al., 2013; Tang et al., 2004).

Numerous investigations have been conducted concerning the issue of chlorine ions in zinc hydrometallurgical production (Liu et al., 2016; Zhao et al., 2022). Wu et al. (2013) have selected copper plates and Ag/AgCl as working and opposite electrodes, respectively, to remove Cl ions in the zinc sulphate solution. They have reported that under optimum conditions such as t=3 h, potential of 0.6 V, and ultrasonic stirring intensity of 50 W, 54.5% of chloride ions were removed successfully. Ahmadi et al. (2018) have investigated the effect of temperature, stirring speed, and potential on Cl ions removal efficiency using copper as an anode and cathode with 99.99% purity. They have found the optimum experiment conditions at pH=5, t= 4 h, optimal potential 0.8 V, stirring speed of 200 rpm, and T= 25 °C, which led to the 42.6% Cl removal from the initial concentration of 295 mg/L in the electrolysis solution. Dong et al. (2024) investigated the chlorine-deep removal in zinc sulfate solution using highly active copper from copper slag. They obtained a dichlorination rate of 90.41% under the optimum conditions such as; 30 g/L solution acidity, t= 30 mins, T = 20 °C, and the ratio of copper slag to zinc powder = 7:6. Furthermore, they found that increasing the amount of zinc powder eight times resulted in a dichlorination of 95.43%.

In this study, we investigated a new method to reduce chlorine in zinc concentrate using several different approaches and dichlorination steps. This research was initiated due to the economic aspects of zinc production and also a potential alternative method for dichlorination using copper or silver, which have significant chlorine ion removal efficiency, albeit they are not cost-effective in the zinc production industry.

2. Materials and methods

2.1. Material

Sodium carbonate (Na_2CO_3) (98%) and sulfuric acid (H_2SO_4) (98%) were purchased from Mojallali Co., and used as received without any additional purification. The primary material used in the experiments was chlorine bearing zinc concentrate, which contains approximately 17.5% zinc. This concentrate was supplied by Zanjan Zinc Khales Sazan Industries Company (ZZKICo), located in Zanjan, Iran

2.2. Experimental Procedure

The dichlorination step was conducted using a beaker, and each approach was done in a 350 g/L pulp density, T=60 °C, and t=1 h. A mechanical stirrer and a heater were applied to stir the pulp and adjust the desired experimental temperature. Noteworthy is the fact that for those approaches that were

required to heat the concentrate, the chlorine bearing zinc concentrate was subjected to direct heating and facilitated the dichlorination process by allowing the desired reactions. Soon after the concentrate heated up, it was added to the beaker due to the dichlorination process. Consequently, upon the expiration of the mentioned dichlorination time, the contents of the beaker were filtered immediately, and the filtrate was subjected to analysis of chlorine and zinc concentration in the solution. Subsequently, the filtercake that remained undergoes a second dichlorination step. After a two-step dichlorination process, the filtercake that remained from the second dichlorination was subjected to acidic leaching using sulfuric acid at a pH around 1. The leaching process's other parameter conditions were conducted under the same conditions as the dichlorination, such as T=60 °C, t=1 h, using a mechanical stirrer and a heater to obtain the desired experimental temperature. As soon as the expiration of leaching time, the solution was filtered briskly, and the filtrate was subjected to analysis to determine the concentration of Zn and chlorine that was entered into the solution during the leaching process.

3. Results and Discussion

The conditions and results of the experiments conducted were presented in Tables 1 to 4. A glance at the Tables supplied reveals some striking information concerning the dichlorination in the zinc hydrometallurgical process. According to Table 1, the first approach involved a two-step dichlorination process using water alone. This method resulted in the dissolution of 15 g/L of chlorine in the first step and 2 g/L in the second step. However, 1.1 g/L of chlorine remained in the leaching solution after this process, indicating limited effectiveness in chlorine removal by water washing.

Table 1. The results of dichlorination using water at T=60 °C and t=1 h

Steps	Concentrate weight (g)	Volume of water (cc)	Volume of filtrate (cc)	Zinc concentration (mg/L)	Chlorine concentration (g/L)
First dichlorination	350	1000	985	55	15.4
Second dichlorination	Filtercake of first step	1000	1024	26	2
Leaching	383.24	1000	865	57000	1.1

In the second dichlorination approach, which is illustrated in Table 2, the chlorine bearing zinc concentrate was heat treated for 1 h before undergoing the two-step dichlorination with water. This approach yielded slightly better results, with 17.4 g/L of chlorine dissolved in the first step and 3.5 g/L in the second step. Despite this improvement, the remaining chlorine in the leaching solution was still 1.1 g/L, suggesting that heating did not significantly enhance the dichlorination efficiency.

Table 2. The results of dichlorination after heat treating the concentrate

Steps	Concentrate weight (g)	Volume of water (cc)	Volume of filtrate (cc)	Zinc concentration (mg/L)	Chlorine concentration (g/L)
First dichlorination	350	1000	795	73	17.4
Second dichlorination	Filtercake of first step	1000	840	32	3.5
Leaching	438	1000	805	59000	1.1

The introduction of sodium carbonate (Na_2CO_3), as given in Table 3, marked a turning point in the results. When 350 g of the chlorine-bearing zinc concentrate was mixed with 20 g of Na_2CO_3 and heated, the two-step dichlorination process resulted in a dissolution of 20.3 g/L in the first step and 2.6 g/L in the second step. Notably, only 0.625 g/L of chlorine remained in the leaching solution, indicating a substantial improvement in chlorine removal efficiency compared to the water washing method.

Table 3. The results of dichlorination after heat treating the mixture of concentrate and Na_2CO_3

Steps	Concentrate weight (g)	Volume of water (cc)	Volume of filtrate (cc)	Zinc concentration (mg/L)	Chlorine concentration (g/L)
First dichlorination	350	1000	735	121	20.3
Second dichlorination	Filtercake of first step	1000	875	13	2.6
Leaching	408	1000	805	58000	0.675

The most effective approach involved dissolving 20 g of Na_2CO_3 in 1000 cc of water and conducting the dichlorination at 60°C for 1 hour. This method achieved remarkable results, which are illustrated in Table 4, with 18.8 g/L of chlorine removed in the first step and 3.4 g/L in the second step, leaving less than 0.5 g/L of chlorine in the leaching solution. This was the lowest concentration of chlorine remaining across all tested methods, demonstrating the effectiveness of using Na_2CO_3 in the dichlorination process.

Table 4. The results of dichlorination using water along with 20g/L Na_2CO_3 at T=60°C and t=1 hour.

Steps	Concentrate weight (g)	Volume of water (cc)	Volume of filtrate (cc)	Zinc concentration (mg/L)	Chlorine concentration (g/L)
First dichlorination	350	1000	875	120	18.8
Second dichlorination	Filtercake of first step	1000	935	298	3.4
Leaching	387	1000	790	62000	0.48

Figure 1 illustrates the dichlorination efficiency for each approach. Dichlorination, which was conducted after heating the concentrate in the absence of Na_2CO_3, does not have a salient dichlorination efficiency compared to other approaches and resulted in 94.98% dichlorination. With clarity, using sodium carbonate (Na_2CO_3) has significantly improved the dichlorination efficiency, both along with the thermal effect and adding to water, which resulted in 96.93 and 98.10 % dichlorination efficiency, respectively. Dichlorination using water containing Na_2CO_3 had a striking dichlorination, which was the most effective approach. The overall dichlorination efficiency was significantly enhanced when sodium carbonate was used. The efficiency reached 96.93% and 98.10% for the methods involving Na_2CO_3, compared to 94.98% for the method without it. This highlights the critical role of sodium carbonate in improving the dichlorination process.

According to Figure 2, which demonstrates the concentration of chlorine in the leaching solution, dichlorination using water and also after heating the concentrate had the highest remaining chlorine in the leaching solution, which was 1.1 g/L for both of the mentioned approaches. Dichlorination using Na_2CO_3, which was conducted in two different approaches, had lower chlorine remaining in the leaching solution. This amount was 0.48 g/L in dichlorination using water along with 20 g/L Na_2CO_3

and 0.675 g/L in dichlorination after heating the mixture of concentrate and Na_2CO_3. As discussed above, the most significant approach to remove chlorine from chlorine-bearing zinc concentrate was the one in which 20g/L Na_2CO_3 was solubilized in water and used in dichlorination.
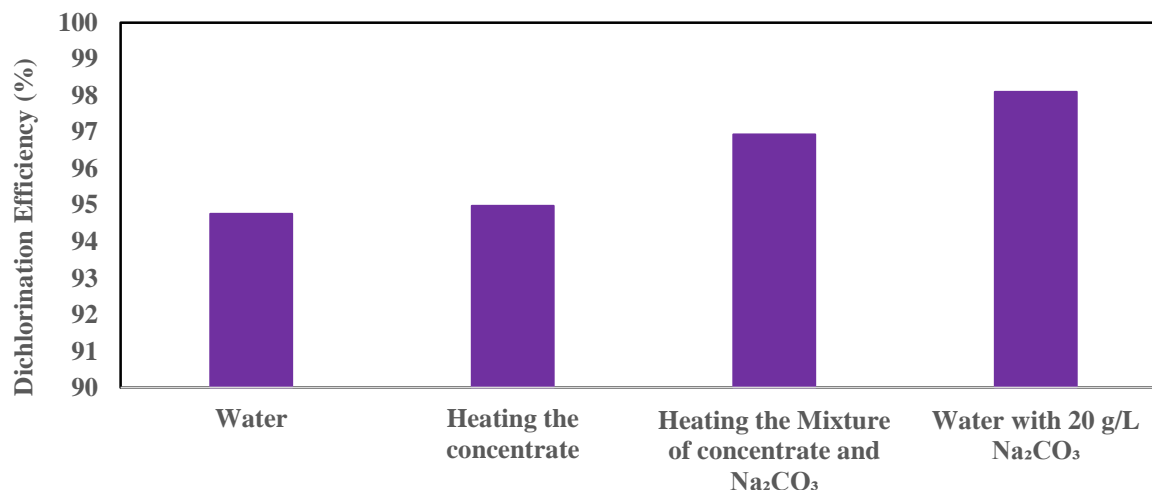

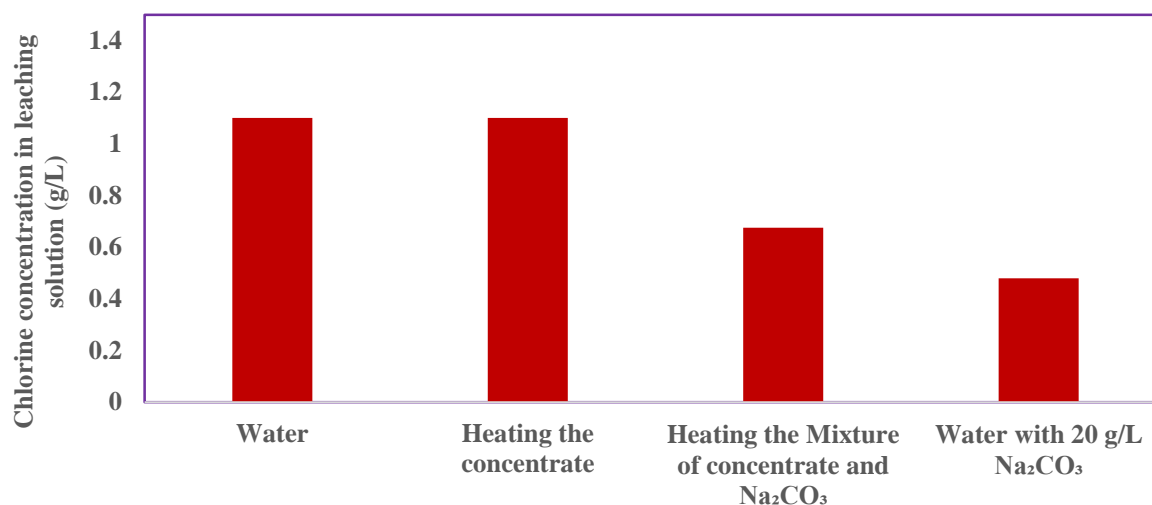Figure 1. Dichlorination efficiency for each approach.

Figure 2. The amount of chlorine in the leaching solution for each approach.

4. Conclusions

In this research, different approaches were investigated concerning the dichlorination of chlorine bearing zinc concentrate. The results showed that in almost all of the employed approaches, significant dichlorination efficiencies were obtained, and more than 90 % of the chlorine was removed. Dichlorination using 20 g/L Na_2CO_3 solved in water at T=60 °C, and 1 hour of dichlorination resulted in approximately the highest dichlorination efficiency of 98.10% and the lowest concentration of chlorine in the leaching solution, 0.48 g/L. So, it was selected as the appropriate approach compared to the others. Concerning traditional procedures that used copper and silver in the dichlorination of zinc PLS, this approach had satisfactory efficiency, particularly in the economic aspects of the

produced zinc. The obtained results suggest a potential alternative to traditional dichlorination procedures, especially on an industrial scale.

References

Ahmadi, R., Khoshkhati, F., & Kia, M. R. (2018). Dechlorination from sulphate aqueous solutions of zinc electrolysis by electrochemical method. *Asian Journal of Water, Environment and Pollution*, *15*(2), 23–28.

Antuñano, N., Herrero, D., Arias, P. L., & Cambra, J. F. (2013). Electrowinning studies for metallic zinc production from double leached Waelz oxide. *Process Safety and Environmental Protection*, *91*(6), 495–502. https://doi.org/10.1016/j.psep.2012.10.014

Ashtari, P., & Pourghahramani, P. (2015). Zinc extraction from zinc plants residue using selective alkaline leaching and electrowinning. *Journal of The Institution of Engineers (India): Series D*, *96*, 179–187.

Balesini Aghdam, A. A., Yoozbashizadeh, H., & Moghaddam, J. (2020). Simple separation method of Zn(II) and Cd(II) from brine solution of zinc plant residue and synthetic chloride media using solvent extraction. *Chinese Journal of Chemical Engineering*, *28*(4), 1055–1061. https://doi.org/10.1016/j.cjche.2019.12.003

Behnajady, B., & Moghaddam, J. (2017a). Separation of arsenic from hazardous As-bearing acidic leached zinc plant purification filter cake selectively by caustic baking and water leaching. *Hydrometallurgy*, *173*, 232–240. https://doi.org/10.1016/j.hydromet.2017.08.016

Behnajady, B., & Moghaddam, J. (2017b). Selective leaching of zinc from hazardous As-bearing zinc plant purification filter cake. *Chemical Engineering Research and Design*, *117*, 564–574. https://doi.org/10.1016/j.cherd.2016.11.019

Behnajady, B., & Moghaddam, J. (2023). Synthesizing Zinc Arsenate and Its Application in Cobalt Purification Process. *Metallurgical and Materials Transactions B*, *54*(3), 1113–1121.

Behnajady, B., & Moghaddam, J. (2024). The Synthesis of Crystalline, Mono-Phase Copper and Zinc Arsenates (III). *Archives of Metallurgy and Materials*, 1359–1365.

Behnajady, B., Najafi, M., & Karimi, S. (2024). Green leaching of cold filter cakes using choline chloride–maleic acid deep eutectic solvent and molecular dynamics simulation. *Physical Chemistry Chemical Physics*, *26*(37), 24407–24422.

Dai, D. Q., Xiu, Z., & Li, H. M. (2018). Study on sources and control of fluorine and chlorine in zinc hydrometallurgy. *Jiangsu Sci Technol Inform*, *35*(2), 39–41.

Dong, Q., He, J., Zhang, C., Fu, G., Li, J., Li, X., Qu, H., Gu, L., Zhang, T., & Yin, W. (2024). A new process of chlorine deep removal in zinc sulfate by highly active copper from copper slag. *JOM*, *76*(7), 3905–3916.

Dongxia, X., Wei, P., Shiqiang, Z., & Yang, L. (2023). Experimental Removal of Chlorine from Hydro-Zinc Smelting System. *Multipurpose Utilization of Mineral Resources*, *44*(6), 184–186.

Hu, Y., Wang, H., Wang, Y., & Wang, H. (2018). Simultaneous removal of fluorine and chlorine from zinc sulfate solution in iron precipitation process. *Journal of Sustainable Metallurgy*, *4*, 95–102.

Liu, W., Zhang, R., Liu, Z., & Li, C. (2016). Removal of chloride from simulated zinc sulfate electrolyte by ozone oxidation. *Hydrometallurgy*, *160*, 147–151.

Nusen, S., Yottawee, N., Cheng, C. Y., & Chairuangsri, T. (2015). Characterisation of Zinc Plant, Cold-Purification Filter Cake and Leaching of Indium by Aqueous Sulphuric Acid Solution. *CHIANG MAI JOURNAL OF SCIENCE*, *42*(3), 718–729.

Su, S., & Chen, H. Q. (2013). Research on removal of fluoride and chloride in zinc hydrometallurgy.

Hunan Nonferrous Metals, 29(1), 40–43.

Tang, D. W., Mao, X. H., & Huang, B. F. (2004). Study on F−, Cl− purification processes from zinc sulfate solution. *J Guizhou Univ Technol (Natural Science Edition)*, 33(1), 15–22.

Wu, X., Liu, Z., & Liu, X. (2013). Chloride ion removal from zinc sulfate aqueous solution by electrochemical method. *Hydrometallurgy*, 134, 62–65.

Yin, R. H., Zhai, A. P., & Li, F. (2011). Investigation and control of F and Cl in zinc hydrometallurgy. *China Nonferrous Metall*, 2, 34–36.

Zhao, M., Wang, S., & Zhang, L. (2022). Removal of chlorine from zinc sulfate solution: a review. *Environmental Science and Pollution Research*, 29(42), 62839–62850.

Evaluation of the Designed Frother for the Feed of Takht-e-Gonbad Copper Plant on Recovery and Separation Efficiency in the Flotation Process

Shahin KazemZadeh[1*], Ali Farahmand[2], Niloofar Ghaedfozooni[1]

* taxinparto.co@gmail.com

Abstract:

In mineral beneficiation through the flotation process, selecting appropriate chemical reagents plays a crucial and decisive role in improving grade, efficiency, and separation performance. Among these reagents, the choice of a suitable frother is of high importance due to its role as the connecting link between bubbles and collectors, as well as its impact on bubble size and the volume of bubbles producedan aspect that has often been overlooked. In this study, by replacing two frothers, KF60N in the rougher stage and KF50 in the scavenger stage, instead of the MIBC frother, the concentrate grade of the produced copper remained constant, while the recovery increased to approximately 84.26% and the separation efficiency improved to 82.02%.

Keywords: Frother, flotation, separation efficiency, copper recovery

1. Introduction

Frothers play a significant and effective role in the flotation process [1, 2]. They help stabilize bubbles and facilitate the attachment of particles to air bubbles, while also stabilizing the attachment of mineral particles to collectors [3]. The type of foam formed and its stability directly influences the separation of valuable material from tailings and the efficiency of the flotation process [4]. Certain minerals, such as molybdenite or graphite, possess a special structure that inherently imparts hydrophobic properties, allowing them to float easily on the water's surface [5, 6]. However, extracting most valuable minerals and metals requires the addition of appropriate collectors and frothers to the flotation cell [7].

The properties of frothers depend on various parameters, including the structure of the hydrocarbon chain, the number of carbons, chain length, and the power and type of hydrophilic agent in the chain [8]. Their performance in the flotation process is also influenced by the characteristics of the tested ore, particle size, pH, type of tailings accompanying the valuable material, residence time, and other effective parameters. Therefore, frothers should be selected in a way that aligns with the conditions of the feed to the plant and the flotation line, achieving the best results [9, 10].

One of the most effective methods for concentrating copper ores is flotation. Copper ores are categorized into two types: oxidized (malachite, azurite) and sulfide (chalcopyrite). The Takht-e-Gonbad copper deposit falls under the category of sulfide ores, with the primary copper mineral being chalcopyrite at an average grade of 0.38%.

So far, the importance of the type of frother in flotation processes has been overlooked in many processing plants, where only the methyl isobutyl carbonate (MIBC) frother is used. In this research, two frothers suitable for the feed of the Takht-e-Gonbad copper plant were designed based on the structure of the ore, the minerals present in it, and the surface interactions among these minerals in an

aqueous environment [11]. One of these frothers, named KF60N, was used in the rougher stage, and KF50 in the scavenger stage of the flotation line. This change in frother had a significant impact on the separation efficiency and final recovery in the flotation line.

2. Material and methods

2.1. Material

The feed ore from the Takht-e-Gonbad copper mine, sized below 100 micrometers, was used. A flotation cell with a capacity of 2600 milliliters, lime with a purity of 93.75% and lime activity of 89.37%, 5% sulfuric acid, collectors SPAX and Z11, collector aid 4132, Chinese MIBC frother, and synthesized frothers F90, F70S, KF60N, and KF80 were utilized, as well as the frother aid K515.

2.2. Flotation test method

A pulp with a solid percentage of 28% and an amount of 880 grams of the Takht-e-Gonbad copper ore sample obtained from a ball mill was added to the flotation cell. The density of the feed used was 2.61 g/cm³. The mixing time of the pulp was 5 minutes, at a temperature of 25 degrees Celsius, with an impeller speed of 800 rpm in the rougher cell and 1344 rpm in the scavenger cell, and an initial pH of 8. During the chemical preparation stage, the total preparation time was 30 minutes with a mixing speed of 11 Hz. To adjust the pH to 11.65, 0.2 grams of lime were added at 60-second intervals 15 times. After adjusting the pH to 11.65, the flotation process was performed by adding the mentioned collectors and frothers as outlined in Table 1. A total of 4 frothing operations were performed, with 2 corresponding to the rougher cell and 2 to the scavenger cell. The amount and type of chemicals used in each test are detailed in Table 1.

Table 1: Conditions for performing flotation tests

Test Number	Frother Used	Amount Of Frother (gr/ton)	The Second Frother Used	Amount Of Second Frother gr/ton))	Co-Frother Used	Amount Of Co-Frother (gr/ton)	Collector Used	Amount Of Collector (gr/ton)	Co-Collector Used	Amount Of Co-Collector (gr/ton)
1	MIBC	7	_	_	F515	15	Z11	25	C4132	10
2	MIBC	10	_	_	F515	15	Z11	25	C4132	10
3	MIBC	15	_	_	F515	15	Z11	25	C4132	10
4	F90	7	_	_	F515	15	Z11	25	C4132	10
5	F90	10	_	_	F515	15	Z11	25	C4132	10
6	F90	15	_	_	F515	15	Z11	25	C4132	10
7	F50	7	_	_	F515	15	Z11	25	C4132	10
8	F50	10	_	_	F515	15	Z11	25	C4132	10
9	F50	15	_	_	F515	15	Z11	25	C4132	10
10	F70S	7	_	_	F515	15	Z11	25	C4132	10
11	F70S	10	_	_	F515	15	Z11	25	C4132	10
12	F70S	15	_	_	F515	15	Z11	25	C4132	10
13	MIBC	15	_	_	F515	15	SIPX	10	C4132	10
14	MIBC	15	_	_	F515	15	SIPX	15	C4132	10
15	MIBC	15	_	_	F515	15	SIPX	20	C4132	10
16	MIBC	15	_	_	F515	15	PEX	10	C4132	10
17	MIBC	15	_	_	F515	15	PEX	15	C4132	10

18	**MIBC**	15	_	_	F515	15	**PEX**	**20**	C4132	10
19	**KF60N**	7	_	_	F515	15	Z11	25	C4132	10
20	**KF60N**	10	_	_	F515	15	Z11	25	C4132	10
21	**KF60N**	15	_	_	F515	15	Z11	25	C4132	10
22	**KF80**	7	_	_	F515	15	Z11	25	C4132	10
23	**KF80**	10	_	_	F515	15	Z11	25	C4132	10
24	**KF80**	15	_	_	F515	15	Z11	25	C4132	10
25	**MIBC**	15	_	_	F515	15	**SIPX**	**10**	C4132	10
26	**KF60N**	15	_	_	F515	15	Z11	25	C4132	10
27	**KF60N**	12	**KF50**	3	F515	15	Z11	25	C4132	10
28	**KF60N**	11	**KF50**	4	F515	15	Z11	25	C4132	10
29	**KF60N**	12	**KF50**	3	F515	15	Z11	25	C4132	10
30	**KF60N**	11	**KF50**	4	F515	15	Z11	25	C4132	10
31	**KF60N**	12	**KF50**	3	F515	15	Z11	25	C4132	10
32	**KF60N**	10	**KF50**	5	F515	15	Z11	25	C4132	10
33	**KF60N**	11	**KF50**	4	F515	15	Z11	25	C4132	10
34	**KF60N**	12	**KF50**	3	F515	15	**SIPX**	25	C4132	10
35	**KF60N**	14	**KF50**	4	F515	15	**SIPX**	25	C4132	10
36	**KF60N**	15	**KF50**	5	F515	15	**SIPX**	25	C4132	10
37	**KF60N**	12	**KF50**	6	F515	15	**SIPX**	25	C4132	10
38	**KF60N**	12	**KF50**	3	F515	15	**SIPX**	25	C4132	10
39	**KF60N**	12	**KF50**	3	F515	15	**SIPX**	25	C4132	10
40	**KF60N**	12	**KF50**	3	F515	15	**SIPX**	25	C4132	10
41	**KF60N**	12	**KF50**	3	**F515**	**12**	**SIPX**	25	C4132	10
42	**KF60N**	12	**KF50**	3	F515	15	**SIPX**	25	C4132	10
43	**KF60N**	12	**KF50**	3	F515	15	**SIPX**	25	C4132	10
44	**KF60N**	12	**KF50**	3	F515	15	**SIPX**	25	**C4132**	**12**
45	**KF60N**	12	**KF50**	3	F515	15	**SIPX**	25	**C4132**	**12**
46	**KF60N**	12	**KF50**	3	F515	15	**SIPX**	25	C4132	10
47	**MIBC**	12	**KF50**	3	F515	15	**SIPX**	25	C4132	10
48	**KF60N**	24	**MIBC**	6	F515	15	**SIPX**	25	C4132	10
49	**KF60N**	22	**KF50**	9	F515	15	**SIPX**	25	C4132	10

3. Results and Discussion

3.1. Particle Characterizations

Three samples from the Takht-e-Gonbad copper plant feed were prepared and sent for XRD analysis.

Figure 1: XRD analysis of sample 1

Figure 2: XRD analysis of sample 2

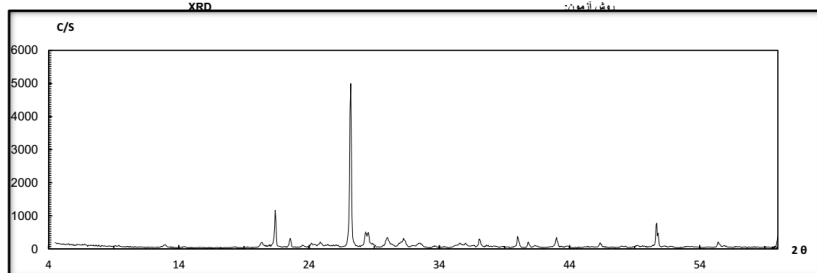| Zarazma Mahan | Client: شرکت محترم فراوری مس درخشان تخت گنبد
403ZK1982
1403/06/18
1403/06/18
1403/07/03
1403/07/03
XRD | تاریخ درخواست:
تاریخ دریافت نمونه:
تاریخ انجام آزمون:
تاریخ صدور نتیجه:
روش آزمون: |
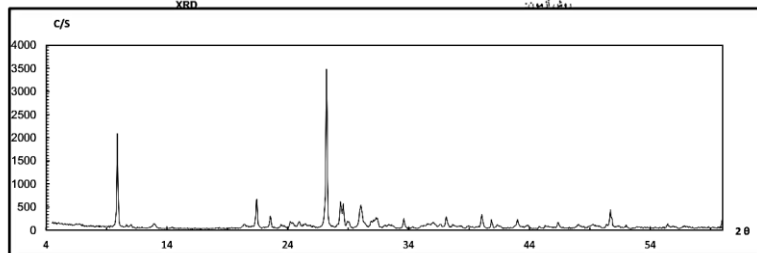
Sample:	Phase(s)	Phase(s)	Phase(s)
CL3-03/06/10	Quartz (33-1161) = 36%	Chlorite (29-0701) = 4%	Illite (26-0911) = 10%
LAB :	SiO2	(Mg,Fe)6(Si,Al)4O10(OH)8	(K,H3O)Al2Si3AlO10(OH)2
Date :	Albite (09-0466) = 12%	Calcite (05-0586) = 7%	Kaolinite (29-1488) = 9%
13.5.2024	NaAlSi3O8	CaCO3	Al2Si2O5(OH)4
kV = 40	Potassium Feldspar = 3%	Dolomite (36-0426) = 5%	Siderite (29-0696) = 6%
mA = 30	KAlSi3O8	CaMg(CO3)2	FeCO3
Ka. = Cu	Amphibol Group (45-1371) = 2%	Pyrite (06-0710) = 3%	Chalcopyrite (37-0471) = 1% ??
	Ca2(Fe.Mg)4Al(Si7Al)O22,(OH)2	FeS2	CuFeS2

Figure 3: XRD analysis of sample 3

According to the XRD analysis results of the submitted samples, they contain quartz, albite, potassium feldspar, and amphibole group minerals, with quartz and silicate minerals being the main gangue associated with them. Additionally, dolomite and calcite were found in the samples, which may impact the flotation process.

Three samples from the Takht-e-Gonbad copper plant feed were also sent for XRF analysis. The analysis results indicated that the sample contains approximately 0.37% copper. The main gangue associated with copper in this sample includes iron, clay, and some calcite and dolomite.

Table 2: XRF analysis for the Takht Gonbad Derakhshan copper plant feed

Sample	Cu (%)	SO₃ (%)	P₂O₅ (%)	SiO₂ (%)	Al₂O₃ (%)	MgO (%)	Na₂O (%)
CL1-03/06/10	0.27	3.24	0.08	54.55	13.56	2.49	1.78
CL2-03/06/10	0.32	3.48	0.05	60.36	11.49	1.67	1.85
CL3-03/06/10	0.41	4.23	0.06	57.93	11.72	1.73	1.41
Sample	LOI (%)	K₂O (%)	CaO (%)	Fe₂O₃ (%)	Cr₂O₃ (%)	TiO₂ (%)	BaO (%)
CL1-03/06/10	7.16	0.77	8.16	7.3	0.02	0.36	<0.01
CL2-03/06/10	6.12	1.27	5.11	7.79	0.02	0.28	0.01
CL3-03/06/10	6.25	1.25	5.54	8.91	0.01	0.33	0.01

3.2. Flotation Test Results

After conducting flotation tests under the conditions outlined in Table 1, the results of concentrate and tailing assays, as well as the recovery and separation efficiency for each test, were summarized in Table 3.

Table 3: Flotation test results

Test Number	Frother Used	Amount Of Frother (gr/ton)	The Second Frother Used	Amount Of Second Frother gr/ton))	Collector Used	Amount Of Collector (gr/ton)	Feed Grade (%)	Tailing Grade (%)	Concentrate Grade (%)	Recovery (%)	Weight Recovery (%)	Separation efficiency (%)
1	MIBC	7	_	_	Z11	25	0.38	0.08	11.077	79.522	2.754	77.585
2	MIBC	10	_	_	Z11	25	0.38	0.09	11.258	76.931	2.783	75.151
3	MIBC	15	_	_	Z11	25	0.38	0.11	10.826	71.782	2.868	70.163
4	F90	7	_	_	Z11	25	0.38	0.11	11.628	71.731	2.583	70.24
5	F90	10	_	_	Z11	25	0.38	0.12	10.636	69.202	2.747	67.667
6	F90	15	_	_	Z11	25	0.38	0.11	9.392	71.895	3.249	69.992
7	F50	7	_	_	Z11	25	0.38	0.11	8.938	71.938	3.41	69.927
8	F50	10	_	_	Z11	25	0.38	0.11	7.937	72.051	3.827	69.754
9	F50	15	_	_	Z11	25	0.38	0.11	10.141	71.832	3.055	70.088
10	F70S	7	_	_	Z11	25	0.38	0.11	9.76	71.863	3.145	70.041
11	F70S	10	_	_	Z11	25	0.38	0.12	9.664	69.281	3.18	67.57
12	F70S	15	_	_	Z11	25	0.38	0.11	8.466	71.988	3.54	69.851
13	MIBC	15	_	_	SIPX	10	0.38	0.11	10.043	71.839	2.823	70.076
14	**MIBC**	**15**	_	_	**SIPX**	**15**	**0.38**	**0.1**	**8.21**	**74.416**	**2.93**	**72.55**
15	MIBC	15	_	_	SIPX	20	0.38	0.094	9.177	76.042	3.618	73.859
16	MIBC	15	_	_	PEX	10	0.38	0.09	8.872	77.098	3.203	74.769
17	MIBC	15	_	_	PEX	15	0.38	0.12	9.072	69.338	2.953	67.5
18	MIBC	15	_	_	PEX	20	0.38	0.13	8.562	66.804	3.106	64.986
19	KF60N	7	_	_	Z11	25	0.38	0.12	8.605	69.389	3.403	67.438
20	KF60N	10	_	_	Z11	25	0.38	0.11	8.575	71.976	3.401	69.869
21	KF60N	15	_	_	Z11	25	0.38	0.08	9.663	79.606	3.48	77.347
22	KF80	7	_	_	Z11	25	0.38	0.11	6.703	72.238	3.817	69.468
23	KF80	10	_	_	Z11	25	0.38	0.1	9.049	74.508	2.793	72.379
24	KF80	15	_	_	Z11	25	0.38	0.12	10.736	69.194	2.734	67.676
25	MIBC	15	_	_	SIPX	10	0.37	0.08	8.487	79.124	3.757	76.617
26	KF60N	15	_	_	Z11	25	0.37	0.08	9.34	79.056	3.263	76.803
27	KF60N	12	KF50	3	Z11	25	0.37	0.1	8.19	73.875	3.723	71.603
28	KF60N	11	KF50	4	Z11	25	0.37	0.11	9.423	71.1	2.915	69.296
29	KF60N	12	KF50	3	Z11	25	0.37	0.06	10.527	84.264	2.559	82.023
30	KF60N	11	KF50	4	Z11	25	0.37	0.13	7.646	65.987	4.153	64.034
31	KF60N	12	KF50	3	Z11	25	0.37	0.1	8.88	73.804	3.376	71.728
32	KF60N	10	KF50	5	Z11	25	0.37	0.1	8.395	73.853	3.011	71.642
33	KF60N	11	KF50	4	Z11	25	0.37	0.06	6.879	84.521	4.33	80.929
34	KF60N	12	KF50	3	SIPX	25	0.37	0.11	7.274	71.349	3.706	68.939
35	KF60N	14	KF50	4	SIPX	25	0.37	0.11	5.175	71.796	5.333	68.288
36	KF60N	15	KF50	5	SIPX	25	0.37	0.13	6.248	66.243	4.725	63.798
37	KF60N	12	KF50	6	SIPX	25	0.37	0.1	8.095	73.886	3.693	71.584

38	KF60N	12	KF50	3	SIPX	25	0.37	0.08	6.577	79.344	4.75	76.022
39	KF60N	12	KF50	3	SIPX	25	0.37	0.08	6.346	79.379	5.157	75.926
40	KF60N	12	KF50	3	SIPX	25	0.37	0.11	5.844	71.618	3.999	68.549
41	KF60N	12	KF50	3	SIPX	25	0.37	0.11	6.354	71.508	4.498	68.709
42	**KF60N**	**12**	**KF50**	**3**	**SIPX**	**25**	**0.37**	**0.07**	**7.899**	**81.806**	**4.423**	**78.908**
43	KF60N	12	KF50	3	SIPX	25	0.37	0.11	6.061	71.569	4.412	68.621
44	KF60N	12	KF50	3	SIPX	25	0.37	0.08	6.618	79.337	4.421	76.039
45	KF60N	12	KF50	3	SIPX	25	0.37	0.1	5.011	74.459	5.916	70.556
46	KF60N	12	KF50	3	SIPX	25	0.37	0.1	6.417	74.128	4.549	71.152
47	MIBC	12	KF50	3	SIPX	25	0.37	0.08	5.847	79.466	4.882	75.689
48	KF60N	24	MIBC	6	SIPX	25	0.37	0.08	5.626	79.509	5.733	75.571
49	KF60N	22	KF50	9	SIPX	25	0.37	0.09	5.138	77.025	5.768	72.957

In tests 1, 2, 3, 13, 14, 15, 16, 17, 18, and 25, the Chinese MIBC frother was used, while synthesized frothers from Taksin Petrochemical were utilized in the remaining tests. Initially, tests were conducted with a single type of frother, showing minimal performance differences between the Chinese frother and synthesized frothers. However, from tests 27 to 49, the use of two types of frothers in the rougher and scavenger cells exhibited noticeable effects; the recovery and separation efficiency increased relative to earlier tests.

Notably, as indicated in Table 3, by keeping the quantity and type of collector, collector aid, and frother constant, merely changing the frother and its amount led to an increase in recovery and separation efficiency without a significant drop in concentrate grade. For example, in tests 42 and 14, all conditions were identical except for the type of frother, resulting in an increase in recovery from 74.41% to 81.8% and separation efficiency from 72.5% to 78.9%. It is worth noting that the initial grade of the feed in test 14 was approximately 0.38%, while in test 42 it was around 0.37%. The highest recovery achieved with the Chinese MIBC frother was 79.5%, while the highest separation efficiency with the synthesized frothers reached 84.26% and 82.02% in the best conditions.

4. Conclusions

This research demonstrated that the type of frother used and its compatibility with the plant feed can be critically important, significantly impacting the final flotation results. Additionally, the amount and duration of each frother's use can affect the final flotation outcomes, resulting in a 5% increase in recovery and separation efficiency.

5. References

1.   Klimpel RR, Hansen RD. Frothers. Reagents in mineral technology: Routledge; 2018. p. 385-409.

2.   Smar V, Klimpel R, Aplan F. Evaluation of chemical and operational variables for the flotation of a copper ore Part I—Collector concentration, frother concentration, and air flow rate. International journal of mineral processing. 1994;42(3-4):225-40.

3.   Kowalczuk PB, Drzymala J. Selectivity and power of frothers in copper ore flotation. Physicochem Probl Miner Process. 2017;53(1):515-23.

4.   Corin KC, Tetlow S, Manono MS. Considering the action of frothers under degrading water quality. Minerals Engineering. 2022;181:107546.

5.   Corin K, Wiese J. Investigating froth stability: A comparative study of ionic strength and frother dosage. Minerals Engineering. 2014;66:130-4.

6.   Jeldres RI, Uribe L, Cisternas LA, Gutierrez L, Leiva WH, Valenzuela J. The effect of clay minerals on the process of flotation of copper ores-A critical review. Applied Clay Science. 2019;170:57-69.

7.   Yuanlun P, Shisheng L, Kehua L. Industrial Application of Special Frother BK208 in a Copper Mine of Yunnan. Nonferrous Metals (Mineral processing section). 2022(1).

8.   Feng Q, Yang W, Wen S, Wang H, Zhao W, Han G. Flotation of copper oxide minerals: A review. International Journal of Mining Science and Technology. 2022;32(6):1351-64.

9.   Chandra A, Gerson A. A review of the fundamental studies of the copper activation mechanisms for selective flotation of the sulfide minerals, sphalerite and pyrite. Advances in colloid and interface science. 2009;145(1-2):97-110.

10.   Szyszka D. Frother critical coalescence concentration and dose in flotation of copper-bearing carbonaceous shale. Mining Science. 2019;26.

11.   Abramov A, Forssberg K. Chemistry and optimal conditions for copper minerals flotation: Theory and practice. Mineral Processing & Extractive Metall Rev. 2005;26(2):77-143.

Upgrading Hirad gold sample, using gravity and flotation approaches

Hassan Behrouzi[1]*, Mohammad Noaparast[2], Mostafa Mahroomi[3], Maryam Shokrzadeh[4]

[1]M.Sc. Student in Mineral Processing, School of Mining Engineering, University of Tehran

[2]Professor, School of Mining Engineering, University of Tehran

[3]Ph.D. Candidate in Mineral Processing, School of Mining Engineering, University of Tehran

[4]Laboratory Expert in Mineralography, School of Mining Engineering, University of Tehran

*Corresponding author: hassanbehrouzi@ut.ac.ir (Hassan Behrouzi)

Abstract:

Nowadays, various beneficiation processes, including gravity separation, flotation, and cyanidation are normally employed for the extraction and processing of gold-bearing ores. In this study, a sample from Gold Mine No. 3, in the Hirad deposit was investigated to determine convenient upgrading methods. Mineralogical results revealed that the metallic minerals in the sample mainly consist of pyrite, arsenopyrite, and minor amounts of chalcopyrite, galena, and sphalerite. Additionally, gold was found primarily as fine microscopic particles within sulfide minerals, and to a lesser extent, in free form. Microscopic studies indicated that the sulfide minerals in the sample have fine particle sizes (approximately -106 +75 microns), and gold is predominantly trapped within these minerals. The gold grade in prepared sample was 2.03 ppm. Experimental results demonstrated that the gravity separation method was not suitable, whereas flotation achieved a higher recovery. During the flotation experiments, various parameters, including the type and dosage of collectors and frother were investigated. The results showed that using 50 g/t of Z6 collector led to a gold recovery of 62.2% with a gold grade of 12.58 ppm, while using 50 g/t of Z11 collector resulted in a recovery of 46.0% with gold grade of 7.32 ppm. Furthermore, increasing the dosage of the frother polypropylene glycol (A65) from 50 to 100 g/t improved the gold recovery from 62.2% to 77.5% and increased the gold grade from 12.58 ppm to 13.41 ppm, as well.

Keywords: Gold, Hirad deposit, Flotation, Gravity separation

1. Introduction

Gold is an element located in the sixth period of the transition metals group in the periodic table, with an atomic number of 79. It crystallizes in the cubic system, and its crystals have a face-centered cubic lattice arrangement, but gold also exists in filamentous and branched forms. The element gold is known by the chemical symbol Au which is derived from its Latin name, Aurum, meaning "glow of dawn". Gold is a soft, dense, and ductile metal with a bright, shiny yellow color and is classified as a precious metal. From ancient times to the present, this metal has attracted human attention due to its brilliant color and chemical stability (Altinkaya, 2021). Gold extraction methods have advanced over the times, like other parts of the mining industry, and despite the decrease in gold grade and the increase in mining depth, gold extraction remains economical. In fact, with the advancement of science and technology, the economic cut-off grade of gold has decreased from 20 ppm to 0.5 ppm which of course presents its significance. Gold is usually found in siliceous veins, as well as in placers and sedimentary veins, along with quartz and pyrite. Due to the significant difference in specific gravity between gold and its associated minerals, the first method used for processing and extracting this element was gravity separation, and it was generally extracted from alluvial and placer deposits (Safari, 2021).

Given that gold plays a beneficial and effective role in stabilizing the regional and global economic market, it has always been sought new and technologically advanced approached to increase the production and efficiency of gold. Due to the decline of high-grade gold reserves worldwide and its increasing economic value following the expansion of its applications, gold extraction from low-grade sources is becoming increasingly important (Fazlavi, 2001).

The Hirad gold mining area is located in South Khorasan province, Iran, 140 km south of Birjand. This area was first introduced as a gold anomaly in 2001 based on the regional geochemical studies and economic geological surveys. By further studies, four gold-bearing mineral zones were identified as Gold Target 1 to 4 (Eshraghi et al.,2005; Askari and Feiz, 2011, Emami Jafari et al., 2023). Fig. 1 shows the geographical location of the study area. The target of this study is to process the gold bearing sample supplied from Hirad deposit, in order to verify the procedures of upgrading approaches.
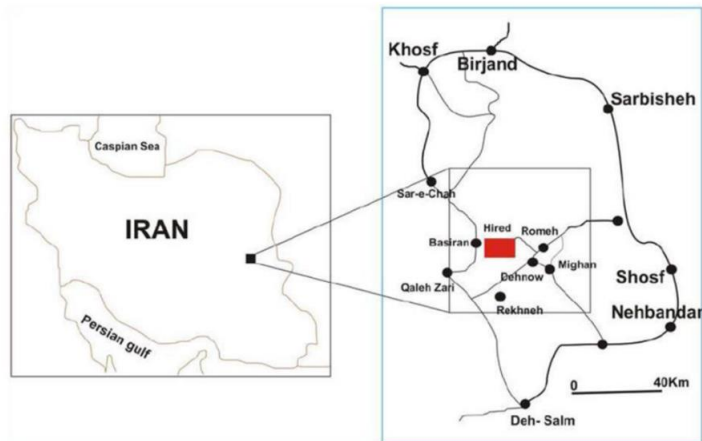
Fig. 1. Geographical location of Hirad region

2. Gold Beneficiation Methods

Gravity separation is a physical process used to separate one or more minerals from associated tailings based on the relative movement of particles in a fluid, influenced by gravity, centrifugal force, and certain other forces. In addition to specific gravity, the weight, shape, size of particles, and the resistance force of fluid layers are also important parameters in determining the relative movement of particles in this process. Although the flotation method has expanded and diminished its importance, gravity separation offers significantly lower costs, method simplicity, less environmental pollution, and the absence of chemical usage compared to flotation.

Taggart presented Equation 1 regarding the applicability of gravity methods which can be used to obtain criteria for assessing the quality of concentration. In this equation, CC is the concentration criterion, ΔH is the specific gravity of the heavy mineral, ΔF is the specific gravity of the fluid, and ΔL is the specific gravity of the light mineral (Rezaei, 1998).

$$CC = \frac{(\Delta H - \Delta F)}{(\Delta F - \Delta L)} \tag{1}$$

In the equation above, if the coefficient CC is greater than 2.7, gravity concentration is accordingly recommended. Consequently, based on this equation, gravity concentration would be suitable for gold particles separation. In this method some parameters should be optimized, such as operating parameters to find out the best grade and recovery (Abdollahi, 2005).

Froth flotation is the most efficient and widely used mineral processing method, enabling the exploitation of large, low-grade ore deposits with complex mineralization. This method was initially used for sulfide ores of copper, lead, and zinc, and then expanded to oxide and non-metallic ores

(Nematollahi, 2008). Froth flotation is a mineral separation method that operates based on the physicochemical properties of solid surfaces with using chemicals as collectors and frothers in an agitated environment (Rezaei, 1996).

The example of refractory gold-bearing sulfide minerals flotation is in the Muteh gold mine. It was carried out by determining effective parameters such as particle size, collector concentration, frother concentration, pH, and time. The optimal flotation process conditions were collector concentration of 30 to 35 g/t, frother concentration of 25 to 30 g/t, and time of 9 to 10 minutes in neutral environment (Ebrahimi Basabi and Mesroghli, 2021).

The dissolution of gold by cyanide has been known since the beginning of the 19th century, but it was not economically used until the late 1980s. Minerals containing free gold were processed by direct cyanidation, with exceeding 80% recovery (Augusto and Martins, 2001; Jeffrey and Breuer, 2000). In this method, the ore is typically crushed to a size of about 60-75% passing 74 microns, and then is directly conducted to the cyanidation process (Yannopoulos, 2012). Cyanidation is considered the simplest and most economical method for gold leaching. Despite its high efficiency, its toxicity and environmental effects necessitate alternatives. Currently, thiosulfate leaching of gold is used at the Goldstrike mine in Nevada, and thiourea is used in other mines such as the New England antimony and Quebec mines (Azizitorghabeh et al., 2021). Thiocyanate has been introduced as a less hazardous alternative for humans and aquatic organisms, and its advantages include lower cost, lower toxicity, and selective performance. Compared to thiourea and thiosulfate, thiocyanate leaching systems require less reagent consumption and lower costs and are more stable (Azizitorghabeh et al., 2021).

3. Sample Characterization

3.1. Sample Preparation

To perform identification tests, a representative sample, approximately 1000 kg (1 ton) was prepared, and presented to mineral processing laboratory of the University of Tehran for further studies. This sample, after passing through three crushing stages by primary and secondary jaw crushers and a roll crusher, reached to size finer than 3360 microns. Then, using mixing and riffle splitting approaches, it was divided into 2-kilogram samples. Also, using a pycnometer, the true specific gravity of the sample was determined which was approximately 2.73 g/cm^3.

3.2. Property Analysis

X-ray Diffraction (XRD), X-ray Fluorescence (XRF), Fire assay, and ICP analyses were performed on the Hirad gold ore sample. According to the Fire assay results, the prepared representative feed sample contains 2.03 ppm of gold.
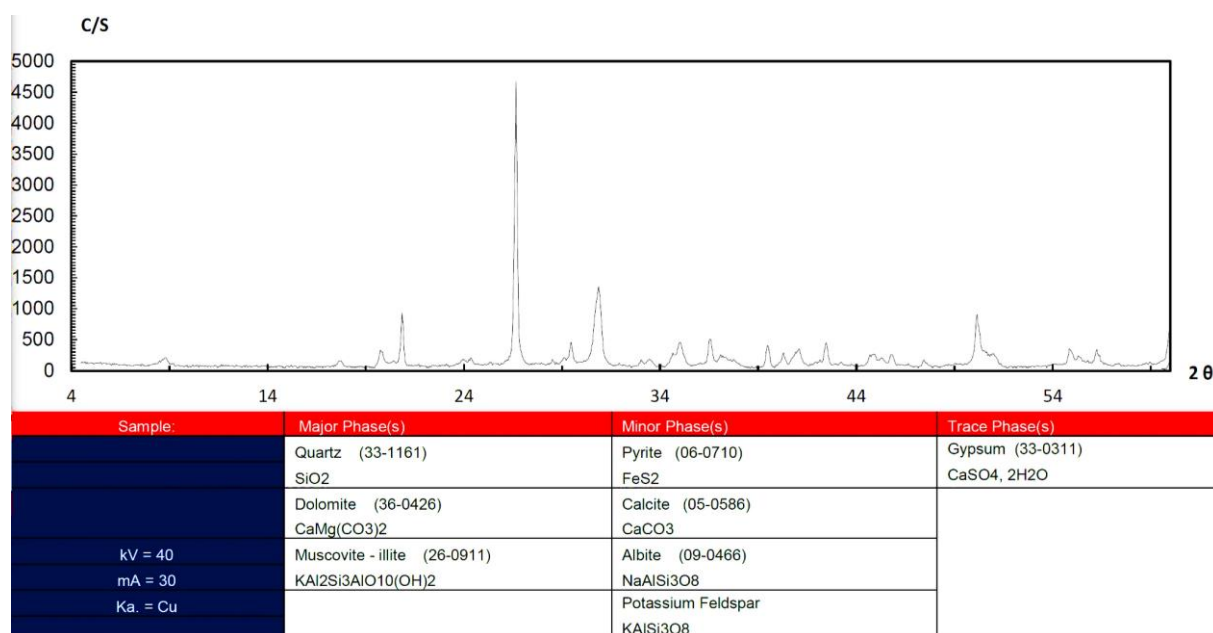
Fig. 2. XRD analysis results

According to the XRD analysis, the graph presented in Fig. 2, the main minerals in the sample are Quartz, Dolomite, and Muscovite-illite, while the accessory minerals include Pyrite, Calcite, Albite, and Potassium Feldspar.

Table 1. XRF analysis results

Element	SiO$_2$	Al$_2$O$_3$	CaO	Fe$_2$O$_3$	K$_2$O	MgO	MnO	Na$_2$O	P$_2$O$_5$	SO$_3$	TiO$_2$	LOI
Percentage	49.30	9.63	7.92	5.46	3.14	4.48	0.23	0.09	0.13	5.83	0.48	13.5

According to the XRF analysis results in Table 1, the major component is SiO$_2$, constituting approximately 49.30% of the sample. This finding is confirmed by comparison with the XRD analysis results, as well. The results of ICP chemical analysis are presented in Table 2. As can be seen, iron, calcium, and aluminum are the main components of this ore.

Table 2. ICP analysis results

Element	Ag	Al	As	Ba	Be	Bi	Ca	Cd	Ce	Co	Cr	Cs	Cu	Dy
Percentage	0.4	618.3	100>	305	0.9	0.1<	41722	2.9	31	11.7	15	12.8	22	3.1
Element	Er	Eu	Fe	Gd	Hf	In	K	La	Li	Lu	Mg	Mn	Mo	Na
Percentage	1.9	1.11	36776	3.5	1.9	0.5<	23478	16	40	0.3	%2>	1584	1.5	475
Element	Nb	Nd	Ni	P	Pb	Pr	Rb	S	Sb	Sc	Se	Sm	Sn	Sr
Percentage	5	12.7	4	593	13	3.34	147	%3>	%0.01>	15.9	0.5<	4	1.7	218
Element	Ta	Tb	Te	Th	Ti	Tl	Tm	U	V	W	Y	Yb	Zn	Zr
Percentage	71	159	1.63	15.8	7.5	118	1.4	0.4	1	2941	7.9	0.5<	0.6	4.1

3.3. Mineralogical Studies

Mineralogical and petrological studies are the normal steps of characterizing the sample which is to be processed in further tests. This is due to the importance of understanding the phase formation of the valuable mineral which plays a crucial role in order to select the appropriate processing method (Hasani Pak, 2001).

Microscopic studies were conducted using transmitted polarized light microscopes (Olympus model) and reflected light microscopes (Leitz model) with a maximum magnification of approximately 630x. The degree of liberation of pyrite and arsenopyrite minerals was determined as shown in Table 3. It indicates that for size fraction of -53+38 microns the liberation degree is 90-95% for pyrite and 74-78% for arsenopyrite.

Table 3. Degree of liberation of gold bearing minerals in different fractions

Fraction (micron)	Pyrite liberation (%)	Arsenopyrite liberation (%)
-210+150	40-45	-
-150+106	70-75	-
-106+75	80-85	20-25
-75+53	88-92	65-70
-53+38	90-95	74-78
-38	95>	85-90

The results of the mineralogical studies in different fractions indicated that the metallic-semimetallic mineral phases were mainly of the sulfide type, with occasional oxide-hydroxide and sulfosalt phases. The sulfide phases included pyrite, with minor amounts of arsenopyrite and, rarely sphalerite. The oxide-hydroxide phases consisted of goethite and rutile-anatase. The abundance of pyrite was approximately 2–3% by volume, appearing as euhedral to subhedral crystals, ranging in size from 20 microns to free particles up to a maximum of 300 microns. Pyrite crystals exhibited the optical properties of arsenic-bearing pyrite. Pyrite was mainly associated with transparent gangue minerals, and occasionally, arsenopyrite.

Arsenopyrite was present in trace amounts (0.15–0.4% by volume), occurring as euhedral crystals ranging in size from finer than 15 microns to a maximum of 160 microns. It was entirely associated with transparent minerals, sometimes with pyrite and rarely with rutile-anatase. Sulfosalt-like crystals, finer than 100 microns, were observed in trace amounts, and exhibited the optical characteristics of sulfosalts. The degree of liberation of pyrite in the -210+150 micron size fraction was determined approximately 40–45%, while no free arsenopyrite crystals were observed, as well.

Under transmitted light, the transparent minerals, in order of abundance, were calcite, dolomite, sericite, feldspar remnants, clay minerals, and quartz. Fig. 3 presents examples of the microscopic images. In finer fractions, pyrite, arsenopyrite, and iron oxide-hydroxides, including goethite and rutile-anatase, were observed in trace amounts (finer than 0.5% by volume). Additionally, in this fraction, besides 3.5–4.5% pyrite and 0.1–0.4% arsenopyrite, fine particles of rutile-anatase, hematite, magnetite, and a single free enargite particle were rarely observed.
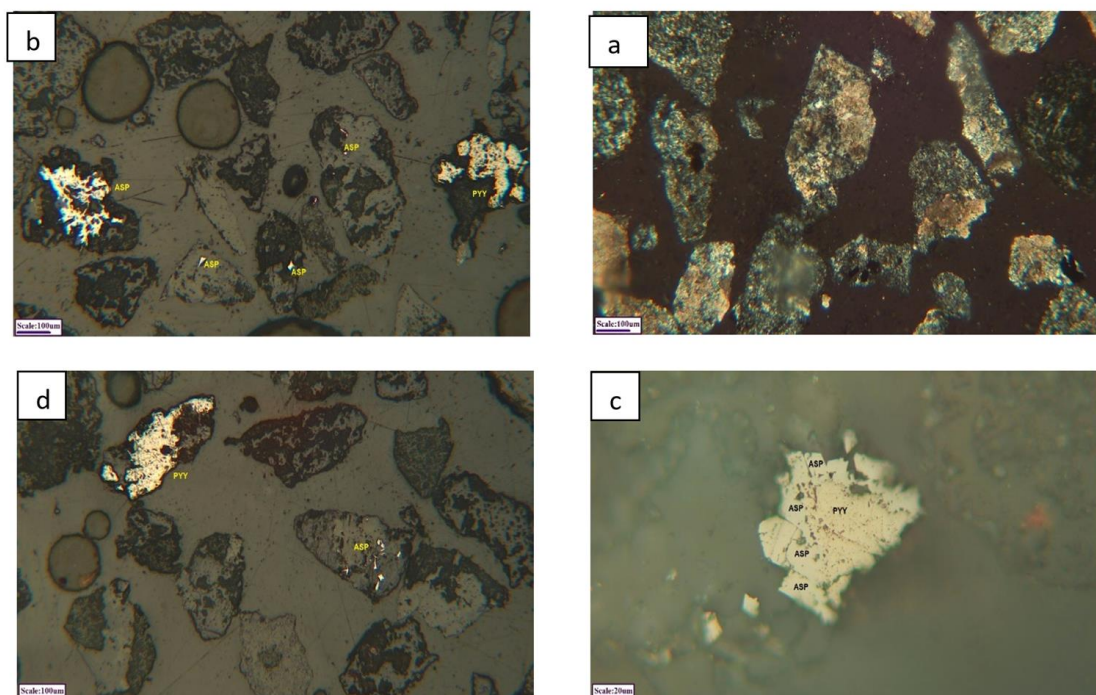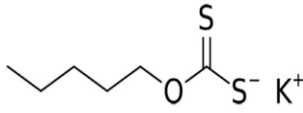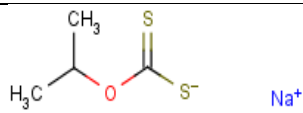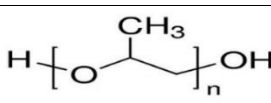
Fig. 3. (a) Transparent minerals, (XPL), (b) Pyrite and arsenopyrite inclusions, (PPL), +150-210 fraction, (c) intergrown pyrite and arsenopyrite crystals, (PPL), (d) Pyrite intergrown with arsenopyrite and transparent non-metallic minerals, (PPL), 150-210 fraction

4. Materials and Methods

4.1. Chemical Reagents

In flotation experiments, potassium amyl xanthate (Z6), and sodium isopropyl xanthate (Z11) were used as collectors, and Polypropylene glycol (A65) was the frother. The specifications of the chemical reagents used are presented in Table 4.

Table 4. Specifications of chemicals used

Chemical Name	Chemical Formula	Trade Name	Function	Structural Formula
potassium amyl xanthate	CH3(CH2)4OCS2K	Z6	collector	
sodium isopropyl xanthate	C3H7OCS2Na	Z11	collector	
Polypropylene glycol	C3H8O2(CH2CH2O)n	A65	frother	

4.2. Experimental Works

4.2.1. Shaking Table

The sample was prepared using a laboratory rod mill in a controlled procedure and screened to a size of approximately d_{80}=600 and 300 microns to be used in shaking table tests. The shaking table was a Wilfley model with dimensions of 129×64 cm. For the experiment, approximately 2 kg of sample with particle sizes of 300 and 600 microns was prepared. The operating conditions were as follows: table slope of 8 degrees, feed water flow rate of 10 liters per minute, and wash water flow rate of 12 liters per minute. After the test, samples of concentrate, middling, and tailing were collected and gold fire assay analysis was employed to determine their gold grades.

4.2.2. Flotation

For flotation tests, the size of sample reached to d_{80}=75 microns by laboratory rod mill. For the experiment, approximately 1 kg of sample was selected, and after adding water, a weight solid percent of 30% was examined. To keep the parameters constant, all experiments were conducted under natural pH, and a frothing time of 5 minutes.

5. Results

The calculations were performed based on the weight and grades of the concentrates and tailings. In order to make sure of evaluation, it was decided to use weight recovery (yield) and grade recovery, by corresponding calculation formulas given in Equations (2) and (3), respectively.

$$Weight\ Recovery\ = \frac{Concentrate\ Weight}{Feed\ Weight} \times 100 \qquad (2)$$

$$Grade\ Recovery\ = \frac{Weight\ Recovery\ \times Concentrate\ Grade}{Feed\ Grade} \times 100 \qquad (3)$$

The Enrichment Ratio (ER) indicates how many times the feed grade has been concentrated in the final product. Therefore, grade recovery serves as an appropriate criterion for evaluating and determining the optimal operating conditions.

Table 5 shows the gold grade and recovery of the products obtained from the shaking table experiments.

Table 5. Results of Shaking Table tests

Test No.	Particle Size Range (μm)	Product	Gold grade (ppm)	Gold Recovery (%)
Test 1	600	Concentrate	4.52	24.6
		Middling	1.95	
		Tailings	1.82	
Test 2	300	Concentrate	3.35	13.8
		Middling	2.25	
		Tailings	2.07	

Table 6 shows the gold grade and recovery of the flotation tests.

Table 6. Results of different flotation tests

Test No.	Collector	Collector Concentration (g/t)	Frother	Frother Concentration (g/t)	Product	Gold grade (ppm)	Gold Recovery
Test 3	Z6	50	A65	50	Concentrate Tailings	12.58 0.54	62.2
Test 4	Z11	50	A65	50	Concentrate Tailings	7.32 1.19	46.0
Test 5	Z6	50	A65	100	Concentrate Tailings	13.41 1.02	77.5
Test 6	Z11	50	A65	100	Concentrate Tailings	11.89 1.22	59.8

6. Discussion

6.1. Shaking Table

As shown in Fig. 4, reducing the particle size from 600 to 300 microns decreased the gold grade from 4.52 to 3.35 ppm, and the recovery also decreased from 24.6% to 13.8%. Consequently, decreasing the particle size did not improve the upgrading process. According to mineralogical studies, this would be postulated by the gold being locked with associated minerals of different specific gravities.
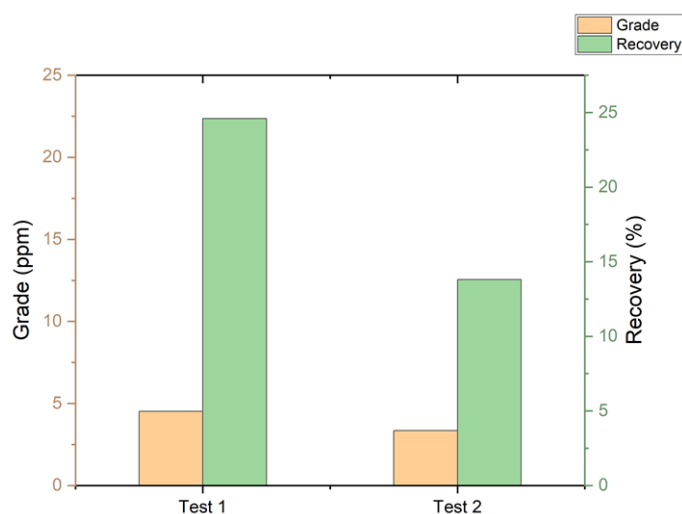
Fig. 4. Comparison of Grade and Recovery of First and Second Shaking Table Tests

6.2. Flotation

6.2.1. Effect of Collector

The effect of collector type was investigated under identical conditions. To investigate more precisely, the frother concentration increased from 50 g/t to 100 g/t, to determine its effect on grade and recovery. Fig. 5 shows that when the frother concentration was 50 g/t, changing the collector from Z6 to Z11 decreased the gold grade from 12.58 to 7.32 ppm, and the recovery also decreased from 62.2% to 46.0%.
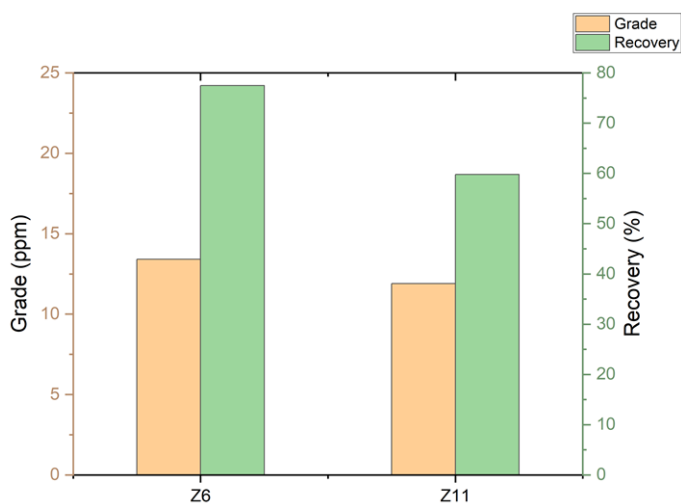
Fig. 5. Comparison of grade and recovery with changing collector, using 50 g/t of frother

In addition, under identical conditions as before, as presented in Fig. 6, only by changing the frother concentration to 100 g/t and changing the collector from Z6 to Z11, the grade decreased from 13.41% to 11.89%, and the recovery also decreased from 77.5% to 59.8%. This is due to the lower floatability of collector Z11 comparing with Z6.
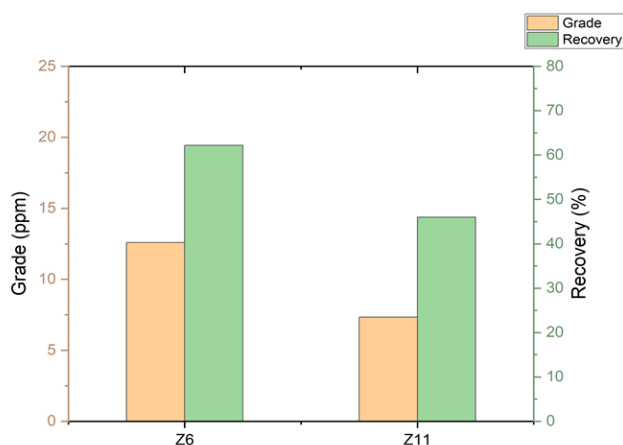
Fig. 6. Comparison of grade and recovery with changing collector, using 100 g/t of frother

6.2.2. Effect of Frother Concentration

Fig. 7 shows that when collector Z11 is used, increasing the frother concentration from 50 to 100 g/t, the gold grade increased from 7.32 to 11.89 ppm, and the recovery also increased from 0.46% to 59.8%.
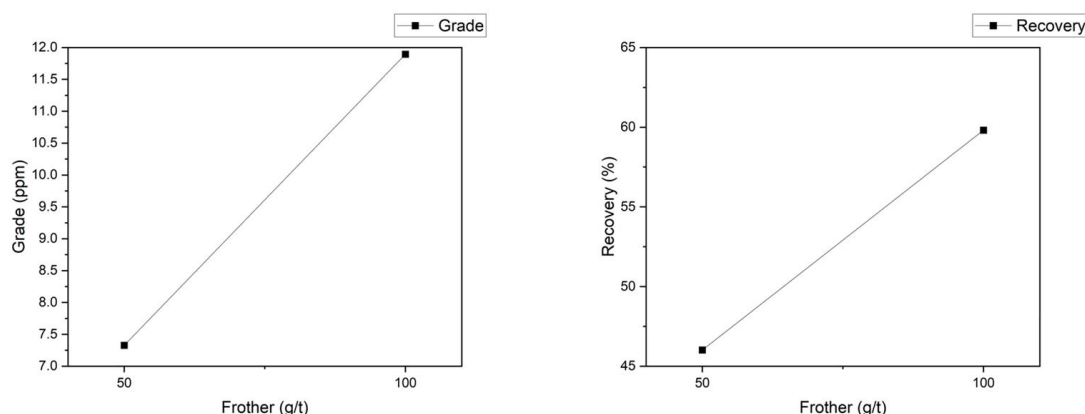
Fig. 7. Changes in grade and recovery with changing frother concentration for collector Z11

Moreover, under different conditions shown in Fig. 8, using collector Z6, increasing the frother concentration from 50 to 100 g/t, increased the gold grade from 12.58% to 13.41%, and the recovery also increased from 62.2% to 77.5%. It is important to note that this is likely due to the flotation of coarse-grained sulfide particles which contained gold.
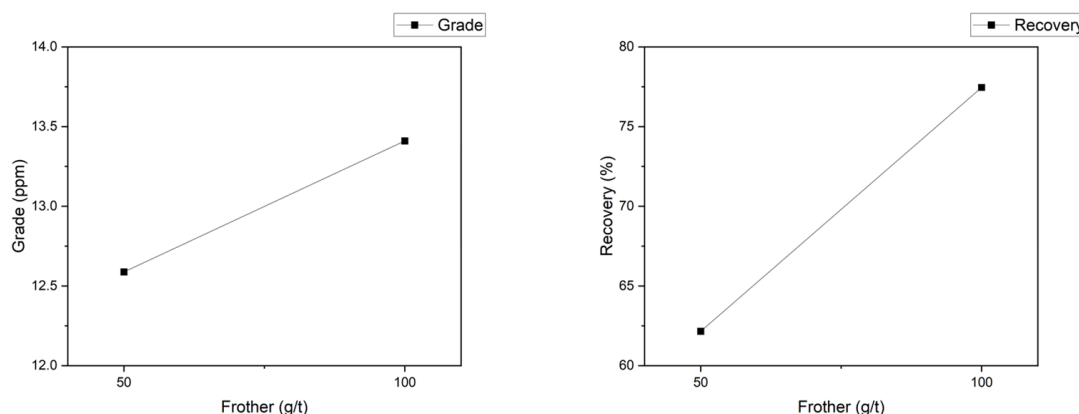
Fig. 8. Changes in grade and recovery with changing frother concentration for collector Z6

7. Conclusion

In this research work, beneficiation approaches such as shaking table and flotation were employed, using the sulfide gold ore sample from Hirad deposit. Different experiments were performed and the following results were made:

- In shaking table tests, it was observed that by decreasing the particle size, the gold recovery in concentrate also decreased. It seems that with the refinement of particle size, optimal separation of gold particles was not possible, and these particles, along with gangue minerals, entered to the middle and tailings parts, which accordingly reduced gold recovery in concentrate.

- In flotation, by changing the type of collector from Z11 to Z6, the recovery increased. Furthermore, by changing the frother concentration from 50 g/t to 100 g/t, the recovery increased due to the flotation of coarse-grained sulfide particles containing gold.

- The results indicated that using 50 g/t of Z6 yielded gold recovery of 62.2% with grade of 12.58 ppm. Using 50 g/t of Z11 produced concentrate with 46.0% recovery and grade of 7.32 ppm. Also, increasing the frother (A65) from 50 to 100 g/t improved the gold recovery from 62.2% to 77.5%, and increased the gold grade from 12.58 ppm to 13.41 ppm.

□ Based on the results of shaking table and flotation tests, the use of flotation with its higher recovery would be recommended.

References

Abdollahi, M., Goleini, M. J., & Zakeri Khatir, M. (2005). Pre-processing of Kooh Zar Damghan Placer Gold by Gravity Methods. Paper presented at the 24th Symposium of Geosciences, Tehran.

Altinkaya, P. (2021). Leaching and recovery of gold from low-grade raw materials in cyanide-free media. Doctoral Dissertation (Thesis), Department of Chemical and Metallurgical Engineering, Aalto University, Espoo, Finland.

Askari, A., & Feiz, M. (2011). Integration Plan of Base Information Layers and Determination of Promising Mineral Points. Detailed Exploration Report of Hirad Gold Deposit (Target 3), Geological Survey and Mineral Exploration of Iran.

Augusto, R. A., & Martins, J. (2001). Innovation features of a new magnetic separator and classifier. Mineral Processing and Extractive Metallurgy Review, 22(1), 231-247.

Azizitorghabeh, A., Wang, J., Ramsay, J. A., & Ghahreman, A. (2021). A review of thiocyanate gold leaching–Chemistry, thermodynamics, kinetics and processing. Minerals Engineering, 160, 106689.

Ebrahimi Basabi, H., & Mesroghli, S. (2021). Optimization of Pre-processing Operations of Gold-Bearing Sulfide Minerals by Flotation Method. Paper presented at the 10th Iranian Mining Engineering Conference, Zahedan.

Emami Jafari, A., Alirezaei, S., Rasa, I., Kolb, J., & Jochen, R. (2023). The Hirad Gold Deposit, Lut Block, Eastern Iran: An Example of an I-Type Reduced Intrusion-Related Gold Deposit. Journal of Earth Sciences, 33(3), 219-242.

Eshraghi, H., Rastad, E., Emami, M. H., & Asgari, A. (2005). Gold Mineralization of Hirad: An Example of Gold Deposits Associated with Reduced Granitoid Intrusions. Paper presented at the 24th Symposium of Geosciences, Tehran.

Fazlavi, A. (2001). Mine Economics (Technical and Economic Evaluation of Mining Projects) (First Edition), in Persian, Sayeh Gostar Publications.

Hasani Pak, A. A. (2001). Mineral Sampling (Exploration, Extraction and Processing), in Persian, University of Tehran Press.

Jeffrey, M. I., & Breuer, P. L. (2000). The cyanide leaching of gold in solutions containing sulfide. Minerals Engineering, 13(10-11), 1097-1106.

Nematollahi, H. (2008). Mineral Processing (4th Edition), in Persian, University of Tehran Press.

Rezaei, B. (1996). Flotation (2nd Edition), in Persian, Hormozgan University Publications.

Rezaei, B. (1998). Mineral Processing Technology (Gravity Concentration), in Persian, Hormozgan University Publications.

Safari, H. (2021). Gold Extraction from Polymetallic Darik Ore. Master's Thesis, in Persian, School of Mining Engineering, University of Tehran.

Yannopoulos, J. C. (2012). The Extractive Metallurgy of Gold. Springer Science & Business Media.

Investigating the Feasibility of Gravity Preconcentration of Miduk copper ore using spiral separator and its effect on the efficiency of flotation process

Reza Rastegarfar[1], Mehdi Shabani[1], Fatemeh Badri Behnoo[1], Javad Ghadami[1], Faraz Soltani[2]*

[1]Miduk Copper Complex, National Iranian Copper Industry Company, Kerman, Iran.

[2]Department of Earth Science Engineering, Arak University of Technology, Arak, Iran.

*Corresponding author: faraz.soltani@arakut.ac.ir (Faraz Soltani)

Abstract:

In this study, the effect of spiral preconcentrating the hydrocyclone overflow sample of the Miduk Copper Complex side flotation plant containing 0.41% total copper (including 0.08% copper oxide) and its effect on increasing the efficiency of the flotation process were investigated. Spiral tests were conducted with 30% solids in four stages, and finally concentrates, middling, and tailing samples were analyzed. Subsequently, flotation tests were conducted under similar conditions on the feed, concentrate, middling, and tailings samples of the spiral test. The results of the spiral test showed that the copper grade was 2.7%, 2%, 1.7%, and 1% in the first to fourth concentrates, respectively (the total copper recovery in all the concentrates was 55.58%). The grade of the middling and tailing samples were 0.17% and 0.27%, respectively. By performing flotation on the spiral concentrate sample, the rougher concentrate grade increased from 1.3% to 5.16% and the flotation process recovery increased from 65 to 85%. The middling and tailing samples also did not responsed the flotation process due to their fine nature (d_{80}=40 micron). The results showed that by performing the spiral preconcentration, 87.76% of the feed intered to the middling and tailing sections. Hence, the flotation plant capacity can be increased by about 8-9 times. Considering the nature of the copper minerals in the tailings of the preconcentration process, this sample is a good candidate for the bioleaching process that needs further investigation.

Keywords: Preconcentration, Copper Sulfide Ore, Spiral Separator, Miduk Copper Plant

1. Introduction

The final extraction processes typically performed on run of mine ores include smelting, hydrometallurgy, flotation, and electro-processes (Poloko, 2019). Due to the refractory nature of the copper sulfide minerals (particularly chalcopyrite), the conventional flotation-smelting method has been used to produce the majority of the world's copper since the 19th century (Neira et al., 2021).

Due to the depletion of high-grade ores, direct processing of ores without preconcentration would be very expensive/energy-intensive (Poloko, 2019, Adewuyi et al., 2020). Physical preconcentration methods include gravity concentration, heavy media separation, magnetic separation, and sensor-based separation methods, etc. (Poloko, 2019). Gravity separation methods are low-cost and environmentally friendly. In recent years, some methods and equipment have been developed for processing very fine materials, including spiral separators for particles as small as 30 µm. In addition, various designs for spiral separators have been proposed based on gravity, particle size, and some other physical properties (Richards et al., 2000).

Due to the widespread use of flotation method for sulfide and some oxide copper ores (Asadi et al., 2019), most of the research on gravity separation methods has been conducted on coal, iron, lead and zinc, gold and some other ores, and few studies have been conducted on copper ores. Nekoee Motlagh et al. (2023), by conducting gravity separation experiments on an IOCG ore containing 0.13% copper, concluded that conventional gravity methods were not suitable for preconcentration of this ore.

A portion of the Miduk copper ore with a lower grade (typically around 0.3 to 0.4 percent) is processed by the Miduk copper complex's side plant (with a nominal capacity of 300 tons per day) by flotation, which presents many challenges for flotation processing (including the low grade of the cleaner concentrate) compared to the ore entering the main plant due to its low grade and challenges in the mineralogy composition. This research aims to investigate and evaluate the effect of using a spiral separator as a preconcentration method in improving the efficiency and capacity of the copper flotation process from the Midoc copper complex's side plant. Using a spiral separator as a method for preconcentration of copper ores is one of the innovative aspects of the present paper. The findings of this research can be used as a guide to improve and optimize the separation and preconcentration processes in the copper processing industry.

2. Material and methods

2.1. Sample preparation and characterization

In this study, about 100 kg representative sample collected from the cyclone overflow of the side flotation plant of the Miduk Copper Complex and prepared for gravity separation tests using the spiral separator from Armis Company (Tehran, Iran). The results of the chemical analysis of the sample is presented in Table 1. According to Table 1, the feed sample contains 0.4% copper (total), of which only 0.08% is in the form of oxide minerals. Therefore, 80% of the total copper in the feed sample is in the sulfide form and only 20% is in the form of copper oxide minerals. The results of microscopic studies also showed that the feed sample contained 8.7% of chalcocite, covellite, chalcopyrite, pyrite, sphalerite, hematite, magnetite metallic minerals, 91.2% non-metallic minerals and 0.14% copper oxide minerals.

Table 1. Grade of Cu and Fe of the feed sample

Component	Percent
Cu	0.4
CuO	0.08
Fe	3.76

The grain size distribution diagram of the feed sample is shown in Figure 1a. According to Figure 1a, the d_{80} of the feed sample is about 101 µm and its d_{100} is about 250 µm. As the particle size becomes finer up to 32 µm, the copper content increases. In other words, the maximum copper grades occur in the finer size fractions, such that the copper grade in the +125 µm size fraction is 0.2% and in the of +32 µm size fraction is 0.62%.
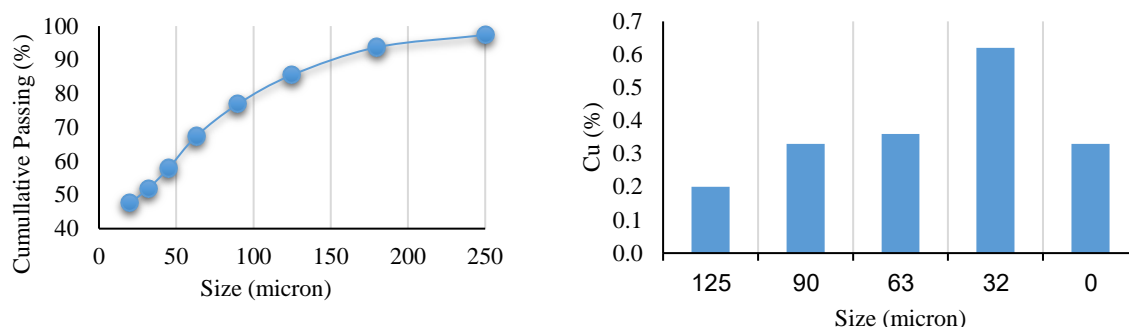
Fig. 1. a) Size distribution of the feed sample and b) Cu grade in different size fractions.

2.2. Spiral separator experiments

Representative sample was processed by flotation method on a laboratory scale to compare the behavior of the sample in the flotation process before and after the spiral separator preconcentration.

Preconcentration test with a spiral (with a solid percentage of about 30%) was carried out in four stages (Figure 2) to achieve the desired grade, which ultimately led to the separation of three final products including four concentrates, a final middling, and a final tailing. All the products were examined in terms of particle size distribution and grade of different size fractions to determine the effect of the spiral separator on the separation of coarse and fine particles.
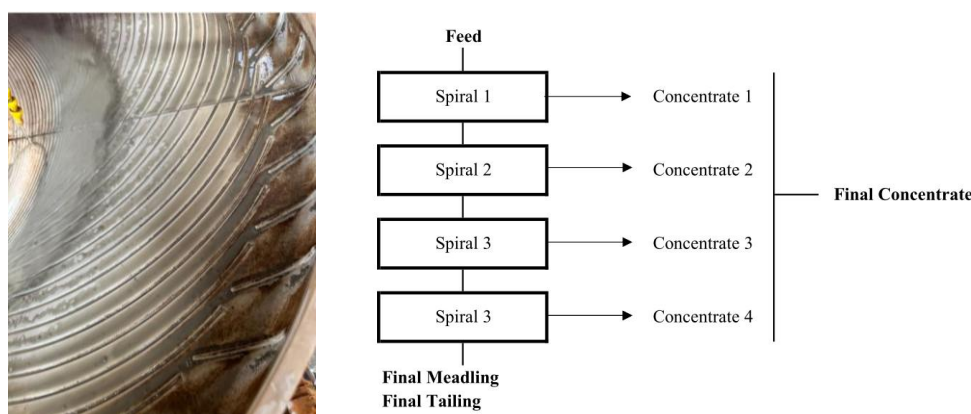
Fig. 2. Flowchart of the spiral tests (right) and a picture of the spiral separator (left).

3. Results and discussion

3.1. Effect of the preconcentration on the Cu grade

Copper grade in different size fractions of concentrates 1 to 4 of the spiral separator is presented in Figure 3. Comparison of the grades of different size fractions in concentrates 1 to 4 showed that, as expected, the grade of the concentrate of the spiral separator decreased from concentrate 1 to 4. It is noteworthy that the maximum grade of 3% copper in the spiral concentrates is in the -32 µm size fraction of the first concentrate. The d_{80} of concentrates 1 to 4 is 118, 110, 131 and 116 µm, respectively, which is coarser compared to the d_{80} of the feed (101 µm), indicating that the particle size of the concentrate is coarser than the input feed. The d_{80} of the middling and the final tailings of the spiral separator experiment were 165 and 40 µm, respectively. The significant difference in the size of tailings particles compared to concentrates and middling products indicates that, given the fine nature of the samples,

particle size also had an effect on the concentration behavior of particles. It means that the particles with a smaller size had a greater tendency to inter the tailings section.
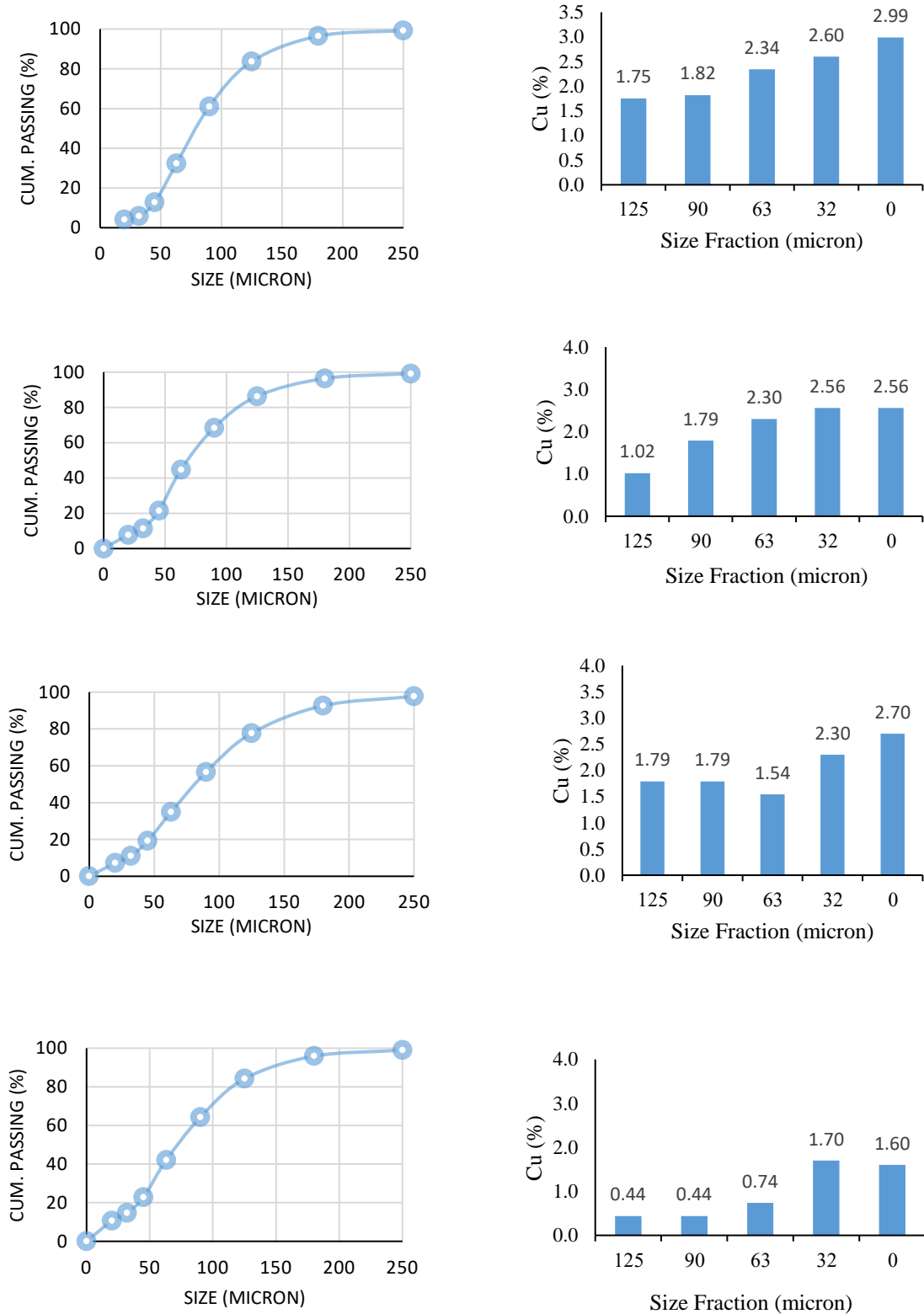
Figure 3. Size distribution and Cu grade in different size fractions of spiral test concentrates.

A notable point about the behavior of fine particles in the concentration process is that heavy particles had a greater tendency to transfer to the concentrate. This is clearly evident from comparing the grade of the concentrate and tailing sections, such that the copper grade in different tailings size fractions ranged from 0.07 in the +250µm size fraction to 0.33 in the -32µm size fraction.

The results showed that the use of the spiral separation method for preconcentration was effective in increasing the copper grade. Furthermore, the recovery of copper in the concentrate, middling and tailings section was also investigated.

3.2. Investigating the possibility of removing tailings with preconcentrating by spiral

The results of the spiral separation experiment are presented in Table 2. According to Table 2, the weight percentage of the total concentrates is 12.25% of the total input feed. Copper grade and recovery of the total concentrates obtained from the spiral experiment is 1.86% and 55.52%, respectively. A notable point in the data presented in Table 2 is the lower grade of the middling section compared to the tailings section. This can be due to the significant difference in particle size of the middling and tailing sections (165 and 40 µm, respectively). On the other hand, 55.77% and 31.99% of the total feed has been entered the tailings and the middling sections, respectively. Therefore, the mixed grade of the middling and tailing sections is about 0.23%.

Table 2. Results of the spiral concentration experiment.

Product	Weight	Wt. %	Cu Grade (%)	Cu Recovery (%)
Feed	85.35	100.00	0.41	100.00
1st Concentrate	2.76	3.23	2.7	21.30
2nd Concentrate	2.57	3.01	2	14.69
3rd Concentrate	2.47	2.89	1.7	12.00
4th Concentrate	2.66	3.12	1	7.60
Middling	27.3	31.99	0.17	13.26
Tailing	47.6	55.77	0.27	36.73

3.3. Effect of preconcentration on the flotation performance

In order to investigate the effect of spiral preconcentration on the flotation process performance, experiments were conducted on the spiral feed sample (cyclone overflow of flotation plant), mixed sample of 4 spiral concentrates, and mixed sample of spiral middling and tailing under similar conditions. According to the results presented in Table 3, by performing flotation operation on spiral concentrate sample, the grade of rougher concentrate increased from 1.3% to 5.16% and the recovery increased from 65% to 85%. It is important to note that the final recovery (spiral + flotation) was about 47.2%. The middling and tailings samples also did not respond well to the flotation process due to their fine nature (with d_{80} of about 40 microns).

The results of the spiral and flotation experiments showed that, considering that one of the important challenges of the Miduk side flotation plant is the low grade of the flotation concentrate, this grade reduction can be overcome by preconcentration using a spiral separator. On the other hand, by performing the spiral preconcentration process, 87.76% of the feed with the grade of 0.23% (middling and tailing sections) is rejected. Hence, the capacity of the flotation plant can be increased by about 8-9

times. Considering the nature of the copper minerals in the tailings of the spiral preconcentration process, this sample is a good candidate for the bioleaching process that needs further investigation.

Table 3. Results of the flotation experiments on the feed and spiral products.

Flotation Feed Type	Cu grade (%)			Cu Recovery (%) in Flotation	Overal Recovery (%) (Spiral+ Flotation)
	Feed	Flotation Concentrate	Flotation Tailing		
Original Feed (Cyclone Overflow)	0.41	1.3	0.18	65	65
Spiral Concentrate	1.86	5.16	0.4	85	47.2
Spiral Middling+Tailing	0.23	0.6	0.12	60	30.0

4. Conclusion

The results of this study showed that in the preconcentration process of Miduk low grade copper ore using four spiral stages, coarse particles with low grade were effectively separated in the middling part of the spiral (separation of the middling product with d_{80} equal to 165 micron and grade of 0.17% from the feed with d_{80} of 101 microns and grade of 0.41%). This separation allowed for the optimization of subsequent processes, especially the flotation stage. Accordingly, the use of this preconcentration method helps to increase the efficiency and effectiveness of the flotation process. In addition, this can lead to optimization of the consumption of chemicals used in copper sulfide flotation, which will significantly reduce costs and increase efficiency. By performing the spiral reconcentration process, 87.76% of the feed with the grade of 0.23% has been rejected. Therefore, the capacity of the flotation plant can be increased by about 8-9 times. Considering the nature of the copper minerals in the tailings of the spiral pretreatment process, this sample is a good candidate for the bioleaching process that should be investigated.

References

Adewuyi, S.O., Ahmed, H. A. M., & Ahmed, H. M. A. (2020). Methods of ore pretreatment for comminution energy reduction. *Minerals*, 10 (5): 423. doi: https://doi.org/10.3390/min10050423.

Asadi, M., Soltani, F., Tavakoli Mohammadi, M. R., Khodadadi, A., & Abdollahy, M. (2019). A successful operational initiative in copper oxide flotation: Sequential sulphidisation-flotation technique. *Physicochemical Problems of Mineral Processing*, 55(2). 356-369. doi: https://doi.org/10.5277/ppmp18137.

Neira, A., Pizarro, D., Quezada, V., & Velásquez-Yévenes, L. (2021). Pretreatment of copper sulphide ores prior to heap leaching: A review. *Metals*, 11(7): 1067. doi: https://doi.org/10.3390/met11071067.

Nekoee Motlagh, M.J., Soltani, F., & Mojeddifar, S. (2024). Iron, copper, and rare earth minerals beneficiation in an IOCG type deposit. *Canadian Metallurgical Quarterly*, 63(4). 1415-1425. doi: https://doi.org/10.1080/00084433.2023.2285199.

Poloko, N. (2019). *Physical separation methods, part 1: A review.* Paper presented at the IOP Conference Series: Materials Science and Engineering.

Richards, R. G., MacHunter, D. M., Gates, P. G., & Palmer, M. K. (2000). Gravity separation of ultra-fine (− 0.1 mm) minerals using spiral separators. *Minerals Engineering*, 13(1): 65-77. doi: https://doi.org/10.1016/S0892-6875(99)00150-8.

Mineralogy and enrichment of some critical elements in processing tailings in the Angouran Zn-Pb deposit, Zanjan

Fariba Tayefi[1], Majid Ghasemi Siani[1], Asghar Dolati1[1], Behrouz Karimi Shahraki[2]

1. Department of Geochemistry, Faculty of Earth Sciences, Kharazmi University, Tehran, Iran

2. Department of Geochemistry, Faculty of Earth Sciences, Kharazmi University, Tehran, Iran

*Corresponding author: tayefi.f85@gmail.com

Abstract

The Angouran Zn-Pb deposit is located in the southwest of Zanjan and in the Sanandaj-Sirjan tectonic zone, and stratigraphically is situated in the Takab Proterozoic metamorphic complex. The schists and dolomites of the Jangutaran are hosts of the ore mineralization. Mineralization in Angouran is divided into two sulfide and non-sulfide (carbonate) ores. Sphalerite and lesser extent galena and pyrite are the most important sulfides. The dominant texture includes massive, vein-veinlet, breccia, colloform and replacement. Smithsonite, hemimorphite, cerussite and mimetite are the dominant minerals in the carbonate ore. Sphalerite and smithsonite are considered the most important hosts of trace and critical elements in sulfide and carbonate ores, respectively, and their extraction is of particular economic importance. Based on microscopic and SEM studies on processing tailings samples, occurrences of critical elements such as Co, Ni, and Cd, and to a lesser extent Ga and Ge, have been identified.

Keywords: Sphalerite, Smithsonite, Critical elements, The Angouran Zn-Pb deposit, the Sanandaj-Sirjan tectonic zone.

1. Introduction

Many of mine tailings, especially those from metalliferous, contain high concentrations of metals or metalloids that can be economically recovered if appropriate solutions are provided. The physical and chemical characteristics of tailings can vary depending on the mineralogy, geochemistry, the type of mining equipment, the particle size of the mineral, and even the humidity content (Lottermoser, 2010). In recent years, given the industrial and economic approaches that govern international societies in the application of elements, a number of low abundance critical raw elements (about 30 elements), including cadmium, indium, germanium, gallium, thallium, rhenium, selenium, and tellurium, are sporadically found in sulfide deposits (Paradis, 2015). Trace elements characteristics in sphalerite can record the effects of ore-forming fluids and distinguish the genetic types of Zn-Pb deposits (Ye et al., 2011; Cook et al., 2009; Li et al., 2023; Zhang et al., 2022). Genetically, sulfide lead-zinc deposits are classified into two major groups: Mississippi Valley Type (MVT) and Sedimentary Exalative (SEDEX) deposits (Leach et al., 2010; Large, 2001). During the oxidation of primary sulfide deposits, non-sulfide (carbonate) deposits are formed, which are divided into hypogene and supergene deposits based on genetically and minelalogical characteristics (Large, 2001; Hitzman et al., 2003; Boni and Mondillo, 2015). The Angouran zinc-lead deposit is one of the largest and most unique zinc-lead mines in Iran, with large sulfide and carbonate reserves of high tonnage and grade, and the presence of recoverable tails with economic potential. Mineralization in the Angouran deposits includes two parts: sulfide and non-sulfide, with the main part of the reserve being non-sulfide (carbonate) mineralization, and based

on the studies of Hitzman (2003) and Karner (2006) placing it in the category of non-sulfide deposits. Sphalerite and smithsonite are the main hosts of the sulfide and non-sulfide (carbonate) mineralization, respectively. To investigate mineralogy and elemental enrichment, geochemical studies of tailing and major host minerals were conducted using ICP-MS analysis and optical and SEM electron microscopy on the processing tailings from the Angouran deposit.

2.   Maaterials and Methods

A total of 25 thin-polished sections were prepared from the processing taillings samples taken from the Angouran mining complex at the Kharazmi University labratory in Tehran. Petrographic and mineralogical studies were performed by SEM and optical microscopy laboratory of Kharazmi University and Iranian Mineral Processing Research Center (IMPRC). Twenty samples were also subjected to X-ray diffraction (XRD) at the Sharif University of Technology Laboratory Services Center and the Iranian Mineral Processing Research Center (IMPRC), for additional mineralogical studies.

3.   Mineralogy

3.1.   Scanning Electron Microscopy (SEM) Studies

3.1.1.   Processing Tailings in Ni-Cd Enrichment

Microscopic and SEM studies of samples from the Ni-Cd enrichment processing tailings have identified the presence of anomalies of Zn, Pb, Ni, U, Ag and strategic elements Cd, Ga, Ge and In within the crystal lattice of sphalerite, galena, smithsonite and cerussite has been identified (Figure 1, A-C). Based on the X-ray maps prepared from this sample, the concentration of Cd and Zn elements is consistent with the location of sphalerite, galena, smithsonite and hemimorphite crystals (Figure 2). Ni, Ga, Cd, Ge and In elements were detected by SEM (Figure 3, A-C). Based on the X-ray maps, the concentration of Cd, Ga, Ge and In elements is consistent with the location of sphalerite, galena and smithsonite crystals (Figure 4).
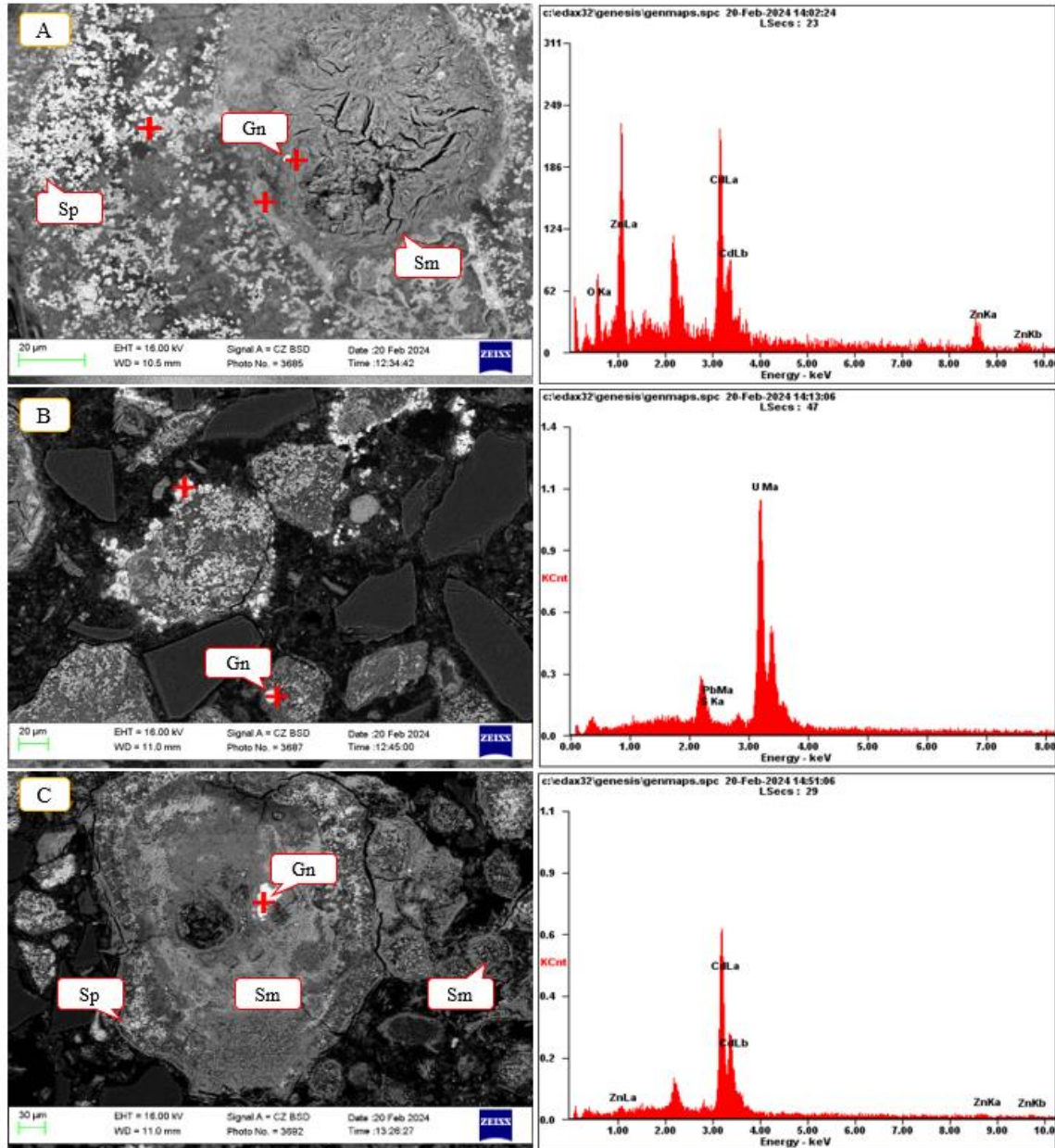
Figure 1. Mineralization of Zn, U and the critical element Cd within the lattice of sphalerite, galena and smithsonite in sample from Ni-Cd-rich processing tailings. Sp: Sphalerite, Gn: Galena, Sm: Smithsonite. Abbreviation is based on Whitney and Evans (2010).
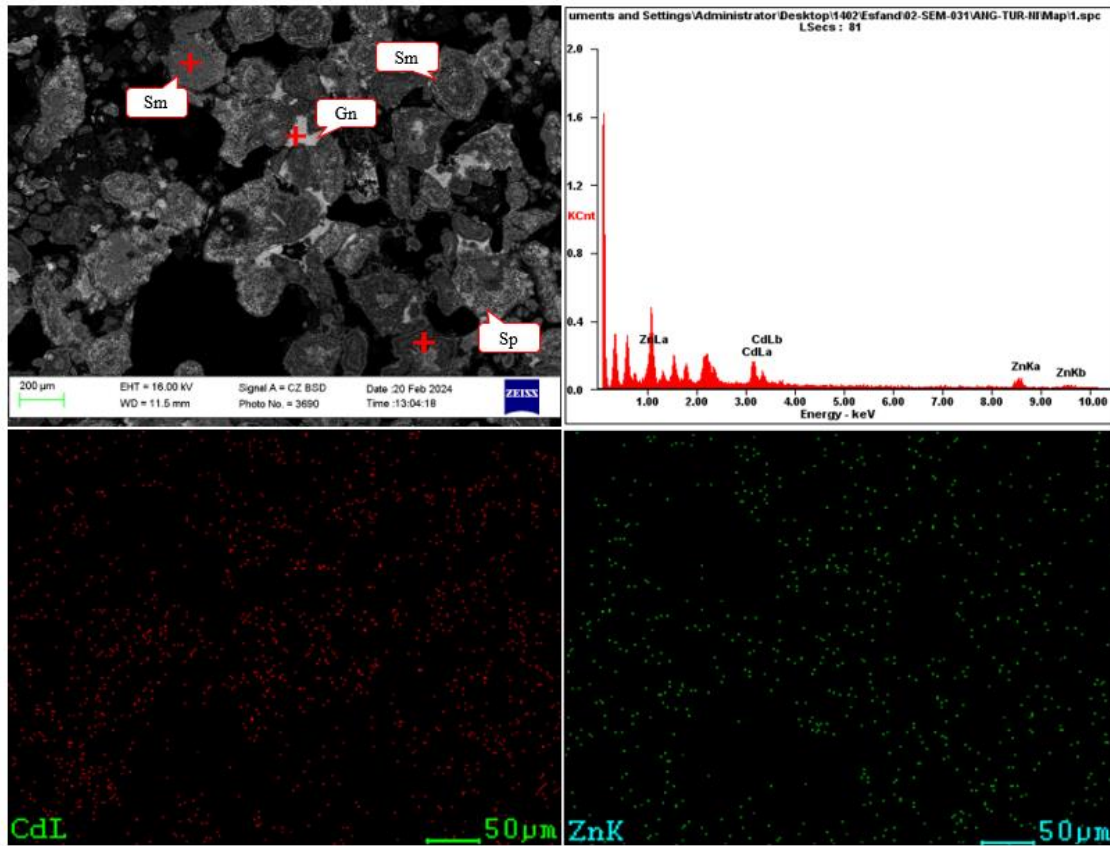
Figure 2. X-ray map of the dispersion of Cd and Zn elements in the Ni-Cd-rich processing tailings sample from the Angouran deposit.
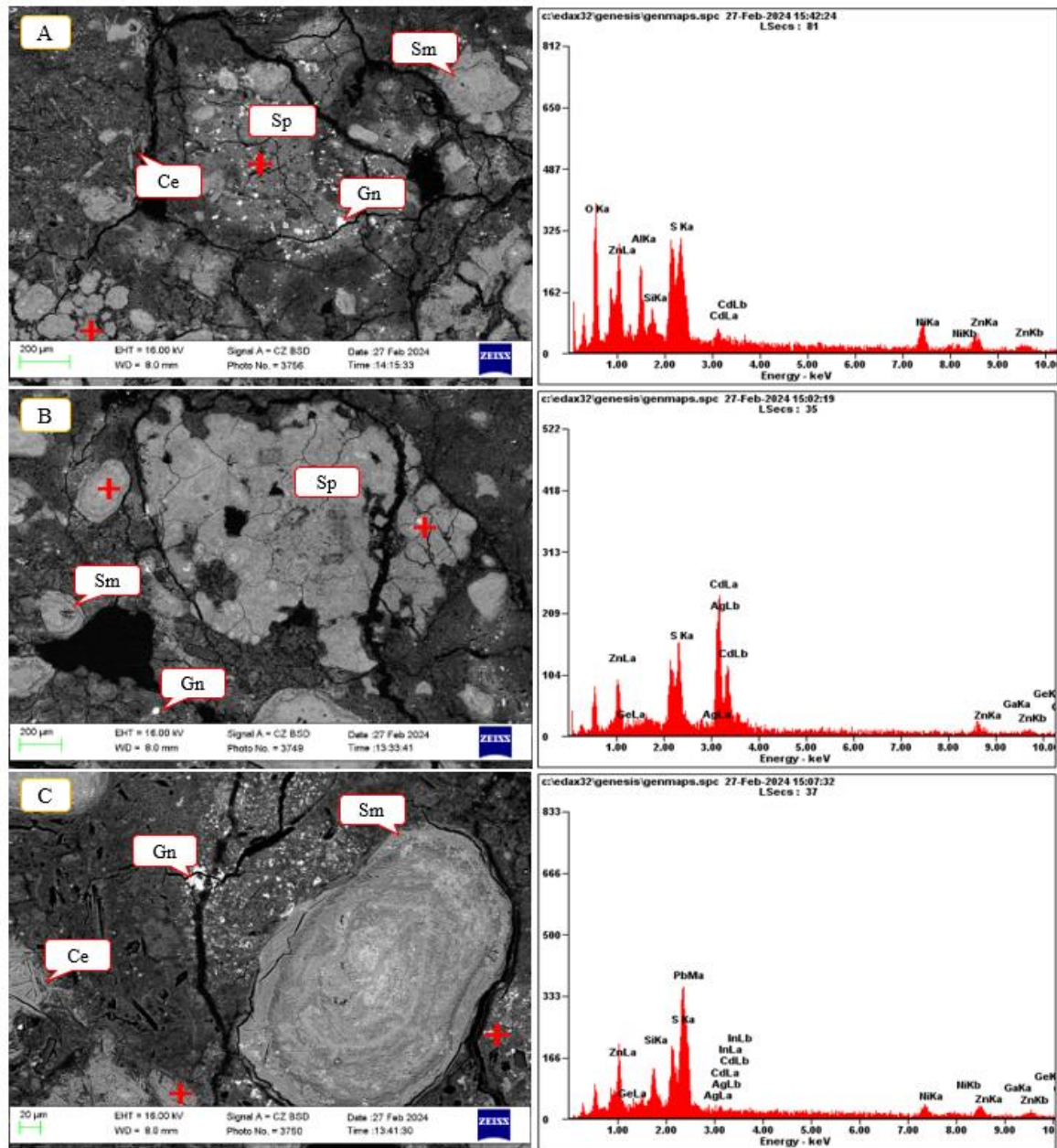
Figure 3. Mineralization of Ni, Ag and the critical elements Ga, Cd, Ge and In within the lattice of sphalerite, galena and smithsonite in Ni-Cd-rich processing tailings. Sp: Sphalerite, Gn: Galena, Sm: Smithsonite, Ce: Cerussite. Abbreviation is based on Whitney and Evans (2010).

Figure 4. X-ray map of the dispersion of the elements Ge, Cd, In and Ga in the Ni-Cd-rich processing tailings from the Angouran deposit.

3.1.2. Co-rich Processing Tailings

Microscopic and SEM studies of Co-rich processing tailings samples indicate the presence of anomalies of Zn, Pb, Fe, Mn, Mg, Se, As, and the critical elements Ga, Ge and Cd within the crystal lattice of the sphalerite, galena and hemimorphite (Figure 5, A-C). In addition, based on X-ray maps prepared from the Co-rich processing tailings sample, the concentrations of the elements Cd, Ga and Ge were correlated with the location of the crystals (Figure 6).
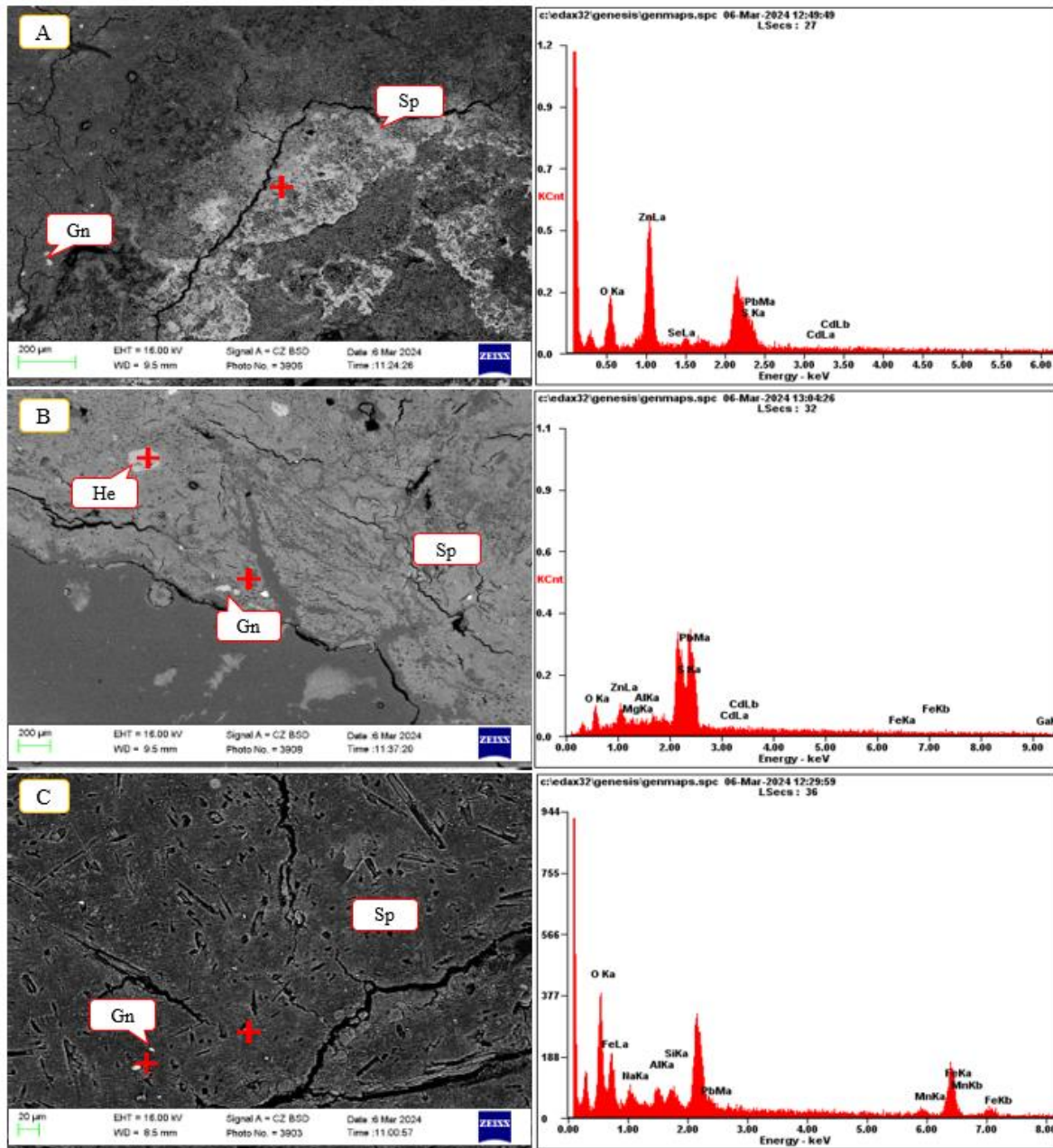
Figure 5. Mineralization of Mn, Mg, Se, As, and the critical elements Ga, Ge, and Cd within the lattice of sphalerite, galena, and hemimorphite in the Co-rich processing tailings from the Angouran deposit. Sphalerite, Gn: Galena, He: Hemimorphite, Ce: Cerussite. Abbreviation is based on Whitney and Evans (2010).
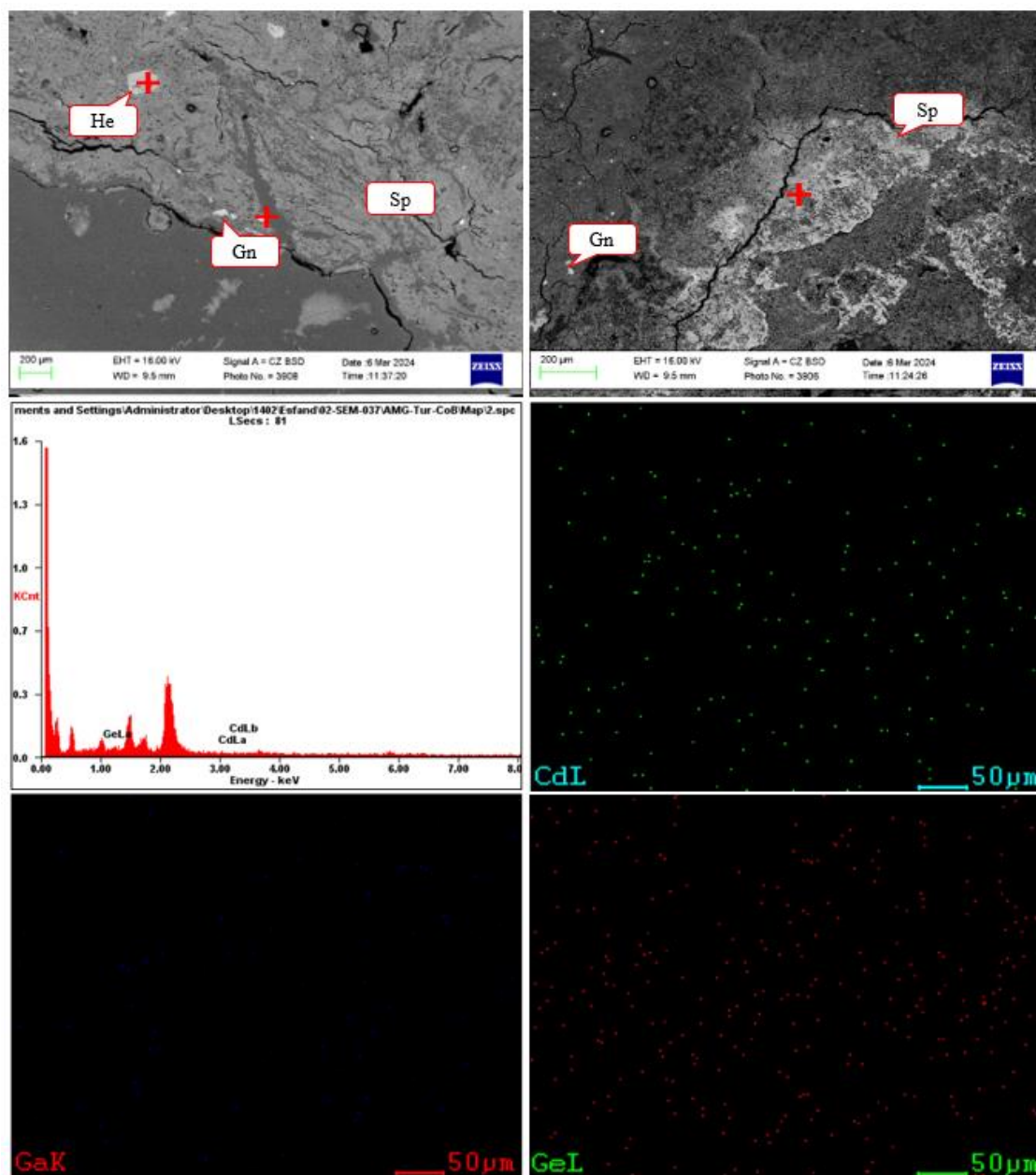
Figure 6. X-ray map of the dispersion of the elements Cd, Ga, and Ge in the Co-rich processing tailings from the Angouran deposit.

3.2. X-ray Diffraction (XRD) Studies

3.2.1. Ni-Cd-rich Processing Tailings

Based on X-ray diffraction (XRD) studies, the trace minerals are zincite and smithsonite which contain Cd, and the gangue minerals calcite and gypsum are clearly visible (Figure 7). In addition, anglesite, and lead oxide are detected, and gypsum, zinc hydroxyoxalate, and cadmium phosphate hydrate are other minerals (Figure 8).
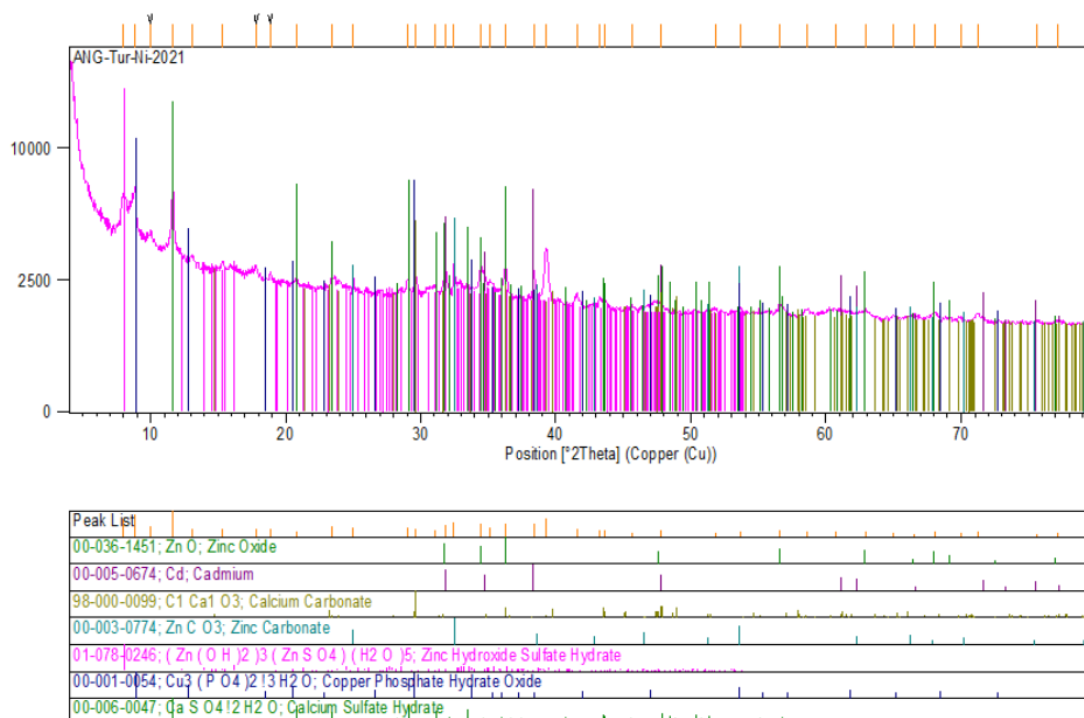
Figure 7. X-ray Diffraction (XRD) diagram of the Ni and Cd-rich processing tailing from the Angouran deposit.
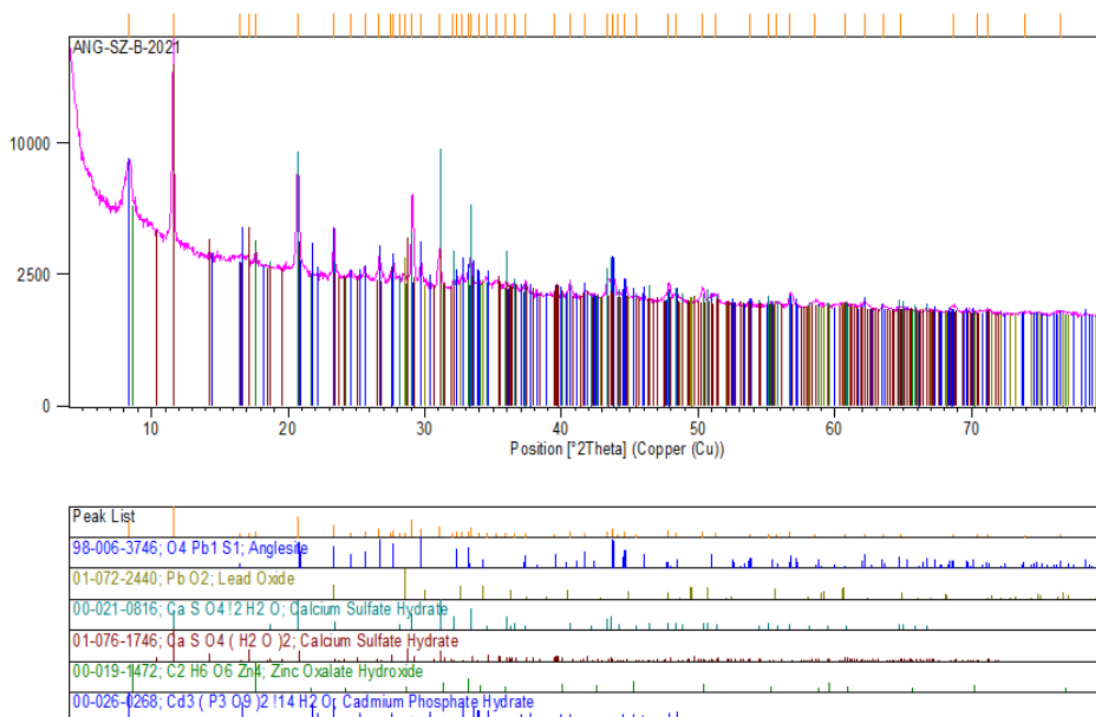
Figure 8. X-ray Diffraction (XRD) diagram of the Ni and Cd-rich processing tailing the Angouran deposit.

3.2.2. Co-rich Processing Tailing

Based on X-ray diffraction (XRD) studies on the Co-rich Processing tailing from the Angouran deposit, gypsum and hydrated magnesium sulfate are clearly visible as the main minerals in this sample (Figure 9).
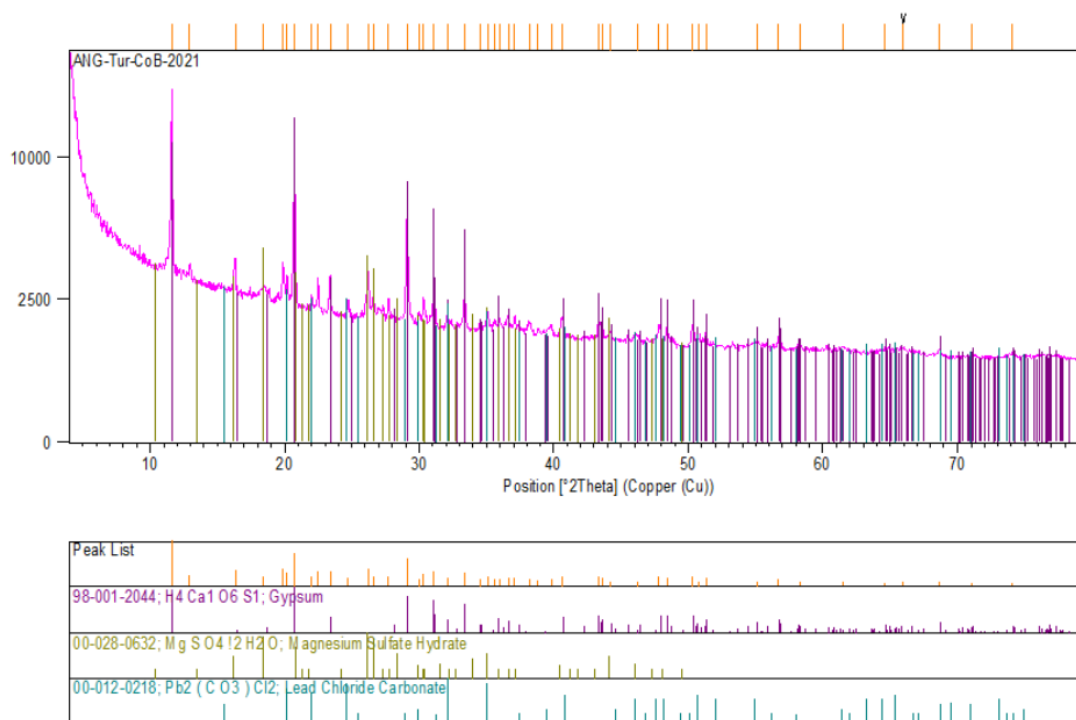
Figure 9. X-ray Diffraction (XRD) diagram of the Co-rich processing tailing from the Angouran deposit.

4. Conclusion

Mineralization at Angouran consists of two parts: sulfide and non-sulfide (carbonate); sphalerite and smithsonite are considered to be the major hosts of high-tech elements (Ga, Ge and In) in sulfide and carbonate ores, respectively. The presence of sphalerite, galena, smithsonite, hemimorphite, cerussite and mimetite as hosts for strategic elements in tailings samples from the Angouran deposit is economically significant. Mineralogical and SEM studies of the tailing's samples have identified the presence of anomalies of high-tech elements (Ga, Ge and In) and other trace elements such as Co, Ni and Cd within the crystal lattice of sulfides and less common carbonates. In addition, based on X-ray diffraction (XRD) studies of the processing tailings samples at the Angouran deposit, Co bearing sphalerite, Cd bearing smithsonite, quartz, gypsum, muscovite and others are clearly observed.

Reference

Boni, M., & Mondillo, N., (2015). "Calamines" and the "Others": The great family of supergene non-sulfide zinc ores. Ore Geology Reviews, 67, p. 208-233. https://doi.org/10.1016/j.oregeorev.2014.10.025

Cook, N.J., Ciobanu, C.L., Pring, A., Skinner, W., Shimizu, M., Danyushevsky, L., & Melcher, F., (2009). Trace and minor elements in sphalerite: A LA-ICPMS study. Geochimica et Cosmochimica Acta, 73(16), p. 4761-4791. doi: https://doi.org/10.1016/j.gca.2009.05.045

Hitzman, M.W., Reynolds, N.A., Sangster, D.F., Allen, C.R., & Carman, C.E., (2003). Classification, genesis, and exploration guides for nonsulfide zinc deposits. Econ Geol 98, p. 685–714. http://dx.doi.org/10.2113/98.4.685

Kärner. K., (2006). The Metallogenesis of the Skorpion Non-Sulphide Zinc Deposit Namibia. Doctoral Thesis, Wittenberg: Universität Halle - Wittenberg.

Large, R.R., Bull, S.W., & Winefield, P.R., (2001). Carbon and oxygen isotope halo in carbonates related to the McArthur River (HYC) Zn-Pb-Ag deposit: Implications for sedimentation, ore genesis, and mineral exploration. Economic Geology 96, p. 1567-1593. http://dx.doi.org/10.2113/96.7.1567

Leach, D.L., Bradley, D.C., Huston, D., Pisarevsky, S.A., Taylor, R.D., & Gardoll, S.J., (2010). Sediment hosted lead-zinc deposits in Earth history. Economic Geology 105, p. 593-625. http://dx.doi.org/10.2113/gsecongeo.105.3.593

Li, G., Zhao, Zh., Wei, J., & Ulrich, Th., (2023). Trace element compositions of galena in an MVT deposit from the Sichuan-Yunnan-Guizhou metallogenic province, SW China: Constraints from LA-ICP-MS spot analysis and elemental mapping. Ore Geology Review 150, 105123. https://doi.org/10.1016/j.oregeorev.2022.105123

Lottermoser, B.G., (2010). "Mine Wastes: Characterization, Treatment and Environmental Impacts", 3rd edition, Springer Heidelberg Dordrecht London New York, 410 p.

Ye, L., Cook, N.J., Ciobanu, C.L., Yuping, L., Qian, Z., Tiegeng, L., Wei, G., Yulong, Y., & Danyushevskiy, L., (2011). Trace and minor elements in sphalerite from base metal deposits in South China: a LA-ICP-MS study. Ore Geol Rev 39, p. 188–217. https://doi.org/10.1016/j.oregeorev.2011.03.001

Zhang, J., Shao, Y., Liu, Zh., & Chen, K., (2022). Sphalerite as a record of metallogenic information using multivariate statistical analysis: Constraints from trace element geochemistry. Journal of Geochemical Exploration 232, 106883. https://doi.org/10.1016/j.gexplo.2021.106883

Sustainable Iron Recovery from Dry Tailings: Application of Advanced Magnetic Separation and Circular Economy Principles, A Case Study of Golgohar Mining and Industrial Company

Pouya Karimi[1]*, Seyed Sajjad Hosseininejad[2], Alireza Farazmand[3]

[1]*PhD in Mineral Processing Engineering | Venture Capital Specialist, Golgohar CVC Fund (GTech)*

[2]*Supervisor of Mineral Processing Laboratory & Pilot Plant, Research & Technology Center, Golgohar Mining & Industrial Company*

[3]*M.Sc. in Mineral Processing Engineering and Head of Mineral Processing Laboratory, Sepanta Development Soreen (STS)*

*Corresponding author: Pouya.karimi62@gmail.com (Pouya Karimi)

Abstract:

This research investigates the challenges of iron recovery from dry tailings of the Golgohar Mining and Industrial Company's concentration plant. Initially, physical (particle size distribution) and chemical (total iron and ferrous oxide) properties were characterized, along with XRD analysis, mineralogical studies, and morphological examinations (SEM, EDAX, and QEMSCAN). The studied tailing sample, produced through magnetic separation processes at a field intensity of 1100 Gauss in plant, had an average iron grade of 11% and a D_{80} of 467 microns. Magnetic separation experiments were conducted using laboratory-scale dry magnetic separators at field intensities of 1200, 3500, and 5000 Gauss in two stages. In the first stage, the effect of magnetic field intensity on iron recovery and product grade was evaluated. The results showed that increasing the magnetic field intensity significantly improved iron recovery, from 4.9% (with an iron grade of 29.9%) to 15.7% (with an iron grade of 18.9%). Based on these findings, a second stage of experiments was performed using an innovative two-stage rougher-cleaner method at field intensities of 3500 and 1200 Gauss, achieving a recovery of 10% with a product iron grade of 40%. This study highlights the importance of advanced recovery methods in optimizing processes and reducing tailings. Furthermore, iron recovery from tailings using magnetic separators aligns with circular economy principles, as it promotes the reuse of mineral resources and minimizes waste. The results of this research can significantly contribute to improving industrial efficiency and reducing the environmental impact of tailings.

Keywords: Iron Recovery, Dry Tailings, Magnetic Separation, Circular Economy, Sustainable Mining

1. Introduction

The mining and mineral processing industry, particularly in the iron ore sector, faces numerous challenges including declining ore grades, increasing volumes of processing tailings, and environmental concerns related to waste disposal (Zhang et al., 2021). In this context, the recovery of iron from dry processing tailings not only enhances economic efficiency but also represents a crucial step toward reducing environmental pollution and implementing circular economy principles (Kirchherr et al., 2017).

The Golgohar mining and industrial complex, with its rich iron ore deposits, stands as one of the most prominent mining and industrial hubs in the Middle East. This region possesses significant potential to become a major competitive player in Iran's mining sector and on the global stage. The area comprises six registered mineral anomalies with a total geological reserve of 1,019 million tons and proven reserves of 1,000 million tons, making it the largest known iron ore deposit in the Middle East (Golgohar Mining Report, 2024). Conventional technologies face limitations in recovering these fine particles, making

advanced high-intensity magnetic separation techniques a promising solution for iron reclamation from these tailings (Xiong et al., 2020).

This research aims to evaluate the feasibility of sustainable iron recovery from Golgohar's dry tailings by combining innovative magnetic separation methods with circular economy principles. Magnetic separation experiments were conducted using laboratory-scale dry magnetic separators at field intensities of 1200, 3500, and 5000 Gauss in two stages. The study investigates the impact of key parameter (magnetic field intensity) and multi-stage separation processes on recovery rates and product grade.

2. Material and methods

For comprehensive physico-chemical and mineralogical characterization of dry tailings from the concentration plant (final tailings from a three-stage dry magnetic separation circuit comprising rougher, cleaner, and scavenger stages, producing three output streams: final dry concentrate, middling's, and final dry tailings), systematic sampling was conducted. Sampling frequency was set at once per working shift (equivalent to 3 samples per day) during the study period from September 1 to September 30, 2022 (Shahrivar 1401). Particle size distribution (D_{80}) was determined using ASTM standard test sieves (1000, 710, 500, 355, 250, and 180 µm) and Laser diffraction analysis (Sympatec GmbH LPS analyzer). Iron content (total Fe) and ferrous oxide (FeO) were quantified through wet chemical methods according to: ASTM E246-10 (Standard Test Methods for Determination of Iron in Iron Ores) and ASTM D3872-05 (Standard Test Method for Ferrous Iron in Iron Ores). In the section of Mineralogical Characterization Advanced analytical techniques were employed using Scanning Electron Microscopy (SEM): EFI ESEM Quanta system, Energy Dispersive X-ray Spectroscopy (EDAX): 2017 silicon drift detector, X-ray Fluorescence (XRF): ASENWARE AW_XDM300 spectrometer and X-ray Mapping for elemental distribution analysis. Dry magnetic separation tests were performed using drum separators (Sepanta Development Soreen Co. [STS]) at varying magnetic field intensities Low-intensity: 1,200 Gauss, Medium-intensity: 3,500 Gauss and High-intensity: 5,000 Gauss.

3. Dry Magnetic Separation Circuit Process Description of factory

The sub-3 mm material from the double-deck screen and underflow of air cyclones is conveyed to the dry magnetic separation section. The feed material is initially stored in eight feed silos, each with a capacity of 189 tons. Each silo is equipped with a chain feeder that continuously supplies material to the magnetic separators. The low-intensity dry magnetic separation system consists of eight parallel processing lines. Each line incorporates a three-stage separation configuration: One rougher, one cleaner and scavenger magnetic separator.

- Feed material characteristics:
  - Particle size distribution: 80% passing 450 µm
  - Bulk density: 2.7 t/m³
- Magnetic separator specifications:
  - Field intensity: 1,100 Gauss (low-intensity)
  - Motor power: 22 kW per separator
- Operational parameters:
  - Drum rotational speeds:
    - Rougher: 5 m/s
    - Cleaner: 6 m/s
    - Scavenger: 3 m/s
  - Operating temperature: 100°C

The material flow through the rougher-cleaner-scavenger circuit produces three product streams: Final concentrate, Middling's product and final tailing. Figure 1 illustrates the feed distribution system and product streams between the rougher, cleaner, and scavenger stages, showing the final concentrate, middling's, and tailings outputs.
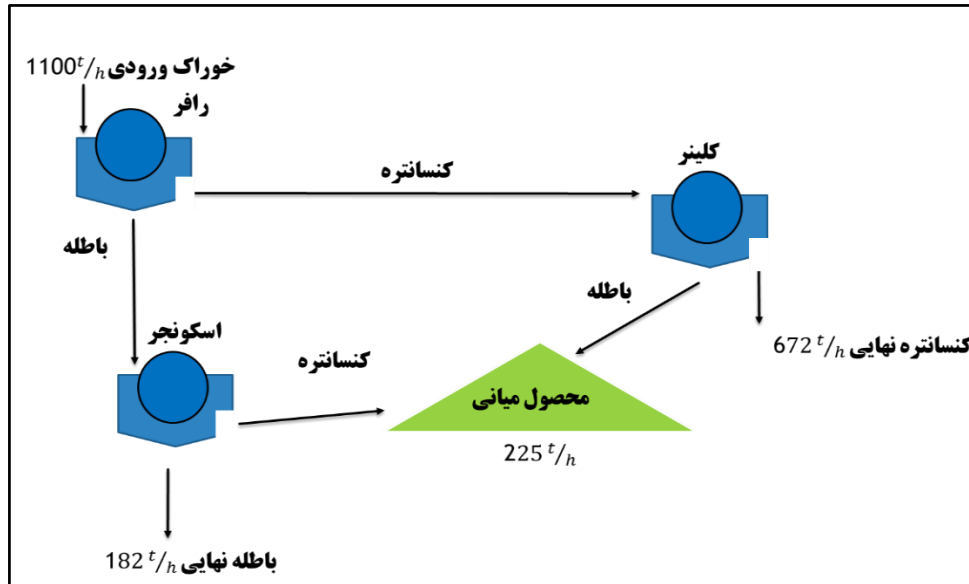

Fig. 1.   Feed material distribution system to low-intensity dry magnetic separators of concentration plant

4.   Results and discussions

4.1. Particle Size Distribution Analysis

Particle size distribution was determined using both laser diffraction analysis (Sympatec GmbH LPS analyzer) and standard ASTM test sieves (1000, 710, 500, 355, 250, and 180 µm). The laser diffraction results revealed the following characteristic diameters: D_{50}: 274 µm and D_{80}: 467 µm. Complementary sieve analysis yielded a D_{80} value of 484 µm, showing good agreement with the laser diffraction method (relative difference: 3.5%). The complete particle size distribution curve of the mentioned dry feed sample is presented in Figure 2.
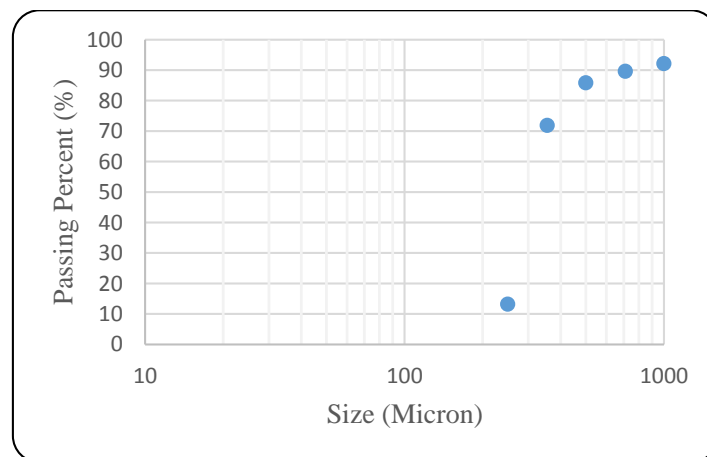
Fig. 2.   Particle size distribution graph of the feed tests

4.2. XRD Mineralogical Analysis

Given the significance of both iron-bearing and gangue mineral types in the investigated tailings sample, XRD analysis was performed. The quantitative phase analysis revealed the Iron-bearing minerals of Hematite (Fe_2O_3): 11 wt%, Magnetite (Fe_3O_4): 4 wt% and Pyrite (FeS_2): 5 wt%. In addition to, the dominant gangue minerals consist of : Spinel ($MgAl_2O_4$): 40 wt%, Biotite ($K(Mg,Fe)_3AlSi_3O_{10}(F,OH)_2$): 20 wt%, Silicon Dioxide (SiO_2): 15 wt% and Vermiculite ($(Mg,Fe,Al)_3(Al,Si)_4O_{10}(OH)_2 \cdot 4H_2O$): 5 wt%. The complete quantitative XRD results are presented in Table 1. Figure 3 shows the diffraction pattern with characteristic peaks of the identified mineral phases, confirming the mineralogical composition.
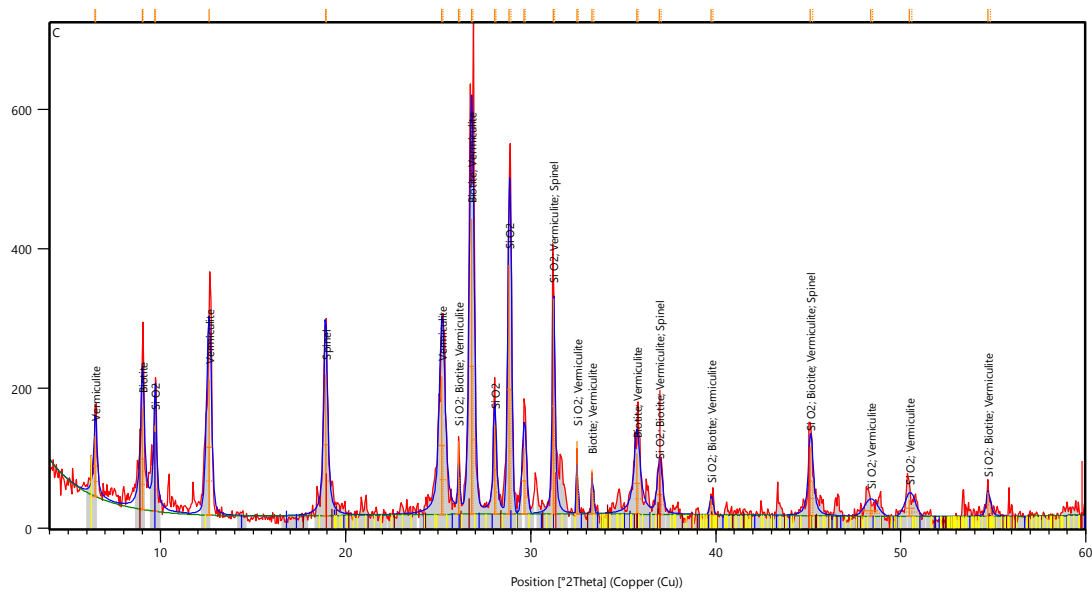
Fig. 3. XRD pattern of Dry tailing sample from the dry magnetic separation circuit of concentration plant

4.3 Chemical and XRF Analysis Results

Given the critical importance of iron content (Fe) and ferrous oxide (FeO) percentages for determining optimal magnetic field intensity to achieve acceptable iron concentrate grade, wet chemical analysis was performed on the tailings sample. The results revealed Total iron (Fe): 10.82 wt% and Ferrous oxide (FeO): 3.80 wt%. These values confirm the predominantly hematitic-magnetitic nature of the tailings sample. Furthermore, X-ray fluorescence (XRF) analysis was conducted to quantify impurity elements (sulfur and phosphorus) and other elemental oxides present in the sample. The complete quantitative results are presented in Table 1.

Table 1. **XRF Chemical Analysis of Investigated Dry Tailings Sample**

Dry Tailing Sample	Fe (%)	FeO (%)	S (%)	SiO_2 (%)	Al2O3 (%)	CaO (%)	MgO (%)	TiO_2 (%)	K_2O (%)	LOI (%)
Value (%)	10.82	3.80	6.304	39.18	8.48	5.11	14.96	.396	1.747	10.1

4.4 SEM, EDAX, and X-Ray Mapping Analyses

To investigate the microstructure, particle morphology, and size distribution of the dry tailings sample at the micron scale, scanning electron microscopy (SEM) was performed. The corresponding

micrographs are presented in Figure 4. Preliminary SEM analysis revealed a particle size distribution ranging from 20 to 650 μm in the examined zones. Energy-dispersive X-ray spectroscopy (EDAX) provided the following elemental composition (wt %): Fe: 11%, Ti: 0.51%, Ca: 4%, K: 1.7%, S: 6.38%, Si: 18%, Al: 7%, Mg: 13%, Na: 1.8% and O: 40%. The EDAX spectrum of sample is shown in Figure 5. As observed, the peaks corresponding to oxygen (O), silicon (Si), sodium (Na), and iron (Fe) exhibited higher intensities compared to other elements. This finding aligns well with the XRD quantitative results, confirming the dominant presence of hematite (Fe_2O_3), silica (SiO_2), and vermiculite in the sample. The X-Ray mapping results (Figure 6) further illustrate the spatial distribution of key elements: Iron (Fe) and Oxygen (O): The strong overlap in their distributions confirms the presence of iron oxides (hematite) as the primary Fe-bearing phase. Sulfur (S): Exhibits coarse-grained clusters, indicating localized concentrations, likely as sulfides (e.g., pyrite). Silicon (Si): Shows both fine and coarse particle distributions, consistent with quartz (SiO_2) and silicate gangue minerals.
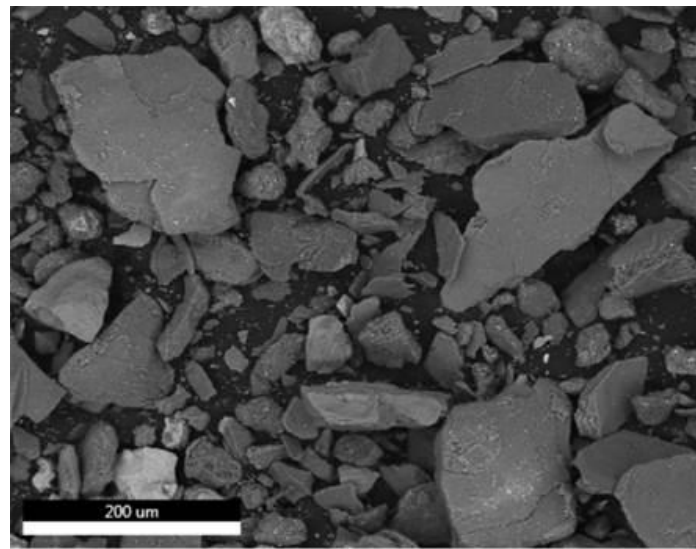
Figure 4. SEM micrographs of dry tailings from the concentration plant
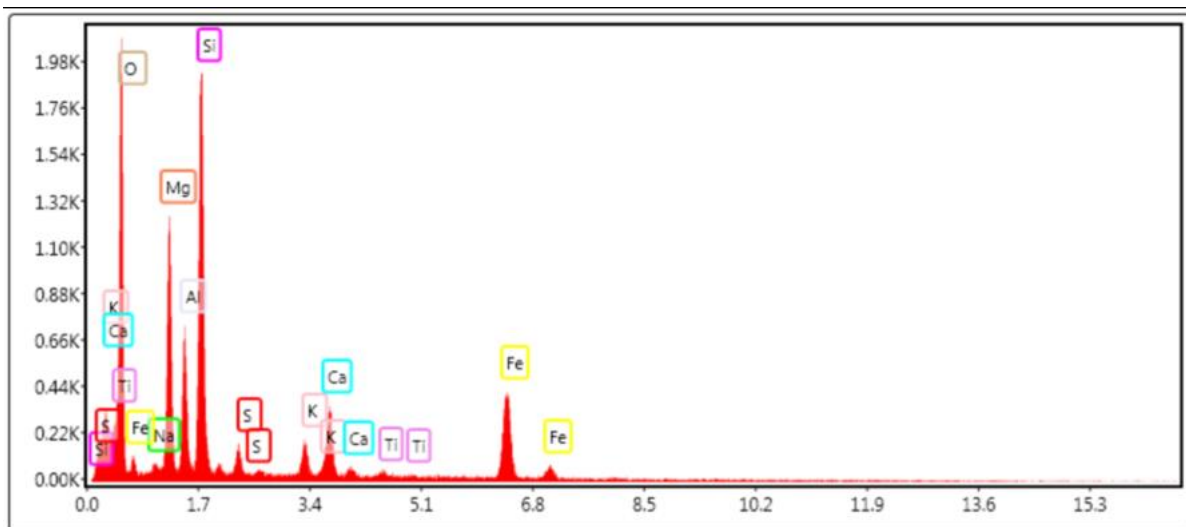
Figure 5. EDS spectrum of the investigated dry tailings sample
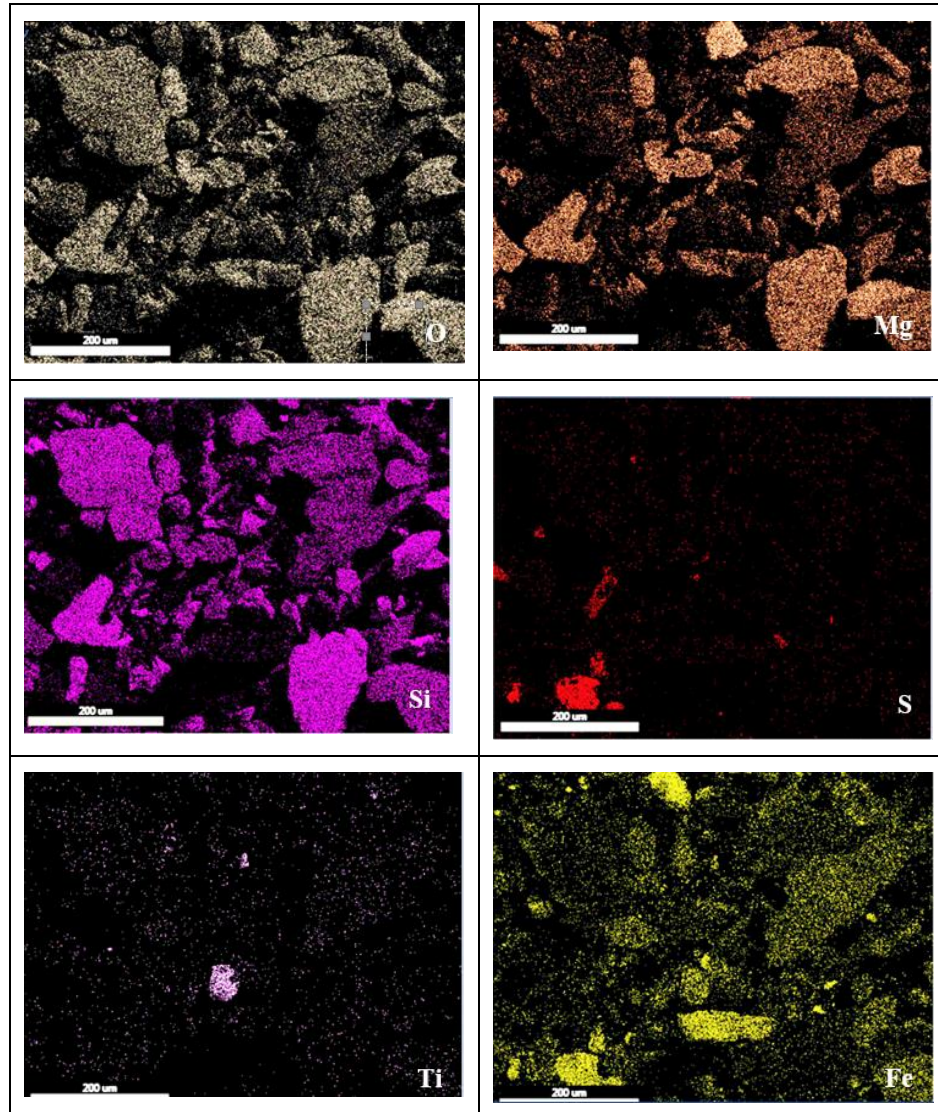
Figure 6. X-ray elemental maps of iron (Fe), oxygen (O), Magnesium (Mg), sulfur (S), silicon (Si), and titanium (Ti) in tailings sample

4.5 Dry Magnetic Separation Experiments

The dry magnetic separation tests were conducted using drum separators under the following experimental conditions: Magnetic Field Intensities of 1,200 Gauss (two configurations, without separation blades and with separation blades), 3,500 Gauss and 5,000 Gauss. Drum Specifications were Diameter: 400 mm and Rotational speed linear velocity of 2 m/s (Angular velocity: 95 rpm (constant across all tests). It must be mention that the dry tailings sample contained 10.82% iron (Fe) grade and 3.80% iron oxide (FeO). Figure 7 (left) demonstrates the iron grade (%) of magnetic separation products across varying magnetic field intensities. As evidenced, increasing the magnetic field intensity from 1,200 G to 5,000 G resulted in a decrease in iron grade from approximately 30% to 19%. This inverse relationship suggests that:

- Higher field intensities capture more weakly magnetic particles, diluting concentrate grade
- The optimal trade-off between recovery and grade occurs at intermediate intensities

Figure 7 (right) presents the mass recovery (%) of dry magnetic separation over the same intensity range (1,200-5,000 G), showing an increase from ~5% to ~16%. This positive correlation indicates:

- Enhanced particle capture efficiency at higher fields
- Progressive liberation of iron-bearing minerals across intensity levels
- Potential for multi-stage separation to balance grade and recovery
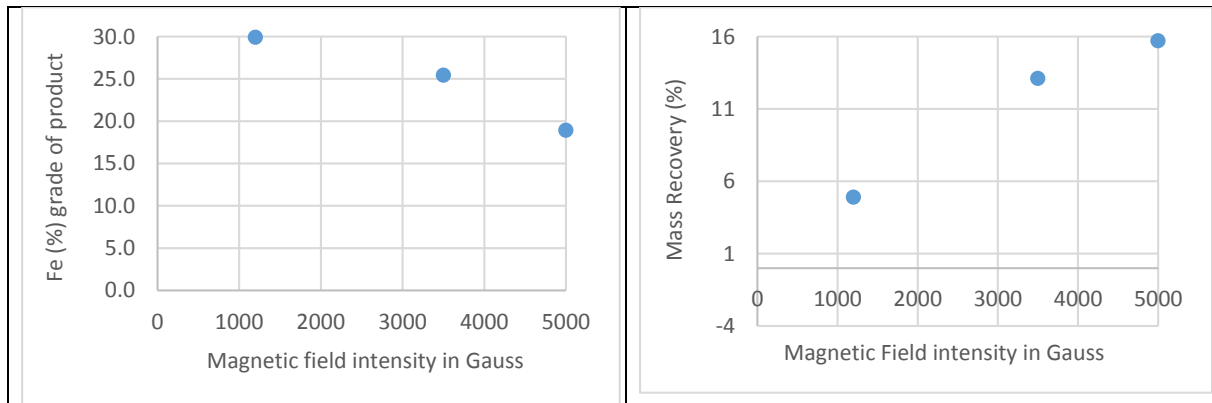
Figure 7. Iron grade (%) of magnetic separation products across varying magnetic field intensities (Left) and mass recovery (%) of dry magnetic separation over intensity ranges (Right)

Based on the first experiments set, a second stage of experiments was performed using an innovative two-stage rougher-cleaner method at field intensities of 3500 and 1200 Gauss, achieving a recovery of 10% with a product iron grade of 40%.

Conclusions

This study systematically evaluated dry magnetic separation for iron recovery from Golgohar's tailings, demonstrating that: Process Optimization of two-stage rougher-cleaner approach (3,500 G → 1,200 G) achieved optimal results, yielding:

- 40% Fe grade (2.7× enrichment from feed)
- 10% recovery rate of total iron content
- Field intensity >3,500 G increased recovery (16% at 5,000 G) but reduced grade (19% Fe), highlighting the grade-recovery tradeoff.

References

1- Zhang, L., Yuan, H., Marhaba, T., & Zhang, W. (2021). Challenges in iron ore processing and environmental impacts. *Minerals engineering, 170,* https://doi.org/10.1016/j.mineng.2021.107034

2- Kirchherr, J., Reike, D., & Hekkert, M. (2017). Conceptualizing the circular economy: An analysis of 114 definitions. *Resources, Conservation and Recycling, 127*, 221–232.

3- Golgohar Mining and Industrial Company. (2024). *Annual technical report on iron ore tailings processing and recovery efficiency* (Report No. GMIC-TR-2024-09). Golgohar Mining Technical Publications.

4- Xiong, D., Lu, L., Holmes, R. J., & Yang, H. (2020). High-intensity magnetic separation for iron recovery from tailings: A comparison of dry and wet processing routes. *Journal of Cleaner Production*, *256*, 120453. DOI: 10.1016/j.jclepro.2020.120453

Investigation of factors affecting the acid leaching of manganese with willow bark reductant

Meysam Naseri[1], Mohammad Baqaeifar[2], Mona Hajilou[3], Akbar Mehdilo[4], Mehdi Irannajad*[5]

[1] Ph.D. Candidate, Department of Mining Engineering, Amirkabir University of Technology, meysam.naseri@aut.ac.ir,

[2] Msc student, Department of Mining Engineering, Amirkabir University of Technology, mohammad.b@aut.ac.ir

[3] Msc student, Department of Mining Engineering, Amirkabir University of Technology, mona.hajilou@aut.ac.ir

[4] Assistant Professor, Department of Mining Engineering, Amirkabir University of Technology, amehdilo@aut.ac.ir

[5] Professor, Department of Mining Engineering, Amirkabir University of Technology, iranajad@aut.ac.ir,

*Corresponding author: iranajad@aut.ac.ir (Mehdi Irannajad)

Abstract:

Manganese is widely used in various industries, including metal alloys, batteries, pigments, glass, ceramics, and the production of cast iron and stainless steel. Leaching is an essential process in mineral processing, which, according to the Pourbaix diagram, should be carried out under acidic and reducing conditions. Different types of reducing agents have been employed for manganese ore leaching, classified into three main categories: chemical reductants, plant-based reductants, and microorganisms. In this study, a manganese concentrate (MnO: 39.76%) was obtained from the Cheragah Amir Tabriz deposit using a shaking table Device. The X-ray diffraction (XRD) and X-ray fluorescence (XRF) analyses of the concentrate showed that the MnO, CaO, and SiO_2 contents were 38.9%, 28.9%, and 4.77%, respectively. The major mineral phases identified in the concentrate were pyrolusite, calcite, and silica. Willow bark was used as a natural reducing agent, and hydrochloric acid was applied as a leaching agent. The effects of key process parameters, including hydrochloric acid concentration, reducing agent dosage, leaching time, and temperature, were systematically investigated. Under the optimal conditions—0.5 M hydrochloric acid concentration, 5 g willow bark, 4 hours of leaching time and a temperature of 75°C—the manganese dissolution efficiency reached 97.06%.

Keywords: Leaching, manganese, hydrochloric acid

1. Introduction

Manganese and its compounds are essential in numerous industries, including metallurgy, chemical manufacturing, battery production, and electronics. However, as demand for manganese-based products rises and high-grade manganese ores become scarcer, the processing of low- and medium-grade ores has become increasingly critical (Naseri et al., 2023). Ranking as the fourth most utilized metal by volume—after iron, aluminum, and copper—manganese faced a significant supply-demand imbalance in 2022. Global demand reached 28.2 million tons, while production lagged at 19.1 million tons (Statista, 2018). This growing disparity is projected to escalate manganese prices in the future. The depletion of high-quality manganese deposits, driven by rising consumption, has contributed to higher costs for the metal, raw ore, and manganese alloys (Ghosh et al., 2018). Additionally, the intricate mineral composition of low-grade ores poses technical and economic challenges for their efficient extraction and processing. Manganese ores are classified into three grades based on manganese content: high-grade (or metallurgical-grade) ores containing 44–48% manganese, medium-

grade ores with 35–44% manganese, and low-grade ores containing less than 35% manganese (Xiong et al., 2018; Acharya et al., 2004).

The extraction of manganese from manganese oxide ore deposits is carried out through pyrometallurgy, hydrometallurgy, and biohydrometallurgy (Zhang, Cheng, 2007). The conventional thermal treatment method involves roasting manganese oxide minerals with carbon at approximately 700–900°C (Timor, 2023). Hydrometallurgy offers advantages over pyrometallurgical and biohydrometallurgical processes and has attracted researchers' attention over the years due to its high efficiency and low energy consumption. Since manganese recovery from manganese ore requires the reduction of manganese oxide, the type of reducing agent used in hydrometallurgical processes has become a key factor in the development of such extraction methods. A major advantage of the leaching method is direct reduction, where the reduction and leaching stages occur in a single step. A wide range of reducing agents have been employed for manganese recovery from various types of manganese ores and secondary sources (Sinha, Purcell, 2019).

The leaching efficiency of manganese oxide ores depends on several factors, among which the choice of reducing agent plays a pivotal role (Sinha, Purcell, 2019). To achieve cost-effective and high-yield manganese extraction, researchers have utilized various reducing agents, broadly categorized into three groups: chemical reducing agents, microorganisms, and plant-based reducing agents Among the plant-based reducing agents used for dissolving manganese oxide ores are sawdust, sugarcane molasses, corn stalks, tea waste, orange peel, and others (Hariprasad et al., 2007; Feng et al., 2016; Hariprasad et al., 2009; Naseri et al., 2023; Zhang et al., 2013).

Relatively few studies have been conducted on the leaching of manganese ore using plant-derived reducing agents. In the present study, the effective parameters of leaching high-grade manganese oxide ore using willow bark were investigated, which had not been investigated in the research reported to date.

## 2. Material and methods

2.1. Sample Preparation

In the leaching experiments, a pyrolusite concentrate was used. After determining the optimal crushing and shaking table conditions, a concentrate with a grade of 38.9% MnO and D80: 180 μm was obtained. The chemical analysis of the concentrate, performed using X-ray fluorescence (XRF), is presented in Table 1. The major impurities in the manganese concentrate were CaO (28.9%) and SiO_2 (4.77%). The mineralogical analysis results (Figure 1) revealed that the primary minerals in the concentrate were pyrolusite, calcite, and silica. The SEM analysis results in Figure 2 confirm the presence of minerals constituting the studied ore. The distribution of manganese (Mn), silicon (Si), sulfur (S) and calcium (Ca) elements is shown in Figure 2.

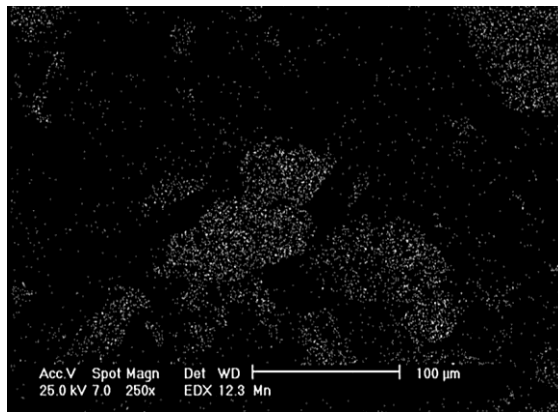Table 1. Chemical analysis of the concentrate by XRF

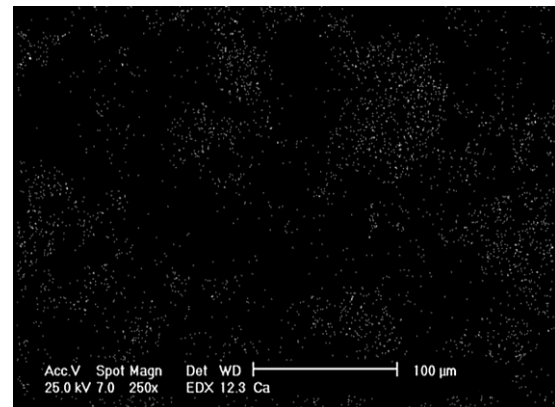| Chemical composition	MnO	CaO	SiO_2	BaO
Content(%)	38.9	28.9	4.77	1.16
Chemical composition	Fe_2O_3	SO_3	MgO	P_2O_5
Content(%)	0.57	0.48	0.35	0.24
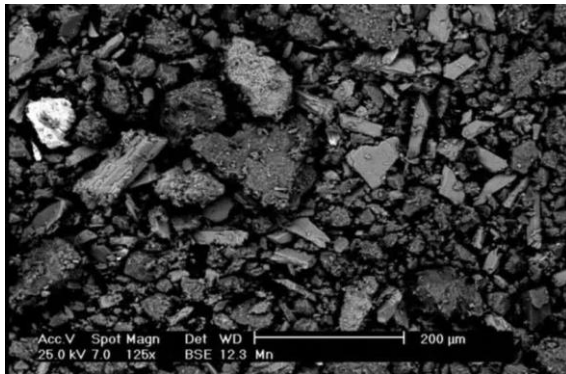
(a) SEM images of the concentrate were obtained
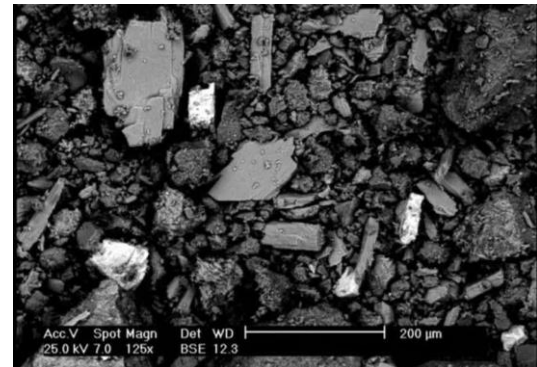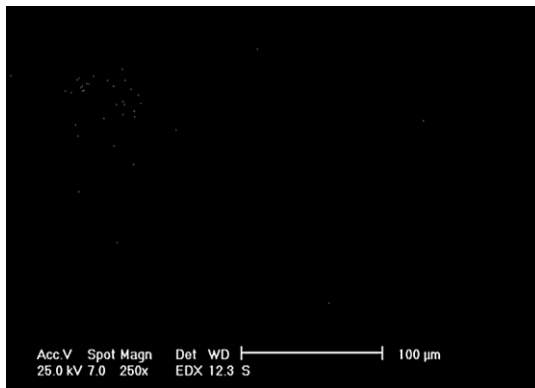

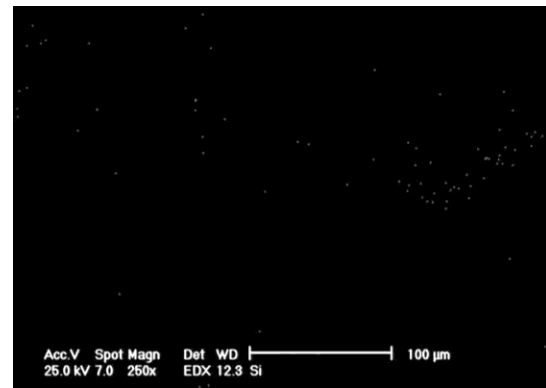(b) SEM images of the concentrate were obtained

(c) Manganese distribution map

(D) Calcium distribution map

(E) Sulfur distribution map

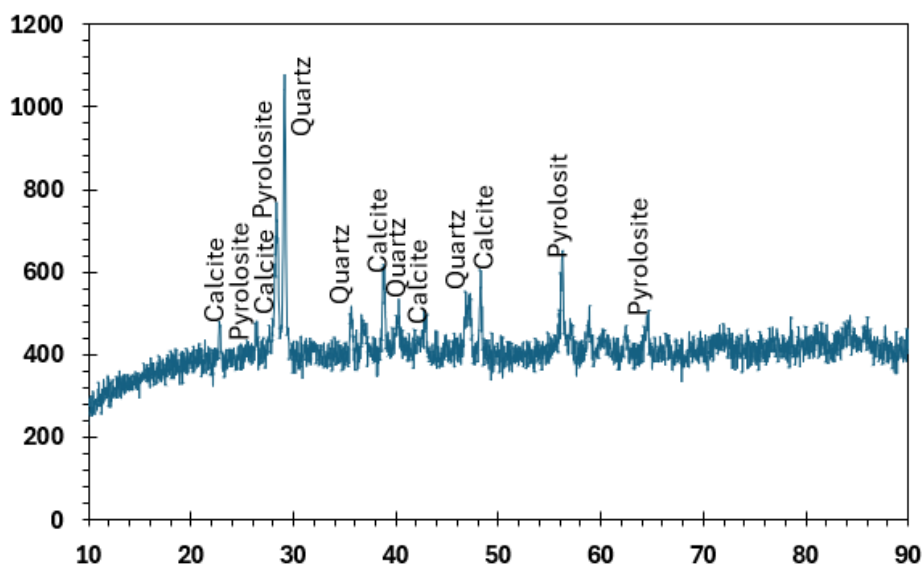(F) Silicon distribution map

Fig. 1. Results of SEM studies

Fig. 2. Mineralogical analysis results by XRD

2.2. Materials and Equipment

The chemical composition of the concentrate was characterized using X-ray fluorescence spectroscopy (XRF) with a PHILIPS X'UNIQUE II spectrometer. For mineral phase identification, X-ray diffraction (XRD) analysis was conducted using a PHILIPS Expert Pro diffractometer. Scanning electron microscopy (SEM) studies were carried out to examine the leaching residues after experiments with willow bark, conducted using an XL 30 microscope (Philips). Atomic absorption spectroscopy (AAS) was applied to determine manganese recovery efficiency, with flame atomic absorption spectroscopy being used for measuring manganese ion concentrations (model: AA240FS). For the leaching experiments with willow bark as a reducing agent, a magnetic hot plate stirrer (model: HSD 330, MTOPS) was utilized. Other equipment used throughout the study included thermometers, pH meters, sieves, beakers, glassware, and related laboratory apparatus.

2.3. Method

The leaching experiments were performed using willow bark as a reducing agent to investigate the effects of key parameters including reaction time, temperature, Hydrochloric acid concentration and Amount of willow bark. The experimental procedure began with the preparation of a leaching solution by adding sulfuric acid to triply distilled water, which was then diluted to a final volume of 250 mL. This solution was transferred to a beaker and heated to the predetermined experimental temperature. Once the target temperature was achieved, 5 g of upgraded manganese concentrate was introduced into the solution. Following a 2-minute equilibration period, the willow bark reducing agent was added to initiate the leaching process, allowing for systematic evaluation of the various parameters under investigation.

3. Results

3.1. Experimental design

The experimental design was carried out using the Taguchi method, and 16 series of experiments were conducted with different combinations of acid (x_1), reducing agent (x_2), temperature (x_3), and time (x_4). The independent variables and their coded/ actual levels are listed in Table 2.

Table 2. Levels of independent variables in the Taguchi design

Parameter	Symbol	Taguchi levels			
		Level1	Level2	Level3	Level4
Acid concentration (M)	x_1	0.5	1	1.5	2
Reducing agent (g)	x_2	1.25	2.5	5	10
Temperature (°C)	x_3	30	45	60	75
Time (min)	x_4	30	60	120	240

3.2. Effect of parameters

Table 3 presents the coded/actual values of the parameters and the experimental results.

Table 3. Taguchi experimental design and parameter optimization results

No	Acid (M)	Reducer (g)	Temp (°C)	Time (min)	Recovery (%)	SNRA1	MEAN1
1	0.5	1.25	30	30	10.68	20.5714	10.68
2	1	2.5	45	30	15.21	23.6426	15.21
3	1.5	5	60	30	18.26	25.2300	18.26
4	2	10	75	30	20.16	26.0898	20.16
5	1	5	30	60	22.21	26.9310	22.21
6	0.5	10	45	60	36.19	31.1718	36.19
7	2	1.25	60	60	28.04	28.9556	28.04
8	1.5	2.5	75	60	39.29	31.8856	39.29
9	1.5	10	30	120	46.23	33.2985	46.23
10	2	5	45	120	40.34	32.1147	40.34
11	0.5	2.5	60	120	32.16	30.1463	32.16
12	1	1.25	75	120	30.24	29.6116	30.24

13	2	2.5	30	240	46.52	33.3528	46.52
14	1.5	1.25	45	240	64.35	36.1710	64.35
15	1	10	60	240	90.54	39.1368	90.54
16	0.5	5	75	240	97.06	39.7408	97.06

Assuming all variables are measurable, the response can be expressed by Equation (1):

$$y = f(x_1. x_2. x_3. x_4) \tag{1}$$

where y is the output response and x_i represents the input variables. The data from the experiments were entered into Minitab software and the final regression model for manganese recovery was derived as Equation (2):

$$Y = 42.37 + 8.23x_1 + 12.45x_2 + 5.67x_3 + 18.32x_4 - 3.12x_1x_2 - 2.45x_1x_3 - 1.78x_1x_4 - 1.23x_2x_3 + 0.89x_2x_4 + 2.34x_3x_4 - 4.56x_1^2 - 3.78x_2^2 - 2.34x_3^2 - 1.89x_4^2 \tag{2}$$

The regression analysis revealed reaction time as the most influential parameter with a coefficient of 18.32, followed by the reducing agent quantity (coefficient: 12.45), highlighting its crucial role in the leaching process. Optimal conditions achieving maximum recovery (97.06%) were obtained with low acid concentration (0.5 M), moderate reducing agent dosage (5 g), high temperature (75°C), and extended duration (240 minutes).

The model demonstrated excellent agreement with experimental data, as evidenced by an R² value of 0.936 (Table 4), while the highly significant p-value (<0.0001) confirmed the statistical validity of the proposed model.

Table 4. parameters of the Taguchi experimental design

R²	R²-adjusted	P-value
0.936	0.853	0.0001

Analysis of variance (ANOVA) reveals that reaction time emerges as the most statistically significant parameter affecting the response, with an F-value of 77.59 and an extremely significant p-value < 0.000003. While temperature (p-value = 0.043) and reducing agent quantity (p-value = 0.026) also demonstrate statistically significant effects, their influence is substantially weaker compared to reaction time (Table 5).

Table 5. ANOVA results of the regression model for metal recovery

Source of Variation	Df	Sum of Squares	Mean Square	F-value	P-value
Regression	4	8437.52	2109.38	22.78529	0.000028
Acid concentration (M)	1	160.06	160.06	1.7291	0.2153
Reducing agent (g)	1	613.24	613.24	6.6243	0.0259

Temperature (°C)	1	481.38	481.38	5.1999	0.0435
Time (min)	1	7182.84	7182.84	77.5904	0.000003
Error	11	1018.31	92.57		
Total	15	9455.83			

Figure 3 clearly shows that time has the greatest impact on the reductive leaching process. The reducing agent (willow bark) and temperature are other influential factors in the reductive leaching of manganese concentrate. Additionally, acid concentration has the least effect on the leaching process.
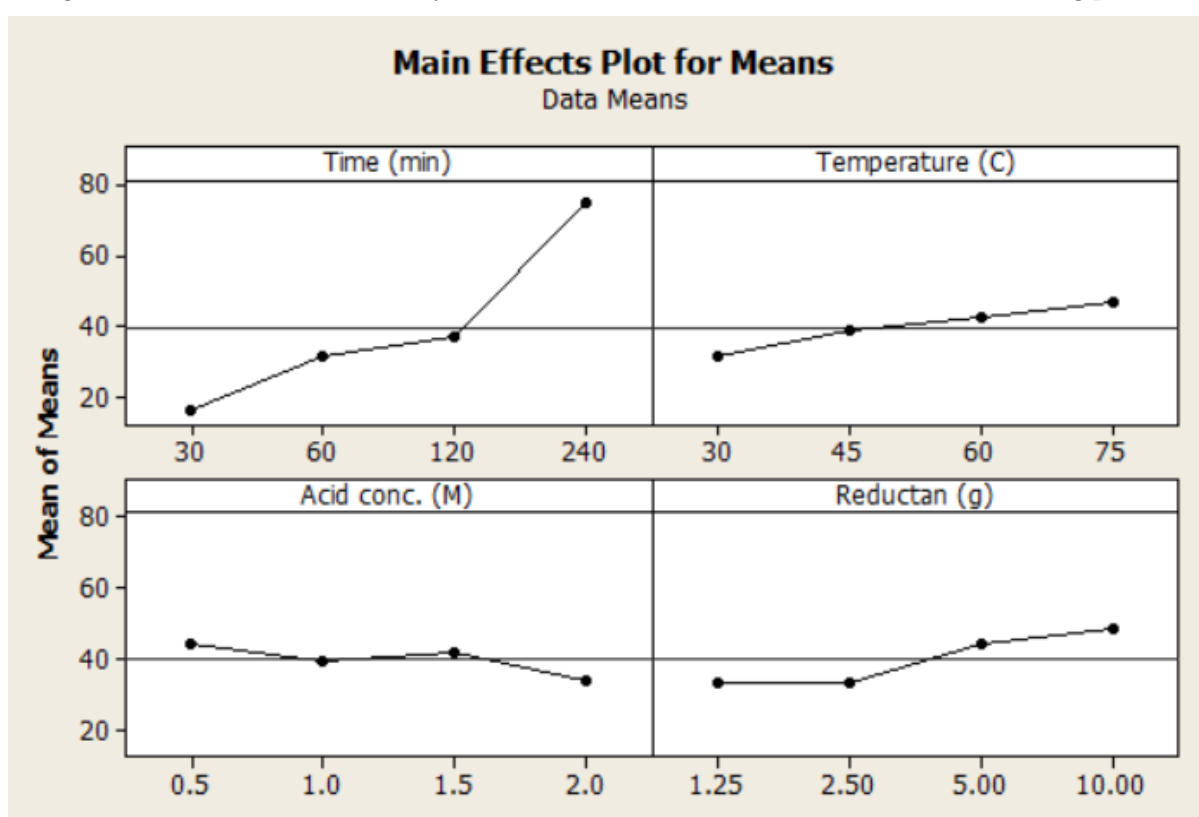
Fig. 3. Effect of factors on manganese recovery

3.3. Interaction Effects of Parameters

3.3.1. Time-Temperature Effects

Figure 4 shows that in the low temperature range (30-40°C) and short duration (less than 50 minutes), the system exhibits the lowest recovery efficiency (less than 20%). Increasing the reaction time to 50-100 minutes within the same temperature range improves the recovery to 20-40%. The optimal operational conditions are observed in the temperature range of 55-75°C and duration of 220-240 minutes, which deliver the highest recovery (>80%).
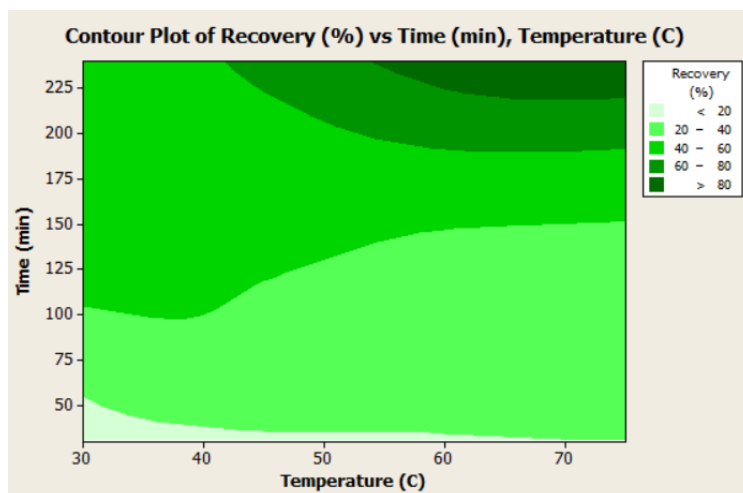
Fig. 4. Investigation of Temperature and Time Effects on Manganese Recovery

3.3.2. Interaction Effects of Acid and Time

As shown in Figure 5, the synergistic relationship between acid concentration and leaching duration significantly influences manganese recovery efficiency. Results from examining different regions indicate that the highest recovery (>80%) is achieved in the acid concentration range of 0.5-1.25 M and reaction time of 220-240 minutes. This optimal range represents conditions where dissolution rate, system stability, and completion of main reactions are in favorable balance. At low acid concentrations (0.5-1.25 M) and short reaction times (less than 50 minutes), recovery below 20% are observed, primarily due to kinetic limitations and incomplete dissolution reactions. When reaction time is increased to 35-145 minutes, the system achieves 20-40% recovery across a wide range of acid concentrations (0.5-1.75 M). At times above 190 to 220 minutes, recovery is in the range of 40 to 60 percent, and at times above 220 minutes, recovery is above 80 percent.
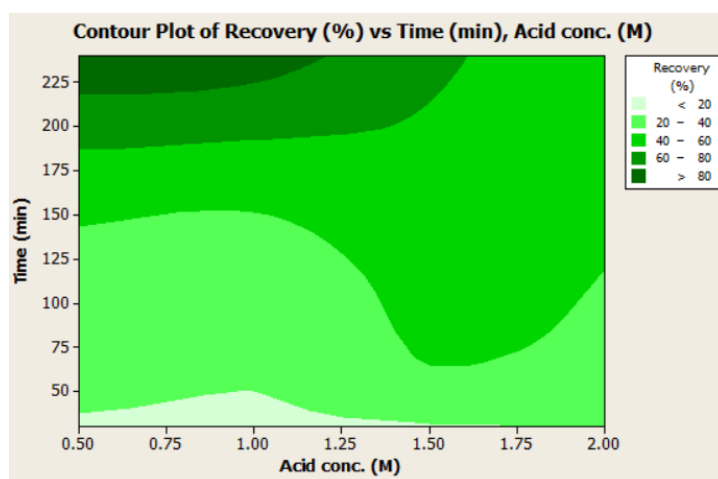

Fig. 5. Effects of Acid Concentration and Time on Manganese Recovery

3.3.3. Interaction Effects of Willow Bark and Time

Figure 6 illustrates the interaction between reaction time and reducing agent quantity on manganese extraction efficiency. The results demonstrate that the highest recovery (>80%) is obtained within the range of 4-10 grams of reducing agent combined with a reaction time of 200-240 minutes. Under conditions of short duration (less than 50 minutes) and moderate reducing agent quantities (2-7 grams), recovery remain below 20%, primarily due to incomplete reduction reactions. When the reaction time is extended to 45-170 minutes, the system achieves recovery of 20-40% across a broad range of reducing agent quantities (1-10 grams). From an operational perspective, these findings indicate that the optimal reducing agent quantity falls within the range of 4-7 grams, with a minimum required reaction time of 200 minutes to achieve desirable recovery.
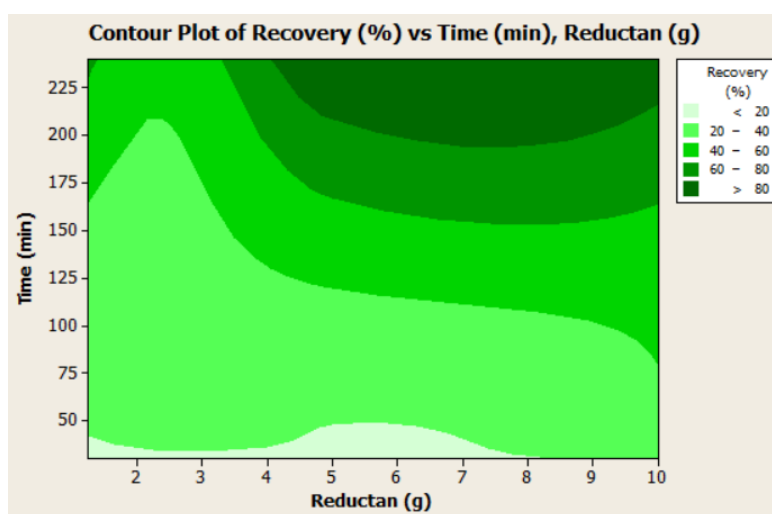

Fig. 6. Investigation of Reducing Agent Concentration and Time Effects on Manganese Recovery

3.3.4. Interaction Effects of Acid Concentration and Temperature

Figure 7 illustrates the interdependent effects of acid concentration and temperature on manganese extraction recovery. The results indicate that the highest recovery (>80%) is achieved within the acid concentration range of 0.75-1 M combined with temperatures of 55-65°C. Under conditions of low acid concentration (0.5-1 M) and reduced temperatures (30-45°C), recovery remain below 20%, primarily due to insufficient activation energy to overcome the reaction's thermodynamic barrier. With gradually increasing the temperature to the range of 45-75°C, the recovery of manganese dissolution reaches 20-60% in a wide range of acid concentrations (0.5-2 M).
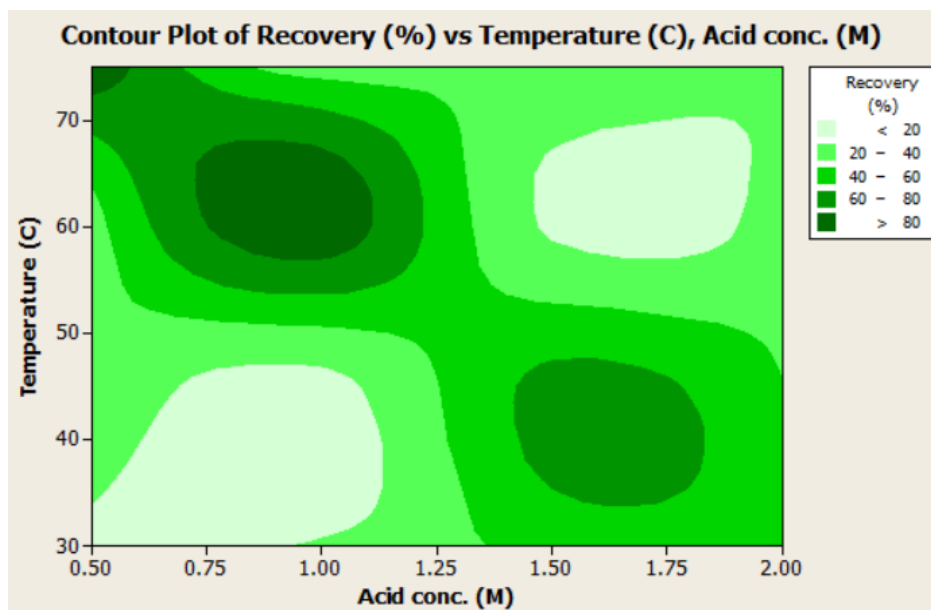
Contour Plot of Recovery (%) vs Temperature (C), Acid conc. (M)

Fig. 7. Investigation of Acid Concentration and Temperature Effects on Manganese Recovery

3.3.5. Interaction Effects of Willow Bark and Temperature

Figure 8 shows the interaction effect of willow bark content and temperature on manganese recovery. The results from the study of different areas indicate that the highest recovery (>80%) is achieved in two specific ranges of reducing agent content of 4-8 g at 75 °C and 10 g at 60-65 °C. At low reducing agent content (2-5 g) and medium temperatures (40-65 °C), recovery is less than 40%, which is due to the limitation in the formation of active manganese complexes. With a gradual increase in reducing agent content to the range of 5-10 g and temperature to 65-75 °C, the recovery increases to 60-80%. The results show that the temperature of 75 °C with 4-8 g of reducing agent is more economically optimal.
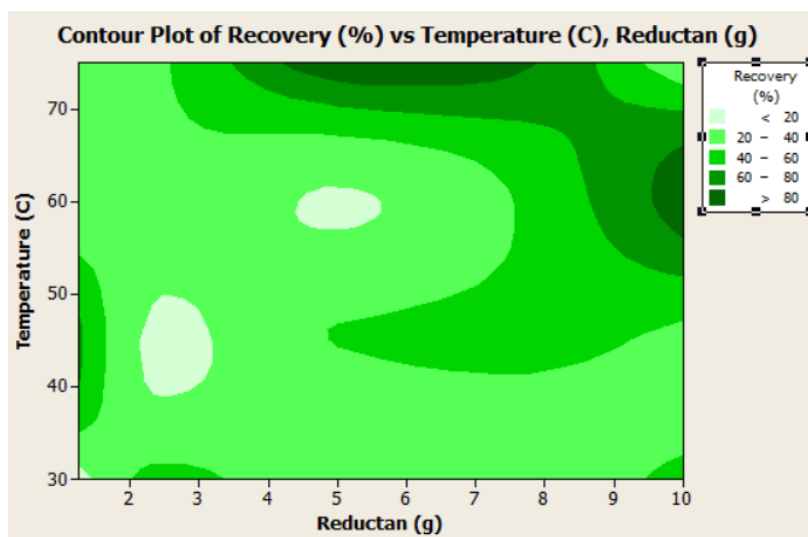
Contour Plot of Recovery (%) vs Temperature (C), Reductan (g)

Fig. 8. Investigation of reducing agent quantity and temperature effects on Manganese recovery

3.3.6. Interaction Effects of Willow Bark and Acid Concentration

Figure 9 shows the interaction of reducing agent amount and acid concentration on manganese extraction recovery. The results from the different regions indicate that the highest recovery (>80%) is achieved in two distinct ranges; reducing agent amount of 4.5-5.8 g with very low acid concentration (0.5-0.6 M) and high reducing agent amount (5.9-10 g) with moderate acid concentration (0.75-1 M). In the low ranges of both parameters (1-6 g reducing agent and 0.5-1.25 M acid), recovery is less than 20%. With a gradual increase in acid concentration to the range of 0.75-2 M and reducing agent amount to 1-10 g, recovery increases to 20-40%.
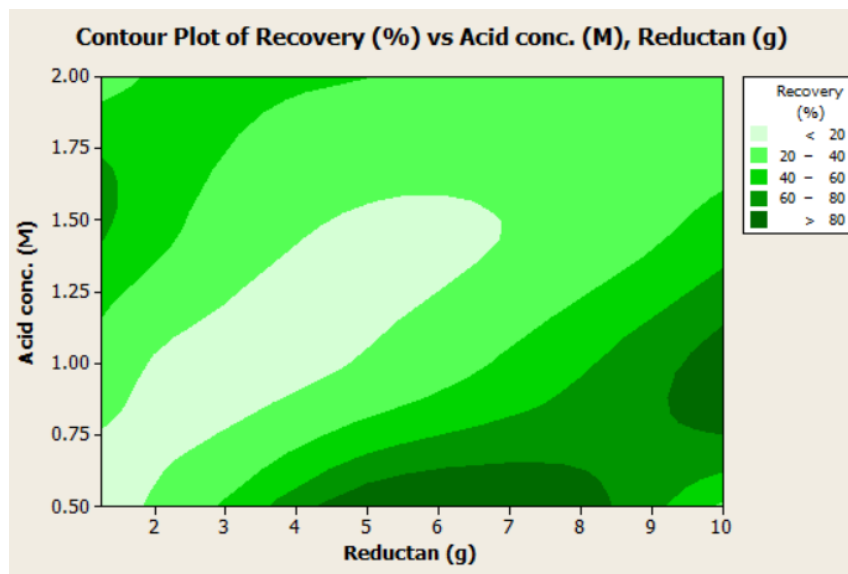

Fig. 9. Investigation of reducing agent quantity and acid concentration effects on Manganese recovery

4. Conclusion

The use of low-grade manganese resources is very important, considering the exhaustion of high-grade manganese mines and the existence of low-grade manganese mines in the country. In the present study, a concentrate with a grade of approximately 40% MnO was prepared from a feed with a grade of 13% MnO using gravity methods. The results of XRF, XRD and SEM studies show that pyrolusite, calcite, quartz and barite are the main minerals constituting the concentrate. In the present study, hydrochloric acid was used as a dissolving agent and willow bark was used as a reducing agent in the manganese ore leaching process. The parameters of time and hydrochloric acid concentration had the greatest and least effect on the reductive leaching process, respectively. The optimal leaching conditions were obtained at a half-molar concentration of hydrochloric acid, a time of 4 hours, a temperature of 75 ° C and an amount of 5 grams of willow bark.

References

Acharya, C., Sukla, L.B., Vibhuti, N., (2004). Fungal leaching of manganese ore. Trans. Indian Inst. Met. 57, 501–508.

Feng, Y., Zhang, S., & Li, H., (2016). Reductive leaching of manganese from low-grade pyrolusite ore in sulfuric acid using pyrolysis-pretreated sawdust as a reductant. Int. J. Miner. Metall. Mater. 23, 241–246.

Ghosh, S., Bal, B., D.A., (2018). Enhancing manganese recovery from low-grade ores by using mixed culture of indigenously isolated bacterial strains. Geomicrobiol 35, 242–6. https://doi.org/https://doi.org/10.1080/01490451.2017.1362080

Hariprasad, D., Dash, B., Ghosh, M. K., & Anand, S., (2007). Leaching of manganese ores using sawdust as a reductant. Miner. Eng. 20, 1293–1295.

Hariprasad Ghosh, M. K., & Anand, S, D., (2009). Dried leaves — Novel reductant for acid leaching of manganese ore. Trans. Indian Inst. Met. 62, 551–554.

Naseri , M; iranajad, M; Mahdilo A., (2023). the importance of manganese dioxide nanoparticles production and its applications, in: In: The 41st Meeting (National Conference) of Earth Sciences, Tehran. (In Persian).

Naseri , M; iranajad, M; Mahdilo A, (2023). The use of agricultural waste and products as a reductant agent in the manganese dioxide leaching process, in: In: The Third National Conference on Green Waste Management. (In Persian)

Sinha, M. K., & Purcell, W., (2019). Reducing agents in the leaching of manganese ores: A comprehensive review. Hydrometallurgy 187, 16186.

Statista, (2018). No Title [WWW Document]. https//www.statista.com/statistics/247624/total-apparent-manganese Consum. (accessed 24 January).

Timor OP, (2023). Leaching optimization of manganese ore from north central timor using H2O2 as a reducing agent.

Xiong, S., Li, X., Liu, P., Hao, S., Hao, F., Yin, Z., L.J., (2018). Recovery of manganese from low-grade pyrolusite ore by reductively acid leaching process using lignin as a low cost reductant. Min. Eng 125, 126–32. https://doi.org/https://doi.org/10.1016/j.mineng.2018.06.003

Zhang, H., Zhu, G., Yan, H., Zhao, Y., Li, T., & Feng, X., (2013). Reduction of low-grade manganese dioxide ore pellets by biomass wheat stalk. Acta Metall. Sin. (English Lett. 26, 167–172.

Zhang, W., Cheng, C.., (2007). Manganese metallurgy review. Part I: leaching of ores/ secondary materials and recovery of electrolytic/chemical manganese dioxide. Hydrometallurgy 89, 137–159.

Extraction of Alumina from Malatya's Diasporic Bauxite by Carbon-Assisted Sintering Method

Shahram Rostami[1]*, Raheleh Hazrati Behnagh[1], Sadegh Marahem[1]

1 *Minerals Application Research Centre in the West of Country, Azarshahr, Iran*

*Corresponding author: e-mail (Shahram Rostami): tetriplex@gmail.com

Abstract:

The Bayer process recovers only 3% of the alumina from Malatya diasporic bauxite. The components of Malatya diasporic bauxite are 4.41% silica, 54.0% alumina, 15.0% iron oxide as ferric oxide and 11.3% loss on ignition. Due to the low silica content of this type of bauxite, it is not necessary to use the lime soda sintering method to avoid creating billet waste and consuming more energy. Therefore, a sintering method with sodium carbonate and carbon was used for selective extraction of alumina. Experimental design was performed by surface response method (RSM) using central composite design. Selected parameters are temperature, soaking time, mass ratio of sodium oxide to bauxite (S/B), mass ratio of carbon to bauxite (C/B). The maximum amount of extraction of alumina from Malatya diasporic bauxite by sintering method is 78.9%, which is obtained in the optimal values of the parameters as follows: A temperature of 1100°C, a soaking time of 31.9 minutes, a mass ratio of sodium oxide to bauxite (S/B) of 1.27 and a mass ratio of carbon to bauxite (C/B) of 0.105. In 31 run experiments, the mixture of materials powder was transferred to an alumina crucible and heated in a muffle furnace at temperatures and soaking times determined by the experimental design. The sintered material was pulverized. The resulting powder was leached by 150 mL of a boiling alkaline solution (NaOH 50g/L) for 30 minutes at a stirring speed of 300rpm. Extracted aluminum from the leaching stage was analyzed by atomic absorption spectrometry.

Keywords: Sintering, Alumina, Malatya diasporic bauxite, Central Composite Design.

1. Introduction

In 2024, global alumina production reached unprecedented levels, with October alone recording a monthly output of 12.61 million tons, marking a 5.6% increase from the previous month and a 3.62% rise compared to October 2023 (Liu, 2025). China led this surge, producing approximately 86.33 million metric tons, followed by Australia and Brazil (SENGUPTA, 2024). This escalation in production underscores the growing demand for alumina, a critical component in various industries, including aluminum production, ceramics, and refractories (Desai, 2024; Liu, 2025).

The importance of efficient alumina extraction methods is underscored by the increasing demand and the environmental implications of traditional extraction processes. Conventional methods, such as the Bayer process, are energy-intensive and generate significant amounts of red mud, posing environmental disposal challenges. Innovations in extraction techniques are essential to address these concerns and to utilize low-grade bauxite ores effectively (Chen et al., 2023; Meher, 2016). Recent research has explored various methods to enhance alumina extraction efficiency (Le et al., 2017a). For instance, studies have investigated the sintering of bauxite residue with additives like soda, metallurgical coke, and other reagents to recover aluminum and sodium (Tam et al., 2019).

Additionally, microwave roasting combined with alkaline leaching has been proposed as a novel approach for extracting alumina from low-grade diasporic bauxite ores (Le et al., 2017b) . These studies highlight the ongoing efforts to develop more sustainable and efficient extraction methods. Recent research has explored various methods to enhance alumina extraction efficiency. For instance, studies have investigated the sintering of bauxite residue with additives like soda, metallurgical coke, and other reagents to recover aluminum and sodium (Kar et al., 2023). Additionally, microwave roasting combined with alkaline leaching has been proposed as a novel approach for extracting alumina from low-grade diasporic bauxite ores (Gu et al., 2018). These studies highlight the ongoing efforts to develop more sustainable and efficient extraction methods.

The carbon-assisted sintering method, also referred to as the calcification–carbonization method, is a novel approach designed to treat low-grade bauxite ores. This process involves the use of carbon as a reducing agent to facilitate the decomposition of bauxite minerals and enhance alumina extraction. The method is particularly effective for diasporic bauxite, which is known for its high silica content and refractory nature (Chen et al., 2023; Weiguang et al., 2016).

Key steps in the process include: calcination, carbonization, sintering, and leaching. The carbon-assisted sintering method generates residues that are rich in calcium carbonate ($CaCO_3$) and calcium silicate ($CaSiO_3$). These residues can be directly utilized in the cement industry, reducing waste disposal challenges (Weiguang et al., 2016). Additionally, the process minimizes red mud generation compared to traditional Bayer methods, contributing to a more sustainable alumina production (Zhou et al., 2023).

The carbon-assisted sintering method offers a promising approach for extracting alumina from Malatya´s diasporic bauxite. By combining calcination, carbonization, sintering, and leaching, this method achieves high alumina recovery rates while reducing environmental impact. Further optimization of process parameters, such as temperature and alkali dosage, is essential to enhance efficiency and sustainability (Sun et al., 2023; Weiguang et al., 2016).

The table 1 highlights the advantages of the carbon-assisted sintering method in terms of alumina recovery and waste reduction.

Table 1: Comparison of Key Parameters in Alumina Extraction Methods

Parameter	Carbon-Assisted Sintering	Traditional Bayer Process	Citation
Alumina Recovery Rate	~81–83%	~70–80%	(Chen et al., 2023; Weiguang et al., 2016)
Silica Reduction	~18–20%	~10–15%	(Ma et al., 2013; Sun et al., 2023)
Energy Consumption	High due to sintering	Moderate	(Sun et al., 2023)
Waste Generation	Low (residue utilized in cement)	High (red mud generation)	(Zhou et al., 2023)

Despite these advancements, a gap remains in the research concerning the extraction of alumina from specific bauxite deposits, such as those found in Malatya, Turkey. The unique mineralogical composition of Malatya's diasporic bauxite presents challenges that are not adequately addressed by existing methods. Furthermore, the potential benefits of carbon-assisted sintering in this context have not been thoroughly investigated. The current research aims to address this gap by exploring the extraction of alumina from Malatya's diasporic bauxite using a carbon-assisted sintering method. This

approach seeks to enhance alumina recovery rates while mitigating environmental impacts associated with traditional extraction techniques. The study will analyze the mineralogical characteristics of the bauxite, optimize sintering parameters, and assess the efficiency of alumina extraction. The central question guiding this research is: Can carbon-assisted sintering effectively improve the extraction efficiency of alumina from Malatya's diasporic bauxite compared to conventional methods? Addressing this question will contribute to the development of more sustainable extraction processes and the effective utilization of low-grade bauxite resources. The structure of the paper is as follows: The next is the methodology section outlines the experimental procedures employed in the study, including sample preparation, experimental design, sintering processes, and analytical techniques. The results section presents the findings of the experiments, followed by a discussion interpreting the results in the context of existing literature. Finally, the conclusion summarizes the key insights and suggests directions for future Material and methods

1.1. Material

Malatya's diasporic bauxite was received from the mine owner. Table 2 shows the chemical composition of this bauxite.

Table 2. Chemical composition of Malatya's diasporic bauxite

	SiO_2%	Al_2O_3%	Na_2O%	K_2O%	Fe_2O_3%	CaO%	LOI
Bauxite	4.41	54.0	0.40	0.42	15.0	0.047	11.3

Industrial grade sodium carbonate with a purity of 99% was used in this research work. The carbon used in these experiments was Graphite Fine Powder from LOBA Chemie with Extra Pure purity.

1.2. Instruments

Atomic absorption spectrometry analysis (Varian 220 Atomic Absorption Spectrometer, Australia) was used to determine the aluminium in the pregnant solution resulting from the leaching of sintered material.

Sintering of the dry powder mixture of materials was carried out in a muffle electric furnace with a capacity of 30 dm^3 manufactured by ATBIN temperature instruments Company (Iran).

Roller crusher and disc mill manufactured by Danesh Faravaran Company (Iran) were used to crush and pulverize mineral rocks and sintered materials.

1.3. Experimental design

The design of experiments was carried out using the response surface methodology (RSM) and the Central Composition Design (CCD) technique using version 19 of Minitab software. Four parameters affecting the process (the number of factors, k = 4) were defined as RSM factors: temperature, soaking time, mass ratio of sodium oxide to bauxite (S/B), mass ratio of carbon to bauxite (C/B). In all experiments, 2 g of bauxite were used. The yield of alumina leached was selected as the response of the model.

The evaluation of the obtained model was carried out by analysis of variance (ANOVA). The modality of the polynomial equation was assessed statistically by the determination coefficient (R^2), and its statistical importance was evaluated by F-test. Table 3 shows Actual and coded values of independent factors. Table 4 shows the design of the experiments.

Table 3. Actual and coded values of independent factors

Factor	Symbol	-α	-1	0	+1	+α
Temperature	A	900°C	950°C	1000°C	1050°C	1200°C
Soaking time	B	0 min	10 min	20 min	30 min	40 min
mass ratio of sodium oxide to bauxite	C	0	0.35	0.70	1.05	1.40
mass ratio of carbon to bauxite	D	0	0.05	0.10	0.15	0.20

Table 4. Design of the experiments

Run	A (T°C)	B (min)	C	D	R%
1	950	10	0.35	0.05	30.4
2	1050	10	0.35	0.05	30.1
3	950	30	0.35	0.05	29.1
4	1050	30	0.35	0.05	29.5
5	950	10	1.05	0.05	45.0
6	1050	10	1.05	0.05	61.7
7	950	30	1.05	0.05	53.5
8	1050	30	1.05	0.05	70.6
9	950	10	0.35	0.15	32.7
10	1050	10	0.35	0.15	31.8
11	950	30	0.35	0.15	32.2
12	1050	30	0.35	0.15	28.6
13	950	10	1.05	0.15	46.6
14	1050	10	1.05	0.15	70.0
15	950	30	1.05	0.15	60.9
16	1050	30	1.05	0.15	67.3
17	900	20	0.7	0.1	43.9
18	1100	20	0.7	0.1	66.1
19	1000	0	0.7	0.1	49.9
20	1000	40	0.7	0.1	61.3
21	1000	20	0.0	0.1	2.25
22	1000	20	1.4	0.1	56.8
23	1000	20	0.7	0.0	55.5
24	1000	20	0.7	0.2	57.7
25	1000	20	0.7	0.1	56.5
26	1000	20	0.7	0.1	58.3
27	1000	20	0.7	0.1	58.8
28	1000	20	0.7	0.1	56.8
29	1000	20	0.7	0.1	59.3
30	1000	20	0.7	0.1	56.8
31	1000	20	0.7	0.1	59.5

1.4. Processing procedure

Each experiment was carried out by mixing the material powder in the amount indicated in Table 3 with 2 g of bauxite powder and subsequently transferring it to a crucible and heating it in the furnace at the temperatures and times determined by the experimental design. Then the furnace was turned off and after cooling, the sintered materials were removed from the crucible and powdered to dimensions below 100 μm. The resulting powder was leached for 30 minutes with 50 mL of boiling alkaline solution (NaOH 50g/L) at a stirring speed of 300 rpm. The leached solution was used to determine the amount of leached alumina by atomic absorption. Finally, the alumina recovery rate was calculated.

1.5. RESULTS AND DISCUSSION

Using the response surface methodology, the role of effective factors and the interaction of factors on alumina extraction is modelled and optimized. . In most cases, a second-order model is obtained by the equation below, where y is the response value of the parameter x.

$$y = \beta_0 + \sum_{i=1}^{q} \beta_i x_i + \sum_{i=1}^{q} \beta_{ii} x_i^2 + \sum\sum_{i<j} \beta_{ij} x_i x_j$$

The factors affecting the process are: temperature, soaking time, mass ratio of sodium oxide to bauxite (S/B), mass ratio of carbon to bauxite (C/B). In the CCD (full factorial two-level design) experimental design method, the number of experiments is obtained from the equation1:

$$N = 2^K + 2K + C \qquad (1)$$

Where N is the number of experiments, K is the number of parameters, and C is the number of central point's repetition.

1.5.1. Statistical analysis

The factor's levels and the experimental conditions are presented in Table 3. In column R%, the amount of alumina extracted by leaching the sintered material is entered as the response (experimental result). The effects of factors affecting response, including temperature, soaking time, mass ratio of sodium oxide to bauxite (S/B), mass ratio of carbon to bauxite (C/B) by the surface response method using the Central Composition Design. Data analysis by RSM provides the following model for the amount of alumina extracted (equation 2):

$R\%$ = -572 + 1.143 A + 2.71 B - 127.7 C + 322 D - 0.000579 A×A - 0.01298 B×B
- 63.81 C×C - 419 D×D
- 0.00234 A×B + 0.2425 A×C
- 0.218 A×D + 0.616 B×C
- 0.96 B×D + 27.5 C×D (2)

where A, B, C, and D, are temperature (°C), soaking time of the reactants at the sintering temperature (min), mass ratio of sodium oxide to bauxite, mass ratio of carbon to bauxite, respectively.

ANOVA was used to evaluate the significance and quality of the obtained model. The p-values smaller than 0.05 at the significance level of 95% indicate the significance of the regression model. For the model of alumina extraction, the p-value was equal to 0.000, which is less than 0.05.

The residual plots (Fig.1) indicate the Gaussian distribution of the residuals and the absence of significant bias in the residuals. The maximum amount of extraction of alumina from Malatya diasporic bauxite was predicted to be 78.9% The model predicts that the maximum amount of alumina extraction will be happened at a temperature of 1100 °C, a soaking time of 32 minutes, a mass ratio of sodium oxide to bauxite of 1.27, and mass ratio of carbon to bauxite of 0.105 (Fig. 2). Plotting the predicted alumina extraction versus the actual values (Fig.3) is linear (R^2 predicted = 0.938). Contour plots (Fig.4) and surface plots (Fig. 5) show changes in the alumina extraction as a function of factors values.
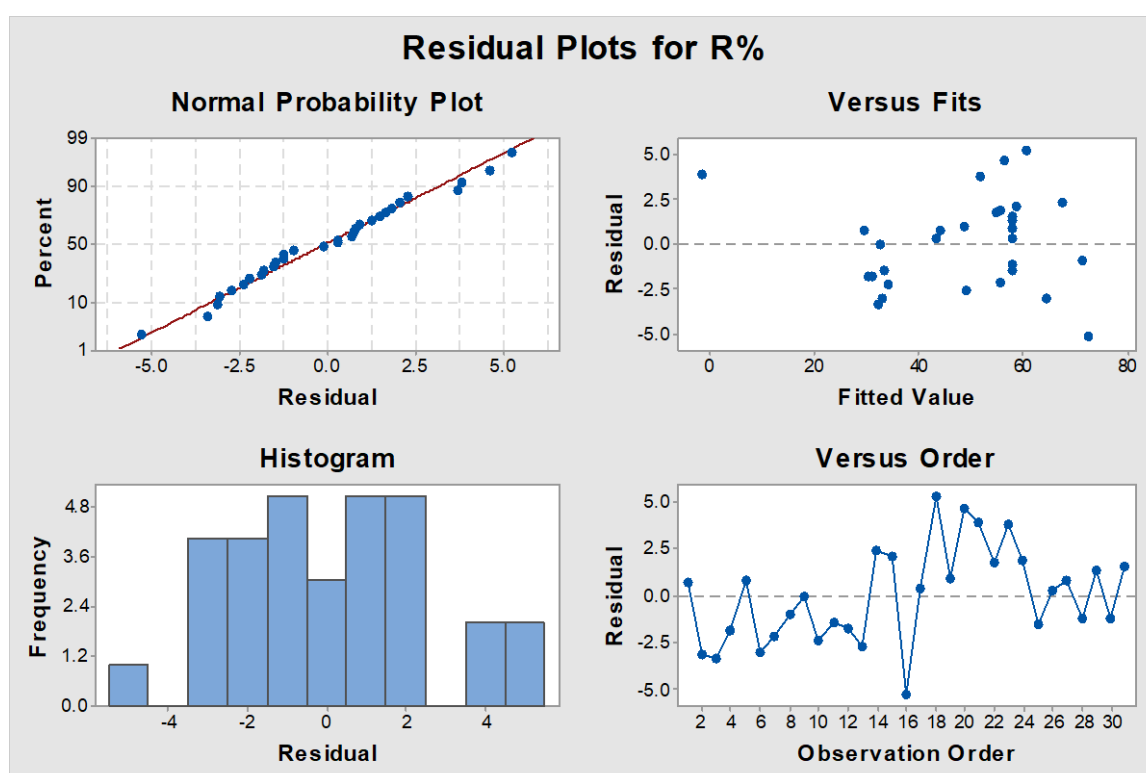
Fig. 1. Residual plots
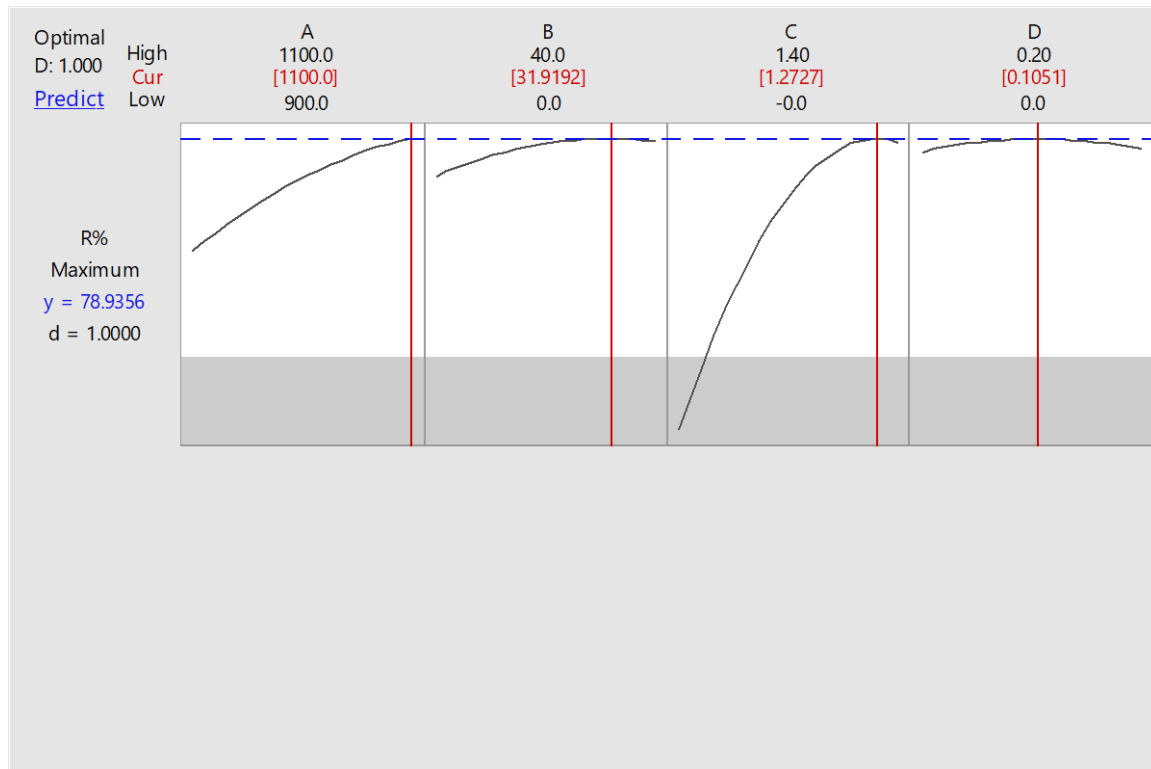
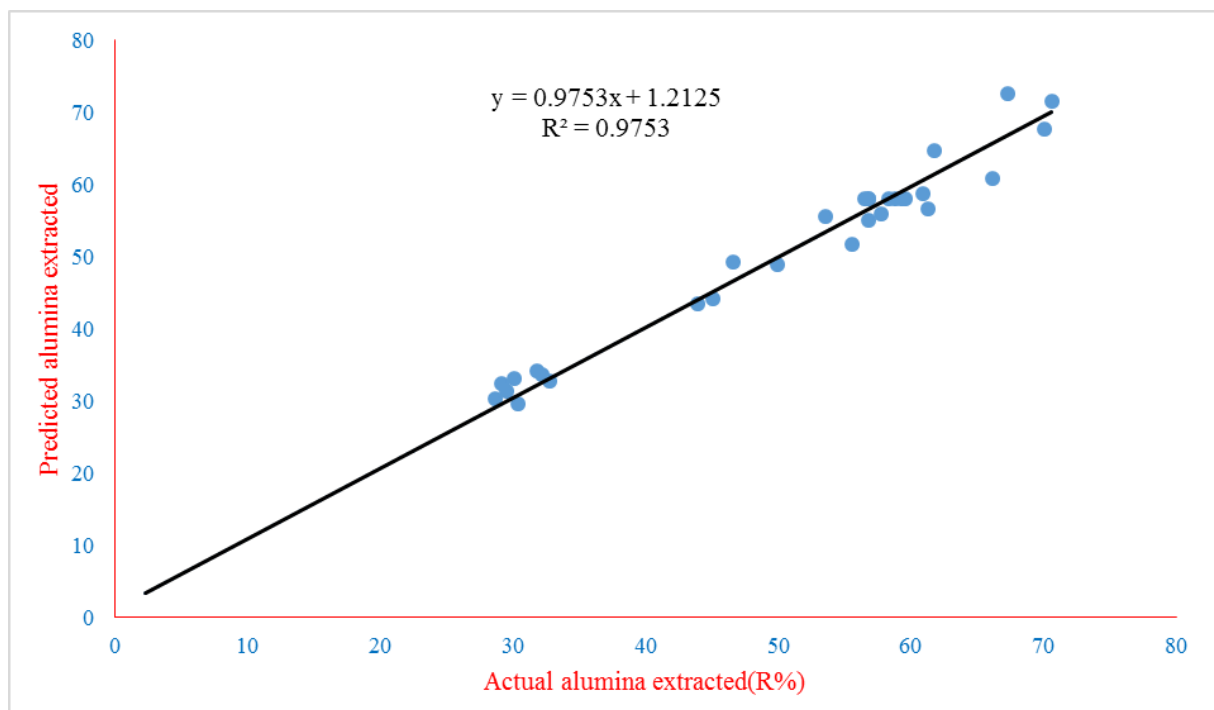**Fig. 2.** Factor's levels at maximum extraction of alumina

Fig. 3. Predicted alumina extraction versus the actual values
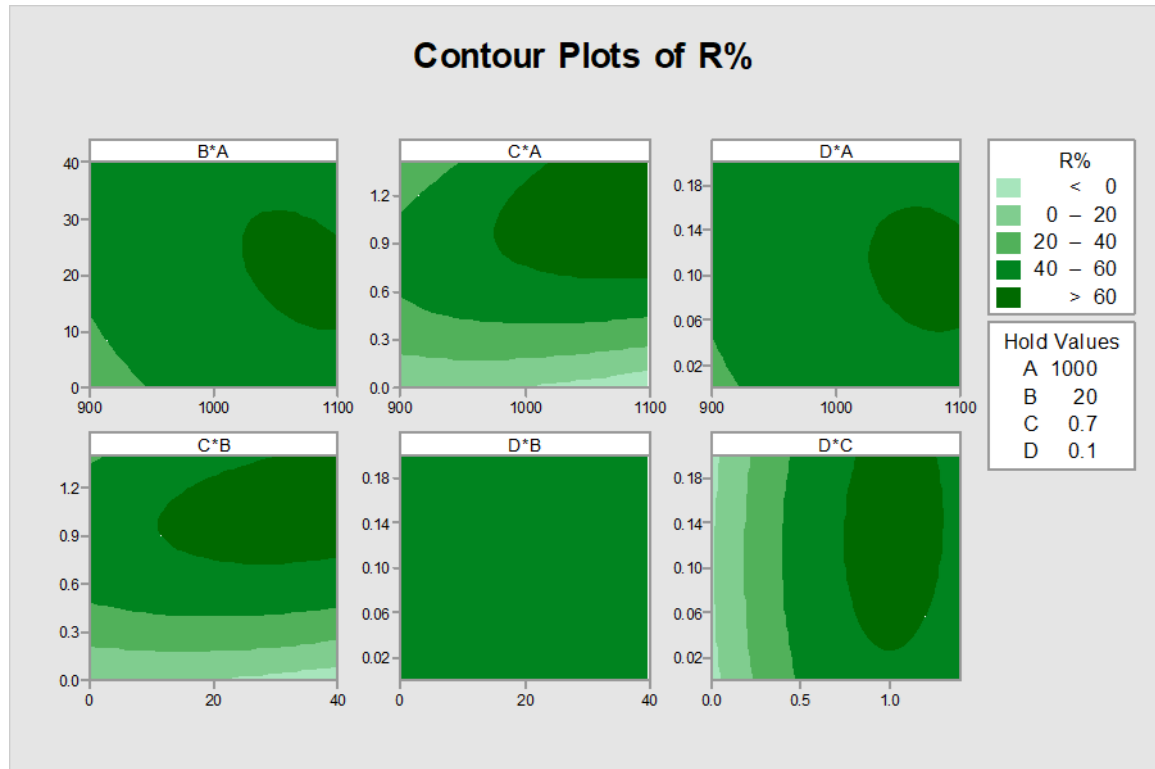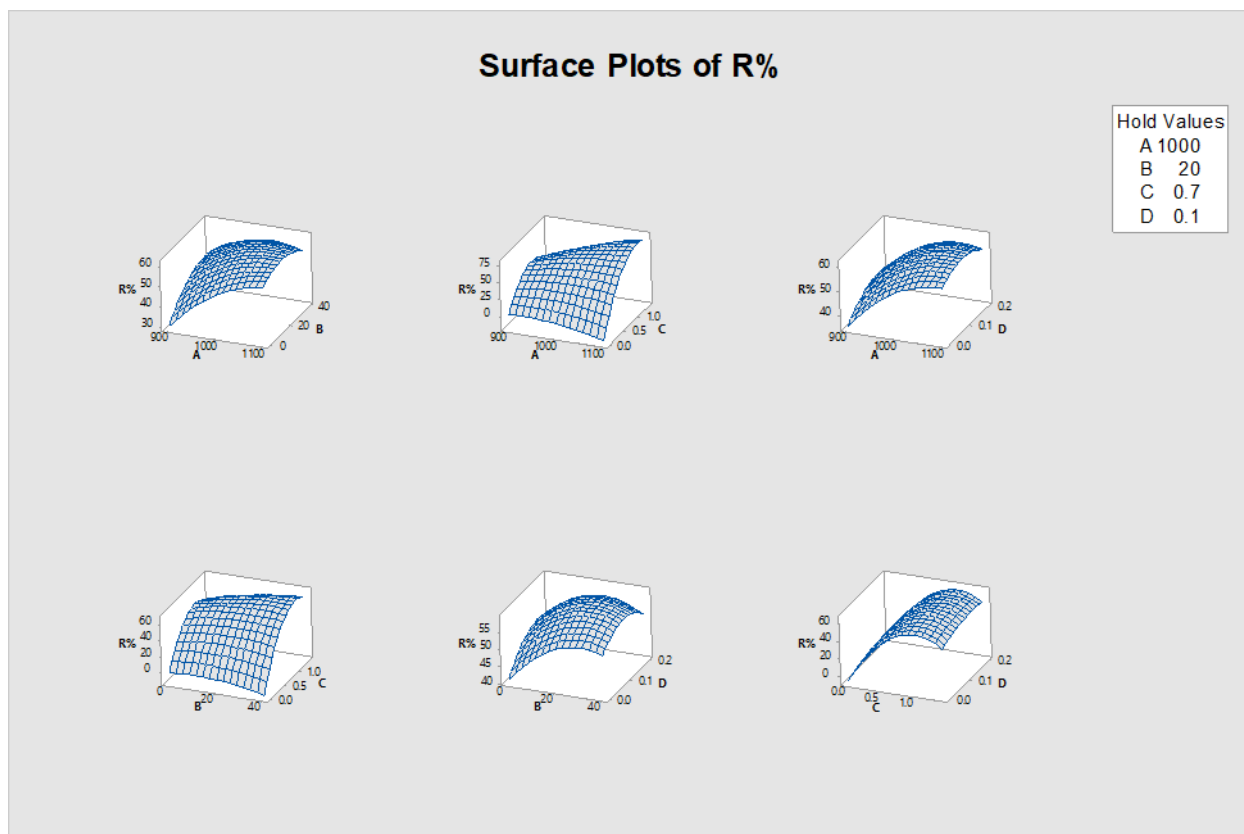
Fig. 4. Contour plots

Fig. 5. The Surface plots

2. Conclusions

This study investigated the extraction of alumina from Malatya's low-grade diasporic bauxite using a carbon-assisted sintering method. The findings demonstrate that this alternative approach can significantly enhance alumina recovery while minimizing environmental impacts associated with conventional methods like the Bayer process. Through optimization using response surface methodology (RSM) and central composite design (CCD), key process parameters—temperature, soaking time, sodium oxide to bauxite ratio (S/B), and carbon to bauxite ratio (C/B)—were systematically evaluated.

The optimal conditions determined for maximum alumina extraction (78.9%) were a temperature of 1100 °C, a soaking time of 31.9 minutes, an S/B ratio of 1.27, and a C/B ratio of 0.105. Statistical analysis confirmed the significance and reliability of the model (p-value < 0.05, R^2 = 0.938), highlighting the influence of each factor and their interactions on the extraction efficiency.

In comparison to traditional methods, the carbon-assisted sintering process demonstrated superior performance in terms of alumina recovery and waste reduction, offering a sustainable alternative particularly suited for low-silica diasporic bauxite. Furthermore, the by-products of the sintering

process, being usable in the cement industry, contribute to the environmental and economic viability of the method.

Future research should focus on scaling up this process, assessing the long-term environmental benefits, and exploring the potential integration of this method into existing alumina production facilities.

Acknowledgments

References

Chen, Y., Long, F., Cao, X., Li, Y., Zhang, W., Zhang, T., & Lv, G. (2023). Exploration of Large-Scale Application of Efficient and Clean Utilization of Low-Grade Bauxite. *Separations*, *10*, 336. https://doi.org/10.3390/separations10060336

Desai, A. L. a. P. (2024). New alumina supplies in 2025 poised to rupture record price rally.

Gu, F., Li, G., Peng, Z., Luo, J., Deng, B., Rao, M., & Zhang, Y. (2018). Upgrading Diasporic Bauxite Ores for Iron and Alumina Enrichment Based on Reductive Roasting. *JOM*, *70*. https://doi.org/10.1007/s11837-018-3000-3

Kar, M. K., Önal, M. A. R., & Borra, C. R. (2023). Alumina recovery from bauxite residue: A concise review. *Resources, Conservation and Recycling*, *198*, 107158. https://doi.org/https://doi.org/10.1016/j.resconrec.2023.107158

Le, T., Ju, S., Lu, L., Peng, J., Zhou, L., & Wang, S. (2017a). A novel process and its mechanism for recovering alumina from diasporic bauxite. *Hydrometallurgy*, *169*. https://doi.org/10.1016/j.hydromet.2016.12.012

Le, T., Ju, S., Lu, L., Peng, J., Zhou, L., & Wang, S. (2017b). A novel process and its mechanism for recovering alumina from diasporic bauxite. *Hydrometallurgy*, *169*, 124-134.

Liu, J. (2025). IAI: Global alumina production falls in Nov 2024 m-o-m.

Ma, Q. X., Zhang, Y. F., Cao, S. T., & Zhang, Y. (2013). Leaching behavior of diaspore bauxite in KOH sub-molten salt. *Guocheng Gongcheng Xuebao/The Chinese Journal of Process Engineering*, *13*, 391-396.

Meher, S. N. (2016). Alumina extraction from red mud by CaCO3 and Na2CO3 sinter process. *International Journal of Chemical Studies*, *4*, 122-127.

SENGUPTA, D. (2024). World alumina production in October surpasses all historical records with highest-ever daily average output. Retrieved 29 November, from

Sun, Y., Pan, A., Ma, Y., & Chang, J. (2023). Extraction of alumina and silica from high-silica bauxite by sintering with sodium carbonate followed by two-step leaching with water and sulfuric acid [10.1039/D3RA03362G]. *RSC Advances*, *13*(33), 23254-23266. https://doi.org/10.1039/D3RA03362G

Tam, P., Panias, D., & Vassiliadou, V. (2019). Sintering Optimisation and Recovery of Aluminum and Sodium from Greek Bauxite Residue. *Minerals*, *9*, 571. https://doi.org/10.3390/min9100571

Weiguang, Z., Ting'an, Z., Guozhi, L., Xuhua, Z., Xiaofeng, Z., Yanxiu, W., & Long, W. (2016). Study on effective extraction of Al and Fe from high-iron bauxite through "calcification-carbonization" method. In E. Williams (Ed.), *Light Metals 2016* (pp. 15-18). Springer International Publishing. https://doi.org/10.1007/978-3-319-48251-4_3

Zhou, G.-t., Wang, Y.-l., Qi, T.-g., Zhou, Q.-s., Liu, G.-h., Peng, Z.-h., & Li, X.-b. (2023). Toward sustainable green alumina production: A critical review on process discharge reduction from

gibbsitic bauxite and large-scale applications of red mud. *Journal of Environmental Chemical Engineering, 11*(2), 109433. https://doi.org/https://doi.org/10.1016/j.jece.2023.109433

Investigation of Strategic and Rare Elements in Keder Porphyry Copper Deposit, Kerman Cenozoic Magmatic Arc

Mansour Adelpour[1]*, Mohsen Rezaie[2]

[1]Assistant Professor, Department of Geology and Exploration, Institute of Strategic Elements, Iranian Research Organization for Science and Technology (IROST), Tehran, Iran

[2]Assistant Professor, Department of Geology, Faculty of Earth Science, Shahid Chamran University of Ahvaz, Ahvaz, Iran *Corresponding author: e-mail (Firstname Lastname)

Abstract:

Porphyry copper deposits (PCDs) are the world's largest Cu and Mo reserves, a major source of Au and Ag, and a key target for exploration of strategic and rare earth elements (REEs). The most important metals commonly extracted from these deposits include Cu, Mo, and Au. Recent studies on porphyry copper systems in different parts of the world have shown that these deposits can also be important for other elements, including Co, Se, Re, Te, REEs, and platinum group elements (PGEs). Therefore, the aim of this study is to investigate the chemistry of sulfide minerals in the phyllic alteration zone of the Keder porphyry copper deposit using scanning electron microscopy–energy dispersive X-ray spectroscopy (SEM-EDX) and electron probe micro-analyzer (EPMA). The Keder deposit is located in the northwest of Kerman province, at the northwest end of Kerman Cenozoic Magmatic Arc (KCMA). Mineralization in this area is associated with a granodiorite to quartzdiorite porphyry intrusive massif of Miocene age that has intruded into Eocene pyroclastic volcanic series. The studies show a trend of changes in the concentration of trace elements in the studied sulfide samples, which can be attributed to the change in the composition of the hydrothermal fluid during the evolution of the hydrothermal systems of this deposit. The results showed that the concentration of Re, Zn and Pb elements is relatively higher in chalcopyrite samples, while Te, Ag, Mo, Co, As and Au elements are mainly concentrated in pyrite samples. The results of this study can help in the processing of strategic elements from PCDs.

1. Introduction

Porphyry deposits are the world's largest reserves of Cu and Mo, a major source of Au and Ag, and a key target for exploration of strategic and rare earth elements. The most important metals typically extracted from porphyry copper deposits (PCDs) include Cu, Mo, and Au (Sillitoe 2010); more than 60% of the world's copper production comes from porphyry copper deposits (Tabelin, Park et al. 2021) and typically contain 100 million tons to more than 20 billion tons of ore (Sillitoe 2010, Taylor, Hammarstrom et al. 2012). Recent studies of porphyry copper systems around the world have shown that these deposits can also be important for other elements, including Co, Se, Re, Te, rare earth elements (REE), and platinum group elements (PGE) (Shan, Cao et al. 2023). In general, porphyry copper and porphyry molybdenum deposits are the largest sources of copper (~60%) and molybdenum (~95%) in the world. Given the large volume of rocks affected by mineralizing hydrothermal systems and the high tonnages of metals obtained from these deposits, other trace element concentrations (such as Re, PGMs, Te, Se, REEs, In, Li, Nb, and Ta) may also become economic in the coming years (John and Taylor 2016). Porphyry copper deposits and the systems containing these deposits have been the subject of much study, and many aspects of these systems have been reviewed in recent papers (Sillitoe 2010). Porphyry copper systems, together with associated skarn, replacement and epithermal deposits, currently provide approximately 3/4 of the world's copper, 1/2 of the world's molybdenum, 1/5 of the gold, about 80% of the world's Re, trace amounts of Se, Te, and minor amounts of Ag, Pd, Pt, Bi, Zn and Pb (Sillitoe 2010). Hydrothermal

activity in porphyry copper systems results in the concentration, redistribution or depletion of dozens of other major and trace elements in rocks that have been affected by hydrothermal fluids (Seedorff, Dilles et al. 2005, Barton 2010). Porphyry copper systems typically have alteration zoning from the center to the periphery of the intrusive mass (Japas et al., 2022). Usually, in porphyry systems, the transition from potassic to phyllic alteration is accompanied by a decrease in temperature and a decrease in the a(K+)/a(H+) activity of hydrothermal fluids (Pirajno, 2009). The mixing of atmospheric and magmatic fluids has long been considered an important factor in the occurrence and development of the phyllic alteration zone (Hemley and Hunt, 1992). It is worth noting that in porphyry systems, the main hypogene mineralization occurs at the end of the potassic alteration zone and in the vicinity of the phyllic alteration zone (Richards, 2012). In Iran, most of the Iranian porphyry copper deposits are located in the Urmia-Dokhtar Magmatic Arc, especially in the southeastern parts, which are called the Cenozoic Kerman Magmatic Arc (Shafiei et al., 2008). Porphyry copper systems in the Urmia-Dokhtar magmatic zone have been studied from various aspects such as petrogenic characteristics or mineral fluid evolution (Shafiei et al., 2008; Asadi et al., 2014; Zarasvandi et al., 2015b). However, so far, fewer studies have been conducted on the physicochemical characteristics of the alteration zones of these deposits, especially the phyllic alteration zones. In this regard, considering the importance of phyllic alteration alteration in porphyry copper systems, this study attempts to characterize the parameters determining the chemistry of philic alteration sulfide minerals in the Keder porphyry copper deposit using modern exploration technologies such as scanning electron microscopy–energy dispersive X-ray spectroscopy (SEM-EDX) and electron probe micro-analyzer (EPMA).

2. Material and methods

2.1. Material

Sampling was carried out on the drill cores of Keder deposit at different depths. Polished thin sections were prepared from 1-2 cm blocks for optical microscopy and electron probe microanalyzer (EPMA) studies. Wavelength-dispersive (WDS) EPMA analyses of the samples were conducted at the Montanuniversität Leoben, Austria using the Jeol JXA 8200 instrument and the following analytical conditions: 15 kV accelerating voltage, 10 nA beam current and beam size set to spot mode (of about 1μm). For analyzing the sericite minerals, the calibration standards were natural adularia, atacamite, rhodonite, titanite, fluorite, labradorite, wollastonite, and olivine for F, Si, Al, Fe, Mg, Ti, Cl, Ba, and Mn. For sulfide analyses including pyrite and chalcopyrite, the calibration standards used were pyrite for Fe and S, chalcopyrite for Cu, pentlandite for Ni, AuTe2 for Au and Te, Bi2Se3 for Se, CoAs3 for Co, GaAs for As, AgBiSe2 for Ag, and ZnS for Zn.

3. Results

The Keder porphyry copper deposit is located in the northwest of Kerman Province and 14 kilometers southwest of Dehaj County (Fig. 1). Alteration-mineralization in this area is associated with a Miocene granodiorite to quartzodiorite porphyry intrusion that intruded Eocene pyroclastic volcanic series. This complex is intruded by a series of younger fine-grained granodiorite dikes (Sadat Mousavi, 2010). The most important structures in the area are NE-SW and E-W trending faults that appear to have controlled mineralization and alteration to some extent. The magmatic series of rocks in the Keder area falls within the medium-K calc-alkaline range. The Keder porphyry deposit is peraluminous and the host volcanic rocks are metaluminous. The semi-deep intrusive rocks and volcanic rocks in the Keder exhibit geochemical characteristics of igneous rocks of a subduction and collisional tectonic setting. Hypogene mineralization in Keder is characterized by the presence of pyrite and some chalcopyrite and a little bornite, covellite, chalcocite, pyrrhotite and small amounts of sphalerite, which are present in the form of veins and stockwork. Hydrothermal alteration in Keder covers an

area of more than 10 Km2 and in this respect is considered one of the largest alteration systems in the Kerman Copper Belt. Phyllic alteration is the most widespread and is especially affected by advanced clay alteration and silicic alteration in the surface zone. Silica forms the prominences of the region in the form of veins and ridges of different dimensions and mostly with shear texture. Potassic alteration is limited in the deep parts, which has been observed in drilling cores. This alteration is characterized by the abundance of biotite and the presence of k-feldspar, magnetite and gypsum-anhydrite veinlets. In addition, propylitic and argillic alteration have also been observed in the region (Sadat Mousavi, 2010).
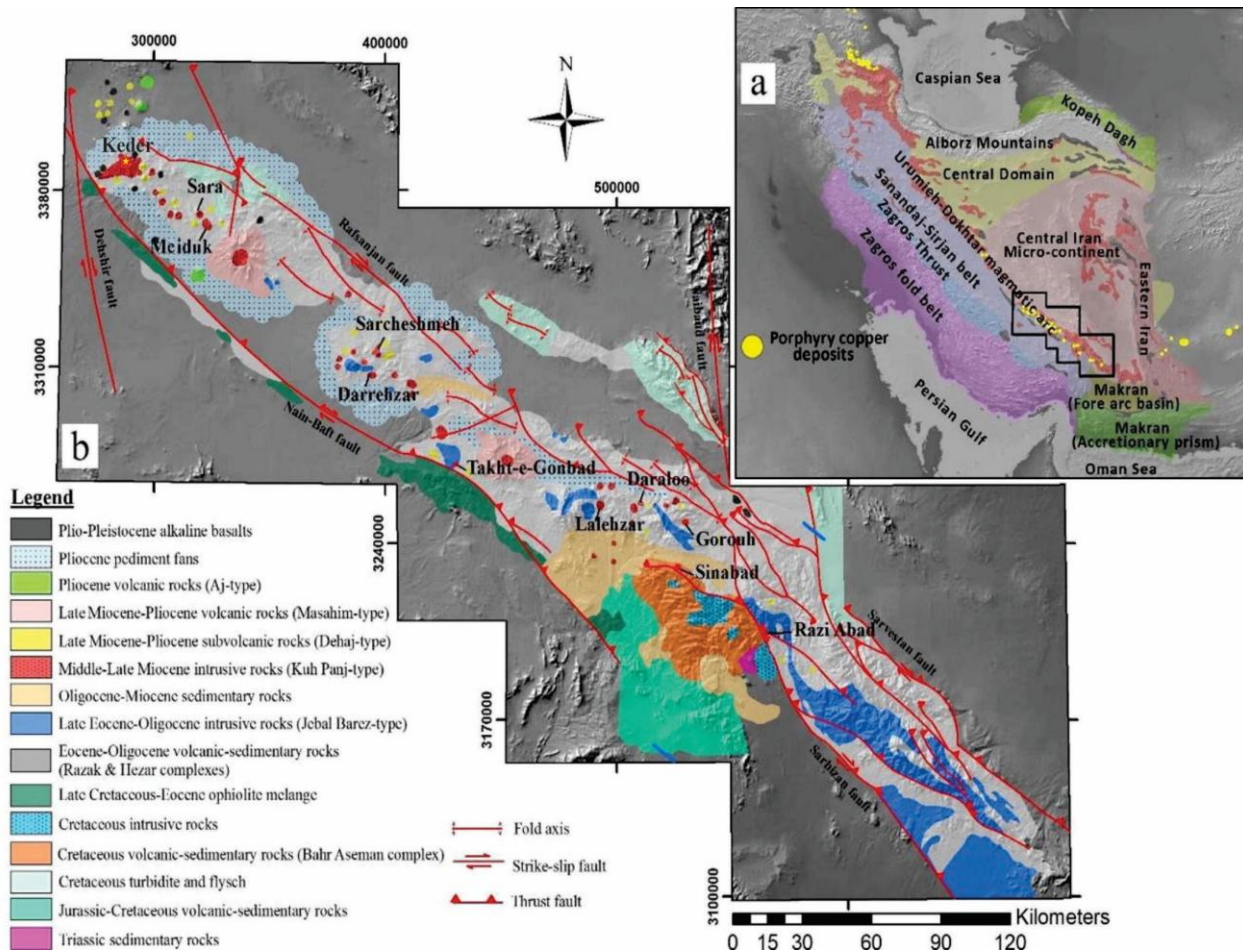

Fig. 1. a) Zagros orogenic and metallogenic belt including three tectonic processes; Urmia-Dokhtar magmatic arc, Sanandaj-Sirjan metamorphic zone and Zagros fold-thrust belt (Hossein et al., 2017) Location of the Keder deposit in the southern part of the Urmia-Dokhtar magmatic belt

Pyrite in the phyllic alteration of the keder deposit can be separated in two distinct generations (I and II). The first generation pyrites (I) in the keder deposits are usually seen as euhedral and cubic in different sizes (Figure 2-a). Also, these pyrites sometimes have porous and uneven surfaces and are found as scattered and shaped grains in areas that have been strongly affected by sericite and siliceous alteration. The second generation pyrites (II) in the Keder deposit are observed as amorphous with fractures (Figure 2-b). In general, the study of phyllic alteration sections of the keder porphyry deposit indicates the predominant occurrence of pyrite and chalcopyrite minerals, along with smaller amounts of pyrrhotite, rutile, hematite, and stibnite. These inclusions and associated minerals were examined and precisely identified using SEM-EDX.

Composition of Sulfides

The most abundant sulfide minerals in the Keder deposit are pyrite and chalcopyrite. These minerals host a wide range of trace elements in their structure, of which Au, Co, Te, As, and Mo are more important (Zarasvandi et al., 2018). According to the results of electron microanalysis (Table 1), in pyrite samples from the Keder deposit, the average Fe is 46.73 wt% and the average S is 52.21 wt%. In the chalcopyrite samples from the Keder deposit, the average values of the main components (in terms of wt%) including Fe, S, and Cu are 28.18, 34.76, and 35.8, respectively. It can be said that the concentrations of the main components in the sulfide samples of the studied deposit are similar to the values previously reported for other Cu, Cu-Au, and Cu-Mo porphyry systems.

Copper, gold, rhenium, and molybdenum are the main trace elements associated with porphyry-type ores (Sillitoe, 2010). According to Zarasvandi et al. (2018), the copper content of pyrite ores in porphyry copper deposits can be an indicator of the fertility of the porphyry system. For example, pyrites from the Meyduk porphyry copper deposit (with significant mineralization; 0.86% Cu, 170 mt; Taghipour et al., 2008) sometimes contain significant amounts of copper (close to 1 wt%) (Zarasvandi et al., 2018). The average copper concentration in pyrite samples from the Keder deposit is 0.0017 wt.% (Table 1). The data show that significant amounts of gold are present in pyrite and chalcopyrite samples of phyllic alteration of this deposit (Table 1). The gold concentration in pyrite samples from the Keder deposit has a maximum of 0.046 wt.% (Table 1). Also, the gold concentration in chalcopyrite samples from the Keder deposit has an average of 0.0169 wt.%. The average Mo concentration in pyrite samples from the Keder deposit is 0.7204 wt.% and in chalcopyrite samples is 0.4855 wt.%.

Table 1. Results of EPMA of pyrite and chalcopyrite in the phyllic alteration of Keder deposit

| Element	Pyrite			Chalcopyrite		
	Min	Max	Average	Min	Max	Average
As	0.0337	0.076	0.04915	0.02	0.03	0.025
Te	0.0031	0.0037	0.0034	0.0014	0.0039	0.0026
S	50.76	53.07	52.215	34.51	35.01	34.76
Fe	46.55	46.92	46.7375	27.99	28.3	28.145
Cu	b.d	0.0068	0.0017	35.11	36.49	35.8
Se	b.d	0.0127	0.003175	b.d	b.d	b.d
Bi	b.d	b.d	b.d	b.d	b.d	b.d
Re	b.d	0.0139	0.004925	0.0105	0.0125	0.0115
Ni	b.d	0.0171	0.0049	0	0	0
Co	0.0919	0.2149	0.13775	0.0494	0.0502	0.0498
Ge	b.d	b.d	b.d	b.d	b.d	b.d
Hg	b.d	b.d	b.d	b.d	b.d	b.d
Au	0.0129	0.046	0.024825	0.0127	0.0212	0.01695
Zn	b.d	0.0004	0.0001	0.0654	0.0801	0.07275
Th	b.d	0.001	0.00025	b.d	b.d	b.d
Sb	b.d	0.0034	0.00085	b.d	b.d	b.d
Ag	b.d	0.0186	0.006875	b.d	0.0012	0.0006
Pb	b.d	b.d	b.d	0.0204	0.0308	0.0256
Mo	0.7116	0.7278	0.720475	0.4568	0.5143	0.48555
Total	98.1632	101.1323	99.91088	98.2466	100.5442	99.39535
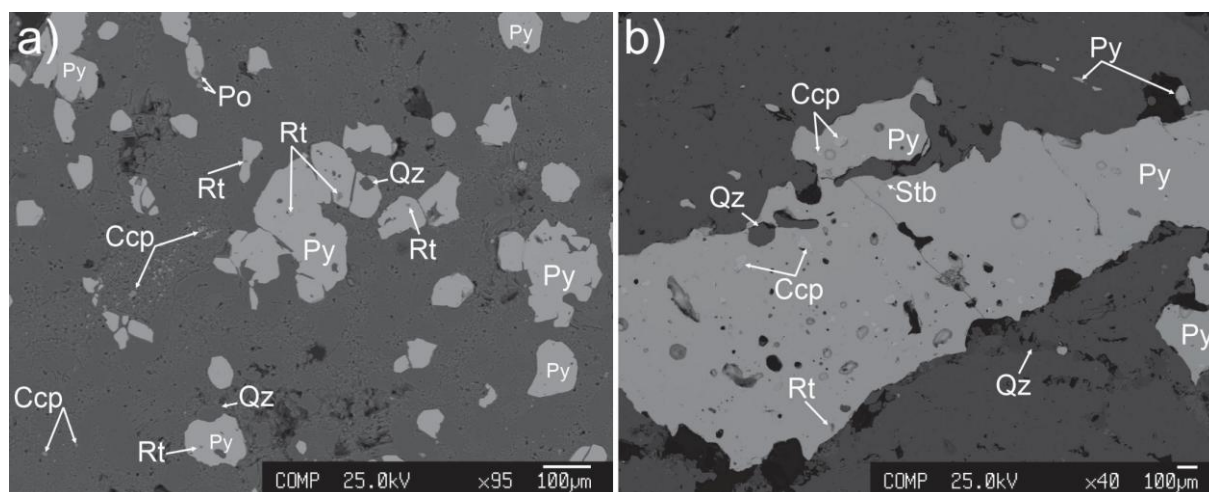
Fig. 2- a & b) SEM-EDX of the Keder deposit minerals. Py: pyrite, Po: pyrrhotite, Ccp: chalcopyrite, Rt: Rutile, Stb: stibnite. Mineral abbreviations are taken from (Whitney and Evans, 2010).

The results of EPMA of pyrite and chalcopyrite showed that the amounts of Re, Pb and Zn elements are higher in chalcopyrite, while the amounts of Mo, Co, As, Te, Ag and Au are higher in pyrite. Most of the pyrite and chalcopyrite samples studied are characterized by relatively high concentrations of Te. For example, the Te values in the Keder pyrite samples have a maximum of 0.0034 wt% and in the Keder chalcopyrite samples the amount of this element is 0.0039 wt%. It is worth noting that these values are above the range of 1.5 to 3 g/t considered as an economic threshold for extraction as a by-product during the copper processing process (Ayres et al., 2002; Cioaca et al., 2014). Previous studies have shown that bornite and chalcopyrite are the most important Ag-carrying minerals in hydrothermal sulfides (Cook et al., 2011; Reich et al., 2013b). The highest average Ag for porphyry copper-gold deposits is reported to be 1.7 wt.% (Cox and Singer, 1988). According to the results of EPMA, the maximum Ag concentration in chalcopyrite and pyrite samples of Keder is 0.0012 wt.% and 0.186, respectively (Table 1). In the samples studied, selenium was only detectable in pyrite samples (maximum 0.0127 wt.%). Studies have shown that in porphyry copper systems, Re is usually concentrated in molybdenite (Zarasvandi et al., 2018). The maximum Re content in pyrite samples from the Keder deposit is 0.0139 wt.% and in chalcopyrite samples is 0.0125 wt.%.

4. Conclusions

Mineralization in the Keder porphyry system is associated with granodiorite to quartzdiorite porphyry intrusive masses that are located. Although the extent of potassic alteration in this deposit is insignificant, phyllic alteration is extremely widespread, such that this alteration is observed from the surface areas to the deepest parts of the drilled boreholes. In general, the phyllic alteration of this deposit shows that quartz-sulfide veins are dominant in the Keder deposit, while anhydrite minerals have a lower occurrence. The results of EPMA on sulfide phases show that significant amounts of Au are present in pyrite and chalcopyrite samples of this deposit. The Au concentration in pyrite samples of the Keder deposit has a maximum of 0.046 wt% and in chalcopyrite samples has a maximum of 0.0212 wt%. The change in the concentration of trace elements in the sulfide phases (pyrite and chalcopyrite) of the phyllic alteration zone indicates the fractionation of trace elements in the sulfide phases during this alteration. The results showed that the concentration of Re, Zn and Pb elements is relatively higher in chalcopyrite samples, while Te, Ag, Mo, Co, As and Au elements are mainly concentrated in pyrite samples.

References

Asadi, S., Moore, F., & Zarasvandi, A., 2014. Discriminating productive and barren porphyry copper deposits in the southeastern part of the central Iranian volcano-plutonic belt, Kerman region, Iran: A review, Earth-Science Reviews, 138(1), 25-46. https://doi.org/10.1016/j.earscirev.2014.08.001

Ayres, R.U., Ayres, L., & Råde, I., 2002. The Life Cycle of Copper, Its Co-products and Byproducts, Eco-Efficiency in Industry and Science, 265p. (http://pubs.iied.org/pdfs/G00740.pdf).

Barton, M. D. (2010). "Broader implications and societal relevance of porphyry copper systems: U.S. Geological Survey Scientific Investigations Report." 126–130.

Cioacă, M.E., Munteanu, M., Qi, L., & Costin, C., 2014. Trace element concentrations in porphyry copper deposits from Metaliferi Mountains, Romania: A reconnaissance study, Ore Geology Reviews, 63, 22–39. DOI:10.1016/J.OREGEOREV.2014.04.016

Cox, D.P., & Singer, D.A., 1988. Distribution of gold in porphyry copper deposits. US Geological Survey, Open-file Report. 10.3133/ofr8846

Japas, M.S .Rubinstein, N.A R.Gómez A.L., 2022. Revisiting reverse osmosis as a mechanism contributing to metal zoning in porphyry copper deposits, Ore Geology Reviews, 143, 104746. https://doi.org/10.1016/j.oregeorev.2022.104746

John, D. A. & R. D. Taylor (2016). "By-products of porphyry copper and molybdenum deposits."

John, D.A., Ayuso, R.A., Barton, M.D., Blakely, R.J., Bodnar, R.J., Dilles, J.H., Gray, F., Graybeal, F.T., Mars, J.L., McPhee, D.K., Seal, R., Taylor, R.D. &. Vikre, P.G., 2010. Porphyry Copper Deposit Model, Chapter B of Mineral Deposit Models for Resource Assessment, U.S. Geological Survey, U.S.A, Report 2010–5070 B, 166 p. 10.3133/ sir20105070B

Pirajno, F., 1992. Hydrothermal mineral deposits, John Wiley and Sons, Sydney. 709 p. https://doi.org/10.1007/978-3-642-75671-9

Reich, M., Deditius, A., Chryssoulis, S., Li, J-W., Ma, Ch-Q., Parada, M.A., Barra, F., & Mittermayr, F., 2013a. Pyrite as a record of hydrothermal fluid evolution in a porphyry copper system: A SIMS/EMPA trace element study, Geochimica et Cosmochimica Acta, 104, 42–62. https://doi.org/10.1016/j.gca.2012.11.006

Reich, M., Kesler, S. E., Utsunomiya, S., Palenik, C., Chryssoulis, S. L., & Ewing, R.C., 2005. Solubility of gold in arsenian pyrite, Geochimica et Cosmochimica Acta, 69(11), 2781–2796. https://doi.org/10.1016/j.gca.2005.01.011

Reich, M., Palacios, C., Barra, F., & Chryssoulis, S., 2013b. Invisible silver in chalcopyrite and bornite from the Mantos Blancos Cu deposit, northern Chile, European Journal of Mineralogy, 25(3), 453–460. https://doi.org/10.1127/ 0935-1221/2013/0025-2287

Richards, J.P., Spell, T., Rameh, E., Razique, A., & Fletcher, T., 2012. High Sr/Y Magmas Reflect Arc Maturity, High Magmatic Water Content, & Porphyry Cu ± Mo ± Au Potential: Examples from the Tethyan Arcs of Central and Eastern Iran and Western Pakistan, Economic Geology, 107(2), 295-332. https://doi.org/10.2113/econgeo.107.2.295

Sadat Mousavi, N., (2010). Study of the porphyry copper deposit of the Kadar region in terms of mineralogical characteristics, alteration, sulfur isotopes and the nature of fluid inclusions. Master's thesis, 2010: p. 180

Seedorff, E., Dilles, J.H., Proffett, J.M., Einaudi, M.T., Zurcher, L., Stavast, W.J.A., Johnson, D.A., & Barton, M.D., 2005. Porphyry deposits: Characteristics and origin of hypogene features, Economic Geology, 100th Anniversary, 251. https://doi.org/10.5382/AV100

Seedorff, E., J. H. Dilles, J. M. Proffett, M. T. Einaudi, L. Zurcher, W. J. Stavast, D. A. Johnson & M. D. Barton (2005). "Porphyry deposits: Characteristics and origin of hypogene features."

Shafiei, B. & Shahabpour, J., 2008. Gold Distribution in Porphyry Copper Deposits of Kerman Region, Southeastern Iran, Journal of Sciences, Islamic Republic of Iran, 19(13) 247-260. https://jsciences.ut.ac.ir/article_31898.html

Shan, P., M. Cao, N. J. Evans, H. Gao, Y. Mao, Y. Gao, L. Salazar, Y. Zhao & K. Qin (2023). "Automated quantitative mineralogy analysis reveals characteristics of Co occurrence in the Jinchang porphyry deposit, NE China." Ore Geology Reviews 158: 105524.

Sillitoe, R. H. (2010). "Porphyry copper systems." Economic geology 105(1): 3-41.

Tabelin, C. B., I. Park, T. Phengsaart, S. Jeon, M. Villacorte-Tabelin, D. Alonzo, K. Yoo, M. Ito & N. Hiroyoshi (2021). "Copper and critical metals production from porphyry ores and E-wastes: A review of resource availability, processing/recycling challenges, socio-environmental aspects, and sustainability issues." Resources, Conservation and Recycling 170: 105610.

Taghipour, N., Aftabi, A., & Mathur, R., 2008. Geology and Re-OS geochronology of Mineralization of the Miduk Poyphyry Deposit, Resource Geology, 58 (2), 143-160. https://doi.org/10.1111/j.1751-3928.2008.00054.x

Taylor, R. D., J. M. Hammarstrom, N. M. Piatak & R. R. Seal II (2012). Arc-related porphyry molybdenum deposit model: Chapter D in Mineral deposit models for resource assessment, US Geological Survey.

Zarasvandi, A., Rezaei, M., Raith, J., Lentz, D., Azimzadeh, A.M., & Pourkaseb, H., 2015b. Geochemistry and fluid characteristics of the Dalli porphyry Cu–Au deposit, Central Iran, Journal of Asian Earth Sciences, 111(1), 175-191.

Zarasvandi, A., Rezaei, M., Raith, J.G., Pourkaseb, H., Asadi, S, Saed, M., & Lentz, D.R., 2018. Metal endowment reflected in chemical composition of silicates and sulfide s of mineralized porphyry copper systems, Urumieh-Dokhtar magmatic arc, Iran. Geochimica et Cosmochimica Acta, 223, 36-59. https://doi.org/10.1016/j.gca.2017.11.012

Optimization of Zarshuran - filtration circuit with pretreatment of tailing pulp by chemical and physical solutions

Ataallah Bahrami[1]*, Fatemeh Kazemi[2], Aylar Najarpour salmasi[3], Mostafa Shiri aq-qalle[4]

[1]Associate Professor, Department of Mining Engineering, Faculty of Engineering, Urmia University, Orumye - Iran

[2]PhD of Mineral Processing, Department of Mining Engineering, Faculty of Engineering, University of Kurdistan, Sanandaj, Iran

[3]MSc of Mineral Processing, Department of Mining Engineering, Faculty of Engineering, Urmia University, Orumye – Iran

[4]Research and Development Unit Manager, Zarshuran Gold Mines and Mining Industries Development Company. Tekab – Iran

*Corresponding author: a.bahrami@urmia.ac.ir (Ataallah Bahrami)

Abstract:

The long duration of the dewatering process (limitations in dewatering equipment) and the Incompatibility in capacity of the dewatering department with processing plant load are the most important current challenges of the tailings dewatering circuit of the Zarshuran gold processing plant (located in West Azerbaijan province). The purpose of this research is to investigate the possibility of increasing the capacity of the dewatering department of the Zarshuran plant using two solutions: 1) chemical pre-treatment of the tailings and 2) changes in the equipment and layout of the current dewatering circuit. In this regard, after measuring the properties of the tailings sample of this plant, pre-treatment-filtration, sedimentation-filtration, hydrocyclone-filtration flotation-sedimentation-filtration tests using chemical agents including various flocculants and surfactants were conducted. Based on the results, the use of all three types of anionic surfactants (SLES, PEG and CTAB) increased the filtration rate and reduced the moisture content of the filter cake. Among them, the best results were obtained with anionic surfactant (SLES) at a concentration of 100 g/t - the moisture content of the filtered cake was less than 26%. By designing the filtration circuit, taking into account processing equipment, including hydrocyclone and thickener, the lowest moisture content in the thickener (without flocculant)-filtration circuit was 32%.

Keywords: Thickener, Filtration, Surfactant, flocculent, Filtration rate

1. Introduction

Water resource management and consumption in the country are strategic and priority issues. Mines and mining industries, as one of the sectors consuming water resources, need policy-making and regulatory and executive measures to address the challenges and damages caused by inappropriate water consumption patterns and wastewater management, as well as environmental issues related to wastewater. In the mining and mineral industries sector, the major water consumption in mineral processing units (such as enrichment and pelletizing, flotation, etc.) and production units in the value chain of mineral and metal products (such as iron and steel, copper, aluminum, lead and zinc, etc.) is as process water and water required for creating a bed for transporting minerals, cooling and temperature control (Bosman, 2016). By examining the quality and quantity of water resources in the mineral industries in the world, it has been determined that among the metals and alloys of iron, steel,

gold, copper, aluminum, cement products and sand, the highest water consumption is related to the production of gold metal, followed by the production of copper metal (Garner et al., 2012).

Considering the need for sustainable management of water resources in mines and mining industries and reforming the consumption pattern in the mining sector, which is an important and priority issue, the quality and quantity of water resources in mines and mining industries in the country have been studied and compared with global standards. Analyses show that in the case of gold, water consumption in Iran is about five times the global consumption; therefore, it is necessary to quickly develop and implement special plans to reduce water consumption in this industry. In general, there are two main solutions for water resource management in the mining sector. The first option is to use saltwater instead of fresh water (seawater desalination), and the second option is to use water recycling processes in industrial-mining factories, including the use of water thickeners and filters (Galvez and Cisternas, 2017; Northey and Haque, 2013).

Dewatering processes (thickeners and filters) are among the most important stages of mineral processing in water recovery and reducing tailings moisture. Improper performance of the dewatering-filtration circuit causes problems such as high tailings moisture and the exit of part of the tailings along with water. On the other hand, the efficiency and performance of these processes in a processing plant determines the volume of water returned to the plant (process water). Given that process water contains a variety of chemicals used during processing processes, returning these chemicals to the plant circuit will not only improve plant performance, but also reduce the environmental impacts of tailings discharge into dams and tailings depots (Stockman et al., 2014; Leonida, 2024). Because high tailings moisture and its discharge into tailings dams can lead to undesirable environmental issues such as the infiltration of mineral drainage into groundwater and surface waters, soil pollution, and even the emission of toxic gases into the air; especially in cases where the tailings and the water with them contain chemicals and toxins (such as gold cyanidation tailings). In addition to the above, the capacity of the plant's water intake section has a significant impact on the overall capacity of the circuit and its work shifts. Increasing the filtration rate will increase the capacity of the water intake circuit and, consequently, the total capacity of the system (Morton, 2023; Cacciuttolo et al., 2023).

In the Zarshuran gold processing plant, after carrying out various gold processing, the process tailings are transferred to two tanks (with a volume of approximately 70 m³). The particle size of the tailings pulp is approximately less than 45 microns and contains various clay minerals, sulfides, activated carbon particles and other minerals present in the plant's primary feed. The outlet suspension from these two tanks is transferred to the filtration unit. The tailings filtration equipment of the Zarshuran processing plant consists of 8 filter press series, with a total capacity of 140 m³ of pulp per hour. The filter plates are made of dense polypropylene with a cross-sectional area of 2.32 - 2.5, which operate under an operating pressure of 100 psi. The filtered cake with a moisture content of 20 to 30 percent is transported to the tailings dam by conveyor belt and truck. Due to the use of a dry stacking system in the Zarshuran processing plant, environmental problems caused by toxic wastewater of this plant have been minimized. Also, a significant portion of the water consumed is recycled to the plant circuit. The recovered water from the filter presses is discharged into concrete pond, than sent to the grinding department. The high moisture content (approximately 30%) of the tailings of the Zarshuran processing plant and the resulting environmental problems indicate the need to optimize the dewatering circuit of the Zarshuran gold tailings. On the other hand, the long duration of the dewatering process (limited dewatering equipment) and the mismatch in capacity between the dewatering depatment and the processing circuit of the plant can be considered the most important current challenges of the dewatering circuit of the Zarshuran. Therefore, increasing the capacity and efficiency of the filtration department of the plant can have a significant impact on the economic profitability of the plant by increasing its production.

In order to improve the dewatering process in mineral processing plants, several studies have been conducted by various researchers to use polyacrylamide (PAM) flocculants to increase the pulp mass percentage and increase the dewatering rate (Vehmaanpera et al., 2018). Also, studies have been

conducted on the hetero-flocculation of tailings such as iron ore, coal, etc. (Mamghaderi et al., 2018; Liu et al., 2019). In general, during the studies and investigations, it was concluded that the use of flocculants and surfactants in dewatering is effective in terms of reducing cake moisture, dewatering kinetics and filtration, and consequently increasing the capacity of the dewatering circuit. The aim of this research, after examining the operational conditions of the circuit and improving it, is to increase the capacity of the plant's dewatering department using pre-treatment tailings by chemical and physical method. In this regard, after determining the chemical composition of the plant's tailings suspension, sedimentation and filtration tests were conducted to investigate the possibility of increasing the sedimentation and filtration speed and consequently increasing the filtration capacity, using chemical agents including various flocculants and surfactants. It should be noted that, given that some of these materials remain in the water returned from the dewatering circuit, consideration has been given to determining the type of material with the least impact on the oxidation and absorption sections.

2. Material and methods

To determine the optimal conditions for dewatering of the Zarshuran filtration circuit, a sample was taken from the tailings dam of the plant (Figure 1). In this sampling, all the instructions related to the removal of tailings from mineral tailings depots and dams were followed. In the first step, identification studies were carried out, including determining the particle size distribution, chemical composition (by XRF method) and mineralogical studies.

Fig. 1. Images of filtration unit and tailing dam of Zarshuran processing plant

Based on the particle size distribution analysis (Figure 2), more than 53% of the particles are concentrated in the -25 micron particle size fraction; followed by the +25-45 micron particle size fraction with 32%, which has the highest particle size in the relevant size range. Based on the curve in Figure 1, more than 95% of the particles are smaller than 90 microns.
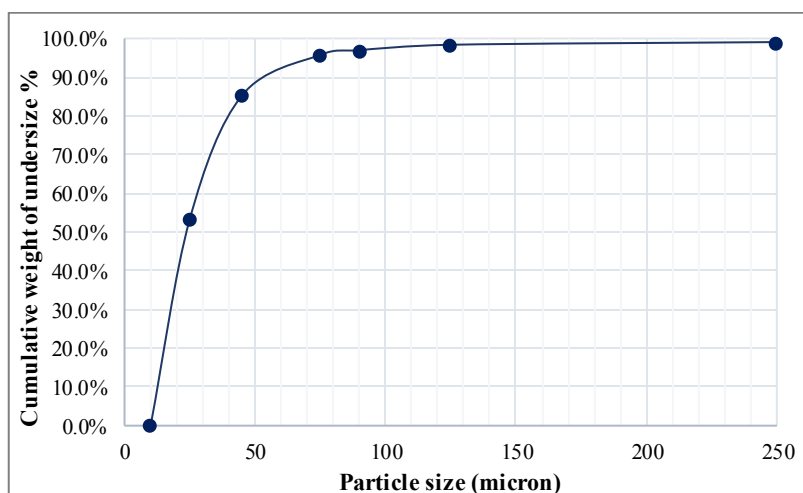
Fig. 2. Particle size distribution curve of the tailings of the Zarshuran gold processing plant

Table 1 shows the results of chemical analysis. Based on the values presented in Table 1, it can be said that most of the minerals in the tailings dam are in the carbonate and silicate phases. Calcium oxide, with a content of more than 40%, is the most important compound identified in the tailings of the Zarshuran gold processing plant. After that, silica is present at a level of approximately 16%, Al_2O_3 (approximately 5%), and Fe_2O_3 and As_2O_3 are the most important compounds.

Table 1. The result of XRF analysis of the tailings of the Zarshuran gold processing plant

Na_2O (%)	SiO_2 (%)	Al_2O_3 (%)	CaO (%)	Fe_2O_3 (%)	As_2O_3 (%)	K_2O (%)	MgO (%)
0.4	15.9	4.9	40.3	2.8	2.4	0.5	0.9
P_2O_5 (%)	SO_3 (%)	Cl (%)	MnO_2 (%)	ZnO (%)	La & Lu (%)	TiO_2 (%)	LOI (%)
<0.01	<0.01	<0.01	0.2	0.3	<0.01	0.4	31.0

Based on mineralogical studies (conducted by polarized transmitted light microscopy), gold-bearing minerals in the Zarshuran tailings include native (free) gold, fine aggregates - probably activated carbon, dispersed sulfide particles - mainly pyrite, arsenopyrite, and small amounts of Realgar and orpiment, iron hydroxides such as goethite and limonite, and silicate minerals. By comparing these studies with the results of particle size analysis, it can be said that the majority of the -25 micron particles are silicate and carbonate minerals.

2.1. Dewatering and filtration tests

In the filtration of tailings from processing plants where the size of waste particles is less than 100 microns; filtration faces the problem of low filter-cake formation rate. One solution to solve this challenge and improve the separation of solutions with fine and colloidal particles is to densify them with chemicals called filter aids. The mechanism of this process is to change the surface properties of the particles, change the properties of the liquid in the solution, or change the interaction between solid and liquid particles. In addition to this solution, changing mechanical and device methods can also be an effective factor in improving the dewatering process. In this research, with the aim of improving the efficiency of the Zarshuran dewatering circuit, the effect of both solutions has been investigated. Figure 3 shows a diagram of the tests conducted in this research to improve the Zarshuran dewatering circuit. It should be noted that all tests were conducted on pulp (20%) prepared from Zarshuran tailings, in accordance with the Zarshuran circuit tailings pulp flow conditions.
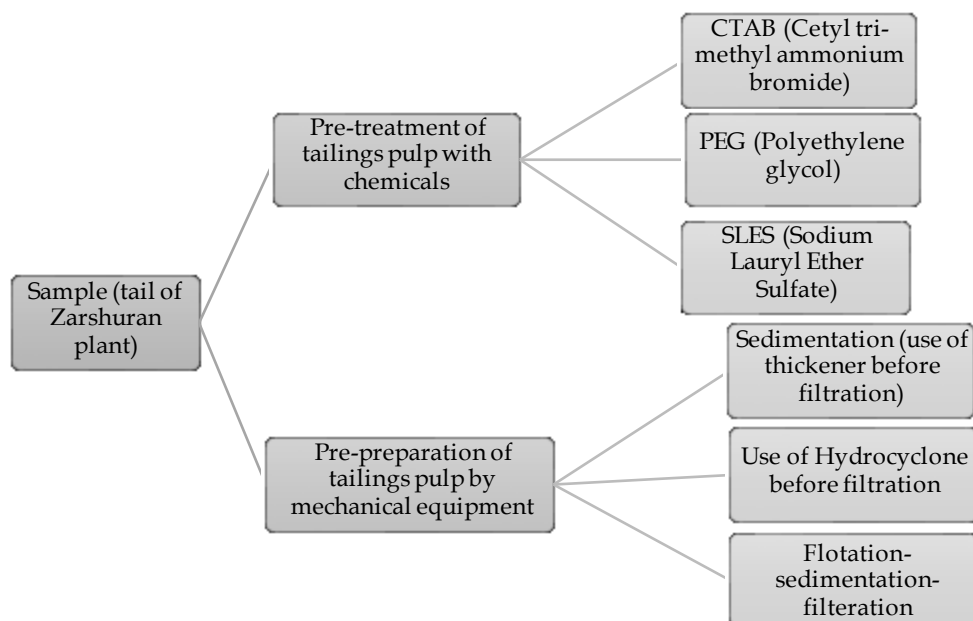
Fig. 3. Schematic of the tests conducted to improve the Zarshuran dewatering circuit

3. Result and discussion

3.1. Optimization of the Zarshuran dewatering circuit using surfactant

Filtration tests were conducted at concentrations of 50, 100, and 150 g/t of chemicals (CTAB, PEG, SLES), at a pH of approximately 8.3 (the same pH as the Zarshuran tailing pulp). Filtration tests were performed using a Merik vacuum pump model MV0006 with a voltage of 220 AC/50 Hz, a power of 1.3 HP, and an ultimate vacuum of $3*10^{-2}$ mbar. The vacuum filtration equipment was on a laboratory scale (Buchner funnel with a diameter of 7.5 cm) and the Top-Feed Leaf method was used for feeding.

Figure 4 shows the results of the filtration tests. The use of CTAB surfactant at all concentrations of 50, 100 and 150 g/t has reduced the percentage of moisture in the filter cake and increased the filtration rate. When this surfactant is used at a concentration of 50 g/t, a significant decrease in the percentage of moisture in the filter cake is observed compared to when the surfactant is not used. For a better understanding of the subject, for example, at a suction time of 10 seconds, the percentage of moisture has decreased from 71.53% to 47.14%, a decrease of 24.39%. At a suction time of 30 seconds, the percentage of moisture has decreased by 24.46%. Also, when this surfactant is used at a concentration of 100 g/t, the percentage of moisture in the cake has decreased similarly to the previous case, and at a suction time of 10 seconds, it has decreased from 71.53% to 50.65%, a decrease of 20.88%. At a suction time of 30 seconds, the difference in moisture percentage was 24.24. The use of CTAB surfactant at a concentration of 150 g/t, similar to the previous two cases, resulted in a decrease in the moisture percentage of the cake. At a suction time of 10 seconds, this decrease was 7.76%, and at a suction time of 30 seconds, a decrease of 11.72% was observed.

In the next case, the tailing pulp of Zarshuran with a solid percentage of 20 was prepared using nonionic surfactant PEG at concentrations of 50, 100 and 150 g/t and then filtered using a Buchner funnel. By comparing the performance of different concentrations of PEG nonionic surfactant, it is concluded that the best results are related to the concentration of 100 g/t and then 50 g/t, and using this surfactant at a concentration of 150 g/t is not economical and logical, considering the changes in moisture percentage.

The use of SLES surfactant in all three concentrations (100, 50 and 150 g/t) has reduced the moisture content of the filter cake and increased the filtration rate. When this surfactant is used in a

concentration of 50 g/t, the moisture content of the filter cake is significantly reduced in all suction times (5-30 seconds) compared to the case without surfactant. When this surfactant is used at a concentration of 100 g/t, a significant decrease in the moisture content of the filter cake is observed compared to the case without surfactant. At a suction time of 10 seconds, the difference in moisture content is 44.67%, and at a suction time of 30 seconds, this difference is 25.04%. It should be noted that the best filtration results are obtained in this case.
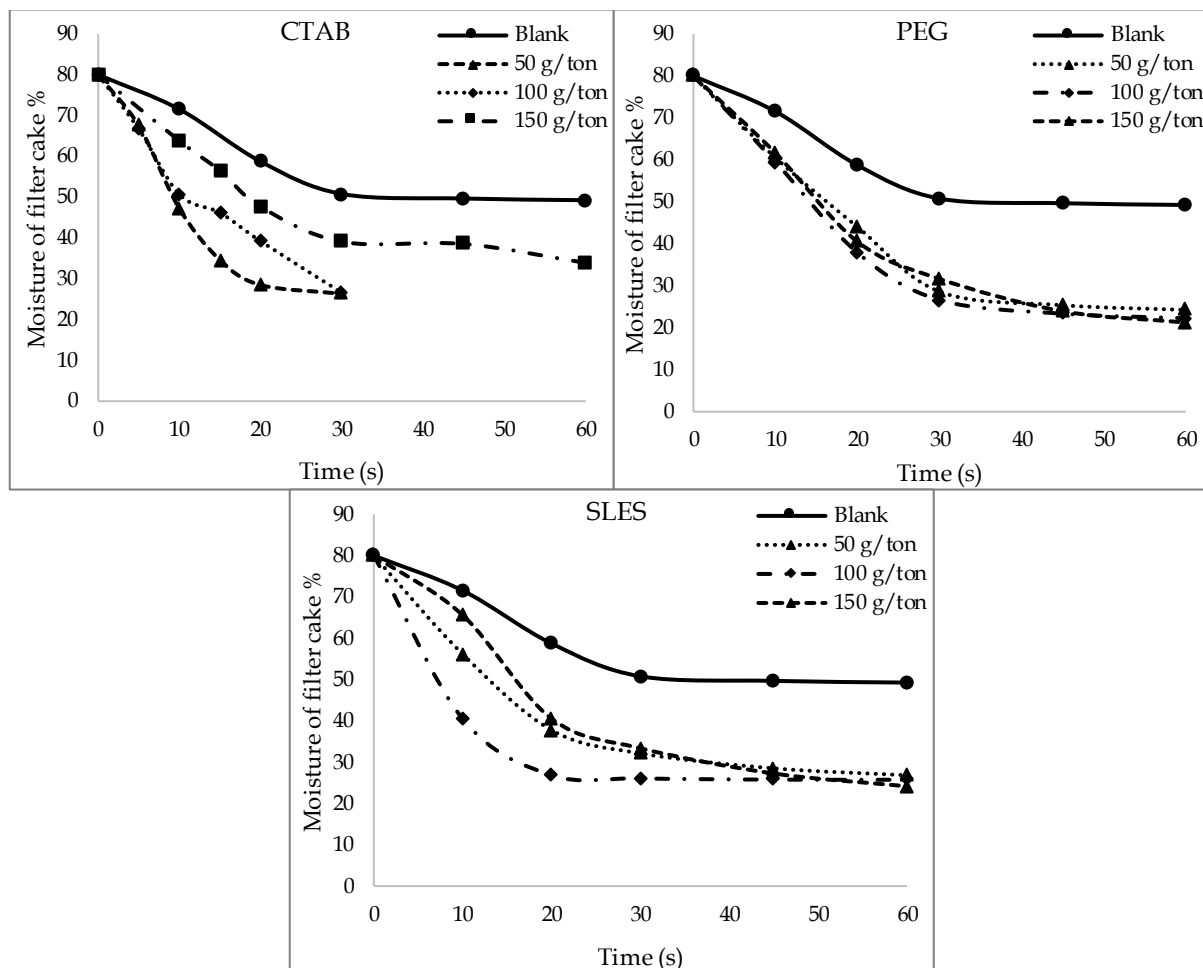
Fig. 4. Changes in filter cake moisture percentage in filtration tests with different surfactants

3.2. Improving the dewatering circuit by re-arranging of equipment

The second solution to improve the efficiency of the dewatering circuit in the Zarshuran gold processing plant is to change the circuit's dewatering equipment. Using a thickener before the filter is an effective solution for improving filtration efficiency and increasing the capacity of circuit. On the sample of Zarshuran tailings dam, sedimentation tests were conducted at different flocculant concentrations to determine the optimal sedimentation mode; the corresponding curves are shown in Figure 5. The sedimentation test using A26 flocculant with a concentration of 100 g/t had a more favorable result than the other cases. In this test, sedimentation occurred at a faster rate.

For sedimentation tests were conducted on the Zarshuran tailings dam without flocculant and with flocculant A26 at concentrations of 50, 100 and 150 g/t, filtration was performed with the same suction time of 45 seconds. Based on the results of previous tests, 45 seconds was considered an optimal time, and after that, with increasing time, the changes in the moisture content of the filter cake were small. Figure 5 shows the results of these tests. It should be noted that the average solids content of the pulp

in these tests was 45%. Based on the results under completely similar test conditions, the lowest moisture content of the filtered cake was related to the case where no flocculant was used for sedimentation. Also, with increasing flocculant concentration, the moisture content of the filter cake increased. The moisture content of the filter cake when no flocculant was used showed the value 32.04%. This value increased with increasing the concentration of flocculant used and reached 53.55% at a concentration of 150 g/t, which is the highest moisture percentage. Therefore, the use of flocculant had a negative impact on the filtration process.
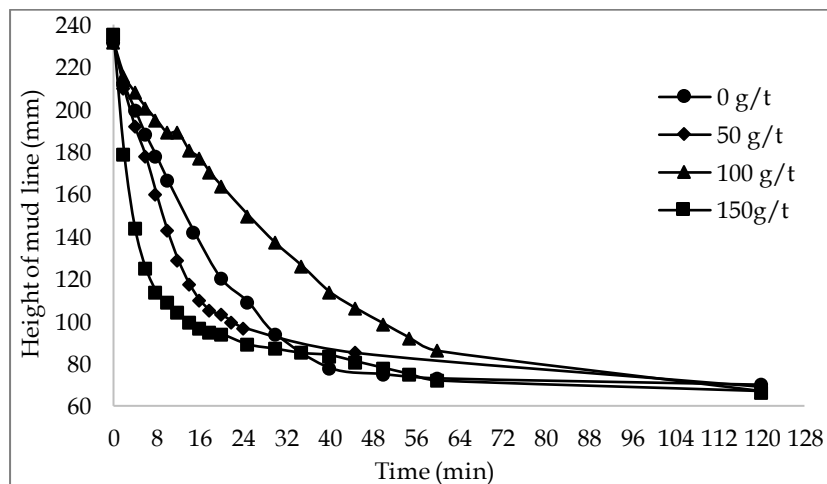

Fig. 5. Sedimentation curves of Zarshuran tailing pulp with using by different concentrations of flocculant A26

Hydrocyclone is another suitable equipment for use in the dewatering circuit. Classification was performed on the Zarshuran tailing pulp by hydrocyclone. Then, filtration tests were performed on the feed, overflow, and underflow of the hydrocyclone. The pulp related to the hydrocyclone feed had a solid percentage of 20, the overflow had a solid percentage of 10, and the solid percentage of the hydrocyclone underflow pulp was 35 percent. Based on Figure 6, it can be concluded that the moisture of the filter cake of feed at the same suction times is higher than the moisture of the underflow - filter cake and lower than overflow - filter cake, which indicates the effect of the particle size distribution on their filterability. Also, the studies showed that the finer particles has lower filtration speed, and the coarser particles has higher filtration speed. For example, at a suction time of 30 seconds, the moisture of the feed, overflow and underflow of the hydrocyclone were 27, 38.49 and 15.98 percent, respectively.
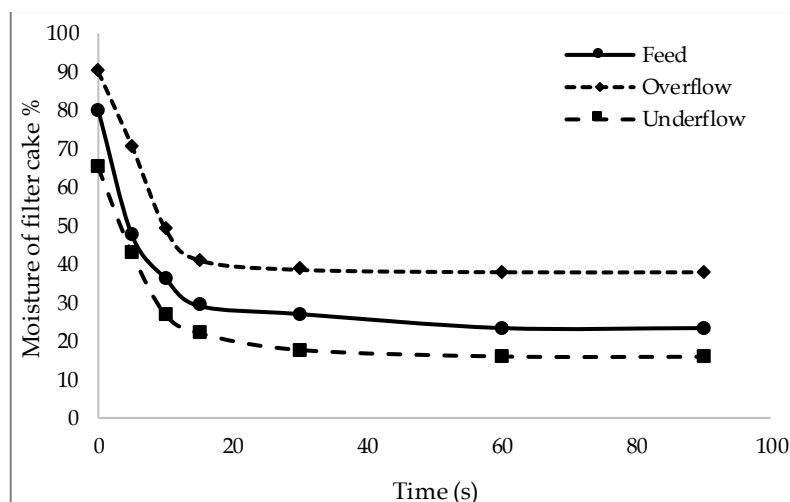

Fig. 6. Filter cake moisture content at different suction times - hydrocyclone feed and products

Mineralogical studies indicate the misreported of fine active carbon (FAC) particles as well as gold in sulfide and silicate phases into the tailings of the Zarshuran circuit. During an experiment with flotation of the Zarshuran tailings, FAC and sulfide minerals were removed and then sedimentation and filtration tests were conducted on the final tailings. Based on the results of sedimentation tests, the use of flocculant B7 has had the most favorable results in the sedimentation of flotation tailing. Therefore, during tests, the filtration of settled particles (in other words, thickener sedimentation) by flocculant B7 and without it, was investigated. In the case of flotation tailings, the moisture percentage has also decreased with increasing suction time. By comparing the moisture percentages of different tests, it can be said that the use of flocculant for settling flotation tailings has a negative effect on the filtration process; such that the moisture content of the filter cake when using flocculant is 52.09 percent and when not using flocculant is 48.85 percent. The formation of flocs using flocculant B7 has been an obstacle to the filtration process.

4. Conclusions

In this study, with the aim of improving the efficiency of the tailings dewatering circuit of the Zarshuran gold processing plant, the use of optimization solutions for the current circuit (using chemicals) and the design of a new circuit (using thickener, hydrocyclone, etc.) were investigated. In the case use of surfactants, in terms of the types of chemicals used, the rate of dewatering and filtration had a direct relationship with the filtration time. A filtration time of 45 seconds was the optimal time because after that, there was not much change in the reduction of filter cake moisture compared to increasing the filtration time. Based on the results, the use of all three types of anionic surfactants (SLES, nonionic polyethylene glycol (PEG), and cationic cetyl tri-methyl ammonium bromide (CTAB) increased the filtration rate and reduced the moisture content of the filter cake. Among them, the best results were obtained with anionic surfactant (SLES) at a concentration of 100 g/t. In this case, the moisture content of the filtered cake was less than 26%. By designing the filtration circuit, taking into account processing equipment, including hydrocyclone and thickener, the lowest moisture content in the thickener (without flocculant)-filtration circuit was 32%. By comparing these results and considering the huge costs of changing and equipping the circuit, it is concluded that using surfactant in the plant's current circuit is the most appropriate solution for improving the dewatering circuit.

References

Bosman, R. (2016). Water footprint of widely used construction materials: steel, cement and glass (*Master's thesis, University of Twente*).

Cacciuttolo, C., Cano, D., & Custodio, M. (2023). Socio-environmental risks linked with mine tailings chemical composition: promoting responsible and safe mine tailings management considering copper and gold mining experiences from Chile and Peru. *Toxics*, *11*(5), p. 462. https://doi.org/10.3390/toxics11050462

Galvez, E.D., & Cisternas, L.A. (2017). Innovative solutions for seawater use in mining operations. *Case Study of Innovative Projects-Successful Real Cases*.

Garner, R., Naidu, T., Saavedra, C., Matamoros, P., & Lacroix, E. (2012). Water management in mining: a selection of case studies. *International Council on Mining & Metals, London*.

Leonida, C. (2024). Mining Companies Turn Attention to Tailings Filtration. *Engineering and Mining Journal*, *225*(6), pp.44-50.

Liu, D., Edraki, M., Malekizadeh, A., Schenk, P.M., & Berry, L. (2019). Introducing the hydrate gel membrane technology for filtration of mine tailings. *Minerals Engineering*, *135*, pp.1-8. https://doi.org/10.1016/j.mineng.2019.02.030

Mamghaderi, H., Gharabaghi, M., & Noaparast, M. (2018). Optimization of role of physical parameters in the filtration processing with focus on the fluid flow from pore. *Minerals Engineering*, *122*, pp. 220-226. https://doi.org/10.1016/j.mineng.2018.03.041

Morton, J. (2023). Pressure Filtration for Tailings Now the Gold Standard?. *Engineering and Mining Journal*, *224*(2), pp.36-40.

Northey, S.A., & Haque, N. (2013). Life cycle based water footprint of selected metal production – Assessing production processes of copper, gold and nickel. In *Water in Mining 2013 conference*, pp. 35-50.

Stockman, C., Soto, J., & Gonzalez, D. (2014). Peruvian Gold-Cyanide Tailings Filtration — A Detailed Cost Comparison. In *Proceedings of the 17th International Seminar on Paste and Thickened Tailings, Vancouver, BC, Canada*, pp.8-12.

Vehmaanperä, P., Safonov, D., Kinnarinen, T., & Häkkinen, A. (2018). Improvement of the filtration characteristics of calcite slurry by hydrocyclone classification. *Minerals Engineering*, *128*, pp. 133-140. https://doi.org/10.1016/j.mineng.2018.08.042

The Effect of Limestone on the Cold Compression Strength (CCS) of Produced Pellets Using Concentrate from Sangan Mines of Khorasan

Amir Doram[1]*, Majid Kermaizdeh[2], Mehrdad Shokouhi[1], Seyyed Ali Shamsi Nia[1]

[1] Sangan Steel Mining Industries Company

[2] Rojan Sanat Alborz

*Corresponding author: a.doram.12@gmail.com (Amir Doram)

Abstract:

In the pelletizing industry, the use of various additives plays a key role in improving the properties of pellets. Bentonite, lime, sodium silicate, and cement are among the common additives used in this process. Additionally, organic materials such as dextrin, sulfite, and bitumen are also widely utilized.

In order to adjust the chemical composition and enhance the reducibility of pellets, the use of calcium and magnesium compounds (such as lime and dolomite) is recommended. Moreover, binding materials like Portland cement and hydrated lime can help improve the mechanical properties and reduce the fines in both raw and fired pellets. However, due to its favorable mechanical and metallurgical properties, bentonite remains the most widely used binder in pelletizing plants.

At the Sangan Iron Ore Pelletizing Plant, bentonite is used as the primary additive, with sodium hydroxide (NaOH) as a supplement. In this study, the use of limestone was investigated to improve pellet quality. For this purpose, raw pellets containing limestone were prepared using a laboratory mixer and disc, and then placed in specialized baskets. The baskets were then sent into the pelletizing furnace, and after firing, they were retrieved from the furnace outlet. The basket test results indicated a significant increase in the quality of pellet strength (CCS). Consequently, based on the positive results of basket tests, the use of lime as an additive was implemented over a specified period to enhance pellet strength (CCS).

Keywords: Pelletizing, Bentonite, Sangan Steel Mining Industries Company, Lime Stone, Cold compressive strength of pellets (CCS)

1. Introduction

In pellet production from iron ore concentrate, a binder is necessary for converting the concentrate into the green pellets. These formed pellets must exhibit an enough drop resistance to ensure they remain intact during handling and transfer to the indurating machine. Moreover, they are required to possess sufficient wet compressive strength (WCS) and dry compressive strength (DSC) so that they maintain their integrity on the travelling grate indurating machine's bed during the drying phase. Ultimately, the binder must contribute to achieving the final fired pellet with the desired overall quality, particularly in terms of strength (Keshavarz Alamdari et al., 2017).

Since the establishment of its pelletizing operations, Sangan Khorasan Steel Company has traditionally used bentonite -the industry's most conventional additive- and supplementary caustic soda to achieve the necessary pellet quality. However, with the subsequent launch of the concentrate plant and the increased use of iron ore concentrate from the Sangan mines, a notable reduction in the cold compressive strength (CCS) of the pellets was observed. Although process modifications were introduced and provided some improvement, the results remained unsatisfactory. Consequently, alternative additives were evaluated. Based on a review of relevant literature and the operational experiences of other companies, limestone was selected for further investigation (QIU et al.2003). To

assess its reliability, a laboratory-scale basket test was conducted wherein green pellets were produced -using a mixer and a laboratory disc- with the limestone additive, then loaded into a basket, sent in to the indurating machine, and recovered at the indurating machine's discharge. Upon observing the satisfactory results from the basket test, this additive was planned and implemented for a trial on the production line (Mehraban et al., 2024).

2. Material and methods

For the laboratory basket test, a predetermined quantity of limestone was procured and subsequently blended with iron ore concentrate from the Sangan mines, water, and caustic soda in a mixer. The resulting mixture was agglomerated into green pellets using a laboratory disc, and after size classification, the pellets were loaded into a Stainless-Steel basket (15 cm in diameter and 25 cm in height). This basket was placed on the pallet car bed alongside other pellets from the production line ensure complete firing during the pelletizing process (Chitsazan and Fathi Mostafa., 2020). After firing, the basket was retrieved from the indurating machine's discharge end and the pellets were forwarded to the laboratory for quality analysis.

2.1. Basket Test Results

The basket tests generated data on several key parameters, including the amounts of bentonite, caustic soda, and limestone used, as well as measurements of CCS, porosity, FeO content, sulfur (S) content, drop number, WCS, and DSC. For example, one set of test results is summarized in the following table:

Table 1. Basket Test Results

Code	Bentonite %	Soda %	Limestone %	CCS	Porosity	FeO	Sulfur	Drop	WCS	DCS
1	1.4	0.02	0	270	13.6	2.12	0.0023	3.8	1953	4747
2	1.4	0.03	0	220	21.035			5.1		
3	1.4	0.03	0	195	19.125			2.5		
4	1.4	0.03	0	264	17.46			2		
5	1.4	0.02	0.7	301	17.605	0.46	0.0072	7.2	1965	5532
6	1.2	0.02	0.7	286	18.81	0.29	0.0132	3.7		
7	1.2	0	0.7	268	16.78	2.13	0.0169	5.3	1600	4271
8	1.2	0.03	1	410	16.775	0.83	0.003	3.2		
9	1.2	0.03	1	338	18.24	0.21	0.0123	3.4		
10	1.2	0.03	0.3	236	22.495	0.42	0.0058	4.8		
11	1.2	0.02	0.8	392	18.8	0.64	0.0057	4		
12	1	0.03	0.7	276	15.07			3		
13	1	0.03	0.7	237	19.23			2.5		

The results clearly indicate that the incorporation of limestone increased pellet strength while maintaining other quality parameters within acceptable limits. Encouraged by these findings, limestone was advanced to a production line trial. For this trial, 400 tons of limestone were procured

from the corresponding mines, processed in a crushing operation, and allocated to two of the four bentonite storage bins feeding the production line.

2.2. Limestone Trial on the Production Line

Figure 1 illustrates the proportion of limestone relative to the overall quantity of additives used. The limestone trial was conducted over a period from the Ordibehesht 20th to the 25rd in 15 working shifts, with comparative data captured both before and after the trial period.
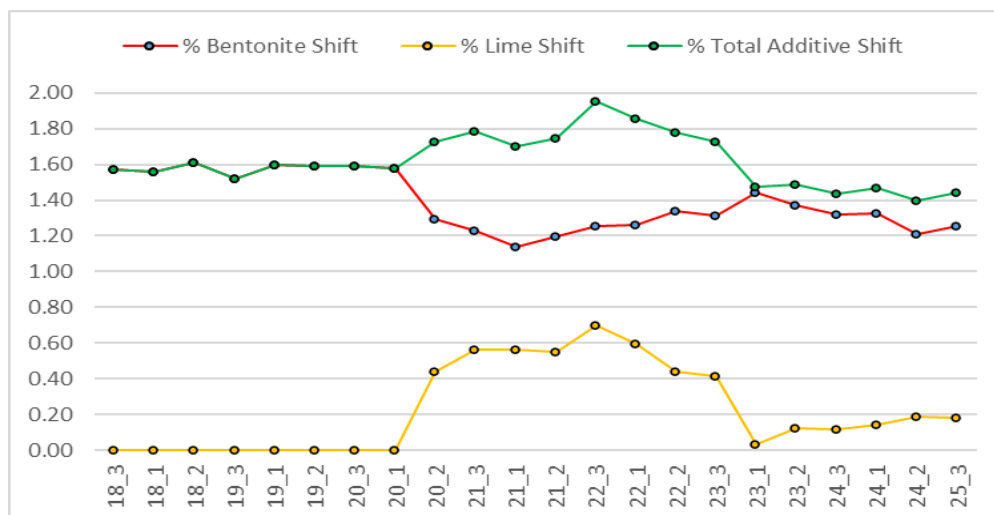

Figure 1: Limestone Usage Versus Total Additives

The impact of limestone on CCS is presented in Figure 2.
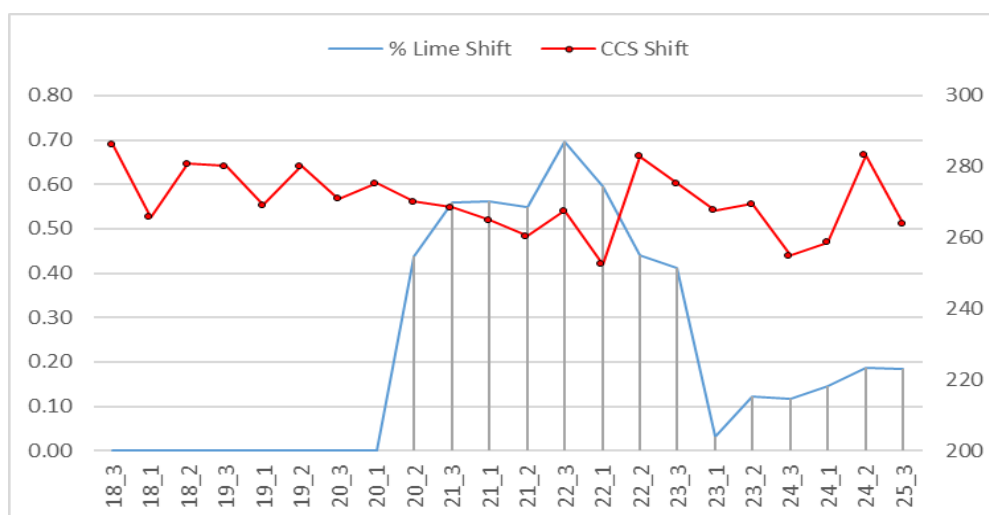
Figure 2: Effect of Limestone on Pellet Strength (CCS)

Figure 2 demonstrates that unlike the basket tests findings, increasing the proportion of limestone in the production line correlated with a marked reduction in the CCS of the fired pellets, alongside heightened fluctuations in strength. Furthermore, high levels of limestone resulted in increased cracking within the fired pellets, resulted in a reduction in CCS. This phenomenon is likely

attributable to the release of carbon dioxide during the firing of the limestone present in the pellets. A reduction in limestone usage was observed to yield an improvement in pellet strength.

During this trial phase, the indurating machine feed rate was established at 700 tons per hour. However, minor variations in the feed rate were noted, reflecting changes in the raw pellet production and the resultant quality of the fired pellets.

During this trial phase, the indurating machine feed rate was established at 700 tons per hour. However, minor variations in the feed rate were noted, reflecting changes in the raw pellet production and the resultant quality of the fired pellets (Figure 3).
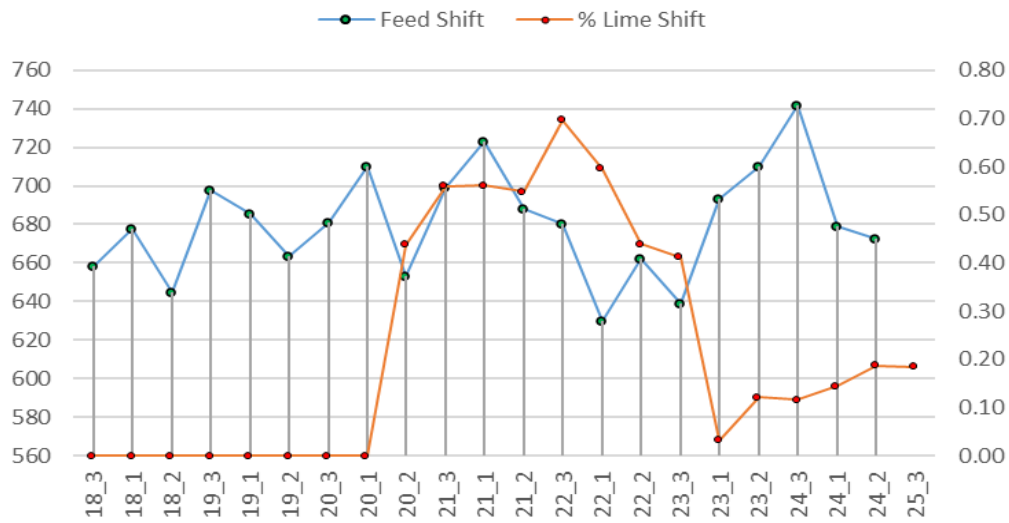

Figure 3: Limestone Usage (%) Versus Indurating Machine Feed Rate (Ton per Hour)

In addition to evaluating pellet strength (CCS), other quality parameters were examined in relation to limestone addition, as depicted in Figures 4, 5, and 6. Notably, while higher limestone content was associated with a decrease in the dry compressive strength (DCS) of green pellets, reducing the limestone usage improved the DCS.
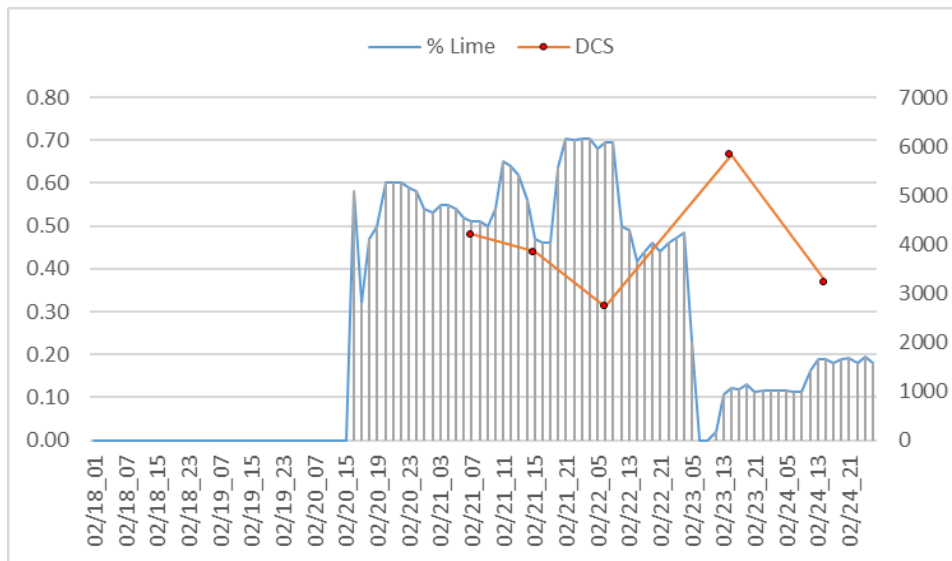

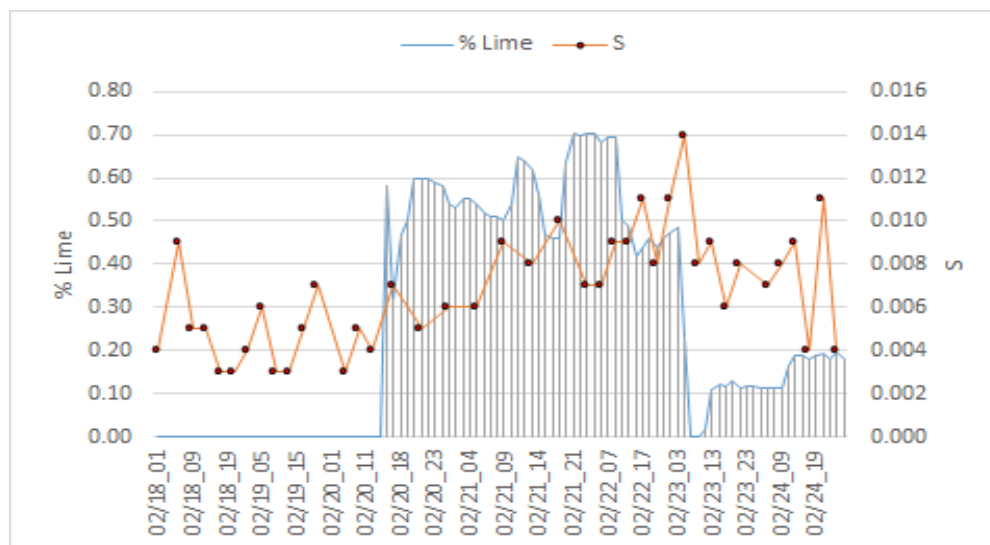Figure 4: Effect of limestone usage (%) and DCS of green pellets (gram per pellet)

Figure 5: Relationship between limestone usage (%) and retained sulfur (S) in fired pellets
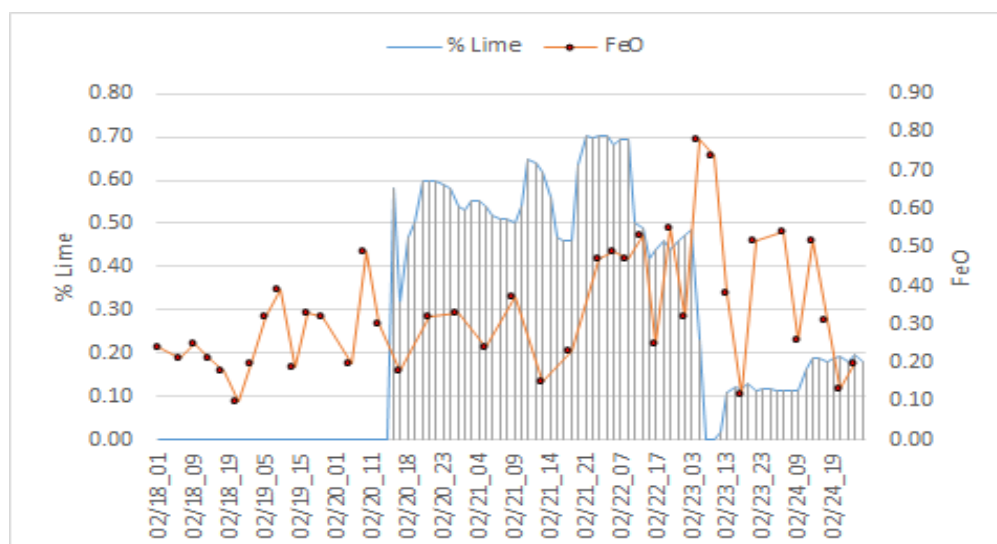

Figure 6: Relationship between limestone usage (%) and retained FeO in fired pellets.

The analyses presented in Figures 5 and 6 suggest that limestone had notable influence on the retained levels of sulfur and FeO in the final product.

3. Conclusions

The data obtained from the production line trial indicate that, in contrast to the promising results observed during laboratory basket tests, limestone adversely affected the CCS of fired pellets, leading to diminished strength, while exerting negligible impact on other critical quality parameters such as retained sulfur and FeO. Based on these findings, the use of limestone in the pelletizing process at Sangan was discontinued, and further research is currently underway to identify a more suitable additive.

References

Chitsazan, B., Fathi, M. (2020). The effect of additives on the physical, chemical, and redox properties of pellets produced from Sanabad iron ore concentrate. 1st International Conference & 4th National Conference on Materials, Metallurgy & Mining, Iran.

Keshavarz Alamdari, E., Razavi, S., Amani, H. (2017). Investigating the effect of additives and the method of preparing iron ore concentrate on the pellet quality in Gol Gohar pelletizing plant. The 6th International Conference Exhibitiion on Metallurgy and Materials Engineering, Iran

Mehraban, M., Mohseni, M., Fallah, M., Ahmadi, S. (2024). Investigating the effect of using new organic binders to reduce bentonite consumption in iron ore pelletizing. 3rd International Conference & 7th National Conference on materials, Metallurgy, Mining, Iran.

QIU, G., JIANG, T., HUANG, Z., ZHU, D., Xiaohui. (2003). Characterization of Preparing Cold Bonded Pellets for Direct Reduction Using an Organic Binder. ISIJ International, Vol. 43, pp. 20–25. doi: 10.2355/isijinternational.43.20

Interaction of Applying Ultrasonic Irradiation in Gilsonite Flotation

Javad Abdi[1], Mohammad Karamoozian[1]

[1] Faculty of mining, petroleum and geophysics engineering, Shahrood University of Technology, Shahrood, Iran

*Corresponding author: djawad.abdi2700@gmail.com (Javad Abdi)

Abstract:

Flotation is a type of mineral separation process that occurs in a water-mineral slurry. The surfaces of the selected minerals are rendered hydrophobic through conditioning with specific reagents. The material used in this study was gilsonite. After the preparation of the samples, two series of with and without irradiation on gilsonite flotation experiments were designed, using the central composite design method. Finally, it was concluded that the ultrasonic method achieves a higher desired recovery amount and lower ash percentage in the concentrate than the normal method in the rougher stage of flotation.

Keywords: Gilsonite, Flotation, Rougher, Ultrasonic irradiation.

1. Introduction

Gilsonite is a crucial, widely used mineraloid with applications across various industries (Lozano-Periera et al. 2023). Due to its chemical composition, naturally occurring gilsonite consists of four fractions and is characterized by a high carbon content (>84%) and a minimal sulfur content (≪0.3%). This material exhibits properties similar to hydrocarbons, including saturated compounds, asphaltenes, resins, and aromatics. Its diverse applications encompass energy production, road paving, inks and paints, oil well drilling, gilsocarbon for nuclear reactors, additives for tire rubber, use in petroleum emulsions, metal smelting, and filters for cyanide ions and toluene retention, among others (Lozano-Periera et al. 2023).

Bahrami et al. conducted experiments in two flotation stages, rougher and cleaner, utilizing different reagents: oil as collector with MIBC[1] as frother and gasoline as collector with pine oil as frother (Bahrami et al. 2019). They also performed a test without any collector and frother to assess the impact of the reagent regime on the kinetic order and flotation rate of a gilsonite sample. The results indicated that the kinetics for the test using oil and MIBC, as well as the test conducted without any collector and frother, were first-order, contrasting with the kinetics observed in the test using gasoline and pine oil (Bahrami et al. 2019). The results indicate that all experiments align closely with the respective models. The kinetic constants (k) during the rougher stage were determined to be 0.1548 (s^{-1}), 0.2300 (s^{-1}), and 0.2163 (s^{-1}) for oil – MIBC, gasoline – pine oil, and tests conducted without any collector or frother, respectively (Bahrami et al. 2019). In the cleaner stage, these values were 0.0450 (s^{-1}), 0.1589 (s^{-1}), and 0.0284 (s^{-1}), respectively (Bahrami et al. 2019). Additionally, the relationship between k, maximum combustible recovery (R_∞), and particle size was investigated. The findings revealed that R_∞ and k were achieved with coarse particle sizes of ($-250 + 106$) mm during the rougher flotation process and ($-850 + 500$) mm in the cleaner flotation process (Bahrami et al. 2019).

Bahrami et al. conducted flotation tests with various reagents, including collectors (gas oil, kerosene, and pine oil), frother (MIBC), and depressants (sodium silicate, tannic acid, sulfuric acid, and sodium cyanide) at different dosages (Bahrami et al. 2021). The findings indicated that the application of kerosene as a collector, MIBC as a frother, and a mixture of sodium silicate, tannic acid, sulfuric acid, and sodium cyanide as a depressant yielded the most favorable outcomes in the flotation of gilsonite during the rougher stage (Bahrami et al. 2021).

---

[1] Methyl IsoButyl Carbinol

Doodran and colleagues carried out flotation tests by examining four factors: the dosage of collector, frother, and depressant, as well as the solid-to-liquid ratio across three different levels (Doodran et al. 2020). The aim was to reduce the ash content and enhance the recovery of Gilsonite. These tests were structured using the Taguchi method, facilitated by Design-Expert software (Doodran et al. 2020). Our findings revealed that the lowest ash content of 5.2% was achieved under conditions that included 200 g/t of Gasoil as the collector, 100 g/t of MIBC as the frother, 300 g/t of sodium silicate as the depressant, and a pulp density corresponding to a 5% solid-to-liquid weight ratio (Doodran et al. 2020).

Bahrami and his team conducted flotation tests during both the rougher and cleaner stages to ascertain the kinetic order and flotation rate of a gilsonite sample (Bahrami et al. 2019). The experiments utilized combinations of oil–MIBC and gas oil–pine oil, with one test performed without a collector and frother (Bahrami et al. 2019). Based on the results, the relationship between the flotation rate constant, maximum combustible recovery, and particle size indicated that the highest flotation combustible recovery and flotation rate occurred within the size range of -250 + 106 μm in both the rougher and cleaner stages (Bahrami et al. 2019). It was observed that the combustible recovery and flotation rate were greater during the rougher flotation process compared to the cleaner stage (Bahrami et al. 2019).

Kazemi and colleagues conducted flotation experiments on samples of gilsonite from Kermanshah province to determine the flotation kinetics and the effect of particle size on it, as well as to examine the relationship between flotation constant, maximum recovery, and particle size (Kazemi et al. 2018). For this purpose, flotation tests were performed using a cleaner flotation process with a collector of kerosene and MIBC frother, a collector of diesel and pine oil frother, and one test was also conducted without using a collector or frother (Kazemi et al. 2018). The results indicate that the maximum recovery and flotation constant in the flotation experiments conducted with gilsonite, without the use of a collector and frother, is associated with particle sizes of -850, +500 μm. In the cleaner tests, the highest k value and recovery were found in the experiment using diesel collector and pine oil frother, with particle sizes of -850, +500 μm (Kazemi et al. 2018).

Bahrami and colleagues conducted flotation experiments to determine the kinetic order and rate of flotation of a Gilsonite sample, performing tests in both rougher and cleaner stages (Bahrami et al. 2020). The experiments utilized combinations of oil-MIBC, gasoil-pine oil, and included one test without any collector or frother (Bahrami et al. 2020). Additionally, the maximum combustible recovery and particle size were analyzed. The results indicated that the maximum flotation combustible recovery and flotation rate were achieved with an intermediate particle size in both the rougher and cleaner flotation processes (Bahrami et al. 2020). Moreover, the combustible recovery and flotation rate during the rougher flotation process were found to be greater than those in the cleaner flotation process (Bahrami et al. 2020).

A key challenge in utilizing raw gilsonite is the reduction of detrimental impurities. Several methods exist for removing these impurities, with flotation being the most important technique for very fine materials. However, despite its widespread use, flotation often fails to reduce impurities (ash) to the desired level. Therefore, this paper investigates the application of ultrasonic irradiation. In flotation technique, hydrophobic particles attach to air bubbles introduced into the pulp and are lifted to a froth layer above the slurry, thereby separating them from the hydrophilic particles (Wills and Finch 2016). To achieve better concentration and recovery, flotation operations can be conducted in one or multiple stages. When flotation is performed in a single stage, it is referred to as "rougher" flotation. In rougher operations, the primary focus is on the recovery parameter, while in the flotation of gilsonite, the undesirable parameter is the ash content. A low ash percentage combined with high recovery indicates an ideal rougher test. The one other technique used for mineral processing is called ultrasound. In this technique, ultrasonic waves are extensively utilized for the preparation and cleaning of mineral surfaces during physical, chemical, and physico-chemical processes, significantly influencing recovery rates. These waves enhance the efficiency of reagents and improve recovery by cleaning particle surfaces (Ebrahimi and Karamoozian 2020). It is proposed to use ultrasonic waves as a pre-treatment method for the flotation of coal with high ash content (Ebrahimi and Karamoozian 2020). Also, in the ultrasonic radiation technique, which is carried out using ultrasonic waves, these waves act as a secondary collector on ore particles, resulting in better attachment of the collector to them (Ebrahimi and Karamoozian 2020). The flotation of gilsonite using the ultrasonic radioactivity method is a very novel approach that has not been applied to gilsonite before. Therefore, the present research holds innovative significance in this field.

2. Material and methods

2.1. Gilsonite Samples

The sample of gilsonite prepared in this research was obtained from the Gilaneh mine located in Ilam province in western Iran. Its precise coordinates are as follows: (33.877778˚N, 46.076944˚E). The gilsonite sample used in this research consists of uncrushed and unclassified feed contained gilsonite powder. This sample was sieved into twelve different size fractions to achieve better results for subsequent tests. The aim of this work was to identify a portion of the initial feed that had the lowest percentage of ash. After conducting a test and measuring the ash content, it was determined that the section (-710, +500) μm matched similar specifications, with an ash content measured at 54.74%. Following this stage, the entire feed was crushed using a laboratory roller crusher, resulting in two different size fractions. To separate these two sizes, the ASTM[2] sieve analysis method was employed, with dimensions as follows: (+500) μm and (-500) μm. In the final stage of the experiment, the ash content of these sizes was again examined and evaluated to obtain more accurate results and to gain a better understanding of the characteristics of this sample. In **Table 1** and **Figure 1**, analysis for screening of gilsonite samples and feed size distribution chart is showed, respectively. **Table 2** shows XRF table for analyzing chemical combinations for detecting of tailing minerals there are into gilsonite smaples. As observed in this table, the concentrations of the chemical compounds CaO and SO_3 exhibit a high percentage abundance in the composition of these gilsonite samples, indicating that the mineral present in this sample is, as tailings, either the mineral anhydrite or gypsum. Also **Figure 2** shows XRD plot for determining frequenccy of each chemical element in samples. XRD analysis of the gilsonite waste revealed two chemical phases: calcium sulfate and calcium oxide. However, since the peaks corresponding to calcium sulfate showed a better match (with a scale factor of 0.723) to the main peaks of the sample than those of calcium oxide (with a scale factor of 0.045), the chemical composition of the mineral of gilsonite tailing is determined to be gypsum.

Table 1. Analysis Table for Screening Gilsonite Samples

Screen Size (μm)	Residual Weight on Screen (g)	Frequency Percentage (%)	Cumulative Percentage on Screen (%)	Cumulative Percentage Passing from Screen (%)
181864	84.68	10.32	10.32	89.68
131064	55.86	6.81	17.13	82.87
35560	25.63	3.12	20.25	79.75
3360	147.21	17.94	38.20	61.80
2380	124.14	15.13	53.33	46.67
1190	85.53	10.43	63.75	36.25
1000	28.74	3.50	67.26	32.74
710	37.57	4.58	71.84	28.16
500	26.11	3.18	75.02	24.98
350	38.02	4.63	79.65	20.35
210	47.80	5.83	85.48	14.52
<210	119.12	14.52	100.00	0.00
Total	820.41			

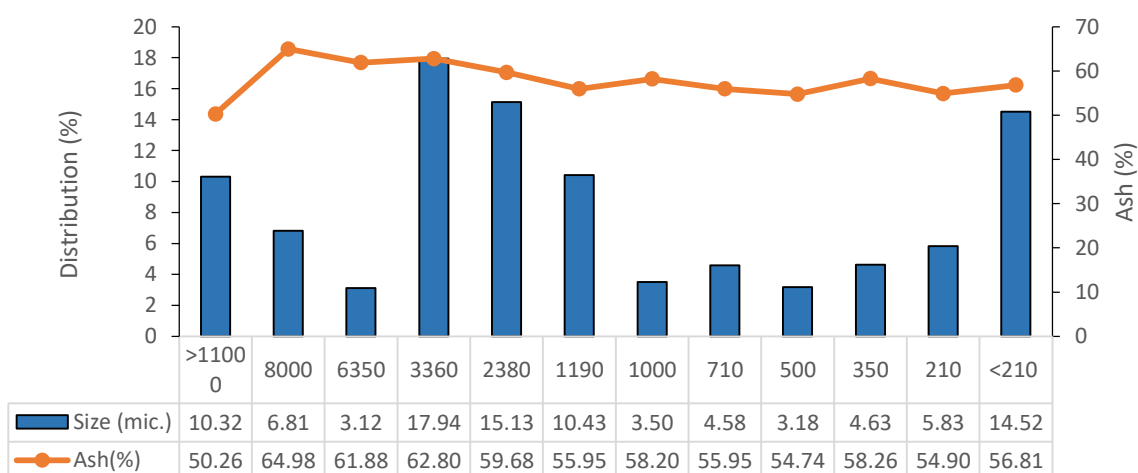[2] American Society for Testing and Materials

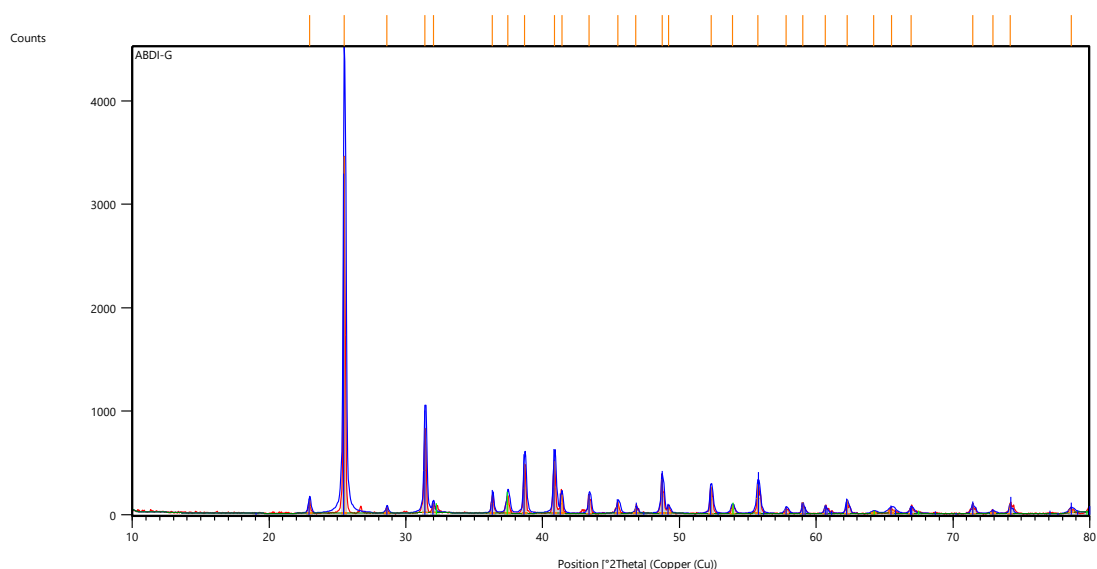**Fig 1.** Feed size distribution and ash content plot

Fig 2. XRD Plot for Gilsonite Samples

2.1.1. Reagents

The chemical reagents used in these flotation experiments are gasoil and MIBC, where gasoil is utilized as a collector and MIBC as a frother.

2.1.2. Flotation Experiments

The flotation experiments conducted in this study utilized a one-step ore flotation method known as "Rougher." To perform the experiments, Denver-type mechanical flotation machines were employed. Regular rougher

experiments were carried out using the 2-liter cell, while ultrasonic rougher experiments were conducted with the 1-liter cell. An ultrasonic bath manufactured by Elma was used for irradiation. Several parameters influence the efficiency of the flotation process, and optimizing conditions can enhance the flotation rate. Additionally, the following fixed parameters were established:

● Selected feed size: (-500) μm

● Solid content: 5 (%);

● Collector type: Gasoil;

● Frother type: MIBC;

● Temperature: room temperature (25°C);

● pH: neutral (7);

● Rotor speed: 1000 RPM;

● Ultrasonic device power: 100 W;

● Preparation time: 8 minutes;

● Initial feed mass: 100 g (In regular rougher) and 52.63 g (In ultrasonic Rougher).

Previous research has shown that reducing the solids content increases recovery; therefore, the minimum possible solids content (5%) was considered in this study (Murhula et al. 2022). Given the number and levels of parameters considered for the flotation experiments, a central composite design technique and response surface methodology were selected, resulting in 20 experiments. Experiments design is showed in **Table 3**; where (R1) is the percentage of gilsonite recovery in regular rougher method and (R2) is the percentage of gilsonite recovery in ultrasonic method.

Table 3. Experimental Design for Gilsonite Rougher

Std	Run	Factor 1 A: Collector	Factor 2 B: Frother	Response 1 R1	Response 2 R2
		g/t	g/t	%	%
1	9	50	50	87.38	93.12
2	3	200	50	85.47	94.54
3	7	50	200	90.34	86.83
4	2	200	200	86.41	83.15
5	5	19	125	84.29	85.59
6	8	231	125	82.86	86.74
7	6	125	19	93.97	96.47
8	1	125	231	80.14	86.69
9	4	125	125	81.80	87.94
10	10	125	125	82.67	87.41

2.1.3. Equations

Equation (1) was used to calculate gilsonite recovery. (Wills and Finch 2016).

$$R = \left(1 - \frac{c \times (f-t)}{f \times (c-t)}\right) \times 100 \quad (1)$$

In this case, the grade of the concentrate (c) is the same as the ash percentage of the concentrate, the grade of the tailings (t) is the same as the ash percentage of the tailings and the grade of the feed (f) is as ash percentage of initial feed.

2.1.4. Process Machine

In these experiments, the process indicator is the DENVER mechanical flotation cell, which consists of three components: an air valve, a stirring blade, and a speed adjustment dial for the flotation stirring. **Figure 3**, shows shows the configuration of the setup system.

Fig 3. The setup system for flotation

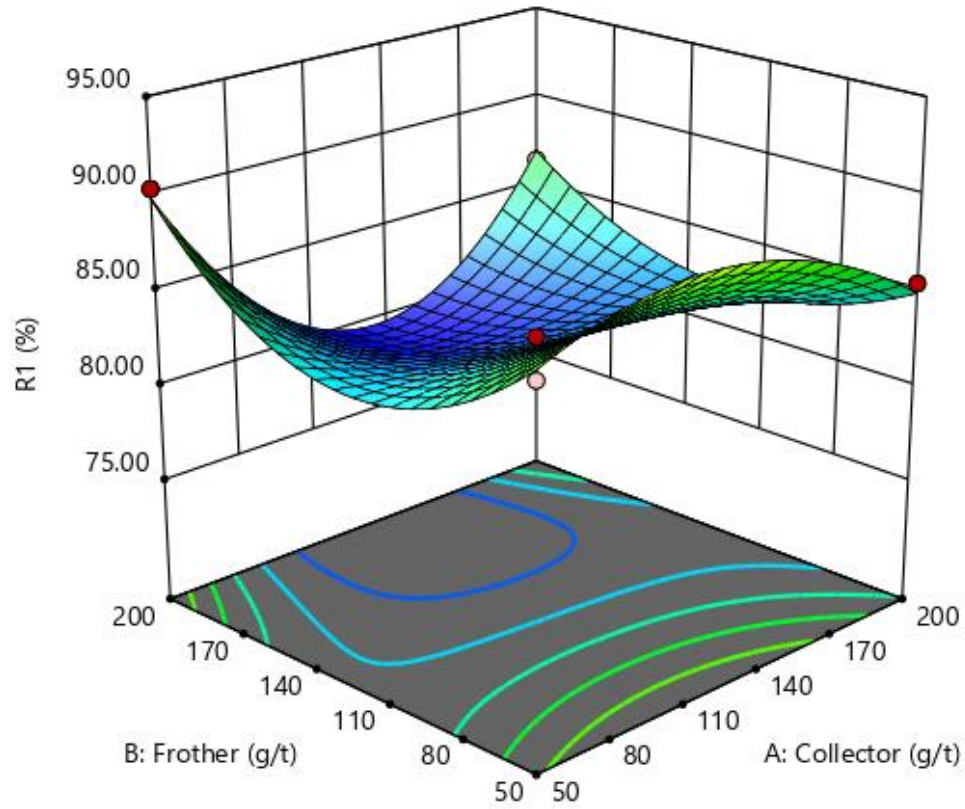## 2.1.5. Results and Discussion

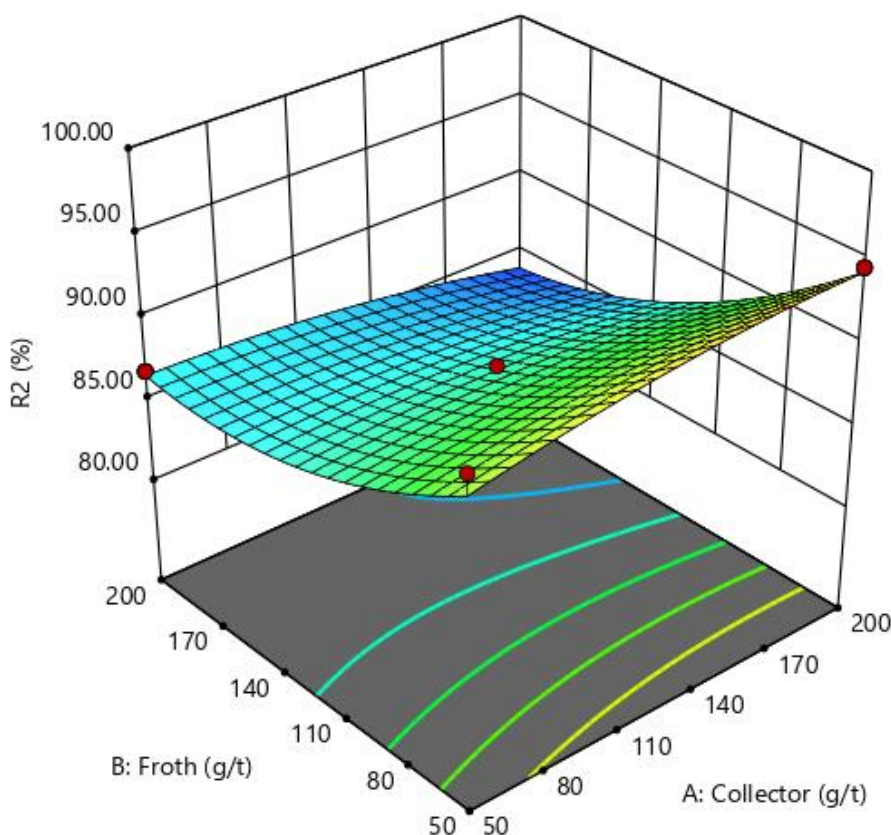**Fig 4**. 3D Surface Plot of Regular Rougher Flotation Tests

Fig 5. 3D Surface Plot of Ultrasonic Rougher Flotation Tests

Figure 4 and **Figure 5** show the graph of changes in the recovery of a regular gilsonite rougher and ultrasonic rougher with respect to the effect and interaction of the variables of collector concentration and foaming agent concentration, respectively. The range of changes in the concentrations of collector and frother agent parameters was between 50 g/ton and 200 g/ton. In Figure 5, by increasing the value of parameter (A) to the optimal point and also decreasing parameter (B) to a certain optimal point, a better recovery rate can be obtained. In Figure 6, by relatively decreasing the values of parameter (A) and increasing the values of parameter (B) to the maximum point, the optimal point can be reached. **Table 4** and **Table 5** perform ANOVA tables for (R1) and (R2) responses. In table 4, the Model F-value of 32.01 indicates that the model is statistically significant, with only a 3.06% probability that an F-value of this magnitude could arise from random noise. P-values below 0.0500 suggest that the corresponding model terms are significant; in this scenario, B, B², and A²B qualify as significant terms. Values exceeding 0.1 indicate that the associated model terms lack significance. If there are multiple insignificant model terms—excluding those necessary to maintain hierarchical structure—considering model reduction may enhance the overall model performance. The Lack of Fit F-value of 2.72 suggests that the lack of fit is not significant when assessed against pure error, with a 34.69% likelihood of obtaining such a large Lack of Fit F-value due to noise. A non-significant lack of fit is favorable; our objective is to ensure that the model fits well. In table 5, The Model F-value of 29.52 indicates that the model is statistically significant, with only a 0.30% likelihood that such a large F-value could arise from random variation. P-values below 0.0500 signify that the model terms are significant; in this instance, the terms B and B² are deemed significant. Conversely, values exceeding 0.1000 suggest that the model terms are not significant. Should there be multiple insignificant model terms—excluding those necessary to maintain hierarchy—reducing the model could enhance its performance. The Lack of Fit F-value of 10.22 suggests that the Lack of Fit is not significant when compared to pure error, with a 22.50% chance that such a Lack of Fit F-value could occur due to random noise. **Table 6** and **Table 7** show suggested models for "R1" and "R2" responses. To find the appropriate model for the desired response, a model is deemed acceptable if it has higher values of R² and adjusted R².

470

Table 4. ANOVA for Reduced Quartic Model of "R1" Response

Source	Sum of Squares	df	Mean Square	F-value	p-value	
Model	157.13	7	22.45	32.01	0.0306	significant
A-collector	1.03	1	1.03	1.47	0.3488	
B-Froth	95.74	1	95.74	136.52	0.0072	
A^2	1.8	1	1.8	2.57	0.2502	
B^2	23.25	1	23.25	33.16	0.0289	
A^2B	68.85	1	68.85	98.18	0.01	
AB^2	1.82	1	1.82	2.6	0.2484	
A^2B^2	8.69	1	8.69	12.38	0.0721	
Residual	1.4	2	0.7013			
Lack of Fit	1.03	1	1.03	2.72	0.3469	not significant
Pure Error	0.3769	1	0.3769			
Cor Total	158.54	9				

Table 5. ANOVA for Reduced Quartic Model of "R2" Response

Source	Sum of Squares	df	Mean Square	F-value	p-value	
Model	163.5	5	32.7	29.52	0.003	significant
A-Collector	0.0491	1	0.0491	0.0443	0.8436	
B-Froth	124.18	1	124.18	112.11	0.0005	
AB	6.52	1	6.52	5.89	0.0723	
A^2	1.75	1	1.75	1.58	0.2773	
B^2	19.92	1	19.92	17.98	0.0133	
Residual	4.43	4	1.11			
Lack of Fit	4.29	3	1.43	10.22	0.225	not significant
Pure Error	0.1399	1	0.1399			
Cor Total	167.93	9				

Table 6. Suggested Model Summary Statisyics for "R1" Response

Source	Std. Dev.	R^2	Adjusted R^2	Predicted R^2	PRESS	
Linear	**4.14**	**0.2426**	**0.0262**	**-0.6345**	**259.14**	**Suggested**
2FI	4.45	0.249	-0.1264	-1.8261	448.05	
Quadratic	4.46	0.4971	-0.1316	-2.5689	565.81	
Cubic	2.13	0.9428	0.7428	-2.5157	557.37	Aliased

Table 7. Suggested Model Summary Statisyics for "R2" Response

Source	Std. Dev.	R^2	Adjusted R^2	Predicted R^2	PRESS	
Linear	2.5	0.7398	0.6655	0.4037	100.13	
2FI	2.49	0.7786	0.668	0.4235	96.81	
Quadratic	**1.05**	**0.9736**	**0.9406**	**0.815**	**31.07**	**Suggested**
Cubic	0.5972	0.9958	0.9809	0.7781	37.26	Aliased

Figure 6 illustrates the Perturbation diagrams of values R1 and R2 corresponding to the optimal values of parameters A and B.
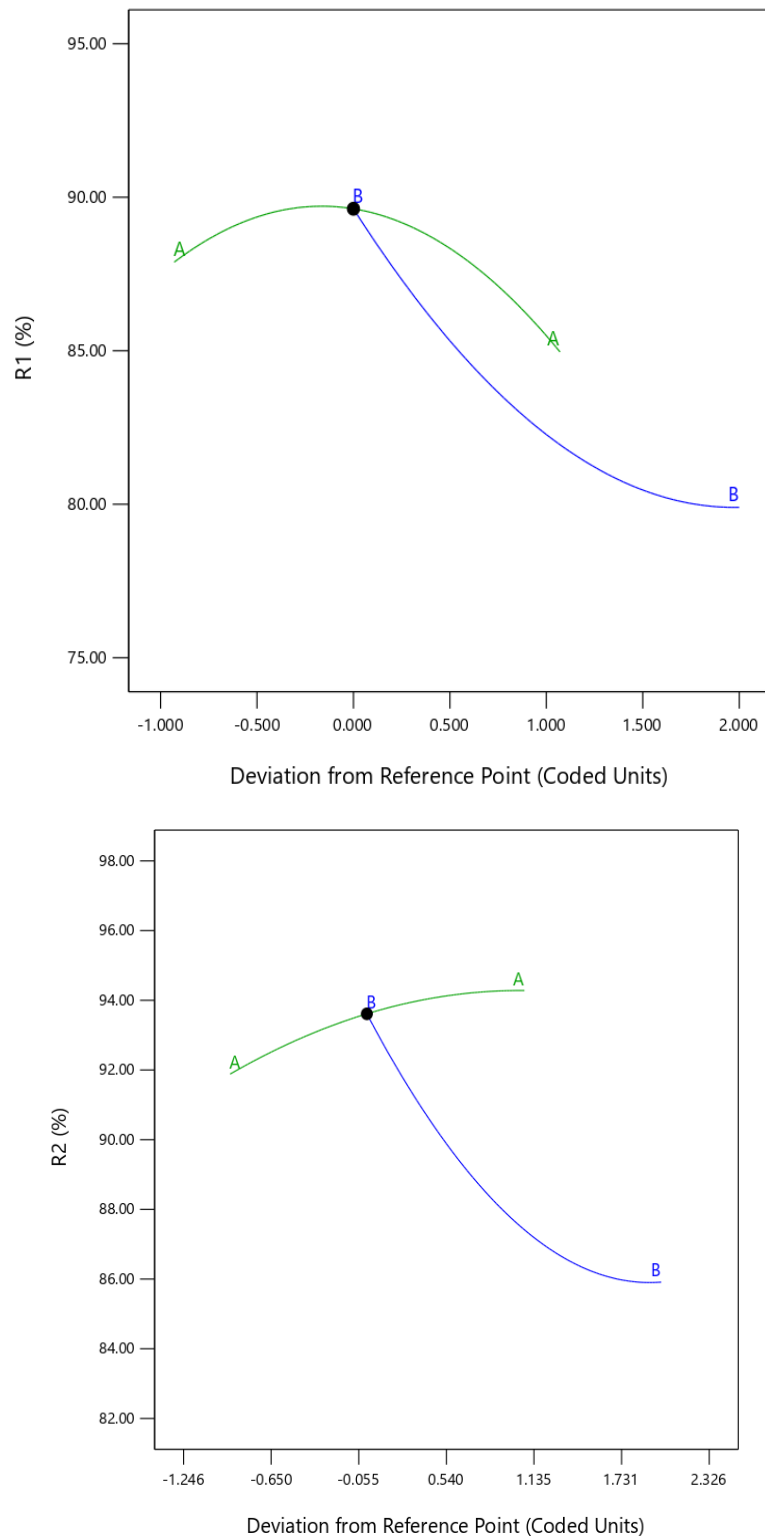
Fig 6. Perturbation Plot for R1 and R2

Figure 7 shows a comparison of the recovery percentage and ash percentage from tests conducted on both normal and ultrasonic rougher sections. According to this chart, test number 7 is the best, exhibiting both optimal recovery (highest recovery) and desirable ash percentage (lowest ash percentage) in both sections.
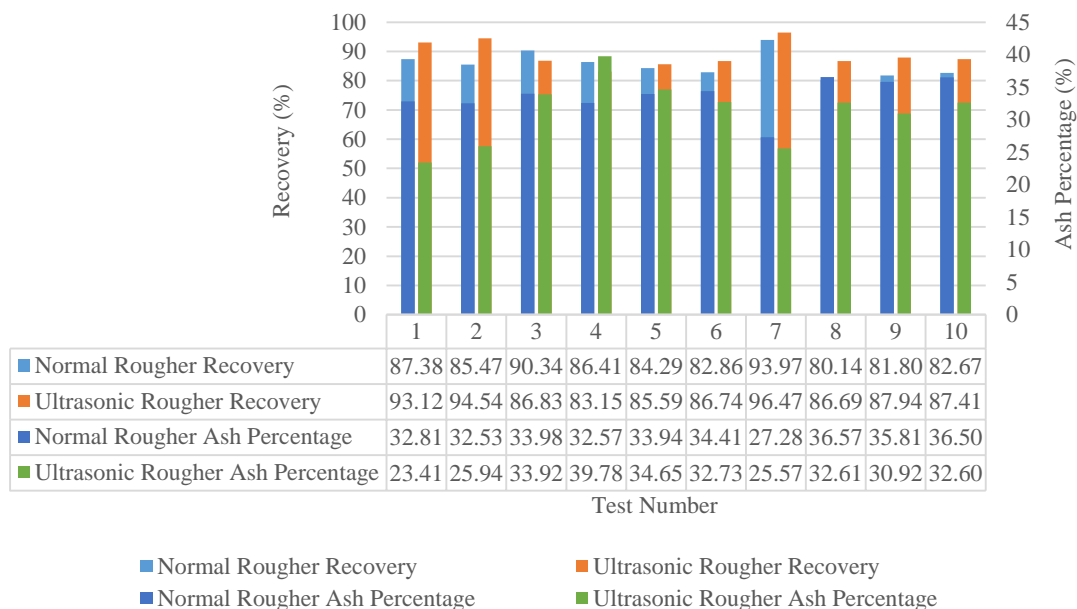

Test Number	1	2	3	4	5	6	7	8	9	10
Normal Rougher Recovery	87.38	85.47	90.34	86.41	84.29	82.86	93.97	80.14	81.80	82.67
Ultrasonic Rougher Recovery	93.12	94.54	86.83	83.15	85.59	86.74	96.47	86.69	87.94	87.41
Normal Rougher Ash Percentage	32.81	32.53	33.98	32.57	33.94	34.41	27.28	36.57	35.81	36.50
Ultrasonic Rougher Ash Percentage	23.41	25.94	33.92	39.78	34.65	32.73	25.57	32.61	30.92	32.60

Fig 7. Recovery-Ash Comparative Plot for Normal and Ultrasonicc Rougher

3.   Conclusions

The examination and analysis of the findings and results are as follows:

1) In the normal rougher, the best recovery percentage and ideal concentrate ash percentage were obtained, 93.97% and 27.28% and in ultrasonic, 96.47% and 25.57%, respectively.
2) In the ultrasonic rougher, the effect of ultrasonic waves caused a much lower ash percentage to be obtained in cases where we did not even have the desired recovery.
3) By using ultrasonic waves, the desired concentrate ash recovery and percentage can be achieved at different dosages of collector and frother.

References

Wills, B. A., and J. A. Finch. 2016. Wills' mineral processing technology. 8th ed. Elsevier Science & Technology Books

Bahrami, A., Kazemi, F., & Ghorbani, Y. (2019). Effect of different reagent regime on the kinetic model and recovery in gilsonite flotation. *Journal of materials research and technology*, *8*(5), 4498-4509.

Bahrami, A., Kazemi, F., Mirmohammadi, M., Ghorbani, Y., & Farajzadeh, S. (2021). Configuration of flowsheet and reagent dosage for gilsonite flotation towards the ultra-low-ash concentrate. *Scientific reports*, *11*(1), 15469.

Doodran, R. J., Khakmardan, S., Shirazi, A., & Shirazy, A. (2020). Minimalization of Ash from Iranian gilsonite by froth flotation. *Journal of Minerals and Materials Characterization and Engineering*, *9*(1), 1-13.

Bahrami, A., Kazemi, F., Ghorbani, Y., & Abdolahi Sharif, J. (2019). The order of kinetic models, rate constant distribution, and maximum combustible recovery in gilsonite flotation. *Mining, Metallurgy & Exploration*, *36*, 1101-1114.

Kazemi, F., Bahrami, A., & Abdollahi Sharif, J. (2018). Study of Flotation Kinetic of Kermanshah State Gilsonite. *Nashrieh Shimi va Mohandesi Shimi Iran*, *37*(1), 197-206.

Bahrami, A., Kazemi, F., & Sharif, J. A. (2020). Investigating the First-Order Flotation Kinetics Models for Iranian Gilsonite. *Iranian Journal of Materials Science & Engineering*, *17*(1).

Lozano-Pereira, H., & Afanasjeva, N. (2023). Gilsonite: An organic mineral with special physical-chemical properties, current uses and future prospects applications. *MATERIALS ENGINEERING*, *25*(1-2023).

Ebrahimi, H., & Karamoozian, M. (2020). Effect of ultrasonic irradiation on particle size, reagents consumption, and feed ash content in coal flotation. *International Journal of Coal Science & Technology*, *7*(4), 787-795.

Murhula, E., Hashan, M., & Otsuki, A. (2022). Effect of solid concentration and particle size on the flotation Kinetics and entrainment of quartz and hematite. Metals, 13(1), 53.

Extraction of cerium from iron ore mine tailings by leaching and solvent extraction method

Mohammad Karimi ¹*, Mohammad Karamoozian²

1.Mohammad Karimi, Master student of mineral processing, Shahrood University of Technology

2.Mohammad Karamoozian, Associate professor in mineral processing, Shahrood University of Technology

*Corresponding author: mohammadkarimi90eng@gmail.com.

Abstract:

This research investigates the process of cerium extraction from tailings that have been separated from iron using a magnetic drum separator, through both acid leaching and solvent extraction methods. Initially, the mineralogical characteristics of the samples were analyzed using microscopic studies. The main minerals identified were feldspar, garnet, calcite, gypsum, amphibole, and secondary minerals such as chlorite, quartz, and apatite. The metallic minerals were included pyrite, chalcopyrite, magnetite, and hematite. The sample was taken from the tailing's damps, then it was crushed to a particle size of less than 800 microns. The sample was then placed in a stirred tank along with water, fed into a spiral separator, and subsequently into a shaking table. The analysis results showed that the cerium grade increased from 320 ppm in the feed to 1364 ppm. In the leaching experiments, the influence of various parameters including temperature, acid concentration, type of acid, leaching time, and particle size on cerium leaching recovery rate was evaluated. The results indicated that temperature and acid concentration had the greatest impact on the leaching rate of cerium. In this stage, 95% of cerium was dissolved. Optimization tests for leaching conditions showed that the best conditions for cerium leaching were using hydrochloric acid at a 1:3 concentration with water, at a temperature of 90°C and a leaching time of 4 hours. In the subsequent phase, an optimization experiment was conducted with the same parameters. Under these conditions, 96.5% of cerium was dissolved. Then, the solvent extraction process was examined using organic solvents, di(2-ethylhexyl) phosphoric acid and tributyl phosphate. The results showed that the highest cerium extraction rate (81%) was achieved when di(2-ethylhexyl) phosphoric acid was used, considering parameters such as pH 3, organic-to-aqueous phase ratio of 1:1, 20-minute extraction time, 25°C temperature, and stirring speed of 300 rpm. Finally, the results of this research contribute to the optimization of the cerium extraction process and provide suggestions for improving the efficiency of this process.

Keywords: Iron tailings, cerium extraction, acid leaching, solvent extraction.

1. Introduction

Rare Earth Elements (REEs) are a group of 17 chemical elements in the periodic table, consisting of 15 lanthanides (from lanthanum to lutetium) along with scandium and yttrium. Due to their similar chemical and physical properties, these elements are commonly found together in various minerals and ores. Based on their geochemical behavior, rare earth elements are categorized into two groups: light rare earth elements (LREEs) and heavy rare earth elements (HREEs). The LREE group includes lanthanum (La), cerium (Ce), praseodymium (Pr), neodymium (Nd), and samarium (Sm). The HREE

group includes europium (Eu), gadolinium (Gd), terbium (Tb), dysprosium (Dy), holmium (Ho), erbium (Er), thulium (Tm), ytterbium (Yb), lutetium (Lu), and yttrium (Y) [1].

Cerium, one of the rare earth elements and a member of the lanthanide series, is represented by the symbol "Ce" and atomic number 58 in the periodic table [2]. It is classified as a soft, lustrous metal and is highly stable in combination with oxygen in the form of cerium oxide (CeO_2). Cerium is considered one of the most important metals in the rare earth industry and is widely used in various sectors, including alloy production, catalysts, pigments, solar panels, light-emitting diodes (LEDs), and glass polishing [3]. It is also used in the manufacture of permanent magnets and phosphorescent powders. Due to its unique chemical and physical properties, cerium plays a vital role in many industrial and technological processes, particularly in the automotive and electronics industries [4].

Cerium is primarily extracted from rare earth-containing minerals such as bastnäsite, monazite, and loparite. Major reserves of this element are found in China, the United States, and Australia [5]. Given the growing demand for cerium and its compounds, particularly in advanced technology industries, its separation and purification have become a major challenge in materials science and chemistry. Various techniques such as solvent extraction, ion exchange, adsorption, and precipitation are employed to extract and purify cerium from other rare earth elements and impurities [6].

During mining activities and the operation of crushing and magnetic beneficiation plants, waste dumps with different mineralogical compositions are formed, which certainly exhibit different behaviors during beneficiation processes. Therefore, the first step is to identify the samples and determine their mineralogical characteristics and processing behavior.

The aim of this study is the separation of cerium from the loaded leach solution using solvent extraction. In this regard, two extractants di-(2-ethylhexyl) phosphoric acid (D2EHPA) and tributyl phosphate (TBP) in kerosene as a diluent were used, and the effects of various parameters were investigated. Also, in order to increase the cerium grade prior to the leaching process, a pre-concentration stage is carried out using gravity separation techniques, including spiral separators and shaking tables.

Gravity Separation of Cerium

Gravity separation is one of the traditional and cost-effective methods for separating heavy minerals—including cerium-bearing minerals such as monazite and bastnäsite—from ore or lighter impurities. This method is based on the density differences between particles and the influence of gravitational force. Gravity separation is often employed as the initial step in the beneficiation of rare earth minerals.

Stages of Gravity Separation

Gravity separation techniques assist in isolating heavy minerals like monazite and bastnäsite (with densities ranging from 4.5 to 5 g/cm³) from lighter impurities such as silica and quartz (with densities around 2.7 g/cm³). This process utilizes water, air, or another medium that enhances the effect of gravity. The ore is first crushed into finer particles to ensure full liberation of the minerals. Heavier particles settle to the bottom, while lighter ones are separated and removed [7].

Common Equipment Used in Gravity Separation:

✓ Spiral Separator:
This equipment is suitable for fine particles, such as rare earth minerals, and operates based on spiral water flow and gravitational force. The main component of the spiral separator is a helical or spiral-shaped trough, typically made from wear-resistant materials.

The spiral has a gentle slope that guides the particles downward. Mineral feed enters the spiral separator, usually with the assistance of water or a dilute solution to facilitate particle movement.

Heavier particles (which generally contain the target minerals) are discharged from the lower part of the equipment, while lighter particles are collected at the upper sections.

To aid in particle movement and create a continuous flow along the spiral path, water or a dilute solution is constantly introduced into the system.

✔ Shaking Table:

A shaking table typically consists of an inclined surface with an adjustable slope. This inclination assists in particle movement and guides them in the desired direction. The table is equipped with a vibration mechanism, usually powered by a motor or an electrical system, which transmits oscillating motion to the table surface.

As the particles move across the table, they are discharged into specific channels that separate heavier and lighter materials. Several collection basins or buckets are located beneath the table to gather the separated materials.

The shaking table is an effective device for mineral recovery using gravity-based methods. It is particularly suitable for the separation of rare earth elements such as cerium, as well as precious metals, from ores with varying densities.

However, to achieve optimal results, operational parameters—such as table inclination and vibration intensity—must be precisely controlled.

Hydrometallurgical Processing:

✔ Acidic Leaching

Acids such as sulfuric acid, nitric acid, and hydrochloric acid are used to dissolve cerium and other rare earth elements into solution.

✔ Solvent Extraction:

Solvent extraction is a chemical process that involves two main steps: extraction and stripping. During the extraction step, the metal ions present in the aqueous phase react with an organic reagent to form metal-organic complexes. As a result, the metal components transfer from the aqueous phase into the organic phase. In the organic phase, metals do not form covalent bonds with carbon atoms, but instead coordinate with atoms such as oxygen, nitrogen, sulfur, or hydrogen through dative (coordinate) bonds.

The reverse of the extraction process is called stripping, where metals are removed from the organic phase back into an aqueous phase.

Solvent extraction is typically a continuous process and is mainly applied to clear and relatively concentrated solutions. It has a moderate operating cost and is widely used for the recovery of many metals. This method is especially useful in cases of high contamination levels or when a high-purity product is required [8].

Cerium-bearing ores are first dissolved in aqueous solutions. Then, organic solvents such as di(2-ethylhexyl) phosphoric acid (DEHPA) are employed to extract cerium from the aqueous phase. During this process, the organic solvent selectively binds with rare earth elements like cerium, separating them from the aqueous solution.

Subsequently, cerium is stripped from the organic phase and converted into usable compounds such as cerium oxide (CeO_2) [9]

2-Material and methods

A total of 500 kg of samples were collected from various parts of the tailings dump for experimental studies. Since the particle size was 10 mm, the sample was ground in a ball mill to below 800 microns in a controlled manner. After homogenization, riffle splitting, and dividing the sample to obtain a representative portion, it was sent to the laboratory for ICP-MS, XRD, and thin polished section analysis. The results showed that the cerium grade in the tailings was 320 ppm.

Subsequently, 10 kg of sample was prepared for gravity separation tests using spiral and shaking table methods. Gravity separation is a technique that utilizes the difference in mineral densities to separate and extract cerium and other rare earth elements from mineral matrices. This method is particularly effective for ores containing both heavy and light mineral phases.

After conducting the spiral and shaking table tests to increase the cerium grade, it was observed that iron grade also increased along with cerium. To reduce the iron content, a dry magnetic separator was employed, and the magnetic fraction (magnetite-rich) was separated from the tailings.

2-1 XRD Analysis

X-ray diffraction (XRD) analysis was performed on the representative tailings sample from the iron ore processing plant. The analyses conducted using the XRD method on the submitted sample are presented in Table 1, and the corresponding XRD graphs can be seen in Figure 1.

Table 1 The results of the X-ray diffraction (XRD) analysis

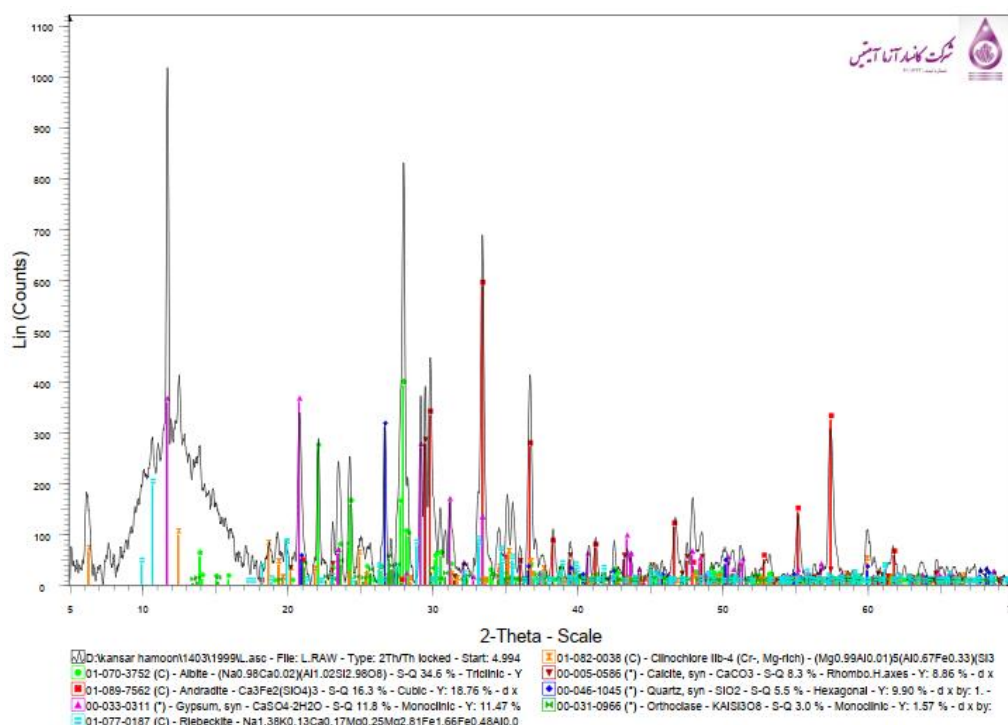|	
-Albite	(Na0.98Ca0.02)(Al1.02Si2.98O8)
-Andradite	Ca3Fe2(SiO4)3
-Gypsum	CaSO4·2H2O
-Riebeckite	Na1.38K0.13Ca0.17Mg0.25Mg2.81Fe1.66Fe0.48Al0.04Si7.94O22(OH)2
-Clinochlore	(Mg0.99Al0.01)5(Al0.67Fe0.33)(Si3.02Al0.98)O10(OH)8
-Calcite	CaCO3
-Quartz	SiO2
Amorphous phase	-

Figure 1 XRD graph

.

2-2 Thin Polished Section Analysis

Macroscopic description: The sample was in powder form, which was molded and then prepared as a thin polished section.

- Main minerals: feldspar, garnet, calcite, gypsum, amphibole
- Accessory minerals: chlorite, quartz, opaque minerals
- Metallic minerals: pyrite, chalcopyrite, magnetite, hematite

Microscopic description:

As shown in Figure 2,3,4, The examined sample predominantly consists of feldspar, garnet, calcite, and amphibole, with lesser amounts of chlorite, gypsum, quartz, and opaque phases. These minerals appear as fine-grained and highly fractured. Feldspar is observed as fragmented crystals, probably albite, sometimes showing polysynthetic twinning. Garnet occurs as fine grains and occasionally subhedral fragmented crystals, approximately 600 microns in size.

Fragments of gypsum and calcite are seen as independent particles and occasionally in association. Carbonate-rich zones are also present. Amphibole appears as fibrous, green-colored crystals up to 200 microns, often associated with garnet and albite.

opaque minerals appear as discrete grains up to 1 mm and are also embedded in rock fragments. Under reflected light, they were identified as pyrite, chalcopyrite, magnetite, and hematite.

- **Pyrite** appears as isolated grains with a spongy texture, up to 1 mm, and also as amorphous infillings in magnetite.
- **Chalcopyrite**, with lower abundance, fills spaces between garnet crystals.
- **Magnetite** appears subhedral, often undergoing replacement by hematite.

A cluster of fine particles with high relief and strong birefringence, likely monazite, was observed at the edge of a carbonate fragment, although it was lost during section preparation. Accurate identification of this phase requires complementary analyses such as SEM or EPMA.
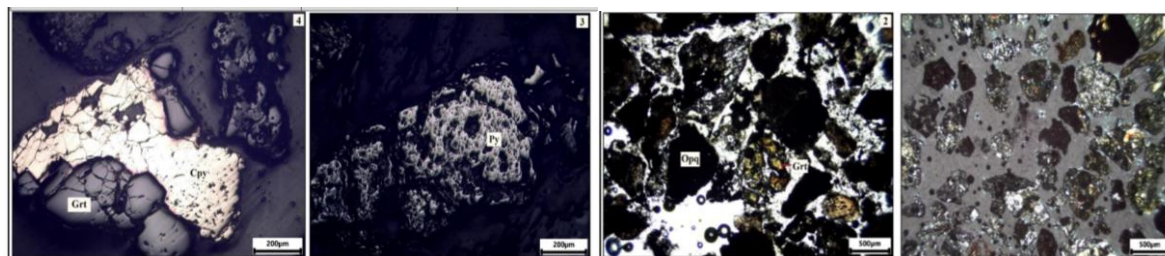
Figure 2   *Figure 3*
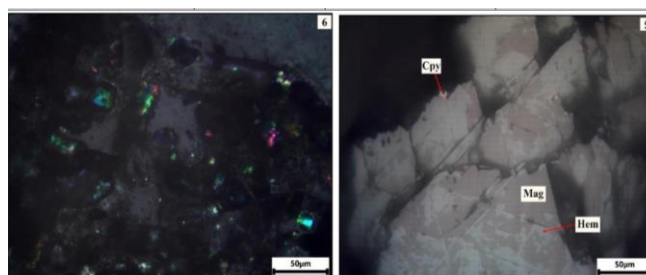
Figure 4

2-3 Leaching Test Procedure

Following the spiral and shaking table gravity separation tests, the concentrate sample was ground using a ball mill in a controlled manner to two particle sizes: -50 microns and -100 microns, in preparation for leaching experiments.

The leaching experiments were conducted on the representative samples using 100 mL beakers placed on hot plates equipped with magnetic stirrers capable of controlling stirring speed. In the first stage, a total of 16 leaching tests were designed and performed.

The procedure for each leaching test was as follows:

Initially, acid solutions of sulfuric acid, nitric acid, and hydrochloric acid were prepared based on predefined concentrations. Then, **5** grams of the representative mineral sample were mixed with a specific volume of the prepared acid solution according to a set solid percentage. This mixture was transferred into the beaker.

After adjusting the stirring speed, the solution was stirred for a predetermined period of time. Upon completion of the leaching process, the resulting pulp was filtered, and the liquid phase (leachate**)** was sent to the laboratory for ICP-MS analysis to determine the cerium content**.**

This experiment was conducted at temperatures of 25, 45, 60, and 90°C, using three types of acids: hydrochloric acid, nitric acid, and sulfuric acid. It was carried out at different durations (1, 2, 3, and 4 hours), with various water-to-acid ratios (1:1, 1:2, 1:3, 1:4, 1:5), and using two particle sizes (-50 and -100 microns), across a total of 16 experiments.

The influence of important parameters on the leaching process

Temperature:

In leaching processes, temperature is one of the most critical parameters that significantly affects metal recovery efficiency. For cerium, increasing the temperature leads to an enhancement in the rate of chemical reactions, resulting in higher recovery. As temperature rises, reaction rates increase. Chemical reactions generally proceed faster at higher temperatures due to increased molecular kinetic energy, which raises the probability of collisions between molecules and ions.

Furthermore, solubility increases at elevated temperatures. Many minerals and compounds—particularly metallic compounds like cerium—dissolve better in solvents under such conditions. As a result, more metals are transferred into the solution, improving overall recovery [10].

As shown in Figure 5, the leaching rate of cerium increases with temperature.
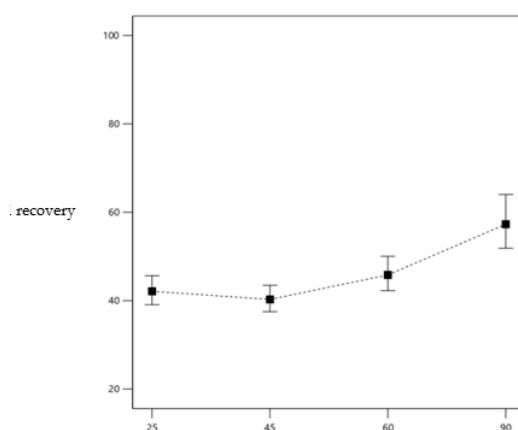

Figure 5 The effect of temperature changes

Acid Type:

The type of acid used in the cerium leaching process is one of the key factors in determining the extraction efficiency of this element. Different acids, due to their distinct chemical properties, have varying effects on cerium extraction. In this study, sulfuric acid, nitric acid, and hydrochloric acid were used. Based on the recovery rates, hydrochloric acid showed the highest efficiency in cerium leaching.

Figure 6 illustrates the effect of acid type on the leaching process.

Figure 6 Effect of acid type
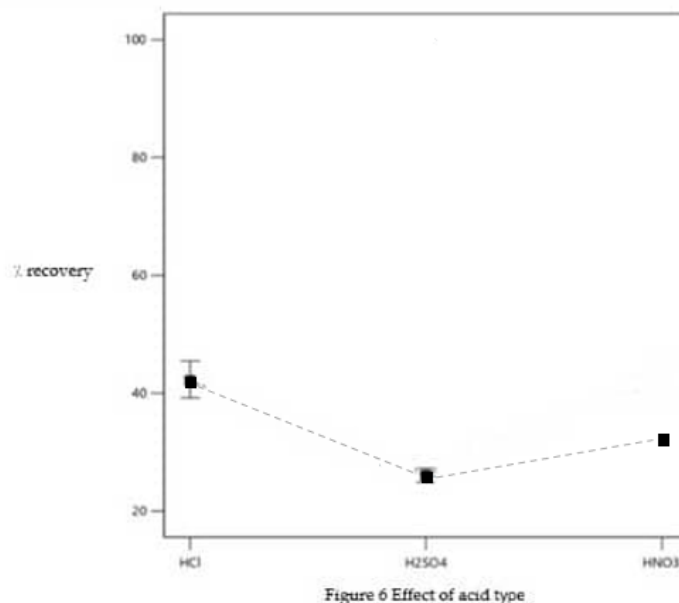
Particle Size:

The particle size in the cerium leaching process is an important factor that can significantly influence extraction efficiency and reaction kinetics. The size of the mineral particles directly affects the contact surface between the material and the leaching solution, which can either enhance or reduce the performance of the leaching process. As particle size decreases, the surface area available for reaction increases, resulting in shorter extraction times for cerium.

This is particularly important in slow chemical reactions. Finer particles lead to a reduction in leaching time and an increase in extraction rate. These smaller particles, having a larger surface area, can react more rapidly and extensively with acid or other leaching agents, thereby increasing the dissolution rate and overall recovery of cerium.

In this study, two particle sizes were used: under 50 microns and under 100 microns. As shown in Figure 7, the leaching recovery rate was higher for the -50-micron particle size.

Figure 7 Effect of Particle Size
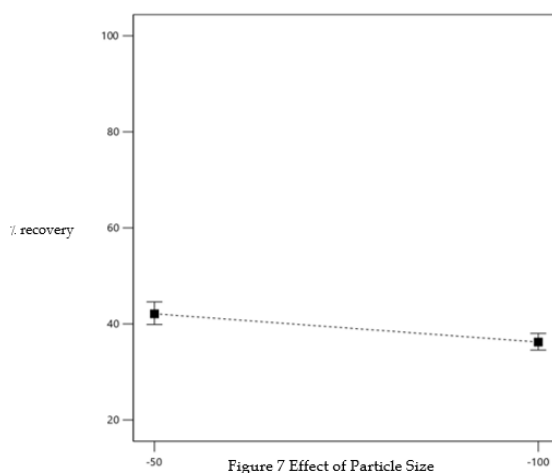
Time:

Leaching time has a direct impact on the rate of chemical reactions. These reactions typically occur more rapidly during the initial stages of the process and then slow down over time as the dissolution of cerium progresses. This phenomenon is due to changes in the contact surface area and the concentration of the solution.

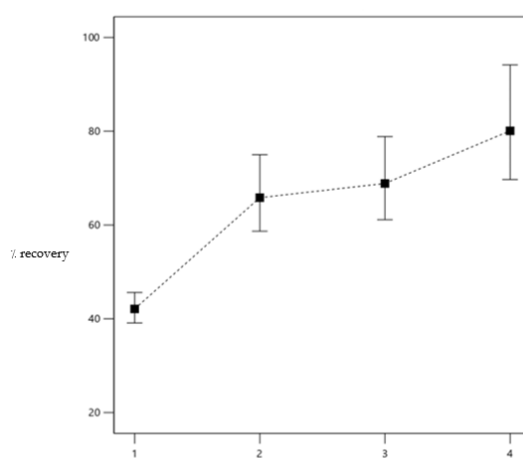As shown in Figure 8, cerium recovery increases with increasing leaching time.

Figure 8 Effect of Time (hour)

Acid concentration:

The acid concentration plays a key role in optimizing cerium extraction processes. It significantly influences the rate of chemical reactions, solvent selectivity, process efficiency, and the overall recovery of cerium. This section discusses in detail the effect of acid concentration on the leaching rate of cerium.

In cerium leaching processes, acid acts as the leaching agent, dissolving cerium compounds from the mineral matrix. As acid concentration increases, the rate of chemical reactions typically rises. This is because a higher acid concentration enhances the acid's ability to dissolve mineral compounds, particularly cerium-bearing phases.

An increase in acid concentration leads to a higher dissolution rate of cerium due to a greater number of acid molecules available in the solution, which in turn increases the frequency of chemical interactions.

As shown in Figure 9, the highest cerium recovery was achieved at a 1:3 solid-to-acid ratio.
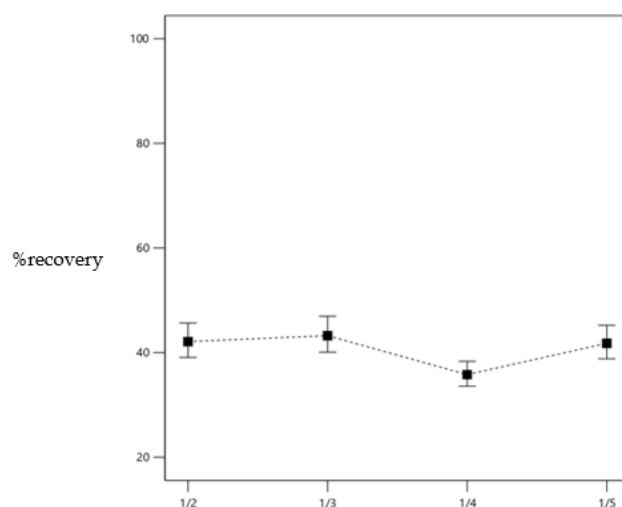

Figure 9 Acid concentration

Based on the results of the optimization experiments, the optimal conditions for cerium leaching are generally as follows:

- **Type of acid:** Hydrochloric acid
- **Acid concentration:** 1:3 (acid to water ratio)
- **Operating temperature:** 90°C
- **Leaching time:** 4 hours
- **Particle size:** 50 microns

Based on the analysis of the results and the optimization of factors affecting the acidic leaching of cerium, an experiment was conducted under the following conditions: hydrochloric acid, a water-to-acid ratio of 1:3, leaching time of 4 hours, particle size of 50 microns, and a temperature of 90°C. The cerium recovery in this experiment reached 96.5%.

2-4 Solvent extraction:

As shown in Table 2,In this solvent extraction experiment, all parameters—including temperature, time, stirring speed, pH, and the organic-to-aqueous phase ratio—were kept constant, while only the ratio of D2EHPA (di-(2-ethylhexyl) phosphoric acid) to TBP (tributyl phosphate) was varied. The main objective of this study is typically to investigate the effect of changes in the ratio of these two extractants on recovery, compound transfer, and the thermodynamic aspects of the extraction process.

Table 2 solvent extraction results

number	(RPM) Stirrer speed	Temperature Centigrade	o/a	Dehpha/TBP Ratio	Time (min)	Extraction (%)
1				D2EHPA		81.46
2				TBP		80.28
3	300	25	1:1	TBP 1:1D2EHPA	20	69.25
4				TBP 1:3 D2EHPA		35.50
5				TBP 3:1 D2EHPA		25.33

According to the results of the solvent extraction, as observed, the highest extraction percentage is 81%, which corresponds to the case where D2EHPA is used alone as the extractant in the reaction.

Conclusions:

The results obtained from the pre-processing using the spiral and shaking table:

The results obtained from the spiral and shaking table tests, as presented in the table, show that the cerium grade increased from 320 ppm to 1364 ppm. Additionally, the weight recovery reached 6%, and the metallurgical recovery was 25%, indicating that the performance of the spiral and shaking table was relatively good.

The results obtained from the leaching and solvent extraction processes.

1. The effects of key operational parameters—including leaching agent concentration, leaching temperature, leaching time, acid concentration, type of acid, and particle size—were investigated. The findings indicated that among the studied factors, leaching temperature, acid concentration, acid type, and leaching time had the most significant impact on cerium recovery through acidic leaching.
2. The maximum cerium recovery rate in the leaching experiments was 95%, achieved under the operating conditions of 400 RPM stirring speed, a water-to-acid ratio of 1:3, leaching temperature of 90°C, a liquid-to-solid ratio of 10, and a leaching duration of 4 hours.
3. The optimized leaching experiment resulted in the dissolution of 96.5% of cerium, with all optimal conditions being considered in this test.
4. The highest cerium extraction rate (81%) using the organic solvent D2EHPA was obtained under the conditions of 300 rpm stirring speed, pH = 3, temperature of 25°C, an organic-to-aqueous phase ratio of 1, and an extraction time of 20 minutes.
5. The synergistic effect of organic solvents on cerium extraction was studied using two binary mixtures of organic extractants: tributyl phosphate (TBP) and D2EHPA. In both cases, the results showed that the cerium extraction rate using D2EHPA alone was higher than that achieved using the synergistic solvent extraction system. Therefore, based on these findings, cerium extraction using D2EHPA alone was preferred over the synergistic extraction method.

References

[1] Mohammadzadeh, M., & Kouhsari, A. H. (2017). A study of rare earth element resources with the aim of evaluating the feasibility of their extraction in Iran. Paper presented at the 2nd National Conference on Geology and Resource Exploration, Shiraz, Iran: Hamayeshnegar Scientific Conference

[2] Berzelius, J. J., & Hisinger, W. (2008). "On the Discovery of Cerium." Annals of Philosophy, 9, 358-360.

[3] Klaproth, M. H. 1995, "Über das Cerium." Annalen der Chemie und Pharmacie, 19, 325-330.

[4] Liu, X (2020). "Cerium-Based Materials for Energy Applications: Synthesis, Properties, and Future Perspectives." Energy Materials, 8(3), 56-72

[5] Wang, L., et al. (2020). "Global Cerium Resources and Production." Resources Policy, 68, 101743.

[6] Gupta, C. K., & Krishnamurthy, N. (2018). "Extractive Metallurgy of Rare Earths." CRC Press.56,60

[7] Wills, B.A., & Finch, J.A. (2015). Wills' 'ineral Processing Technology. Elsevier.Gupta, C.K., & Krishnamurthy, N. (2005). Extractive Metallurgy of Rare Earths. CRC Press.

[8] Gupta, C.K., & Krishnamurthy, N. (2005). Extractive Metallurgy of Rare Earths. CRC Press.Xie, F., Zhang, T.A., Dreisinger, D., & Doyle, F. (2014). "Solvent Extraction of Rare Earths.Minerals Engineering.

[9] Zhang, Y., & Zhang, L. (2011). "Solvent extraction of cerium using organophosphorus extractants"." Solvent Extraction and Ion Exchange, 29(2), 167-179. Wong, P. K., & Zhang, X. (2016). "Separation of cerium from other rare earths using organic solvents"." Hydrometallurgy, 167, 72-80.

[10] S. Radhika, B.N. Kumar, M.L. Kantam, B.R. Reddy,2010, Liquid–liquid extraction and separationpossibilities of heavy and light rare-earths from phosphoric acid solutions with acidic organophosphorus reagents, Separation and Purification Technology 295-302

Ammonia Leaching for Potassium Removal from Alunite and investigation of Ammonia Recovery

Seyed Mahdi Latifi[1]*, Alireza Salehirad[1], Fatemeh Torkian[1], Abbas Jafari[2], Hamidreza Ebrahimi Basavi, Mohammadreza Karimi

[1]Iranian Research Organization for Science and Technology (IROST)

[2]Iran Mineral Materials Procurement and Production Company (IMPASCO)

**Corresponding author: latifi@irost.ir (Seyed Mahdi Latifi)

Abstract:

Alunite is considered a promising alternative to bauxite for producing metal-grade alumina. However, due to the detrimental presence of potassium in alumina, its removal during refining is essential. In this study, potassium was eliminated from alunite through ammonia leaching, with key parameters—such as solid-to-liquid ratio and ammonia concentration—investigated. Results demonstrated that ~95% of K_2O was removed at a solid-to-liquid ratio of 1:3 and an ammonia concentration of 60 g/L. Additionally, a recycling loop leaching process was evaluated and it was found by applying a dilution ratio of 2 and fully make up ammonia, potassium removal efficiency is comparable to that of single-stage leaching.

Keywords: Aunite, Alumina, Alkaline Leaching

1. Introduction

As the demand for aluminum continues to rise across various industries, the need for efficient and sustainable sources of alumina has become increasingly critical. Alunite serves as a promising alternative to traditional bauxite ores, which are the primary source of alumina [1]. Alunite, a sulfate mineral composed primarily of potassium aluminum sulfate [2], has gained significant attention in the field of alumina production due to its unique chemical composition and properties. Alunite deposits are found in various geological settings around the world, making it a widely available resource. This abundance can help meet the growing global demand for alumina, which is essential for aluminum production [3].

Composed mainly of potassium aluminum sulfate, alunite contains a significant amount of potassium, which poses challenges for its direct use in alumina extraction processes. The presence of potassium not only complicates the refining process but also affects the quality of the alumina produced. Therefore, the effective removal of potassium from alunite is crucial to enhance its usability in aluminum production. There are several methods to remove potassium content from alunite ore namely, acid leaching [4], alkaline leaching [5], mechanical activation [2], water leaching [6], etc. Among the mentioned methods alkaline leaching is notable due to its advantages, such as high efficiency, selective extraction [7], energy efficiency [5] and environmental impact [7].

One of the alkaline methods for extracting potassium from alunite involves leaching with ammonia, which offers several benefits over other routes. In this work the influencing factors on alunite leaching recovery has been investigated and suitable operating ranges for them were defined.

2. Material and Methods

2.1. Material

Alunite ore was supplied from Haft Sandoogh district, North Takestan,Qazvin Province, Iran. Ammonia solution (25 wt%) was obtained from Neutron Company (Iran).

2.2. Leaching Condition

Before leaching, alunite ore was classified into particles around 0.3 mm in size and then calcined at 600 °C for 1 h. Leaching experiments were conducted in a hot plate stirrer system at 90 °C for 1 h. After the leaching process, the product was filtered, and the solid residue was washed with distilled water, dried at 70 °C overnight, and then analyzed with multi-acid digestion and the ICP-OES method.

3. Results and Discussion

Table 1 presents the specification for the alunite ore as received.

Table 1. Alunite Composition obtained from Haft Sandoogh district

SiO_2	Al_2O_3	K_2O	Fe_2O_3	Na_2O	SO_3	TiO_2	LOI
45.78	21.08	5.35	0.76	0.64	21.80	0.49	24.86

As can be seen in Table 1, the magnitude of the K_2O is more than 5 wt% that is not appropriate for the alumina being used in the aluminum production industry. In order to reduce the content level of potassium in alunite, leaching experiments were carried out at ratios of solid/liquid= 1:1, 1:2 and 1:3. Also the initial concentration of ammonia in the leaching solutions was set at amounts of 15, 30 and 60 g/l. Figure 1 shows the results of alunit leaching with ammonia at different of solid-to-liquid ratios and ammonia concentrations.
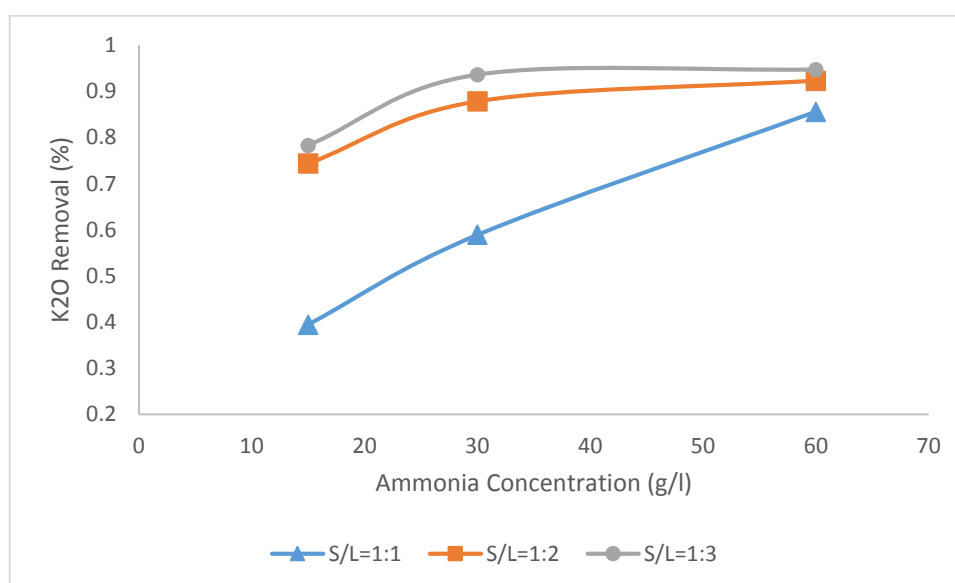

Figure 1. K_2O Removal at various S/l ratios and ammonia concentrations

As observed in Figure 1, during the leaching process, increasing the liquid-to-solid ratio from 1 to 2 noticeably increases the removal of K_2O. However, increasing this ratio from 2 to 3 does not result in a significant change in K_2O removal. Increasing the initial ammonia concentration in the leaching solution further improves K_2O removal, although this increase was slight for solid-to-liquid ratios of 1:2 and 1:3, especially when the concentration increased from 30 to 60 g/l.
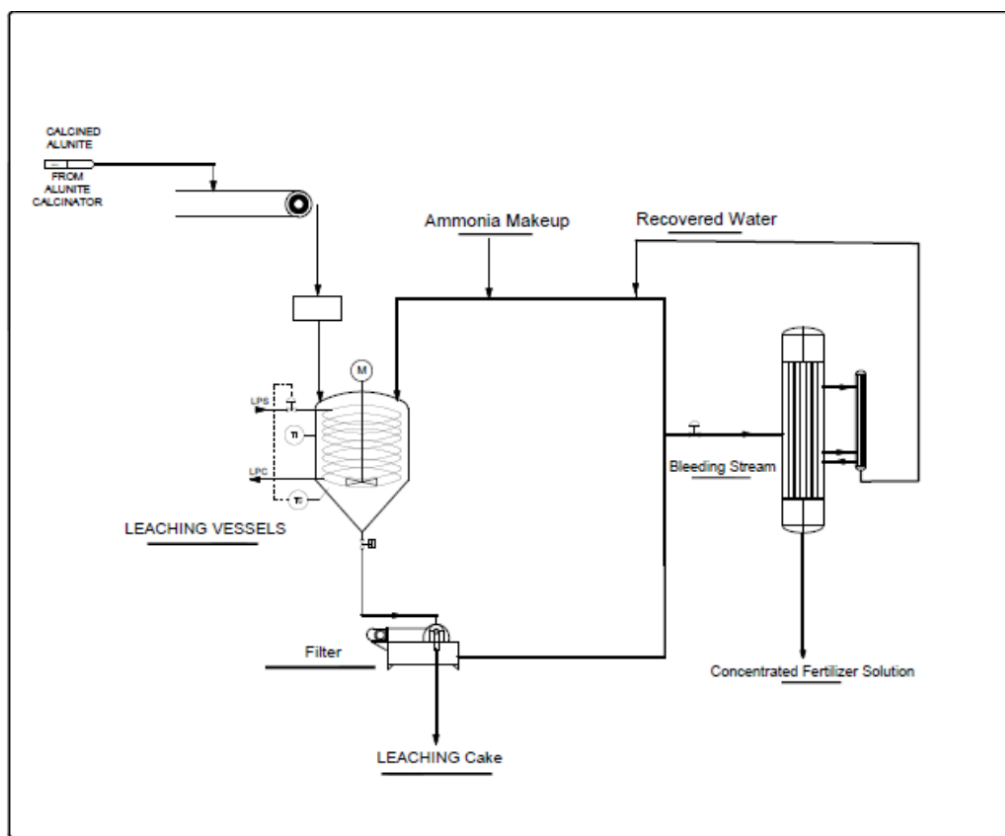
Figure 2. Designed recycling loop for ammonia solution

To investigate the recovery of the used ammonia solution several experiments were conducted to represent a recycling loop shown in Figure 2. As shown in Figure 2, during the recycling loop, the ammonia solution is diluted, and make up ammonia is also added. To achieve appropriate values for the dilution rate and the amount of ammonia make up, various values were applied for these variables, and their performance in removing K_2O removal was evaluated (Figure 3). As shown in Figure 3, for a dilution ratio of 2, adding 100% of the initial ammonia as make up can bring the K_2O removal level to that of a one-stage leaching (without a recycling loop). According to Figure 3 by adding this amount of make up ammonia, the removal performance will be even higher than that of one-stage leaching when the dilution ratio is 5.
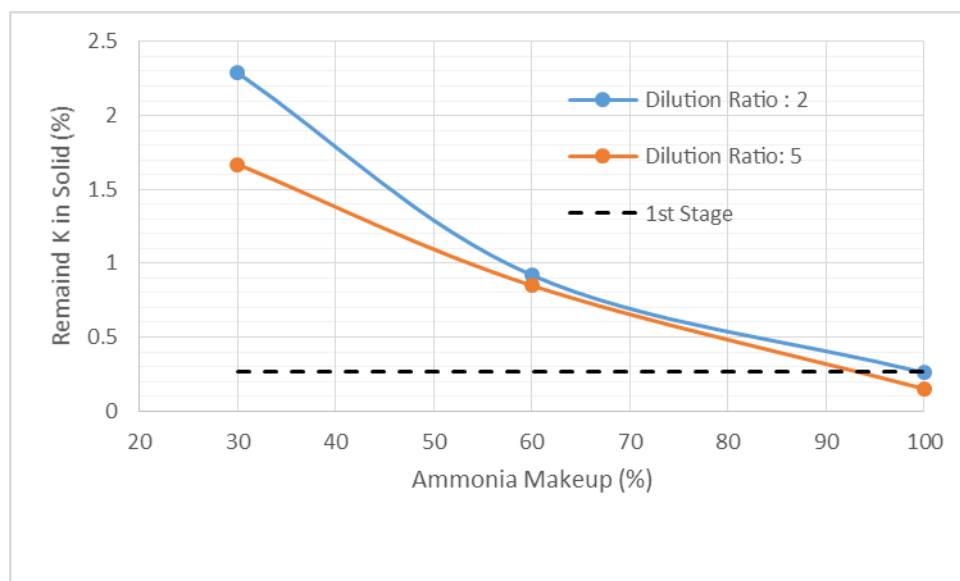
Figure 3. Effect of dilution ratio and ammonia make up on potassium removal in recycling loop

Conclusion

The alkaline leaching of alunite with an ammonia solution was investigated, demonstrating its effectiveness in potassium removal. A study of the influencing variables revealed that increasing the liquid-to-solid ratio reduces the impact of ammonia concentration on potassium extraction. Additionally, ammonia recovery tests indicated that nearly all the initial ammonia was consumed during the process. This suggests to maintain potassium removal in a recycling loop, a 100% ammonia makeup input would be required.

References

1. Gamidov, R. G., Teymurova, E. A., Jafarov, Y. I., Ibragimov, A. A., Ibragimova, F. S., Mammadov, A. N., & Abdullaev, N. I. (2023). DEVELOPMENT OF AMMONIA-ALKALINE METHOD OF COMPLEX PROCESSING OF ALUNITE ORE. Azerbaijan Chemical Journal, (1), 122-128. DOI: 10.32737/0005-2531-2023-1-122-128

2. Liu, L., Wang, Y., & Cai, C. (2021). Study on decomposition kinetics of activated alunite concentrate from copper tailings and leaching behavior of valuable elements. Cleaner Materials, 1, 100008. doi.org/10.1016/j.clema.2021.100008

3. Geidarov, A. A., Alyshanly, G. I., Gulieva, A. A., Tagieva, L. T., & Alieva, V. A. (2020). Kinetic laws of the dissolution of alunite from alunite ores with an alkali solution. Russian Metallurgy (Metally), 2020(9), 933-937. doi.org/10.1134/S0036029520090050

4. Kuang, G.,Hu, S.,Cai, Y.-Y.,Li, H. (2016). Utilizing alunite comprehensively from Zijin copper tailings by directly pressure acid leaching. Chinese Journal of Nonferrous Metals, 2412-2419

5. Mohammadi, M., & Salarirad, M. M. (2013). Kinetics of direct leaching of natural alunite in KOH. Industrial & Engineering Chemistry Research, 52(40), 14359-14365. doi.org/10.1021/ie401549w

6. Zhao, W., Yao, X., Zhong, S., Zhu, Y., Yang, X., Yi, L., ... & Qi, T. (2015). Extraction of Al and K salts from associated alunite tailings by an acid calcination-water leaching method. Journal of Cleaner Production, 107, 786-792. doi.org/10.1016/j.jclepro.2015.05.103

7. Luo, M., Liu, C., Jiang, Y., Xue, J., Li, P., & Yu, J. (2017). Green recovery of potassium and aluminum elements from alunite tailings using gradient leaching process. Journal of Cleaner Production, 168, 1080-1090. doi.org/10.1016/j.jclepro.2017.09.090

The Enrichment Plan of Simidco Iron Ore Concentrate Plant

Mehdi Parvan[1]* Alireza Yazdanpanah[1] , Vahid ghalandari[1], Amer javanshiri[1]

[1]Sanabad Comprehensive Development Industrial and Mining Company

*Corresponding author: mahdi.parvan@gmail.com (Mahdi Parvan),

Abstract:

The industrial and mining sectors are pivotal in shaping a country's economic future, providing capital for modernization and reducing reliance on oil-based economies. However, the declining grade of iron ore and increasing mineralogical complexity have led to higher processing and beneficiation costs. This has amplified the need to maximize the value-added to products. In the Sanabad Comprehensive Development Concentrate Plant, which plays a key role in supplying raw materials for upstream steel industries, efforts were made to enhance concentrate grade and quality due to declining product grades and Net Present Value (NPV). This study focuses on maximizing the value-added of the plant's production. Given the current processing flowsheet, the mined ore undergoes multiple crushing and classification stages before entering the magnetic separation stages, where 2700 Gauss drum separators enhance the concentrate grade through four steps. Challenges in achieving target concentrate grades led to the formation of a specialized working group to address process inefficiencies. After extensive lab testing and discussions, it was determined that adjusting the plant's flowsheet and layout was the only viable solution. Three proposed circuits are being pilot-tested at the Iran Mineral Processing Research Center to determine the most effective configuration for improving plant efficiency.

Keywords: Iron Ore Processing, Beneficiation Costs, Concentrate Grade, Magnetic Separation, Efficiency Improvement

1. Introduction

The industrial and mining sectors are among the most significant and impactful industries in a country, playing a vital role in shaping its economic path and destiny. These industries provide the necessary capital for modernization and development, significantly contributing to increased production and a stable economy independent of oil. The gradual decline in the grade of iron ore resources and the increasing complexity of their mineralogy have led to rising costs in crushing and beneficiation processes at processing plants. Moreover, with higher sales, labor, and raw material costs—resulting in increased final product prices—maximizing the value-added of the produced product has become imperative.

In recent years, extensive research has been conducted in most processing plants and steel industries to optimize processes, enhance the grade and quality of final products, and consequently increase value-added. In the Senabad Comprehensive Development Concentrate Plant, which plays a crucial role in supplying raw materials for pelletizing plants, smelting, and upstream steel industries, efforts were made to improve the grade and quality of products due to declining grades and Net Present Value (NPV). This study aimed to maximize the value-added of the concentrate produced by the Senabad Comprehensive Development Company.

In this plant, based on the design and layout of the concentrate production line, extracted ore undergoes several stages of crushing (gyratory, cone, and high-pressure roller mill) and classification by dry and wet screens and hydrocyclones before entering the beneficiation stages. In iron ore processing and beneficiation sites, magnetic separators are among the most critical and essential equipment. These drums play a vital role in recovering and upgrading the produced concentrate. In this plant, particles are processed through 2700 Gauss magnetic drums over four beneficiation stages. The waste materials are separated from the concentrate, which then enters the sulfur removal circuit and, finally, ceramic disc filters for dewatering.

For years, the managers and staff of this large complex have aimed to enhance the grade, recovery, and efficiency of the produced product. This research focuses on examining, feasibility analysis, concluding, and ultimately deciding on three proposed circuits and providing appropriate solutions to improve circuit efficiency after pilot testing at the Iran Mineral Processing Research Center.

Specialized workgroups comprising R&D, production, process, quality control, and laboratory units were formed to address the issue of declining concentrate grades and offer solutions to resolve it. After extensive discussions during meetings, changes to all process parameters, and numerous laboratory-scale tests yielding unsatisfactory results, it was decided and approved that the only operational solution to improve the final concentrate grade of the Senabad Comprehensive Development Company would be changes to the plant's flowsheet and layout. Three different circuits were proposed by the workgroup for pilot testing, with the initial feasibility studies to be conducted by the research, technology, and optimization units. Subsequently, semi-industrial tests were carried out at the Iran Mineral Processing Research Center in Karaj.
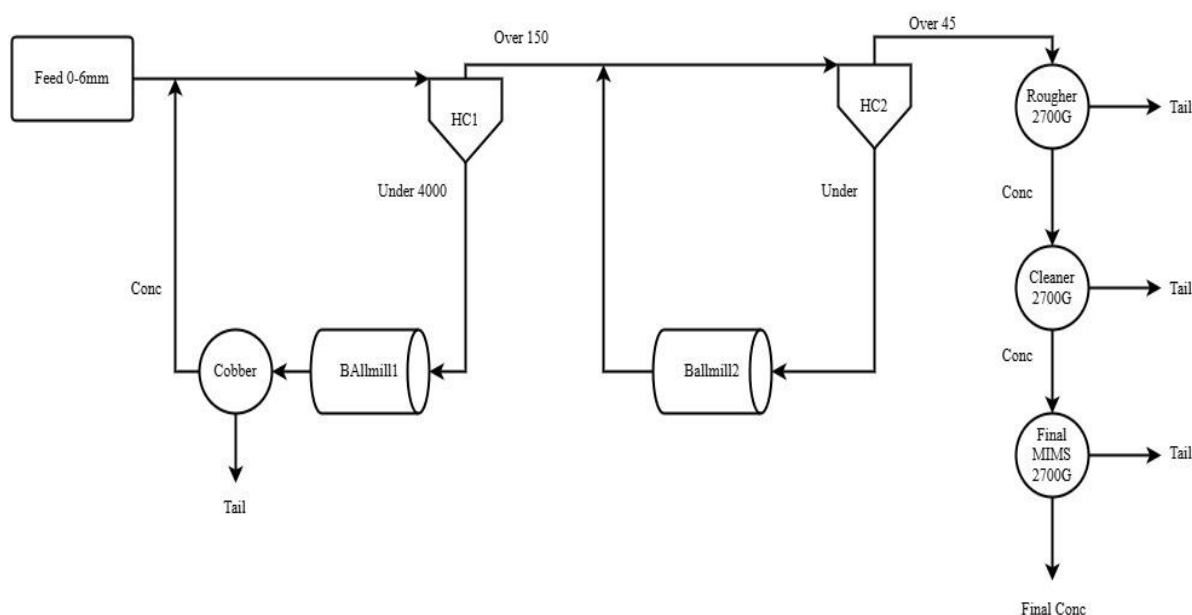

Fig. 1. Beneficiation Circuit of Simidco's Concentrate Plant.

2. Material and methods

2.1. Material

The ore with approved composition and specifications was collected behind the crushing platform. After being crushed by gyratory and cone crushers and reaching the desired size, it was transferred to the Senabad Comprehensive Development site and stockpiled near hopper 114 in the Blending area.

This 1000-ton stockpile was sent to the concentrate production line on 19/05/1403 with coordination from the specialized working group members.

Simultaneously with feeding this material, arrangements were made with the laboratory and quality control units to ensure regular sampling from all streams of the concentrate production line. The grade and particle size distribution results of all samples taken on that day were reported by the laboratory unit and are accessible in the laboratory's daily performance report table.

During the injection of ore into the concentrate production line, samples of 2 tons were taken from the designated stockpile every 20 minutes and collected separately. After 12 hours of continuous sampling of the feed and its simultaneous injection into the concentrate production line, a total of 80 tons of ore samples were collected and stockpiled. The stockpile had a coarse particle size distribution of **D80=35**, which needed to be reduced to a finer size (0-6 mm) for semi-industrial testing. Consequently, after necessary coordination with the transport and raw material supply units, the required ore was sent to the crushing site (Berkarar site) at Simidco Company and reduced to the particle size range of 0-6 mm.

Again, while crushing the 80 tons of ore, the required sampling for a 25-ton sample was conducted, ensuring the sample was completely homogeneous, comprehensive, and representative. This crushed sample was then loaded and sent to the Iran Mineral Processing Research Center for further processing and testing.

2.2. methods

In semi-industrial tests conducted at the Iran Mineral Processing Research Center, initial steps included assessing the layout, equipment installation, and proper configuration of the circuit based on the proposed flowsheets from the Senabad Comprehensive Development Company. Upon starting the circuit, it was observed that the particle size of the output from the primary ball mill was finer than desired. Subsequent adjustments to feed rate, solids percentage, and mill rotation speed did not yield satisfactory results. It was ultimately decided to replace the ball size, discharging the previous balls and charging 40 and 60-micron balls instead. After retesting, the particle size distribution results were acceptable.

Despite changes made and the placement of a 4-inch cyclone at the start of the circuit, the cyclone underflow exceeded the desired amount. Therefore, a curved screen was used at the mill's output instead of a hydrocyclone. With these changes, the Loop 1 output particle size of 150 microns was achieved. During the test, the critical parameters were continuously monitored and adjusted to optimal levels.

Once process stability was confirmed in each test, sampling from the entire circuit began after 30 minutes. Samples were taken manually from specific points in the circuit, including feed entering the circuit, feed and product of the ball mills, and feed, concentrate, and tailings of the magnetic drums. Sampling continued for 5 hours, with intervals of 15 minutes, in accordance with standard sampling procedures. Images of the sampling points from various streams were captured.

The collected samples were sent to the research center's laboratory to determine grade and particle size distribution. Additionally, a portion of the samples was sent to Simidco's laboratory for validation, and results were compared between the two laboratories.

During the sampling process, operational parameters such as circuit feed tonnage, recirculating load tonnage, ball mill rotation speed, drum speed, and the control of cyclone overflow and underflow sizes were monitored. To study the effect of particle size distribution on improving concentrate grade, all three proposed circuits by Simidco were tested at 45 and 60-micron size distributions. Operational parameters were reviewed during the process.

Control and monitoring of material density and solids percentage were key factors affecting recovery and grade. To evaluate this, the solids percentage in magnetic drums, ball mills, and hydrocyclones was set to an optimal value of 30%.
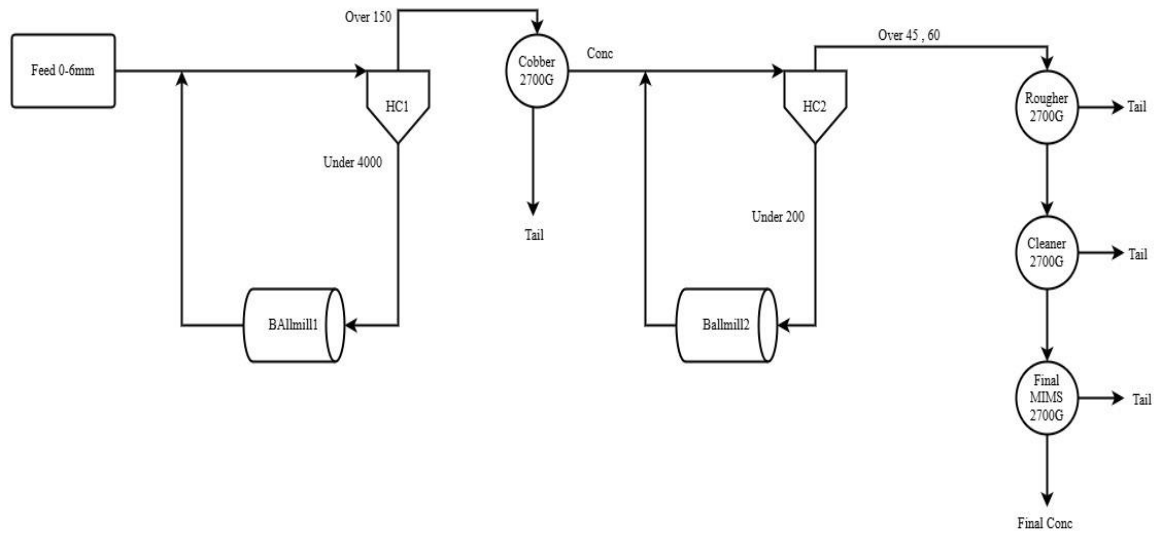
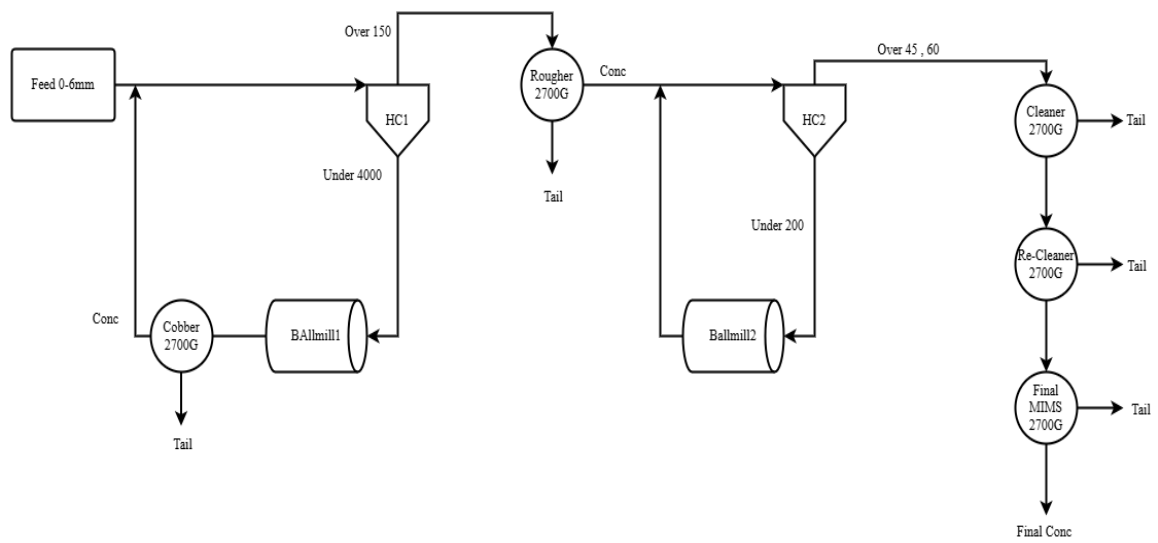Fig. 2. Circuit No. 1 involves moving the cobber to a position after Hydrocyclone 1

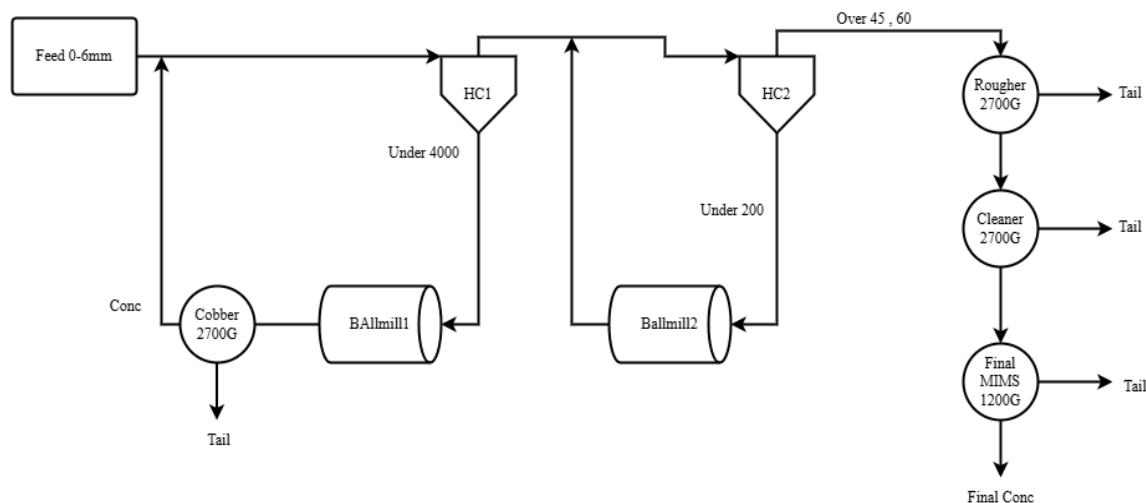Fig. 3. Circuit 2 involves adding a separator after Hydrocyclone 1.

Figure. 4. Circuit 3 includes replacing the final separators with 1200 Gauss magnetic separators.

3.   Discussion and Results

The initial sample, with a particle size distribution of D80 = 4436 microns, was considered as the feed for the proposed pilot circuits. The feed capacity was set to 370 kg/h for Circuit 1 and 336 kg/h for Circuits 2 and 3, with an average iron grade of 43.8%.

3.1. Comparison of the Grade Impact of Circuits on Process Efficiency

According to results reported by the laboratory at the Iran Mineral Processing Research Center, a comparison of the grades of the three proposed circuits at a particle size distribution of 45 microns shows an increase in the grade of Circuit 2 in the copper, rougher, cleaner, and re-cleaner concentrates. Similarly, at a coarser particle size distribution (60 microns), Circuit 2 demonstrates superior grades across all mentioned magnetic separators compared to the other two circuits. This improvement is attributed to the fact that Circuit 2 includes an additional magnetic separator compared to the other circuits, enabling five stages of beneficiation for the particles, whereas the other circuits only achieve four stages. Another contributing factor is the removal of coarse-grained tailings at the beginning of the circuit, allowing higher-grade particles to enter Loop 2. In Circuit 2, grade improvement occurs in the initial stages, leading to an overall higher grade by the end of the circuit. Undoubtedly, increasing the grade of the feed at the start of the circuit directly results in a higher grade at the end of the stream.

Table 1. Comparison of Proposed Circuits' Grade with Factory Product

Circuit	Concentrate Plant Grade (%)	Pilot Test Grade (%)	Grade Improvement (%)
Circuit 1	62.66	66.90	+0.28
Circuit 2	62.66	68.00	+1.40
Circuit 3	62.66	67.67	+1.05

What stands out in this test is the grade improvement of Circuit 3 at coarser particle sizes. The reason for this enhancement is that, in magnetic separators operating at lower intensities (1200 Gauss), optimal coarser particles tend to achieve higher grades. These separators are more effective in separating waste particles from the concentrate. The slight grade difference between Circuit 2 and Circuit 3 can be attributed to the higher-grade feed in Circuit 2.
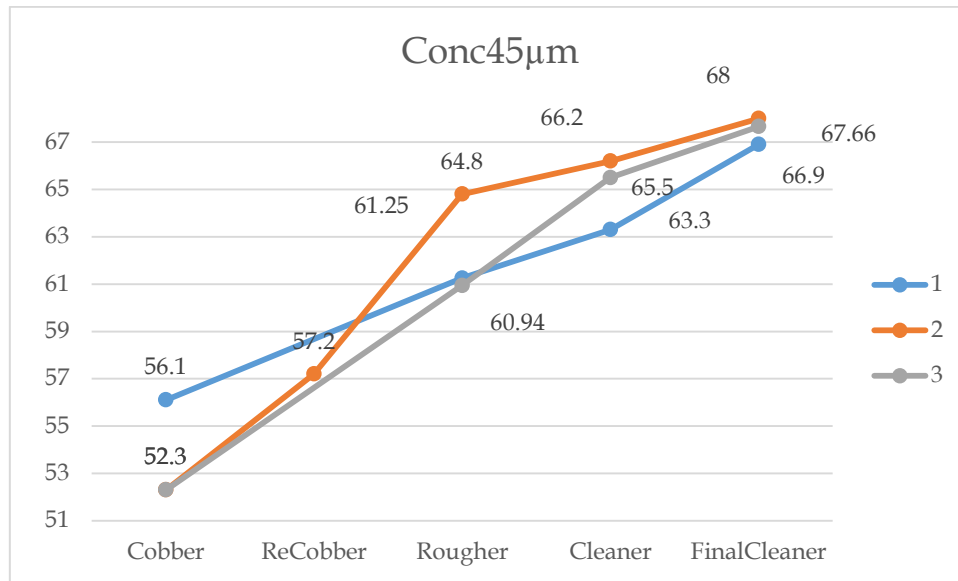
Figure. 5. Comparison of the Grade Impact of Circuits on Process Efficiency

3.2. Comparison of Tailings Impact on Circuit Efficiency

A comparison of the proposed circuits' tailings shows that Circuit 3 consistently produces the lowest iron grade in tailings, especially in final tailings, for both particle size distributions of 60 and 45 microns. This reduction in tailings grade reflects an improvement in recovery and production tonnage for this circuit. The primary reason for this improvement is the inclusion of a 1200 Gauss magnetic drum in the re-cleaner section, which maximizes particle capture. The grade analysis results indicate that Circuit 2, at the 45-micron particle size, has the highest iron grade in tailings, which increases progressively towards the end of the circuit. This suggests lower recovery and efficiency in Circuit 2. Since cleaner tailings are discharged into the thickener and ultimately exit the concentrate plant, this translates to iron loss. Furthermore, the data highlights that the iron grade in tailings across all circuits is higher at finer particle sizes (45 microns). This increase is attributed to the effect of finer particles, which elevates tailings grade due to the greater generation of slimes.
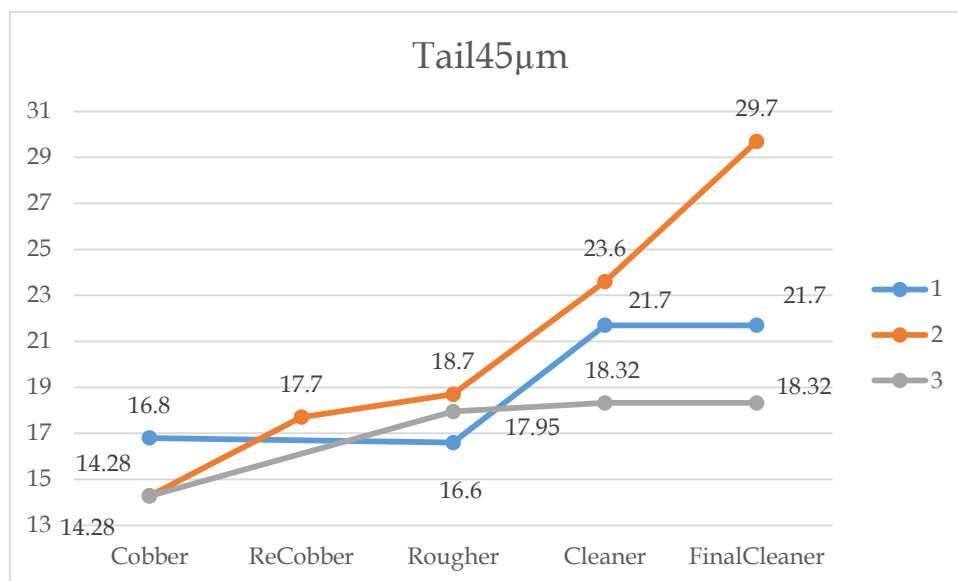

Figure. 6. Comparison of Tailings Impact on Circuit Efficiency

3.3. Study on the Effect of Iron Recovery in Circuits

Examining the effect of iron recovery is one of the critical factors impacting system efficiency. This section of the research focuses on analyzing the influence of iron recovery.

Iron recovery can be calculated using the following formula:

$R = 100 \cdot Cc/Ff$

Where:

R: Iron recovery

C: Weight of extracted concentrate (kg)

c: Grade of extracted concentrate (%)

F: Weight of input feed (kg)

f: Grade of input feed (%)

The experimental results and charts indicate that Circuit 3 achieves the highest iron recovery. The primary reason for this success is the increased production tonnage enabled by the 1200 Gauss magnetic separator in this circuit. Improved iron recovery translates into enhanced product value, making this factor highly significant in the overall process. Two critical factors—grade and tonnage—play a decisive role in iron recovery. Both the feed grade and tonnage, along with the concentrate grade and tonnage, have significant impacts.
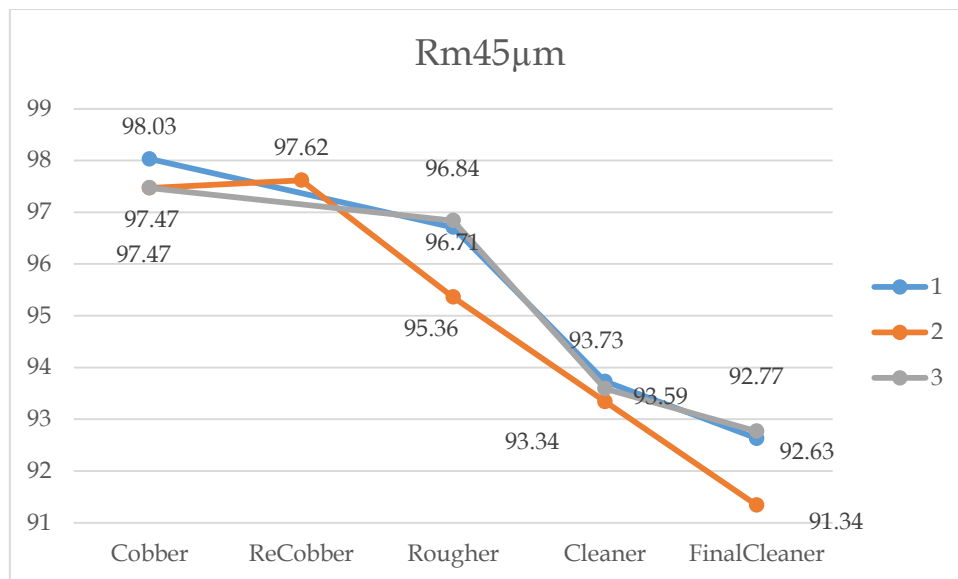

Figure. 7. Study on the Effect of Iron Recovery in Circuits

Analysis of the charts indicates that Circuit 3 consistently achieves the highest iron recovery across both tested particle size distributions. This higher recovery correlates with enhanced value-added in Circuit 3. At a finer particle size of 45 microns, Circuit 1 ranks second in iron recovery. However, at coarser sizes (60 microns), Circuits 2 and 1 switch places in terms of recovery efficiency.

According to findings from the Iran Mineral Processing Research Center, iron recovery is higher at coarser particle sizes. While coarser size distributions may show a decrease in grade, increased tonnage compensates by boosting iron recovery. Conversely, reducing particle size diminishes this effect.

3.4. Comparison of Mass Recovery

Mass recovery is another significant factor influencing the efficiency of processing plant circuits. The annual production tonnage of an industrial facility is often a key concern for its management. Mass recovery can be calculated using the formula:

R=100·C/F

Where:

- R: Mass recovery

- C: Tonnage of produced concentrate

- F: Tonnage of input feed

In this analysis:

- Circuit 1 achieved the highest mass recovery at finer particle sizes, with a value of 60.65. This indicates that Circuit 1 can potentially yield the highest annual production at a particle size of 45 microns.

- As particle size increases, Circuit 3 exhibits greater mass recovery. This highlights that the 1200 Gauss magnetic separator in Circuit 3 effectively enhances mass recovery under these conditions.
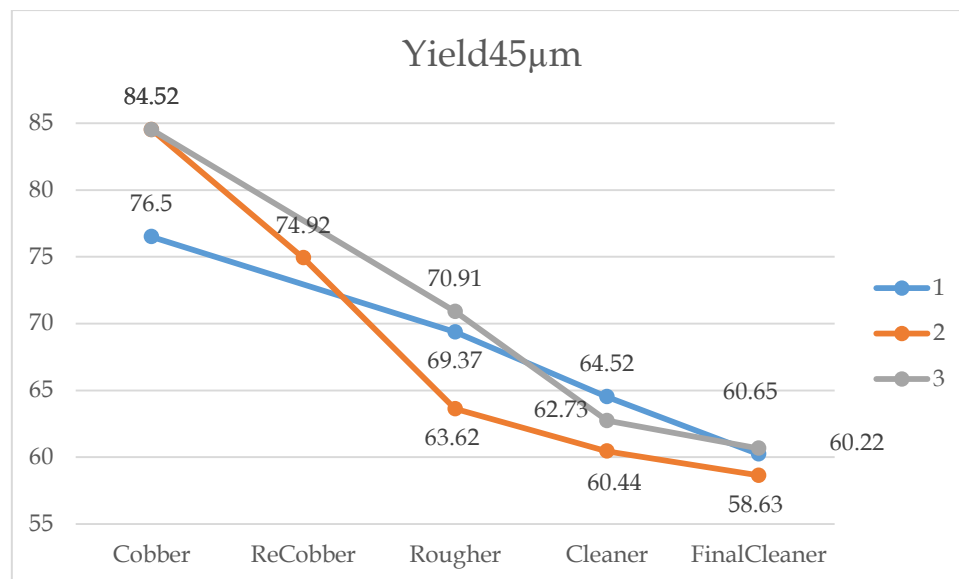

Figure. 8. Study on the Effect of Mass Recovery in Circuits

c

3.5. Comparison of Crushing Levels Across Circuits

1. Circuit 1:

    o Due to the line layout, a closed loop is formed between the ball mill and the primary cyclone, excluding the copper separator, and cyclone overflow enters the copper separator. This configuration requires an increase in crushing capacity by 192 tons per hour compared to the current line, resulting in higher production costs and increased product prices.

o Additionally, finer particles are produced in Loop 2, leading to higher slimes and "tailing following," ultimately reducing the grade of the produced concentrate.

2. Circuit 2:

o In Circuit 2, adding a 2700 Gauss magnetic separator at the beginning of Loop 2 can remove 64 tons per hour of coarse-grained tailings and send them directly to the thickener. This makes Loop 2 operate at lower, lighter tonnage.

o If higher production capacity is needed, input tonnage to the line can be increased. However, the main issue is that this increased tonnage overloads Loop 1, which requires operational solutions from production and process teams to address.

3. Circuit 3:

o Circuit 3 does not introduce additional crushing, and its crushing costs are similar to the current conditions of Simidco's concentrate plant. However, removing fine tailings may slightly increase particle size distribution.

3.6. Comparison of Circuit Production Levels

Based on mass balance analysis across all circuit flows, assuming equal feed tonnage (612 tons per hour) and identical working days (320 days annually) for all circuits:

Table 2. Comparison of Circuit Production Levels

Circuit	Daily Production (tons)	Annual Production (tons)
Circuit 1	7700	2,464,000
Circuit 2	7580	2,425,600
Circuit 3	7739	2,476,480

Key Insights:

- Circuit 3 achieves the highest production, making it the most efficient in terms of annual tonnage.

- Circuits 1 and 2 follow, with Circuit 1 slightly outperforming Circuit 2 in daily and annual production.

3.7. profit and loss based on tonnage and grade

Table 3. Comparison of Costs and Profits in Proposed Circuits

Title	Baseline	Circuit 1	Circuit 2	Circuit 3
Daily Production (tons)	7,800	7,700	7,580	7,329
Added Value Increase Compared to Baseline (Rials)	35,000,000	49,000,000	70,415,000	1,890,000
Active Production Grade (%)	66.62	66.9	68	67.7
Grade Difference from Production	N/A	-0.28	+1.38	+1.08

Line (%)				
Annual Operating Days	320	320	320	320
Annual Production (tons)	2,496,000	2,464,000	2,425,600	2,345,280
Annual Added Value (Rials)	87,500,000,000	87,447,000,000	90,132,800,000	91,407,347,000
Added Value Difference (Rials)	N/A	-53,000,000	+2,632,800,000	+3,907,347,000
Daily Production Difference (tons)	N/A	-10	-220	-61

Observations:

Circuit 3 has the highest annual added value, although it has the lowest daily production.

Circuit 2 offers the most significant grade increase (+1.38%) compared to the production line.

Circuit 1 strikes a balance but shows the least improvement in metrics.

Comparison of Grade and Mass Recovery in the Proposed Circuits

Circuit	Traditional Theory	Daily Production Theory	Transitional Recovery	Weight Recovery	Chemical Recovery
plant	328	7800	85.15	58.39	60.13
Circuit 1	321	7700	80.94	52.51	49.35
Circuit 2	316	7580	81.00	51.70	49.30
Circuit 3	322	7729	82.33	52.78	50.07

Plan 1: Due to a reduction in grade and an increase in production, it will experience a **21.7% decline** in daily production value.

Plan 2: Will result in a **7.5% increase** in the price of the produced concentrate.

Plan 3: Will see an **8.3% increase** in the price of the produced concentrate.

Acknowledgments

This study aimed to better understand the beneficiation process of the concentrate production plant and provide operational recommendations to improve its efficiency. The key findings are as follows:

Proposal for Temporary Implementation: It is suggested to temporarily replace one of the final magnetic drums with a 1200 Gauss separator instead of the 2700 Gauss separator. The results of this magnetic separator should be analyzed and monitored continuously over a one-month period. If the desired and expected outcomes are achieved, other magnetic separators can be replaced at the appropriate time, and Circuit 3 can be implemented.

Alternative Plan: If the 1200 Gauss drum is installed and its results do not meet the approval and satisfaction of the specialized working group within the designated timeframe, Circuit 2 should be designed and implemented.

References

Journal Articles Giblett, A., & Morrell, S. (2016). The influence of particle size and liberation on the recovery of valuable minerals. *Mineral Processing and Extractive Metallurgy*, 125(3), 123-135. doi: 10.1016/j.minpro.2016.03.001 Habib, M., Martinez, J., & Smith, R. (2020). Advances in flotation techniques for mineral processing. *International Journal of Mining and Mineral Engineering*, 12(4), 245-260. doi: 10.1007/s12345-020-00456

Smith, J., Brown, A., & Taylor, R. (2020). Magnetic drum separators: Applications and advancements. *Mineral Processing Journal*, *45*(3), 123-135. doi: 10.1234/mpj.2020.56789

Conference Papers Chuanyao, S., & Kuangdi, X. (2023). Sustainability in mineral processing: Challenges and opportunities. Paper presented at the *International Conference on Mineral Processing*, Beijing, China. Fujita, T., Higashitani, K., & Matsusaka, S. (2019). Magnetic separation advancements in mineral processing. Paper presented at the *World Mining Congress*, Tokyo, Japan.

Jones, P., & Lee, K. (2019). Innovations in magnetic drum separator design. Paper presented at the *International Conference on Mineral Engineering*, Sydney, Australia.

Books Simate, G., & Ndlovu, S. (2021). *Acid Mine Drainage: Formation, Dissemination, and Control*. (Vol. 3): Taylor & Francis. Makino, H., & Matsusaka, S. (2019). *Powder Technology Handbook*. (Vol. 2): Springer.

Williams, D., & Harris, M. (2018). Magnetic Separation Techniques. (*Vol. 2*): Springer.

Book Sections Gwenzi, W. (2016). Environmental impacts of mineral processing. *Sustainability in the Mineral and Energy Sectors* (pp. 45-67): Elsevier. Higashitani, K., & Fujita, T. (2019). Electromagnetic forces in mineral separation. *Powder Technology Handbook* (pp. 123-145): Springer.

Clark, T., & Evans, S. (2021). Magnetic drum separators in mineral processing. *Advances in Separation Technology* (pp. 45-67): Elsevier.

.

www.imprs.ir

Secretariat Address: Iran, Mineral Processing Research Center
Phone: (+98)2632106211   Email: imprs2025@imprc.ir
Exhibition Secretariat: Tel(+98) 21885448845   Mobile:(+98) 9394221003